DYNAMICS OF PLANETS, STARS, AND BLACK HOLE BINARIES: TIDES, SPIN RESONANCES, AND GRAVITATIONAL WAVES

A Dissertation

Presented to the Faculty of the Graduate School

of Cornell University

in Partial Fulfillment of the Requirements for the Degree of

Doctor of Philosophy

by

Yubo Su

August 2022

DYNAMICS OF PLANETS, STARS, AND BLACK HOLE BINARIES: TIDES, SPIN RESONANCES, AND GRAVITATIONAL WAVES

Yubo Su, Ph.D.

Cornell University 2022

Simply by nature of their scale and complexity, astrophysical systems are almost always studied by simplifications and effective, parameterized models. Yet even after this considerable simplification, the resulting systems can still host unusual and exciting phenomena. In this dissertation, I study and characterize analytically and numerically many of these behaviors in few-body systems consisting of planets, stars, and black holes (BHs). My work falls into three broad categories: (i) I carry out a comprehensive theoretical analysis of the spin dynamics of planets by studying the "Colombo's Top" system (a rotating planet whose spin axis precesses around its orbital axis, which itself varies in time). In the course of this analysis, I examine: the dynamics of planetary obliquities when surrounded by a dissipating protoplanetary disk, and the capture probabilities of planetary spins into high-obliquity, stable equilibria due to tidal dissipation in two and many-planet systems. I apply these results to assess the spin dynamics and evolution of planets in various, observationally-relevant architectures, such as super Earths with nearby or distant companions. My work is the first to describe comprehensively the complex resonance capture process responsible for the excitation of large obliquities in both integrable, two-planet systems and chaotic, three-planet systems. My results show that super Earths around solar-type stars have a significant chance of capture into various stable high obliquity states; this will have a large impact on their surface/atmosphere conditions. (ii) I use detailed hydrodynamical simulations to understand the nonlinear internal gravity wave breaking process that is responsi-

ble for tidal dissipation in white dwarf and early-type stellar binaries. I then use my results to understand the circularization of highly eccentric, massive stellar binaries and to calculate the observational effects of tidal heating in compact white dwarf binaries. (iii) I study the observational signatures of the tertiary-induced merger channel for merging BH binaries, in which a distant companion drives the BH binary into a high-eccentricity orbit via the von Zeipel-Lidov-Kozai mechanism, and the binary then merges due to gravitational wave emission. I study both the spin dynamics of the merging BHs when the tertiary is circular as well as the mass ratio distribution when the tertiary is eccentric, with observational comparisons to the BH mergers seen by the LIGO/VIRGO Collaboration.

BIOGRAPHICAL SKETCH

Yubo Su was born in Chengdu, China, but grew up in the USA in Atlanta, Georgia. At River Trail Middle School, he was one of three students in the state of Georgia to receive a perfect score of 25 on the American Mathematics Contest 8, and he continued to participate in local and national math competitions through middle and high school. While completing his secondary education at Northview High School, he ultimately decided to pursue a degree in physics after two years of AP Physics with Mr. Chris Kemp. Around this time, he also conducted research under the supervision of Professor Ken Brown at the Georgia Institute of Technology.

In 2012, he began his undergraduate studies at the California Institute of Technology (Caltech). Here, he completed a double major in physics and computer science while conducting research under the supervision of: (i) Professors William A. Goddard III (Caltech) and Jose L. Mendoza Cortes (Michigan State University) in approximate numerical methods for intermolecular forces, (ii) Drs. Paulett C. Liewer and Eric De Jong (Jet Propulsion Laboratory) in visualization of coronal mass ejections, and (iii) Professor Sunil R. Golwala (Caltech) in modeling systematic uncertainties in surveys using the kinetic Sunyaev-Zeldovich due to foreground subtraction, resulting in a senior undergraduate thesis.

In 2017, after a one-year period of employment at Blend Labs as a software engineer, he began to pursue a PhD in Astronomy under Professor Dong Lai, working first on hydrodynamical simulations then on careful studies of few-body dynamics. Upon the defense of this dissertation, he will begin work as a Lyman Spitzer, Jr. Fellow at Princeton University in September 2022.

Much as with his research interests, Yubo also has dabbled in a large array of hobbies. His spare time is currently largely occupied by running, cooking, practicing piano, and playing Starcraft, but an updated list can (hopefully!) be found on

his current website.

To my parents, who have supported me on every step of this journey. To my late grandfather, who was looking forward so much to seeing a PhD among his grandkids. And to my late and great friend Cassidy Yang, who was one of my partners in crime at Caltech and who left with so much to give the world still.

ACKNOWLEDGEMENTS

I must begin by thanking my adviser, Dong Lai. There is no way to put into words the impact Dong has had on the trajectory of my academic career, let alone in such a brief space. He has been tirelessly dedicated to my growth, providing consistent and pointed guidance. Whether I am working through a month's work in a week or a week's work in a month, he is always nudging me back onto the right track. He has a ceaseless eye for improvement, continually reminding me of all the things I still need to learn to become a successful researcher while still helping me bring my strengths to the questions at hand. He has corrected the unending typos in my equations that I can never seem to find; has consistently found ways to clarify and streamline my writing, whether individual words or entire sections; and has, against my every predisposition, found a way to teach me the value of "telling a story" when communicating my work. A large part of my success as a graduate student is thanks to Dong's advising, and I feel both deeply fortunate and grateful to have worked with him for the past five years.

Next, I thank the other members of the Cornell faculty and staff who have taught me much and given me many opportunities. First, I thank the members of my special committee for their very helpful input and feedback over the years: Jim Cordes, Nikole Lewis, and Ira Wasserman. I thank Phil Nicholson for listening to my research many, many times and for giving me opportunities both to grade for his class and to have many enjoyable conversations. I thank Henrik Spoon for the chance to help build out the IDEOS web portal, which was a unique and fun experience. I thank our department's staff for their infinite patience in the face of my many questions, which have made my travel and other issues so much less stressful: Monica Carpenter, Jessica Jones, Lynda Sovocool, Jill Tarbell, and Bez Thomas.

I thank the collaborators I was fortunate enough to collaborate and correspond

with. I am grateful to Daniel Lecoanet for his patience on my first project in graduate school, in which I rapidly found myself out of my depth and only began to understand the best approach to the problem with his extensive guidance. I am grateful to Bin Liu and Laetitia Rodet for their insightful and careful comments during our collaborations.

I thank my lovely parents, Xiaoli Fu and Ziqiang Su, for twenty-eight long (and at times, difficult) years of raising and supporting me. Thank you for always telling me what you think, even when I do not want to hear it, and supporting me even when I do not listen. Through the hardest and most confusing parts of my PhD journey, you have always lent me your open ears and your candid thoughts, and I hope you know that I would not have been able to make the decisions I did without your support and patience. I also thank my self-proclaimed "coolest cousin" Will Su and his lovely wife Cindy Guan for much helpful advice and for having me over many times over the past few years.

I thank my previous research mentors (listed in the Biographical Sketch). In particular, I thank Sunil Golwala for taking a chance on me when I knew little more than how to LaTeX quickly and for patiently working with me as I struggled to learn how to tackle a class of problems I had never known before. I thank Eric Black and Ken Libbrecht for the support and many long and helpful discussions over the years; I was so fortunate to have had the chance to be a TA for Ph3. I thank Steven Strogatz for incredible applied mathematics classes that taught me tools that I've been able to bring with me to astrophysical dynamics.

I thank Maria Paulene Abundo for the many long hours and late nights together and for all the support through our many triumphs and crises; we will get GM one day, I am sure of it. I thank my fellow group members over the years: J.J. Zanazzi, Kassandra Anderson, Bonan Pu, Michelle Vick, Jiaru Li, Chris O'Connor, and J.T. Laune, all of whom have provided advice, support, and unforgettable com-

pany at different points during my PhD. I thank the friends I've made at Cornell who have made my days and my nights out memorable ones, even if it may have felt like pulling teeth at times: Paul Corlies, Eiden and Maomao Leung, Jack Madden, Dante Iozzo, Eamonn O'Shea, Gabriel Bonilla, Abhinav Jindal, Cristóbal Armanza, Ishan Mishra, Bo Peng, Christopher Rooney, Akshay Suresh, Ngoc Truong, Catie Ball, and Stella Ocker. I thank Michael Lam for helping me prepare for the Philadelphia Marathon in 2019, one the most meaningful things outside that research that I have done in the past few years. I thank Jiseon Min for introducing me to many new ideas, hobbies, and gizmos, and to Arthur Min for being the best boy. I thank the many friends who have helped make research through a pandemic bearable through their companionship, both virtual or in-person: Andy Huang, Gordon KK Huang, Willy Xiao, Jesse Zhao, Cathy An, Jonathan Austin, Maryyann Landlord Crichton and Will Crichton, Sudarshan Muralidhar, Diana Wang and Justin Wang, Dhruva Bavadekar, Richard Kang, Jessica Lim and Chaplin Yi, Joseph Berleant, Dan Chui, Jacob Quinn Shenker, and Patrick Yu. I thank my mentors and colleagues at Blend Labs who have shaped how I approach and solve problems far beyond my former desk at 100 Montgomery: Eugene Marinelli, Eduardo Lopez, Chris Nguyen-Blaser, Nitya Subramanian, Devon Yang, Michael Millerick, Jeff Chen, Albert Lee, and Chao Xue. I thank the so many other friends who I have not been able to thank by name here, of which there are still many; they say that you see farther by standing on the shoulders of giants, and I've been fortunate to have had so many such friends over the years.

Finally, I thank Cornell University for funding the first two years of my thesis work, and the NASA Future Investigators in Earth and Space Science and Technology (FINESST) program for funding the following three.

TABLE OF CONTENTS

LIST OF TABLES

LIST OF FIGURES

CHAPTER 1

INTRODUCTION

The diversity and intractability of phenomena in astrophysics owe their origin to the breadth of scales over which astrophysical systems evolve. Despite these difficulties, the dynamical evolution of such systems is important to understand, as they shape the universe as we observe it today. These systems, consisting of bodies such as planets, stars, and black holes, evolve over characteristic time scales ranging from minutes to years due to effects such as tidal evolution and gravitational wave emission. In principle, these effects are sufficiently well understood that astrophysical dynamics can be solved via direct numerical simulation. In practice, however, numerical integration over times as long as the age of the observable universe and for the wide range of observed system parameters is far beyond the capability of modern computers. As a result, many effective models are developed to bridge the gap between the "microphysics" of these systems, their behavior over these short time scales, and their long-term evolution.

The focus of this dissertation concerns the dynamics of various effective models that are derived under the so-called "secular" approximation. In systems consisting of multiple bodies, their mutual gravitational interaction causes the constituent bodies to orbit one another over a wide range of orbital periods. The secular approximation concerns the dynamics when averaged over the system's orbital period(s), turning individual bodies into massive rings. The evolution of these rings occurs over substantially longer time scales than the orbital periods of the original bodies, and so long term study of the system becomes possible. In this dissertation, I apply both analytical and numerical techniques to study the secular dynamics of three classes of systems: (i) the evolution of a planet's spin in a planetary system with multiple planets, (ii) the formation of merging black

hole binaries (detectable by LIGO/VIRGO) from systems consisting of three black holes, and (iii) the evolution of stars in binaries due to their mutual tidal interaction. Below, I motivate and describe my results for each of these three classes of systems.

1.1 The Dynamics of Exoplanetary Spins

First, I introduce my work on the dynamics of an exoplanet's spin. The spin state of a planet is characterized by two attributes, its spin period and orientation. The spin period of a planet determines the length of a day on the planet, while its obliquity (the angle between a planet's spin axis and orbital axes) gives rise to its seasons. Both of these attributes are of general interest, as together they determine the atmospheric and surface conditions of the planet. They are also of dynamical interest as they reflect the evolutionary history of a planet. Within the solar system, the planets' obliquities take on a wide range of values, from nearly zero for Mercury and 3.1° for Jupiter, to 23° for Earth and 26.7° for Saturn, to 30° for Neptune and 98° for Uranus. The origin of these nonzero obliquities has motivated many hypotheses for the formation of each of these planets: for instance, multiple giant impacts are traditionally invoked to generate the large obliquities of the ice giants [Safronov and Zvjagina, 1969, Benz et al., 1989, Korycansky et al., 1990, Morbidelli et al., 2012]. In the case of the gas giants, obliquity excitation may be achieved via certain spin-orbit resonances, where the spin and orbital precession frequencies of the planet become commensurate as the system evolves [Ward and Hamilton, 2004, Hamilton and Ward, 2004, Ward and Canup, 2006, Vokrouhlickỳ and Nesvornỳ, 2015, Saillenfest et al., 2020, 2021]. These resonances were first studied in the seminal work of Colombo [1966] and is sometimes referred to as "Colombo's Top", while the equilibria of this system are often known as "Cassini

States" (CSs). Subsequent works have uncovered the rich dynamics of this system [Peale, 1969, 1974, Ward, 1975, Henrard and Murigande, 1987].

Shifting focus beyond the solar system, there are about 5000 confirmed exoplanets as of May 2022[1]. Which among these planets may be habitable has recently become a question of great interest. A key factor in assessing a planet's habitability is its obliquity, and so it is important to understand the dynamical processes that affect the obliquity. Observationally, these obliquities are challenging to measure, and to date only loose constraints have been obtained for the obliquities of faraway planetary-mass companions [Bryan et al., 2020, 2021]. Nevertheless, there are prospects for better constraints on exoplanetary obliquities in the coming years [Snellen et al., 2014, Bryan et al., 2018, Seager and Hui, 2002]. Furthermore, there is ongoing work towards inferring exoplanetary obliquities via thermal phase curve modeling [Adams et al., 2019, Ohno and Zhang, 2019] and via indirect dynamical evidence [Millholland and Laughlin, 2018, 2019, Millholland and Spalding, 2020]. From a theory perspective, substantial obliquities may arise even during the earlest phase of planet formation if protoplanetary disks are turbulent and twisted [Tremaine, 1991, Jennings and Chiang, 2021]. They can also arise due to giant impacts or planet collisions as a result of dynamical instabilities of planetary orbits [Safronov and Zvjagina, 1969, Benz et al., 1989, Korycansky et al., 1990, Dones and Tremaine, 1993, Morbidelli et al., 2012, Li and Lai, 2020, Li et al., 2021]. However, many processes can still change these obliquities before they reach their present-day values.

In this dissertation, I consider three mechanisms by which this primordial obliquity can be related to present-day obliquities. In Chapter 2, I consider the obliquity evolution of an oblate planet due to gravitational interactions both with

[1] https://exoplanetarchive.ipac.caltech.edu/

its host star and with an exterior, dissipating (mass-losing) protoplanetary disk. Obliquity excitation occurs as the system passes through a resonance between the planet's secular spin and orbital precession frequencies as the disk dissipates. This scenario was recently studied by Millholland and Batygin [2019], who focused on the special case of small initial obliquities. However, the primordial obliquity is not necessarily small, as argued above; the objective of Chapter 2 is to determine the final obliquity of the planet as a function of an arbitrarily oriented initial spin. When the disk dissipation is sufficiently gradual (adiabatic), I show that the principle of conservation of phase space area combined with the theory of probabilistic separatrix encounter [Henrard, 1982] is able to completely predict the final obliquities and their associated probabilities for arbitrary initial conditions. On the other hand, when the disk dissipates rapidly, I show that the obliquity is instead excited impulsively. I provide analytical expressions for the obliquity excitation in both of these regimes as well as for the boundary of the two regimes.

In Chapter 3, I consider a different mechanism for obliquity excitation, where an inner planet with a single outer companion planet experiences tidal dissipation in addition to gravitational torques from its host star and companion. The effect of tidal dissipation both acts to drive the planet's obliquity towards zero (spin-orbit alignment) and to drive the planet's spin rate towards synchronization (i.e. drive the spin frequency towards the planet's orbital frequency). In the absence of spin-orbit resonances, planets experiencing tidal dissipation are thus expected to evolve towards low obliquities and become tidally locked. However, in the presence of additional planets, the planet may remain in a high-obliquity, asynchronously-rotating spin state if it is evolves into the so-called "Cassini State 2" (CS2) that is stable to tidal dissipation [Fabrycky et al., 2007, Levrard et al., 2007, Peale, 2008]. For a general initial spin orientation, the planet evolves into one of either CS2 or the low-obliquity CS1 via a probabilistic process. I show that

the probabilities of reaching each of the two CSs outcomes can be analytically calculated via a generalization of Henrard's seminal work of resonance capture [Henrard, 1982]. I derive a simple closed-form expression for the case where the initial spin orientation is isotropically distributed. I apply my results to show that the common super Earth-cold Jupiter systems (Zhu and Wu, 2018, Bryan et al., 2019; but see Rosenthal et al., 2021) may often host an oblique super Earth. I also show that the proposed formation scenarios for WASP-12b and ultra-short-period planets via obliquity-enhanced tidal dissipation [Millholland and Laughlin, 2018, Millholland and Spalding, 2020] are disfavored due to the low probability of being captured into CS2.

In Chapter 4, I generalize the discussion in Chapter 3 to include an additional planet, considering systems of either three super Earths or two super Earths and one cold Jupiter. In systems consisting of three or more planets, it is well-known that the planetary obliquities can evolve chaotically in the absence of dissipation [e.g. that of Mars Touma and Wisdom, 1993, Laskar and Robutel, 1993]. However, the obliquity dynamics in the presence of tidal dissipation are not well-understood. Via numerical integration, I show that the occurence rate of oblique planets is generally enhanced by the presence of additional planets. I find that this is due to a novel class of resonances that are not CSs, and that I term "mixed-mode resonances." I derive an analytic relation for the obliquities of these resonances.

1.2 Tidal Evolution in Stellar Binaries

Second, I introduce my work on the tidal evolution of stellar binaries, including those consisting of two white dwarfs (WDs). About half of stars detected today have detectable binary companions [e.g. Gao et al., 2014, Yuan et al., 2015]. In a

stellar binary, the changing tidal gravitational field between the two stars generates fluid motion within both component stars. As this fluid motion experiences dissipation due to radiative and turbulent damping, energy is transferred between the binary orbit and the individual stars. The first theoretical models for tidal dissipation studied the equilibrium tide [Alexander, 1973, Hut, 1981]. Here, the stars develop a hydrostatic bulge due to their mutual gravitational force, and the motion of this bulge results in dissipation.

While simple and sufficient for weak tidal interactions, this model becomes inaccurate for sufficiently close binaries [see Ogilvie, 2014 for a review]. In particular, internal gravity waves (IGWs), oscillations in the stellar fluid restored by buoyancy, play an important role in several types of binary systems. In solar-type stars with radiative cores and convective envelopes, IGWs are excited by tidal forcing at the radiative-convective boundary and propagate inward; as the wave amplitude grows due to geometric focusing, nonlinear effects can lead to efficient damping of the wave [Goodman and Dickson, 1998, Barker and Ogilvie, 2010, Essick and Weinberg, 2015]. In early-type main-sequence stars, with convective cores and radiative envelopes, IGWs are similarly excited at the convective-radiative interface but travel toward the stellar surface; nonlinearity develops as the wave amplitude grows, leading to efficient dissipation [Zahn, 1975, 1977]. WDs do not have convective regions, and IGWs are instead generated at changes in the WD's composition. For these outward-traveling IGWs, one important nonlinear effect arises when the fluid displacement becomes comparable to the wavelength of the wave. When this threshold is reached, the waves break, like ocean waves on the shore, and deposit their energy and angular momentum. This wave breaking process is complex and turbulent, requiring numerical simulations to be well characterized. However, despite its ubiquity and importance, wave breaking has typically only been included in a parameterized fashion [e.g. Fuller and Lai,

2012a, Burkart et al., 2013, Vick et al., 2017].

In Chapter 5, I use well-resolved numerical simulations to study the detailed wave breaking process. While I primarily consider the case of binary WDs [following the work of Fuller and Lai, 2011, 2012a, 2013], the qualitative behavior is likely to be similar for early-type stars. Specifically, I develop quantitative prescriptions for both the location and the spatial extent of the energy deposited by the breaking IGWs. In my simulations, I generate IGWs from the bottom of a 2D isothermal atmosphere. As these IGW propagate upwards, they grow in amplitude and eventually break. I find that this wave breaking naturally generates a sharp critical layer (CL), a thin region of fluid separating the lower stationary region (with no mean flow) and the upper "synchronized" region (with the mean flow velocity equal to the horizontal IGW phase speed). Waves incident on the CL are absorbed efficiently, depositing their energy and momentum flux within the CL. I show that the width of this CL is mediated by the onset of the Kelvin-Helmholtz instability (carried by the IGW). Furthermore, the CL propagates downwards to accommodate the absorbed momentum flux, and the fluid synchronizes from top-to-bottom, as first hypothesized by Goldreich and Nicholson [1989]. However, the IGW absorption at the CL is not absolute, and I compute reflection and transmission coefficients for the IGW at the CL from my simulations.

In Chapter 6, I then present analytical expressions for the tidal evolution of a massive star in a compact, eccentric binary. Due to the compactness of the binary, the IGWs excited from the convective core of the star are expected to propagate outwards through the radiative envelope and break near the stellar surface. The tidal torque in circular binaries has recently been revised into a simpler and more accurate form [Kushnir et al., 2017]. However, the inclusion of eccentricity significantly complicates the evaluation of the tidal torque, generally requiring a sum

over many Fourier harmonics [Vick et al., 2017]. I show that these two results can be combined to yield an accurate closed-form approximation to the eccentric tidal torque. I apply my results to the system PSR J0045-7319, which consists of a pulsar and massive main-sequence star and exhibits detectable orbital decay [Kaspi et al., 1994, Bell et al., 1995]. I conclude that the star must be rapidly and differentially rotating in order for the tidal torque to be consistent with the observed orbital decay rate.

1.3 Tertiary-Induced Formation of Black Hole Binaries

Third, I introduce my work on the formation of black hole (BH) binaries. Since it first detected gravitational waves (GWs) in 2015, the LIGO/VIRGO Collaboration (LVC) has since detected a total of 90 compact object coalescences to date, the large majority of which are mergers of two BHs [The LIGO Scientific Collaboration et al., 2021b]. As the catalog of events grows, it is increasingly fruitful to pose the question of how these BH binaries are formed. The canonical scenario posits that these BH binaries initially form as wider stellar binaries that undergo a common envelope phase and subsequently experience orbital decay to form compact BH binaries that can then merge via GW emission [e.g. Belczynski et al., 2016]. However, such a process has numerous uncertainties, and many studies have explored alternatives that do not require an efficient common envelope phase. I focus on the so-called "tertiary-induced" merger scenario, where a wide black hole binary experiences von Zeipel-Lidov-Kozai [ZLK von Zeipel, 1910, Lidov, 1962, Kozai, 1962] oscillations due to gravitational interactions with a distant tertiary companion over very long, secular time scales. During these ZLK oscillations, the eccentricity of the inner binary varies between small values to values very near

unity. If the maximum eccentricity is sufficiently large, the enhanced GW emission near pericenter can dramatically shrink the binary orbit, and the binary can then merge in isolation via GW radiation alone.

In this dissertation, I consider the distributions both of the spin orientations and of the mass ratio of the component BHs for binaries formed via the tertiary-induced merger channel. In Chapter 7, I study the spin evolution of BH binaries undergoing ZLK oscillations. Previously, Liu and Lai [2018] used numerical integrations to study the final spin orientations of BHs in binaries that form via the tertiary-induced channel. They found that, when the spins are initially aligned with the orbital angular momentum axis and the octupole-order corrections to the ZLK effect are negligible (this is accurate when either the tertiary's orbit is circular or the inner binary has equal masses), the spins of the BHs tend to lie in the orbital plane (i.e. normal to the angular momentum axis) upon merger. I show via analytical arguments that this behavior is due to conservation of an approximate adiabatic invariant, which is well-conserved as long as the system coalesces over many ZLK cycles. If this condition is satisfied, I solve for the final spin orientation for an arbitrary initial spin orientation. I also quantify the deviation from this prediction for systems that merge non-adiabatically. While the spin distribution from the LVC significantly prefers spin-orbit alignment, there is still ongoing study concerning whether there may be a sub-population of BH mergers with perpendicular spin and orbit axes [Roulet et al., 2021, The LIGO Scientific Collaboration et al., 2021a]. Such a sub-population is consistent with formation via the tertiary-induced channel.

In Chapter 8, I study the mass-ratio distribution in the tertiary-induced merger channel. This distribution is sensitive to the octupole-order corrections neglected in Chapter 7. In systems where the octupole-order terms are more important,

the inner binary can more readily attain extreme eccentricities. The strength of these octupole-order terms scales inversely with the binary's mass ratio (i.e. binaries with more unequal masses experience stronger octupole-order effects). As a result, it is evident that the tertiary-induced merger scenario is more efficient at producing BH binaries with unequal component masses. This trend is opposite to that seen by the LVC, which has observed more systems with equal masses than systems with unequal masses. This may not entirely rule out tertiary-induced mergers as a formation channel for BH binaries, however: the mass-ratio distribution of wide BH binaries is unknown, so the enhanced formation rate may be unable to overcome a natural paucity of small-mass-ratio BH binaries. I also show that the formation rate enhancement for unequal-mass binaries is much weaker when the inner binary is somewhat compact, which also can slightly ease the tension with the observed mass-ratio distribution. Finally, note that the octupole-order corrections are negligible when the tertiary is sufficiently distant, e.g. when the binary is on a distant orbit around a supermassive BH.

CHAPTER 2

DYNAMICS OF COLOMBO'S TOP: GENERATING EXOPLANET OBLIQUITIES FROM PLANET-DISK INTERACTIONS

Originally published in:

Yubo Su and Dong Lai. Dynamics of Colombo's Top: Generating exoplanet obliquities from planet-disk interactions. *ApJ*, 903(1):7, Oct 2020. doi: 10.3847/1538-4357/abb6f3

2.1 Introduction

2.1.1 Colombo's Top

A rotating planet is subjected to gravitational torque from its host star, making its spin axis precess around its orbital (angular momentum) axis. Now suppose the orbital axis precesses around another fixed axis—such orbital precession could arise from gravitational interactions with other masses in the system (e.g. planets, external disks, or binary stellar companion). What is the dynamics of the planetary spin axis? How does the spin axis evolve as the spin precession rate, the orbital precession rate, or their ratio, gradually changes in time?

Colombo [1966] was the first to point out the importance of the above simple model in the study of the obliquity (the angle between the spin and orbital axes) of planets and satellites. Subsequent works [Peale, 1969, 1974, Ward, 1975, Henrard and Murigande, 1987] have revealed rich dynamics of this model. With appropriate modification, this model can be used as a basis for understanding the evolution of rotation axes of celestial bodies. Indeed, many contemporary problems in planetary/exoplanetary dynamics can be cast into a form analogous to this simple model or its variants [e.g. Ward and Hamilton, 2004, Fabrycky et al., 2007, Batygin and

Adams, 2013, Lai, 2014, Anderson and Lai, 2018, Zanazzi and Lai, 2018].

In this paper we present a systematic investigation on the secular evolution of Colombo's top, starting from general initial conditions. Our study includes several new analytical results that go beyond previous works. While our results are general, we frame our study in the context of generating exoplanet obliquities from planet-disk interaction with a dissipating disk.

2.1.2 Planetary Obliquities from Planet-Disk Interaction

It is well recognized that the obliquity of a planet may provide important clues to its dynamical history. In the the Solar System, a wide range of planetary obliquities are observed, from nearly zero for Mercury and 3.1° for Jupiter, to 23° for Earth and 26.7° for Saturn, to 98° for Uranus. Multiple giant impacts are traditionally invoked to generate the large obliquities of ice giants [Safronov and Zvjagina, 1969, Benz et al., 1989, Korycansky et al., 1990, Morbidelli et al., 2012]. For gas giants, obliquity excitation may be achieved via spin-orbit resonances, where the spin and orbital precession frequencies of the planet become commensurate as the system evolves [Ward and Hamilton, 2004, Hamilton and Ward, 2004, Vokrouhlickỳ and Nesvornỳ, 2015]. Such resonances may also play a role in generating the obliquities of Uranus and Neptune [Rogoszinski and Hamilton, 2020]. For terrestrial planets, multiple spin-orbit resonances and their overlaps can make the obliquity vary chaotically over a wide range [e.g. Laskar and Robutel, 1993, Touma and Wisdom, 1993, Correia et al., 2003]

Obliquities of extrasolar planets are difficult to measure. So far only loose constraints have been obtained for the obliquity of a faraway ($\gtrsim 50$ au) planetary-mass companion [Bryan et al., 2020]. But there are prospects for constraining

exoplanetary obliquities in the coming years, such as using high-resolution spectroscopy to obtain $v \sin i$ of the planet [Snellen et al., 2014, Bryan et al., 2018] and using high-precision photometry to measure asphericity of the planet [Seager and Hui, 2002]. Finite planetary obliquities have been indirectly inferred to explain the peculiar thermal phase curves [see e.g. Adams et al., 2019, Ohno and Zhang, 2019] and tidal dissipation in hot Jupiters [Millholland and Laughlin, 2018] and in super Earths [Millholland and Laughlin, 2019].

It is natural to imagine some of the mechanisms that generate planetary obliquities in the Solar System may also operate in exoplanetary systems. Recently, Millholland and Batygin [2019] studied the production of planet obliquities via a spin-orbit resonance, where a dissipating protoplanetary disk causes resonance capture and advection. In their work, a planet is accompanied by an inclined exterior disk; as the disk gradually dissipates, the planetary obliquity increases, reaching 90° for what the authors characterize as adiabatic resonance crossings.

The Millholland & Batygin study assumes a negligible initial planetary obliquity. This assumption is intuitive, since the planet attains its spin angular momentum from the disk. But it may not always be satisfied. In particular, the formation of rocky planets through planetesimal accretion can lead to a wide range of obliquities, especially if the final spin is imparted by a few large bodies [Dones and Tremaine, 1993, Lissauer et al., 1997, Miguel and Brunini, 2010]. Such "stochastic" accretion likely happened for terrestrial planets in the Solar System. Giant impacts may have also played a role in the formation of the close-in multiple-planet systems diskovered by the Kepler satellite [e.g. Inamdar and Schlichting, 2015, Izidoro et al., 2017].

2.1.3 Goal of This Paper

In this paper, we consider a wide range of initial planetary obliquities in the Millholland-Batygin dissipating disk scenario, and examine how the obliquity evolves toward the "final" value as the exterior disk dissipates. We provide an analytical framework for understanding the final planetary obliquity for arbitrary initial spin-disk misalignment angles. We also consider various dissipation timescales, and examine both "adiabatic" (slow disk dissipation) and "non-adiabatic" evolution. We calibrate these analytical results with numerical calculations. On the technical side, our paper extends previous works [such as Henrard, 1982, Henrard and Murigande, 1987, Millholland and Batygin, 2019] in several aspects. Two of our main results are: (i) a careful accounting of the phase space area across sepratrix to analytically describe the rich dynamics of adiabatic evolution, and (ii) using the concept of "partial adiabatic resonance advection" to fully capture the dynamics in the non-adiabatic limit.

It is important to note that while we focus on a specific scenario of generating/modifying planetary obliquities from planet-disk interactions, our analysis and results have a wide range of applicability. For example, a dissipating disk is dynamically equivalent to an outward-migrating external companion.

The paper is organized as follows. In Section 2.2, we review the relevant spin-orbit dynamics and key concepts that are used in the remainder of the paper. In Sections 2.3 and 2.4, we study the evolution of the system when the disk dissipates on different timescales, from highly adiabatic to nonadiabatic. Analytical results are presented to explain the numerical results in both limits. We discuss the implications of our results in Section 2.5. Our primary physical results consist of Fig. 2.5 in the adiabatic limit and Fig. 2.12 in the nonadiabatic limit. Some

detailed calculations are relegated to the appendices, including a leading-order estimate of the final planetary obliquities given small initial spin-disk misalignment angles in Appendix A.2.

2.2 Theory

2.2.1 Equations of Motion

We consider a star of mass $M_\star$ hosting an oblate planet (mass M_p, radius R_p and spin angular frequency Ω_p) at semimajor axis a_p, and a protoplanetary disk of mass M_d. For simplicity, we treat the disk as a ring of radius r_d, but it is simple to generalize to a disk with finite extent [see Millholland and Batygin, 2019]. Denote $\mathbf{S}$ the spin angular momentum and $\mathbf{L}$ the orbital angular momentum of the planet, and $\mathbf{L}_\mathrm{d}$ the angular momentum of the disk. The corresponding unit vectors are $\hat{\mathbf{s}} \equiv \mathbf{S}/S$, $\hat{\mathbf{l}} \equiv \mathbf{L}/L$, and $\hat{\mathbf{l}}_\mathrm{d} \equiv \mathbf{L}_\mathrm{d}/L_\mathrm{d}$.

The spin axis $\hat{\mathbf{s}}$ of the planet tends to precess around its orbital (angular momentum) axis $\hat{\mathbf{l}}$, driven by the gravitational torque from the host star acting on the planet's rotational bulge. On the other hand, $\hat{\mathbf{l}}$ and the disk axis $\hat{\mathbf{l}}_\mathrm{d}$ precess around each other due to gravitational interactions. We assume $S \ll L \ll L_\mathrm{d}$, so $\hat{\mathbf{l}}_\mathrm{d}$ is nearly constant and $\hat{\mathbf{l}}$ experiences negligible backreaction torque from $\hat{\mathbf{s}}$. The equations of motion for $\hat{\mathbf{s}}$ and $\hat{\mathbf{l}}$ in this limit are [Anderson and Lai, 2018]

$$\frac{\mathrm{d}\hat{\mathbf{s}}}{\mathrm{d}t} = \omega_\mathrm{sl}\left(\hat{\mathbf{s}}\cdot\hat{\mathbf{l}}\right)\left(\hat{\mathbf{s}}\times\hat{\mathbf{l}}\right) \equiv \alpha\left(\hat{\mathbf{s}}\cdot\hat{\mathbf{l}}\right)\left(\hat{\mathbf{s}}\times\hat{\mathbf{l}}\right), \tag{2.1}$$

$$\frac{\mathrm{d}\hat{\mathbf{l}}}{\mathrm{d}t} = \omega_\mathrm{ld}\left(\hat{\mathbf{l}}\cdot\hat{\mathbf{l}}_\mathrm{d}\right)\left(\hat{\mathbf{l}}\times\hat{\mathbf{l}}_\mathrm{d}\right) \equiv -g\left(\hat{\mathbf{l}}\times\hat{\mathbf{l}}_\mathrm{d}\right), \tag{2.2}$$

where

$$\omega_{\rm sl} \equiv \frac{3GJ_2M_pR_p^2M_\star}{2a_p^3I_p\Omega_p} = \frac{3k_{\rm qp}}{2k_{\rm p}}\frac{M_\star}{m_{\rm p}}\left(\frac{R_{\rm p}}{a_{\rm p}}\right)^3\Omega_{\rm p}, \tag{2.3}$$

$$\omega_{\rm ld} \equiv \frac{3M_{\rm d}}{4M_\star}\left(\frac{a_{\rm p}}{r_{\rm d}}\right)^3 n. \tag{2.4}$$

In Eq. (4.4), $I_p = k_pM_pR_p^2$ (with k_p a constant) is the moment of inertia and $J_2 = k_{\rm qp}\Omega_p^2(R_p^3/GM_p)$ (with k_{qp} a constant) the rotation-induced (dimensionless) quadrupole of the planet [for a body with uniform density, $k_p = 0.4, k_{qp} = 0.5$; for giant planets, $k_p \simeq 0.25$ and $k_{qp} \simeq 0.17$ [e.g. Lainey, 2016]]. In other studies, $3k_{\rm qp}/2k_{\rm p}$ is often notated as $k_2/2C$ [e.g. Millholland and Batygin, 2019]. In Eq. (2.4), $n \equiv \sqrt{GM_\star/a_{\rm p}^3}$ is the planet's orbital mean motion, and we have assumed $r_d \gg a_p$ and included only the leading-order (quadrupole) interaction between the planet and disk. We define three relative inclination angles via

$$\hat{\mathbf{s}}\cdot\hat{\mathbf{l}} \equiv \cos\theta, \quad \hat{\mathbf{s}}\cdot\hat{\mathbf{l}}_{\rm d} \equiv \cos\theta_{\rm sd}, \quad \hat{\mathbf{l}}\cdot\hat{\mathbf{l}}_{\rm d} \equiv \cos I. \tag{2.5}$$

In our model, I is a constant. Following standard notation [e.g. Colombo, 1966, Peale, 1969, Ward and Hamilton, 2004], we have defined $\alpha \equiv \omega_{\rm sl}$ and $g \equiv -\omega_{\rm ld}\cos I$.

We can combine Eqs. (7.20) and (2.2) into a single equation by transforming into a frame rotating about $\hat{\mathbf{l}}_{\rm d}$ with frequency g. In this frame, $\hat{\mathbf{l}}_{\rm d}$ and $\hat{\mathbf{l}}$ are fixed, and $\hat{\mathbf{s}}$ evolves as:

$$\left(\frac{{\rm d}\hat{\mathbf{s}}}{{\rm d}t}\right)_{\rm rot} = \alpha\left(\hat{\mathbf{s}}\cdot\hat{\mathbf{l}}\right)\left(\hat{\mathbf{s}}\times\hat{\mathbf{l}}\right) + g\left(\hat{\mathbf{s}}\times\hat{\mathbf{l}}_{\rm d}\right). \tag{2.6}$$

We define the dimensionless time τ as

$$\tau \equiv \alpha t, \tag{2.7}$$

and the frequency ratio η

$$\begin{aligned}\eta &\equiv -\frac{g}{\alpha} \\ &= 2.08\left(\frac{k_{\rm p}}{k_{\rm qp}}\right)\left(\frac{\rho_{\rm p}}{\rm g/cm^3}\right)\left(\frac{M_{\rm d}}{0.01M_\odot}\right)\left(\frac{a_{\rm p}}{5\,\rm AU}\right)^{9/2} \\ &\quad\times\left(\frac{r_{\rm d}}{30\,\rm AU}\right)^{-3}\left(\frac{M_\star}{M_\odot}\right)^{-3/2}\left(\frac{P_p}{10\,\rm hrs}\right)\cos I,\end{aligned} \tag{2.8}$$

where $\rho_p = 3M_p/(4\pi R_p^3)$ and $P_p = 2\pi/\Omega_p$ is the planet's rotation period. In Eq. (2.8), we have introduced the fiducial values of variable parameters for the application considered in this paper. Eq. (3.5) then becomes

$$\left(\frac{{\rm d}\hat{\mathbf{s}}}{{\rm d}\tau}\right)_{\rm rot} = \left(\hat{\mathbf{s}}\cdot\hat{\mathbf{l}}\right)\left(\hat{\mathbf{s}}\times\hat{\mathbf{l}}\right) - \eta\left(\hat{\mathbf{s}}\times\hat{\mathbf{l}}_{\rm d}\right). \tag{2.9}$$

Throughout this paper, we consider α constant, but allow g to vary in time. In the dispersing disk scenario of Millholland and Batygin [2019], $|g|$ decreases in time due to the decreasing disk mass. We consider a simple exponential decay model

$$M_{\rm d}(t) = M_{\rm d}(0)e^{-t/t_{\rm d}}, \tag{2.10}$$

with $t_{\rm d}$ constant. This implies

$$\frac{{\rm d}\eta}{{\rm d}t} = -\eta/t_{\rm d}, \text{ or } \frac{{\rm d}\eta}{{\rm d}\tau} = -\epsilon\eta, \tag{2.11}$$

where

$$\begin{aligned}\epsilon &\equiv \frac{1}{\alpha t_{\rm d}} \\ &= 0.106\left(\frac{k_{\rm p}}{k_{\rm qp}}\right)\left(\frac{\rho_{\rm p}}{\rm g/cm^3}\right)\left(\frac{a_{\rm p}}{5\,\rm AU}\right)^3\left(\frac{P_{\rm p}}{10\,\rm hrs}\right)\left(\frac{t_{\rm d}}{\rm Myr}\right)^{-1}.\end{aligned} \tag{2.12}$$

Eqs. (2.9) and (2.11) together constitute our system of study.

In the next two subsections, we summarize the theoretical background relevant to our analysis of the evolution of the system.

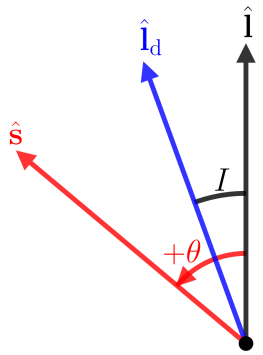

Figure 2.1: Definition of angles in the Cassini state configuration and the adopted sign convention for θ. Traditionally, $\theta \in [-\pi, \pi]$.

2.2.2 Cassini States

Spin states satisfying $(\mathrm{d}\hat{\mathbf{s}}/\mathrm{d}\tau)_\mathrm{rot} = 0$ are referred to as *Cassini States* (CSs) [Colombo, 1966, Peale, 1969]. They require that $\hat{\mathbf{s}}$, $\hat{\mathbf{l}}$, and $\hat{\mathbf{l}}_\mathrm{d}$ be coplanar. There are either two or four CSs, depending on the value of η. They are specified by the obliquity θ and the precessional phase of $\hat{\mathbf{s}}$ around $\hat{\mathbf{l}}$, denoted by ϕ. Following the standard convention and nomenclature (see Figs. 2.1 and 3.1), CSs 1, 3, 4 have $\phi = 0$ and $\theta < 0$, corresponding to $\hat{\mathbf{s}}$ and $\hat{\mathbf{l}}_\mathrm{d}$ being on opposite sides of $\hat{\mathbf{l}}$, while CS2 has $\phi = \pi$ and $\theta > 0$, corresponding to $\hat{\mathbf{s}}$ and $\hat{\mathbf{l}}_\mathrm{d}$ being on the same side of $\hat{\mathbf{l}}$. The CS obliquity satisfies

$$\sin\theta\cos\theta - \eta\sin(\theta - I) = 0. \tag{2.13}$$

When $\eta < \eta_\mathrm{c}$, where

$$\eta_\mathrm{c} \equiv \left(\sin^{2/3} I + \cos^{2/3} I\right)^{-3/2}, \tag{2.14}$$

all four CSs exist, and when $\eta > \eta_\mathrm{c}$, only CSs 2, 3 exist. The CS obliquities as a function of η are shown in Fig. 3.1.

Of the four CSs, 1, 2, 3 are stable while 4 is unstable. Appendix A.1 gives the libration frequencies and growth rates, respectively, near these CSs.

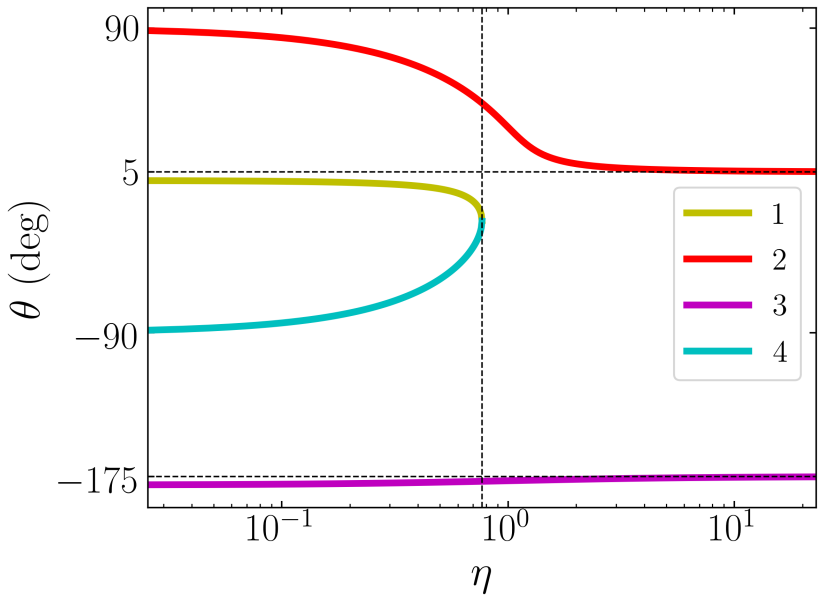

Figure 2.2: Cassini state obliquities as a function of η for $I = 5°$. The thin vertical dashed line indicates η_c (= 0.766 for $I = 5°$), where CS1 and CS4 merge and annihilate, and the thin horizontal dashed lines indicate $\theta = I$ and $I - 180°$, the asymptotic values for CSs 2 and 3 for $\eta \gg \eta_c$.

2.2.3 Separatrix

The Hamiltonian (in the rotating frame) of the system is

$$\begin{aligned}\mathscr{H}(\phi, \cos\theta) &= -\frac{1}{2}\left(\hat{\mathbf{s}}\cdot\hat{\mathbf{l}}\right)^2 + \eta\left(\hat{\mathbf{s}}\cdot\hat{\mathbf{l}}_d\right) \\ &= -\frac{1}{2}\cos^2\theta + \eta\left(\cos\theta\cos I - \sin I\sin\theta\cos\phi\right). \end{aligned} \tag{2.15}$$

Here, ϕ and $\cos\theta$ are canonically conjugate variables. Trajectories in the phase space $(\phi, \cos\theta)$ satisfy H = constant (see Fig. 2.3).

When $\eta < \eta_c$, CS4 exists and is a saddle point. The two trajectories originating and ending at CS4 are the only two infinite-period orbits in the phase space. Together, these two critical trajectories are referred to as the *separatrix* and divide phase space into three zones. In Fig. 2.3, we show the separatrix, the three zones, and their relations to the CSs. Trajectories in zone II librate about CS2 while

those in zones I and III circulate.

Since $(\phi, \cos\theta)$ are canonically conjugate, the integral $\oint \cos\theta \, \mathrm{d}\phi$ along a trajectory is an adiabatic invariant (see Section 2.3). The unsigned areas $\left(\left|\int \cos\theta \, \mathrm{d}\phi\right|\right)$ of the three zones (as defined in Fig. 2.3) can be computed analytically. If we define

$$z_0 = \eta \cos I, \qquad \chi = \sqrt{-\frac{\tan^3\theta_4}{\tan I} - 1}, \tag{2.16a}$$

$$\rho = \chi \frac{\sin^2\theta_4 \cos\theta_4}{\chi^2 \cos^2\theta_4 + 1}, \qquad T = 2\chi \frac{\cos\theta_4}{\chi^2 \cos^2\theta_4 - 1}, \tag{2.16b}$$

then the areas for $\eta < \eta_\mathrm{c}$ are given by [Ward and Hamilton, 2004]

$$\mathscr{A}_\mathrm{I} = 2\pi(1 - z_0) - \frac{\mathscr{A}_\mathrm{II}}{2}, \tag{2.17a}$$

$$\mathscr{A}_\mathrm{II} = 8\rho + 4 \arctan T - 8 z_0 \arctan \frac{1}{\chi}, \tag{2.17b}$$

$$\mathscr{A}_\mathrm{III} = 2\pi(1 + z_0) - \frac{\mathscr{A}_\mathrm{II}}{2}. \tag{2.17c}$$

These are plotted as a function of η in Fig. 2.4. While the zones are not formally defined for $\eta > \eta_\mathrm{c}$ since the separatrix disappears, a natural extension exists: evolve an initial phase space point p under adiabatic decrease of η until the separatrix appears at $\eta = \eta_\mathrm{c}$, then identify p with the zone it is in at η_c. Since phase space area is conserved under adiabatic evolution, this extension implies $\mathscr{A}_\mathrm{j}(\eta > \eta_\mathrm{c}) = \mathscr{A}_\mathrm{j}(\eta_\mathrm{c})$. The boundary between these extended zones is denoted by the dashed black line in panel (a) of Fig. 2.3, where no separatrix exists.

2.3 Adiabatic Evolution

In this section, we study the evolution of the planetary obliquity θ when the parameter η [or the disk mass M_d; see Eqs. (2.8) and (2.11)] decreases sufficiently slowly that the evolution is adiabatic. Intuitively, this requires the disk evolu-

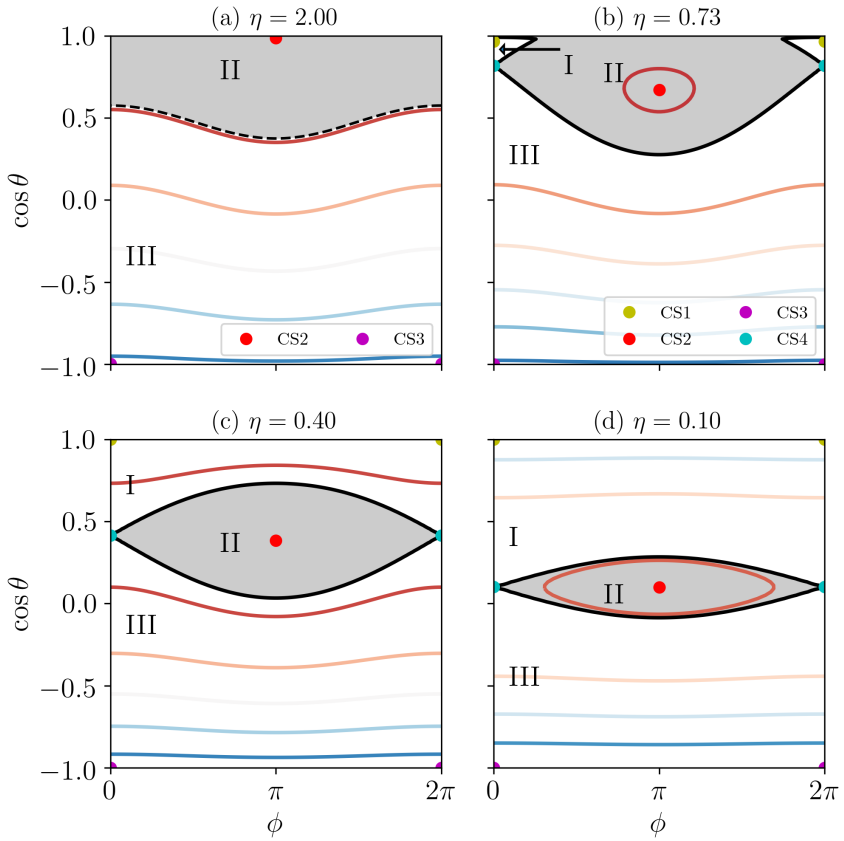

Figure 2.3: Level curves of $\mathscr{H}(\phi, \cos\theta)$ [Eq. (3.8)] for $I = 5°$, where warmer colors denote more positive values. The black solid line is the separatrix, which only exists for $\eta < \eta_c = 0.766$. The three zones (I, II, III), divided by the separatrix, are labeled. The Cassini states are denoted by filled circles and have the same colors as in Fig. 3.1. The interior of the separatrix, shaded in grey, is formally only defined for $\eta < \eta_c$, but we may identify the points in phase space that flow into zone II when evolved forward in time (decreasing η adiabatically); this is the shaded region in panel (a), bounded by the black dotted line.

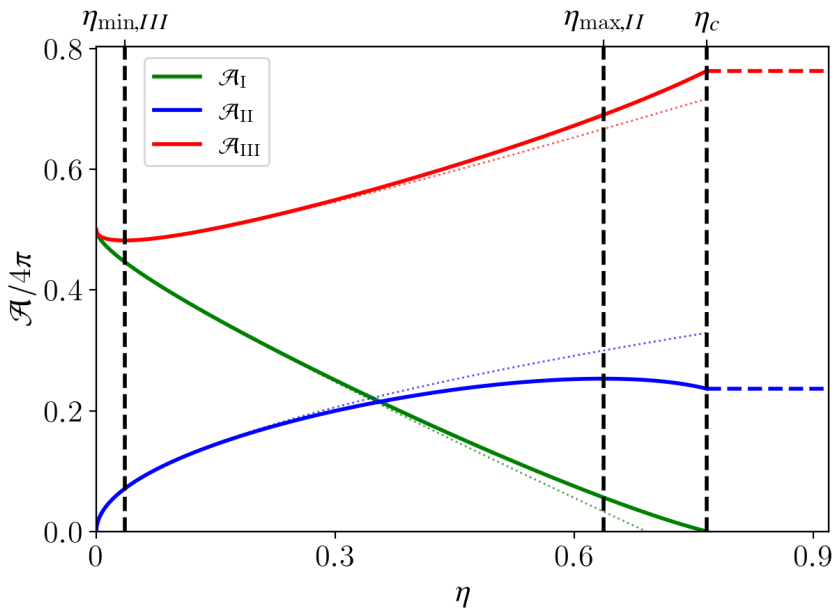

Figure 2.4: Plot of fractional areas of each of the zones $\mathscr{A}_{\mathrm{j}}(\eta)/4\pi$ as given by Eqs. (2.17) for $I = 5°$. The colored dotted lines correspond to small η approximations used in Appendix A.2. The colored dashed lines for $\eta > \eta_{\mathrm{c}}$ are the effective values of $\mathscr{A}_{\mathrm{II}}, \mathscr{A}_{\mathrm{III}}$ for $\eta > \eta_{\mathrm{c}}$, denoting the points that would flow into either area under adiabatic decrease of η from $\eta > \eta_{\mathrm{c}}$ (see the text). The vertical black dashed lines correspond to $\eta = \eta_{\mathrm{c}}$ [Eq.(2.14)] and the values of η for which $\mathscr{A}_{\mathrm{II}}$ is maximized ($\eta_{\mathrm{max,II}}$) and for which $\mathscr{A}_{\mathrm{III}}$ is minimized ($\eta_{\mathrm{min,III}}$, Eq. (2.30)).

tion time t_d [Eq. (2.10)] be much larger than the spin precession period, $2\pi/\alpha$, i.e. $\epsilon = 1/(\alpha t_\mathrm{d}) \ll 1/(2\pi)$.

More rigorously, adiabaticity requires t_d be much larger than all timescales of the dynamical system governed by the Hamiltonian [Eq. (3.8)]. This is of course not possible in all cases, as the motion along the separatrix has an infinite period. In practice, as η evolves, the system only crosses the separatrix once or twice, while it spends many orbits inside one of the three zones and far from the separatrix. Thus, a *weak adiabaticity criterion* is that, for all equilibria/fixed points, the local circulation/libration periods are much shorter than the timescale for the motion of the equilibria due to changing η. If this criterion is satisfied, then the system will evolve adiabatically for most of its evolution save one or two separatrix crossings.

As shown in Appendix A.1.2, libration about CS2 is slower than that about CS1 or CS3. As such, it has the smallest characteristic frequency in the system. The weak adiabaticity criterion is equivalent to requiring that, at all times other than separatrix crossing, the obliquity of CS2 (θ_2) evolve over a longer timescale than the local libration period about CS2, i.e.

$$\left|\frac{\mathrm{d}\theta_2}{\mathrm{d}\tau}\right| \ll \frac{\omega_\mathrm{lib}}{2\pi}, \tag{2.18}$$

where

$$\omega_\mathrm{lib} = \sqrt{\eta \sin I \sin\theta_2 \left(1 + \eta \sin I \csc^3\theta_2\right)}, \tag{2.19}$$

is the libration frequency about CS2 for a given η (Appendix A.1.2). This formula differs from that given in Millholland and Batygin [2019], where the $\csc^3\theta_2$ term is neglected and the square root is missing[1]. Differentiating Eq. (2.13) gives

$$\frac{\mathrm{d}\theta_2}{\mathrm{d}\tau} = -\epsilon \frac{\eta \sin(\theta_2 - I)}{\cos(2\theta_2) - \eta\cos(\theta_2 - I)}, \tag{2.20}$$

[1]The missing $\csc^3\theta_2$ term can be traced to a $\theta \gg I$ approximation made in Eq. (3) of Hamilton and Ward [2004]. Since $\theta_2 \sim I$ for $\eta \gg 1$ (Fig. 3.1), this approximation is not always valid.

where $\epsilon = -\mathrm{d}(\ln\eta)/\mathrm{d}\tau$ [Eq. (2.12)]. Eq. (2.18) is most constraining at $\eta \sim 1$, i.e. it will be satisfied for all η if it is satisfied near $\eta \sim 1$, where $|\mathrm{d}\theta_2/\mathrm{d}\tau| \sim \epsilon$. Thus, weak adiabiticity requires

$$\epsilon \ll \epsilon_{\rm c} \equiv \left(\frac{\omega_{\rm lib}}{2\pi}\right)_{\eta=1} \simeq \frac{1}{2\pi\sqrt{2}}\sqrt{\sin I\,(1+8\sin I)}, \tag{2.21}$$

where in the last equality we have used $\sin\theta_2 \simeq 1/2$ at $\eta = 1$ (e.g. when $I = 5^\circ$ and $\eta = 1$, $\theta_2 \approx 31^\circ$). For $I = 5^\circ$, we obtain $\epsilon_{\rm c} \approx 0.0433$. Since our criterion is only a weak condition for adiabaticity, we use $\epsilon = 3\times10^{-4}$ in our "adiabatic" calculations below. We explore the consequences of nonadiabatic evolution in Section 2.4.

2.3.1 Adiabatic Evolution Outcomes

We consider the evolution of a system with arbitrary initial spin-disk misalignment angle $\theta_{\rm sd,i}$ and initial $\eta_{\rm i} \gg 1$. We are interested in the final spin obliquities $\theta_{\rm f}$ after η gradually decreases to $\eta_{\rm f} \ll 1$ (i.e. after the disk has dissipated to a negligible mass). Note that when $\eta_{\rm i} \gg 1$, $\hat{\mathbf{l}}$ precesses around $\hat{\mathbf{l}}_{\rm d}$ much faster than the spin-orbit precession ($|\omega_{\rm ld}| \gg |\omega_{\rm sl}|$), and the spin obliquity θ varies rapidly. It is thus more appropriate to use $\theta_{\rm sd,i}$ rather than θ to specify the initial spin orientation. We explore the entire range $\theta_{\rm sd,i} \in [0,\pi]$ and choose $\epsilon = 3\times10^{-4}$ (see above).

To obtain the distribution of the final obliquities $\theta_{\rm f}$, we evenly sample 101 values of $\theta_{\rm sd,i}$, and for each $\theta_{\rm sd,i}$ value, we pick 101 evenly spaced orientations of $\hat{\mathbf{s}}$ approximately from the ring of initial conditions having angular distance $\theta_{\rm sd,i}$ to $\hat{\mathbf{l}}_{\rm d}$[2]. To be concrete, we choose $\eta_{\rm i} = 10\eta_{\rm c}$ where $\eta_{\rm c}$ is given by Eq. (2.14) and

[2]The actual procedure we adopt to choose the initial conditions is the natural extension of this description to finite $\eta_{\rm i}$. Note that the center of libration of $\hat{\mathbf{s}}$ is CS2, which, since $\eta_{\rm i}$ is finite, is different from $\hat{\mathbf{l}}_{\rm d}$. Furthermore, the libration is not exactly circular. As a result, the libration trajectories for initial conditions on the circular ring of points having angular distance $\theta_{\rm sd,i}$ from $\hat{\mathbf{l}}_{\rm d}$ are not the same and will each enclose slightly different initial phase space areas $A_{\rm i}$. Since our analytical theory assumes exact conservation of the initially enclosed phase space area $A_{\rm i}$

evolve Eqs. (2.9) and (2.11) until η reaches its final value 10^{-5}. At such a small η, $\hat{\mathbf{s}}$ is strongly coupled to $\hat{\mathbf{l}}$ and the final obliquity $\theta_{\rm f}$ is frozen. The mapping between $\theta_{\rm sd,i}$ and $\theta_{\rm f}$ is our primary result, and is shown for $I = 5^\circ$, 10°, and 20° in Figs. 2.5 and 2.6 respectively. The blue dots represent the results of the numerical calculation. The colored tracks are calculated semi-analytically using the method discussed in the following subsection.

2.3.2 Analytical Theory for Adiabatic Evolution

The evolutionary tracks that govern the $\theta_{\rm f}$-$\theta_{\rm sd,i}$ mapping correspond to various sequences of separatrix crossings. They can be understood using the principle of adiabatic invariance, combined with (i) how the enclosed phase space area by the trajectory evolves across each separatrix crossing, and (ii) the associated probabilities with each separatrix crossing.

Governing Principle: Evolution of Enclosed Phase Space Area

First, we consider how the enclosed phase space area by a trajectory evolves over time. In the absence of separatrix encounters, the enclosed phase space area $\oint \cos\theta \, {\rm d}\phi$ is an adiabatic invariant. We adopt convention where

$$A \equiv \oint (1 - \cos\theta) \, {\rm d}\phi. \tag{2.22}$$

Note that A can be negative when ${\rm d}\phi/{\rm d}t < 0$, unlike the unsigned areas $\mathscr{A}_{\rm i}$ [Eqs. (2.17)] which are positive by definition. This definition of A has two advantages: (i) it is

for each $\theta_{\rm sd,i}$ (see Section 2.3.2), this diskrepancy introduces an extra deviation from the analytical prediction. To guarantee all points for a particular $\theta_{\rm sd,i}$ have the same $A_{\rm i}$, we instead choose initial conditions on the libration cycle going through $(\theta_2 + \theta_{\rm sd,i}, \phi_2)$ [where (θ_2, ϕ_2) are the coordinates of CS2]. This ensures that all initial conditions for a given $\theta_{\rm sd,i}$ enclose the same initial $A_{\rm i}$. As $\eta_{\rm i} \to \infty$, this procedure generates initial conditions on the ring having angular distance $\theta_{\rm sd,i}$ to $\hat{\mathbf{l}}_{\rm d}$, recovering the procedure given in the text.

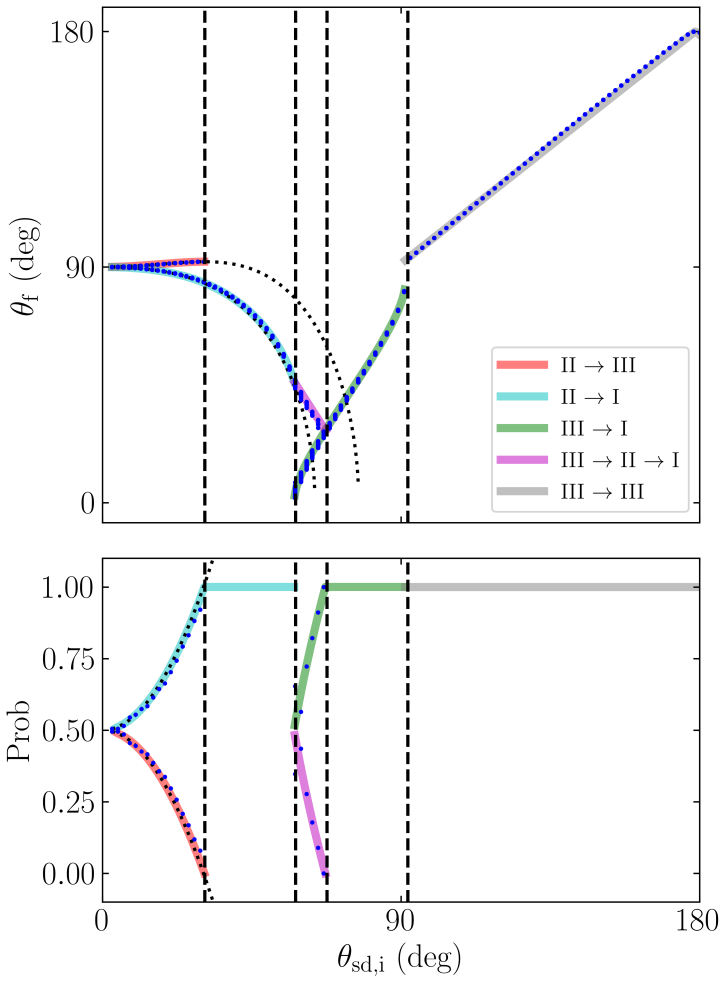

Figure 2.5: Top: The final spin obliquity θ_f as a function of the initial spin-disk misalignment angle $\theta_{sd,i}$ for systems evolving from initial $\eta_i \gg 1$ to $\eta_f \ll 1$, for $I = 5°$. The blue dots are results of numerical calculations (Section 2.3.1), and the colored tracks are semi-analytical results (Section 2.3.2). Bottom: The probabilities of different outcomes. Where a particular $\theta_{sd,i}$ corresponds to multiple tracks, the system evolves probabilistically. The track that a particular system evolves along in a numerical simulation can be measured by examining its final obliquity. The dots represent the inferred probabilities from measured final obliquities in our simulations, while the colored tracks denote the semi-analytic probability of the system evolving along each track. There are five regimes of $\theta_{sd,i}$ values for which different tracks are accessible. In both plots, the vertical dashed black lines denote semi-analytical calculations of the boundaries of these regimes (see Section 2.3.2), while the black dotted lines represent analytical approximations valid in the small-$\theta_{sd,i}$ limit (see Appendix A.2).

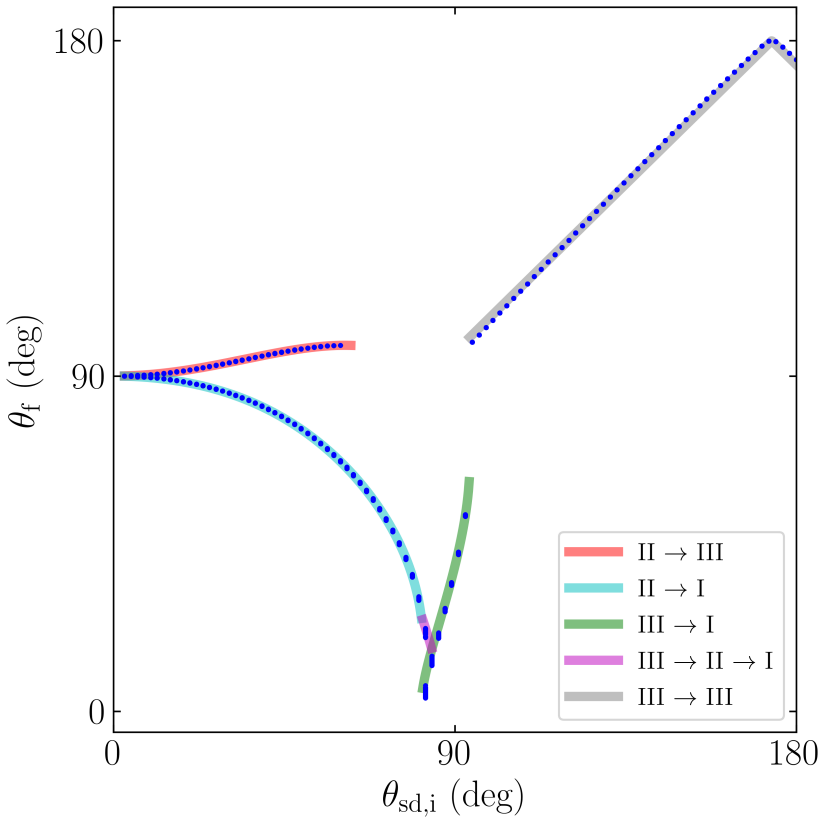

Figure 2.6: Same as the top panel of Fig. 2.5 but for $I = 20^\circ$ and with fewer annotations.

continuous across transitions from circulating to librating that cross the North pole ($\cos\theta = 1$), and (ii) the areas of the three zones are equal in absolute value to the expressions given in Eqs. (2.17). The path over which the integral is taken is either a libration or circulation cycle. When $\eta_\mathrm{i} \gg 1$, trajectories librate about $\hat{\mathbf{I}}_\mathrm{d}$ with constant θ_sd, meaning they enclose initial phase space area

$$A_\mathrm{i} = 2\pi\left(1 - \cos\theta_\mathrm{sd,i}\right). \tag{2.23}$$

Complications arise when considering finite η_i, as trajectories near CS2 or CS3 librate about these equilibria, rather than $\hat{\mathbf{I}}_\mathrm{d}$, and Eq. (2.23) is no longer exact. In practice, Eq. (2.23) holds very well when defining $\theta_\mathrm{sd,i}$ as the angular distance to CS2; an exception is discussed in Section 2.3.2.

Beginning at the last separatrix crossing, the final enclosed phase space area A_f will be conserved for all time. As $\eta \to 0$, trajectories circulate about $\hat{\mathbf{I}}$ at constant obliquity θ_f, related to A_f by

$$2\pi\left(1 - \cos\theta_\mathrm{f}\right) = A_\mathrm{f}. \tag{2.24}$$

The enclosed phase space area is not conserved when the trajectory encounters the separatrix. However, the change is easily understood [Henrard, 1982]. In essence, when the trajectory crosses the separatrix, it continues to evolve adjacent to the separatrix. So if a separatrix crossing results in a zone I trajectory (see Fig. 2.3), the new area can be approximated by integrating Eq. (2.22) along the upper leg of the separatrix. Pictorially, this can be seen in the bottom panels of Fig. 2.7.

Governing Principle: Probabilistic Separatrix Crossing

When a trajectory experiences separatrix crossing, it transitions into nearby zones probabilistically. This process is studied in the adiabatic limit by Henrard [1982] and Henrard and Murigande [1987]. Their results may be summarized as follows: if zone i is shrinking while adjacent zones j,k are expanding such that the sum of their areas is constant, the probabilities of transition from zone i to zones j and k are given by

$$\Pr(i \to j) = -\frac{\partial \mathscr{A}_\mathrm{j}/\partial\eta}{\partial \mathscr{A}_\mathrm{i}/\partial\eta}, \tag{2.25a}$$

$$\Pr(i \to k) = -\frac{\partial \mathscr{A}_\mathrm{k}/\partial\eta}{\partial \mathscr{A}_\mathrm{i}/\partial\eta}. \tag{2.25b}$$

Note that $\Pr(i \to j) + \Pr(i \to k) = 1$. Eqs. (2.25) can be used in conjunction with Eqs. (2.17) to understand for what initial conditions each track can be observed and with what probabilities.

As an example, consider a system in zone II in panel (d) of Fig. 2.3. As η decreases, zone II will shrink while zones I and III will expand until the trajectory crosses the separatrix. Suppose the trajectory exits zone II at some $\eta_\star$, then the probability of the II $\to$ I transition is $\Pr(\mathrm{II} \to \mathrm{I}) = -\dot{A}_\mathrm{I}/\dot{A}_\mathrm{II}$, while the II $\to$ III transition occurs with probability $\Pr(\mathrm{II} \to \mathrm{III}) = -\dot{A}_\mathrm{III}/\dot{A}_\mathrm{II}$.

Evolutionary Trajectories

Returning to the evolution of $\hat{\mathbf{s}}$, we can classify trajectories by the sequence of separatrix encounters. Initially, in the $\eta > \eta_\mathrm{c}$ regime, only zones II and III exist; as $\eta \to 0$, only zones I and III exist (see Fig. 2.3). There are five distinct evolutionary tracks:

1. II → I (see Fig. 2.7 for an example). The spin axis $\hat{\mathbf{s}}$ initially circulates in zone II (snapshot a), and then starts librating about CS2 as η decreases (snapshot b), enclosing some initial phase space area A_i. This libration continues until the separatrix expands (due to decreasing η) to "touch" the trajectory (snapshot c), at which $\mathscr{A}_\mathrm{II}(\eta_\star) = A_\mathrm{i}$. As $\hat{s}$ moves to a circulating trajectory in zone I immediately bordering the separatrix, it will encompass $-\mathscr{A}_\mathrm{I}(\eta_\star)$ phase space area. The final obliquity θ_f is then given by Eq. (2.24), with $A_\mathrm{f} = -\mathscr{A}_\mathrm{I}\left(\eta_\star\right)$. An analytical approximation to θ_f is derived in Appendix A.2 and is

$$(\cos\theta_\mathrm{f})_{\mathrm{II}\to\mathrm{I}} \simeq \left(\frac{\pi\theta_{\mathrm{sd,i}}^2}{16}\right)^2 \cot I + \frac{\theta_{\mathrm{sd,i}}^2}{4}. \tag{2.26}$$

The transition probability is

$$\Pr(\mathrm{II}\to\mathrm{I}) = -\left(\frac{\partial\mathscr{A}_\mathrm{I}/\partial\eta}{\partial\mathscr{A}_\mathrm{II}/\partial\eta}\right)_{\eta=\eta_\star}. \tag{2.27}$$

This track can only occur when the initial condition begins in zone II, requiring $A_\mathrm{i} < \mathscr{A}_\mathrm{II}(\eta_\mathrm{c})$, where $\mathscr{A}_\mathrm{II}\left(\eta_c\right)$ is given by Eq. (2.17b) evaluated at $\eta = \eta_c$. Since $\partial\mathscr{A}_\mathrm{I}/\partial\eta < 0$ everywhere, while $\partial\mathscr{A}_\mathrm{II}/\partial\eta > 0$ at all possible $\eta_\star$ for an initial condition starting in zone II, this track always has nonzero probability.

2. II → III (see Fig. 2.8). This track is similar to the II → I track; the only difference is that, upon separatrix encounter, the trajectory follows the circulating trajectory in zone III bordering the separatrix, upon which it will encompass area $\mathscr{A}_\mathrm{I}(\eta_\star) + \mathscr{A}_\mathrm{II}(\eta_\star) = A_\mathrm{f}$. The final obliquity is still given by Eq. (2.24), and the analytical approximation derived in Appendix A.2 is

$$(\cos\theta_\mathrm{f})_{\mathrm{II}\to\mathrm{III}} \simeq \left(\frac{\pi\theta_{\mathrm{sd,i}}^2}{16}\right)^2 \cot I - \frac{\theta_{\mathrm{sd,i}}^2}{4}. \tag{2.28}$$

The transition probability is

$$\Pr(\mathrm{II}\to\mathrm{III}) = -\left(\frac{\partial\mathscr{A}_\mathrm{III}/\partial\eta}{\partial\mathscr{A}_\mathrm{II}/\partial\eta}\right)_{\eta=\eta_\star}. \tag{2.29}$$

Again, this track can only occur when $A_\mathrm{i} < \mathscr{A}_\mathrm{II}(\eta_\mathrm{c})$, but a further constraint arises when we consider the transition probability. Upon examination of Fig. 2.4, it is clear that $\partial\mathscr{A}_\mathrm{III}/\partial\eta > 0$ for a large range of η, which would give a negative transition probability—implying a forbidden transition. Define

$$\eta_{\mathrm{min},III} \equiv \mathrm{argmin}\,\mathscr{A}_\mathrm{III}(\eta), \tag{2.30}$$

which is labeled in Fig. 2.4. Thus, the II → III track is permitted only if $\eta_\star <, \eta_{\mathrm{min,III}}$.

3. III → I (see Fig. 2.9). The trajectory encounters the separatrix when $\mathscr{A}_\mathrm{I}(\eta_\star) + \mathscr{A}_\mathrm{II}(\eta_\star) = A_\mathrm{i}$, upon which it transitions to a zone I trajectory enclosing $A_\mathrm{f} = -\mathscr{A}_\mathrm{I}$. The final obliquity is again given by Eq. (2.24).

   This track can only occur if $A_\mathrm{i} > \mathscr{A}_\mathrm{II}(\eta_\mathrm{c})$, but is also constrained by requiring A_i be sufficiently small so that it will encounter the separatrix (if A_i is too large, it will never encounter the separatrix, and we simply have a III → III transition). This condition is $A_\mathrm{i} < \max(\mathscr{A}_\mathrm{I} + \mathscr{A}_\mathrm{II}) = 4\pi - \min(\mathscr{A}_\mathrm{III})$. Since $\partial\mathscr{A}_\mathrm{I}/\partial\eta < 0$ and $\partial\mathscr{A}_\mathrm{III}/\partial\eta > 0$ for all accessible $\eta_\star$, this track is always permitted.

4. III → II → I (see Fig. 2.10). That $\mathscr{A}_\mathrm{II}(\eta)$ is not a monotonic function of η (see Fig. 2.4) is key to the existence of this track. Consider a trajectory originating in zone III that first encounters the separatrix at η_1, when $\mathscr{A}_\mathrm{I}(\eta_1) + \mathscr{A}_\mathrm{II}(\eta_1) = A_\mathrm{i}$, such that it transitions into zone II enclosing intermediate phase space area $A_\mathrm{m} = \mathscr{A}_\mathrm{II}(\eta_1)$. Such a transition has probability

$$\Pr(\mathrm{III} \to \mathrm{II}) = -\left(\frac{\partial\mathscr{A}_\mathrm{II}/\partial\eta}{\partial\mathscr{A}_\mathrm{III}/\partial\eta}\right)_{\eta=\eta_1}, \tag{2.31}$$

   which is nonnegative (i.e. the transition is permitted) if $\eta_1 \in [\eta_{\mathrm{max,II}}, \eta_\mathrm{c}]$. Equivalently, this requires $A_\mathrm{i} \in \left[\mathscr{A}_\mathrm{II}\left(\eta_\mathrm{c}\right), \mathscr{A}_\mathrm{II,max}\right]$. Then, as η continues to decrease, a second η_2 value exists for which $A_\mathrm{m} = \mathscr{A}_\mathrm{II}(\eta_2)$, upon which the

trajectory is ejected to zone I and $A_f = -\mathscr{A}_I(\eta_2)$. Note that $\eta_2 < \eta_{max,II}$ necessarily, as zone II must be shrinking in order for the trajectory to be ejected. The final obliquity is given by Eq. (2.24). Graphical inspection of Fig. 2.4 shows that $\partial\mathscr{A}_{II}/\partial\eta$ and $\partial\mathscr{A}_{III}/\partial\eta$ have the same signs for $\eta < \eta_{max,II}$, and therefore the complementary II → I transition is guaranteed. Overall, the III → II → I track is permitted so long as the first transition is permitted, or $A_i \in \left[\mathscr{A}_{II}\left(\eta_c\right), \mathscr{A}_{II,max}\right]$.

5. III → III. This track is the trivial case where no separatrix encounter occurs, and A is constant throughout the evolution ($A_f = A_i$) except for a jump by 4π when crossing the South pole ($\cos\theta = -1$) due to the coordinate singularity. This requires $A_i > \max(\mathscr{A}_I + \mathscr{A}_{II})$. In the limit of $\eta_i \to \infty$ and $\eta_f \to 0$ we have $\theta_f = \theta_{sd,i}$. For finite η_i, the initial enclosed phase space area for III → III trajectories is not given exactly by using $\theta = \theta_{sd,i}$ in Eq. (2.23). This is because the initial orbits for such trajectories are better described as librating about CS3 with angle of libration $\Delta\theta - \theta_{sd,i}$ rather than about CS2 with angle of libration $\theta_{sd,i}$. Here, $\Delta\theta$ is the angular distance between CS2 and CS3 and is not equal to 180° except when $\eta_i \to \infty$. This finite-η_i effect is responsible for the small cusp at the very right ($\theta_{sd,i} \to 180°$) of Figs. 2.5 and 2.6.

In summary, starting from an initial condition with phase space area A_i at $\eta = \eta_i \gg 1$, the five evolutionary tracks are:

1. $A_i \in \left[0, \mathscr{A}_{II}\left(\eta_{min,III}\right)\right]$: Both the II → III and the II → I tracks are possible.
2. $A_i \in \left[\mathscr{A}_{II}\left(\eta_{min,III}\right), \mathscr{A}_{II}(\eta_c)\right]$: Only the II → I track.
3. $A_i \in \left[\mathscr{A}_{II}(\eta_c), \mathscr{A}_{II,max}\right]$: Both the III → I and III → II → I are possible.
4. $A_i \in \left[\mathscr{A}_{II,max}, \max(\mathscr{A}_I + \mathscr{A}_{II})\right]$: Only the III → I track.
5. $A_i > \max(\mathscr{A}_I + \mathscr{A}_{II})$: Only the III → III track.

In all cases, the corresponding ranges for $\theta_{\rm sd,i}$ can be computed via Eq. (2.23). The boundaries between these ranges are overplotted in Fig. 2.5, where they can be seen to agree well with the numerical results.

2.4 Nonadiabatic Effects

In Section 2.3, we have examined the spin axis evolution in the limit where $\epsilon \ll \epsilon_{\rm c}$ [see Eq. (7.37)] and the evolution is mostly adiabatic (except at separatrix crossings). We now consider nonadiabatic effects.

2.4.1 Transition to Non-adiabaticity: Results for $\epsilon \lesssim \epsilon_{\rm c}$

To illustrate the transition to nonadiabaticity, we carried out a suite of numerical calculations for several values of ϵ. The results for two of these values are shown in Figs. 2.11 and 2.12.

As ϵ increases (see Fig. 2.11), nonadiabaticity manifests as a larger scatter of final obliquities near the tracks predicted from adiabatic evolution. This scatter first sets in for trajectories starting in zone III, as these trajectories encounter the separatrix at larger η compared to those originating in zone II. This means the obliquity of CS2 θ_2 is smaller for these trajectories, and the adiabaticity criterion is stricter [see Eq. (7.37)]. Physically, approaching the adiabaticity criterion corresponds to the separatrix crossing process becoming sensitive to the *phase* of the libration/circulation cycle at the crossing: if the trajectory crosses the separatrix when the obliquity is at its maximum, the final obliquity will also be relatively larger.

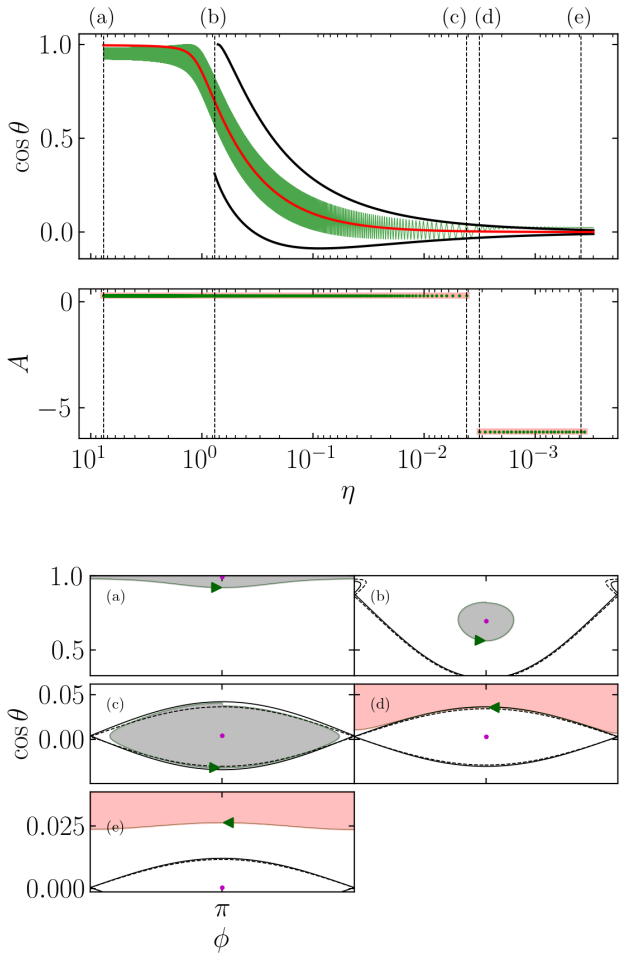

Figure 2.7: An example of the II → I evolutionary track for $I = 5°$ and $\theta_{\rm sd,i} = 17.2°$. Upper panel: The thin green line shows $\cos\theta$ as a function of η, obtained by numerical integration (with $\epsilon = 3 \times 10^{-4}$). Overlaid are the location of Cassini State 2 (dashed red) and the upper and lower bounds on the separatrix (dotted black). The trajectory tracks CS2 to a final obliquity of 88.57°. The black vertical dashed lines denote instants in the simulation portrayed in bottom panels. Middle panel: The enclosed separatrix area obtained by integrating the simulated trajectory (green dots) and adiabatic theory (red line). Lower plot: Snapshots in $(\cos\theta, \phi)$ phase space of one circulation/libration cycle of the trajectory, shown in dark green with an arrow indicating direction. The snapshots correspond to the start of the simulation (a), the appearance of the separatrix (b), two panels depicting the separatrix crossing process (c-d), and a final snapshot at $\eta = 10^{-3.5}$ (e). The separatrices at the beginning and end of the portrayed cycle in each snapshot are shown in solid/dashed black lines respectively. Also labeled is CS2 at the start of each cycle (filled red circle). Finally, the enclosed phase space area is shaded in grey ($A > 0$) and red ($A < 0$).

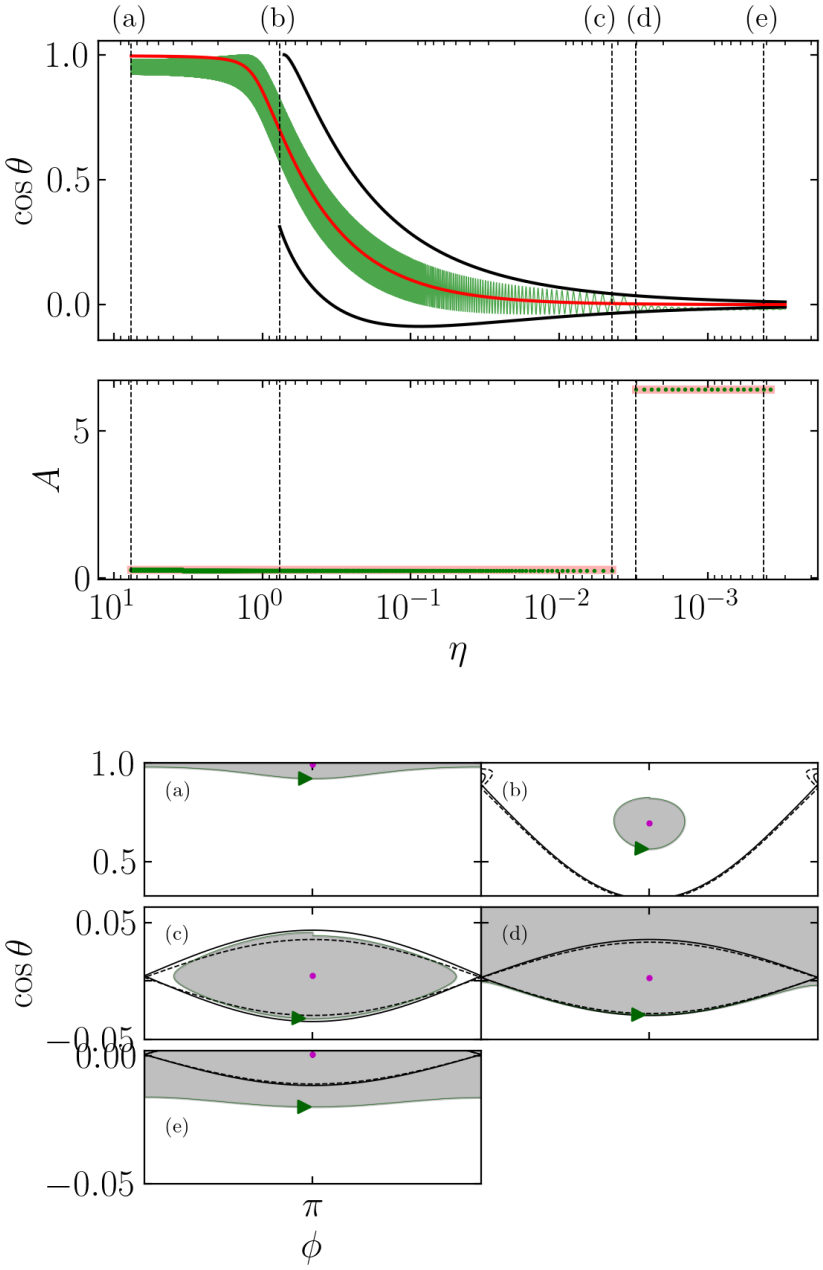

Figure 2.8: Same as Fig. 2.7 but for the II → III track. $\theta_{\rm sd,i} = 17.2^\circ$ and $\epsilon = 3.01 \times 10^{-4}$.

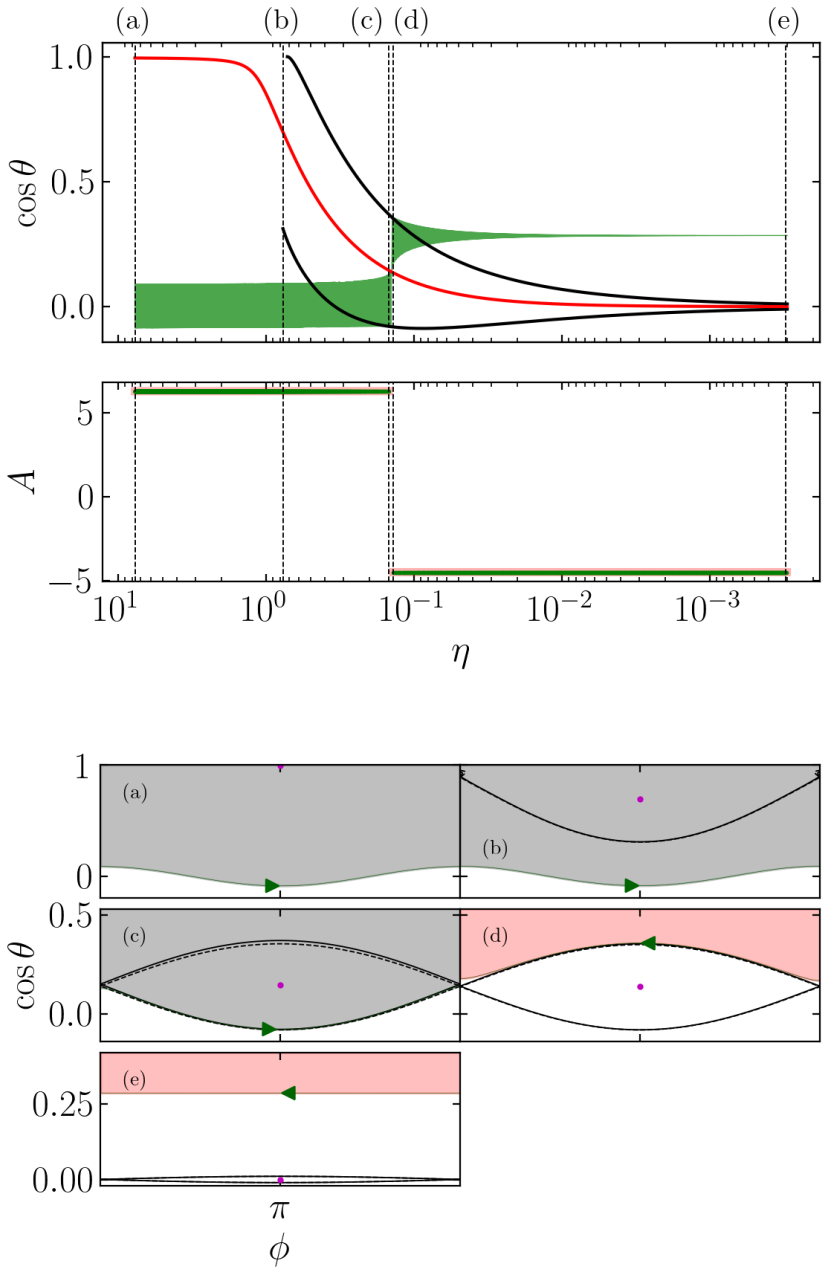

Figure 2.9: Same as Fig. 2.7 but for the III → I track. $\theta_{\rm sd,i} = 89.1°$, and $\epsilon = 3 \times 10^{-4}$.

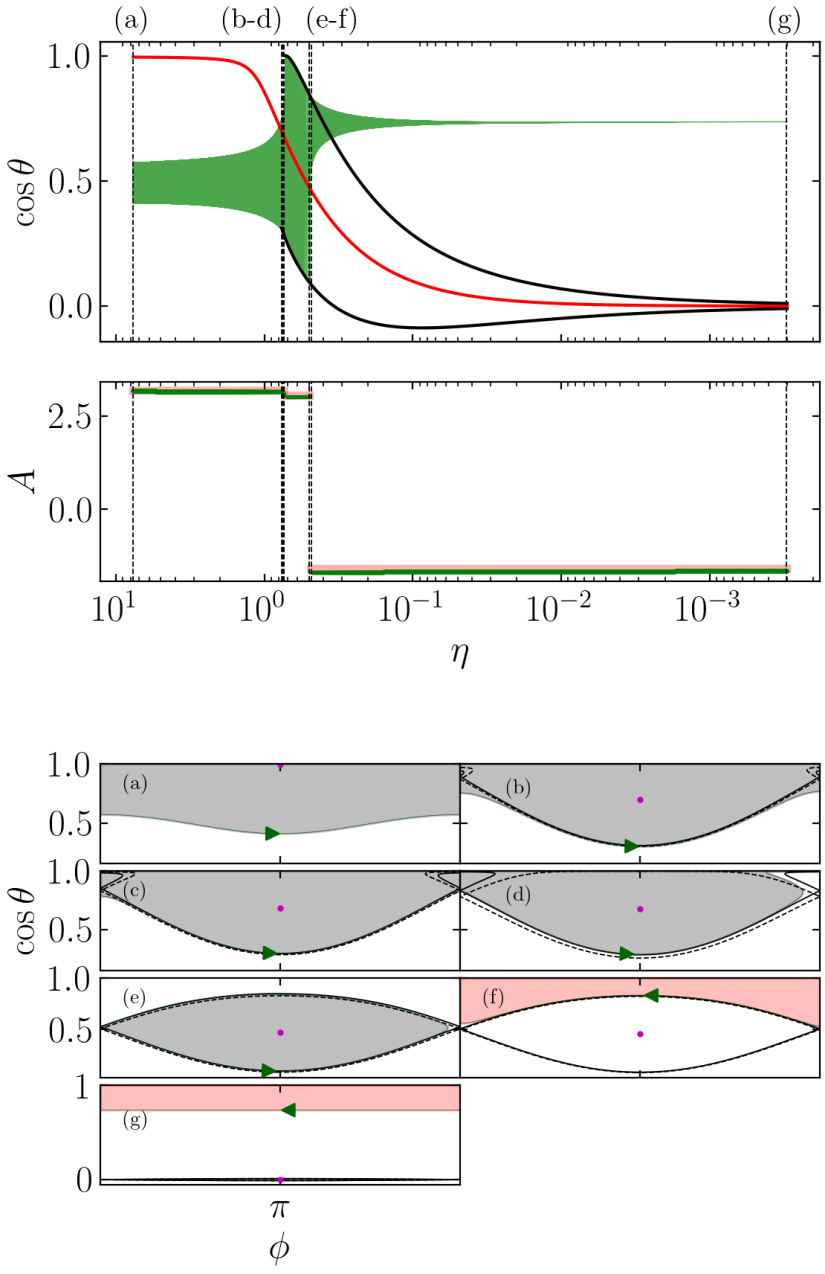

Figure 2.10: Same as Fig. 2.7 but for the III → II → I track. $\theta_{\rm sd,i} = 60°$, and $\epsilon = 3.14 \times 10^{-4}$. Two separatrix crossings are shown, in panels (c-d) and (e-f).

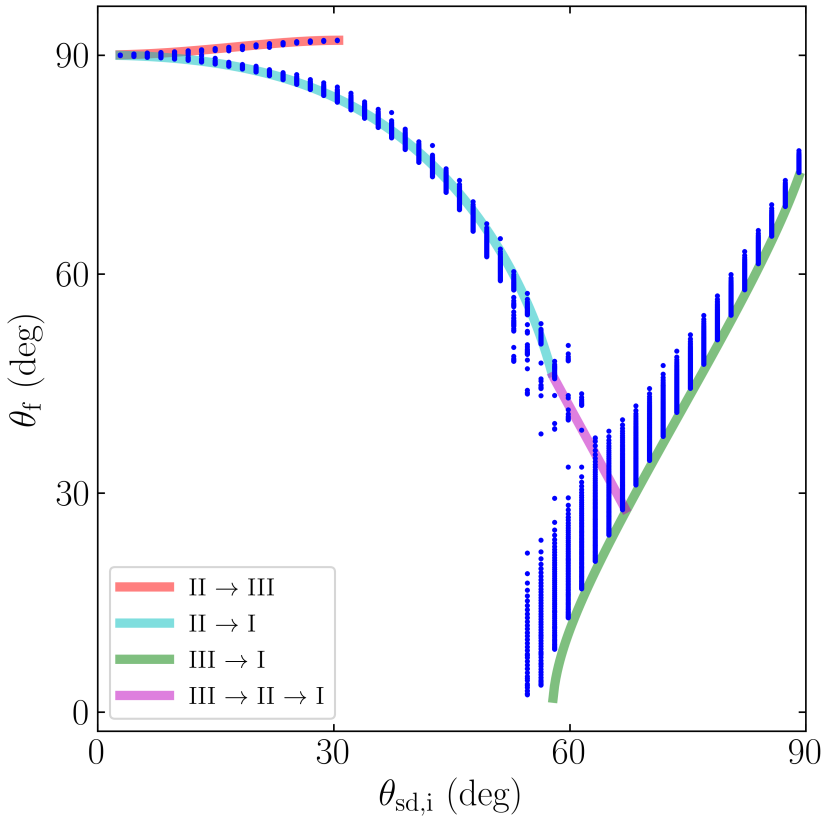

Figure 2.11: Same as Fig. 2.5 but for $\epsilon = 10^{-2.5}$ and restricting $\theta_{\rm sd,i} < 90^\circ$ (blue dots). The colored solid lines are analytical adiabatic results (same as shown in Fig. 2.5). A larger spread from the adiabatic tracks is observed in the numerical results due to the non-adiabaticity effect.

As ϵ increases further (see Fig. 2.12) but still marginally satisfies the weak adiabaticity criterion [Eq. (7.37)], the scatter in $\theta_{\rm f}$ continues to widen. The horizontal banded structure of the final obliquities is a consequence of even stronger phase sensitivity during separatrix crossing: trajectories cross the separatrix at similar phases evolve to similar final obliquities that only depend weakly on on $\theta_{\rm sd,i}$. Finally, in Fig. 2.12, the bottom edge of the data and the III → I track deviate very noticeably. This non-adiabatic effect is the result of the separatrix evolving significantly within the separatrix-crossing orbit, as the tracks computed in Section 2.3 assume that η is constant throughout the separatrix-crossing orbit.

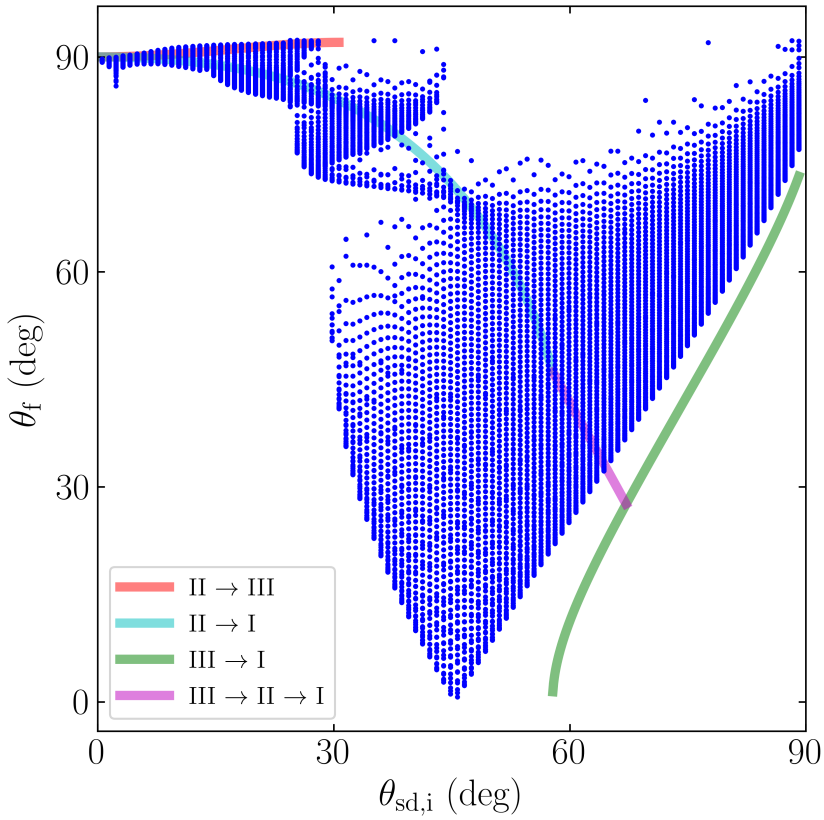

Figure 2.12: Same as Fig. 2.11 but for $\epsilon = 10^{-1.5}$ (i.e. larger non-adiabaticity effect). Some small resemblance to the adiabatic tracks remains, and the deviations appear to have a banded structure.

A sample trajectory following in the style of Fig. 2.7 but for $\epsilon = 0.3$ (violating even weak adiabaticity) is provided in Fig. 2.13. It is clear that the trajectory does not track the level curves of the Hamiltonian during each individual snapshot. This results from CS2 migrating more quickly than the trajectory can librate about CS2, violating the weak adiabaticity criterion.

2.4.2 Non-adiabatic Evolution: Result for $\epsilon \gtrsim \epsilon_{\rm c}$

In general, numerical calculations are needed to determine the non-adiabatic obliquity evolution ($\epsilon \gtrsim \epsilon_{\rm c}$). However, some analytical results can still be obtained when the obliquity change is small.

We start from Eq. (2.9), which governs the evolution of the spin axis in the rotating frame. We choose coordinate axes such that $\hat{\mathbf{l}} = \hat{\mathbf{z}}$ and $\hat{\mathbf{l}}_{\rm d} = \hat{\mathbf{z}}\cos I + \hat{\mathbf{x}}\sin I$, giving

$$\left(\frac{{\rm d}\hat{\mathbf{s}}}{{\rm d}\tau}\right)_{\rm rot} = \left[\left(\eta\cos I - \cos\theta\right)\hat{\mathbf{z}} + \eta\sin I\,\hat{\mathbf{x}}\right] \times \hat{\mathbf{s}}. \tag{2.32}$$

Defining $S = \hat{s}_{\rm x} + i\hat{s}_{\rm y}$, we find

$$\frac{{\rm d}S}{{\rm d}\tau} = i\left(\eta\cos I - \cos\theta\right)S - i\eta\sin I\cos\theta. \tag{2.33}$$

To proceed, we assume the obliquity is roughly constant, $\cos\theta \approx \cos\theta_{\rm i}$. Eq. (2.33) can then be solved explicitly, starting from the initial value $S(\tau_{\rm i})$:

$$S(\tau)e^{-i\Phi(\tau)} - S(\tau_{\rm i}) \simeq -i\sin I\cos\theta_{\rm i}\int_{\tau_{\rm i}}^{\tau}\eta(\tau')e^{-i\Phi(\tau')}\,{\rm d}\tau', \tag{2.34}$$

where

$$\Phi(\tau) \equiv \int_{\tau_{\rm i}}^{\tau}\left(\eta(\tau')\cos I - \cos\theta_{\rm i}\right)\,{\rm d}\tau'. \tag{2.35}$$

We now invoke the stationary phase approximation, so that $\Phi(\tau) \simeq \Phi(\tau_0) + (1/2)\ddot{\Phi}(\tau_0)(\tau - \tau_0)^2$, where τ_0 is determined by $\dot{\Phi} = 0$, occurring when $\eta_0 = \cos\theta_i/\cos I$. We then

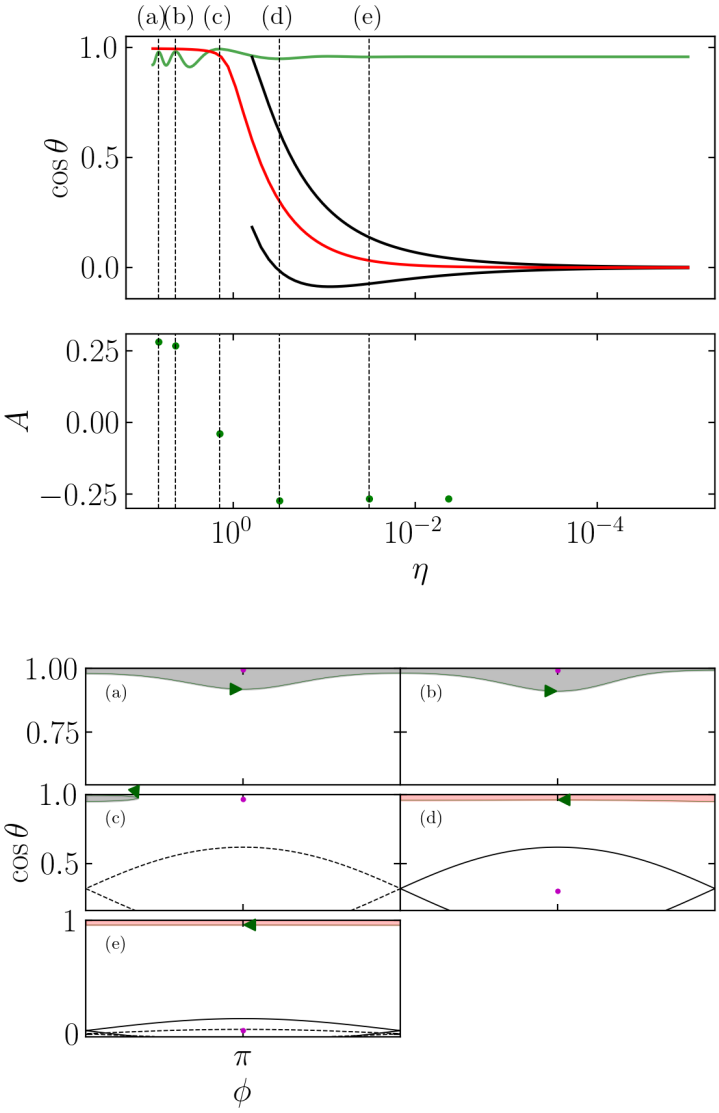

Figure 2.13: Same as Fig. 2.7 but for a nonadiabatic case, with $\epsilon = 0.3$. In the top panel, it is evident that the libration cycle about CS2 is unable to keep up with the swift migration of CS2 as η changes, decreasing the obliquity excitation compared to the adiabatic simulation. In the middle panel, the trajectory only undergoes six libration/circulation cycles before $\eta < 10^{-5}$, and the enclosed phase space area is clearly not conserved. In the bottom panel, we can see that individual trajectories do not lie along level curves of the Hamiltonian, as the Hamiltonian phase space changes quickly compared to the period of circulation cycles.

find, for $\tau \gg \tau_0$,

$$S(\tau)e^{-i\Phi(\tau)} - S(\tau_\mathrm{i}) \simeq -i\eta(\tau_0)\sin I\cos\theta_\mathrm{i}\, e^{-i\Phi(\tau_0)}\sqrt{\frac{2\pi}{i\ddot{\Phi}(\tau_0)}}. \tag{2.36}$$

Using $\dot{\eta} = -\epsilon\eta$ [Eq. (2.11)] and $\ddot{\Phi}(\tau_0) = \dot{\eta}(\tau_0)\cos I = -\epsilon\cos\theta_i$, we have

$$S(\tau)e^{-i\Phi(\tau)} - S(\tau_\mathrm{i}) \simeq -i^{3/2}\tan I(\cos\theta_\mathrm{i})^{3/2} e^{-i\Phi(\tau_0)}\sqrt{\frac{2\pi}{\epsilon}}. \tag{2.37}$$

The final obliquity θ_f is then given by

$$\sin\theta_\mathrm{f} \simeq \left|\sin\theta_i + e^{-i\varphi_0}\tan I(\cos\theta_\mathrm{i})^{3/2}\sqrt{\frac{2\pi}{\epsilon}}\right|, \tag{2.38}$$

where $\varphi_0 = \Phi(\tau_0) + \pi/4$ is a constant phase. If the initial obliquity is much smaller than the final obliquity ($\sin\theta_\mathrm{i} \ll \sin\theta_\mathrm{f}$), we obtain

$$\sin\theta_\mathrm{f} \simeq \sqrt{\frac{2\pi}{\epsilon}}\tan I(\cos\theta_\mathrm{i})^{3/2}. \tag{2.39}$$

This expression is valid only if $\cos\theta \approx \cos\theta_\mathrm{i}$ throughout the evolution. This corresponds to the limit where θ_f is not much larger than θ_i, which requires ϵ not to be too small. Numerically, this is consistent with the system being in the nonadiabatic regime $\epsilon \gtrsim \epsilon_\mathrm{c}$ (see Fig. 2.14).

The above calculation applies for a specific initial θ_i, but, as discussed at the beginning of Section 2.3.1, the initial spin orientation is more appropriately described by $\theta_\mathrm{sd,i}$ since $\eta_i \gg 1$. The correct way to predict the final obliquity for a given $\theta_\mathrm{sd,i}$ using Eq. (2.38) is somewhat subtle but yields good agreement with numerical results.

First consider the case with $\theta_\mathrm{sd,i} = 0$. This corresponds to a well-defined initial obliquity $\theta_i = I$ (more precisely, the initial condition is CS2). The final obliquity in this case, denoted θ_0f, is given by

$$\begin{aligned}\sin\theta_\mathrm{0f} &\simeq \sin I\left|1 + e^{-i\varphi_0}\sqrt{\frac{2\pi\cos I}{\epsilon}}\right|, \\ &\approx \sin I\sqrt{\frac{2\pi\cos I}{\epsilon}},\end{aligned} \tag{2.40}$$

where the second equality assumes $\sqrt{2\pi/\epsilon} \gg 1$. Fig. 2.14 shows the final obliquity as function of ϵ for $\theta_{\rm sd,i} = 0$ and $I = 5^\circ$. We see that the agreement between the numerical results and Eq. (2.40) is excellent. For $\epsilon \ll \epsilon_{\rm c}$, we find $\theta_{\rm f} \simeq 90^\circ$, in agreement with the result of adiabatic evolution (see Fig. 2.5).

When $\theta_{\rm sd,i} \neq 0$, we find that the final obliquity $\theta_{\rm f}$ spans a range of values for a given $\theta_{\rm sd,i}$, as can be seen in Fig. 2.15. The range can be described by

$$\left|\theta_{0\rm f} - \theta_{\rm sd,i}\right| \lesssim \theta_{\rm f} \lesssim \theta_{0\rm f} + \theta_{\rm sd,i}. \tag{2.41}$$

Eq. (2.41) can be understood as follows (see Fig. 2.16). In the beginning ($\eta = \eta_{\rm i} \gg 1$), the initial spin vector precesses around $\hat{\mathbf{l}}_{\rm d}$ on a cone with opening half-angle $\theta_{\rm sd,i}$ (more precisely, the cone is centered on CS2, which coincides with $\hat{\mathbf{l}}_{\rm d}$ as $\eta_{\rm i} \to \infty$). Note that for $\eta \gg 1$, the adiabaticity condition is easily satisfied: using $\theta_2 \simeq I + \eta^{-1} \sin I \cos I$ (see Section A.1), Eq. (2.19) gives $\omega_{\rm lib} \simeq \eta$ while Eq. (2.20) gives $|{\rm d}\theta_2/{\rm d}\tau| \simeq \left(\epsilon/\eta\right) \sin I \cos I \ll \omega_{\rm lib}$. As η decreases, the system will transition from being adiabatic to being nonadiabatic, since $\epsilon \gtrsim \epsilon_{\rm c}$. The evolution of the system can thus be decomposed into two phases: (i) when the evolution is adiabatic, the spin vector will precess around the slowly-moving CS2; (ii) when the evolution becomes nonadiabatic, the spin vector stops tracking the quickly-evolving CS2. During the adiabatic evolution of phase (i), the angle between CS2 and the spin vector is approximately unchanged due to conservation of phase space area[3]. Once the evolution enters phase (ii), the precession axis quickly (on timescale $\ll 1/\omega_{\rm lib}$) changes to $\hat{\mathbf{l}}$ (as η decreases to $\eta_{\rm f} \ll 1$). Precession about $\hat{\mathbf{l}}$ does not change the obliquity, so the range of obliquities at the end of phase (i) is frozen in as the range of final obliquities. We refer to this two-phase evolution as *partial adiabatic*

[3]This approximation assumes sufficiently small $\theta_{\rm sd,i}$ such that libration about CS2 remains approximately circular throughout phase (i) (initially, when $\eta \to \infty$, all librations are circular about $\hat{\mathbf{l}}_{\rm d}$). This assumption breaks down when $\theta_{\rm sd,i}$ is sufficiently large that librating orbits become noncircular as η decreases before the end of phase (i) (Fig. 2.3 illustrates that the libration cycles farther from CS2, corresponding to a larger $\theta_{\rm sd,i}$, are less circular for a given η). This causes the deviation of the numerical results in Fig. 2.15 from Eq. (2.41) for $\theta_{\rm sd,i} \gtrsim 45^\circ$.

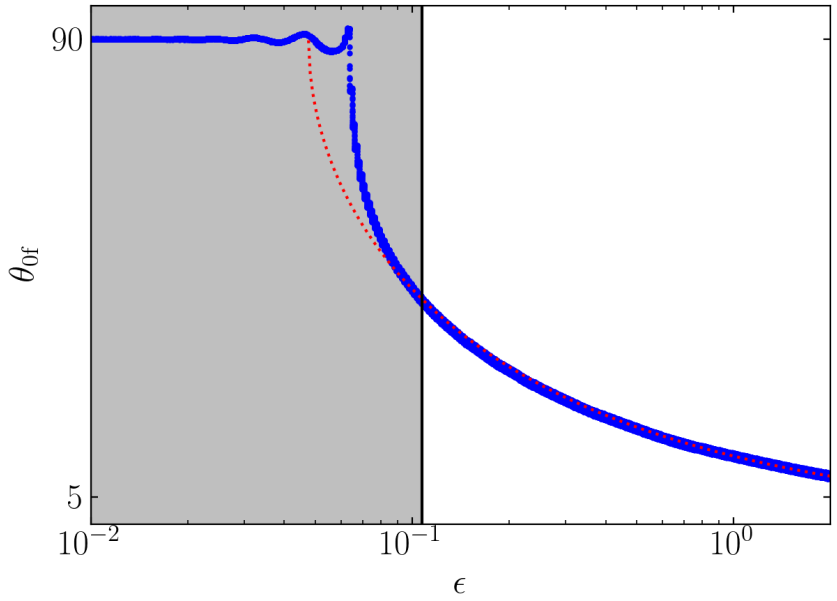

Figure 2.14: Final obliquity θ_f as a function of ϵ for $\theta_{sd,i} = 0$ and $I = 5°$. The shaded area, bordered by the black line, corresponds to the adiabatic regime estimated by Eq. (7.37). The blue dots are numerical results, and the red dashed line corresponds to Eq. (2.40), which is in good agreement with numerical results for $\epsilon > \epsilon_c \approx 0.1$ (the nonadiabatic regime). Note that $\theta_f \simeq 90°$ in the adiabatic regime ($\epsilon \ll \epsilon_c$).

resonance advection.

Fig. 2.15 shows the numerical result of θ_f vs $\theta_{sd,i}$ for $I = 5°$ and $\epsilon = 0.3$. We see that Eq. (2.41) provides good lower and upper bounds of the final obliquity for $\theta_{sd,i} \lesssim 45°$ (see footnote 3).

2.5 Summary

In this paper, we have studied the excitation of planetary obliquities due to gravitational interaction with an exterior, dissipating (mass-losing) protoplanetary disk. Obliquity excitation occurs as the system passes through a secular reso-

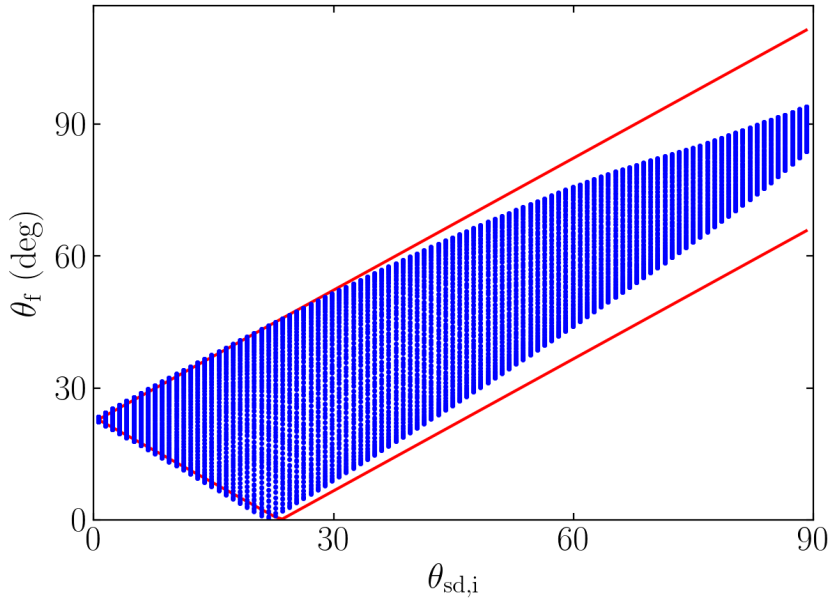

Figure 2.15: Final obliquity $\theta_{\rm f}$ vs $\theta_{\rm sd,i}$ for $I = 5^\circ$ and $\epsilon = 0.3$ (firmly in the nonadiabatic regime). The blue dots represent numerical results, and the two red lines show the analytical lower and upper bounds given by Eq. (2.41).

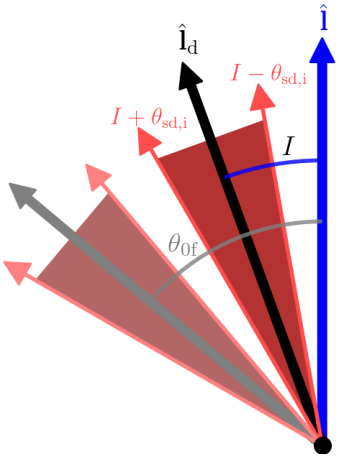

Figure 2.16: Schematic picture for understanding nonadiabatic obliquity evolution when $\theta_{\rm sd,i} > 0$ assuming $\eta_{\rm i} \gg 1$. The figure shows a projection onto the plane containing both $\hat{\mathbf{l}}$ and $\hat{\mathbf{l}}_{\rm d}$. When $\theta_{\rm sd,i} = 0$, the initial spin vector points along $\hat{\mathbf{l}}_{\rm d}$ and evolves into the final spin vector (grey), which has obliquity $\theta_{0\rm f}$ [Eq. (2.40)]. When $\theta_{\rm sd,i} \neq 0$, the set of initial conditions for the spin vector forms a cone (solid red area) centered on $\hat{\mathbf{l}}_{\rm d}$ with opening half-angle $\theta_{\rm sd,i}$. Under nonadiabatic evolution, the set of final spin vectors forms a new cone, still with opening half-angle $\theta_{\rm sd,i}$, centered on $\theta_{0\rm f}$ (light red area).

nance between spin precession and orbital (nodal) precession. This scenario was recently studied by Millholland and Batygin [2019], who focused on the special case of small initial obliquities. In contrast, we consider arbitrary initial misalignment angles in this paper, motivated by the fact that planet formation through core accretion can lead to a wide range of initial spin orientations. We present our result as a mapping from $\theta_{\rm sd,i}$ to $\theta_{\rm f}$, where $\theta_{\rm sd,i}$ is the initial misalignment angle between the planet's spin axis and the disk's orbital angular momentum axis, and $\theta_{\rm f}$ is the final planetary obliquity. We have derived analytical results that capture the behavior of this mapping in both the adiabatic and nonadiabatic limits:

1. In the adiabatic limit (i.e. the disk dissipates at a sufficiently slow rate), we reproduce the known result $\theta_{\rm f} \simeq 90^\circ$ for $\theta_{\rm sd,i} \simeq 0$. We demonstrate (via numerical calculation and analytical argument) the dual-valued behavior of $\theta_{\rm f}$ for nonzero $\theta_{\rm sd,i}$ (see Fig. 2.5). We show for the first time that both the final $\theta_{\rm f}$ values and the probabilities of achieving each value can be understood analytically via careful accounting of adiabatic invariance and separatrix crossing dynamics.
2. As the disk dissipates more rapidly, the adiabatic condition [Eq. (7.37)] breaks down, we find that a broad range of final obliquities can be reached for a given $\theta_{\rm sd,i}$ (see Fig. 2.15). We understand this result via the novel concept of partial adiabatic resonance advection and provide an analytical expression of the bounds on $\theta_{\rm f}$ in Eq. (2.41).

As noted in Section 2.1, while in this paper we have examined a specific scenario of generating/modifying planetary obliquities from planet-disk interactions, the dynamical problem have studied is more general [Colombo, 1966, Peale, 1969, 1974, Ward, 1975, Henrard and Murigande, 1987]. Our work goes beyond these previous works and provides the most general solution to the evolution of "Colombo's

top" as the system evolves from the "weak spin-orbit coupling" regime ($\eta \gg 1$) to the "strong spin-orbit coupling" regime ($\eta \ll 1$). The new analytical results presented in this paper can be adapted to other applications.

Concerning the production of planetary obliquity with a dissipating disk, when there are multiple planets in a system, the nodal precession rate g for the planet of interest never decays below the Laplace-Lagrange rate driven by planet-planet secular interactions [Millholland and Batygin, 2019]. Therefore, η has a minimum value at late times. This does not affect the methodology of our analysis, but can affect the detailed results. For example, the adiabaticity criterion must be modified slightly as $\mathrm{d}\ln\eta/\mathrm{d}t$ is no longer constant but asymptotes to zero as η decreases; the planet may never undergo separatrix crossing if their $\eta_\star$ (which depends on $\theta_{\mathrm{sd,i}}$) in the absence of the companions is too small; the planetary obliquity will oscillate even when the disk has fully evaporated (as $\hat{\mathbf{l}}$ is no longer constant). The spin dynamics can be even more complex if the two planets are in mean motion resonance [e.g. Millholland and Laughlin, 2019].

CHAPTER 3

DYNAMICS OF COLOMBO'S TOP: TIDAL DISSIPATION AND RESONANCE CAPTURE, WITH APPLICATIONS TO OBLIQUE SUPER-EARTHS, ULTRA-SHORT-PERIOD PLANETS AND INSPIRALING HOT JUPITERS

Originally published in:
Yubo Su and Dong Lai. Dynamics of Colombo's Top: Tidal dissipation and resonance capture, with applications to oblique super-Earths, ultra-short-period planets and inspiraling hot Jupiters. *MNRAS*, 509(3):3301–3320, November 2021. ISSN 0035-8711. doi: 10.1093/mnras/stab3172

3.1 Introduction

It is well recognized that the obliquity of a planet, the angle between the spin and orbital axes, likely reflects its dynamical history. In our Solar System, planetary obliquities (hereafter just "obliquities") range from 3.1° for Jupiter to 26.7° for Saturn to 98° for Uranus. The obliquities of exoplanets are challenging to measure, and so far only loose constraints have been obtained for the obliquity of a faraway ($\gtrsim 50$ AU) planetary-mass companion [Bryan et al., 2020]. Nevertheless, there are prospects for better constraints on exoplanetary obliquities in the coming years, such as using high-resolution spectroscopy to measure $v \sin i$ for planetary rotation [Snellen et al., 2014, Bryan et al., 2018] and using high-precision photometry to measure the asphericity of a planet [Seager and Hui, 2002]. Substantial obliquities are of increasing theoretical interest for their proposed role in explaining peculiar thermal phase curves [see e.g. Adams et al., 2019, Ohno and Zhang, 2019], in enhancing tidal dissipation in hot Jupiters [Millholland and Laughlin, 2018] and super Earths [Millholland and Laughlin, 2019], and in the formation of ultra-short-period planets [USPs; Millholland and Spalding, 2020].

While nonzero obliquities are sometimes attributed to one or many giant impacts/collisions [e.g. Safronov and Zvjagina, 1969, Benz et al., 1989, Korycansky et al., 1990, Dones and Tremaine, 1993, Morbidelli et al., 2012, Li and Lai, 2020, Li et al., 2021], some studies suggest that large planetary obliquities may be produced by spin-orbit resonances. In this scenario, a rotating planet is subjected to a gravitational torque from its host star, making its spin axis precess around its orbital (angular momentum) axis. At the same time, the orbital axis precesses around another fixed axis under the gravitational influence of other masses in the system, e.g. additional planets or a protoplanetary disk. When the two precession frequencies become comparable, a resonance can occur that excites the obliquity to large values. This model is known as "Colombo's Top" after the seminal work of Colombo [1966], and subsequent works have investigated the rich dynamics of this system [Peale, 1969, 1974, Ward, 1975, Henrard and Murigande, 1987]. Such resonances have been invoked to explain the obliquities of both the Solar System gas giants [Ward and Hamilton, 2004, Hamilton and Ward, 2004, Ward and Canup, 2006, Vokrouhlickỳ and Nesvornỳ, 2015, Saillenfest et al., 2020, 2021] and the ice giants [Rogoszinski and Hamilton, 2020].

In a previous paper [Su and Lai, 2020, hereafter Paper I], we presented a systematic and general investigation of the dynamics of Colombo's Top when the two precession frequencies of the system evolve through a commensurability. We obtained a semi-analytic mapping between the (arbitrary) planetary spin orientation and the final obliquity after a resonance encounter. We applied our results to investigate the generation of exoplanetary obliquities via a dissipating protoplanetary disk. However, our model did not consider the effect of additional torques in the system. In particular, tidal dissipation in the planet can cause the planet's spin frequency to approach its orbital frequency and drive the planet's spin axis towards its orbital axis, complicating the evolution of Colombo's Top [Fabrycky

et al., 2007, Levrard et al., 2007, Peale, 2008]. In this paper, we extend these previous works to present a comprehensive study on how tidal dissipation influences the equilibria (called "Cassini States") of the system and drive its long-term evolution. Our new results (summarized in Section 3.6) include a stability analysis of tide-modified Cassini States and a novel, analytic description/calculation of the resonance encounter process. We apply our general theoretical results to assess how obliquity tides may affect different types of exoplanetary systems.

Our paper is organized as follows. In Section 3.2, we briefly review the basic setup and non-dissipative dynamics of Colombo's Top. In Section 3.3, we investigate the effect of adding a simple alignment torque to Colombo's Top. The resulting dynamics captures the essential behavior that emerges due to tidal dissipation. In Section 3.4, we solve for the dynamics of the system including the full effect of tidal dissipation. In Section 3.5, we apply our results to three exoplanetary systems/scenarios of interest: (i) a super Earth with an exterior companion, (ii) the formation of USPs via obliquity tides, and (iii) the rapid orbital decay of the hot Jupiter WASP-12b. We summarize and discuss in Section 3.6.

3.2 Spin Evolution Equations and Cassini States: Review

In this section, we briefly review the spin dynamics of a planet in the presence of a distant perturber and introduce our notations; see Paper I for more details. We consider a star of mass $M_\star$ hosting an inner oblate planet of mass m and radius R on a circular orbit with semi-major axis a and an outer perturber of mass $m_{\rm p}$ on a circular orbit with semi-major axis $a_{\rm p}$. The two orbits are mutually inclined by the angle I. Denote $\mathbf{S}$ the spin angular momentum and $\mathbf{L}$ the orbital angular momentum of the planet, and $\mathbf{L}_{\rm p}$ the angular momentum of the perturber. The

corresponding unit vectors are $\hat{\mathbf{s}} \equiv \mathbf{S}/S$, $\hat{\mathbf{l}} \equiv \mathbf{L}/L$, and $\hat{\mathbf{l}}_\mathrm{p} \equiv \mathbf{L}_\mathrm{p}/L_\mathrm{p}$. The spin axis $\hat{\mathbf{s}}$ of the planet tends to precess around its orbital (angular momentum) axis $\hat{\mathbf{l}}$, driven by the gravitational torque from the host star acting on the planet's rotational bulge. On the other hand, $\hat{\mathbf{l}}$ and $\hat{\mathbf{l}}_\mathrm{p}$ precess around each other due to gravitational interactions. Assuming $S \ll L$, the equations of motion for $\hat{\mathbf{s}}$ and $\hat{\mathbf{l}}$ are

$$\frac{\mathrm{d}\hat{\mathbf{s}}}{\mathrm{d}t} = \omega_\mathrm{sl} \left(\hat{\mathbf{s}} \cdot \hat{\mathbf{l}}\right) \left(\hat{\mathbf{s}} \times \hat{\mathbf{l}}\right) \equiv \alpha \left(\hat{\mathbf{s}} \cdot \hat{\mathbf{l}}\right) \left(\hat{\mathbf{s}} \times \hat{\mathbf{l}}\right), \tag{3.1}$$

$$\frac{\mathrm{d}\hat{\mathbf{l}}}{\mathrm{d}t} = \omega_\mathrm{lp} \left(\hat{\mathbf{l}} \cdot \hat{\mathbf{l}}_\mathrm{p}\right) \left(\hat{\mathbf{l}} \times \hat{\mathbf{l}}_\mathrm{p}\right) \equiv -g \left(\hat{\mathbf{l}} \times \hat{\mathbf{l}}_\mathrm{p}\right), \tag{3.2}$$

where

$$\omega_\mathrm{sl} \equiv \alpha = \frac{3GJ_2 m R^2 M_\star}{2a^3 \mathscr{I} \Omega_\mathrm{s}} = \frac{3k_q}{2k} \frac{M_\star}{m} \left(\frac{R}{a}\right)^3 \Omega_\mathrm{s}, \tag{3.3}$$

$$\omega_\mathrm{lp} \equiv -\frac{g}{\cos I} = \frac{3m_\mathrm{p}}{4M_\star} \left(\frac{a}{a_\mathrm{p}}\right)^3 n. \tag{3.4}$$

In Eq. (4.4), Ω_s is the spin frequency of the inner planet, $\mathscr{I} = kmR^2$ (with k the normalized moment of inertia, often notated as C_N) is its moment of inertia and $J_2 = k_\mathrm{q}\Omega_\mathrm{s}^2(R^3/Gm)$ (with k_q a constant, related to the hydrostatic Love number k_2 by $k_\mathrm{q} = k_2/3$) is its rotation-induced (dimensionless) quadrupole moment [for a fluid body with uniform density, $k = 0.4, k_\mathrm{q} = 0.5$; for the Earth, $k \simeq 0.331$ and $k_\mathrm{q} \simeq 0.31$; for Jupiter, $k \simeq 0.27$ and $k_\mathrm{q} \simeq 0.18$ [e.g. Groten, 2004, Lainey, 2016]]. In other studies, $3k_\mathrm{q}/2k$ is often notated as $k_2/2C_\mathrm{N}$ [e.g. Millholland and Batygin, 2019]. In Eq. (3.4), $n \equiv \sqrt{GM_\star/a^3}$ is the inner planet's orbital mean motion, and we have assumed $a_\mathrm{p} \gg a$ and included only the leading-order (quadrupole) interaction between the inner planet and perturber (Section 3.5.2 discusses modifications to Eq. 3.4 when $a_\mathrm{p} \gtrsim a$). Eq. (3.2) neglects the back-reaction torque on $\hat{\mathbf{l}}$ from $\hat{\mathbf{s}}$; this is justified since $L \gg S$ (see Anderson and Lai, 2018 for the case when $L \sim S$). In Eq. (4.4) (and throughout Sections 3.2–3.4), we assume $L_\mathrm{p} \gg L$ so that $\hat{\mathbf{l}}_\mathrm{p}$ is a constant (Section 3.5.3 discusses the case of $L \simeq L_\mathrm{p}$). Following the standard notations, we have defined $\alpha = \omega_\mathrm{sl}$ and $g \equiv -\omega_\mathrm{1p} \cos I$ [e.g. Colombo, 1966].

As in Paper I, we combine Eqs. (4.2)–(3.2) into a single equation by transforming into a frame rotating about $\hat{\mathbf{l}}_\mathrm{p}$ with frequency g. In this frame, $\hat{\mathbf{l}}_\mathrm{p}$ and $\hat{\mathbf{l}}$ are both fixed, and $\hat{\mathbf{s}}$ evolves as

$$\left(\frac{\mathrm{d}\hat{\mathbf{s}}}{\mathrm{d}t}\right)_\mathrm{rot} = \alpha\left(\hat{\mathbf{s}}\cdot\hat{\mathbf{l}}\right)\left(\hat{\mathbf{s}}\times\hat{\mathbf{l}}\right) + g\left(\hat{\mathbf{s}}\times\hat{\mathbf{l}}_\mathrm{p}\right). \tag{3.5}$$

We choose the coordinate system such that $\hat{\mathbf{z}} = \hat{\mathbf{l}}$ and $\hat{\mathbf{l}}_\mathrm{p}$ lies in the $\hat{\mathbf{x}}$-$\hat{\mathbf{z}}$ plane. We describe $\hat{\mathbf{s}}$ in spherical coordinates using the polar angle θ, the planet's obliquity, and ϕ, the precessional phase of $\hat{\mathbf{s}}$ about $\hat{\mathbf{l}}$, defined so that when $\phi = 0°$, $\hat{\mathbf{l}}_\mathrm{p}$ and $\hat{\mathbf{s}}$ are on opposite sides of $\hat{\mathbf{l}}$.

The equilibria of Eq. (3.5) are referred to as *Cassini States* [CSs; Colombo, 1966, Peale, 1969]. We follow the notation of Paper I and introduce the parameter

$$\eta \equiv -\frac{g}{\alpha} = \frac{1}{2}\frac{k}{k_\mathrm{q}}\frac{m_\mathrm{p} m}{M_\star^2}\left(\frac{a}{a_\mathrm{p}}\right)^3\left(\frac{a}{R}\right)^3\frac{n}{\Omega_\mathrm{s}}\cos I. \tag{3.6}$$

For a given value of η, there can be either two or four CSs, all of which require $\hat{\mathbf{s}}$ lie in the plane of $\hat{\mathbf{l}}$ and $\hat{\mathbf{l}}_\mathrm{p}$. In the standard nomenclature, CSs 1, 3, and 4 have $\theta < 0$, implying that $\hat{\mathbf{s}}$ and $\hat{\mathbf{l}}_\mathrm{p}$ are on opposite sides of $\hat{\mathbf{l}}$, while CS2 has $\theta > 0$, implying that $\hat{\mathbf{s}}$ and $\hat{\mathbf{l}}$ are on the same side of $\hat{\mathbf{l}}$. We depart from the standard convention and simply label the CSs using the polar angles θ and ϕ (with $\theta \in [0, \pi]$): Figure 3.1 shows the CS obliquities as a function of η. CS1 and CS4 do not exist when $\eta > \eta_\mathrm{c}$, where

$$\eta_\mathrm{c} \equiv \left(\sin^{2/3} I + \cos^{2/3} I\right)^{-3/2}. \tag{3.7}$$

The Hamiltonian corresponding to Eq. (3.5) is

$$\begin{aligned} H &= -\frac{\alpha}{2}\left(\hat{\mathbf{s}}\cdot\hat{\mathbf{l}}\right)^2 - g\left(\hat{\mathbf{s}}\cdot\hat{\mathbf{l}}_\mathrm{p}\right) \\ &= -\frac{\alpha}{2}\cos^2\theta - g\left(\cos\theta\cos I - \sin I\sin\theta\cos\phi\right). \end{aligned} \tag{3.8}$$

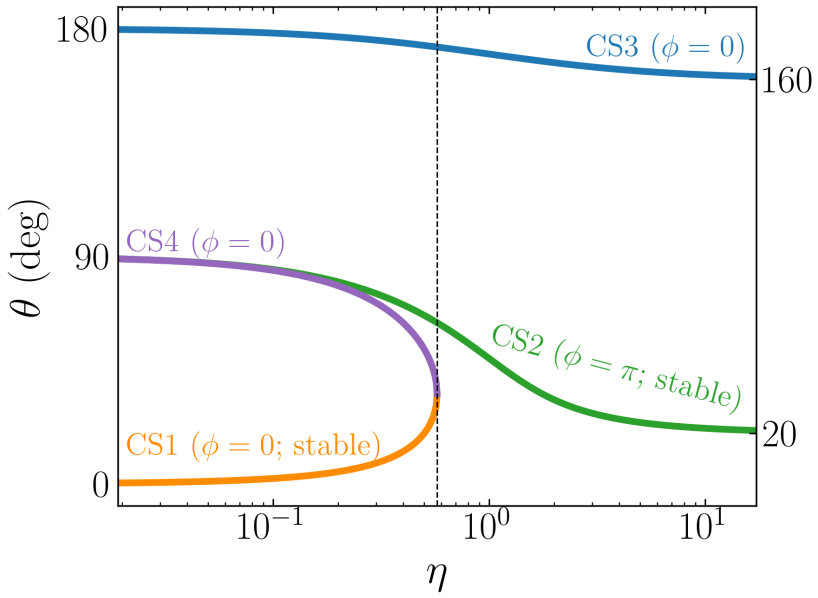

Figure 3.1: Cassini State obliquities θ as a function of $\eta \equiv -g/\alpha$ (Eq. 8.5) for $I = 20°$. The vertical dashed line denotes η_c, where the number of Cassini States changes from four to two (Eq. 3.7). The y-axis labels on the right of the plot show the asymptotic obliquities for CS2 and CS3, I and $180° - I$ respectively. Note that θ does not follow the standard convention (e.g. Colombo, 1966, Paper I) and is simply the angle between $\hat{\mathbf{s}}$ and $\hat{\mathbf{l}}$, while $\phi = 0$ corresponds to $\hat{\mathbf{s}}$ and $\hat{\mathbf{l}}_p$ being on opposite sides of $\hat{\mathbf{l}}$. While CSs 1–3 are "dynamically" stable, only CS1 and CS2 are stable and attracting in the presence of the spin-orbit alignment torque (see Section 3.3.2).

Here, $\cos\theta$ and ϕ form a canonically conjugate pair of variables. Figure 3.2 shows the level curves of this Hamiltonian for $I = 20°$, for which $\eta_c \approx 0.574$ (Eq. 3.7). When $\eta < \eta_c$, CS4 exists and is a saddle point. The infinite-period orbits originating and ending at CS4 form the *separatrix* and divide phase space into three zones. The angle ϕ librates for trajectories in zone II and circulates for trajectories in zones I and III. On the other hand, when $\eta > \eta_c$, the separatrix is absent and all trajectories circulate. When the separatrix exists, we divide it into two curves: $\mathscr{C}_+$, the boundary between zones I and II, and $\mathscr{C}_-$, the boundary between zones II and III.

3.3 Spin Evolution with Alignment Torque

In this section, we consider a simplified dissipative torque that isolates the important new phenomenon presented in this paper. We assume that the spin magnitude of the planet is constant, so α and g are both fixed, while the spin orientation $\hat{\mathbf{s}}$ experiences an alignment torque towards $\hat{\mathbf{l}}$ on the alignment timescale $t_{\rm al}$:

$$\left(\frac{d\hat{\mathbf{s}}}{dt}\right)_{\rm tide} = \frac{1}{t_{\rm al}}\hat{\mathbf{s}} \times \left(\hat{\mathbf{l}} \times \hat{\mathbf{s}}\right). \tag{3.9}$$

The full equations of motion for $\hat{\mathbf{s}}$ in the coordinates θ and ϕ can be written as

$$\frac{d\theta}{dt} = -g \sin I \sin\phi - \frac{1}{t_{\rm al}} \sin\theta, \tag{3.10}$$

$$\frac{d\phi}{dt} = -\alpha\cos\theta - g\left(\cos I + \sin I \cot\theta \cos\phi\right). \tag{3.11}$$

3.3.1 Modified Cassini States

If the alignment torque is weak ($|g|\, t_{\rm al} \gg 1$), then the fixed points of Eqs. (3.10)–(3.11) are slightly modified CSs. To leading order, all of the CS obliquities $\theta_{\rm cs}$ are

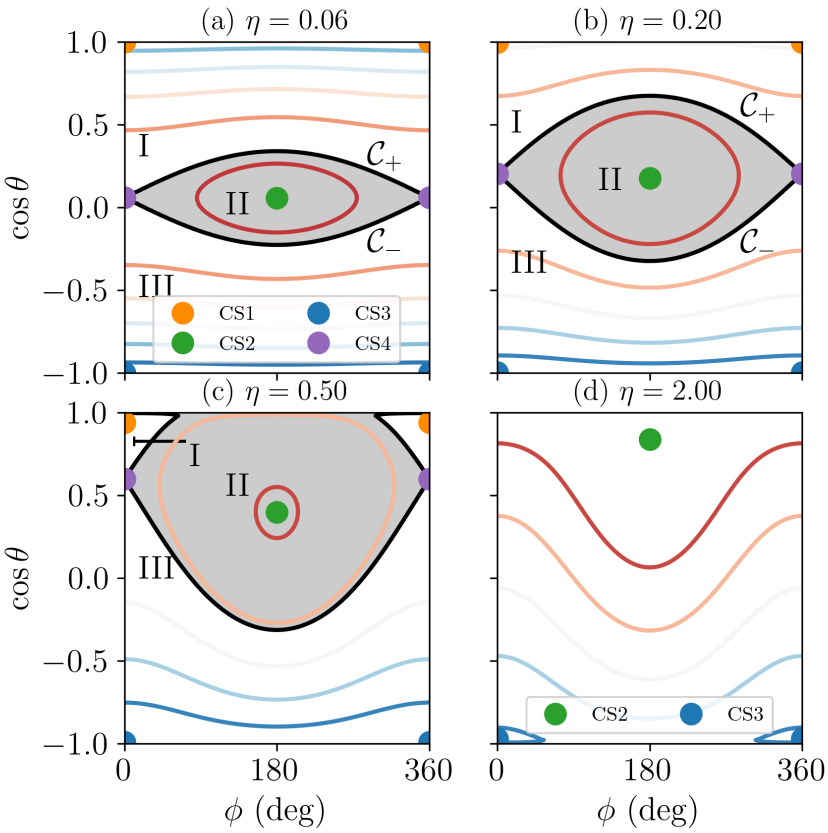

Figure 3.2: Level curves of the Hamiltonian (Eq. 3.8) for $I = 20°$, for which $\eta_c \approx 0.57$ (Eq. 3.7). For $\eta < \eta_c$, there are four Cassini States (labeled), while for $\eta > \eta_c$ there are only two. In the former case, the existence of a *separatrix* (solid black lines) separates phase space into three numbered zones (I/II/III, labeled). We denote the upper and lower legs of the separatrix by $\mathscr{C}_\pm$ respectively, as shown in the upper two panels.

unchanged while the azimuthal angle $\phi_{\rm cs}$ for each CS now satisfies

$$\sin\phi_{\rm cs} = \frac{\sin\theta_{\rm cs}}{\sin I\,|g|\,t_{\rm al}}. \tag{3.12}$$

We can see that if $t_{\rm al}$ is longer than the critical alignment timescale $t_{\rm al,c}$, given for a particular $\theta_{\rm cs}$ by

$$t_{\rm al,c} \equiv \frac{\sin\theta_{\rm cs}}{|g|\sin I}, \tag{3.13}$$

then Eq. (3.12) will always have solutions for $\phi_{\rm cs}$, and the alignment torque does not change the number of fixed points of the system. If $t_{\rm al}$ is decreased below $t_{\rm al,c} \sim |g\sin I|^{-1}$, CS2 and CS4 cease to be fixed points when $\eta \lesssim 1$ [as noted in Levrard et al., 2007, Fabrycky et al., 2007], as $\theta_{\rm cs} \sim 90^\circ$ for these (see Fig. 3.1). On the other hand, the other CSs have small $\sin\theta_{\rm cs}$ and are only slightly modified. Figure 3.3 shows the obliquity and azimuthal angle for each of the CSs when $\eta = 0.2$, obtained via numerical root finding of Eqs. (3.10–3.11), where it can be seen that CS2 and CS4 collide and annihilate when $t_{\rm al}$ reaches $t_{\rm al,c}$. The phase shifts $\phi_{\rm cs}$ for CS2 and CS4 for $t_{\rm al} > t_{\rm al,c}$ can be predicted to good accuracy using Eq. (3.12) and $\theta_{\rm cs} \approx \pi/2 - \eta\cos I \approx 79^\circ$ [Su and Lai, 2020]; these are shown as the dashed lines in the bottom panel of Fig. 3.3. For the remainder of this section, we will consider the case where $t_{\rm al} \gg t_{\rm al,c}$ and the CSs only differ slightly from their unmodified locations.

3.3.2 Linear Stability Analysis

We next seek to characterize the stability of small perturbations about each of the CSs in the presence of the weak alignment torque. We can linearize Eqs. (3.10–

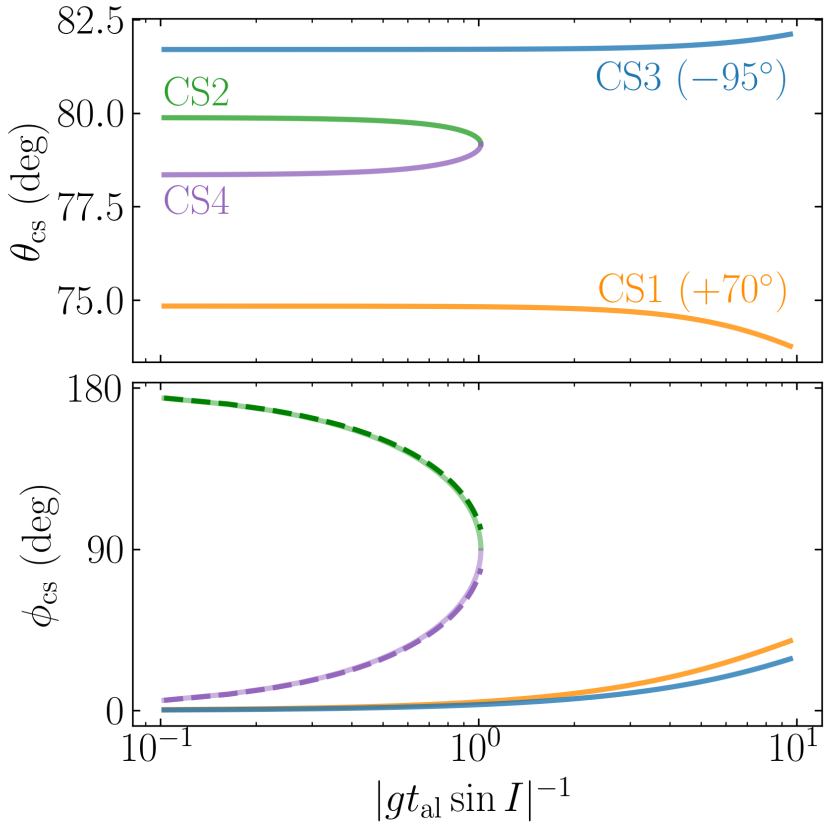

Figure 3.3: Modified CS obliquities (top) and azimuthal angles (bottom) for $I = 20°$ and $\eta = 0.2$, where the CS1 and CS3 obliquities have been offset (as labeled) to improve clarity of the plot. In both panels, the solid lines give the result when applying a numerical root finding algorithm to the full equations of motion, Eqs. (3.10–3.11), while the dotted lines in the bottom panel give the CS2 and CS4 azimuthal angles according to Eq. (3.12). At $|gt_{\rm al}\sin I| = 1$, CS2 and CS4 collide and annihilate (see Eq. 3.13).

3.11) about a shifted CS, yelding

$$\frac{\mathrm{d}}{\mathrm{d}t}\begin{bmatrix}\Delta\theta\\ \Delta\phi\end{bmatrix} = \begin{bmatrix}-\frac{\cos\theta}{t_{\rm al}} & -g\sin I\cos\phi\\ \alpha\sin\theta + g\frac{\sin I\cos\phi}{\sin^2\theta} & 0\end{bmatrix}_{\rm cs}\begin{bmatrix}\Delta\theta\\ \Delta\phi\end{bmatrix}, \tag{3.14}$$

where the "cs" subscript indicates evaluating at a CS, $\Delta\theta = \theta - \theta_{\rm cs}$, and $\Delta\phi = \phi - \phi_{\rm cs}$. The eigenvalues λ of Eq. (3.14) satisfy the equation

$$0 = \left(\lambda + \frac{\cos\theta_{\rm cs}}{t_{\rm al}}\right)\lambda - \lambda_0^2, \tag{3.15}$$

where

$$\lambda_0^2 \equiv \left(\alpha\sin\theta_{\rm cs} + g\sin I\csc^2\theta_{\rm cs}\cos\phi_{\rm cs}\right)\left(-g\sin I\cos\phi_{\rm cs}\right). \tag{3.16}$$

When $t_{\rm al}$ is large, we can simplify Eq. (3.15) to

$$\lambda \approx -\frac{\cos\theta_{\rm cs}}{t_{\rm al}} \pm \sqrt{\lambda_0^2}. \tag{3.17}$$

The stability of a CS depends on the real part of λ in Eq. (3.17). Equation (3.17) λ_0^2 is a generalization of Eq. (A4) in Paper I and generally has the same behavior: it is negative for CSs 1–3 and positive for CS4, as shown in Fig. 3.4. Thus, CS4 is always "dynamically" unstable (i.e. unstable even in the limit of $t_{\rm al} \to \infty$), as there will always be at least one positive solution for λ. On the other hand, CSs 1–3 are dynamically stable, and their overall stabilities in the presence of the alignment torque are determined by the sign of $\cos\theta_{\rm cs}$. Using Fig. 3.1, we conclude that CS1 and CS2 are stable and attracting while trajectories near CS3 are driven away by the alignment torque. These calculations quantify the results long used in the literature [e.g. Ward, 1975, Fabrycky et al., 2007].

3.3.3 Spin Obliquity Evolution Driven by Alignment Torque

With the above results, we are equipped to ask questions about the dynamics of Eqs. (3.10–3.11): what is the long-term evolution of $\hat{\mathbf{s}}$ for a general initial $\hat{\mathbf{s}}_{\rm i}$?

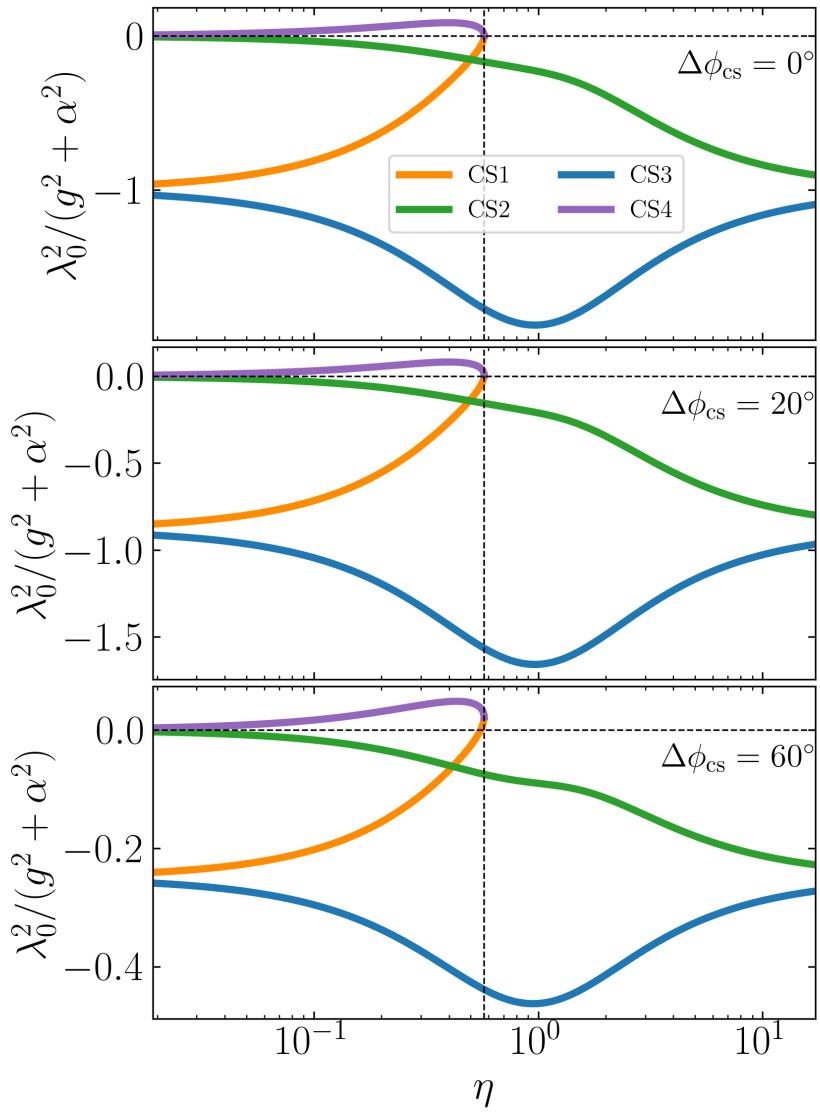

Figure 3.4: λ_0^2 (Eq. 3.16) as a function of η for the four CSs, for three different values of the shift in $\phi_{\rm cs}$ (e.g. for $\Delta\phi_{\rm cs} = 60°$, the phase angles are $\phi_{\rm cs} = 120°$ for CS2 and $\phi_{\rm cs} = 60°$ for CSs 1, 3, and 4). The values of $\Delta\phi_{\rm cs}$ are labeled ($\Delta\phi_{\rm cs} = 0$ corresponds to the unmodified CSs).

For $\eta > \eta_c$, the only stable (and attracting) spin state is CS2, and all initial conditions will evolve asymptotically towards it.

For $\eta < \eta_c$, both CS1 and CS2 are stable (assuming the alignment torque is sufficiently weak that CS2 remains a fixed point; see Section 3.3.1), and spin evolution may involve separatrix crossing. To explore the fate of various initial $\hat{\mathbf{s}}$ orientations, we numerically integrate Eqs. (3.10–3.11) for many random initial conditions uniformly distributed in $\left(\cos\theta_i, \phi_i\right)$ and determine the nearest CS for each integration after $10t_{al}$. In Fig. 3.5, we show the results of this procedure for $\eta = 0.2$, and $I = 20^\circ$ (we use $t_{al} = 10^3/|g|$, but the results are unchanged as long as $t_{al} \gg |g|^{-1}$). It is clear that initial conditions in zone I evolve into CS1, those in zone II evolve into CS2, while those in zone III have a probabilistic outcome. These can be understood as follows:

For initial conditions in zone I, the spin orientation circulates, and $\dot{\theta}$ is negative everywhere during the cycle. Thus θ decreases until the trajectory has converged to CS1. This is intuitively reasonable, as CS1 is stable and attracting (see Section 3.3.2).

For initial conditions in zone II, our stability analysis in Section 3.3.2 shows that when $\hat{\mathbf{s}}$ is sufficiently near CS2, it will converge to CS2 since CS2 is stable and attracting. In fact, this result can be extended to all initial conditions inside the separatrix, as shown in Appendix B.1.

For initial conditions in zone III, since there are no stable CSs in zone III, the system must evolve through the separatrix to reach either CS1 or CS2. The outcome of the separatrix encounter is probabilistic and determines the final CS. Intuitively, this can be understood as probabilistic resonance capture, as first studied in the seminal work of Henrard [1982]: for $\eta \lesssim \eta_c \sim 1$, we have that $\alpha \gtrsim -g$, but

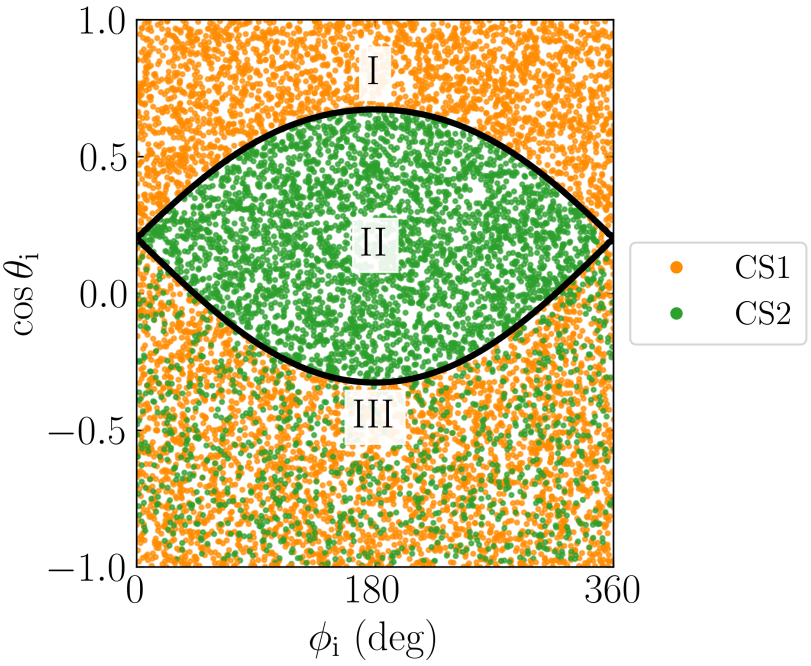

Figure 3.5: Asymptotic outcomes of spin evolution driven by an alignment torque for different initial spin orientations (θ_i and ϕ_i) for a system with $\eta = 0.2$ and $I = 20°$. Each dot represents an initial spin orientation, and the coloring of the dot indicates which stable Cassini State (legend) the system evolves into: initial conditions in Zone I evolve into CS1, those in Zone II evolve into CS2, and those in Zone III have a probabilistic outcome.

$\alpha \cos\theta$ can become commensurate with $-g$ if $\cos\theta$ becomes small. This is achieved as θ evolves from an initially retrograde obliquity through 90° towards 0° under the influence of the alignment torque.

While similar in behavior to previous studies of probabilistic resonance capture [Henrard, 1982, Su and Lai, 2020], the underlying mechanism is different: In these previous studies, the phase space structure itself evolves and causes the system to transition among different phase space zones; here in the problem at hand, a non-Hamiltonian, dissipative perturbation causes the system to transition among fixed phase space zones. In the following subsection, we present an analytic calculation to determine the probability distribution of outcomes upon separatrix encounter. Readers not interested in the technical details can simply examine the resulting Fig. 3.7.

3.3.4 Analytical Calculation of Resonance Capture Probability

Before discussing our quantitative calculation, we first present a graphical understanding of the separatrix encounter process. Figure 3.6 shows how the perturbative alignment torque generates the two outcomes upon separatrix encounter, i.e. the zone III to zone II and the zone III to zone I transition. The critical trajectories in Fig. 3.6 are calculated numerically by integrating from a point infinitesimally close to CS4 forward and backward in time. In the absence of the alignment torque, these trajectories would evolve along the separatrix, but in the presence of the alignment torque, they are perturbed slightly and cease to overlap. It can be seen in Fig. 3.6 that this splitting opens a path from zone III into both zones I and II: the coloring scheme indicates that the trajectories within the orange and

green regions of phase space stay within their respective colored regions.

To understand this process more concretely, and to compute the associated probabilities of the two possible outcomes, we consider the evolution of the value of the *unperturbed* Hamiltonian (Eq. 3.8) as the spin evolves due to the alignment torque. A point in zone III evolves such that H is increasing until $H \approx H_{\rm sep}$, where $H_{\rm sep}$ is the value of H along the separatrix, given by

$$\begin{aligned} H_{\rm sep} &\equiv H\left(\cos\theta_4, \phi_4\right) \\ &\approx g\sin I + \frac{g^2}{2\alpha}\cos^2 I + \mathcal{O}\left(\eta^2\right), \end{aligned} \tag{3.18}$$

where

$$\theta_4 \simeq \pi/2 - \eta\cos I \tag{3.19}$$

(see Section A.1 of Paper I) and $\phi_4 = 0$ are the coordinates of CS4. As the system evolves closer to the separatrix, the change in H over each circulation cycle can be approximated by ΔH_-, the change in H along $\mathscr{C}_-$ (see Fig. 3.2). In general, we define the quantities $\Delta H_\pm$

$$\Delta H_\pm \equiv \oint_{\mathscr{C}_\pm} \frac{{\rm d}H}{{\rm d}t}\,{\rm d}t. \tag{3.20}$$

Using

$$\begin{aligned} \frac{{\rm d}H}{{\rm d}t} &= \frac{\partial H}{\partial(\cos\theta)}\frac{{\rm d}(\cos\theta)}{{\rm d}t} + \frac{\partial H}{\partial\phi}\frac{{\rm d}\phi}{{\rm d}t} \\ &= \left(\frac{{\rm d}(\cos\theta)}{{\rm d}t}\right)_{\rm tide}\frac{{\rm d}\phi}{{\rm d}t} \end{aligned} \tag{3.21}$$

and Eq. (3.10), we find

$$\Delta H_\pm = \mp\frac{1}{t_{\rm al}}\int_0^{2\pi}\sin^2\theta\,{\rm d}\phi, \tag{3.22}$$

where $\theta = \theta\left(\phi\right)$ is evolved along $\mathscr{C}_\pm$. Thus, if we evaluate H every time that a trajectory originating in zone III crosses $\phi = 0$, we see that will initially be $< H_{\rm sep}$ and increase for each circulation cycle until the system encounters the separatrix.

At the beginning of the separatrix-crossing orbit, the initial value of H, denoted by H_{i}, must be greater than $H_{\mathrm{sep}} - \Delta H_{-}$ to encounter the separatrix on the current orbit. We thus require

$$H_{\mathrm{i}} \in \left[H_{\mathrm{sep}} - \Delta H_{-}, H_{\mathrm{sep}}\right]. \tag{3.23}$$

The values of $\cos\theta$ corresponding to the lower and upper bounds in this range are shown as the black and purple dots on the left of Fig. 3.6 respectively.

During the separatrix-crossing orbit, the trajectory first evolves approximately along $\mathscr{C}_{-}$ and then along $\mathscr{C}_{+}$, after which the final value of H, denoted by H_{f}, is approximately equal to

$$H_{\mathrm{f}} = H_{\mathrm{i}} + \Delta H_{+} + \Delta H_{-}. \tag{3.24}$$

There are two outcomes depending on the value of H_{f}:

- If $H_{\mathrm{f}} < H_{\mathrm{sep}}$, then, since $H < H_{\mathrm{sep}}$ corresponds to the exterior of the separatrix, this implies that the trajectory has ended outside of the separatrix. This outcome thus corresponds to a zone III to zone I transition. In Fig. 3.6, the evolution within the orange shaded regions exhibits such an outcome.
- If $H_{\mathrm{f}} > H_{\mathrm{sep}}$, then the trajectory has instead ended inside of the separatrix and has executed a zone III to zone II transition. This corresponds to evolution within the green shaded regions in Fig. 3.6.

These two possibilities can be re-expressed in terms of H_{i}: if H_{i} is in the interval $[H_{\mathrm{sep}} - \Delta H_{-},\ H_{\mathrm{sep}} - \Delta H_{-} - \Delta H_{+}]$, then the system executes a III $\rightarrow$ I transition, and if it is in the interval $[H_{\mathrm{sep}} - \Delta H_{-} - \Delta H_{+},\ H_{\mathrm{sep}}]$, then the system executes a III $\rightarrow$ II transition. We see that there is a critical value of H_{i},

$$(H_{\mathrm{i}})_{\mathrm{crit}} = H_{\mathrm{sep}} - \Delta H_{-} - \Delta H_{+}, \tag{3.25}$$

that separates the two possible outcomes of the separatrix encounter within the interval given by Eq. (3.23). The value of $\cos\theta$ for which H is equal to $H_{\rm sep} - \Delta H_- - \Delta H_+$ is shown as the blue dot on the left of Fig. 3.6. Finally, if the alignment torque is weak, then $|\Delta H_\pm| \propto t_{\rm al}^{-1}$ is small compared to any variation in the value of H (e.g. when changing the initial $\phi_{\rm i}$ or $\theta_{\rm i}$ by a small amount), and $H_{\rm i}$ can be effectively considered as randomly chosen from a uniform distribution over the range $\left[H_{\rm sep} - \Delta H_-, H_{\rm sep}\right]$. As a consequence we obtain the probability of the III → II transition:

$$P_{\rm III\to II} = \frac{\Delta H_- + \Delta H_+}{\Delta H_-}. \tag{3.26}$$

To evaluate Eq. (3.26) analytically, we use the approximate expression for the separatrix $\eta \ll 1$ (see Eq. B5 of Paper I)[1]:

$$(\cos\theta)_{\mathscr{C}_\pm} \approx \eta\cos I \pm \sqrt{2\eta\sin I\left(1-\cos\phi\right)}. \tag{3.27}$$

Using Eq. (3.22), we find

$$\Delta H_- \approx \frac{2\pi}{t_{\rm al}}\left(1 - 2\eta\sin I\right) + \mathscr{O}(\eta^{3/2}), \tag{3.28}$$

$$\Delta H_+ + \Delta H_- \approx \frac{32\eta^{3/2}\cos I\sqrt{\sin I}}{t_{\rm al}} + \mathscr{O}\left(\eta^{5/2}\right), \tag{3.29}$$

and thus

$$P_{\rm III\to II} \approx \frac{16\eta^{3/2}\cos I\sqrt{\sin I}}{\pi\left(1-2\eta\sin I\right)}. \tag{3.30}$$

To compare Eq. (3.30) with numerical results, we perform numerical integrations of Eqs. (3.10–3.11) while restricting the initial conditions to those in zone III. In Fig. 3.7, we display Eq. (3.30) alongside the computed $P_{\rm III\to II}$ using 1000 initial conditions in zone III for each of 60 values of η. Excellent agreement is observed.

[1] A more exact expression valid for all $\eta \le \eta_{\rm c}$ can be obtained by using the exact analytical solution to Colombo's Top, see Ward and Hamilton [2004]. We forgo this approach due to the significant complexity of the expression involved for a small extension in the regime of validity: our expression is sufficiently accurate when $\eta \lesssim 0.3$, while $\eta_{\rm c} \lesssim 1$.

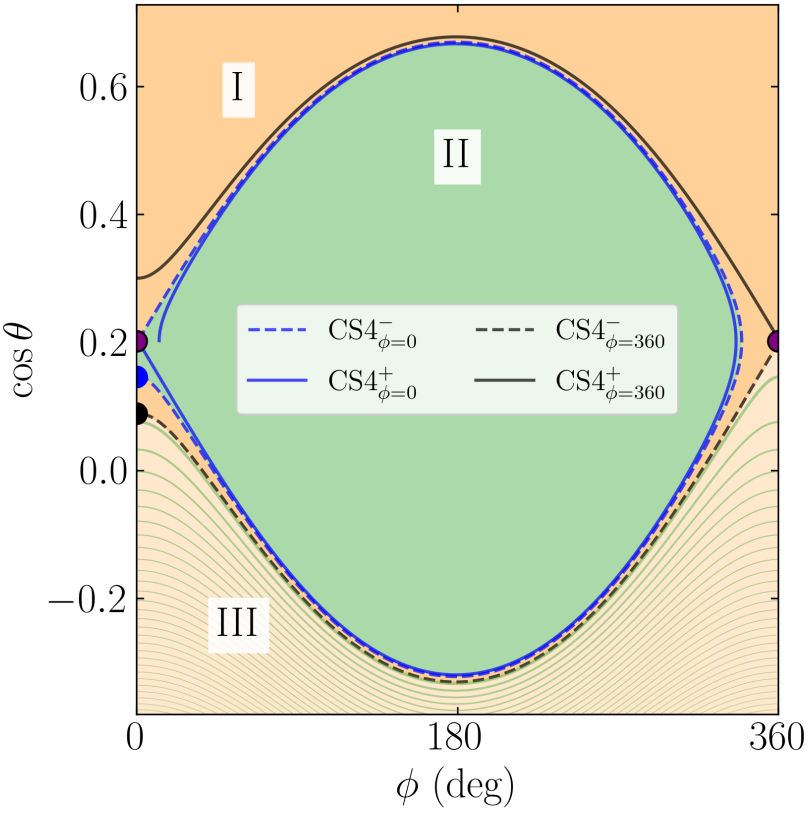

Figure 3.6: Plot illustrating the probabilistic origin of separatrix (resonance) capture for a system with $\eta = 0.2$ and $I = 20°$. The orange regions converge to CS1, and the green to CS2. The purple dots denote CS4, a saddle point. The boundaries separating the CS1 and CS2-approaching regions consist of four critical trajectories (labeled in the legend) that are evolved starting from infinitesimal displacements from CS4 along its stable and unstable eigenvectors going forwards and backwards in time: e.g. the trajectory labeled $\text{CS4}^+_{\phi=0}$ starts at $\phi = \epsilon$ (for some small, positive ϵ) and evolves forwards in time (with $t_{\text{al}} = 10^3\,|g|^{-1}$), while the trajectory labeled $\text{CS4}^-_{\phi=360}$ starts at $\phi = 360° - \epsilon$ and evolves backwards in time. The blue and black dots denote the intersections of $\text{CS4}^-_{\phi=0}$ and $\text{CS4}^-_{\phi=360}$ critical trajectories with the vertical line $\phi = 0$. These critical trajectories can be used to understand the probabilistic outcomes that trajectories originating in zone III experience upon separatrix encounter, illustrated by the tightly spaced orange and green bands in zone III; see Section 3.3.4 for additional details.

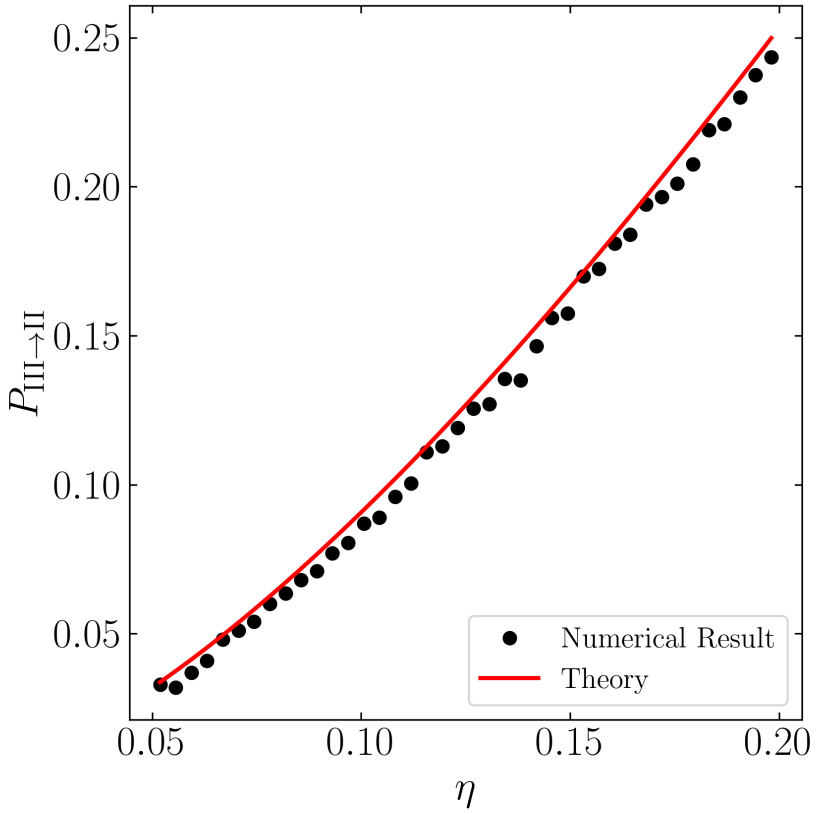

Figure 3.7: Zone III to Zone II transition probability $P_{\mathrm{III}\to\mathrm{II}}$ upon separatrix encounter as a function of η driven by an alignment torque. For each η, 1000 initial random $(\theta_{\mathrm{i}}, \phi_{\mathrm{i}})$ values in zone III are evolved until just after separatrix encounter, where the outcome of the encounter is recorded. The red line shows the analytical result, Eq. (3.30).

The rigorous connection between the above calculation, focusing on the evolution of H along the two legs of the separatrix $\mathscr{C}_{\pm}$, and the graphical picture illustrated in Fig. 3.6 is provided by *Melnikov's Method* [Guckenheimer and Holmes, 1983]. Melnikov's Method is a general calculation that gives the degree of splitting of a "homoclinic orbit" (here, the separatrix) of a Hamiltonian system induced by a small, possibly time-dependent, perturbation. At a qualitative level, we can state the connection succinctly (see Fig. 3.6):

- The trajectory labeled $\mathrm{CS4}^{-}_{\phi=360}$ is evolved backwards in time from CS4 (where the Hamiltonian has the value H_{sep}) along $\mathscr{C}_{-}$, and thus the black dot labels the start of a separatrix-crossing orbit with the initial value of the Hamiltonian $H_{\mathrm{i}} = H_{\mathrm{sep}} - H_{-}$. According to Eq. (3.23), this is exactly the minimum H_{i} such that a trajectory experiences a separatrix-crossing orbit. This is consistent with Fig. 3.6, where it is clear that any trajectories below the black dot at $\phi = 0$ will not experience a separatrix encounter on its current circulation cycle.
- The trajectory labeled $\mathrm{CS4}^{-}_{\phi=0}$ is the one evolving backwards in time from CS4 along first $\mathscr{C}_{+}$ then $\mathscr{C}_{-}$, and thus the blue dot labels the start of a separatrix-crossing orbit with $H_{\mathrm{i}} = H_{\mathrm{sep}} - \Delta H_{-} - \Delta H_{+}$. According to Eq. (3.25), this is exactly the critical value of H_{i} that separates trajectories executing a III→II transition and a III→I transition. This is also consistent with Fig. 3.6, where the region above $\mathrm{CS4}^{-}_{\phi=0}$ is colored green while the region below is colored orange.

3.4 Spin Evolution with Weak Tidal Friction

3.4.1 Tidal Cassini Equilibria (tCE)

Having understood the effect of the alignment torque on the spin evolution (Section 3.3), we now implement the full effect of tidal dissipation, including both tidal alignment and spin synchronization. We use the weak friction theory of equilibrium tides [e.g. Alexander, 1973, Hut, 1981]. In this model, tides cause both the spin orientation $\hat{\mathbf{s}}$ and frequency $\Omega_{\rm s}$ to evolve on the characteristic tidal timescale $t_{\rm s}$ following [see Lai, 2012]:

$$\left(\frac{\mathrm{d}\hat{\mathbf{s}}}{\mathrm{d}t}\right)_{\rm tide} = \frac{1}{t_{\rm s}}\left[\frac{2n}{\Omega_{\rm s}} - \left(\hat{\mathbf{s}}\cdot\hat{\mathbf{l}}\right)\right]\hat{\mathbf{s}}\times\left(\hat{\mathbf{l}}\times\hat{\mathbf{s}}\right), \tag{3.31}$$

$$\frac{1}{\Omega_{\rm s}}\left(\frac{\mathrm{d}\Omega_{\rm s}}{\mathrm{d}t}\right)_{\rm tide} = \frac{1}{t_{\rm s}}\left[\frac{2n}{\Omega_{\rm s}}\left(\hat{\mathbf{s}}\cdot\hat{\mathbf{l}}\right) - 1 - \left(\hat{\mathbf{s}}\cdot\hat{\mathbf{l}}\right)^2\right], \tag{3.32}$$

where $t_{\rm s}$ is given by

$$\frac{1}{t_{\rm s}} \equiv \frac{1}{4k}\frac{3k_2}{Q}\left(\frac{M_\star}{m}\right)\left(\frac{R}{a}\right)^3 n, \tag{3.33}$$

with k_2 and Q the tidal Love number[2] and tidal quality factor, respectively. We neglect orbital evolution (thus, $t_{\rm s}$ is a constant) in this section since the time scale is longer than $t_{\rm s}$ by a factor of $\sim L/S \gg 1$ (we discuss the effect of orbital evolution in Section 3.5.3). We will continue to consider the case where tidal dissipation is slow, i.e. $|g|\,t_{\rm s} \gg 1$. The full equations of motion including weak tidal friction can

[2]Note that for rocky planets, the tidal k_2 and the hydrostatic k_2 (which is equal to the $3k_{\rm q}$) need not be equal, e.g. for the Earth, $k_2^{\rm tidal} \approx 0.29$ [Lainey, 2016] while the hydrostatic $k_2^{\rm rotational} = 0.94$ [Fricke, 1977]. This is due to the Earth's appreciable rigidity. For higher-mass, more "fluid" planets, $k_2^{\rm tidal} \simeq k_2^{\rm rotational}$.

be written in component form as

$$\frac{\mathrm{d}\theta}{\mathrm{d}t} = g\sin I\sin\phi - \frac{1}{t_\mathrm{s}}\sin\theta\left(\frac{2n}{\Omega_\mathrm{s}} - \cos\theta\right), \tag{3.34}$$

$$\frac{\mathrm{d}\phi}{\mathrm{d}t} = -\alpha\cos\theta - g\left(\cos I + \sin I\cot\theta\cos\phi\right), \tag{3.35}$$

$$\frac{1}{\Omega_\mathrm{s}}\frac{\mathrm{d}\Omega_\mathrm{s}}{\mathrm{d}t} = \frac{1}{t_\mathrm{s}}\left[\frac{2n}{\Omega_\mathrm{s}}\cos\theta - \left(1+\cos^2\theta\right)\right]. \tag{3.36}$$

Equation (3.36) shows that, at a given obliquity, tides tend to drive Ω_s towards the pseudo-synchronous equilibrium value, given by

$$\frac{\Omega_\mathrm{s}}{n} = \frac{2\cos\theta}{1+\cos^2\theta} \quad \left(\dot{\Omega}_\mathrm{s} = 0\right). \tag{3.37}$$

On the other hand, Eq. (3.34) shows that the spin-orbit alignment timescale t_al is related to t_s by

$$t_\mathrm{al}^{-1} = t_\mathrm{s}^{-1}\left(\frac{2n}{\Omega_\mathrm{s}} - \cos\theta\right). \tag{3.38}$$

Thus, $\dot{\theta}_\mathrm{tide} < 0$ for $2n/\Omega_\mathrm{s} > \cos\theta$ and $\dot{\theta}_\mathrm{tide} > 0$ for $2n/\Omega_\mathrm{s} < \cos\theta$.

To understand the long-term evolution of the system, we first consider its behavior near a CS. Specifically, we wish to understand whether initial conditions near a CS stay near the CS as the evolution of Ω_s causes the CSs (and separatrix) to evolve. We first note that the evolution of Ω_s alone does not drive $\hat{\mathbf{s}}$ towards or away from CSs: As long as it evolves sufficiently slowly (adiabatically; see Paper I), conservation of phase space area ensures that trajectories will remain at fixed distances to stable equilibria of the system. Thus, Eq. (4.16) or (3.34) alone determine whether the system evolves towards or away from a nearby CS as Ω_s evolves. Then, from Eq. (3.38), we see that CS2 is still always stable (and attracting), while CS1 is becomes unstable for $\Omega_\mathrm{s} > 2n\cos\theta_1 \approx 2n$, where $\theta_1 \approx \eta\sin I$ (Paper I) is the obliquity of CS1.

With this consideration, we can identify the long-term equilibria of the system when tidal torques drive the evolution of both the obliquity and Ω_s (and thus η):

these equilibria must satisfy $\dot{\Omega}_{\rm s} = 0$ and be a CS that is stable in the presence of the tidal torque (i.e. satisfying $\mathrm{d}\hat{\mathbf{s}}/\mathrm{d}t = 0$); we call such long-term equilibria *tidal Cassini Equilibria* (tCE). Figure 3.8 depicts the evolution of the system following Eqs. (4.16–4.17) in $(\Omega_{\rm s}, \theta)$ space starting from several representative initial conditions, along with the locations of CS1 and CS2. The circled points in Fig. 3.8 denote the two tCEs (tCE1 and tCE2, depending on whether it lies on CS1 or CS2).

The obliquities of the tCE and the evolutionary track in the θ-$\Omega_{\rm s}$ plane depend on the parameter

$$\begin{aligned}\eta_{\rm sync} &\equiv \left(\eta\right)_{\Omega_{\rm s}=n} = \eta\frac{\Omega_{\rm s}}{n} \\ &= \frac{k}{2k_{\rm q}}\frac{m_{\rm p}m}{M_\star^2}\left(\frac{a}{a_{\rm p}}\right)^3\left(\frac{a}{R}\right)^3\cos I. \end{aligned} \tag{3.39}$$

In Fig. 3.8, $\eta_{\rm sync} = 0.06$; Figs. 3.9–3.10 illustrate the cases with $\eta_{\rm sync} = 0.5$ and 0.7 respectively.

The tCE obliquities as a function of $\eta_{\rm sync}$ are shown in Fig. 3.11 for $I = 20^\circ$ and $I = 5^\circ$. In fact, an analytical expression for the tCE2 obliquity and rotation rate for $\eta_{\rm sync} \ll 1$ can be obtained using Eqs. (3.37)–(3.39) and $\cos\theta_2 \simeq \eta\cos I$ (valid for $\eta \ll 1$; see Appendix of Paper I):

$$\cos\theta_{\rm tCE2} \simeq \sqrt{\frac{\eta_{\rm sync}\cos I}{2}}, \tag{3.40}$$

$$\frac{\Omega_{\rm s,tCE2}}{n} \simeq \sqrt{2\eta_{\rm sync}\cos I}. \tag{3.41}$$

This approximation for $\theta_{\rm tCE2}$ is shown as the blue dashed line in Fig. 3.11, indicating good agreement with the numerical result obtained via root finding of Eqs. (3.34)–(3.36) while assuming $|g|\,t_{\rm s} \gg 1$.

There are two important conditions that can influence the existence and stability of the tCE. First, if $\eta_{\rm sync} > \eta_{\rm c}$ (where $\eta_{\rm c}$ is given by Eq. 3.7), then tCE1 will

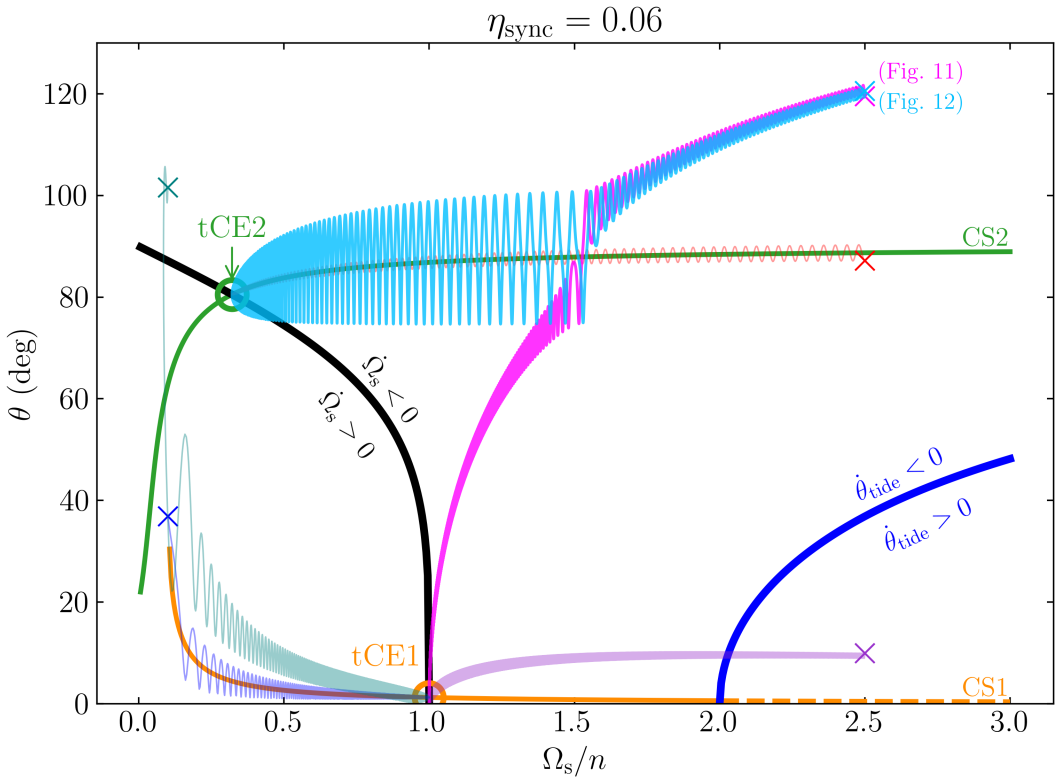

Figure 3.8: Schematic depiction of the effect of tidal friction on the planet's spin evolution in the θ-$\Omega_{\rm s}$ plane for a system with $I = 20°$ (corresponding to $\eta_{\rm c} = 0.574$; see Eq. 3.7) and $\eta_{\rm sync} = 0.06$ (see Eq. 3.39). The black and blue lines denote where the tidal $\dot{\Omega}_{\rm s}$ and $\dot{\theta}$ change signs (see Eqs. 3.34 and 3.37). The orange and green lines give the CS1 and CS2 obliquities respectively (these are the two CSs that can be stable in the presence of tidal dissipation). Note that when $\dot{\theta}_{\rm tide} > 0$, CS1 becomes unstable, denoted by the dashed orange line. The points that lie on CSs and satisfy $\dot{\Omega}_{\rm s} = 0$ are called tidal Cassini Equilibria (tCE), which are circled and labeled. The various colored crosses and their associated colored lines represent a few characteristic examples of the spin evolution under weak tidal friction (for illustrative purposes, we have used $|g|\, t_{\rm s} = 10^2$ and evolved each example for $5t_{\rm s}$). The phase space evolution of the two thicker evolutionary trajectories (cyan and pink; those beginning at $\theta_{\rm i} = 120°$) are shown in Figs. 3.12–3.13.

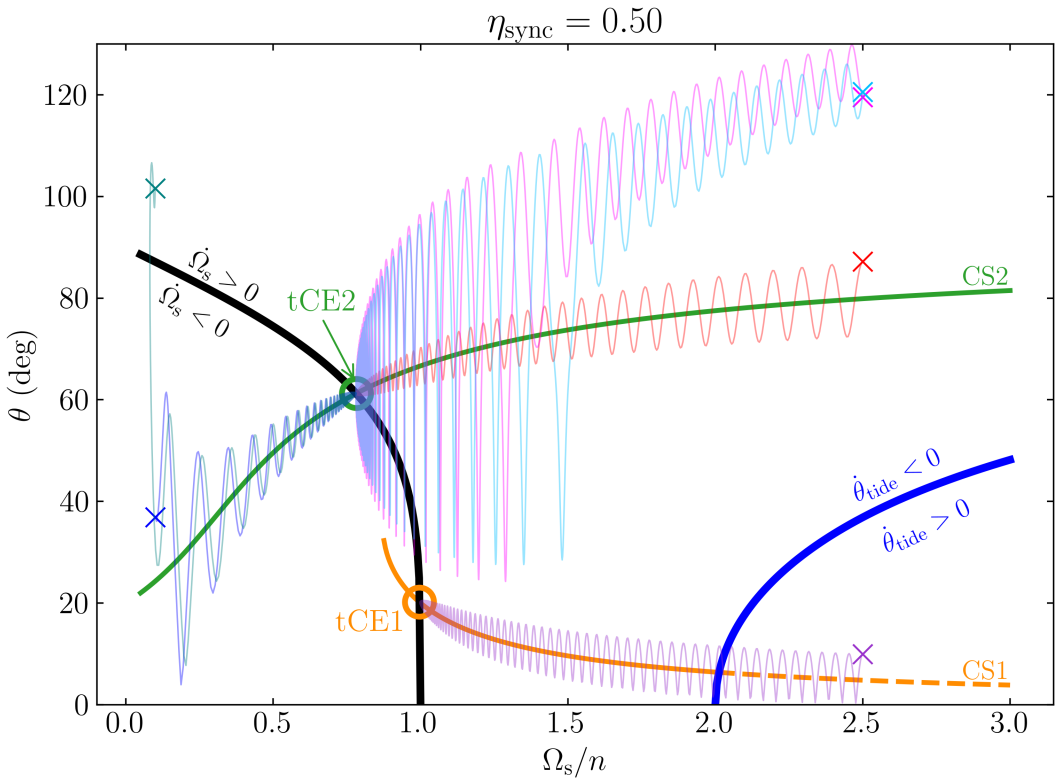

Figure 3.9: Same as Fig. 3.8 but for $\eta_{\rm sync} = 0.5$. The crosses and lines correspond to evolutionary trajectories using the same initial conditions as those shown in Fig. 3.8.

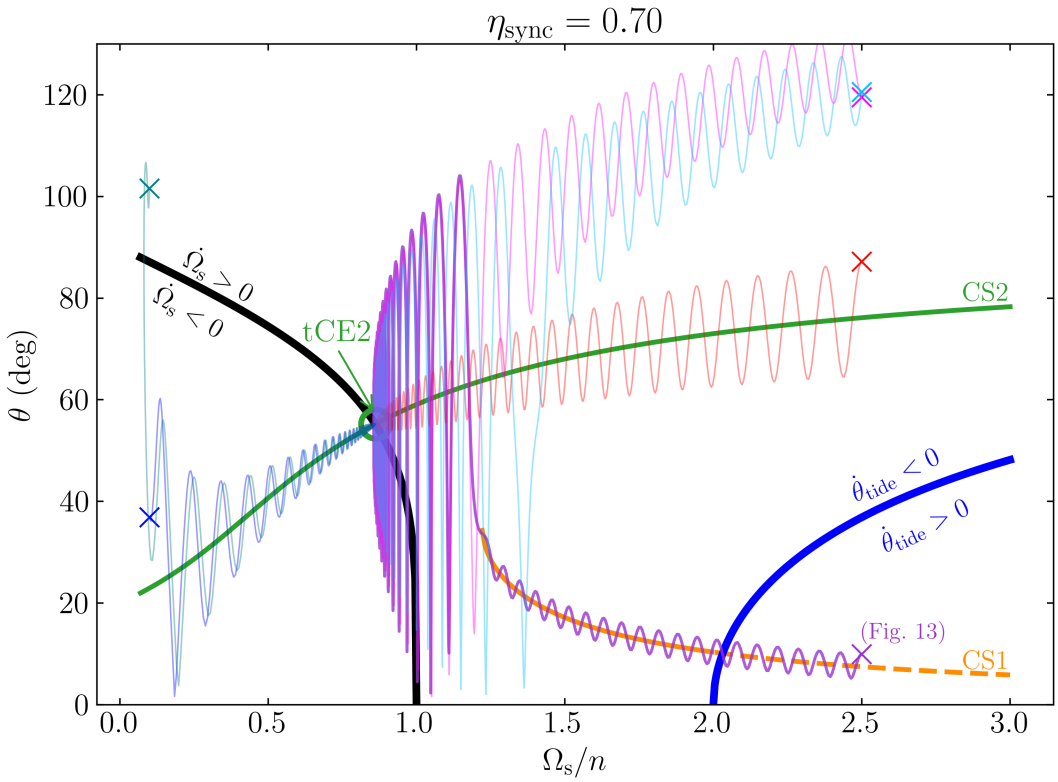

Figure 3.10: Same as Figs. 3.8 but for $\eta_{\rm sync} = 0.7$. Note that $\eta_{\rm sync} = 0.7 > \eta_{\rm c} = 0.574$ and tCE1 does not exist. The phase space evolution of the thick purple trajectory (starting at $\theta_{\rm i} = 10°$) is shown in Fig. 3.14.

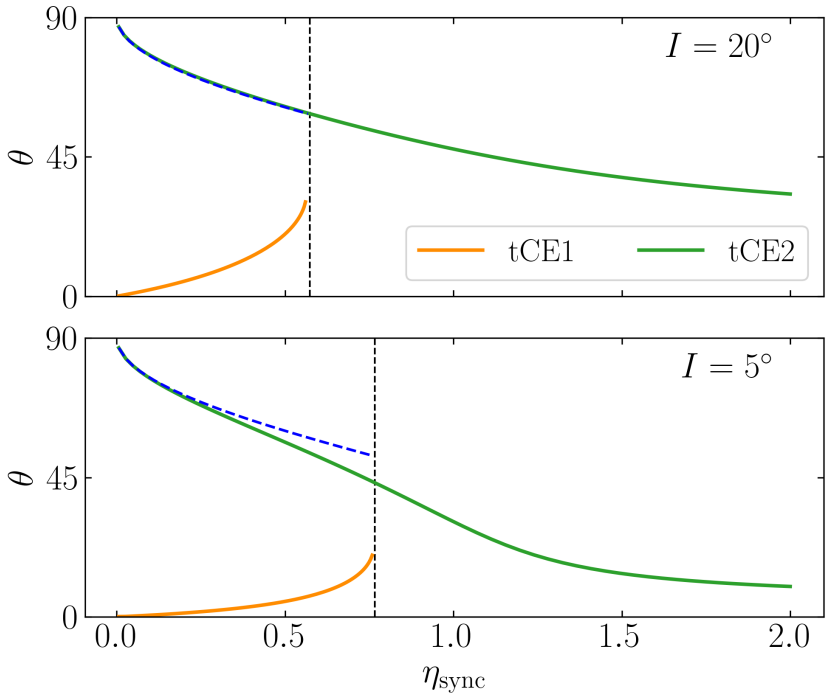

Figure 3.11: Obliquities of the two tCE as a function of $\eta_{\rm sync}$ (defined in Eq. 3.39) for $I = 20°$ (top) and $I = 5°$ (bottom). The blue dashed lines denote the analytical approximation given by Eq. (3.40) and is only valid for $\eta_{\rm sync} \ll 1$. The vertical dashed lines denote where $\eta_{\rm sync} = \eta_{\rm c}(I)$, above which tCE1 ceases to exist.

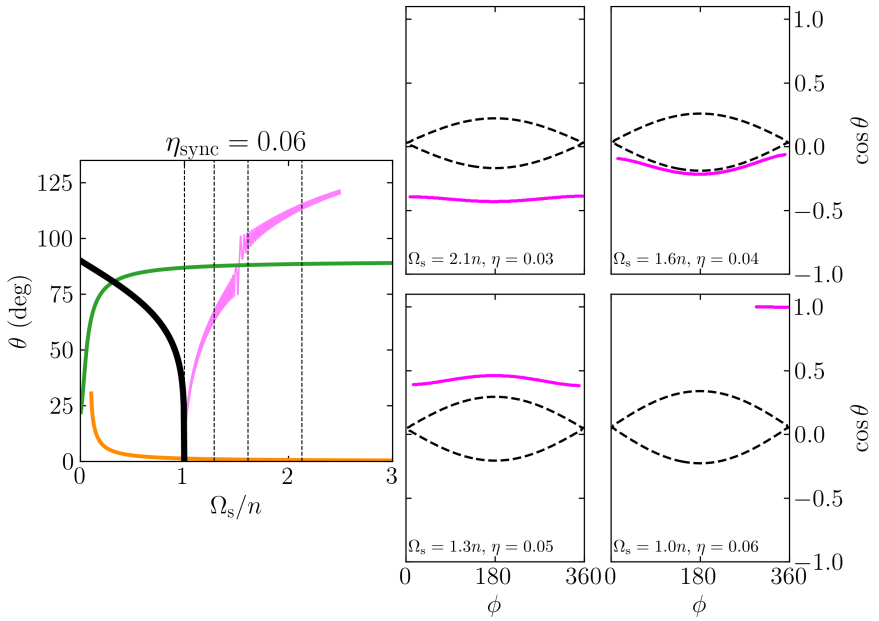

Figure 3.12: Phase space evolution of the pink trajectory in Fig. 3.8, for which $\eta_{\rm sync} = 0.06$ and $I = 20^\circ$ (corresponding to $\eta_{\rm c} = 0.574$). The initial conditions are $\Omega_{\rm s,i} = 2.5n$, $\theta_{\rm i} = 120^\circ$, and $\phi_{\rm i} = 0^\circ$, and we have used $|g|\,t_{\rm s} = 10^2$ and have evolved the system for $5t_{\rm s}$. In the left-most panel, the trajectory's evolution in the θ-$\Omega_{\rm s}$ plane along with the curves indicating CS1, CS2, and $\dot{\Omega}_{\rm s} = 0$ are re-displayed from Fig. 3.8. The vertical dashed lines denote the values of $\Omega_{\rm s}/n$ for which a few phase space snapshots of the system are displayed in the right four panels. In each of these right four panels, the trajectory's evolution for a single circulation/libration cycle is displayed in the $\cos\theta$-ϕ plane for the labeled value of $\Omega_{\rm s}$ (and the corresponding value of η). The system encounters the separatrix, undergoes a III $\rightarrow$ I transition, and converges to tCE1.

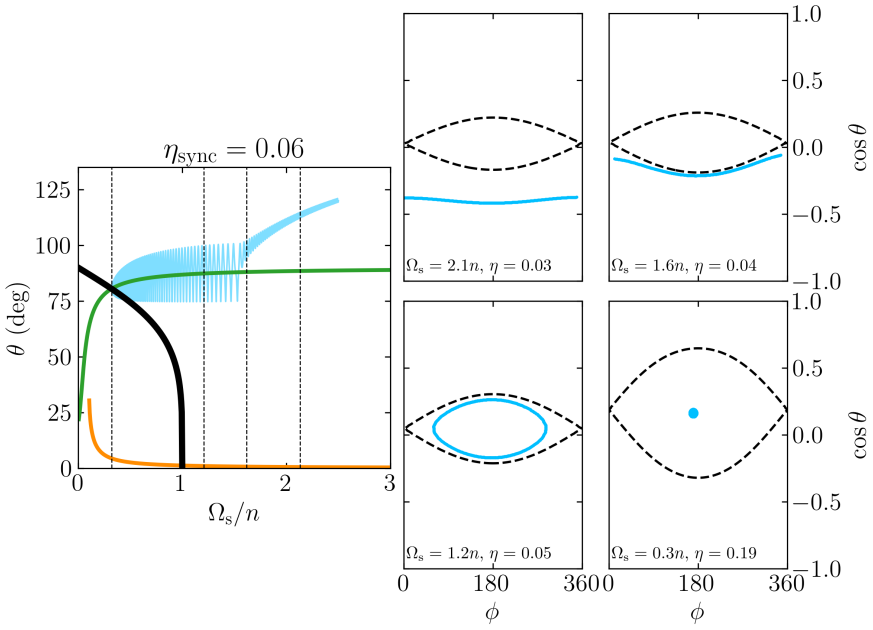

Figure 3.13: Same as Fig. 3.12 but for $\phi_{\rm i} = 286°$, corresponding to the cyan trajectory in Fig. 3.8. The system encounters the separatrix, undergoes a III → II transition, and converges to tCE2. The small ϕ offset of tCE2 from 180° arises from the alignment torque (see Fig. 3.3). Note that the initial condition of this trajectory and that displayed in Fig. 3.12 have the same initial $\theta_{\rm i}$ and $\Omega_{\rm s,i}$ but different precessional phases $\phi_{\rm i}$.

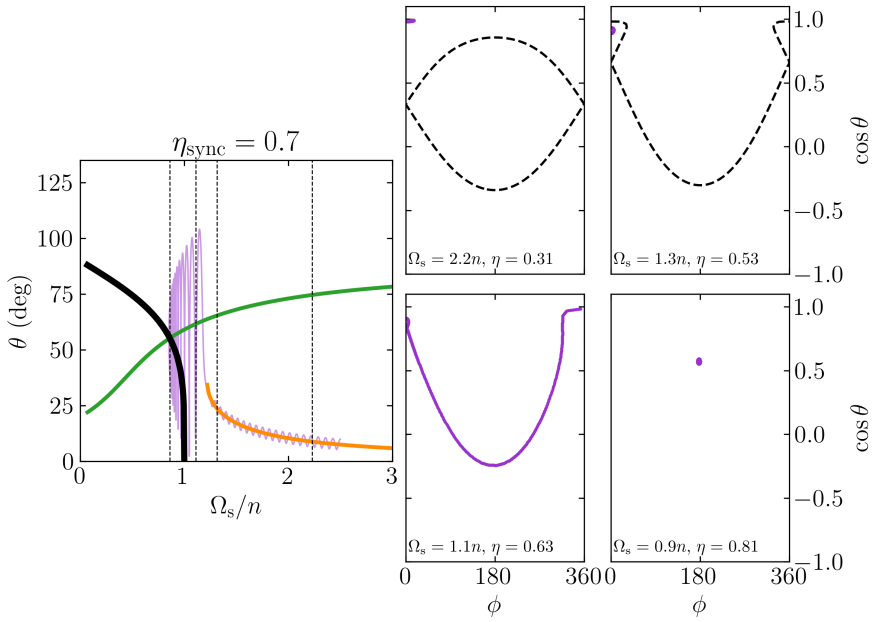

Figure 3.14: Same as Fig. 3.12 but for $\eta_{\rm sync} = 0.7$ and $\theta_{\rm i} = 10°$, corresponding to the purple trajectory shown in Fig. 3.10. Here, the system evolves along CS1 until the separatrix disappears, upon which it experiences large obliquity variations that damp due to tidal dissipation. The highly asymmetric shape in the third panel arises due to the strong tidal dissipation used in this simulation ($|g|\,t_{\rm s} = 10^2$). The system finally converges to tCE2, the only tCE that exists for this value of $\eta_{\rm sync}$.

not exist (Fig. 3.10 gives an example)[3]. Second, tCE2 may not be stable if the phase shift due to the alignment torque (see Section 3.3.1) is too large. Applying the results of Section 3.3.2 (see Eqs. 3.12–3.13), we find that tCE2 is stable as long as $t_s \geq t_{s,c}$ where

$$t_{s,c} \equiv \frac{\sin\theta_{tCE2}}{|g|\sin I}\left(\frac{2n}{\Omega_{s,tCE2}} - \cos\theta_{tCE2}\right). \tag{3.42}$$

When $\eta_{sync} \ll 1$, we can use Eqs. (3.40–3.41) to further simplify $t_{s,c}$ to[4]

$$t_{s,c} \simeq \frac{\tan\theta_{tCE2}}{|g|\sin I} \approx \frac{1}{|g|\sin I}\sqrt{\frac{2}{\eta_{sync}\cos I}}. \tag{3.43}$$

3.4.2 Spin and Obliquity Evolution as a Function of Initial Spin Orientation

We can now study the final fate of the planet's spin as a function of the initial condition. We begin by examining the example trajectories shown in Figs. 3.8, for which we have integrated the equations of motion (combining Eqs. 3.5 and 4.16 to give $d\hat{\mathbf{s}}/dt$, and Eq. 4.17) and set $I = 20°$, $t_s = 100\,|g|^{-1}$. We discuss each of the six trajectories in turn:

- The trajectory with the initial condition $\Omega_{s,i} = 2.5n$ and $\theta_i = 10°$ (purple) has an initially prograde spin (i.e. in zone I, see Fig. 3.2) and directly evolves to tCE1, with the final $\Omega_s/n \simeq 1$ and $\theta = \theta_{CS1} \simeq \eta_{sync}\sin I$ (for $\eta_{sync} \ll 1$; see Appendix A of paper I).
- The trajectory with $\Omega_{s,i} = 2.5n$ and $\theta_i = 90°$ (red) has an initial condition inside the resonance / separatrix (zone II) and evolves to tCE2. Note that

[3] Strictly speaking, η_{sync} can be slightly smaller than η_c, as the planet's spin is slightly subsynchronous at tCE1 (see Eq. 3.37).

[4] Note that Eq. (3.43) for the critical t_s agrees with Eq. (16) of Levrard et al. [2007].

the obliquity is trapped in a high value due to the stability of CS2 under the alignment torque, as shown in Section 3.4.1.

- We have chosen two trajectories, both with the initial condition $\Omega_{s,i} = 2.5n$ and $\theta_i = 120^\circ$, but with different initial precessional phases ϕ_i. Consider first the pink trajectory, for which $\phi_i = 0^\circ$. It originates in zone III, evolves towards the separatrix as tidal friction damps the obliquity, and crosses the resonance (separatrix) without being captured, upon which the obliquity continues to damp until the system converges to tCE1. The detailed phase space evolution of this trajectory is shown in Fig. 3.12, where the outcome of the separatrix encounter is very visible.

- The light blue trajectory also has $\Omega_{s,i} = 2.5n$ and $\theta_i = 120^\circ$ (like the pink trajectory) but with the initial precessional phase $\phi_i \approx 286^\circ$. It also originates in zone III, encounters the separatrix but is captured into the resonance (zone II), upon which tidal friction drives the system towards tCE2. The detailed phase space evolution of this trajectory is shown in Fig. 3.13, where the resonance capture is displayed. Also visible in the final panel of Fig. 3.13 is the slight phase offset of CS2, i.e. $\phi_{cs} < 180^\circ$, in agreement with the result of Section 3.3.1 (see Fig. 3.3).

- For completeness, we also examine some trajectories for initially subsynchronous spin rates. The trajectory with $\Omega_{s,i} = 0.1n$ and $\theta_i = 35^\circ$ (blue) has its obliquity rapidly damped to zero by tidal friction as it spins up to spin-orbit synchronization, eventually converging to tCE1. A subtlety of initially subsynchronous spins can be seen here: since the initial $\eta_i = 0.6 > \eta_c$ (= 0.574), the separatrix and CS1 do not exist initially. As such, naively, one expects initial convergence to CS2 and subsequent obliquity evolution along CS2 as the spin increases. However, due to the strong tidal dissipation adapted in the calculation and the proximity of η_i to η_c, CS1 appears

within a single circulation cycle, and the obliquity quickly damps to, and continues to evolve along CS1.

- The trajectory with $\Omega_{s,i} = 0.1n$ and $\theta_i = 100^\circ$ (teal) also has its obliquity damped toward tCE1 as it approaches spin-orbit synchronization. We note that if we adopt $t_s = 10^3 |g|^{-1}$, the same initial condition will converge to tCE2, agreeing with the intuitive analysis given in the previous paragraph.

In Figs. 3.9–3.10 we show, for each of the six initial conditions, the evolutionary trajectories for the $\eta_{sync} = 0.5$ and $\eta_{sync} = 0.7$ cases. The qualitative behaviors of these six examples change in several important ways, so we will discuss a few points of interest:

- For both $\eta_{sync} = 0.5$ and $\eta_{sync} = 0.7$, we see that the initial conditions with $\theta_i = 120^\circ$ ($\phi_i = 0$, pink; and $\phi_i = 286^\circ$, blue) converge to tCE2. In fact, for these values of η_{sync}, all initial conditions with $\theta_i = 120^\circ$ will converge to tCE2 regardless of ϕ_i.
- The two subsynchronous initial conditions evolve to tCE2 for both $\eta_{sync} = 0.5$ and $\eta_{sync} = 0.7$, as in both cases $\eta_i \gg \eta_c$ and CS2 is the only low-obliquity spin equilibrium. The system then continues to evolve along CS2 toward tCE2.
- Of particular interest is the trajectory starting from the initial condition $\Omega_{s,i} = 2.5n$ and $\theta_i = 10^\circ$ (purple) in the case of $\eta_{sync} = 0.7$. Figure 3.14 shows the detailed phase space evolution of this trajectory, where it can be seen that the system initially evolves along the stable CS1, but is ejected when Ω_s becomes sufficiently small that CS1 ceases to exist, upon which large obliquity variations eventually lead to convergence to tCE2, the only tCE that exists.

From the above examples, we see that the spin evolution driven by tides can be complex and varies greatly depending on the various system parameters and initial conditions. In the case where the initial spin is subsynchronous, the detailed outcome depends sensitively on the initial value of η and the tidal dissipation rate. In the following, we restrict our discussion to the more astrophysically common regime of $\Omega_{\rm s,i} \gg n$, and we adopt the fiducial value $\Omega_{\rm s,i} = 10n$.

Having developed an intuition for a few different possible evolutionary trajectories, we can attempt to draw general conclusions about the final fate of the planet's spin as a function of its initial conditions. We do this by again integrating Eqs. (3.5, 4.16–4.17) for many initial $\theta_{\rm i}$ and $\phi_{\rm i}$ and examining the final outcomes. In contrast to the examples shown in Figs. 3.8–3.14, we use a more gradual tidal dissipation rate of $|gt_{\rm s}| = 10^3$. In Fig. 3.15, we show the final outcome for many randomly chosen $\theta_{\rm i}$ and $\phi_{\rm i}$ for $\eta_{\rm sync} = 0.06$ and $I = 20^\circ$. We see that the behaviors seen in the example trajectories of Fig. 3.8 are general: tCE1 is generally reached for spins initially in zone I (like the purple trajectory in Fig. 3.8), tCE2 is generally reached for spins initially in zone II (like the red trajectory in Fig. 3.8), and a probabilistic outcome is observed for spins initially in zone III (like the light blue and pink trajectories in Fig. 3.8). Figures 3.16 and 3.17 show similar results for $\eta_{\rm sync} = 0.2$ and $\eta_{\rm sync} = 0.5$. As $\eta_{\rm sync}$ is increased, more initial conditions reach tCE2. This is both because there are more systems initially in zone II and because systems initially in zone III have a higher probability of executing a III $\rightarrow$ II transition upon separatrix encounter. Note also that in Fig. 3.17, even initial conditions in zone I are able to reach tCE2; we comment on the origin of this behavior in the next section.

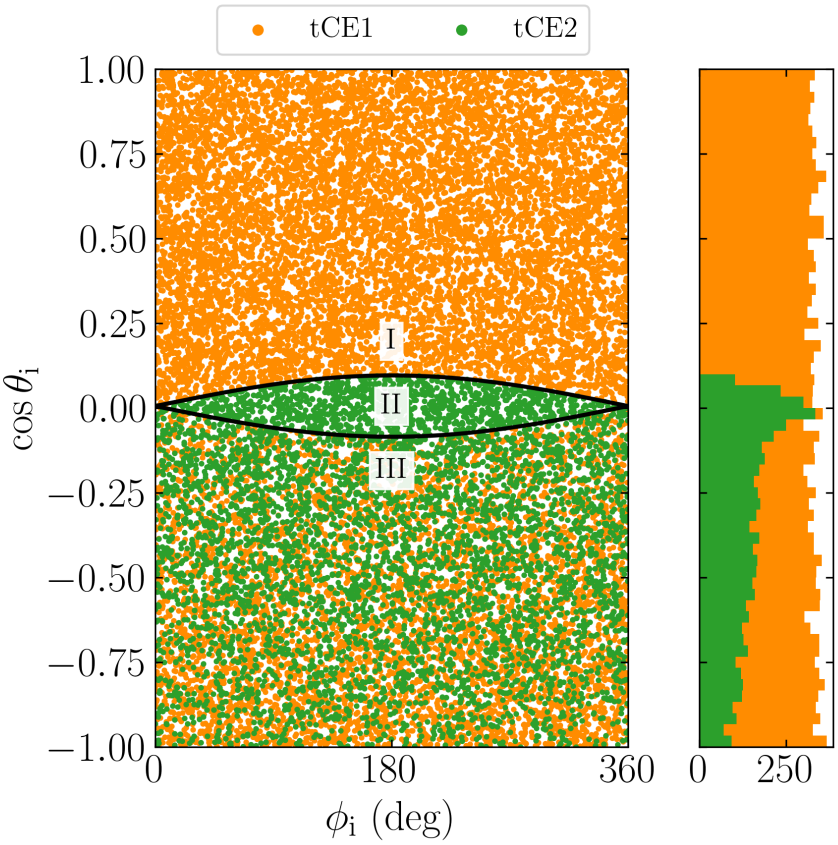

Figure 3.15: *Left:* Asymptotic outcomes of spin evolution in the presence of weak tidal friction for different initial spin orientations (θ_i and ϕ_i) for a system with $\eta_{\rm sync} = 0.06$ and $I = 20°$. Each dot represents an initial spin orientation, and the coloring of the dot indicates which tCE (legend) the system evolves into. Similarly to Fig. 3.5 initial conditions in Zone I evolve into CS1, those in Zone II evolve into CS2, and those in Zone III have a probabilistic outcome. *Right:* Histogram of the final tCE that a given initial obliquity θ_i evolves into, averaged over ϕ_i.

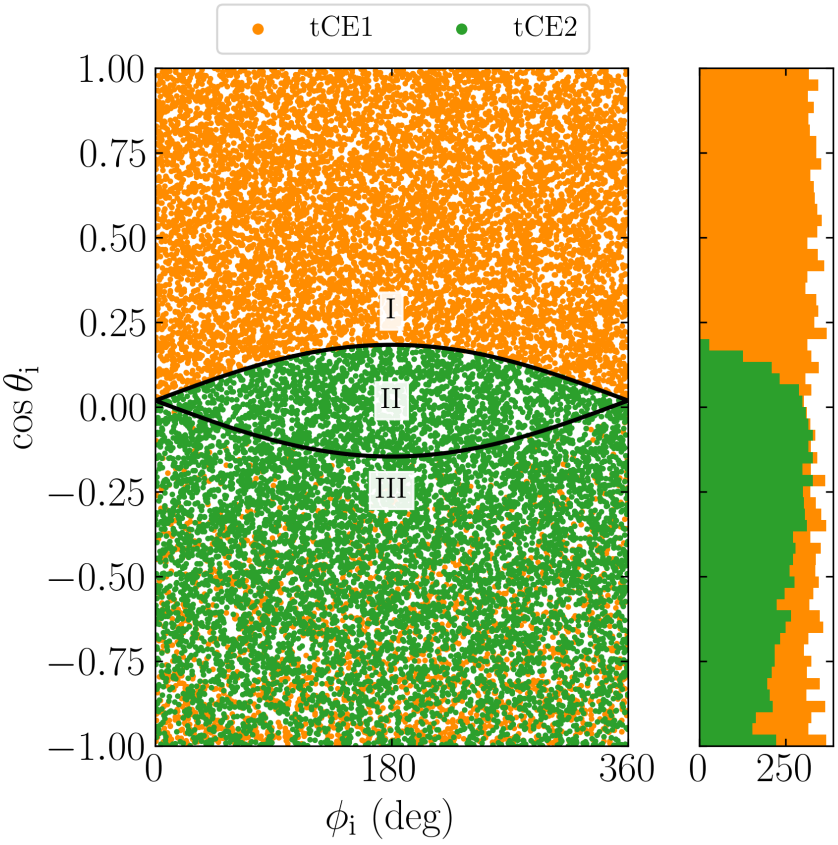

Figure 3.16: Same as Fig. 3.15 but for $\eta_{\rm sync} = 0.2$.

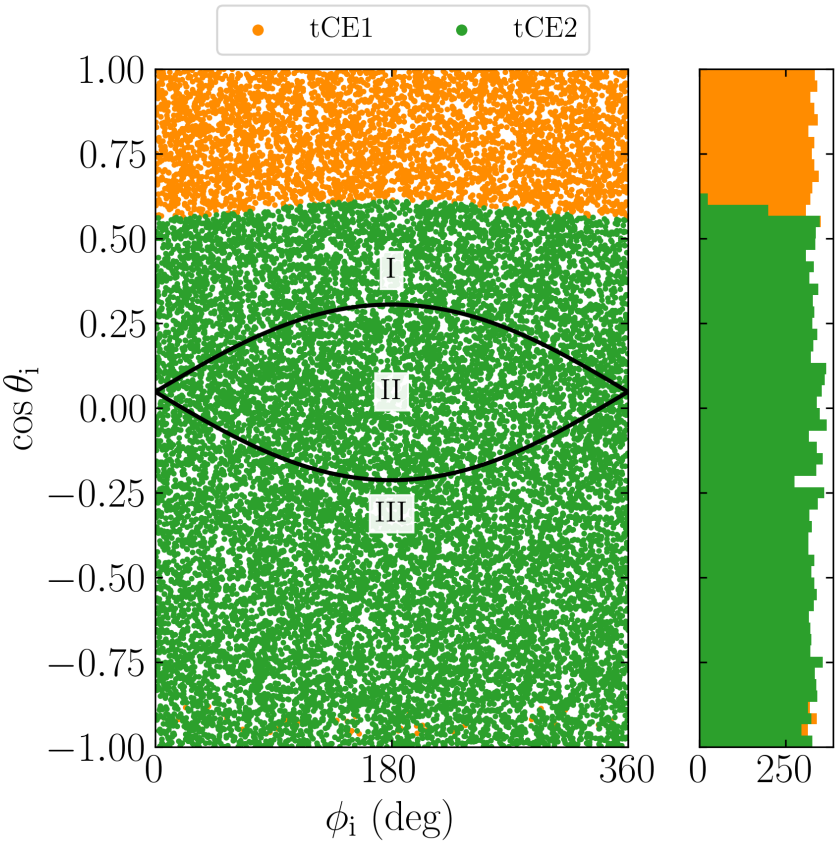

Figure 3.17: Same as Fig. 3.15 but for $\eta_{\rm sync} = 0.5$. Note that even points above the separatrix can evolve towards tCE2 here.

3.4.3 Semi-analytical Calculation of Resonance Capture Probability

Even when including the evolution of Ω_s, and therefore the parameter η (see Eq. 8.5), the probabilities of the III $\rightarrow$ I and III $\rightarrow$ II transitions upon separatrix encounter can still be obtained semi-analytically. The calculation resembles that presented in Section 3.3.4 but involves several new ingredients. We describe the calculation below.

In Section 3.3.4, we found that the evolution of H, the value of the unperturbed Hamiltonian, allowed us to calculate the probabilities of the various outcomes of separatrix encounter. Specifically, the outcome upon separatrix encounter is determined by the value of H at the start of the separatrix-crossing orbit relative to $H_{\rm sep}$, the value of H along the separatrix. However, when the spin Ω_s is also evolving, $H_{\rm sep}$ also changes during the separatrix-crossing orbit, and the calculation in Section 3.3.4 must be generalized to account for this. Instead of focusing on the evolution of H along a trajectory, we instead follow the evolution of

$$K \equiv H - H_{\rm sep}. \tag{3.44}$$

Note that $K > 0$ inside the separatrix, and $K < 0$ outside. With this modification, the outcome of the separatrix-crossing orbit can be determined in the same way as in Section 3.3.4. First, we must compute the change in K along the legs of the separatrix. We define $\Delta K_\pm$ by generalizing Eq. (3.20) in the natural way:

$$\Delta K_\pm = \oint_{\mathscr{C}_\pm} \left[\frac{{\rm d}H}{{\rm d}t} - \frac{{\rm d}H_{\rm sep}}{{\rm d}t} \right] {\rm d}t. \tag{3.45}$$

Here, however, note that the contours $\mathscr{C}_\pm$ depends on the value of Ω_s at separatrix encounter (or the corresponding value $\eta = \eta_{\rm cross}$). Since there is no closed form solution for $\Omega_s(t)$, the probabilities of the various outcomes cannot be expressed

as a simple function of the initial conditions.

Continuing the argument presented in Section 3.3.4, we consider the outcome of the separatrix-crossing orbit as a function of K_i, the value of K at the start ($\phi = 0$) of the separatrix-crossing orbit. We find that if $-\Delta K_+ - \Delta K_- < I_{\rm i} < 0$, then the system undergoes a III $\rightarrow$ II transition and eventually evolves towards tCE2, and if $-\Delta K_- < K_i < -\Delta K_- - \Delta K_+$, then the system undergoes a III $\rightarrow$ I transition and ultimately evolves towards tCE1. Thus, we find that the probability of a III $\rightarrow$ II transition is given by

$$P_{\rm III \rightarrow II} = \frac{\Delta K_+ + \Delta K_-}{\Delta K_-}. \tag{3.46}$$

Again, since $\Delta K_\pm$ are evaluated at resonance encounter, and $\Omega_{\rm s}$ is evolving, there is no way to express $\Delta K_\pm$ in a closed form of the initial conditions. In fact, since many resonance encounters occur when $\eta = \eta_{\rm cross}$ is $\gtrsim 0.2$, even an approximate calculation of $\Delta K_\pm$ using Eq. (3.27) (which is valid only for $\eta \ll 1$) is inaccurate, and we instead calculate $\Delta K_\pm$ along the numerically-computed $\mathscr{C}_\pm$ for arbitrary η. Note that Eqs. (3.45, 3.46) are equivalent to the separatrix capture result of Henrard [1982] when $\dot{\theta}_{\rm tide} = 0$ (see also Henrard and Murigande, 1987 and Paper I). In other words, we argue that this classic calculation can be unified with the calculation given in Section 3.3.4 to give an accurate prediction of separatrix encounter outcome probabilities in the presence of both dissipative perturbation and parametric evolution of the Hamiltonian.

We note that Levrard et al. [2007] also presented an analytical expression for the resonance capture probability (their Eq. 14) following the method of Goldreich and Peale [1966]. However, their expression is incomplete, as it does not account for the contribution of the tidal alignment torque to the change of the integral of motion over a single orbit.

To validate the accuracy of Eq. (3.46), we can compare with direct numerical integration of Eqs. (3.5, 4.16–4.17) for many initial conditions while evaluating $P_{\mathrm{III}\to\mathrm{II}}$ (and thus also obtaining $P_{\mathrm{III}\to\mathrm{I}} = 1 - P_{\mathrm{III}\to\mathrm{II}}$) for each simulation at the moment it encounters the separatrix, if it does so. If the theory is correct, the total numbers of systems converging to each of tCE1 and tCE2 should be equal to those predicted by the calculated probabilities. In Fig. 3.18, we show the agreement of this semi-analytic procedure with the numerical result displayed in the right panel of Fig. 3.15. Figure 3.19 depicts the same for the parameters of Figs. 3.16, also showing satisfactory agreement. Thus, we conclude that the outcomes of separatrix encounter are accurately predicted by Eq. (3.46).

With the above calculation, we can understand why even some initial conditions in zone I may converge to tCE2 in certain situations (see Fig. 3.17). As long as the initial spin is sufficiently large ($\geq 2n$), Eq. (3.34) shows that when $\cos\theta > 2n/\Omega_{\mathrm{s}}$, the obliquity can increase. In particular, when the critical obliquity $\cos\theta = 2n/\Omega_{\mathrm{s}}$ is inside the separatrix, tidal alignment acts to drive initial conditions in both zones I and III towards the critical obliquity and into the separatrix, and also towards larger H. As such, when this effect is sufficiently strong, Eq. (3.45) shows that both $\Delta K_{\pm} > 0$, and both III $\to$ II and I $\to$ II transitions are guaranteed upon separatrix encounter (Eq. 3.46).

3.4.4 Spin Obliquity Evolution for Isotropic Initial Spin Orientations

In Sections 3.4.2–3.4.3, we considered the outcome of the spin evolution driven by tidal torque as a function of the initial spin orientation, specified by θ_{i} and ϕ_{i}. Here, we calculate the probability of evolution into tCE2 when averaging over a

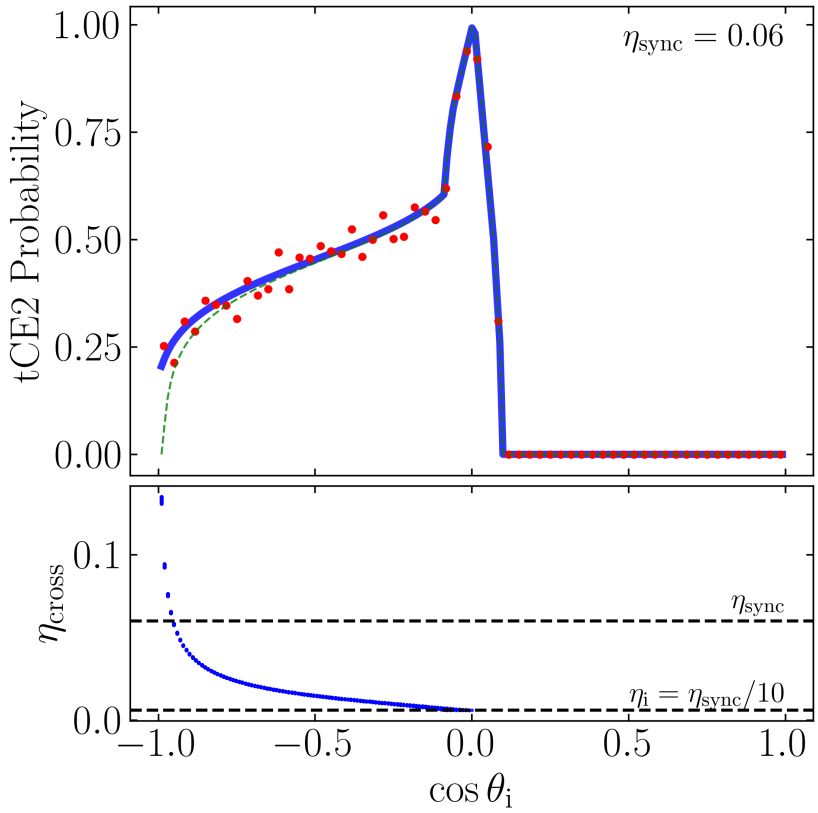

Figure 3.18: Comparison of the fraction of systems converging to tCE2 obtained via numerical simulation (red dots) and obtained via a semi-analytic calculation (blue line) for $\eta_{\rm sync} = 0.06$, $I = 20°$, and $\Omega_{\rm s,i} = 10n$ (see right panel of Fig. 3.15). The semi-analytic calculation is performed by numerically integrating Eqs. (3.5, 4.16–4.17) on a grid of initial conditions uniform in $\cos\theta_{\rm i}$ and $\phi_{\rm i}$ until the system reaches the separatrix, then calculating the probability of reaching tCE2 for each integration using Eq. (3.46). The green dashed line in the top panel shows the result of using the analytical expression (Eq. B.7) for $\Delta K_{\pm}$, and the bottom panel shows the distribution of values of $\eta_{\rm cross}$, the value of η when a trajectory starting at $\theta_{\rm i}$ encounters the separatrix.

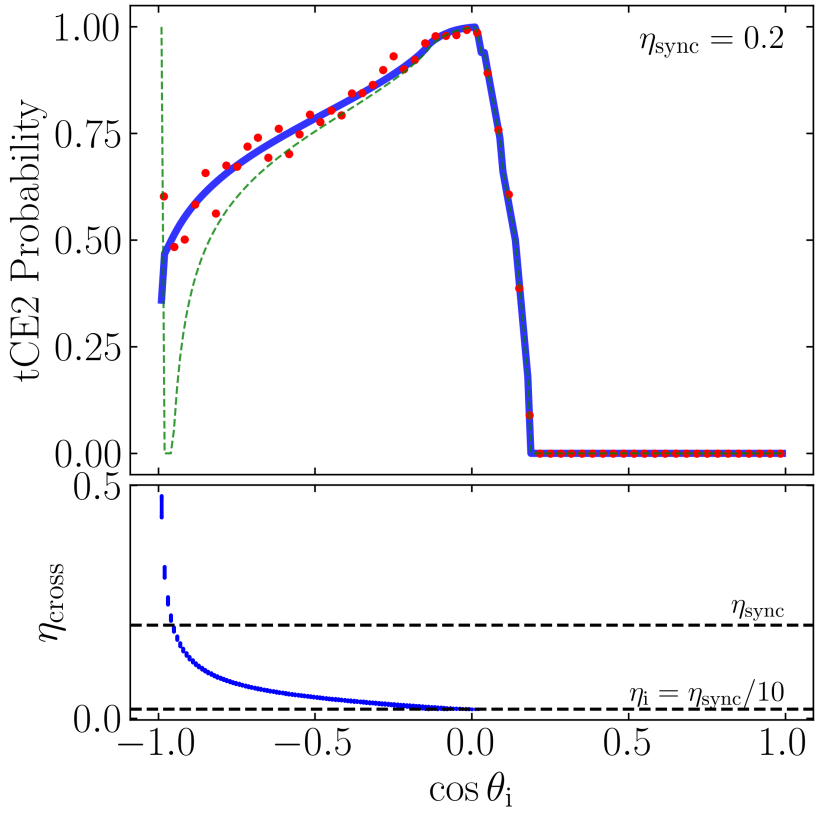

Figure 3.19: Same as Fig. 3.18 but for $\eta_{\rm sync} = 0.2$, corresponding to the right panel of Fig. 3.16. Note that the analytical equation (Eq. B.7; green dashed line) exhibits significantly poorer agreement than in Fig. 3.18 when $\eta_{\rm cross} \gtrsim 0.2$.

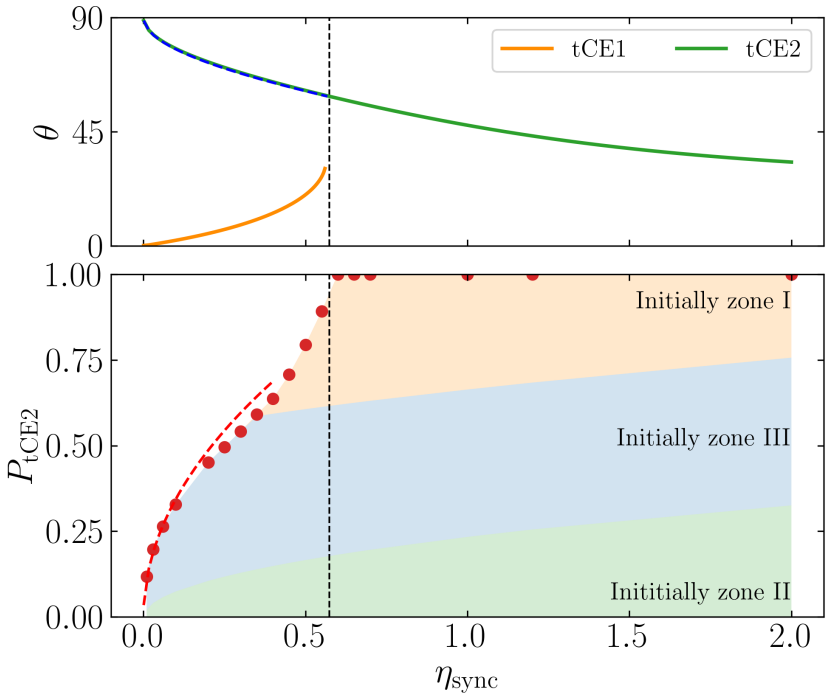

Figure 3.20: *Top:* Same as top panel of Fig. 3.11. *Bottom:* Total probability of the system ending up in tCE2 ($P_{\rm tCE2}$; red dots) as a function of $\eta_{\rm sync}$ (Eq. 3.39), averaged over an isotropic initial spin orientation and taking $\Omega_{\rm s,i} = 10n$. The red dashed line shows the analytical prediction Eq. (3.47). The three shaded regions denote the contributions of initial conditions in zones I/II/III (labeled) to the total tCE2 probability. For example, among systems that converge to tCE2 for $\eta_{\rm sync} = 0.06$, more originate in zone III than zone II, and none originate in zone I.

distribution of initial spin orientations, which we denote by $P_{\rm tCE2}$. For simplicity, we assume $\hat{\mathbf{s}}$ to be isotropically distributed (see Section 3.6 for discussions concerning impact of more physically realistic distributions of $\hat{\mathbf{s}}$). The bottom panel of Fig. 3.20 shows $P_{\rm tCE2}$ for $I = 20^\circ$ as a function of $\eta_{\rm sync}$. We see that, e.g., tCE2 with a large obliquity ($\sim 70^\circ$) can be reached with substantial probability ($\gtrsim 50\%$).

When $\eta_{\rm sync} \ll 1$ and $\Omega_{\rm s,i} \gtrsim n$, an approximate analytical formula for $P_{\rm tCE2}$ can

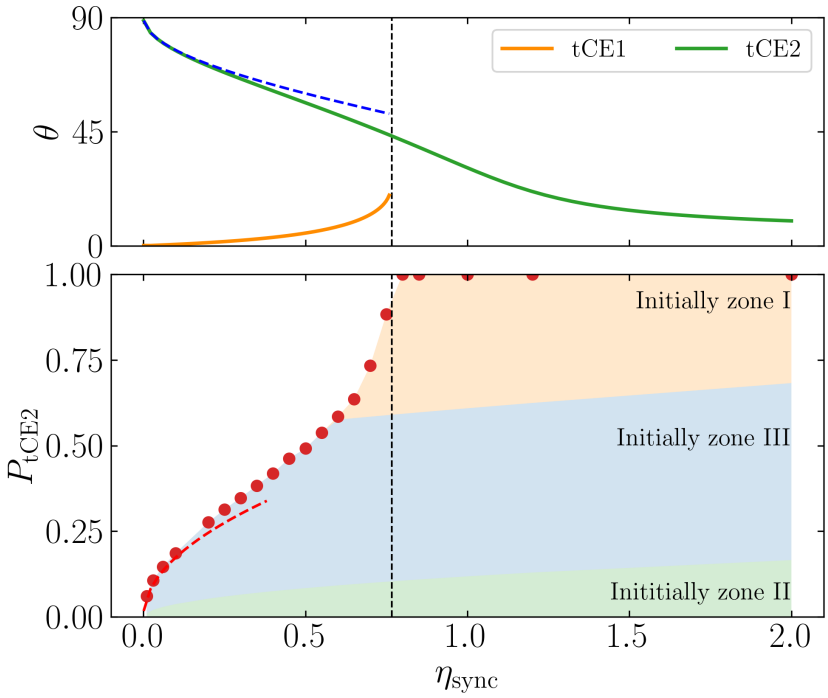

Figure 3.21: Same as Fig. 3.20 but for $I = 5°$.

be obtained (see Appendix B.2):

$$P_{\rm tCE2} \simeq \frac{4\sqrt{\eta_{\rm sync}\sin I}}{\pi}\left[\sqrt{n/\Omega_{\rm s,i}} + \frac{3}{2\left(1+\sqrt{n/\Omega_{\rm s,i}}\right)}\right]. \tag{3.47}$$

Eq. (3.47) is shown in Figs. 3.20–3.21 as the red dashed lines; it agrees well with the numerical results (red dots) for $\eta_{\rm sync} \lesssim 0.4$. To illustrate the predicted values of $P_{\rm tCE2}$ for small $\eta_{\rm sync}$, we display $P_{\rm tCE2}$ for $\eta_{\rm sync} \in [10^{-4}, 0.4]$ for both $I = 20°$ and $I = 5°$ in Fig. 3.22. Note that for $\eta_{\rm sync} \leq 10^{-2}$, numerical results for $P_{\rm tCE2}$ are difficult to obtain, as the integration of Eqs. (3.34)–(3.36) slows down dramatically due to the rapid precession of $\hat{\mathbf{s}}$ about $\hat{\mathbf{l}}$.

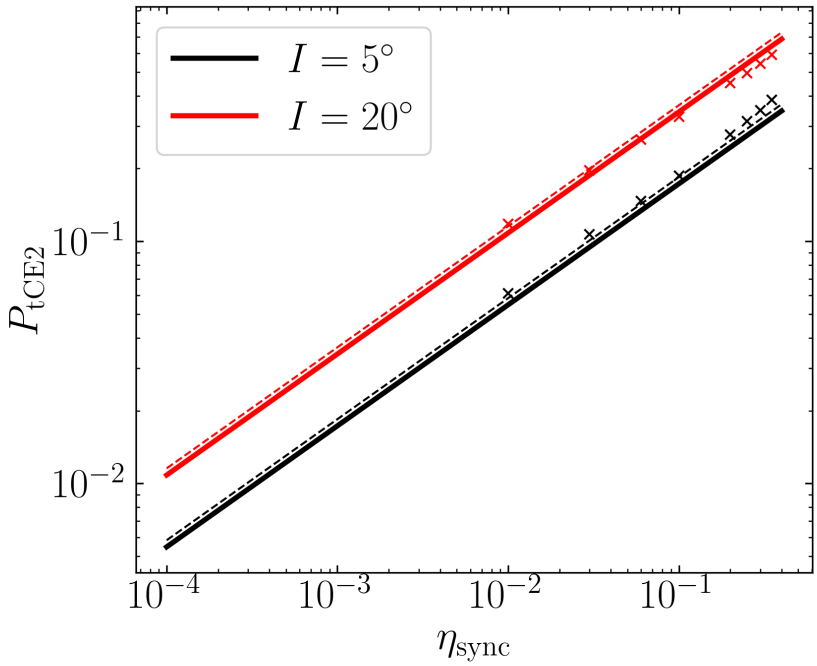

Figure 3.22: $P_{\rm tCE2}$ as a function of $\eta_{\rm sync}$ for $I = 5°$ and $I = 20°$ shown on a log-log plot, to emphasize the scaling at small $\eta_{\rm sync}$. The crosses are the results of numerical integrations as shown in Figs. 3.20–3.21, the solid lines are Eq. (3.47) for $\Omega_{\rm s,i} = 10n$ and the dashed lines are for $\Omega_{\rm s,i} = 3n$.

3.5 Applications

3.5.1 Obliquities of Super-Earths with Exterior Companions

Consider a system consisting of an inner Super-Earth (SE) with semi-major axis $a \lesssim 0.5\,\mathrm{AU}$ and an exterior companion. For concreteness, we assume the companion (with mass m_p) to be a cold Jupiter (CJ) with $a_\mathrm{p} \gtrsim 1\,\mathrm{AU}$. Such systems are quite abundant [Zhu and Wu, 2018, Bryan et al., 2019]. A phase of giant impacts may occur in the formation of such SEs [Inamdar and Schlichting, 2015, Izidoro et al., 2017], leading to a wide range of initial obliquities for the SEs. We are interested in the "final" obliquities of the SEs driven by tidal dissipation.

For typical SE parameters, the spin evolution timescale due to tidal dissipation is given by

$$\begin{aligned}\frac{1}{t_\mathrm{s}} &\simeq \frac{1}{3\times 10^7\,\mathrm{yr}}\left(\frac{1}{4k}\right)\left(\frac{2k_2/Q}{10^{-3}}\right)\left(\frac{M_\star}{M_\odot}\right)^{3/2}\left(\frac{m}{4M_\oplus}\right)^{-1}\\ &\quad\times\left(\frac{R}{2R_\oplus}\right)^3\left(\frac{a}{0.4\,\mathrm{AU}}\right)^{-9/2}.\end{aligned} \tag{3.48}$$

This occurs well within the age of SE-CJ systems. On the other hand, the orbital evolution of the SE occurs on the timescale [e.g. Lai, 2012]

$$\begin{aligned}-\frac{\dot a}{a} &= \frac{3k_2}{Q}\frac{M_\star}{m}\left(\frac{R}{a}\right)^5 n\left(1-\frac{\Omega_\mathrm{s}}{n}\cos\theta\right)\\ &\simeq \frac{1}{7\times 10^{14}\,\mathrm{yr}}\left(1-\frac{\Omega_\mathrm{s}}{n}\cos\theta\right)\left(\frac{2k_2/Q}{10^{-3}}\right)\left(\frac{M_\star}{M_\odot}\right)^{3/2}\\ &\quad\times\left(\frac{m}{4M_\oplus}\right)^{-1}\left(\frac{R}{2R_\oplus}\right)^5\left(\frac{a}{0.4\,\mathrm{AU}}\right)^{-13/2}.\end{aligned} \tag{3.49}$$

Thus, a does not evolve within the age of the SE-CJ system (for $a \gtrsim 0.06\,\mathrm{AU}$), and we shall treat a as a constant in this subsection (but see Sections 3.5.2–3.5.3).

With typical SE-CJ parameters, Eq. (3.39) can be evaluated:

$$\eta_{\rm sync} = 0.303 \cos I \left(\frac{k}{k_{\rm q}}\right)\left(\frac{m_{\rm p}}{M_{\rm J}}\right)\left(\frac{m}{4M_\oplus}\right)\left(\frac{M_\star}{M_\odot}\right)^{-2}\left(\frac{a}{0.4\,{\rm AU}}\right)^{6} \times \left(\frac{a_{\rm p}}{5\,{\rm AU}}\right)^{-3}\left(\frac{R}{2R_\oplus}\right)^{-3}. \tag{3.50}$$

We see from Figs. 3.20 and 3.21 that this value of $\eta_{\rm sync}$ can lead to a high-obliquity tCE2 with significant probability, assuming the SE has a wide range of initial obliquities. In addition, Eq. (3.43) shows that tCE2 is stable if $t_{\rm s} \gtrsim t_{\rm s,c}$, where

$$\frac{1}{t_{\rm s,c}} = \frac{\sin I \cos^2 I}{3\times 10^5\,{\rm yr}}\left(\frac{k}{k_{\rm q}}\right)\left(\frac{m_{\rm p}}{M_{\rm J}}\right)^{3/2}\left(\frac{m}{4M_\oplus}\right)^{1/2} \times \left(\frac{M_\star}{M_\odot}\right)^{-3/2}\left(\frac{a}{0.4\,{\rm AU}}\right)^{6}\left(\frac{a_{\rm p}}{5\,{\rm AU}}\right)^{-9/2}\left(\frac{R}{2R_\oplus}\right)^{-3/2}. \tag{3.51}$$

In Fig. 3.23, we show the value of $\eta_{\rm sync}$ in the regions of $(a, a_{\rm p})$ parameter space that satisfy the stability condition for tCE2. We see that a generous portion of parameter space is able to generate and sustain SEs in stable tCE2 with significant obliquities. In summary, we predict that a large fraction of SEs with exterior CJ companions can have long-lived, significant obliquities ($\gtrsim 60^\circ$) due to being trapped in tCE2.

3.5.2 Formation of Ultra-short-period Planet Formation via Obliquity Tides

Ultra-short period planets (USPs), Earth-sized planets with sub-day periods, constitute a statistically distinct subsample of Kepler planets [e.g. Winn et al., 2018, Dai et al., 2018]. It is generally thought that USPs evolved from close-in SEs through orbital decay, driven by tidal dissipation in their host stars [Lee and Chiang, 2017] or in the planets [Petrovich et al., 2019, Pu and Lai, 2019]. In particular, Pu and Lai [2019] showed that a "low-eccentricity migration" mechanism can

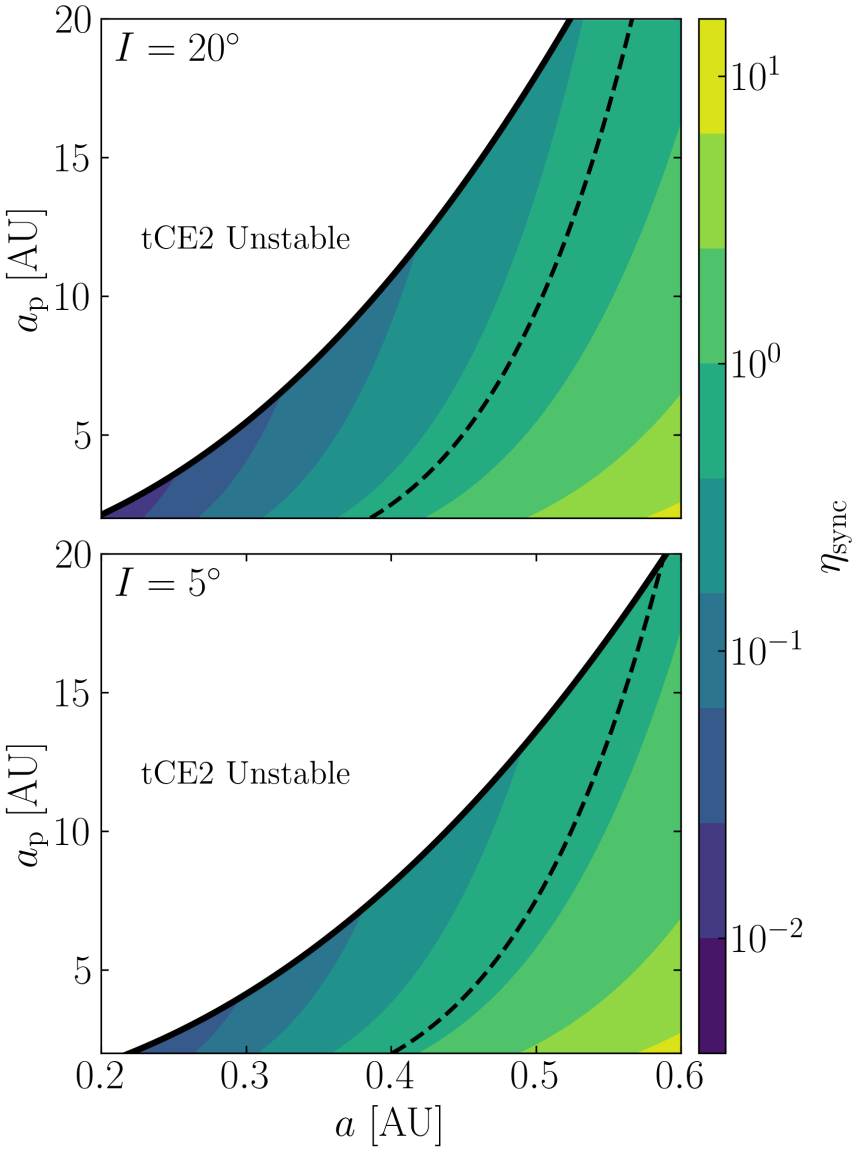

Figure 3.23: Depiction of the values of $\eta_{\rm sync}$ for the Super Earth + Cold Jupiter systems as a function of a and $a_{\rm p}$ for $I = 20°$ (top) and $I = 5°$ (bottom). The SE is taken to have $m = 4M_\oplus$ and $R = 2R_\oplus$ while the CJ is taken to have $m_{\rm p} = M_{\rm J}$, and we have taken $k \approx k_{\rm q}$ for the SE. We only show the regions satisfying $t_{\rm s} \geq t_{\rm s,c}$ (the stability condition for tCE2; Eqs. 3.48–3.51). The line satisfying $\eta_{\rm sync} = \eta_{\rm c}$ (Eq. 3.7) is shown as the black dashed line. Systems with $\eta_{\rm sync} \gtrsim 0.1$ have appreciable probabilities of being captured in permanent tCE2 with significant obliquities (see Figs. 3.20–3.22).

successfully produce USPs with the observed properties. In this scenario, USPs evolve from a subset of SE systems: a low-mass planet with an initial period of a few days maintains a small but finite eccentricity due to secular forcings from exterior companion planets (SEs or sub-Neptunes) and evolve to become a USP due to orbital decay driven by tidal dissipation.

Millholland and Spalding [2020] proposed an alternative formation mechanism of USPs based on obliquity tides (instead of eccentricity tides as in Pu and Lai, 2019). This mechanism consists of three stages:

- A proto-USP (with two external companions) is assumed to be rapidly captured into CS2 with appreciable obliquity and a pseudo-synchronous spin rate.
- The inner planet undergoes runaway tidal migration as a result of the decreasing semi-major axis and increasing obliquity while following CS2.
- The inward migration stalls when the tidal torque becomes sufficiently strong to destroy CS2.

Here, we evaluate the viability of the obliquity-driven migration scenario for USPs using the general results presented earlier in this paper.

First, the spin evolution timescale for typical proto-USP parameters is

$$\frac{1}{t_{\rm s}} = \frac{1}{1200\,{\rm yr}}\left(\frac{1}{4k}\right)\left(\frac{2k_2/Q}{10^{-3}}\right)\left(\frac{M_\star}{M_\odot}\right)^{3/2}\left(\frac{\rho}{\rho_\oplus}\right)^{-1}\left(\frac{a}{0.035\,{\rm AU}}\right)^{-9/2}. \tag{3.52}$$

where ρ is the density of the proto-USP, $\rho_\oplus$ is the density of the Earth, and we have adopted the (approximately) largest possible value for a (the semi-major axis of the proto-SE) to ensure that orbital decay can happen within the age of the system (see Eq. 3.56). This is much shorter than the age of the system, and so the proto-USP can quickly evolve into one of the stable tCE (either tCE1 or tCE2).

Next, to determine which tCE the planet evolves into, we need to evaluate $\eta_{\rm sync}$ (see Eq. 3.39). For simplicity, we consider the case where the proto-USP is surrounded by a single external planetary companion with $a_{\rm p} \gtrsim a$ (typical of Kepler multi-planet systems) but with $L_{\rm p} \gg L$ (this condition can easily be relaxed; see Section 3.5.3). To account for such a close-by companion, Eq. (3.4) must be modified to [see e.g. Lai and Pu, 2017]:

$$\omega_{\rm lp} = \frac{3m_{\rm p}}{4M_\star}\left(\frac{a}{a_{\rm p}}\right)^3 n f(\alpha), \tag{3.53}$$

where $\alpha = a/a_{\rm p}$ and

$$f(\alpha) \equiv \frac{b^{(1)}_{3/2}(\alpha)}{3\alpha} \approx 1 + \frac{15}{8}\alpha^2 + \frac{175}{64}\alpha^4 \ldots \tag{3.54}$$

with $b^{(1)}_{3/2}$ the Laplace coefficient. With this modification, $\eta_{\rm sync}$ (Eq. 3.39) is given by

$$\begin{aligned}\eta_{\rm sync} = 0.011 f(\alpha)\left(\frac{k}{k_{\rm q}}\right)\left(\frac{\rho}{\rho_\oplus}\right)\left(\frac{a}{0.035\,{\rm AU}}\right)^3 \cos I \\ \times \left(\frac{m_{\rm p}}{10M_\oplus}\right)\left(\frac{1.3a}{a_{\rm p}}\right)^3\left(\frac{M_\star}{M_\odot}\right)^{-2},\end{aligned} \tag{3.55}$$

where we have normalized $a_{\rm p}/a$ to 1.3 (corresponding to a period ratio $P_{\rm p}/P = 1.5$), for which $f(\alpha) \approx 5.5$. As $k/k_{\rm q} \sim 1$ (see footnote 1) for the close-in proto-USP, we have $\eta_{\rm sync} \lesssim 0.06$, much less than $\eta_{\rm c} \sim 1$ under most conditions[5]. As such, if the initial planetary obliquity is prograde, the planet is guaranteed to evolve into tCE1, and not tCE2 (see Figs. 3.15, 3.18–3.19). If we assume instead a randomly oriented initial planetary spin, Figs. 3.22–3.20 suggest that the probability of capture into tCE2 is small ($\lesssim 20\%$). A more sophisticated calculation including the effect of a third planet does not greatly modify these results.

[5]One can make $\eta_{\rm sync}$ larger by choosing a larger initial value for a, e.g. $a = 0.05\,{\rm AU}$. However, the planet would not be able to experience orbital decay for such a large value, see Eq. (3.56). Also note that Kepler systems of SEs have adjacent period ratios in the range of 1.3–4 [Fabrycky et al., 2014], corresponding to semi-major axis ratios of 1.2–2.5.

The second stage of the proposed mechanism, runaway inward migration after attaining tCE2, requires that the initial orbital decay timescale be sufficiently fast. Evaluating Eq. (3.49) for the relevant physical parameters, we find

$$-\frac{\dot{a}}{a} = \frac{1}{8\times10^8\,\mathrm{yr}}\left(1-\frac{\Omega_\mathrm{s}}{n}\cos\theta\right)\left(\frac{2k_2/Q}{10^{-3}}\right)\left(\frac{M_\star}{M_\odot}\right)^{3/2} \times\left(\frac{m}{M_\oplus}\right)^{-1}\left(\frac{R}{R_\oplus}\right)^5\left(\frac{a}{0.035\,\mathrm{AU}}\right)^{-13/2}. \tag{3.56}$$

For $\eta_\mathrm{sync} \ll \eta_\mathrm{c}$, Eqs. (3.41) imply that $\Omega_\mathrm{s}\cos\theta/n \ll 1$ in tCE2, so indeed the orbit of the proto-USP is able to decay within the lifetime of the system. On the other hand, in tCE1, $\omega_\mathrm{s} \approx n$ and $\cos\theta \simeq 1-\eta_\mathrm{sync}^2\sin^2 I/2$, so $\dot{a}/a$ is suppressed by a factor of $\sim \eta_\mathrm{sync}^2\sin^2 I$. This shows that a proto-USP in tCE1 is unable to initiate runaway orbital decay within the age of the system. Note that this constraint also implies η_sync (Eq. 3.55) cannot be increased by considering proto-USPs with larger values of a, as the initial orbital decay will become too slow.

Finally, we compute the orbital separation at which tCE2 becomes unstable when the tidal alignment torque is too strong. Evaluating Eq. (3.43), we find that tCE2 breaks ($t_\mathrm{s} \lesssim t_\mathrm{s,c}$) when the semi-major axis is smaller than a_break, where

$$\begin{aligned} a_\mathrm{break} &\simeq \left[\frac{k_\mathrm{q}}{k^3 f^3(\alpha)}\right]^{1/18}\left(\frac{2k_2}{Q}\right)^{1/9}\left(\sin I\cos^2 I\right)^{-1/9} \times\left(\frac{M_\star^2}{m_\mathrm{p}m}\right)^{1/6}\left(Ra_\mathrm{p}\right)^{1/2} \\ &\simeq 0.028\,\mathrm{AU}\left(\frac{2k_2/Q}{10^{-3}}\right)^{1/9}\left(\sin I\cos^2 I\right)^{-1/9}\left(\frac{M_\star}{M_\odot}\right)^{1/3} \times\left(\frac{m_\mathrm{p}}{10M_\oplus}\right)^{-1/6}\left(\frac{\rho}{\rho_\oplus}\right)^{-1/6}\left(\frac{a_\mathrm{p}}{0.05\,\mathrm{AU}}\right)^{1/2}, \end{aligned} \tag{3.57}$$

where we have used $k \sim k_\mathrm{q} \sim 0.4$ and $\alpha = 0.028/0.05$. Once the system exits tCE2, it rapidly evolves to tCE1, in which orbital decay is severely suppressed (Eq. 3.56). This final orbital separation does not qualify as a USP ($P \lesssim$ day). To reduce a_break to 0.0195 AU (corresponding to a 1 day orbital period for $M_\star = 1M_\odot$) would require the value of $a_\mathrm{p}/m_\mathrm{p}^{1/3}$ to be ~ 2 times smaller than that adopted in Eq. (3.57) (e.g. for

$m_{\rm p}$ to be larger by a factor of 8 for the same $a_{\rm p}$). Note that observed USPs almost always have $a_{\rm p}/a \gtrsim 3$ [Steffen and Farr, 2013, Winn et al., 2018].

In summary, our results suggest that only proto-USPs with large primordial obliquities have a nonzero probability of evolving into tCE2 initially[6]. More importantly, proto-USPs that successfully initiate runaway tidal migration after reaching tCE2 will likely cease their inward migration before becoming a USP.

3.5.3 Orbital decay of WASP-12b Driven by Obliquity Tides

WASP-12b is a hot Jupiter (HJ) with mass $m = 1.41 M_{\rm J}$ and radius $R = 1.89 R_{\rm J}$ orbiting a host star (with mass $M_\star = 1.36 M_\odot$ and radius $R_\star = 1.63 R_\odot$) on a $P = 1.09$ day ($a = 0.023$ AU) orbit [Hebb et al., 2009, Maciejewski et al., 2013]. Long-term observations have revealed that its orbit is undergoing decay with $P/\dot{P} = -3.2$ Myr [Maciejewski et al., 2016, Patra et al., 2017, Patra et al., 2020, Turner et al., 2021]. Such a rapid orbital decay puts useful constraints on the physics of tidal dissipation in the host star [e.g. Weinberg et al., 2017, Barker, 2020].

Millholland and Laughlin [2019] considered the possibility that the measured orbital decay of WASP-12b is caused by tidal dissipation in the HJ trapped in a high-obliquity CS due to an undetected planetary companion. We now evaluate the plausibility of this scenario. We begin with the planetary spin evolution timescale, which is given by (see Eq. (4.16)):

$$\frac{1}{t_{\rm s}} = \frac{1}{6000\,{\rm yr}} \left(\frac{1}{4k}\right) \left(\frac{2k_2/Q}{10^{-6}}\right) \left(\frac{M_\star}{1.36 M_\odot}\right)^{3/2} \times \left(\frac{m}{1.41 M_{\rm J}}\right)^{-1} \left(\frac{R}{1.89 R_{\rm J}}\right)^{3} \left(\frac{a}{0.023\,{\rm AU}}\right)^{-9/2}. \tag{3.58}$$

[6]The probability is small even for isotropic primordial obliquities. This low probability may not be an issue, as the occurence rate of USPs is only $\sim 0.5\%$ around solar type stars [Sanchis-Ojeda et al., 2014, Winn et al., 2018].

Thus, the spin of WASP-12b has plenty of time to find a tCE. We also wish to calculate $\eta_{\rm sync}$, but there are two uncertainties: (i) the properties of the hypothetical planet companion (mass $m_{\rm p}$) to WASP-12b are unknown, and it is likely that $L_{\rm p}$ is smaller than L; and (ii) we should evaluate $\eta_{\rm sync}$ using the "primordial" / initial value of a for WASP-12b at the start of its orbital migration, not necessarily its present day value. Concerning (i), we express the precession of $\hat{\mathbf{l}}$ about $\mathbf{J} = J\hat{\jmath} \equiv \mathbf{L} + \mathbf{L}_{\rm p}$, the total angular momentum axis, as

$$\frac{{\rm d}\hat{\mathbf{l}}}{{\rm d}t} = \omega_{\rm lp} \frac{J}{L_{\rm p}} \left(\hat{\mathbf{l}} \times \hat{\jmath}\right) \cos I, \tag{3.59}$$

where $\omega_{\rm lp}$ is given by Eq. (3.53). Thus, we see that the precession frequency g in Sections 3.2–3.4 is changed to (cf. Eq. 3.4)

$$g = -\omega_{\rm lp} \frac{J}{L_{\rm p}} \cos I = -\frac{3 m_{\rm p}}{4 M_\star} \left(\frac{a}{a_{\rm p}}\right)^3 n f(\alpha) \frac{J}{L_{\rm p}} \cos I. \tag{3.60}$$

Concerning (ii), we use the fiducial values for the initial semi-major axis $a_{\rm i} = 0.038\,{\rm AU}$ and initial semi-major axis ratio $a_{\rm p}/a_{\rm i} = 1.29$, to be justified *a posteriori*. Assuming $J/L_{\rm p} \simeq L/L_{\rm p}$ (i.e. $L \gg L_{\rm p}$), we have

$$\begin{aligned} \eta_{\rm sync,i} &\simeq \frac{k}{2k_{\rm q}} \left(\frac{m}{M_\star}\right)^2 \left(\frac{a_{\rm i}}{a_{\rm p}}\right)^{7/2} \left(\frac{a_{\rm i}}{R}\right)^3 f(\alpha_{\rm i}) \cos I, \\ &= 0.015 f(\alpha_{\rm i}) \left(\frac{m}{1.41 M_{\rm J}}\right)^2 \left(\frac{M_\star}{1.36 M_\odot}\right)^{-2} \\ &\quad \times \left(\frac{a_{\rm i}}{0.038\,{\rm AU}}\right)^3 \left(\frac{a_{\rm p}}{1.29 a_{\rm i}}\right)^{-7/2} \left(\frac{R}{1.89 R_{\rm J}}\right)^{-3} \cos I, \end{aligned} \tag{3.61}$$

where we have used $k/k_{\rm q} \simeq 1$. For the adopted fiducial of $a_{\rm i}$ and $a_{\rm p}$, $\alpha_{\rm i} = a_{\rm i}/a_{\rm p}$ and $f(\alpha_{\rm i}) \simeq 5$.

We next work towards justifying these choices of fiducial parameters. There are four physical and observational constraints on the "WASP-12b + companion" system (see Fig. 3.24):

(i) The HJ must have had a sufficiently small initial semi-major axis such that its orbital decay timescale is less than the age of the system. The orbital decay

rate is given by

$$-\left(\frac{\dot{a}}{a}\right)_{\rm i}=\frac{1}{\rm Gyr}\left(\frac{2k_2/Q}{10^{-6}}\right)\left(\frac{M_\star}{1.36M_\odot}\right)^{3/2}\left(\frac{m}{1.41M_{\rm J}}\right)^{-1}$$
$$\times\left(\frac{R}{1.89R_{\rm J}}\right)^{5}\left(\frac{a_{\rm i}}{0.038\,{\rm AU}}\right)^{-13/2}\left(1-\frac{\Omega_{\rm s}}{n}\cos\theta\right). \tag{3.62}$$

Thus, the initial semi-major axis for the HJ cannot exceed 0.038 AU even when $(1-\Omega_{\rm s}\cos\theta/n)\approx 1$.

(ii) The exterior planet must be sufficiently massive to keep the HJ in the high-obliquity tCE2 today, i.e. the tCE2 must be stable under the influence of the exterior planet. With the amended precession frequency $|g|$ given by Eq. (3.60), the stability of tCE2 requires (see Eq. 3.43)

$$\frac{1}{t_{\rm s}}\lesssim\omega_{\rm lp}\cos I\frac{J}{L_{\rm p}}\sin I_{\rm J}\sqrt{\frac{\eta_{\rm sync}\cos I_{\rm J}}{2}}, \tag{3.63}$$

where $\cos I_{\rm J}\equiv\hat{\mathbf{l}}\cdot\hat{\jmath}$. Using $\sin I_{\rm J}=\left(L_{\rm p}/J\right)\sin I\ll 1$ for $L\gg L_{\rm p}$, this yields

$$\frac{a_{\rm p}}{a}\lesssim\left[\frac{(kf(\alpha))^{3/2}}{k_{\rm q}^{1/2}}\sin I\cos^{3/2}I\frac{Q}{2k_2}\frac{m_{\rm p}m^2}{M_\star^3}\left(\frac{a}{R}\right)^{9/2}\right]^{4/19}$$
$$\simeq 3.5\left[\frac{k^3f^3(\alpha)}{k_{\rm q}}\right]^{2/19}\left(\sin I\cos^{3/2}I\right)^{4/19}\left(\frac{m}{1.41M_{\rm J}}\right)^{8/19}$$
$$\times\left(\frac{m_{\rm p}}{80M_\oplus}\right)^{4/19}\left(\frac{M_\star}{M_\odot}\right)^{-12/19}\left(\frac{2k_2/Q}{10^{-6}}\right)^{-4/19}$$
$$\times\left(\frac{a}{0.023\,{\rm AU}}\right)^{18/19}\left(\frac{R}{1.89R_{\rm J}}\right)^{-18/19}, \tag{3.64}$$

where in the second equality, we have used the currently observed values for a, m, R, and $M_\star$, and have set $\left(k^3f^3/k_{\rm q}\right)^{2/19}\simeq 1$.

(iii) The RV signal of the exterior planet must be smaller than the residuals of the published RVs, ~ 16 m/s [Hebb et al., 2009, Husnoo et al., 2011, Knutson et al., 2014, Bonomo et al., 2017]. This requires

$$\left(\frac{a_{\rm p}}{0.076\,{\rm AU}}\right)^{-1/2}\left(\frac{m_{\rm p}}{80M_\oplus}\right)\left(\frac{M_\star}{1.36M_\odot}\right)^{-1/2}\left(\frac{\sin i_{\rm p}}{1/\sqrt{2}}\right)\lesssim 1, \tag{3.65}$$

where $i_{\rm p}$ is the line-of-sight inclination angle of $m_{\rm p}$. Here, we have taken $a_{\rm p}$ to be the maximum value (3.3×0.023 AU) permitted by Eq. (3.64). For these extreme values of $a_{\rm p}$ and $m_{\rm p}$, we still have $L_{\rm p}/L \simeq 0.4$, and so $L \gg L_{\rm p}$ is satisfied for the permitted parameter space.

(iv) Finally, we require that the initial orbital configuration of the two planets be dynamically stable. We use the Hill stability criterion [e.g. Gladman, 1993, Petit et al., 2020],

$$a_{\rm p} - a_{\rm i} > 2\sqrt{3}\left(\frac{a_{\rm p}+a_{\rm i}}{2}\right)\left(\frac{m+m_{\rm p}}{3M_\star}\right)^{1/3}. \tag{3.66}$$

Assuming $m_{\rm p} \ll m$, this yields

$$\frac{a_{\rm p}}{a_{\rm i}} > 1.29. \tag{3.67}$$

The combination of the two constraints in Eqs. (3.62, 3.67) justify the fiducial parameters used in Eq. (3.64).

We next address the implications of the rather small "initial" $\eta_{\rm sync}$ value found in Eq. (3.61). When evaluating $\eta_{\rm sync,i}$, it is possible that R is larger today than its "primordial" value (at semi-major axis $a_{\rm i} > a$) due to inflation induced by increased stellar irradiation. However, if a smaller value of R is used in Eq. (3.61), the value of $a_{\rm i}$ must also be decreased such that $R^5/a_{\rm i}^{13/2}$ is constant in order to maintain the same $(\dot{a}/a)_{\rm i}$ (see Eq. 3.62), which further decreases $\eta_{\rm sync,i}$.

For $\eta_{\rm sync,i} \sim 0.075$ (corresponding to the fiducial parameters used in Eq. 3.61), we can infer that prograde primordial obliquities will evolve towards tCE1 (see Figs. 3.15, 3.20–3.21). On the other hand, if the primordial obliquity of the HJ is assumed to be isotropically distributed, then Fig. 3.20 suggests that the probability of entry into tCE2 is $\lesssim 25\%$ even if the perturbing planet is misaligned by $I_{\rm J} \sim I \sim 20^\circ$. In reality, $\sin I_{\rm J} = \left(L_{\rm p}/J\right)\sin I \ll \sin I$ for $L_{\rm p} \ll L$, so the probability is likely much smaller (see Eq. 3.47 with I replaced by $I_{\rm J}$).

Figure 3.24 illustrates the joint constraints on the possible companion to WASP-12b and the resulting range of $\eta_{\rm sync,i}$ values. These small $\eta_{\rm sync,i}$ values suggest that capture of WASP-12b into the high-obliquity tCE2 is unlikely from either an isotropic or prograde-favoring initial obliquity distribution, and the observed orbital decay of WASP-12b is unlikely to be driven by obliquity tides in the planet. For obliquity tides to be operating today, we would have to imagine a scenario where dynamical effects when the WASP-12b system was young may have preferentially generated tCE2-producing systems, i.e. systems with $\theta_{\rm i} \simeq 90^\circ$. While the scenario considered by Millholland and Batygin [2019] and Su and Lai [2020] with an exterior, dissipating protoplanetary disk does not directly apply here due to the slow disk dispersal time scale, a similar effect (decreasing η) can be accomplished by simultaneous disk-driven migration of an inner HJ and exterior companion. The exploration of such a scenario in the context of HJ formation is beyond the scope of this paper.

3.6 Summary and Discussion

We have presented a comprehensive study on the evolution of a planet's spin (both magnitude and direction) due to the combined effects of tidal dissipation and gravitational interaction with an exterior companion/perturber. This paper extends our previous study [Su and Lai, 2020] of Colombo's Top ("spin + companion" system) to include dissipative tidal effects, for which we have adopted the weak friction theory of the equilibrium tide. Our paper contains several new general theoretical results that can be adapted to various situations, as well as three applications to exoplanetary systems of current interest.

We summarize our general theoretical results and provide a guide to the key

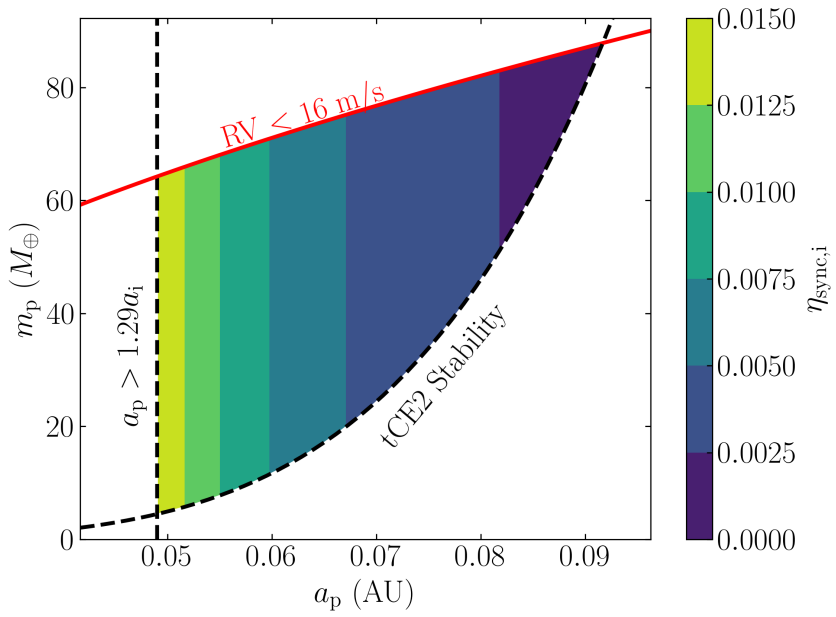

Figure 3.24: Constraints on the companion of WASP-12b and the values of $\eta_{\rm sync,i}$ (Eq. 3.61) in the obliquity tidal decay scenario. The right dashed line is from Eq. (3.64), required for the current system to be locked in a stable tCE2; the left vertical line is from Eq. (3.67), required for the dynamical stability of the "primordial" system; the red line is from Eq. (3.65). The probability of capture into tCE2 (starting from a isotropic distribution of spin orientation) is proportional to $\eta_{\rm sync,i}^{1/2}$ (see Eq. 3.47 with I replaced by $I_{\rm J}$, and note that $I_{\rm J} \ll 1$ for the WASP-12b system). The plot adopts the largest possible value of $a_{\rm i}$ ($= 0.038\,{\rm AU} > 0.023\,{\rm AU} = a$); using a smaller $a_{\rm i}$ would significantly reduce $\eta_{\rm sync,i}$, making capture into tCE2 even less likely.

equations and figures as follows:

1. In the presence of a spin-orbit alignment torque (such as that arising from tidal dissipation), our linear analysis (Section 3.3.2) shows explicitly that only two of the equilibrium spin orientations (called "Cassini States", CSs) are stable and attracting (see Fig. 3.1): the "simple" CS1 (which typically has a low obliquity) and the "resonant" CS2 (which can have a large obliquity). The latter arises from the spin-orbit resonance, which occurs when the spin precession frequency of the planet is comparable to the orbital precession frequency driven by the companion. However, when the alignment torque is too strong (or the alignment timescale $t_{\rm al}$ too short), the CSs themselves can be significantly modified. In particular, when $t_{\rm al}$ is shorter than a critical value (of order the planet's orbital precession period; see Eq. 3.13), CS2 becomes destabilized and ceases to exist.

2. We compute the long-term evolution of the planetary spin obliquity driven by the alignment torque for an arbitrary initial spin orientation (Section 3.3.3). When neglecting the evolution of the planet's spin magnitude, which implies that the spin and orbital precession frequencies α, g (see Eqs. 4.4–3.4) and the ratio $\eta = -g/\alpha$ are held constant, the asymptotic outcomes of the obliquity evolution (CS1 or CS2) can be analytically determined from the initial spin orientation (see Fig. 3.5), and we have obtained a new analytical expression for the probability of resonance capture into CS2 (Eq. 3.30 and Fig. 3.7).

3. In general, tidal torques act on both the obliquity and magnitude of the planetary spin, thus the ratio $\eta = -g/\alpha$ (which determines the phase-space structure of the system) evolves in time. Still, there are at most two equilibrium configurations (spin magnitude and obliquity) that are stable under

the effect of tidal dissipation. We call these *tidal Cassini Equilibria* (tCE; see Fig. 3.8). The locations of these equilibria are determined by the system architecture and are parameterized by $\eta_{\rm sync}$ (Eq. 3.39), the ratio η evaluated for $\Omega_s = n$ (fully synchronized spin rate).

4. We show that if tCE1 exists (which requires $\eta_{\rm sync} < \eta_{\rm c}$, where $\eta_{\rm c}$ is given by Eqs. 3.7; Section 3.4.1), which tCE a given initial planetary spin configuration asymptotically evolves towards depends on which of the phase space zones (see Fig. 3.2) the initial spin orientation belongs to (see Figs. 3.15–3.17): (i) If the spin originates in zone I, then it generally evolves towards tCE1 (unless $\eta_{\rm sync}$ very near $\eta_{\rm c}$, e.g. see Fig. 3.17); (ii) if the spin originates in zone II, then it evolves towards tCE2 (which has a nontrivial obliquity); and (iii) if the spin originates in zone III, the outcome is generally probabilistic.

5. For initial conditions in zone III, the probability of approaching either tCE can be determined by careful study of the dynamics upon separatrix encounter (Sections 3.3.4 and 3.4.3); Figs. 3.18 and 3.19 give two example results. Assuming that the initial spin orientation is isotropically distributed, we have computed the overall probability of the system evolving into tCE2 as a function of $\eta_{\rm sync}$: Figs. 3.20 and 3.21 give the results for two different planet mutual inclinations, and Eq. (3.47) gives an approximate analytical expression valid for $\eta_{\rm sync} \ll 1$.

Applying our general theoretical results to three types of exoplanetary systems, our key findings are (see Section 3.5):

1. We show that over a wide range of parameter space, a super Earth (SE) with an exterior cold Jupiter companion (or other types of companions with a similar $m_{\rm p}/a_{\rm p}^3$) has a substantial probability of being trapped in a permanent

tCE2 with a significant obliquity, assuming that SEs have a wide range of primordial obliquities (e.g. due to giant impacts or collisions).

2. We show that, in general, the formation of ultra-short-period planets (USPs) via runaway orbital decay driven by obliquity tides is difficult due to the low probability of capture into the high-obliquity tCE2. More importantly, proto-USPs that happen to be captured into tCE2 and initiate runaway tidal migration will likely break away from tCE2 and cease their inward migration before becoming a USP.
3. The hot Jupiter WASP-12b is unlikely to be undergoing enhanced orbital decay due to obliquity tides, as the capture into tCE2 has a low probability or requires rather special initial conditions.

Finally, we mention some possible caveats of our study. We have adopted dissipative tidal torques according to the (parameterized) weak friction theory of the equilibrium tide. Other mechanisms of tidal dissipation may be dominant, depending on the internal property of the planet and the nature of tidal forcing [e.g. Papaloizou and Ivanov, 2010, Ogilvie, 2014, Storch and Lai, 2013]. We expect that, with proper parameterization and rescaling, our theoretical results presented in Sections 3.3–3.4 are largely unaffected by the details of the tidal model. In any case, a different tidal model is amenable to the same analysis as presented in this paper: The tCEs can still be found by an analysis similar to that shown in Fig. 3.8, and the probabilistic outcome of a separatrix encounter can still be solved using the techniques developed in Sections 3.3.4 and 3.4.3.

Some of results presented in Section 3.4, such as Figs. 3.20–3.22, pertain to the probabilistic outcomes of an initially isotropic distribution of spin orientations, assuming that giant impacts or planet collisions effectively randomize a planet's primordial spin. More physically accurate distributions can be used in

the case of planetary mergers [Li and Lai, 2020] or many smaller impacts [Dones and Tremaine, 1993]. Figures 3.20–3.21 can be updated accordingly by convolving any initial obliquity distribution with the tCE2 capture probability distributions, such as those shown in the right panels of Figs. 3.15–3.17 or the upper panels of Figs. 3.18–3.19. The qualitative results are unlikely to change, though the detailed probabilities for tCE2 capture can increase (decrease) if the initial obliquity distribution favors (disfavors) $\theta_{\rm i} \approx 90^\circ$ compared to the isotropic distribution.

CHAPTER 4

DYNAMICS OF COLOMBO'S TOP: NON-TRIVIAL OBLIQUE SPIN EQUILIBRIA OF SUPER-EARTHS IN MULTI-PLANETARY SYSTEMS

Originally published in:
Yubo Su and Dong Lai. Dynamics of Colombo's Top: Non-trivial oblique spin equilibria of super-Earths in multi-planetary systems. *MNRAS*, 2022a

4.1 Introduction

The obliquity of a planet, the angle between the spin and orbital axes, plays an important role in the atmospheric dynamics, climate, and potential habitability of the planet. For instance, the atmospheric circulation of a planet changes dramatically as the obliquity increases beyond 54°, as the averaged insolation at the poles becomes greater than that at the equator [Ferreira et al., 2014, Lobo and Bordoni, 2020]. Variations in insolation over long timescales can also affect the habitability of an exoplanet [Spiegel et al., 2010, Armstrong et al., 2014]. In the Solar System, planetary obliquities range from nearly zero for Mercury and 3.1° for Jupiter, to 23° for Earth and 26.7° for Saturn, to 98° for Uranus. The obliquities of exoplanets are challenging to measure, and so far only loose constraints have been obtained for the obliquities of faraway planetary-mass companions [Bryan et al., 2020, 2021]. Nevertheless, there are prospects for better constraints on exoplanetary obliquities in the coming years [Snellen et al., 2014, Bryan et al., 2018, Seager and Hui, 2002]. Substantial obliquities are of great theoretical interest for their proposed role in explaining peculiar thermal phase curves of transiting planets [Adams et al., 2019, Ohno and Zhang, 2019] and various other open dynamical puzzles [Millholland and Laughlin, 2018, 2019, Millholland and Spalding, 2020, Su and Lai, 2021].

The obliquity of a planet reflects its dynamical history. Some obliquities could be generated in the earliest phase of planet formation, when/if proto-planetary disks are turbulent and twisted [Tremaine, 1991, Jennings and Chiang, 2021]. Large obliquities are commonly attributed to giant impacts or planet collisions as a result of dynamical instabilities of planetary orbits [Safronov and Zvjagina, 1969, Benz et al., 1989, Korycansky et al., 1990, Dones and Tremaine, 1993, Morbidelli et al., 2012, Li and Lai, 2020, Li et al., 2021]. Repeated planet-planet scatterings could also lead to modest obliquities [Hong et al., 2021, Li, 2021]. Substantial obliquity excitation can be achieved over long (secular) timescales via spin-orbit resonances, when the spin precession and orbital (nodal) precession frequencies of the planet become comparable [Ward and Hamilton, 2004, Hamilton and Ward, 2004, Ward and Canup, 2006, Vokrouhlickỳ and Nesvornỳ, 2015, Millholland and Batygin, 2019, Saillenfest et al., 2020, Su and Lai, 2020, Saillenfest et al., 2021]. Such resonances are likely responsible for the obliquities of the Solar System gas giants and may have also played a role in generating obliquities of ice giants [Rogoszinski and Hamilton, 2020]. For terrestrial planets, multiple spin-orbit resonances and their overlaps can make the obliquity vary chaotically over a wide range [Laskar and Robutel, 1993, Touma and Wisdom, 1993, Correia et al., 2003].

A large fraction ($30-90\%$) of Sun-like stars host close-in super Earths (SEs), with radii $1-4R_\oplus$ and orbital distances $\lesssim 0.5$ AU, mostly in multi-planetary (≥ 3) systems [e.g. Lissauer et al., 2011, Howard et al., 2012, Zhu et al., 2018, Sandford et al., 2019, Yang et al., 2020, He et al., 2021]. In these systems, the SE orbits are mildly misaligned with mutual inclinations $\sim 2^\circ$ [Lissauer et al., 2011, Tremaine and Dong, 2012, Fabrycky et al., 2014], which increase as the number of planets in the system decreases [Zhu et al., 2018, He et al., 2020]. In addition, ~ 30–40% of the SE systems are accompanied by cold Jupiters [CJs; masses $\gtrsim 0.5M_{\rm J}$ and

semi-major axes $\gtrsim 1\,\mathrm{AU}$ Zhu and Wu, 2018, Bryan et al., 2019] with significantly inclined ($\gtrsim 10^\circ$) orbits relative to the SEs [Masuda et al., 2020].

SEs are formed in gaseous protoplanetary disks, and likely have experienced an earlier phase of giant impacts and collisions following the dispersal of disks [e.g. Liu et al., 2015b, Inamdar and Schlichting, 2016, Izidoro et al., 2017]. As a result, the SEs' initial obliquities are expected to be broadly distributed [Li and Lai, 2020, Li et al., 2021]. However, due to the proximity of these planets to their host stars, tidal dissipation can change the planets' spin rates and orientations substantially within the age of the planetary system. Indeed, the tidal spin-orbit alignment timescale is given by

$$t_{\rm al} \simeq (30\,{\rm Myr})\left(\frac{Q/2k_2}{10^3}\right)\left(\frac{M_\star}{M_\odot}\right)^{-3/2} \times \left(\frac{m}{4m_\oplus}\right)\left(\frac{R}{2R_\oplus}\right)^{-3}\left(\frac{a}{0.4\,{\rm AU}}\right)^{9/2}, \tag{4.1}$$

where m, R, k_2, Q, and a are the planet's mass, radius, tidal Love number, tidal quality factor, and semi-major axis respectively, and $M_\star$ is the stellar mass. In a previous paper [Su and Lai, 2021], we have studied the combined effects of spin-orbit resonance and tidal dissipation in a two-planet system (i.e. a SE with a companion), and showed that the planet's spin can only evolve into to two possible long-term equilibria ("Tidal Cassini Equilibria"), one of which can have a significant obliquity. In this paper, we extend our analysis to three-planet systems consisting of either three SEs or two SEs and a CJ. In addition to the equilibria analogous to those of the two-planet case, we discover a novel class of oblique spin equilibria unique to multi-planet systems. Such equilibria can substantially increase the occurrence rate of oblique SEs in these architectures.

This paper is organized as follows. In Section 4.2, we summarize the evolution of a SE in a multi-planetary system. In Section 4.3, we introduce a tidal alignment

torque that damps the SE's obliquity and investigate the resulting steady-state behavior. In Section 4.4, we evolve both the SE spin rate and orientation according to weak friction theory of the equilibrium tide. We show that the qualitative dynamics are similar to the simpler model studied in Section 4.3. We summarize and discuss in Section 4.5.

4.2 Spin Equations of Motion

The unit spin vector $\hat{\mathbf{S}}$ of an oblate planet orbiting a host star precesses around the planet's unit angular momentum $\hat{\mathbf{L}}$ following the equation

$$\frac{\mathrm{d}\hat{\mathbf{S}}}{\mathrm{d}t} = \alpha\left(\hat{\mathbf{S}}\cdot\hat{\mathbf{L}}\right)\left(\hat{\mathbf{S}}\times\hat{\mathbf{L}}\right), \tag{4.2}$$

where the characteristic spin-orbit precession frequency α is given by

$$\begin{aligned}\alpha &= \frac{3GJ_2mR^2M_\star}{2a^3C\Omega_\mathrm{s}} = \frac{3k_q}{2k}\frac{M_\star}{m}\left(\frac{R}{a}\right)^3\Omega_\mathrm{s} \\ &= \frac{1}{150\,\mathrm{yr}}\left(\frac{k_\mathrm{q}}{k}\right)\left(\frac{M_\star}{M_\odot}\right)^{3/2} &(4.3)\\ &\quad\times\left(\frac{m}{2M_\oplus}\right)^{-1}\left(\frac{R}{1.2R_\oplus}\right)^3\left(\frac{a}{0.1\,\mathrm{AU}}\right)^{-9/2}\frac{\Omega_\mathrm{s}}{n}. &(4.4)\end{aligned}$$

In Eq. (4.4), Ω_s is the rotation rate of the planet, $C = kmR^2$ is its moment of inertia (with k the normalized moment of inertia), $J_2 = k_\mathrm{q}\Omega_\mathrm{s}^2(R^3/Gm)$ (with k_q a constant) is its rotation-induced (dimensionless) quadrupole moment, and $n \equiv \sqrt{GM_\star/a^3}$ is its mean motion. For a SE, we adopt $k \sim k_\mathrm{q} \sim 0.3$ [e.g. Groten, 2004, Lainey, 2016].

The orbital axis $\hat{\mathbf{L}}$ also evolves in time, precessing and nutating about the total angular momentum axis of the exoplanetary system, which we denote by $\hat{\mathbf{J}}$. When there are just two planets, this precession is uniform (with rate g and constant inclination angle between $\hat{\mathbf{L}}$ and $\hat{\mathbf{J}}$), and the spin dynamics of the planet is described by the well-studied "Colombo's Top" system [Colombo, 1966, Peale,

1969, 1974, Ward, 1975, Henrard and Murigande, 1987]. The spin equilibra of this system are termed "Cassini States" (CSs), and the number of CSs and their obliquities depend on the ratio $\eta \equiv |g|/\alpha$. In the presence of a tidal spin-orbit alignment torque, up to two equilibria are stable and attracting, as shown in [Su and Lai, 2021; see also Fabrycky et al., 2007, Levrard et al., 2007, Peale, 2008]: for $\eta \gg 1$, only CS2 is stable, with $\hat{\mathbf{S}}$ nearly aligned with $\hat{\mathbf{J}}$; for $\eta \lesssim 1$, $\hat{\mathbf{S}}$ can evolve towards two possible states, the "trivial" CS1 with a small spin-orbit misalignment angle $\theta_{\rm sl}$, or the "resonant" CS2 with significant $\theta_{\rm sl}$ (which approaches 90° for $\eta \ll 1$).

When the SE is surrounded by multiple companions, the precession of $\hat{\mathbf{L}}$ occurs on multiple characteristic frequencies [see Murray and Dermott, 1999]. In this case, the spin dynamics given by Eq. (4.2) is complex and can lead to chaotic behavior [e.g. the chaotic obliquity evolution of Mars Laskar and Robutel, 1993, Touma and Wisdom, 1993]. But what is the final equilibrium state of $\hat{\mathbf{S}}$ in the presence of tidal alignment? In this paper, we focus on the case where the SE has two planetary companions. If the mutual inclinations among the three planets are small, then the explicit solution for $\hat{\mathbf{L}}(t)$ can be written as [Murray and Dermott, 1999]

$$\begin{aligned}\mathscr{I} &\equiv I\exp(i\Omega)\\ &= I_{\rm (I)}\exp\left[ig_{\rm (I)}t+i\phi_{\rm (I)}\right]+I_{\rm (II)}\exp\left[ig_{\rm (II)}t+i\phi^{\rm (II)}\right], \qquad (4.5)\\ \hat{\mathbf{L}} &= \Re(\mathscr{I})\hat{\mathbf{X}}+\Im(\mathscr{I})\hat{\mathbf{Y}}+\sqrt{1-|\mathscr{I}|^2}\,\hat{\mathbf{Z}}. \qquad (4.6)\end{aligned}$$

Here, I is the inclination of $\hat{\mathbf{L}}$ relative to $\hat{\mathbf{J}}$, $\mathscr{I}$ is the complex inclination, the quantities $I_{\rm (I,II)}$, $g_{\rm (I,II)}$ and $\phi_{\rm (I,II)}$ are the amplitudes, frequencies, and phase offsets of the two inclination modes, indexed by (I) and (II), and the Cartesian coordinate system XYZ is defined such that $\hat{\mathbf{J}} = \hat{\mathbf{Z}}$. Without loss of generality, we denote mode I as the dominant mode, with $I_{\rm (I)} \geq I_{\rm (II)}$. For simplicity, we fix $\phi_{\rm (I)} = \phi_{\rm (II)} = 0$.

4.3 Steady States Under Tidal Alignment Torque.

Since SEs are close to their host stars, tidal torques tend to drive $\hat{\mathbf{S}}$ towards alignment with $\hat{\mathbf{L}}$ and $\Omega_{\rm s}$ towards synchronization with the mean motion (see Eq. 4.1). As the evolution of $\Omega_{\rm s}$ also changes α (Eq. 4.4) and the underlying phase-space structure, we first consider the dynamics when ignoring the spin magnitude evolution. In this case, the planet's spin orientation experiences an alignment torque, which we describe by

$$\left(\frac{{\rm d}\hat{\mathbf{S}}}{{\rm d}t}\right)_{\rm al} = \frac{1}{t_{\rm al}}\hat{\mathbf{S}}\times\left(\hat{\mathbf{L}}\times\hat{\mathbf{S}}\right), \tag{4.7}$$

where $t_{\rm al}$ is given by Eq. (4.1). Note that $t_{\rm al}$ is significantly longer than all precession timescales in the system.

With two precessional modes for $\hat{\mathbf{L}}(t)$, we expect that the tidally stable spin equilibria (steady states) correspond to the stable, attracting CSs for each mode, when they exist. In other words, if we denote the CS2 corresponding to mode I by CS2(I), then we expect that the tidally stable equilibria are among the four CSs: CS1(I) (if it exists), CS2(I), CS1(II) (if it exists), and CS2(II). The corresponding CS obliquities $\theta_{\rm sl}\equiv\cos^{-1}(\hat{\mathbf{S}}\cdot\hat{\mathbf{L}})$ are given by

$$\alpha\cos\theta_{\rm sl} = -g_{\rm (I,II)}\left(\cos I_{\rm (I,II)} + \sin I_{\rm (I,II)}\cot\theta_{\rm sl}\cos\phi_{\rm sl}\right), \tag{4.8}$$

where the azimuthal angle $\phi_{\rm sl}$ of $\hat{\mathbf{S}}$ around $\hat{\mathbf{L}}$ is $\phi_{\rm sl}=0$ (corresponding to $\hat{\mathbf{S}}$ and $\hat{\mathbf{J}}$ being coplanar but on opposite sides of $\hat{\mathbf{L}}$) for CS1 and $\phi_{\rm sl}=\pi$ for CS2 [note that because of the tidal alignment torque, the actual $\phi_{\rm sl}$ value is slightly shifted from 0 or π; see Su and Lai, 2021].

To confront this expectation, we integrate Eqs. (4.2), (4.6), and (4.7) numerically starting from various spin orientations. Figure 4.1 shows two evolutionary trajectories for a system with $I_{\rm (I)}=10^\circ$, $I_{\rm (II)}=1^\circ$, $\left|g_{\rm (I)}\right|=0.1\alpha$, and $\left|g_{\rm (II)}\right|=0.01\alpha$.

Such a system can be realized, for instance, by three SEs with masses $M_\oplus$, $3M_\oplus$, and $3M_\oplus$ and semi-major axes 0.1 AU, 0.15 AU, and 0.4 AU (see the left panels of Fig. C.1 in the Appendix[1]). We see that the initially retrograde spin is eventually captured into a steady state centered around CS1 or CS2 of the dominant mode (i.e. mode I), with $\phi_{\rm sl}$ librating around 0 or π, respectively. The small oscillation of the final $\theta_{\rm sl}$ is the result of perturbations from mode II.

In addition to CS1(I) and CS2(I), we find that the spin can also settle down into other equilibria (steady states) with different librating angles. In general, we define the resonant phase angle

$$\phi_{\rm res} \equiv \phi_{\rm sl} - g_{\rm res} t. \tag{4.9}$$

The examples shown in Fig. 4.1 correspond to $g_{\rm res} = 0$. In Fig. 4.2, we show three evolutionary trajectories (with three different initial spin orientations) of a system with the same parameters as in Fig. 4.1 but with $g_{\rm (II)} = -\alpha$. Such a system can be realized, for instance, by two warm SEs orbited by a cold Jupiter (see the right panels of Fig. C.3 in the Appendix where α_3 is small). Among these three examples, the first is captured into a resonance with $g_{\rm res} = 0$ [i.e. CS2(I)], the second is captured into a resonance with $g_{\rm res} = \Delta g \equiv g_{\rm (II)} - g_{\rm (I)}$, and the third is captured into a resonance with $g_{\rm res} = \Delta g/2$.

To explore the regimes under which various resonances are important, we numerically determine [by integrating Eqs. (4.2), (4.6), and (4.7)] the final spin equilibria (steady states) for systems with different mode parameters ($I_{\rm (I)}$, $I_{\rm (II)}$, $g_{\rm (I)}$, and $g_{\rm (II)}$), starting from all possible initial spin orientations. Fig. 4.3 shows some examples of such a calculation for $I_{\rm (I)} = 10^\circ$, $I_{\rm (II)} = 1^\circ$, $g_{\rm (I)} = -0.1\alpha$ (the same as

[1]Note that the mode amplitudes $I_{\rm (I)}$ and $I_{\rm (II)}$ in Fig. C.1 are closer in magnitude than the case we consider here. We exaggerate the inclination hierarchy for a more intuitive physical picture, and explore the case where the modes are of comparable amplitudes later in the paper and in Appendix C.2.

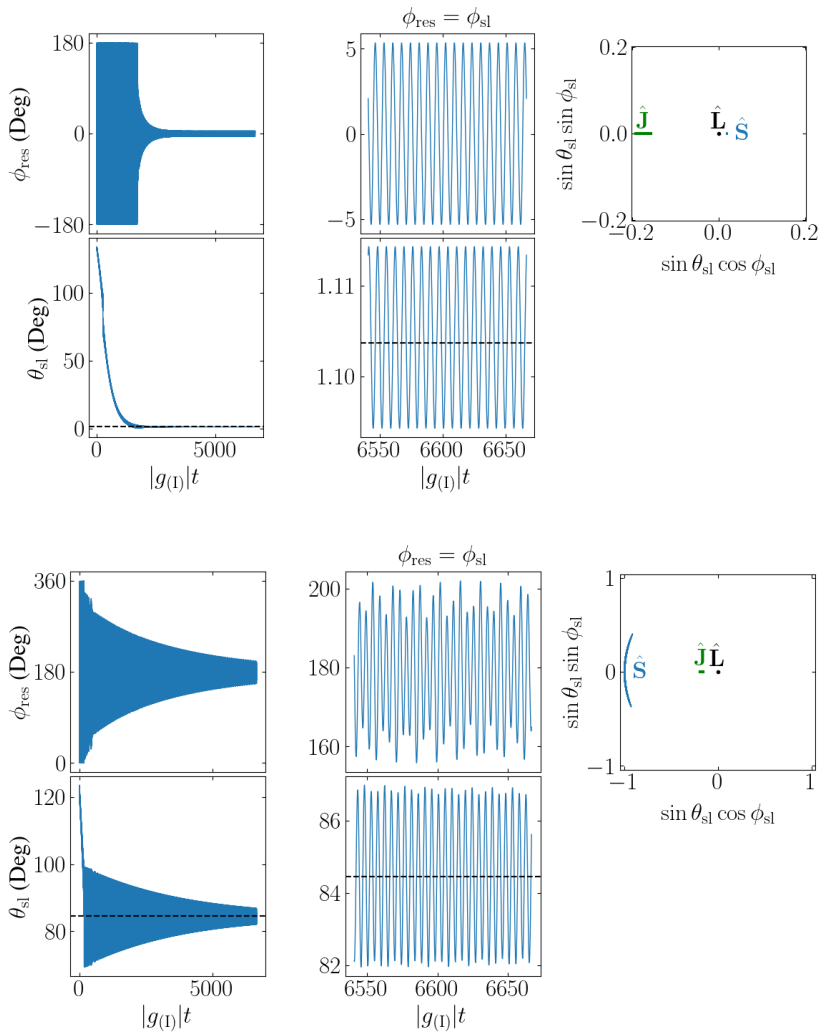

Figure 4.1: Two evolutionary trajectories of $\hat{\mathbf{S}}$ showing capture into mode I resonances (CSs). In both cases, the mode parameters describing the evolution of $\hat{\mathbf{L}}$ (see Eq. 4.6) are $I_{(\rm I)} = 10°$, $I_{(\rm II)} = 1°$, $g_{(\rm I)} = -0.1\alpha$, and $g_{(\rm II)} = 0.1g_{(\rm I)}$, while the initial spin orientations differ. In the top group of plots showing capture into CS1(I) [i.e. Cassini State 1 of mode I], the left four panels show the evolution of the spin obliquity $\theta_{\rm sl}$ and the resonant phase angle $\phi_{\rm res}$; in this case, $\phi_{\rm res}$ equals $\phi_{\rm sl}$, the azimuthal angle of $\hat{\mathbf{S}}$ around $\hat{\mathbf{L}}$, defined so that $\phi_{\rm sl} = 0$ corresponds to $\hat{\mathbf{S}}$ and $\hat{\mathbf{J}}$ being coplanar with $\hat{\mathbf{L}}$ but on opposite sides of $\hat{\mathbf{L}}$. The horizontal black dashed line shows the theoretically predicted obliquity of CS1(I), given by Eq. (4.8). The right panel shows the final steady-state spin axis projected onto the orbital plane (perpendicular to $\hat{\mathbf{L}}$). In these coordinates, $\hat{\mathbf{L}}$ (black dot) is stationary, while $\hat{\mathbf{J}}$ (green line) librates with a fixed orientation, and $\hat{\mathbf{S}}$ is shown in blue. The bottom group of panels shows the same but for capture into the CS2(I) resonance.

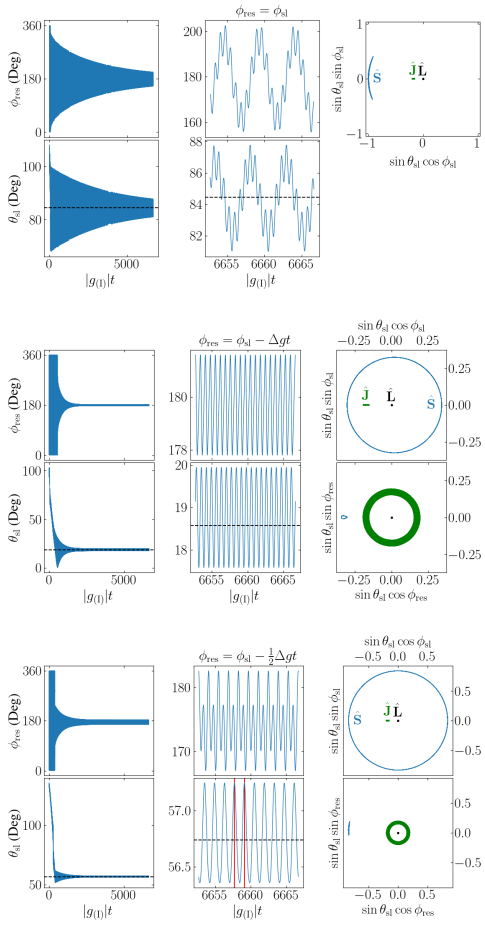

Figure 4.2: Three evolutionary trajectories for a system with the same parameters as in Fig. 4.1, except for $g_{(\mathrm{II})} = -\alpha = 10g_{(\mathrm{I})}$. The three examples correspond to capture into CS2(I) (with $\phi_{\mathrm{res}} = \phi_{\mathrm{sl}}$), a resonance with $\phi_{\mathrm{res}} = \phi_{\mathrm{sl}} - \Delta g t$ [corresponding to CS2(II)], and a "mixed mode" resonance with $\phi_{\mathrm{res}} = \phi_{\mathrm{sl}} - \Delta g t/2$, where $\Delta g = g_{(\mathrm{II})} - g_{(\mathrm{I})}$. In the bottom two groups of plots, ϕ_{sl} is not the resonant angle, so the spin axis encircles $\hat{\mathbf{L}}$ in the top-right plots. For these two cases, we also display in the bottom-right panels the projection of the steady-state spin axis onto the $\hat{\mathbf{L}}$ plane but with ϕ_{res} as the azimuthal angle. In these two panels, $\hat{\mathbf{J}}$ encircles $\hat{\mathbf{L}}$ (as shown by the green ring), but the spin can be seen not to encircle $\hat{\mathbf{L}}$, indicating that ϕ_{res} is indeed librating. Finally, for the mixed-mode example (bottom group), the vertical red lines in the bottom-middle panel are separated by $2\pi/|g_{\mathrm{res}}| = 4\pi/|\Delta g|$, denoting the period of oscillation in θ_{sl}.

in Figs. 4.1–4.2), but with the four different values of $g_{(\mathrm{II})} = \{0.1, 2.5, 3.5, 10\} \times g_{(\mathrm{I})}$. We identify three qualitatively different regimes:

- When $|g_{(\mathrm{II})}| \ll |g_{(\mathrm{I})}|$ (top-left panel of Fig. 4.3), mode II serves as a slow, small-amplitude perturbation to the dominant mode I, and the spin evolution is very similar to that studied in Su and Lai [2021]: prograde initial conditions (ICs) outside of the mode-I resonance evolve towards CS2(I), ICs inside the resonance evolve to CS2(I), and retrograde ICs outside of the mode-I resonance reach one of the two probabilistically.
- When $|g_{(\mathrm{II})}| \sim |g_{(\mathrm{I})}|$ (see the top-right and bottom-left panels of Fig. 4.3), the resonances corresponding to the two modes overlap, chaotic obliquity evolution occurs [see Touma and Wisdom, 1993, Laskar and Robutel, 1993], and we expect that CS2(I) becomes less stable[2]. Indeed we see that in this regime, fewer ICs evolve into the high-obliquity CS2(I) equilibrium of the dominant mode I, and most ICs lead to the low-obliquity CS1(I).
- When $|g_{(\mathrm{II})}| \gg |g_{(\mathrm{I})}|$ (see the bottom-right panel of Fig. 4.3), the separatrix for mode II does not exist, we see that all ICs inside the separatrix of mode I again converge successfully to CS2(I), and CS2(II) becomes the preferred low-obliquity equilibrium. Additionally, a narrow band of ICs with $\cos\theta_{\mathrm{sl},0} \sim 0.6$ and some other scattered ICs with $\cos\theta_{\mathrm{sl},0} \lesssim 0.6$ evolve to the mixed-mode equilibrium with $g_{\mathrm{res}} = \Delta g/2$, which has $\theta_{\mathrm{eq}} \approx 60^\circ$. A second mixed-mode resonance with $g_{\mathrm{res}} = \Delta g/3$ is also observed (with $\theta_{\mathrm{eq}} \approx 67^\circ$) for a sparse set of ICs.

Towards a better understanding of how systems are captured into these mixed-

[2] An more precise resonance overlap condition can be obtained by comparing the separatrix widths, as the mode-II resonance is much narrower even when $g_{(\mathrm{I})} = g_{(\mathrm{II})}$. Such a condition would require $g_{(\mathrm{I})} \sin I_{(\mathrm{I})} \sim g_{(\mathrm{II})} \sin I_{(\mathrm{II})}$. Thus, the onset of chaos due to resonance overlap occurs somewhere in the range $I_{(\mathrm{II})}/I_{(\mathrm{I})} \lesssim g_{(\mathrm{II})}/g_{(\mathrm{I})} \lesssim 1$.

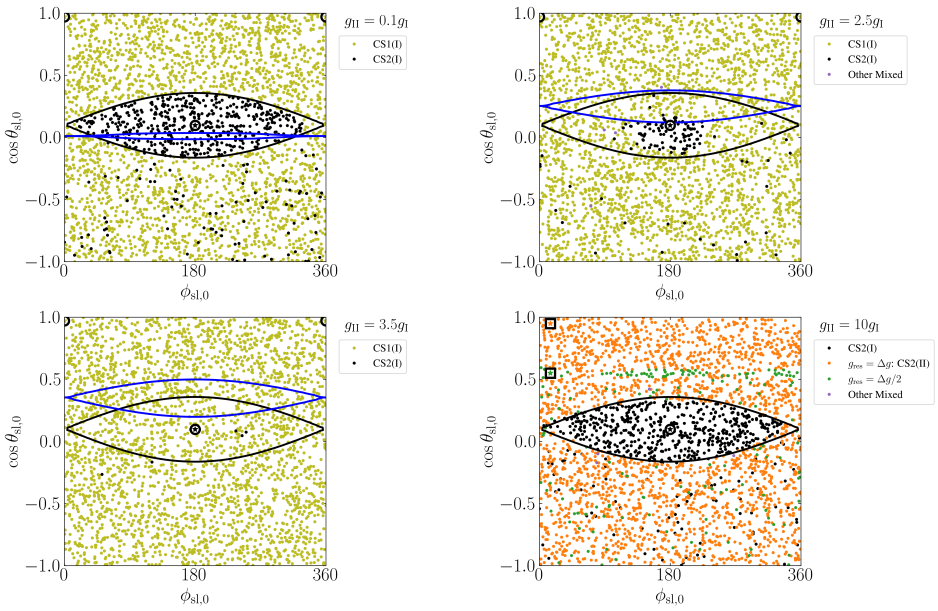

Figure 4.3: Asymptotic outcomes of spin evolution driven by tidal alignment torque for different initial spin orientations (described by $\theta_{\rm sl,0}$ and $\phi_{\rm sl,0}$) for a system with $I_{\rm (I)} = 10^\circ$, $I_{\rm (II)} = 1^\circ$, $\alpha = 10\left|g_{\rm (I)}\right|$, and $g_{\rm (II)} = \{0.1, 2.5, 3.5, 10\} \times g_{\rm (I)}$ in the top-left, top-right, bottom-left, and bottom-right panels respectively (as labeled). Each dot represents an initial spin orientation, and the coloring of the dot indicates which Cassini State (CS) and which mode (legend) the system evolves into. The obliquity and $\phi_{\rm sl}$ values of the mode-I CSs are labeled as the circled stars, with the same colors as in the legend. The obliquities of the other equilibria are labeled as the boxed stars at the left edges of the right-bottom panel, with the same colors as in the legend; a small, arbitrary offset in $\phi_{\rm sl}$ is added to reflect the fact that these equilibria do not have fixed $\phi_{\rm sl}$ values. The separatrices for the mode I and mode II resonances are given in the black and blue lines respectively.

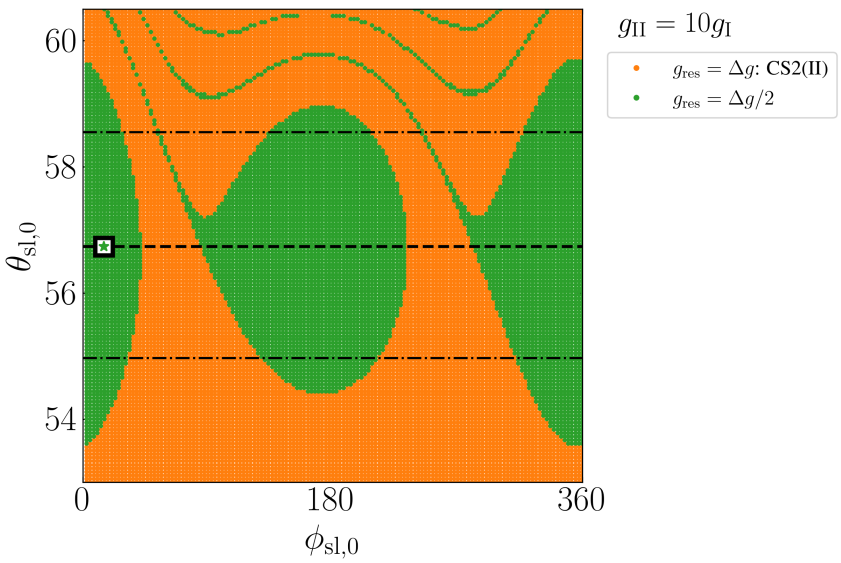

Figure 4.4: Same as the bottom right panel of Fig. 4.3 but zoomed-in to a narrow range of initial obliquities near $\theta_{\rm eq} \approx 57^\circ$ (horizontal dashed line) for the $g_{\rm res} = \Delta g/2$ mixed mode equilibrium as predicted by Eq. (4.15). The horizontal dash-dotted lines indicate the amplitude of oscillation of the mode (see Fig. 4.2). It is clear that there are two basins of attraction for this mixed-mode resonance near $\phi_{\rm sl,0} = 0$ and $\phi_{\rm sl,0} = 180^\circ$.

mode equilibria, we numerically calculate the "basin of attraction" by repeating the procedure for producing Fig. 4.3 but instead use a fine grid of ICs with $\theta_{\rm sl,0}$ near the average obliquity of the equilibrium. This results in a "zoomed-in" version of the bottom-right panel of in Fig. 4.3 and doubles as a numerical stability analysis of the equilibrium. Figure 4.4 shows the result of this procedure applied to the $g_{\rm res} = \Delta g/2$ resonance, where we have zoomed in to $\theta_{\rm sl,0}$ near the $\theta_{\rm eq} \approx 60^\circ$ associated with the resonance. We see that the resonance is reached consistently from some well-defined regions in the $(\theta_{\rm sl}, \phi_{\rm sl})$ space.

Figure 4.5 summarizes the equilibrium obliquities $\theta_{\rm eq}$ of various resonances achieved for the system depicted in the bottom-right panel of Fig. 4.3. For a trajectory that reaches a particular equilibrium, we compute $\theta_{\rm eq} = \langle \theta_{\rm sl} \rangle$ by averaging over the last $100/\max\left(\left|g_{\rm (I)}\right|, |\Delta g|\right)$ of the integration. We obtain the corresponding "resonance" frequency by $g_{\rm res} \simeq \langle \dot{\phi}_{\rm sl} \rangle$.

In fact, the relation between $\theta_{\rm eq}$ and $g_{\rm res}$ can be described analytically. We consider the equation of motion in the rotating frame where $\hat{\mathbf{L}} = \hat{\mathbf{z}}$ is constant and $\hat{\mathbf{J}}$ lies in the xz plane (i.e. $\hat{\mathbf{J}} = -\sin I\hat{\mathbf{x}} + \cos I\hat{\mathbf{z}}$):

$$\left(\frac{\mathrm{d}\hat{\mathbf{S}}}{\mathrm{d}t}\right)_{\rm rot} = \alpha\left(\hat{\mathbf{S}}\cdot\hat{\mathbf{L}}\right)\left(\hat{\mathbf{S}}\times\hat{\mathbf{L}}\right) + \hat{\mathbf{S}}\times\left(\dot{\Omega}\hat{\mathbf{J}} + \dot{I}\hat{\mathbf{y}}\right). \tag{4.10}$$

Let $\hat{\mathbf{S}} = \sin\theta_{\rm sl}\left(\cos\phi_{\rm sl}\hat{\mathbf{x}} + \sin\phi_{\rm sl}\hat{\mathbf{y}}\right) + \cos\theta_{\rm sl}\hat{\mathbf{z}}$. The evolution of $\phi_{\rm sl}$ then follows

$$\begin{aligned}\frac{\mathrm{d}\phi_{\rm sl}}{\mathrm{d}t} = &-\alpha\cos\theta_{\rm sl} - \dot{\Omega}\left(\cos I + \sin I\cot\theta_{\rm sl}\cos\phi_{\rm sl}\right)\\ &- \dot{I}\cot\theta_{\rm sl}\sin\phi_{\rm sl}.\end{aligned} \tag{4.11}$$

Note that the single-mode CSs satisfy Eq. (4.11) where $\dot{\Omega} = g$, $\dot{I} = 0$, and $\phi_{\rm sl}$ is either equal to 0° or 180° (Eq. 4.8). For the general, two-mode problem, if $\phi_{\rm res} = \phi_{\rm sl} - g_{\rm res}t$ is a resonant angle, then it must satisfy

$$\left\langle\frac{\mathrm{d}\phi_{\rm res}}{\mathrm{d}t}\right\rangle = \left\langle\frac{\mathrm{d}\phi_{\rm sl}}{\mathrm{d}t}\right\rangle - g_{\rm res} = 0, \tag{4.12}$$

where the angle brackets denote an average over a libration period. Since $\phi_{\rm sl}$ circulates when $g_{\rm res} \neq 0$, $\langle\cos\phi_{\rm sl}\rangle = \langle\sin\phi_{\rm sl}\rangle = 0$. Furthermore, if $I_{\rm (II)}/I_{\rm (I)} \equiv \epsilon \ll 1$, we can expand Eq. (4.5) to obtain

$$\dot{\Omega} = g_{\rm (I)} + \Delta g\epsilon\cos(\Delta g t) + \mathcal{O}\left[\epsilon^2\right], \tag{4.13}$$

$$I = I_{\rm (I)}\left(1 + \epsilon\cos(\Delta g t) + \mathcal{O}\left[\epsilon^2\right]\right), \tag{4.14}$$

where $\Delta g \equiv g_{\rm (II)} - g_{\rm (I)}$. To leading order, we have $\dot{\Omega} \simeq g_{\rm (I)}$ and $I \simeq I_{\rm (I)}$, so Eq. (4.11) reduces to

$$\alpha\cos\theta_{\rm eq} \simeq -g_{\rm (I)}\cos I_{\rm (I)} - g_{\rm res}. \tag{4.15}$$

This is Eq. (4.15) in the main text, and is shown in Fig. 4.5. Good agreement between the analytic expression and numerical results is observed. Note that setting $g_{\rm res} = \Delta g$ in Eq. (4.15) does not yield the mode II CSs, as the mode I inclination is still being used, and the $\phi_{\rm sl}$ terms are averaged out in the mixed mode calculation while being nonzero in the CS obliquity calculation.

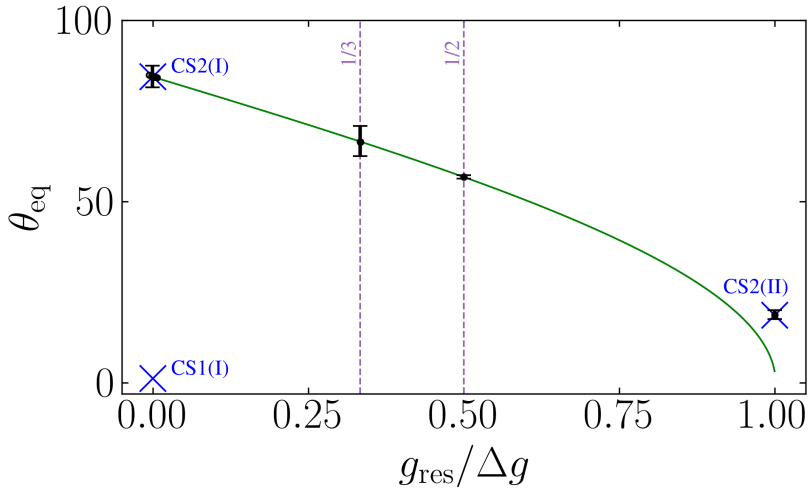

Figure 4.5: "Equilibrium" obliquity as a function of the resonant frequency (Eq. 4.9) for a system with $I_{(\rm I)} = 10°$, $I_{(\rm II)} = 1°$, $\alpha = 10\,|g_{(\rm I)}|$, and $g_{(\rm II)} = 10 g_{(\rm I)}$ (corresponding to the bottom-right panel of Fig. 4.3). The green line is the analytical result given by Eq. (4.15). The error bars denote the amplitude of oscillation of $\theta_{\rm sl}$ when the spin has reached a steady state (e.g. Figs. 4.1–4.2). The blue crosses denote the CSs for the two inclination modes.

The four systems shown in Fig. 4.3 demonstrate that the characteristic spin evolution depends strongly on the ratio $g_{(\rm II)}/g_{(\rm I)}$. To understand the transition between these different regimes, we vary $g_{(\rm II)}$ over a wide range of values (while keeping the other parameters the same as in Fig. 4.3). For each $g_{(\rm II)}$, we numerically determine the steady-state (equilibrium) obliquities and compute the probability of reaching each equilibrium by evolving 3000 initial spin orientations drawn randomly from an isotropic distribution. Figure 4.6 shows the result. Two trends can be seen: the probability of long-lived capture into the CS2(I) resonance decreases as $|g_{(\rm II)}|$ is increased from $|g_{(\rm II)}| \ll |g_{(\rm I)}|$ to $|g_{(\rm II)}| \sim |g_{(\rm I)}|$, and mixed-mode resonances become significant, though non-dominant, outcomes for $|g_{(\rm II)}| \gg |g_{(\rm I)}|$.

Having discussed how the spin evolution changes when $g_{(\rm II)}$ is varied, we now explore the effect of different values of $I_{(\rm II)}$. In Fig. 4.7, we display the final out-

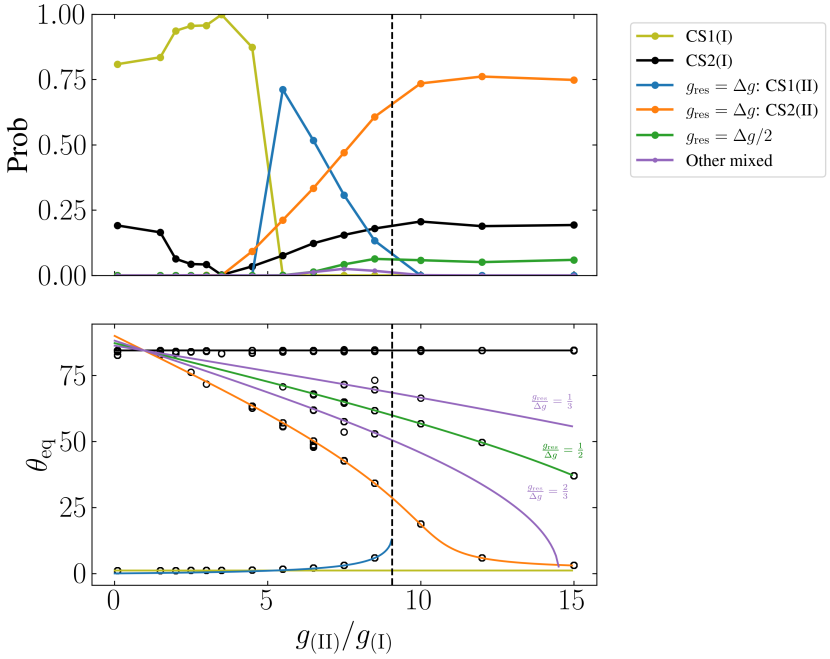

Figure 4.6: Final outcomes of spin evolution under tidal alignment torque for a 3-planet system with inclination mode parameters $I_{\rm (I)} = 10°$, $I_{\rm (II)} = 1°$, $\alpha = 10\left|g_{\rm (I)}\right|$ (same as Figs. 4.1–4.5) and varying $g_{\rm (II)}/g_{\rm (I)}$. The top panel shows the probability of each of the possible steady-state outcomes for 3000 initial spin orientations sampled from an isotropic distribution. The vertical dashed line shows the value of $\left|g_{\rm (II)}\right|$ above which CS1(II) no longer exists. The bottom panel shows the final equilibrium obliquities (open black circles) for each $g_{\rm (II)}/g_{\rm (I)}$. For the mixed-mode resonances ($g_{\rm res} \neq 0, \Delta g$), the equilibrium obliquities are given by Eq. (4.15) and are shown as the solid green and purple lines for the labeled values of $g_{\rm res}$. The other lines are the equilibrium $\theta_{\rm eq}$ for "pure" CSs (as labeled), whose equilibria satisfy Eq. (4.8). Not all observed mixed-mode resonances are plotted (e.g. for $g_{\rm (II)} = 7.5 g_{\rm (I)}$, there is an outcome with $g_{\rm res}/\Delta g = 3/4$).

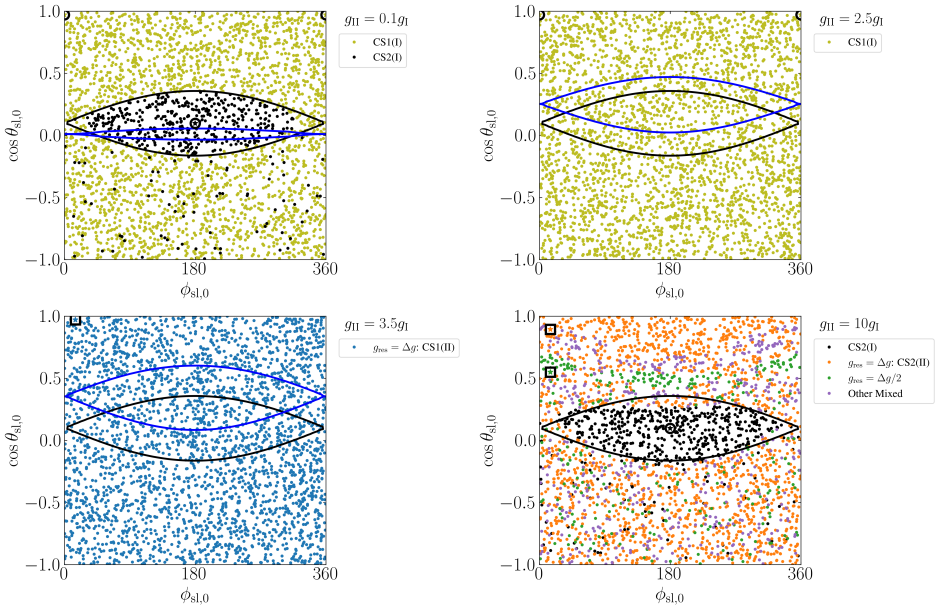

Figure 4.7: Same as Fig. 4.3 but for $I_{(II)} = 3°$.

comes as a function of the initial spin orientation for the same $g_{(II)}$ values as in Fig. 4.3, but for $I_{(II)} = 3°$. Comparing the bottom-left panels of Figs. 4.3 and 4.7 (with $g_{(II)} = 3.5g_{(I)}$), we find that the favored low-obliquity CS changes from CS1(I) to CS1(II) when using $I_{(II)} = 3°$. In both cases, CS2(I) is destabilized such that most initial conditions converge to the low-obliquity CS, either CS1(I) or CS1(II). In the bottom-right panel, we find that many initial conditions converge to other mixed modes than the $g_{res} = \Delta g/2$ mode. The values of g_{res} observed for the system are shown in Fig. 4.8, where we find that many low-order rational multiples of $g_{res}/\Delta g$ are obtained. While the amplitude of oscillation in the final θ_{sl} is substantial (and larger than in Fig. 4.5), we find that the predictions of Eq. (4.15) are consistent up to the range of oscillation of θ_{sl}. In Fig. 4.9, we summarize the outcomes of spin evolution as a function of $g_{(II)}/g_{(I)}$ for $I_{(II)} = 3°$. We identify the same two qualitative trends as seen in Fig. 4.6: the instability of CS2(I) when $g_{(II)} \sim g_{(I)}$ and the appearance of mixed modes when $|g_{(II)}| \gg |g_{(I)}|$.

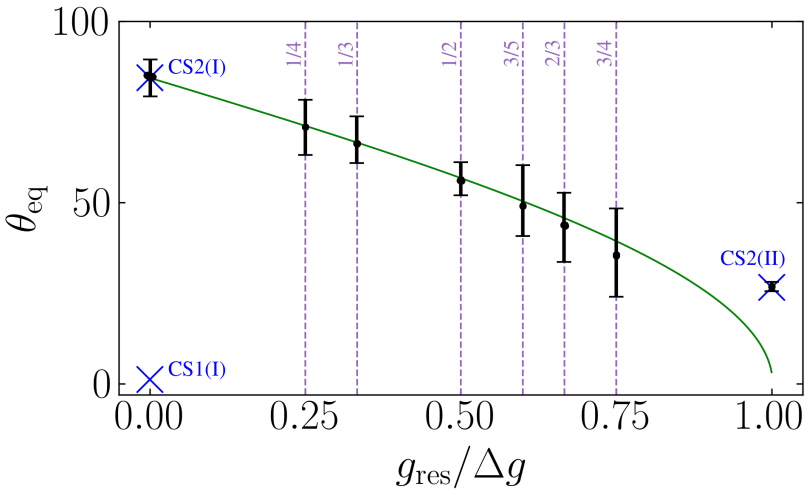

Figure 4.8: Same as Fig. 4.5 but for $I_{\rm (II)} = 3°$.

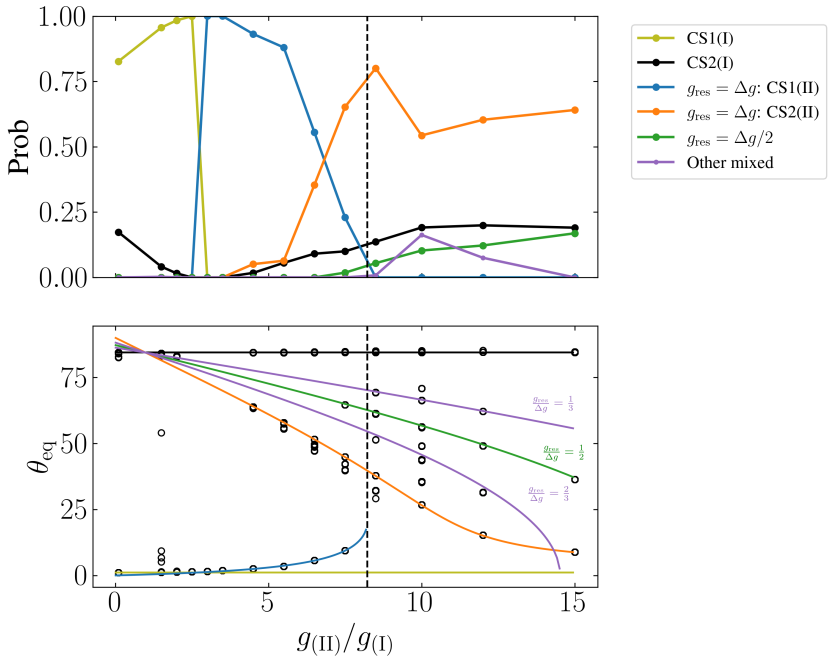

Figure 4.9: Same as Fig. 4.6 but for $I_{\rm (II)} = 3°$. Note that the agreement of the black open circles with the theoretical obliquities in the bottom panel is slightly worse than in Fig. 4.6 but still well within the ranges of oscillation of the obliquities (see Fig. 4.8 for the characteristic ranges).

4.3.1 Summary of Various Outcomes

In summary, the spin evolution in a 3-planet system driven by a tidal alignment torque depends largely on the frequency of the smaller-amplitude mode, $g_{(\mathrm{II})}$, compared to that of the larger-amplitude mode, $g_{(\mathrm{I})}$. In the regime where $|g_{(\mathrm{I})}| \lesssim \alpha$, we find that:

- When $|g_{(\mathrm{II})}| \ll |g_{(\mathrm{I})}|$, the low-amplitude and slow (II) mode does not significantly affect the spin evolution, and the results of [Su and Lai, 2021] are recovered. The two possible outcomes are the tidally stable CS1(I) (generally low obliquity) and CS2(I) (generally high obliquity). Prograde initial spins converge to CS1(I), spins inside the mode I resonance converge to CS2(I), and retrograde initial spins attain one of these two tidally stable CSs probabilistically. For the fiducial parameters used for Fig. 4.6, approximately 20% of systems are trapped in the high-obliquity CS2(I).
- When $g_{(\mathrm{II})} \sim g_{(\mathrm{I})}$, CS2(I) is increasingly difficult to attain due to the interacting mode I and mode II resonances, and the probability of attaining CS2(I) can be strongly suppressed (see Fig. 4.6, where the probability of a high-obliquity outcome goes to zero for $g_{(\mathrm{II})}/g_{(\mathrm{I})} = 3.5$).
- When $|g_{(\mathrm{II})}| \gtrsim |g_{(\mathrm{I})}|$, there are three classes of outcomes. The highest-obliquity outcome is still CS2(I), and is attained for initial conditions inside the mode I resonance (separatrix; see Fig. 4.5). The lowest-obliquity outcome is generally CS2(II)[3] and is the most favored outcome (see Fig. 4.6). The third possible outcome are mixed modes with $g_{\mathrm{res}}/\Delta g$ a low-order rational number (see Eq. 4.9). These mixed modes only appear for $|g_{(\mathrm{II})}| \gg |g_{(\mathrm{I})}|$, and generally have obliquities between those of CS2(I) and CS2(II) (see Fig. 4.3). For the

[3] This may not be the case when $I_{(\mathrm{II})} \lesssim I_{(\mathrm{I})}$ while $g_{(\mathrm{II})} \gg g_{(\mathrm{I})}$; see Fig. C.7 in the Appendix

fiducial parameters used for Fig. 4.6, the mixed-mode resonances increase the probability of obtaining a substantial ($\gtrsim 45^\circ$) obliquity from $\sim 20\%$ to $\sim 30\%$.

4.4 Weak Tidal Friction

We now briefly discuss the spin evolution of the system incorporating the full tidal effects. In the weak friction theory of the equilibrium tide, the spin orientation and frequency jointly evolve following [Alexander, 1973, Hut, 1981, Lai, 2012]

$$\left(\frac{\mathrm{d}\hat{\mathbf{S}}}{\mathrm{d}t}\right)_{\rm tide} = \frac{1}{t_{\rm s}}\left[\frac{2n}{\Omega_{\rm s}} - \left(\hat{\mathbf{S}}\cdot\hat{\mathbf{L}}\right)\right]\hat{\mathbf{S}}\times\left(\hat{\mathbf{L}}\times\hat{\mathbf{S}}\right), \tag{4.16}$$

$$\frac{1}{\Omega_{\rm s}}\left(\frac{\mathrm{d}\Omega_{\rm s}}{\mathrm{d}t}\right)_{\rm tide} = \frac{1}{t_{\rm s}}\left[\frac{2n}{\Omega_{\rm s}}\left(\hat{\mathbf{S}}\cdot\hat{\mathbf{L}}\right) - 1 - \left(\hat{\mathbf{S}}\cdot\hat{\mathbf{L}}\right)^2\right], \tag{4.17}$$

where

$$\frac{1}{t_{\rm s}} \equiv \frac{1}{4k}\frac{3k_2}{Q}\left(\frac{M_\star}{m}\right)\left(\frac{R}{a}\right)^3 n, \tag{4.18}$$

(see Eq. 4.1, but with $4k = 1$).

Since $\alpha \propto \Omega_{\rm s}$ evolves in time, we describe the spin-orbit coupling by the parameter

$$\alpha_{\rm sync} \equiv [\alpha]_{\Omega_{\rm s}=n}\,. \tag{4.19}$$

To facilitate comparison with the previous results, we use $\alpha_{\rm sync} = 10\left|g_{\rm (I)}\right|$ and $\left|g_{\rm (I)}\right| t_{\rm s} = 300$. Note that for the physical parameters used in Eqs. (4.4) and (4.18), $g_{\rm (I)} t_{\rm s} \sim 10^4$; we choose a faster tidal timescale to accelerate our numerical integrations. The initial spin is fixed $\Omega_{\rm s,0} = 3n$. We then integrate Eqs. (4.2), (4.6), and (4.16–4.17) starting from various initial spin orientations and determine the final outcomes. Figure 4.10 shows the results for a few select values of $g_{\rm (II)}$ and for $I_{\rm (II)} = 3^\circ$. Similar behaviors to Figs. 4.3 and 4.7 are observed. The probabilities

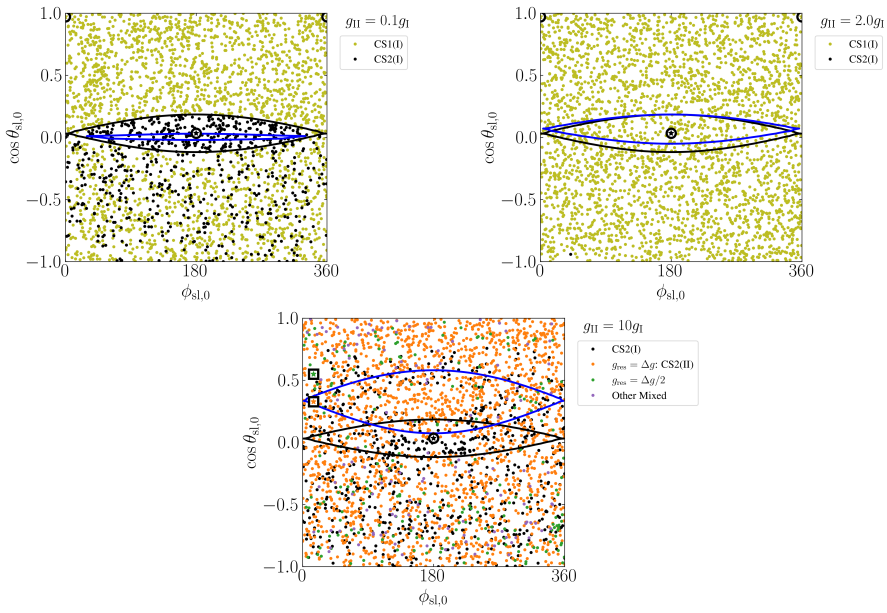

Figure 4.10: Similar to Figs. 4.7 but including full tidal effects on the planet's spin, with $\alpha_{\rm sync} = 10\,|g_{(\rm I)}|$ (Eq. 4.19), $I_{(\rm II)}3^\circ$, and initial spin $\Omega_{\rm s,0} = 3n$. In the three panels, $g_{(\rm II)} = \{0.1, 2, 10\} \times g_{(\rm I)}$ respectively. Note that the plotted separatrices (blue and black lines) use the initial value of α.

and obliquities of the various equilibria are shown in Fig. 4.11. Note that each equilibrium obliquity has a corresponding equilibrium rotation rate, given by

$$\frac{\Omega_{\rm eq}}{n} = \frac{2\cos\theta_{\rm eq}}{1+\cos^2\theta_{\rm eq}}. \tag{4.20}$$

The probabilities shown in Fig. 4.11 exhibit qualitative trends that are quite similar to those seen for the evolution driven by the tidal alignment torque alone: when $|g_{(\rm II)}| \ll |g_{(\rm I)}|$, the results of [Su and Lai, 2021] are recovered; when $g_{(\rm II)} \sim g_{(\rm I)}$, the probability of attaining CS2(I) is significantly suppressed; and when $|g_{(\rm II)}| \gg |g_{(\rm I)}|$, mixed modes appear.

4.5 Summary and Discussion

In this work, we have shown that the planetary spins in compact systems of multiple super Earths (SEs), possibly with an outer cold Jupiter companion, can be

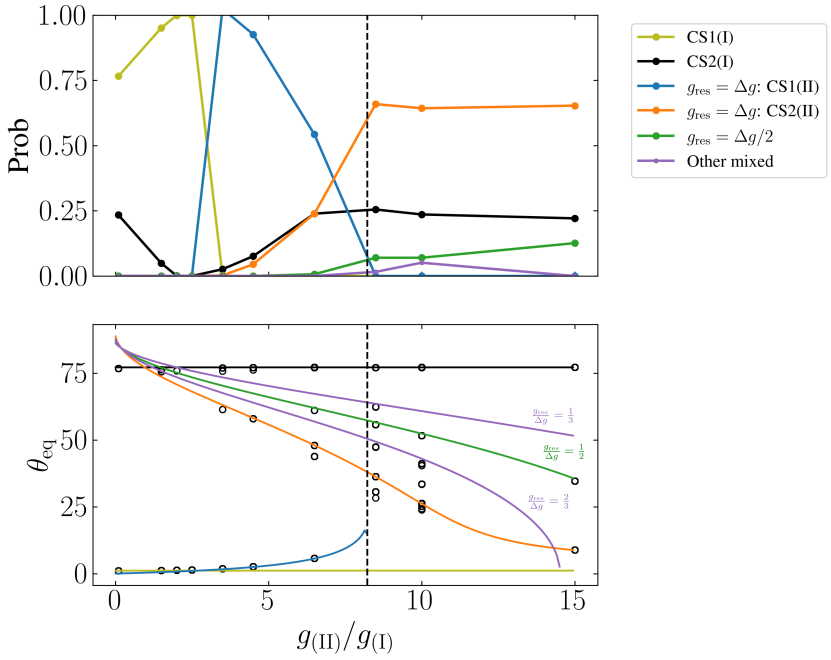

Figure 4.11: Similar to Fig. 4.9 but with weak tidal friction.

trapped into a number of spin-orbit resonances when evolving under tidal dissipation, either via a tidal alignment torque (Section 4.3) or via weak tidal friction (Section 4.4). In addition to the well-understood tidally-stable Cassini States associated with each of the orbital precession modes, we have also discovered a new class of "mixed mode" spin-orbit resonances that yield substantial obliquities. These additional resonances constitute a significant fraction of the final states of tidal evolution if the planet's initial spin orientation is broadly distributed, a likely outcome for planets that have experienced an early phase of collisions or giant impacts. For instance, for the fiducial system parameters shown in Fig. 4.6, these mixed-mode equilibria increase the probability that a planet retains a substantial ($\gtrsim 45°$) obliquity from 20% to 30%. A large equilibrium obliquity has a significant influence on the planet's insolation and climate. For planetary systems surrounding cooler stars (M dwarfs), the SEs (or Earth-mass planets) studied in this work lie in the habitable zone [e.g. Dressing et al., 2017, Gillon et al., 2017],

and the nontrivial obliquity can impact the habitability of such planets.

In a broader sense, the mixed-mode equilibria discovered in our study represent a novel astrophysical example of subharmonic responses in parametrically driven nonlinear oscillators. In equilibrium, the planetary obliquity oscillates with a period that is an integer multiple of the driving period $2\pi/|\Delta g|$ (see Appendix C.2 for further discussion). Such subharmonic responses are often seen in nonlinear oscillators [e.g. in the classic van der Pol and Duffing equations Levenson, 1949, Flaherty and Hoppensteadt, 1978, Hayashi, 2014].

Throughout this paper, we have adopted fiducial parameters where $\left|g_{(\mathrm{I})}\right| \lesssim \alpha$, which is generally expected for the SE systems being studied. If instead $\left|g_{(\mathrm{I})}\right| \gtrsim \alpha$, then there is no resonance for the dominant (larger-amplitude) mode I. There are then a few possible cases: if $\left|g_{(\mathrm{II})}\right| \lesssim \alpha$, mode II is both slower than mode I and has a smaller amplitude, so it will not affect the mode I dynamics significantly. On the other hand, if $\left|g_{(\mathrm{II})}\right| \gtrsim \alpha$, then mode II also has no resonance, and both CS2(I) and CS2(II) have low obliquities, implying that the system will always settle into a low-obliquity state.

CHAPTER 5

PHYSICS OF TIDAL DISSIPATION IN EARLY-TYPE STARS AND WHITE DWARFS: HYDRODYNAMICAL SIMULATIONS OF INTERNAL GRAVITY WAVE BREAKING IN STELLAR ENVELOPES

Originally published in:
Yubo Su, Daniel Lecoanet, and Dong Lai. Physics of tidal dissipation in early-type stars and white dwarfs: Hydrodynamical simulations of internal gravity wave breaking in stellar envelopes. *MNRAS*, 495(1):1239–1251, May 2020. ISSN 0035-8711. doi: 10.1093/mnras/staa1306

5.1 Introduction

The physical processes responsible for tidal evolution in close binaries often involve the excitation and dissipation of internal waves, going beyond the "weak friction" of equilibrium tides [see Ogilvie, 2014, for a review]. In particular, internal gravity waves (IGWs), arising from buoyancy of stratified stellar fluid, play an important role in several types of binary systems. In solar-type stars with radiative cores and convective envelopes, IGWs are excited by tidal forcing at the radiative-convective boundary and propagate inward; as the wave amplitude grows due to geometric focusing, nonlinear effects can lead to efficient damping of the wave [Goodman and Dickson, 1998, Barker and Ogilvie, 2010, Essick and Weinberg, 2015]. In early-type main-sequence stars, with convective cores and radiative envelopes, IGWs are similarly excited at the convective-radiative interface but travel toward the stellar surface; nonlinearity develops as the wave amplitude grows, leading to efficient dissipation [Zahn, 1975, 1977]. As the outgoing wave deposits its angular momentum to the stellar surface layer, a critical layer may form and the star is expected to synchronize from outside-in [Goldreich and Nicholson, 1989].

Tidal dissipation can also play an important role in compact double white dwarf (WD) binary systems (with orbital periods in the range of minutes to hours). Such binaries may produce a variety of exotic astrophysical systems and phenomena, ranging from isolated sdB/sdO stars, R CrB stars, AM CVn binaries, high-mass neutron stars and magnetars (created by the accretion-induced collapse of merging WDs), and various optical transients (underluminous supernovae, Ca-rich fast transients, and type Ia supernovae) [e.g. Livio and Mazzali, 2018, Toloza et al., 2019]. The outcomes of WD mergers depend on the WD masses and composition, but tidal dissipation can strongly affect the pre-merger conditions of the WDs and therefore the merger outcomes. Tidal dissipation may also influence the evolution of eccentric WD-massive black hole binaries prior to the eventual tidal disruption of the WD [Vick et al., 2017].

Recent studies have identified nonlinear dissipation of IGWs as the key tidal process in compact WD binaries [Fuller and Lai, 2012a, 2013, 2012b, Burkart et al., 2013]: IGWs are tidally excited mainly at the composition transitions of the WD envelope; as these waves propagate outwards towards the WD surface, they grow in amplitude until they break, and transfer both energy and angular momentum from the binary orbit to the outer envelope of the WD. However, these previous works parameterized the wave breaking process in an ad hoc manner. The details of dissipation, namely the location and spatial extent of the wave breaking, affect the observable outcomes: dissipation near the surface of the WD can be efficiently radiated away and simply brightens the WD, while dissipation deep in the WD envelope causes an energy buildup that results in energetic flares [Fuller and Lai, 2012b]. An important goal of this paper is to elucidate the details of the nonlinear IGW breaking process; the result of this "microphysics" study will help determine the thermal evolution and the observational manifestations of tidally heated binary WDs.

In this paper, we perform numerical simulations of IGW breaking in a plane-parallel stratified atmosphere (a simple model for a stellar envelope). We use the pseudo-spectral code Dedalus [Burns et al., 2016, Burns et al., 2020] and a 2D Cartesian geometry, and consider IGWs propagating into an isothermal fluid initially at rest. We find that, after an initial transient phase, a *critical layer* naturally develops, separating a lower zone that has no horizontal mean flow and an upper zone with mean flow at the horizontal phase velocity of the IGW. The major part of our paper is dedicated to characterizing the behavior of the critical layer when interacting with a continuous train of IGW excited from the bottom of the atmosphere. IGWs are generally *anti*-diffusive, in that they steepen shear flows [Lindzen and Holton, 1968, Couston et al., 2018] and act to narrow the critical layer. We find this steepening is counter-balanced by the Kelvin-Helmholtz instability and turbulence within the narrow critical layer. By careful accounting of the momentum flux budget about the critical layer, we are able to model the reflection and absorption of the incident IGW, and the slow downward propagation of the critical layer.

While the motivation of our study is to understand tidal dissipation in WD and early-type stellar binaries, the IGW breaking process studied in this paper is also quite relevant to the circulation dynamics of planetary atmospheres [see e.g. Lindzen, 1981, Holton, 1983, Baldwin et al., 2001].

This paper is organized as follows. In Section 5.2 we present the system of equations used in our simulations. In Section 5.3, we review the existing understanding of wave breaking and present analytical results characterizing IGW behavior near a critical layer. In Section 5.4 we describe our numerical setup and in Section 5.5 we validate our method in the weak-forcing limit against linear theory. In Section 5.6, we present the results of simulations of IGW breaking and our

characterization of the critical layer. We summarize and conclude in Section 5.7.

5.2 Problem Setup and Equations

We consider a incompressible, isothermally stratified fluid representing a stellar envelope or atmosphere. We study dynamics in 2D, so that fluid variables depend only on the Cartesian coordinates x and z. While it is well known that waves break differently in 2D versus 3D [Klostermeyer, 1991, Winters and D'Asaro, 1994], the dynamical effect of the breaking process is likely to be similar in 2D [Barker and Ogilvie, 2010]. We approximate the gravitational field as uniform, pointing in the $(-\hat{\mathbf{z}})$ direction. The plane-parallel approximation is justified since wave breaking generally occurs near the stellar surface. The background density stratification is given by

$$\overline{\rho} = \overline{\rho}_0 e^{-z/H}, \tag{5.1}$$

with $\overline{\rho}_0$ some reference density. We denote background quantities with overbars and perturbation quantities with primes.

The Euler equations for an incompressible fluid in a uniform gravitational field are

$$\nabla \cdot \mathbf{u} = 0, \tag{5.2a}$$

$$\frac{\mathrm{D}\rho}{\mathrm{D}t} = 0, \tag{5.2b}$$

$$\frac{\mathrm{D}\mathbf{u}}{\mathrm{D}t} + \frac{\nabla P}{\rho} + g\hat{\mathbf{z}} = 0, \tag{5.2c}$$

where $\mathrm{D}/\mathrm{D}t = \partial/\partial t + (\mathbf{u}\cdot\nabla)$ is the Lagrangian or material derivative, and $\mathbf{u}, \rho, P$ denote the velocity field, density and pressure respectively. The constant gravitational acceleration is $(-g\hat{\mathbf{z}})$. Note that these equations conserve the same wave energy as the commonly used anelastic equations [Ogura and Phillips, 1962, Brown

et al., 2012] and thus give the same wave amplitude growth. Appendix D.1 provides a derivation of these equations and justification for using them.

For this isothermal background, hydrostatic equilibrium implies $\overline{P}(z) = \overline{\rho}(z)gH$. We assume there is initially no background flow, so $\mathbf{u} = \mathbf{u}'$. Physically, this assumption corresponds to a non-rotating star.

For convenience, we introduce the dimensionless density variable Υ and the reduced pressure ϖ [e.g. Lecoanet et al., 2014] via

$$\Upsilon \equiv \ln \frac{\rho}{\bar{\rho}}, \tag{5.3}$$

$$\varpi \equiv \frac{P}{\rho}. \tag{5.4}$$

These variables automatically enforce $\rho > 0$ and eliminate the stiff term $\nabla P/\rho$ in the Euler equation. In terms of Υ and ϖ, the second two equations in (5.2) become

$$\frac{\mathrm{D}\Upsilon}{\mathrm{D}t} + u_z \frac{\partial \ln \overline{\rho}}{\partial z} = 0, \tag{5.5a}$$

$$\frac{\mathrm{D}\mathbf{u}}{\mathrm{D}t} + \nabla\varpi + \varpi\nabla\Upsilon - \frac{\varpi}{H}\hat{\mathbf{z}} + g\hat{\mathbf{z}} = 0. \tag{5.5b}$$

Hydrostatic equilibrium corresponds to $\Upsilon = 0, \overline{\varpi} = gH$.

5.3 Internal Gravity Waves: Theory

5.3.1 Linear Analysis

In the small perturbation limit, we may linearize Eq. (5.5). The resulting equations admit the canonical IGW solution [Drazin, 1977, Dosser and Sutherland, 2011b]

$$u_z'(x,z,t) = Ae^{z/2H}\cos(k_x x + k_z z - \omega t), \tag{5.6}$$

where A is a constant amplitude, and the frequency ω and the wave number (k_x, k_z) satisfy the dispersion relation

$$\omega^2 = \frac{N^2 k_x^2}{k_x^2 + k_z^2 + (2H)^{-2}}. \tag{5.7}$$

Our equations are valid in the limit of large sound speed ($c_s \to \infty$), in which the *Brunt-Väisälä frequency*, N, is given by

$$N^2 \equiv g^2 \left(\frac{\mathrm{d}\rho}{\mathrm{d}P} - \frac{1}{c_s^2} \right) = \frac{g}{H}, \tag{5.8}$$

and is constant. Other dynamical quantities are simply related to u_z'.

In the short-wavelength/WKB limit ($|k_z H| \gg 1$), the solution exhibits the following characteristics:

1. The amplitude of the wave grows with z as $e^{z/2H}$. Thus, the linear approximation always breaks down for sufficiently large z.

2. The phase and group velocities are given by:

$$\mathbf{c}_p = (k_x \hat{\mathbf{x}} + k_z \hat{\mathbf{z}}) \frac{\omega}{k_x^2 + k_z^2 + (2H)^{-2}}, \tag{5.9}$$

$$\mathbf{c}_g = N \frac{\left[k_z^2 + (2H)^{-2}\right] \hat{\mathbf{x}} - (k_x k_z \hat{\mathbf{z}})}{\left[k_x^2 + k_z^2 + (2H)^{-2}\right]^{3/2}}. \tag{5.10}$$

   The additional $(2H)^{-2}$ term in the denominator accounts for the growing amplitude of the IGW in the z direction (as the z wavenumber is effectively $k_z - i/(2H)$). We note $\mathbf{c}_p \cdot \mathbf{c}_g = \mathcal{O}\left[(k_z H)^{-2}\right] \approx 0$. In the Boussinesq approximation where terms of order $\mathcal{O}\left(H^{-2}\right)$ are ignored, the phase and group velocities are exactly orthogonal [Drazin, 1977, Dosser and Sutherland, 2011a]. We use the convention where upward propagating IGW have $c_{g,z} > 0$, $k_z < 0, k_x > 0$.

3. The averaged horizontal momentum flux F (in the $+\hat{\mathbf{z}}$ direction) carried by the IGW is defined by

$$F(z,t) \equiv \left\langle \rho u_x' u_z' \right\rangle_x \equiv \frac{1}{L_x} \int_0^{L_x} \rho u_x' u_z' \, \mathrm{d}x. \tag{5.11}$$

The notation $\langle \ldots \rangle_x$ denotes averaging over the x direction. For the linear solution (Eq. 5.6), this evaluates to

$$F \approx -\frac{A^2}{2} \overline{\rho}_0 \frac{k_z}{k_x}, \tag{5.12}$$

Thus, indeed $F > 0$ for an upward propagating IGW ($c_{g,z} > 0$).

5.3.2 Wave Generation

To model continuous excitation of IGWs deep in the stellar envelope propagating towards the surface, we use a volumetric forcing term to excite IGW near the bottom of the simulation domain. Our forcing excites both IGWs propagating upwards, imitating a wave tidally excited deeper in the star, and downwards, which are not physically relevant in binaries. In our simulations, these downward propagating waves are dissipated by a damping zone described in Section 5.4.2.

As not to interfere with the incompressibility constraint, we force the system on the density equation. We implement forcing with strength C localized around height z_0 with small width σ by replacing Eq. (5.5a) with

$$\frac{\mathrm{D}\Upsilon}{\mathrm{D}t} + u_z \frac{\partial \ln \overline{\rho}}{\partial z} = C e^{-\frac{(z-z_0)^2}{2\sigma^2}} \cos(k_x x - \omega t). \tag{5.13}$$

Using a narrow Gaussian profile excites a broad z power spectrum, but only the k_z satisfying the dispersion relation (Eq. 5.7) for the given k_x and ω will propagate.

In the linearized system, the effect of this forcing can be solved exactly (see Appendix D.2). In the limit $|k_z H| \gg 1, \sigma \ll H$, the solution can be approximated

as two plane waves propagating away from the forcing zone

$$u_z(x,z,t) \approx \frac{C}{2k_z}\frac{gk_x^2}{\omega^2}\exp\left(-\frac{k_z^2\sigma^2}{2}\right)\sqrt{2\pi\sigma^2} \times \begin{cases} e^{\frac{z-z_0}{2H}}\sin\left(k_x x + k_z(z-z_0) - \omega t + \frac{k_z\sigma^2}{2H}\right) & \text{for } z > z_0, \\ e^{\frac{z-z_0}{2H}}\sin\left(k_x x - k_z(z-z_0) - \omega t + \frac{k_z\sigma^2}{2H}\right) & \text{for } z < z_0. \end{cases} \tag{5.14}$$

The $z > z_0$ region contains an upward propagating IGW wavetrain. The x component of the velocity can be obtained by the incompressibility constraint (Eq. 5.2a).

5.3.3 Wave Breaking Height

As the upward propagating IGW grows in amplitude ($|\mathbf{u}| \propto e^{z/2H}$), it is expected to break due to nonlinear effects. We can estimate the height of wave breaking using the condition $|\mathbf{u}| \sim \omega/|\mathbf{k}|$. This can be rewritten using the Lagrangian displacement $\boldsymbol{\xi} = \mathbf{u}/(-i\omega)$:

$$|\xi_z k_z| \sim 1. \tag{5.15}$$

Drazin [1977], Klostermeyer [1991], Winters and D'Asaro [1994] describe the onset of wave breaking in some detail. At intermediate amplitudes, wave breaking occurs via triadic resonances, transferring energy from the "parent" IGW to "daughter" waves on smaller length scales that efficiently damp. The horizontal momentum flux decreases from F to 0 over this breaking region. The lost flux is deposited into a horizontal mean flow

$$\overline{U}(z,t) \equiv \langle u_x \rangle_x . \tag{5.16}$$

As the mean flow grows, a *critical layer* may form, as discussed below.

5.3.4 Critical Layers

A horizontal shear flow $\overline{U}(z,t)\hat{\mathbf{x}}$ enters the fluid equations via the Lagrangian derivative, which can be decomposed as

$$\frac{\mathrm{D}}{\mathrm{D}t} = \frac{\partial}{\partial t} + \overline{U}\frac{\partial}{\partial x} + \left(\mathbf{u}' \cdot \nabla\right), \tag{5.17}$$

where $\mathbf{u}'$ is the velocity field *without* the shear flow. Thus, $\overline{U}$ has the effect of Doppler shifting the time derivative into the frame comoving with the mean flow. If $\overline{U}$ is roughly constant, then the behavior of a linear plane-wave perturbation satisfies the modified dispersion relation

$$\left(\omega - \overline{U}k_x\right)^2 = \frac{N^2 k_x^2}{k_x^2 + k_z^2 + (2H)^{-2}}. \tag{5.18}$$

This is just Eq. (5.7) with $\omega \to \omega - \overline{U}k_x$. It is apparent that if $\overline{U} = \overline{U}_c$, where

$$\overline{U}_c \equiv \frac{\omega}{k_x}, \tag{5.19}$$

then the dispersion relation is singular and the linear solution breaks down. Physically, this corresponds to the Doppler-shifted frequency of the IGW being zero. Anywhere $\overline{U} = \overline{U}_c$ is called a *critical layer*.

The behavior of an IGW incident upon a critical layer was first studied in the inviscid, linear regime in Booker and Bretherton [1967], which found nearly complete absorption of the IGW. The amplitude reflection and transmission coefficients are given by

$$\mathscr{R} = \exp\left(-2\pi\sqrt{\mathrm{Ri} - \frac{1}{4}}\right), \qquad \mathscr{T} = \exp\left(-\pi\sqrt{\mathrm{Ri} - \frac{1}{4}}\right), \tag{5.20}$$

where Ri is the local Richardson number evaluated at the critical layer height z_c:

$$\mathrm{Ri} \equiv \left.\frac{N^2}{\left(\partial\overline{U}/\partial z\right)^2}\right|_{z_c}. \tag{5.21}$$

In the $\mathrm{Ri} \gg 1$ limit, $\mathscr{R}, \mathscr{T} \ll 1$ and the incident wave is almost completely absorbed. This result also applies to viscous fluids [Hazel, 1967]. However, weakly nonlinear theory [Brown and Stewartson, 1982] and numerical simulations [Winters and D'Asaro, 1994] suggest that nonlinear effects may significantly enhance reflection and transmission.

Consider now the long-term evolution of the critical layer due to continuous horizontal momentum transfer by IGWs. Any incident horizontal momentum flux absorbed by the fluid, denoted $F_a(t)$, must manifest as additional horizontal momentum of the shear flow. Additionally, as the mean flow $\overline{U}$ cannot grow efficiently above $\overline{U}_c$ (due to the breakdown of the linear solution), we assume $\overline{U}$ saturates at $\overline{U}_c$, which holds to good accuracy (see Fig. 5.4). In this case, the critical layer must propagate downward in response to the incident momentum flux. The horizontal momentum of the shear flow satisfies

$$\frac{\partial}{\partial t} \int \overline{\rho}(z) \overline{U}(z,t) \, \mathrm{d}z - F_a(t) = 0. \tag{5.22}$$

Assuming $\overline{U}(z > z_c) \approx \overline{U}_c$ and $\overline{U}(z < z_c) \approx 0$, this condition becomes

$$-\overline{\rho}(z_c) \overline{U}_c \frac{\mathrm{d}z_c}{\mathrm{d}t} = F_a(t). \tag{5.23}$$

If F_a is constant in time, the height of the critical layer $z_c(t)$ has analytical solution:

$$z_c(t) = -H \ln \left[\exp\left(-\frac{z_c(t=0)}{H} \right) + \frac{t F_a}{\overline{U}_c H \overline{\rho}_0} \right], \tag{5.24}$$

where $z_c(t=0)$ is the initial critical layer height.

5.4 Numerical Simulation Setup

We use the pseudo-spectral code Dedalus [Burns et al., 2016, Burns et al., 2020] to simulate the excitation and propagation of IGWs (Section 5.5) as well as their

nonlinear breaking and the formation of a critical layer (Section 5.6).

5.4.1 Parameter Choices

We solve Eqs. (5.2a), (5.5b), and (5.13) in a Cartesian box with size L_x,L_z. We choose periodic boundary conditions in both the x and z direction. To mimic the absence of physical boundaries at the top/bottom of the simulation domain, we damp perturbations to zero near the top/bottom using damping zones (see Section 5.4.2). We expand all variables as Fourier series with N_x and N_z modes, and use the 3/2 dealiasing rule to avoid aliasing errors in the nonlinear terms [Boyd, 2001]. We choose $L_z = 12.5H$ (z runs from $-H$ to $11.5H$), and the lower and upper damping zones are active for $z < 0.3H$ and $z > 9.5H$ respectively. The forcing (see Eq. (5.13)) is centered at $z_0 = 2H$ with width $\sigma = 0.078H$, sufficiently far from the lower damping zone and permitting sufficient room for the upward propagating wave to grow as $\propto e^{z/2H}$. Finally, we want similar grid spacing in the x and z directions (i.e. $L_x/N_x \sim L_z/N_z$), guided by the intuition that turbulence generated by wave breaking is approximately isotropic, so we use $L_x = 4H$ and $N_z/N_x = 4$.

The time integration uses a split implicit-explicit third-order scheme where certain terms are treated implicitly and the remaining terms are treated explicitly. A third-order, four-stage DIRK-ERK scheme [Ascher et al., 1997] is used with adaptive timesteps computed from the minimum of $0.1/N$ and the advective Courant-Friedrichs-Lewy (CFL) time. The CFL time is given by $\Delta t = 0.7 \min(\Delta x/u_x, \Delta z/u_z)$, where the minimum is taken over every grid point in the domain, and $\Delta x \equiv L_x/N_x$ and $\Delta z \equiv L_z/N_z$ are the grid spacings in the x and z directions respectively.

We non-dimensionalize the problem such that $H = N = \rho_0 = 1$. The physics of the simulation is then fixed by the four remaining parameters k_x, ω, C, and the

viscosity ν. We describe our choices for these parameters below:

1. k_x: Tidally excited waves in stars generally have $\ell = 2$, corresponding to a horizontal wavenumber $k_\perp \sim 1/R$, where R is the radius of the star. We use the smallest wavenumber in our simulation, $k_x = 2\pi/L_x$.

2. ω: We choose ω by evaluating the dispersion relation $\omega(k_x, k_z)$ for a desired k_z (see Eq. (5.7)). We pick $|k_z H| = 2\pi$ to ensure the waves are very well resolved in all of our simulations. Note however that tidally forced IGWs typically have $\omega \ll N$, or equivalently $k_r/k_\perp \sim k_r R \gg 1$. This requires $|k_z H| \gtrsim 1$, which is only marginally satisfied in our simulations.

3. C: In our weak forcing simulations (Section 5.5), we first choose the forcing strength C (see Eq. (5.13)) to be sufficiently weak such that $|\xi_z k_z| \ll 1$ is satisfied everywhere in the simulation domain. This constrains C by Eq. (5.14). In our wave breaking simulations (Section 5.6), we choose larger C.

4. ν: Nonlinear effects transfer wave energy from the injection wavenumber $\mathbf{k}$ to larger wavenumbers. Our spectral method does not have any numerical viscosity, so diffusivity must be introduced into the equations to regularize the systems at large wavenumbers. We add viscosity and diffusivity to the system in a way that conserves horizontal momentum (see Appendix D.3 for details). We define the dimensionless Reynolds number

$$\mathrm{Re} \equiv \frac{\omega}{\nu k_z^2} = \frac{\omega}{\nu}\left(\frac{H}{2\pi}\right)^2. \tag{5.25}$$

   We use $\mathrm{Re} \gg 1$ in our simulations[1].

Finally, we use initial conditions $\mathbf{u}(x,z,0) = \Upsilon(x,z,0) = 0$ and $\varpi(x,z,0) = 1$, corresponding to hydrostatic equilibrium and no initial fluid motion.

[1]This condition is always satisfied in stars. For example, in WDs, the dominant linear dissipation mechanism of g-modes is radiative damping, with damping rate ranging from 10^{-11}–10^{-4} of the mode frequency [Fuller and Lai, 2011]. This corresponds to a small effective viscosity or $\mathrm{Re} \gg 1$.

5.4.2 Damping Layers

We aim to damp disturbances that reach the vertical boundaries of the simulation domain without inducing nonphysical reflection. To do so, we replace material derivatives in Eq. (5.5) with:

$$\frac{\mathrm{D}}{\mathrm{D}t} \to \frac{\mathrm{D}}{\mathrm{D}t} + \Gamma(z), \tag{5.26}$$

$$\Gamma(z) = \frac{1}{2\tau}\left[2 + \tanh\frac{z - z_T}{\Delta z} + \tanh\frac{z_B - z}{\Delta z}\right], \tag{5.27}$$

where $z_B = 0.3H$ and $z_T = 9.5H$ are the boundaries of the lower and upper damping zones respectively. This damps perturbations below z_B and above z_T with damping time τ and negligibly affects the dynamics between z_B and z_T. Most importantly, horizontal momentum remains conserved between z_B and z_T, and outgoing boundary conditions are imposed at z_B, z_T. We choose the transition width $\Delta z = 0.25H$ and damping time $\tau = 1/(15N)$. This prescription is similar to Lecoanet et al. [2016] and has the advantage of being smooth, important for spectral methods. Further details of our implementation of the fluid equations in Dedalus are described in Appendix D.3.

5.5 Weakly Forced Numerical Simulation

To test our numerical code and implementation, we carry out a simulation in the weakly forced regime with $C = 1.64 \times 10^{-7}$. According to the linear solution (Eq. (5.14)), this generates IGW with $|\xi_z k_z| \approx 5 \times 10^{-5}$ just above the forcing zone. The IGW grows to $|\xi_z k_z| \approx 7.4 \times 10^{-3}$ at the upper damping zone and satisfies $|\xi_z k_z| \ll 1$ in the entire simulation domain. We include a nonzero ν corresponding to $\mathrm{Re} = 10^7$.

We expect the waves to follow the analytical solution given by Eq. (5.14) and the corresponding $u_x(x,z,t)$; we denote this analytical solution $\mathbf{u}_{\text{an}}(x,z,t)$. The amplitude of the observed IGW in the simulation field $\mathbf{u}$ relative to $\mathbf{u}_{\text{an}}$ over some region $z \in [z_b, z_t]$ can be estimated from

$$A_i(t) = \frac{\int_{z_b}^{z_t}\int_0^{L_x} \overline{\rho}(\mathbf{u}\cdot\mathbf{u}_{\text{an}})\,\mathrm{d}x\mathrm{d}z}{\int_{z_b}^{z_t}\int_0^{L_x} \overline{\rho}|\mathbf{u}_{\text{an}}|^2\,\mathrm{d}x\mathrm{d}z}. \tag{5.28}$$

The subscript i denotes the incident wave. If $\mathbf{u} = \mathbf{u}_{\text{an}}$, then $A_i(t) = 1$. The factor of $\bar{\rho}$ inside the integrands in Eq. (5.28) corrects for the $\propto e^{z/2H}$ growth of $\mathbf{u}_{\text{an}}$; without it, $A_i(t)$ would be dominated by the contribution near z_t.

For the weakly forced simulation, we expect $A_i(t) = 1$ when integrated between the forcing and damping zones, i.e. $z_b \gtrsim z_0$ and $z_t \lesssim z_T$ (z_0, z_T are defined in Eq. (5.13) and Eq. (5.27) respectively). For consistency with the nonlinear case later, we choose $z_b = z_0 + 3\sigma$ and $z_t = z_b + H$. Note that using a larger integration domain by choosing $z_t = z_T - \Delta z$ just below the upper damping zone instead does not change the measured A_i. The resulting measurement of $A_i(t)$ is shown in Fig. 5.1, and indeed $A_i \approx 1$ after the initial transient.

The analytical theory (Section 5.3.1) also predicts that the horizontal momentum flux $F(z,t)$ is independent of z between the forcing zone where the wave is generated and the damping zone where it is dissipated. The expected horizontal momentum flux carried by the excited IGW in the linear theory can be computed by simply evaluating Eq. (5.11) for $\mathbf{u}_{\text{an}}$ and is a constant:

$$F_{\text{an}} \equiv \left\langle \rho u_{an,x} u_{an,z} \right\rangle_x. \tag{5.29}$$

Denoting the momentum flux measured in the simulation by $F(z,t)$ (use Eq. (5.11) with velocities taken from the simulation), we expect $F(z,t) = F_{\text{an}}$ between z_0 and z_T. Fig. 5.2 shows agreement with this prediction.

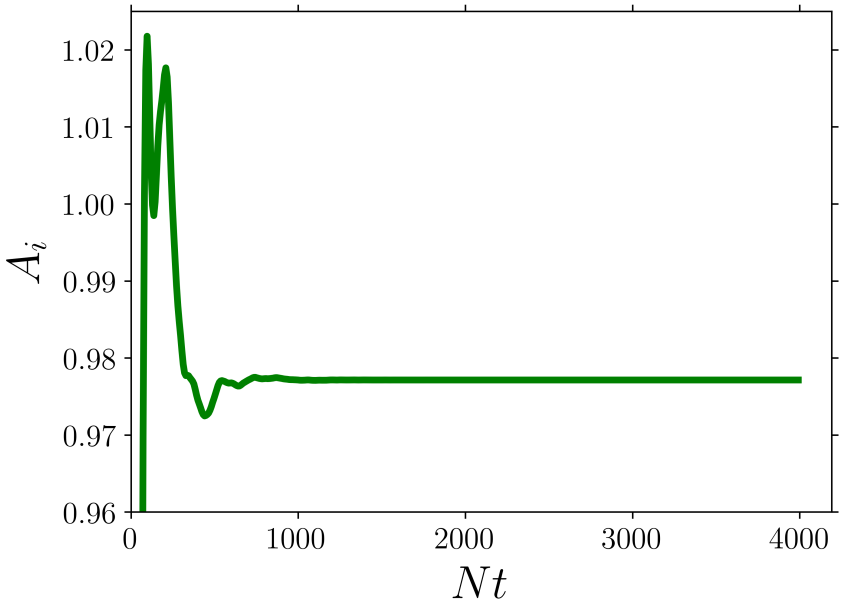

Figure 5.1: Amplitude of the excited IGW over time (in units of N^{-1}) in the weakly forced simulation, computed using Eq. (5.28). $A_i(t) = 1$ corresponds to perfect agreement with the analytical estimate. After an initial transient phase, we observe $A_i(t)$ asymptotes to ≈ 1, implying continuous excitation of identical IGW with the expected amplitude. The small deviation of $A_i(t)$ from unity may be due to truncation error in our implicit timestepping scheme, as a relatively large fixed step size $\Delta t = 0.1/N$ was used for this simulation.

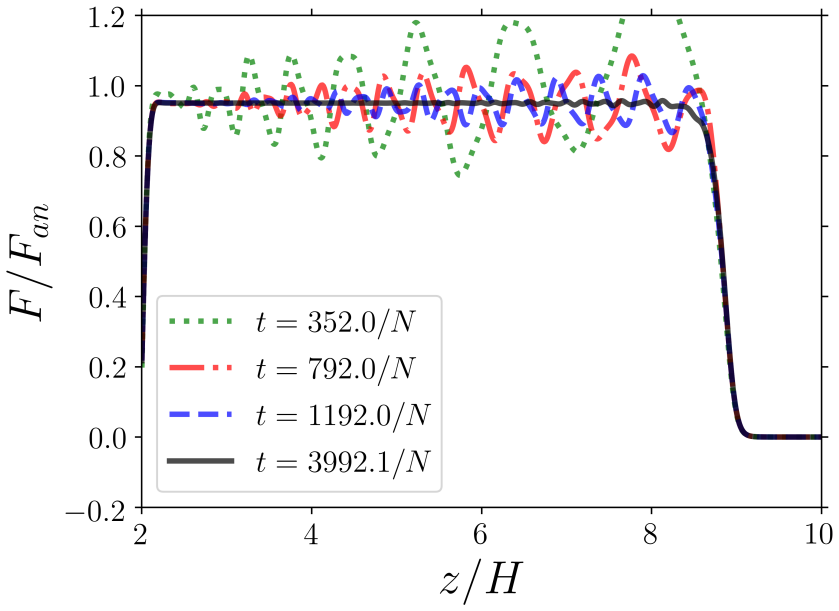

Figure 5.2: F/F_{an} plotted at select times t (in units of N^{-1}). As the initial transient dies out, $F/F_{\text{an}} \approx 1$ to a good approximation above the forcing zone $z > z_0 = 2H$ and below the damping zone $z \lesssim z_T = 9.5H$. The horizontal momentum flux excited in the forcing zone is transported without loss to the top of the domain, where it is dissipated by the damping zone (see Section 5.4.2) without reflection.

Resolution	Re
1024×4096	2048
768×3072	1024
512×2048	512
256×1024	341
256×1024	205
256×1024	146

Table 5.1: Spectral resolutions and Reynolds numbers of simulations of wave breaking.

5.6 Numerical Simulations of Wave Breaking

To perform simulations of wave breaking phenomena, we use the same setup as described in Section 5.4 and Section 5.5 except for different values of C and ν. In particular, we choose C such that $|\xi_z k_z| = 0.1$ in the forcing zone ($z = z_0$). The linear solution predicts $|\xi_z k_z| \sim 4.25$ at the upper damping zone z_T. We choose the viscosity ν for each resolution to be as small as possible while still resolving the shortest spatial scales of the wave breaking. A table of our simulations can be found in Table 5.1.

5.6.1 Numerical Simulation Results

A full video of our simulation with $N_x = 768$, $N_z = 3072$, Re = 1024 is available online[2]. We take this to be our fiducial simulation for the remainder of this paper, though other simulations show qualitatively similar behavior.

In Fig. 5.3, we present snapshots of u_x and Υ at various phases of the simulation. Note that $\Upsilon \lesssim 0.1$, so the density stratification does not deviate significantly from equilibrium. The flow evolves through several distinct stages:

[2] `https://bit.ly/3vuVKNN`

1. At early times (top left panel), the flow resembles a linear IGW lower in the simulation domain but breaks down into smaller-scale features at higher z. Some characteristic swirling motion can be seen in the advected scalar Υ, indicating Kelvin-Helmholtz instabilities.

2. At a slightly later time (top right panel), the mean flow in u_x becomes much more prominent and the critical layer z_c has become much more definite. Small-scale fluctuations are still present in u_x but at smaller amplitudes due to being in a denser region of the fluid.

3. In the bottom left panel, the critical layer transition becomes very sharp, and small swirls of limited vertical extent in Υ at the location of the critical layer suggest that the Kelvin-Helmholtz instability is responsible for regulating the width of this transition. More discussion can be found in Section 5.6.2.

4. At the end of the simulation (bottom right panel), the critical layer has advanced downwards, but otherwise the flow shows very few significant qualitative differences from the previous snapshot. This suggests that the latter phase of the simulation has reached a steady state. Notably, the horizontal banded structure of u_x in the upper, synchronized fluid does not continue to evolve (also visible in the top panel of Fig. 5.4), suggesting that momentum redistribution and mixing within the synchronized fluid are negligible.

In Fig. 5.4, we plot the mean horizontal flow velocity $\overline{U}$ (Eq. (5.16)) and the dimensionless momentum flux F/F_{an} (Eqs. (5.11) and (5.29)) as a function of z at the times depicted in Fig. 5.3. At each time, $\overline{U}$ is close to zero below the critical layer, but then sharply increases to $\overline{U}_c$ at the critical layer (i.e. the flow is "spun-up"). Above the critical layer, $\overline{U}$ varies slightly due to momentum transport within the spun-up layer. This agrees with the expectation discussed in Section 5.3.4.

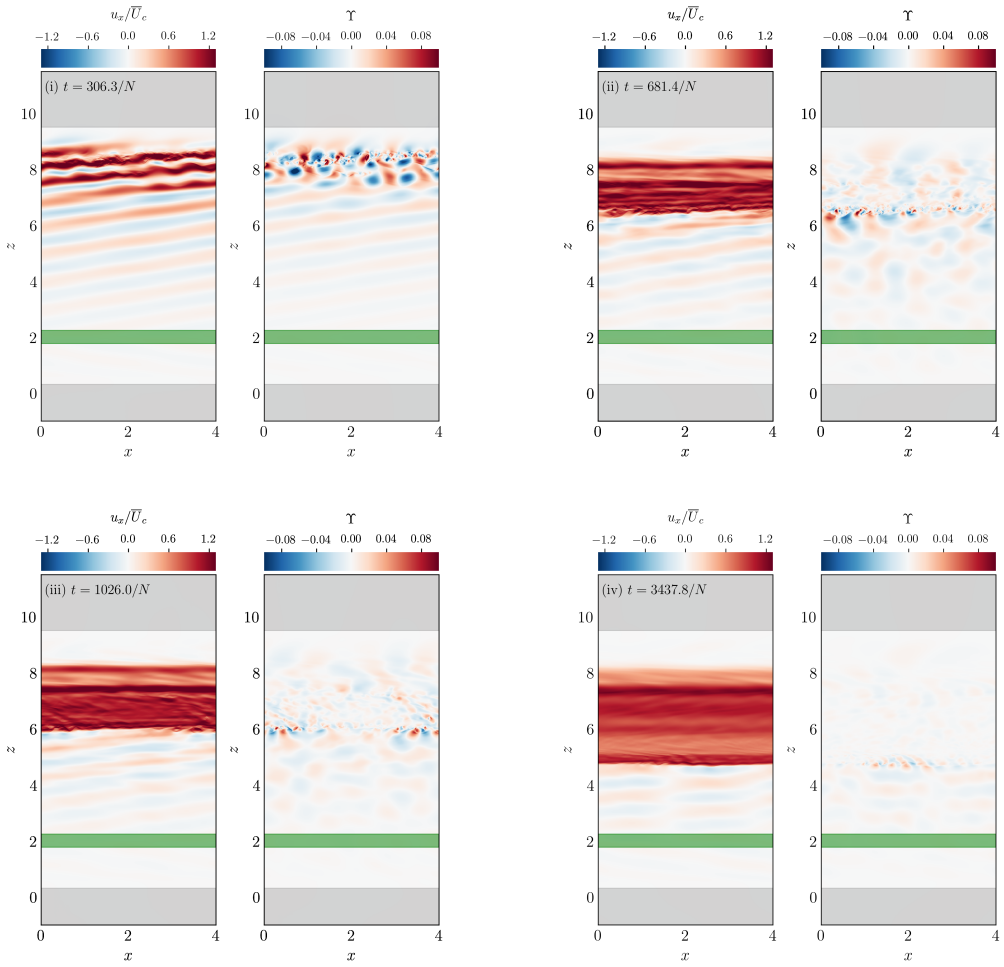

Figure 5.3: Snapshots of u_x and $\Upsilon \equiv \ln\left(\rho/\bar{\rho}\right)$ in the fiducial simulation illustrating distinct phases of the evolution of the flow. See the online PDF for a color version. Damping layers at the top and bottom of the simulation domain are shaded in light grey (see Section 5.4.2), while the forcing zone in the lower middle portion of the simulation domain (see Section 5.3.2) is shaded in light green (boundaries are at $z_0 \pm 3\sigma$). The four panels illustrate (i) the initial transient wave breaking phase, (ii) formation of a distinct critical layer, (iii) steepening of the critical layer, and (iv) downward advance of the critical layer.

Similarly, $F \lesssim F_{\rm an}$ below the critical layer, and then decreases to about zero above the critical layer. However, two notable deviations from the discussion in Section 5.3.4 can be observed: (i) the incident flux on the critical layer fluctuates somewhat temporally, and (ii) there is a small negative flux just above the critical layer at later times. These are addressed in subsequent sections.

5.6.2 Kelvin-Helmholtz Instability and Critical Layer Width

The formation of the critical layer is associated with a strong shear flow. What is the width of this layer? Inspection of Fig. 5.3 suggests the presence of the Kelvin-Helmholtz Instability (KHI) in the critical layer. In a stratified medium, KHI occurs when the Richardson number (Eq. (5.21)) satisfies $\mathrm{Ri} \lesssim 1/4$ [e.g. Shu, 1991]. It is natural to suspect that the shear flow cannot steepen further than the onset of KHI. To test this, we compute the local Ri for the shear flow around the critical layer.

It is difficult to accurately measure the Richardson number, as it depends on the derivative of the velocity. We measure Ri as follows: we first assign an $\mathrm{Ri}_x(x,t)$ for every x in the critical layer, then take the median of Ri for the entire layer. Ri_x is computed using the vertical distance over which the local u_x increases from $0.3\bar{U}_c$ to $\bar{U}_c$ (see Eq. (5.19)). The value 0.3 is necessary to exclude the small mean flow generated in the weakly nonlinear regime far below the critical layer. This

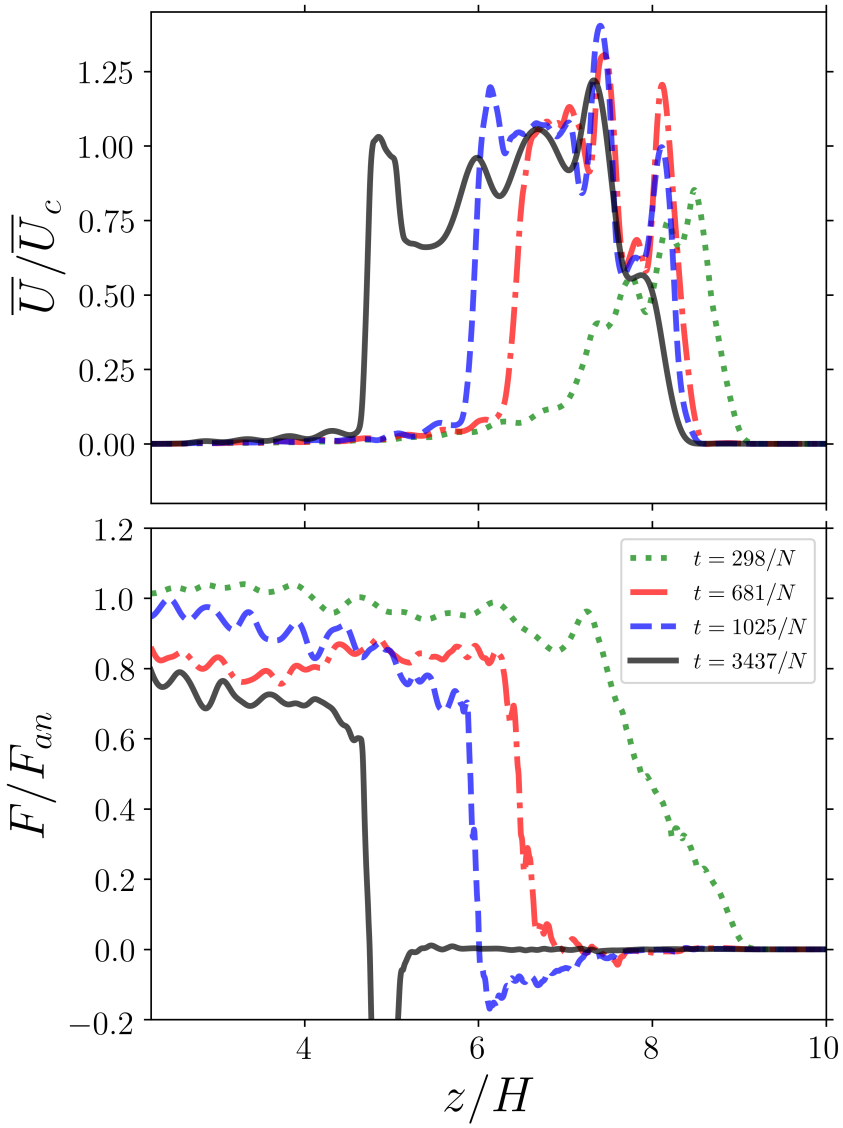

Figure 5.4: The mean horizontal flow velocity $\overline{U}(z,t)$ (Eq. (5.16)) and the dimensionless momentum flux $F(z,t)/F_{\text{an}}$ (Eqs. (5.11) and (5.29)) in our fiducial simulation plotted at the same times as in Fig. 5.3. The two distinct zones of mean flow are separated by a critical layer. The critical layer propagates toward lower z due to momentum transport ($\partial F/\partial z$).

procedure can be written:

$$z_{CL,\min}(x,t) \equiv \min\left\{z \mid u_x(x,z,t) > 0.3\overline{U}_c\right\}, \tag{5.30}$$

$$z_{CL,\max}(x,t) \equiv \max\left\{z \mid u_x(x,z,t) < \overline{U}_c\right\}, \tag{5.31}$$

$$\mathrm{Ri}_x(x,t) \equiv \left(\frac{N^2\left(z_{CL,\max} - z_{CL,\min}\right)^2}{(0.7\overline{U}_c)^2}\right), \tag{5.32}$$

$$\mathrm{Ri}(t) \equiv \underset{x}{\mathrm{med}}\,\mathrm{Ri}(x,t). \tag{5.33}$$

We use the background buoyancy frequency to compute Ri, as fluctuations do not change N^2 significantly ($\sim 1\%$). To understand the variation in Ri over x, we also compute $\min_x \mathrm{Ri}_x(x,t)$ (the maximum is very noisy). Both are shown in Fig. 5.5. Absorption of incident IGWs quickly decreases the Richardson number to between 0.25 and 0.5, characteristic of the onset of the KHI.

This result suggests that the critical layer width is regulated by the competition between steepening induced by IGW breaking and broadening due to shear instability. This width does not vary significantly with resolution in our resolved simulations (see Fig. 5.10). As such, Ri ~ 0.5 can be used to calculate the critical layer width in stars, where N^2 and $\overline{U}_c$ (corresponding to the tidal frequency) are known.

5.6.3 Flux Budget

The downward propagation of the critical layer location $z_c(t)$ is driven by the absorption of horizontal momentum flux at z_c, following Eq. (5.23). The flux budget at the critical layer can be decomposed as

$$F_i(t) = F_a(t) + F_r(t) + F_s(t), \tag{5.34}$$

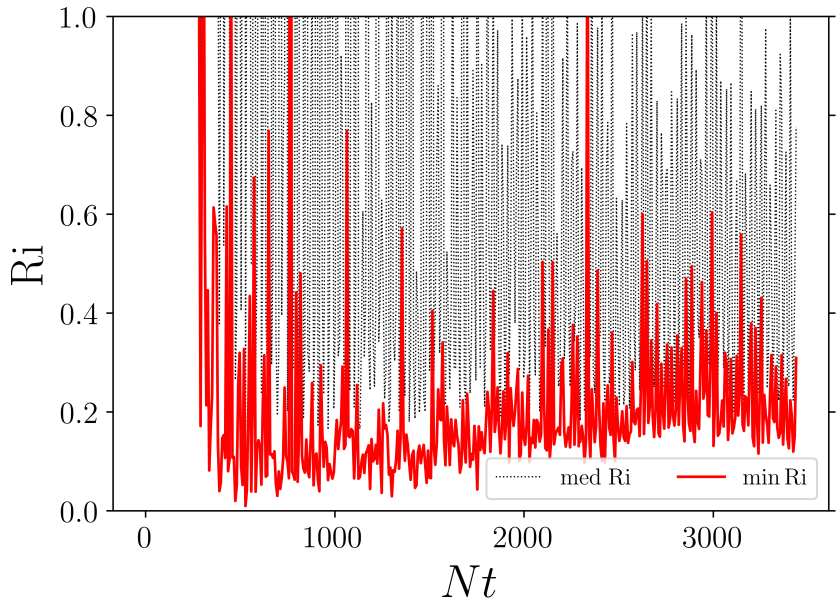

Figure 5.5: Local Richardson number (Eq. (5.33)) of the flow at the critical layer over time (in units of N^{-1}) in our fiducial simulation. The solid red and dotted black lines denote respectively the minimum and median of $\mathrm{Ri}_x(x,t)$. These numbers measure the mean and spread in width of the critical layer over x. Note that $\mathrm{Ri} \sim \frac{1}{4}$ corresponds to the KHI, so this plot suggests the shear at the critical layer does not steepen past the onset of the KHI.

where F_i is the incident flux, F_a is the absorbed flux, F_r is the reflected flux, and F_s is some "redistribution" flux above the critical layer, responsible for momentum redistribution within the synchronized upper layer. Careful accounting of F_s turns out to be important to obtain the correct F_a and resulting critical layer propagation. A more specific physical interpretation of F_s is unclear; it is somewhat tempting but unfounded to identify F_s with the transmitted flux. In these simulations, we find $F_s < 0$, corresponding to net momentum transport *into* the critical layer from the synchronized layer above it.

After measuring z_c (see Section 5.6.4) and $F(z)$ (Eq. (5.11)) at each time step, we determine each of F_i, F_a, F_r, F_s as follows:

$$F_i(t) = F_{\text{an}} A_i^2(t), \tag{5.35}$$

$$F_r(t) = F_i(t) - \frac{1}{H} \int_{z_c - \Delta z - H}^{z_c - \Delta z} F(z,t)\,\mathrm{d}z, \tag{5.36}$$

$$F_s(t) = \frac{1}{\Delta z} \int_{z_c}^{z_c + \Delta z} \min(F(z,t), 0)\,\mathrm{d}z, \tag{5.37}$$

$$F_a(t) = F_i - F_r - F_s. \tag{5.38}$$

Fig. 5.6 depicts the four components of this flux decomposition. Below the critical layer, we average over an interval of length H, also the vertical wavelength. The offset Δz is necessary to make the measurement of the incident flux unaffected by the turbulence within the critical layer itself. The width of the critical layer is limited by $\mathrm{Ri} \lesssim 1$ (see Section 5.6.2), which bounds its vertical extent $\sim \frac{1}{|k_z|}$. We empirically found an offset of $\Delta z = \frac{3}{|k_z|}$ was necessary to be sufficiently far from strong fluctuations near the critical layer.

Above the critical layer, we observe that the F_s feature has varying width (compare e.g. the $t = 1171.4/N$ and $t = 3437.8/N$ lines in the bottom panel of Fig. 5.4) but contributes significantly to the total flux budget. We average only where $F < 0$

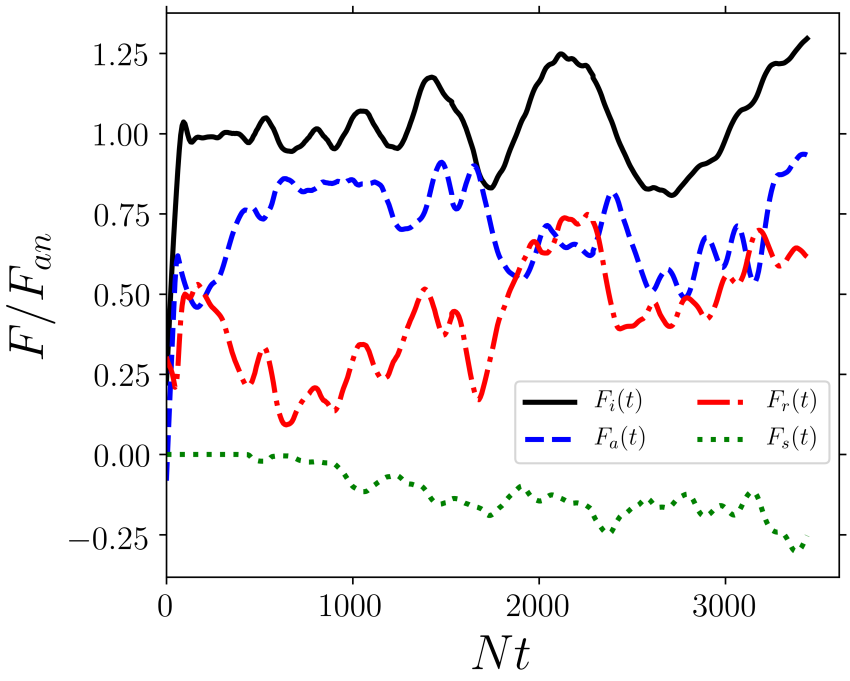

Figure 5.6: Momentum flux decomposition calculated from the simulation. Plotted are the four components of the horizontal momentum flux budget over time (see Eq. (5.34)), in units of the analytical estimate for the incident wave flux F_{an} (Eq. (5.12)): F_i, the flux incident on the critical layer; F_a, the flux absorbed by the critical layer; F_r, the flux reflected at the critical layer; and F_s, the flux inside the synchronized layer.

so that F_s is robust to such width variations. We find that this is an accurate way of measuring F_s and determining F_a.

5.6.4 Critical Layer Propagation

With a careful determination of F_a, we can make predictions for the propagation of $z_c(t)$ and compare to the measured propagation in the simulation. In principle, z_c is the location where the incident flux significantly attenuates. In the simulation, shear turbulence causes F to have significant spatial and temporal fluctuations that translate to large temporal fluctuations in $z_c(t)$. To minimize these spurious

fluctuations, we measure the location of the critical layer using a spatial average of where flux deposition occurs:

$$z_{c,\min}(t) \equiv \min_z \{z : F(z,t) > 0.3F_{\text{an}}\}, \tag{5.39}$$

$$z_{c,\max}(t) \equiv \max_z \{z : F(z,t) < 0.3F_{\text{an}}\}, \tag{5.40}$$

$$z_c(t) \equiv \frac{z_{c,\min}(t) + z_{c,\max}(t)}{2}. \tag{5.41}$$

Measuring z_c in other ways does not significantly change the results of the analysis.

In Fig. 5.7 we plot the numerically measured z_c against numerical integration of Eq. (5.23) using the measured $F_a(t)$. Since the critical layer is still forming at early times, we solve Eq. (5.23) by integrating backwards from the end of the simulation ($t = t_f$), using $z_c(t_f)$ as the initial condition. From Fig. 5.7, we see that the agreement between the measured $z_c(t)$ and its estimate via $F_a(t)$ is excellent.

By time-averaging the numerically measured F_a, we find $\langle F_a \rangle_t \approx 0.71 F_{\text{an}}$. Note that $F_a < F_{\text{an}}$, so momentum flux absorption at the critical layer is incomplete. This is due to reflection of waves off the critical layer, which carry momentum downward.

5.6.5 Non-absorption at Critical Layer

To further understand the behavior at the critical layer, we compare two reflective behaviors observed in the simulation: (i) the presence of a reflected wave with the same frequency as the incident wave (i.e. with wave vector $\mathbf{k}_r = k_x\hat{\mathbf{x}} - k_z\hat{\mathbf{z}}$), and (ii) the reflected flux F_r. The reflected wave amplitude and flux need not agree exactly if some reflected flux is in higher-order modes, which is indeed the case in

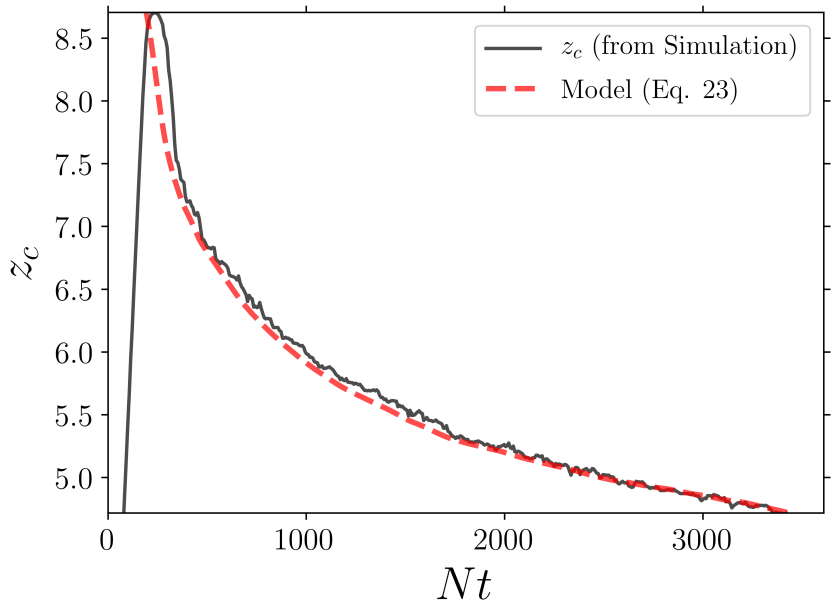

Figure 5.7: Propagation of the critical layer over time. Shown are: (solid black) $z_c(t)$ from simulation data, and (dashed red) model for $z_c(t)$ using direct integration of Eq. (5.23) for $F_a(t)$ measured from simulation data (described in Eq. (5.38)). The model uses the end of the simulation as its initial condition and integrates backwards, as the critical layer is still forming at earlier times. The agreement of the model with the simulation shows Eq. (5.23) is a good description of the evolution of z_c.

our simulations. Both are of physical interest, however: the reflected wave amplitude is essential for setting up standing modes in a realistic star, while the flux is important for accurately tracking angular momentum transfer during synchronization.

To measure the reflected wave amplitude $A_r(t)$, we use an approach similar to the calculation of $A_i(t)$ (Eq. (5.28)):

$$A_r(t) = \max_{\delta x} \frac{\int_{z_b}^{z_t}\int_{0}^{L_x} \overline{\rho}\left(\mathbf{u}\cdot\mathbf{u}_{an,\mathbf{k}_r}\big|_{x=x+\delta x}\right)\,\mathrm{d}x\mathrm{d}z}{\int_{z_b}^{z_t}\int_{0}^{L_x} \overline{\rho}\,|\mathbf{u}_{\mathrm{an}}|^2\,\mathrm{d}x\mathrm{d}z}, \tag{5.42}$$

where $z_b = z_0+3\sigma$ and $z_t = z_b+H$ as before. The primary difference from Eq. (5.28) is the introduction of free parameter δx, the horizontal phase offset of the reflected wave. Since δx is unknown *a priori*, we choose $\delta x \in [0,2\pi]$ that maximizes $A_r(t)$. In our simulation, the phase offset $\phi_r(t) \equiv k_x \delta x(t)$ is consistent with reflection off a moving boundary at z_c, i.e. $\left|\partial\phi_r/\partial t\right| \simeq 2\left|\partial(k_z z_c)/\partial t\right|$.

Fig. 5.8 illustrates the behaviors of A_i and A_r. Both vary significantly in time but their mean values appear to converge towards the end of the simulation.

Since $A_i(t), A_r(t)$ vary somewhat over time, we perform time averaging over interval of four wave periods, denoted by angle brackets. We can then define the amplitude reflectivity

$$\mathscr{R}_A(t) \equiv \frac{\langle A_r\rangle(t)}{\langle A_i\rangle(t)}. \tag{5.43}$$

We compare the square of the reflectivity to the ratios of F_r and $-F_s$ to F_i, as $F \propto A^2$ (Eq. (5.12)). We define

$$\hat{F}_r \equiv \frac{\langle F_r\rangle(t)}{\langle F_i\rangle(t)}, \tag{5.44}$$

$$\hat{F}_s \equiv -\frac{\langle F_s\rangle(t)}{\langle F_i\rangle(t)}. \tag{5.45}$$

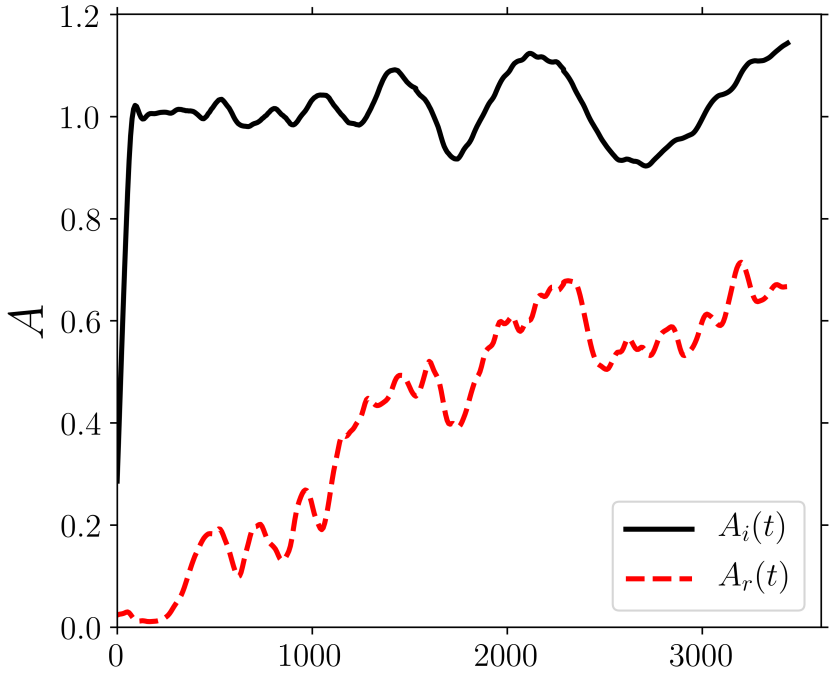

Figure 5.8: The incident wave amplitude $A_i(t)$ (solid black) and the reflected wave amplitude $A_r(t)$ (dashed red) just above the forcing zone.

Fig. 5.9 shows $\mathscr{R}_A^2$, $\hat{F}_r$, and $\hat{F}_s$ as functions of time. The three quantities appear to be roughly stationary for $t \gtrsim 2500/N$. Modest fluctuations ($\sim 20\%$) in A_i do not affect our reflectivity results thanks to the time averaging used in Eqs. (5.43)–(5.45).We see that in general $\hat{F}_r \gtrsim \mathscr{R}_A^2$, conforming with the expectation that the reflected flux consists of the simple reflected mode and higher order modes as well.

5.6.6 Resolution Study

Although throughout this paper we focused on our fiducial simulation with Re = 1024 and resolution $N_x = 768$, $N_z = 3072$, we also ran a suite of simulations varying the resolution and corresponding Reynolds number (Tab. 5.1). We find that

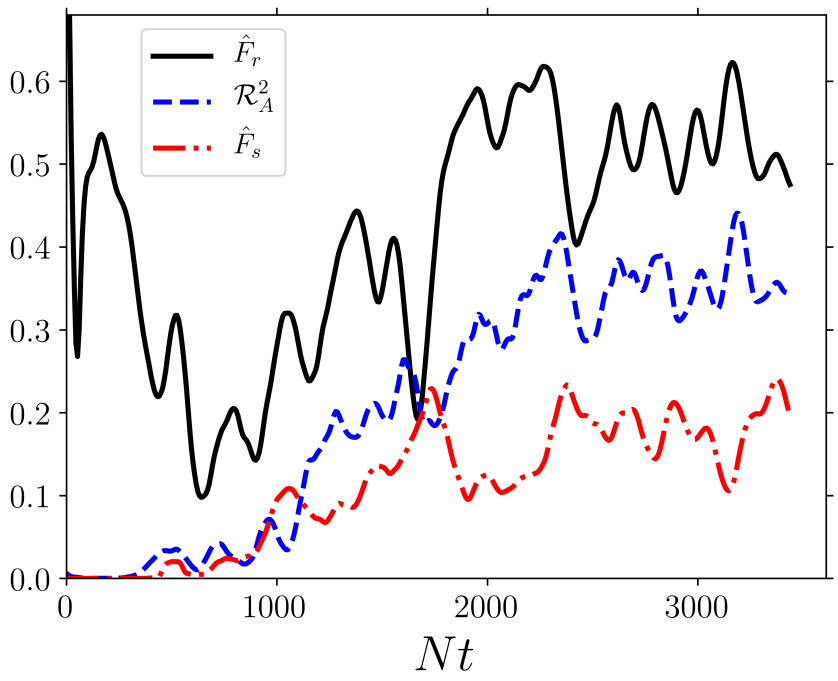

Figure 5.9: $\mathscr{R}_A^2$, $\hat{F}_r$, and redistribution flux $\hat{F}_s$ [Eqs. (5.43–5.45)] as a function of time (in units of N^{-1}). These quantities seem to become comparatively stable past about $t = 2500/N$, indicating that an asymptotic value may have been reached. That $\hat{F}_r \gtrsim \mathscr{R}_A^2$ implies a substantial fraction of reflected flux is in higher-order modes than the reflected IGW.

our global, quantitative measurements in the simulations ($\mathscr{R}_A^2$, F_r, F_s, and Ri) are very similar for our highest Reynolds numbers (1024 and 2048).

For each simulation in Tab. 5.1, we compute the median values of $\mathscr{R}_A^2$, $\hat{F}_r$, $\hat{F}_s$, and Ri [Eqs. (5.43–5.45) and (5.21) respectively] over the last 1/4 of the simulation time, when these quantities have reached their asymptotic values. These results are shown in Fig. 5.10.

As the simulation resolution increases and the viscosity decreases, we find that the Richardson number decreases, while the reflection and redistribution fluxes increase. The Richardson number is roughly constant for $\mathrm{Re} > 200$ with a value of $\mathrm{Ri} \sim 0.4$. The behavior of the fluxes is more complicated. While the fraction of reflected and redistributed flux is similar for our simulations with $\mathrm{Re} = 1024$ and 2048, higher resolution simulations would be required to determine these flux fractions in the limit $\mathrm{Re} \to \infty$.

Nevertheless, the difference in behavior of Ri and the flux reflectivity as Re is varied is in tension with Eq. (5.20). This tension is natural: Eq. (5.20) is derived from a linear theory, while fluid motion within the critical layer is turbulent, so reflection at the critical layer cannot be captured by the linear theory.

5.7 Summary and Discussion

5.7.1 Key Results

In this paper, we have performed numerical simulations of nonlinear breaking of IGWs in a stratified isothermal atmosphere. Such a setup represents the plane-parallel idealization of the outer stellar envelope. Our simulations use the spectral

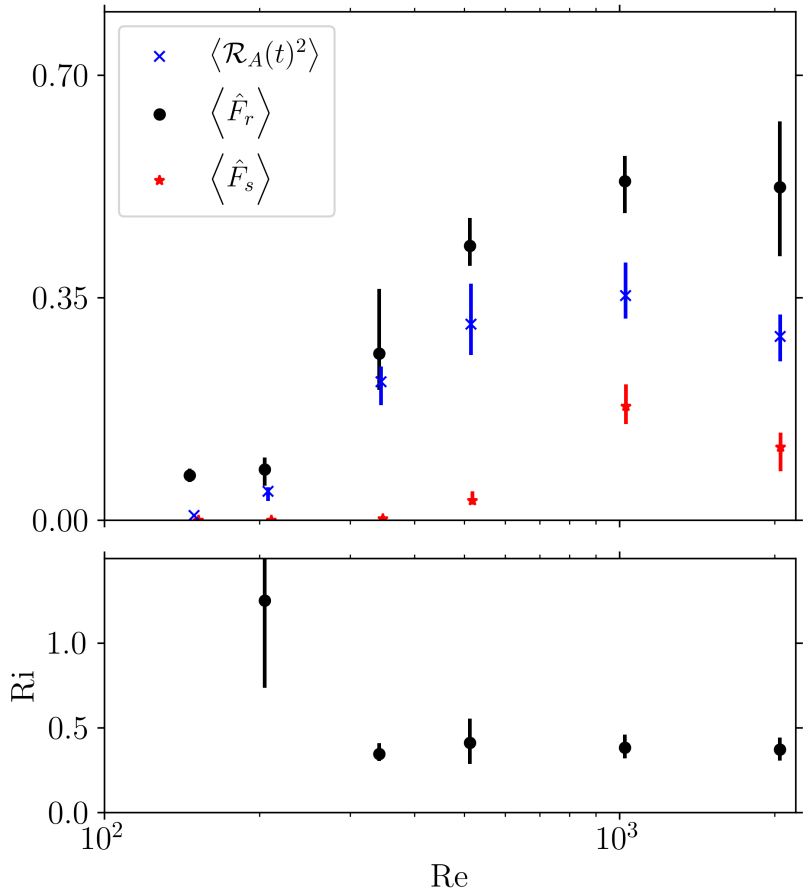

Figure 5.10: Convergence of the median $\hat{F}_r$, $\mathscr{R}_A^2$, $\hat{F}_s$, and Ri (Eqs. (5.43)–(5.45) and (5.21) respectively) in simulations with varying resolution and viscosity as given in Tab. 5.1. Vertical bars show the temporal variation of each measurement between the 16% and 84% range. Small horizontal displacements are made for data points at identical Re for readability. Note that simulations with larger Re correspond to smaller viscosity and are more physically realistic. At the smallest Re value, Ri ≈ 50 is too large to fit on the plot.

code Dedalus [Burns et al., 2016, Burns et al., 2020], and are carried out in 2D. We observe spontaneous formation of a critical layer that separates a "synchronized" upper layer of fluid and a lower layer with no mean horizontal flow. This critical layer then propagates downwards as incident IGWs break and deposit horizontal momentum to the fluid (see Fig. 5.3 for snapshots from our fiducial simulation). Our primary conclusions regarding the evolution of the critical layer are as follows:

1. The width of the turbulent critical layer is determined by requiring the local Richardson number (Eq. (5.21)) Ri ~ 0.5 (see Fig. 5.5).
2. The location of the critical layer $z_c(t)$ can be predicted by careful measurement of the absorbed horizontal momentum flux at the critical layer (see Eq. (5.23) and Fig. 5.7).
3. The absorption of IGW momentum flux at the critical layer is incomplete. The critical layer only absorbs ~ 70% of the incident flux in our highest resolution simulations (see Fig. 5.10). The reflected flux is carried away from the critical layer as both lowest-order reflected waves and waves with larger z wavenumbers.

5.7.2 Discussion

In this paper, we have studied the nonlinear behavior of IGWs with $|k_x/k_z| \sim 1/(2\pi)$ in a plane-parallel geometry. Tidally excited IGWs in binary stars have horizontal wavenumber $k_\perp \sim 1/R$ (where R is the stellar radius) much smaller than the radial wavenumber k_r. While our simulations do not satisfy $|k_x/k_z| \ll 1$, the qualitative behavior is likely to be similar, as the turbulence driving the critical layer dynamics occurs at scales significantly smaller than either $1/k_x$ or $1/|k_z|$. Simulating

IGWs with $k_x \ll |k_z|$ is more challenging numerically and we defer its exploration to future work.

It is interesting to compare our work with that of Barker and Ogilvie [2010], who studied inward-propagating IGWs in solar-type stars and their nonlinear breaking due to geometric focusing. In their numerical simulations in a 2D polar geometry, they found no evidence for reflected waves, contrary to our result. Note that their simulations were run with substantially higher viscosity, or lower resolution, than explored here, and their effective Reynolds number (equal to $1/\lambda$ in their notation) is of order 10. We also find at low Reynolds numbers that there is negligible wave reflection.

Regardless of the limitations inherent in our simulations (e.g. plane-parallel geometry), our results shed light on the physical mechanism of tidal heating in close binaries. In particular, our simulations indicate that energy dissipation occurs in a narrow critical layer. The star heats up from outside-in as the critical layer propagates inwards. This tidal heating profile differs flom that used by Fuller and Lai [2012b]. We plan to study this issue in a future work.

CHAPTER 6

DYNAMICAL TIDES IN ECCENTRIC BINARIES CONTAINING MASSIVE MAIN-SEQUENCE STARS: ANALYTICAL EXPRESSIONS

Originally published in:
Yubo Su and Dong Lai. Dynamical tides in eccentric binaries containing massive main-sequence stars: Analytical expressions. *MNRAS*, 510(4):4943–4951, 2022b

6.1 Introduction

The physics of tidal dissipation in massive, main-sequence (MS) stars (i.e. having a convective core and radiative envelope) under the gravitational influence of a companion was first studied by Zahn [1975] [see also Savonije and Papaloizou, 1983, Goldreich and Nicholson, 1989]. The dominant dissipation mechanism is through the *dynamical tide*, in which the time-dependent tidal potential of the companion excites internal gravity waves (IGWs) at the convective-radiative boundary (RCB). As the wave propagates towards the surface, its amplitude grows, and the wave dissipates efficiently [Zahn, 1975, Goldreich and Nicholson, 1989, Su et al., 2020]. The contribution due to viscous dissipation in the convective core is expected to be subdominant.

The original expression describing the torque due to dynamical tides by Zahn [1975] is very sensitive to the global properties of the star. Kushnir et al. [2017] present an updated derivation of the tidal torque that depends only on the local stellar properties near the RCB, eliminating many uncertainties from the Zahn's original expression. In Zaldarriaga et al. [2018], the authors use the new expression to study tidal synchronization in binaries consisting of a Wolf-Rayet star and a black hole, the likely progenitors to merging black-hole binaries observed by LIGO/VIRGO.

These previous works all apply to nearly circular binaries. However, massive stars can often be found in high-eccentricity (high-e) systems, such as binaries consisting of one MS star and one neutron star (NS). The NS is formed with a large kick velocity [e.g. Lai et al., 2001, Janka et al., 2021], giving rise to a high-e binary. Several such high-e MS-NS systems have been discovered [e.g. Kaspi et al., 1994, Johnston et al., 1994, Champion et al., 2008]. These are the progenitors of double NS systems [e.g. Tauris et al., 2017]. An important issue is to understand whether such high-e systems can circularize prior to mass transfer or a common envelope phase [Vigna-Gómez et al., 2020, Vick et al., 2021].

The purpose of this paper is to derive easy-to-use, analytical expressions for the effects of dynamical tides for high-e binaries with massive MS stellar companions. In Section 6.2, we summarize the equations of dynamical tides involving IGWs in circular binaries and existing techniques for studying high-e systems. In Section 6.3, we evaluate the effect of dynamical tides in high-e systems containing massive MS stellar companions, including the torque and orbital decay rate. In Section 6.4, we apply our results to the pulsar-MS binary PSR J0045-7319, for which a non-zero orbital decay rate has been measured. Finally, we summarize our results and discuss the uncertainties in Section 6.5.

6.2 Dynamical Tides in Massive Stars

6.2.1 Circular Binaries

We first review the case where the binary is circular. Let M be the mass of the MS star, M_2 the mass of the companion, a the semimajor axis of the binary, and Ω the angular frequency (mean motion) of the binary. The tidal torque exerted on

the star by the companion due to tidal excitation of IGWs at the RCB is [Kushnir et al., 2017]

$$T_{\rm circ}(\omega) = T_0 \, {\rm sgn}(\omega) \left| \frac{\omega}{\Omega} \right|^{8/3}, \tag{6.1}$$

where

$$T_0 \equiv \beta_2 \frac{G M_2^2 r_{\rm c}^5}{a^6} \left(\frac{\Omega}{\sqrt{G M_{\rm c}/r_{\rm c}^3}} \right)^{8/3} \frac{\rho_{\rm c}}{\bar{\rho}_{\rm c}} \left(1 - \frac{\rho_{\rm c}}{\bar{\rho}_{\rm c}} \right)^2, \tag{6.2}$$

$$\beta_2 \equiv \left[\frac{r_{\rm c}}{g_{\rm c}} \left(\frac{{\rm d}N^2}{{\rm d}\ln r} \right)_{r=r_{\rm c}} \right]^{-1/3} \left[\frac{3^2 \Gamma^2(1/3)}{40\pi 12^{2/3}} \alpha^2 \right]. \tag{6.3}$$

Here, $\omega \equiv 2\Omega - 2\Omega_{\rm s}$ is the tidal forcing frequency, $\Omega_{\rm s}$ is the spin of the MS star, N is the Brunt-Väisälä frequency, r is the radial coordinate within the star, and $r_{\rm c}$, $M_{\rm c}$, $g_{\rm c}$, $\rho_{\rm c}$, and $\bar{\rho}_{\rm c}$ are the radius of the RCB, the mass contained within the convective core, the gravitational acceleration at the RCB, the stellar density at the RCB, and the average density of the convective core respectively. Γ is the gamma function, α is a numerical constant of order unity given by Eq. (A32) of Kushnir et al. [2017], and $\beta_2 \approx 1$ for a large range of stellar models (Fig. 2 of Kushnir et al., 2017). In Eq. (6.1), we have expressed the various factors such that T_0 contains all the spin-independent terms.

The above result (Eq. 6.1) assumes that tidally excited IGWs dissipate completely as they propagate outwards towards the stellar surface. Such dissipation can happen either through radiative damping or nonlinear effects. Recent hydrodynamical simulations of the IGW breaking process in the stellar envelope [Su et al., 2020] show that the nonlinear damping of the outward-propagating IGWs is due to the development of a narrow critical layer. This critical layer divides the star into a asynchronously-rotating interior and a synchronously-rotating exterior [see Goldreich and Nicholson, 1989], and it efficiently absorbs the angular momentum of the incident IGWs ($\sim 70\%$ of incident flux, Su et al., 2020). If the

IGWs instead reflect before dissipating completely, then standing waves are set up in the stellar interior. These internal oscillations then dissipate due to radiative damping and nonlinear mode couplings (for the former, see e.g. Lai, 1996, 1997, Kumar and Quataert, 1997, 1998, and for the latter, see e.g. O'Leary and Burkart, 2014). Except when a tidal forcing frequency is resonant with a stellar oscillation mode, the traveling-wave assumption represents an upper bound on the tidal torque (see e.g. Yu et al., 2020b, 2021 concerning tidal dissipation in white dwarf binaries).

Note additionally that we use Eq. (6.1) from Kushnir et al. [2017] instead of the classic expression from Zahn [1975], which is given by:

$$T_{\rm circ}^{\rm (Zahn)}(\omega) = \frac{3}{2}\frac{GM_2^2R^5}{a^6}E_2\left(\frac{\omega}{\sqrt{GM/R^3}}\right)^{8/3}, \tag{6.4}$$

where M and R are the mass and radius of the MS star and E_2 is a numerical parameter obtained by integrating over the entire star. The fitting formula $E_2 = 1.592\times10^{-9}(M/M_\odot)^{2.84}$ as given by Hurley et al. [2002] is commonly used, which varies by many orders of magnitude for different stars. Moreover, $T_{\rm circ}^{\rm (Zahn)}$ depends on M and R, properties of the entire star, whereas the tidal torque is entirely generated at the RCB. For these reasons, the expression by Kushnir et al. [2017] is preferred.

6.2.2 Eccentric Binaries

The gravitational potential of an eccentric companion at the quadrupole order can be decomposed as a sum over circular orbits [e.g. Storch and Lai, 2013, Vick et al.,

2017]:

$$U(\mathbf{r},t) = \sum_{m=-2}^{2} U_{2m}(\mathbf{r},t), \tag{6.5}$$

$$\begin{aligned} U_{2m}(\mathbf{r},t) &= -\frac{GM_2W_{2m}r^2}{D(t)^3}Y_{2m}(\theta,\phi)e^{-imf(t)}, \\ &= -\frac{GM_2W_{2m}r^2}{a^3}Y_{2m}\left(\theta,\phi\right)\sum_{N=-\infty}^{\infty}F_{Nm}e^{-iN\Omega t}. \end{aligned} \tag{6.6}$$

Here, the coordinate system is centered on the MS star, (r,θ,ϕ) are the radial, polar, and azimuthal coordinates of $\mathbf{r}$ respectively, $W_{2\pm2} = \sqrt{3\pi/10}$, $W_{2\pm1} = 0$, $W_{20} = -\sqrt{\pi/5}$, $D(t)$ is the instantaneous distance to the companion, f is the true anomaly, and Y_{lm} denote the spherical harmonics. F_{Nm} denote the *Hansen coefficients* for $l = 2$ [also denoted X_{2m}^N in Murray and Dermott, 1999], which are the Fourier coefficients of the perturbing function, i.e.

$$\frac{a^3}{D(t)^3}e^{-imf(t)} = \sum_{N=-\infty}^{\infty}F_{Nm}e^{-iN\Omega t}. \tag{6.7}$$

The F_{Nm} can be written explicitly as an integral over the eccentric anomaly [Murray and Dermott, 1999, Storch and Lai, 2013]:

$$F_{Nm} = \frac{1}{\pi}\int_0^{\pi}\frac{\cos[N(E-e\sin E)-mf(E)]}{(1-e\cos E)^2}\,\mathrm{d}E. \tag{6.8}$$

By considering the effect of each summand in Eq. (6.5), the total torque on the star, energy transfer in the inertial frame, and energy transfer in the star's corotating frame (which is also the tidal heating rate) can be obtained [Storch and Lai, 2013, Vick et al., 2017]:

$$T = \sum_{N=-\infty}^{\infty}F_{N2}^2T_{\mathrm{circ}}(N\Omega-2\Omega_{\mathrm{s}}), \tag{6.9}$$

$$\begin{aligned} \dot{E}_{\mathrm{in}} = \frac{1}{2}\sum_{N=-\infty}^{\infty}\Bigg\{&\left(\frac{W_{20}}{W_{22}}\right)^2 N\Omega F_{N0}^2T_{\mathrm{circ}}(N\Omega) \\ &+N\Omega F_{N2}^2T_{\mathrm{circ}}(N\Omega-2\Omega_{\mathrm{s}})\Bigg\}, \end{aligned} \tag{6.10}$$

$$\dot{E}_{\mathrm{rot}} = \dot{E}_{\mathrm{in}} - \Omega_{\mathrm{s}}T. \tag{6.11}$$

Here, dots indicate time derivatives.

Equations (6.9–6.10) can be used to express the binary orbital decay and circularization rates using

$$\frac{\dot{a}}{a} = -\frac{2a\dot{E}_{\rm in}}{GMM_2}, \tag{6.12}$$

$$\frac{\dot{e}e}{1-e^2} = -\frac{a\dot{E}_{\rm in}}{GMM_2} + \frac{T}{L_{\rm orb}}, \tag{6.13}$$

where $L_{\rm orb} = MM_2\left[Ga(1-e^2)/(M+M_2)\right]^{1/2}$ is the orbital angular momentum. The stellar spin synchronization rate can also be computed assuming that the star rotates rigidly:

$$\dot{\Omega}_{\rm s} = \frac{T}{kMR^2}, \tag{6.14}$$

where kMR^2 is the moment of inertia of the MS star.

6.3 Analytic Evaluation of Tidal Torque and Energy Transfer Rates

We can combine the expressions given in Sections 6.2.1 and 6.2.2 to compute the torque and energy transfer rate due to dynamical tides in an eccentric binary. The tidal torque is obtained by evaluating Eq. (6.9) with the circular torque set to Eq. (6.1), giving:

$$T = \sum_{N=-\infty}^{N=\infty} F_{N2}^2 T_0 \,\mathrm{sgn}\left(N - \frac{2\Omega_{\rm s}}{\Omega}\right)\left|N - \frac{2\Omega_{\rm s}}{\Omega}\right|^{8/3}. \tag{6.15}$$

The energy transfer rate in the inertial frame is obtained by evaluating Eq. (6.10) in the same way, giving:

$$\dot{E}_{\rm in} = \frac{T_0}{2}\sum_{N=-\infty}^{\infty}\left[N\Omega F_{N2}^2 \mathrm{sgn}\left(N - 2\Omega_{\rm s}/\Omega\right)\left|N - \frac{2\Omega_{\rm s}}{\Omega}\right|^{8/3} + \left(\frac{W_{20}}{W_{22}}\right)^2 \Omega F_{N0}^2 |N|^{11/3}\right]. \tag{6.16}$$

These two expressions can be used to obtain the orbital decay, circularization, and spin synchronization rates using Eqs. (6.12–6.14).

While exact, the two sums in Eqs. (6.15–6.16) are difficult to evaluate for larger eccentricities, where one often must sum hundreds or thousands of terms, each of which has a different F_{Nm}. In the following, we obtain closed-form approximations to Eqs. (6.15–6.16) when the eccentricity is large.

6.3.1 Approximating Hansen Coefficients

To simplify Eqs. (6.15–6.16), we seek tractable approximations for both F_{N2} and F_{N0}. Note that while the Hansen coefficients can be evaluated using the integral expression Eq. (6.8), this requires calculating a separate integral for each N. Instead, it is more convenient to use the discrete Fourier Transform of the left hand side of Eq. (6.7) to calculate arbitrarily many N at once [as pointed out by Correia et al., 2014]. Since $F_{(-N)m} = F_{N(-m)}$, we will only study the Hansen coefficient behavior for $m \geq 0$.

$m = 2$ Hansen Coefficients

Figure 6.1 shows F_{N2} vs. N when $e = 0.9$. First, we note that F_{N2} is much larger when $N \geq 0$ than for $N < 0$, so we focus on the behavior for $N \geq 0$. Here, F_{N2} has only one substantial peak. There are only two characteristic frequency scales: Ω and $\Omega_{\rm p}$, the pericentre frequency, defined by

$$\Omega_{\rm p} \equiv \Omega \frac{\sqrt{1+e}}{(1-e)^{3/2}}. \tag{6.17}$$

For convenience, we also define $N_{\rm p}$ as the floor of $\Omega_{\rm p}/\Omega$, i.e.

$$N_{\rm p} \equiv \lfloor \Omega_{\rm p}/\Omega \rfloor, \tag{6.18}$$

We find that the peak of the F_{N2} occurs at $N \sim N_\mathrm{p}$, the only characteristic scale in N over which F_{N2} can vary. When $N \gg N_\mathrm{p}$, the Fourier coefficients must fall off exponentially by the Paley-Wiener theorem, as the left hand side of Eq. (6.7) is smooth [e.g. Stein and Shakarchi, 2009]. When instead $N \ll N_\mathrm{p}$, there are no characteristic frequencies between Ω and Ω_p, so we expect the Hansen coefficients to be scale-free between $N = 1$ and N_p, i.e. a power law in N. The expected behaviors in both of these regimes are in agreement with Fig. 6.1.

Motivated by these considerations, we approximate the Hansen coefficients by

$$F_{N2} \approx \begin{cases} C_2 N^p e^{-N/\eta_2} & N \geq 0, \\ 0 & N < 0, \end{cases} \tag{6.19}$$

for some fitting coefficients C_2, p, and η_2. By performing fits to F_{N2} for varying eccentricities, we find that $p \approx 2$ for modest-to-large eccentricities, and we take $p = 2$ to be fixed for the remainder of this work. For $e = 0.9$, Fig. 6.1 shows that $p = 2$ accurately captures the power-law behavior of the F_{N2} for $N \lesssim N_\mathrm{max}$, where N_max is the value of N for which F_{N2} is maximized. While F_{N2} deviates appreciably from this power law for $N \ll N_\mathrm{max}$, these terms are small in magnitude and are sub-dominant in any sum over the F_{N2}. Thus, our approximation for F_{N2} is sufficiently accurate when evaluating expressions that involve sums over the F_{N2}, such as in Eqs. (6.15–6.16)[1].

To constrain the remaining two free parameters η_2 and C_2, we use the well

[1]There is good reason to expect $p = 2$ for $N \lesssim N_\mathrm{p}$ as long as the eccentricity is sufficiently large. In this regime, we first note that the left-hand side of Eq. (6.7) resembles the second derivative of a Gaussian with width $\sim \Omega_\mathrm{p}^{-1}$, as it is both sharply peaked about $t = 0$ and has zero derivative three times every period (at $t = \epsilon$, $t = P/2$, and $t = P - \epsilon$ for some small $\epsilon \sim \Omega_\mathrm{p}^{-1}$). Secondly, we note that a Gaussian resembles a Dirac delta function over timescales longer than its width (here, $\sim \Omega_\mathrm{p}^{-1}$). Since the Dirac delta function has a flat Fourier spectrum ($\propto N^0$), and time differentiation multiplies by N in frequency space, the second derivative of a Gaussian has a Fourier spectrum $\propto N^2$ for $N \lesssim N_\mathrm{p}$. As F_{N2} is the Nth Fourier coefficient for the left-hand side of Eq. (6.7), we do indeed expect $F_{N2} \propto N^2$ for $N \lesssim N_\mathrm{p}$.

known Hansen coefficient moments [e.g. Eqs. 22, 23 of Storch and Lai, 2013]

$$\sum_{N=-\infty}^{\infty} F_{N2}^2 = \frac{f_5}{\left(1-e^2\right)^{9/2}}, \tag{6.20}$$

$$f_5 \equiv 1 + 3e^2 + \frac{3e^4}{8}, \tag{6.21}$$

$$\sum_{N=-\infty}^{\infty} F_{N2}^2 N = \frac{2f_2}{\left(1-e^2\right)^{6}}, \tag{6.22}$$

$$f_2 \equiv 1 + \frac{15e^2}{2} + \frac{45e^4}{8} + \frac{5e^6}{16}. \tag{6.23}$$

Applying Eq. (6.19) to Eqs. (6.20, 6.22), we obtain the coefficients η_2 and C_2

$$\eta_2 = \frac{4f_2}{5f_5\left(1-e^2\right)^{3/2}} \sim \frac{1}{2(1-e)^{3/2}}, \tag{6.24}$$

$$C_2 = \left[\frac{4f_5}{3\left(1-e^2\right)^{9/2}\eta_2^5}\right]^{1/2}. \tag{6.25}$$

Figure 6.1 illustrates the agreement of Eq. (6.19) using these two values of η_2 and C_2 with the numerical F_{N2}. The good agreement for $N \gtrsim N_\mathrm{p}/10$ (which is where F_{N2} is large) is especially impressive as there are no fitting parameters in Eq. (6.19), as C_2, η_2, and p are all analytically constrained. Finally, note that the maximum of the F_{N2} occurs at $N = \lfloor 2\eta_2 \rfloor \sim (1-e)^{-3/2} \sim N_\mathrm{p}$.

$m = 0$ Hansen Coefficients

We now turn to the $m = 0$ Hansen coefficients, F_{N0}, which are shown in Fig. 6.2. We know that $F_{N0} = F_{(-N)0}$, so we consider only $N \geq 0$. From the figure, we see that the F_{N0} decay exponentially. There is only one characteristic scale available for this decay, namely N_p. Therefore, we naturally assume the F_{N0} coefficients can be approximated by a function of form:

$$F_{N0} = C_0 e^{-|N|/\eta_0}. \tag{6.26}$$

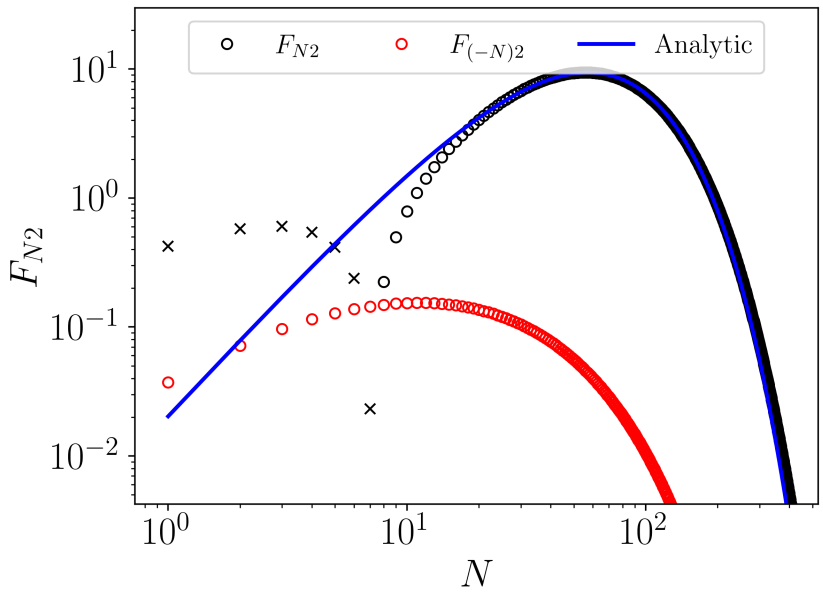

Figure 6.1: Plot of Hansen coefficients F_{N2} for $e = 0.9$. The red circles denote negative N, while the black circles and crosses denote positive and negative F_{N2}. The blue line is the formula given by Eq. (6.19) with $p = 2$ and with η_2 and C_2 given by Eqs. (6.24–6.25).

The two free parameters C_0 and η_0 are constrained by the identities

$$\sum_{N=-\infty}^{\infty} F_{N0}^2 = \frac{f_5}{\left(1-e^2\right)^{9/2}}, \tag{6.27}$$

$$\sum_{N=-\infty}^{\infty} F_{N0}^2 N^2 = \frac{9e^2}{2\left(1-e^2\right)^{15/2}} f_3, \tag{6.28}$$

$$f_3 = \frac{1}{2} + \frac{15e^2}{8} + \frac{15e^4}{16} + \frac{5e^6}{128}. \tag{6.29}$$

Applying Eq. (6.26) to Eqs. (6.27–6.28), we obtain

$$\eta_0 = \left[\frac{9e^2 f_3}{\left(1-e^2\right)^3 f_5}\right]^{1/2}, \tag{6.30}$$

$$C_0 = \left[\frac{f_5}{\left(1-e^2\right)^{9/2} \eta_0}\right]^{1/2}. \tag{6.31}$$

Figure 6.2 illustrates the agreement of Eq. (6.26) using these two values of η_0 and $C_0$with the numerically computed F_{N0}.

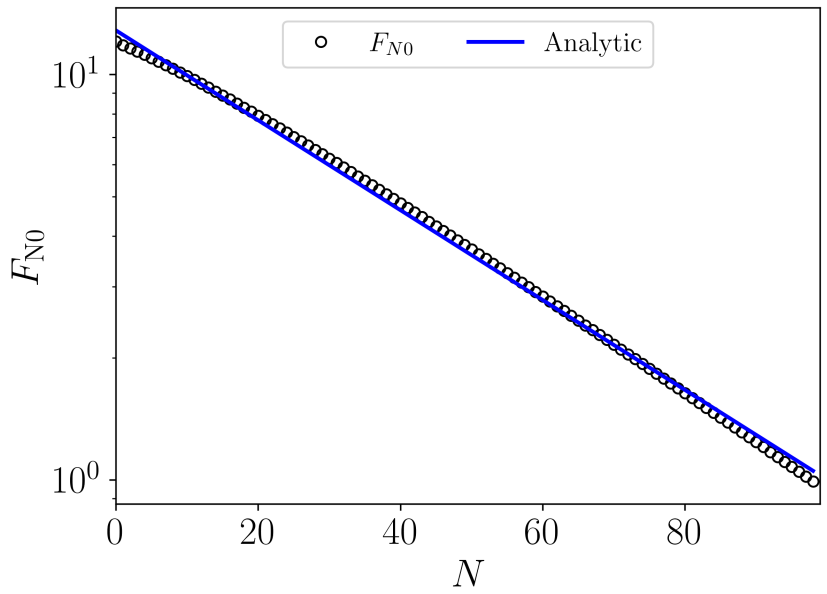

Figure 6.2: Plot of F_{N0} (black circles) for $e = 0.9$. Since $F_{N0} = F_{(-N)0}$, we only show positive N. The blue line is given by Eq. (6.26) with η_0 and C_0 given by Eqs. (6.30–6.31).

6.3.2 Approximate Expressions for Torque and Energy Transfer

Having found good approximations for the Hansen coefficients, we now apply them to simplify the expressions for the torque and the energy transfer rate in Eqs. (6.15–6.16).

Tidal Torque

To simplify Eq. (6.15), we replace F_{N2} with Eq. (6.19) and the sum with an integral, obtaining

$$T \approx T_0 \int_0^\infty C_2^2 N^4 e^{-2N/\eta_2} \operatorname{sgn}(N - 2\Omega_s/\Omega) |N - 2\Omega_s/\Omega|^{8/3} \, \mathrm{d}N. \tag{6.32}$$

This expression is already easier to evaluate than Eq. (6.15), but we can use further approximations to obtain a closed form. We first analyze Eq. (6.32) in the small-spin limit, where it can be integrated analytically[2], giving

$$T\left(|\Omega_{\rm s}| \ll \Omega_{\rm p}\right) \simeq T_0 \frac{f_5(e)(\eta_2/2)^{8/3}}{(1-e^2)^{9/2}} \frac{\Gamma(23/3)}{4!}. \tag{6.33}$$

Note that this has the scaling $T \sim T_0 (1-e)^{-17/2} \sim T_{\rm p}\Omega/\Omega_{\rm p}$, where $T_{\rm p}$ is the torque exerted by a circular orbit with separation equal to the pericentre separation $a_{\rm p} \equiv a(1-e)$, i.e.

$$T_{\rm p} = \beta_2 \frac{G M_2^2 r_{\rm c}^5}{a_{\rm p}^6} \left(\frac{\Omega_{\rm p}}{\sqrt{G M_{\rm c}/r_{\rm c}^3}}\right)^{8/3} \frac{\rho_{\rm c}}{\bar{\rho}_{\rm c}} \left(1 - \frac{\rho_{\rm c}}{\bar{\rho}_{\rm c}}\right)^2 \sim T_0 (1-e)^{-10}. \tag{6.34}$$

The top panel of Fig. 6.3 compares Eq. 6.33 to the integral of Eq. (6.32) and to the direct sum of Eq. (6.15) as a function of the eccentricity. It can be see that both the integral and the analytic closed form perform well for moderate-to-large eccentricities, but both over-predict the torque at small $e \lesssim 0.2$ (at $e = 0.2$, the torque is over-predicted by $\sim 20\%$). This discrepancy is expected: there are only a few non-negligible summands in Eq. (6.15) when e is small, so replacing the sum over N with an integral is expected to introduce significant inaccuracy that appears in both the integral and closed-form expressions.

Eq. (6.33) is valid so long as $|\Omega_{\rm s}/\Omega| \ll N_{\rm max}$ (or equivalently, $\left|\Omega_{\rm s} \ll \Omega_{\rm p}\right|$), where $N_{\rm max} = 10\eta_2/3$ is where the integrand is in Eq. (6.32) maximized. If instead $|\Omega_{\rm s}/\Omega| \gg N_{\rm max}$, the torque can be evaluated directly using Eq. (6.15) and the known Hansen coefficient moments, giving:

$$T\left(|\Omega_{\rm s}| \gg \Omega_{\rm p}\right) \simeq -T_0 \,\mathrm{sgn}(\Omega_{\rm s})\, |2\Omega_{\rm s}/\Omega|^{8/3} \frac{f_5(e)}{(1-e^2)^{9/2}}. \tag{6.35}$$

The bottom panel of Fig. 6.3 compares this formula to the integral of Eq. (6.32) and to the direct sum of Eq. (6.15) as a function of the eccentricity, where $\Omega_{\rm s}/\Omega = 400$.

[2]The key to the success of our approach is that sums of form $\sum_{n=-\infty}^{\infty} F_{N2}^2 N^p$ can be approximated for non-integer p in terms of the Γ function, since $\int_0^\infty x^p e^{-x}\,\mathrm{d}x = \Gamma(p-1)$.

Here, $N_{\max} \ll 400$ for all eccentricities shown. We see that direct summation, the integral expression, and Eq. (6.35) agree very well for all eccentricities.

Having obtained closed-form expressions of Eq. (6.32) for small and large spins, we can further derive a single expression joining these two limits. To do this, we first assume that the spin is small but non-negligible. In this regime, we make the approximation

$$N - 2\Omega_{\rm s}/\Omega \simeq \frac{N}{N_{\max}}\left(N_{\max} - \frac{2\gamma_T \Omega_{\rm s}}{\Omega}\right), \tag{6.36}$$

for some free parameter γ_T. With this, we can integrate Eq. (6.32) in closed form. We can fix γ_T by requiring our expression reproduce the large spin limit (Eq. 6.35) when taking $|\Omega_{\rm s}| \to \infty$. This procedure gives an expression for the torque that agrees with both limiting forms (Eq. 6.33–6.35) and is given by

$$T \simeq T_0 \frac{f_5(e)(\eta_2/2)^{8/3}}{(1-e^2)^{9/2}} \operatorname{sgn}\left(1 - \gamma_T \frac{\Omega_{\rm s}}{\eta_2 \Omega}\right) \left|\frac{4}{\gamma_T}\left(1 - \gamma_T \frac{\Omega_{\rm s}}{\eta_2 \Omega}\right)\right|^{8/3}, \tag{6.37}$$

where

$$\gamma_T = 4\left(\frac{4!}{\Gamma(23/3)}\right)^{3/8} \approx 0.691. \tag{6.38}$$

Figure 6.4 compares this expression to the integral of Eq. (6.32) and to the direct sum of Eq. (6.15) at fixed $e = 0.9$ and varying $\Omega_{\rm s}$. We see that Eq. (6.37) agrees well with the integral and sum for both large and small spins, and is also reasonably accurate for intermediate spins. However, Eq. (6.32) is more accurate than Eq. (6.37) when T changes signs and $|T|$ is small. This is also expected: T changes signs when the spin approaches *pseudosynchronization* (Section 6.3.2) because large contributions to the sum in Eq. (6.15) have opposite signs and mostly cancel out. Thus, small inaccuracies in the summand result in significant discrepancies in the total torque. The integral approximation, Eq. (6.32), is expected to be in good agreement with the direct sum, Eq. (6.15), as the accuracy of the Hansen coefficient approximation in Section 6.3.1 is good for large eccentricities, thus guaranteeing term-by-term accuracy. On the other hand, the closed-form expression,

Eq. (6.37), is more approximate when $\Omega_s/\Omega \sim N_{\max} \sim \eta_2$. In fact, Eq. (6.37) predicts $dT/d\Omega_s \approx 0$ near pseudosynchronization. This is not accurate and is an artifact of our factorization ansatz in Eq. (6.36).

In summary, the tidal torque must be evaluated with explicit summation (Eq. 6.15) when $e \lesssim 0.2$ (see discussion after Eq. 6.33), can be approximated by the integral expression (Eq. 6.32) when e is large for all values of Ω_s, and otherwise can be approximated by the closed-form expression given by Eq. (6.37). Recall that when e is small, the explicit summation of Eq. (6.15) is quite simple, as good accuracy can be obtained with just the first few terms in the summation (e.g. for $e = 0.2$, including just the three terms $N \in [2,4]$ results in 98% accuracy).

Pseudosynchronization

In general, the exact torque as given by Eq. (6.15) vanishes for a single Ω_s, which we call the *pseudo-synchronized* spin frequency. An approximation for the pseudo-synchronized spin can be directly read off from Eq. (6.37):

$$\frac{\Omega_{\rm ps}}{\Omega} = \frac{\eta_2}{\gamma_T} = \frac{4 f_2(e)}{5\gamma_T f_5(e)\left(1-e^2\right)^{3/2}}. \tag{6.39}$$

This has the expected scaling $\Omega_{\rm ps} \sim \Omega_{\rm p}$ (the pericentre orbital frequency). Figure 6.5 compares this prediction for the pseudo-synchronized spin to the exact one obtained by applying a root finding algorithm to Eq. (6.15). We see that Eq. (6.39) is a reasonable approximation for the pseudo-synchronized spin frequency when $e \gtrsim 0.1$.

In passing, we note that, in the standard weak friction theory of equilibrium tides, the pseudo-synchronized spin is given by [Alexander, 1973, Hut, 1981]

$$\frac{\Omega_{\rm ps}^{\rm (Eq)}}{\Omega} = \frac{f_2(e)}{f_5(e)\left(1-e^2\right)^{3/2}}. \tag{6.40}$$

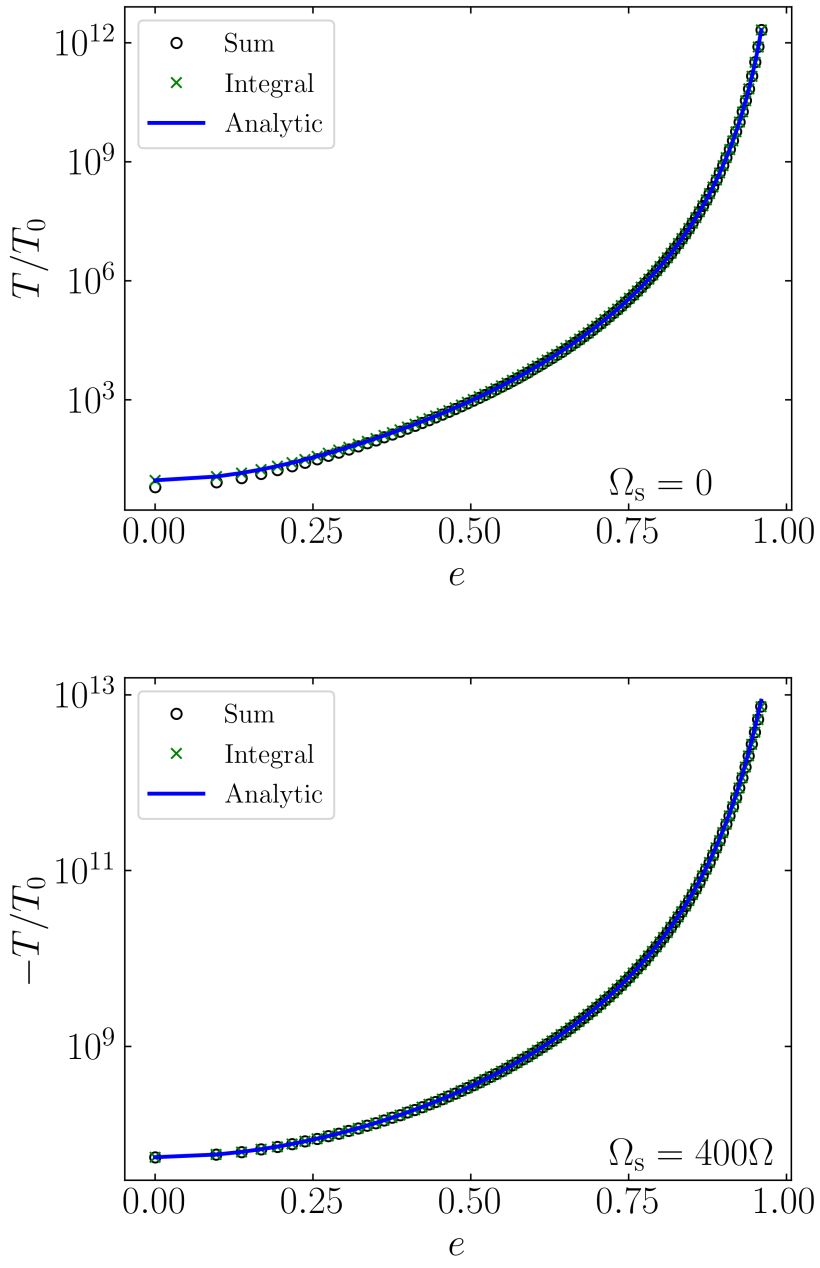

Figure 6.3: The tidal torque on a non-rotating (top) and rapidly rotating (bottom) star due to a companion with orbital eccentricity e. Black circles represent direct summation of Eq. (6.15), green crosses are evaluated using the integral approximation Eq. (6.32), and the blue line is Eq. (6.37). In the small and large spin limits, Eq. (6.37) reduces to Eq. (6.33) and Eq. (6.35) respectively.

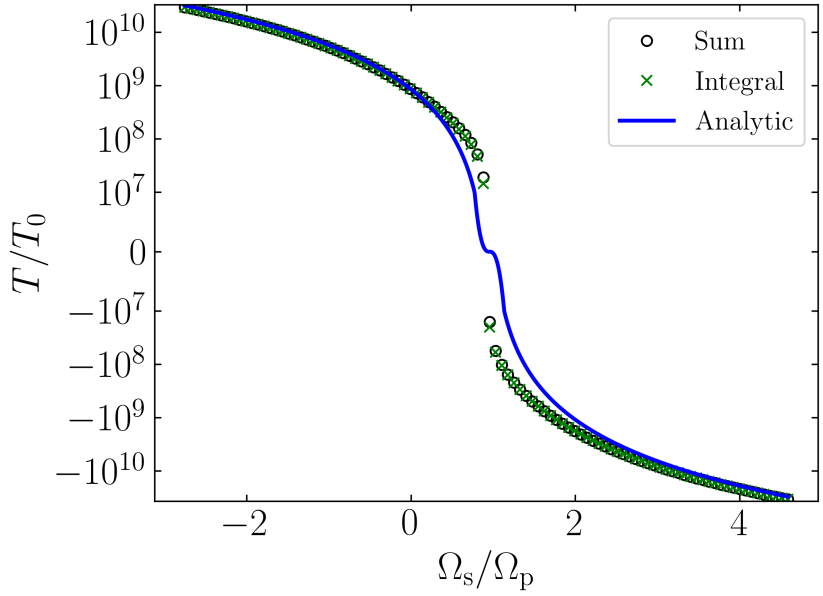

Figure 6.4: The tidal torque as a function of the stellar spin for a highly eccentric $e = 0.9$ companion. The black circles represent direct summation of Eq. (6.15), green crosses the integral approximation (Eq. 6.32), and the solid line the analytic closed-form expression Eq. (6.37). The spin is normalized by the pericentre orbital frequency $\Omega_p \approx 43\Omega$ (Eq. 6.17).

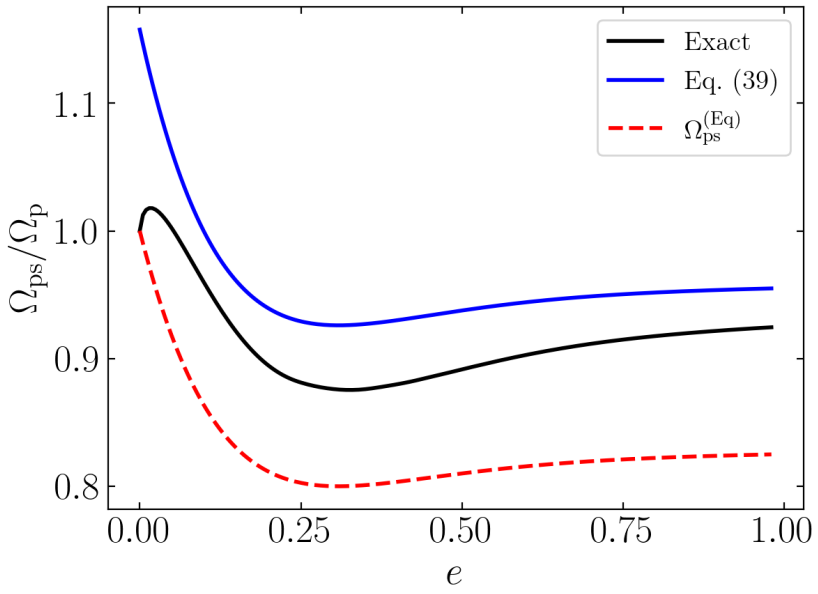

Figure 6.5: The spin frequencies $\Omega_{\rm ps}$ normalized by the pericentre frequency $\Omega_{\rm p}$ (Eq. 6.17) as a function of eccentricity. The blue line is given by Eq. (6.39). The black line shows the exact solution, obtained by using a root finding algorithm to solve for the zero of Eq. (6.9). The red dashed line shows the spin frequency predicted by the weak friction theory of equilibrium tides (Eq. 6.40).

Though describing a different tidal phenomenon, this only differs from Eq. (6.39) by a factor of $4/(5\gamma_T) \approx 1.15$. We show it for comparison as the red dotted line in Fig. 6.5.

Energy Transfer

We now turn our attention to Eq. (6.10) and replace F_{N2} and F_{N0} with their respective approximations (Eqs. 6.19 and 6.26) to obtain the energy transfer rate

$$\dot{E}_{\rm in} = \frac{T_0\Omega}{2}\int_0^\infty \Big[C_2^2 N^5 e^{-2N/\eta_2}\,\mathrm{sgn}\,(N-2\Omega_{\rm s}/\Omega)\,|N-2\Omega_{\rm s}/\Omega|^{8/3} + 2\left(\frac{W_{20}}{W_{22}}\right)^2 C_0^2 e^{-2N/\eta_0} N^{11/3}\Big]\,\mathrm{d}N. \tag{6.41}$$

We evaluate the $m=2$ and $m=0$ contributions to this expression separately.

We first examine the $m=2$ contribution using the same procedure in Section 6.3.2 for the torque. If the spin is moderate, i.e. $|\Omega_{\rm s}/\Omega| \lesssim N_{\rm max}$ where now $N_{\rm max} = 23\eta_2/6$, we make the approximation

$$N - 2\Omega_{\rm s}/\Omega \simeq \frac{N}{N_{\rm max}}\left(N_{\rm max} - \frac{2\gamma_E\Omega_{\rm s}}{\Omega}\right), \tag{6.42}$$

where γ_E is a free parameter. This lets us integrate the $m=2$ contribution to Eq. (6.41) analytically. We constrain γ_E by requiring agreement with the large-spin limit: for $|\Omega_{\rm s}/\Omega| \gg N_{\rm max}$, we have

$$\dot{E}_{\rm in}^{(m=2)}\left(|\Omega_{\rm s}| \gg \Omega_{\rm p}\right) \simeq -\frac{T_0\Omega}{2}\,\mathrm{sgn}(\Omega_{\rm s})|2\Omega_{\rm s}/\Omega|^{8/3}\frac{2f_2(e)}{(1-e^2)^6}. \tag{6.43}$$

This fixes γ_E and we obtain the complete $m=2$ contribution to Eq. (6.41):

$$\dot{E}_{\rm in}^{(m=2)} \simeq \frac{T_0\Omega f_5(e)(\eta_2/2)^{11/3}}{2(1-e^2)^{9/2}} \times \mathrm{sgn}\left(1-\gamma_E\frac{\Omega_{\rm s}}{\eta_2\Omega}\right)\left|\frac{4}{\gamma_E}\left(1-\gamma_E\frac{\Omega_{\rm s}}{\eta_2\Omega}\right)\right|^{8/3}, \tag{6.44}$$

where

$$\gamma_E = 4\left(\frac{5!}{\Gamma(26/3)}\right)^{3/8} \approx 0.5886. \tag{6.45}$$

Note that, when $\Omega_s \approx 0$, Eq. (6.44) gives the expected scaling of $\dot{E}_{\rm in}^{(m=2)} \sim T_p \Omega$ where T_p is the torque exerted by a circular companion at the pericentre separation, given by Eq. (6.34).

The $m = 0$ contribution to Eq. (6.41) can be straightforwardly integrated using the parameterization Eq. (6.26). The sum of the two contributions then gives the total energy transfer rate:

$$\begin{aligned}\dot{E}_{\rm in} = \frac{T_0 \Omega}{2}\Bigg[& \frac{f_5(e)(\eta_2/2)^{11/3}}{(1-e^2)^{9/2}} \\ & \times \mathrm{sgn}\left(1-\gamma_E \frac{\Omega_s}{\eta_2 \Omega}\right)\left|\frac{4}{\gamma_E}\left(1-\gamma_E \frac{\Omega_s}{\eta_2 \Omega}\right)\right|^{8/3} \\ & + \frac{f_5(e)\Gamma(14/3)}{(1-e^2)^{10}}\left(\frac{3}{2}\right)^{8/3}\left(\frac{e^2 f_3(e)}{f_5(e)}\right)^{11/6}\Bigg].\end{aligned} \tag{6.46}$$

The two panels of Fig. 6.6 compare this expression with the integral form Eq. (6.41) and the direct sum Eq. (6.16) for small and large spins. The agreements are excellent except that, when the spin and eccentricity are small, both the integral and closed form expressions over-predict the energy transfer rate. Figure 6.7 compares these three expressions as a function of spin for $e = 0.9$. The performance of Eq. (6.46) degrades when the system is near pseudosynchronization ($\Omega_s \simeq \Omega_p$), but generally captures the correct behavior of the exact result, while Eq. (6.41) is accurate for all spins. As was the case with the tidal torque, we see that the evaluation of the energy transfer rate when $e \lesssim 0.2$ requires direct summation (Eq. 6.16), and the evaluation when e is substantial but the spin is near pseudosynchronization can be performed using the integral approximation (Eq. 6.41), and otherwise the evaluation can be performed using the closed-form expression (Eq. 6.46).

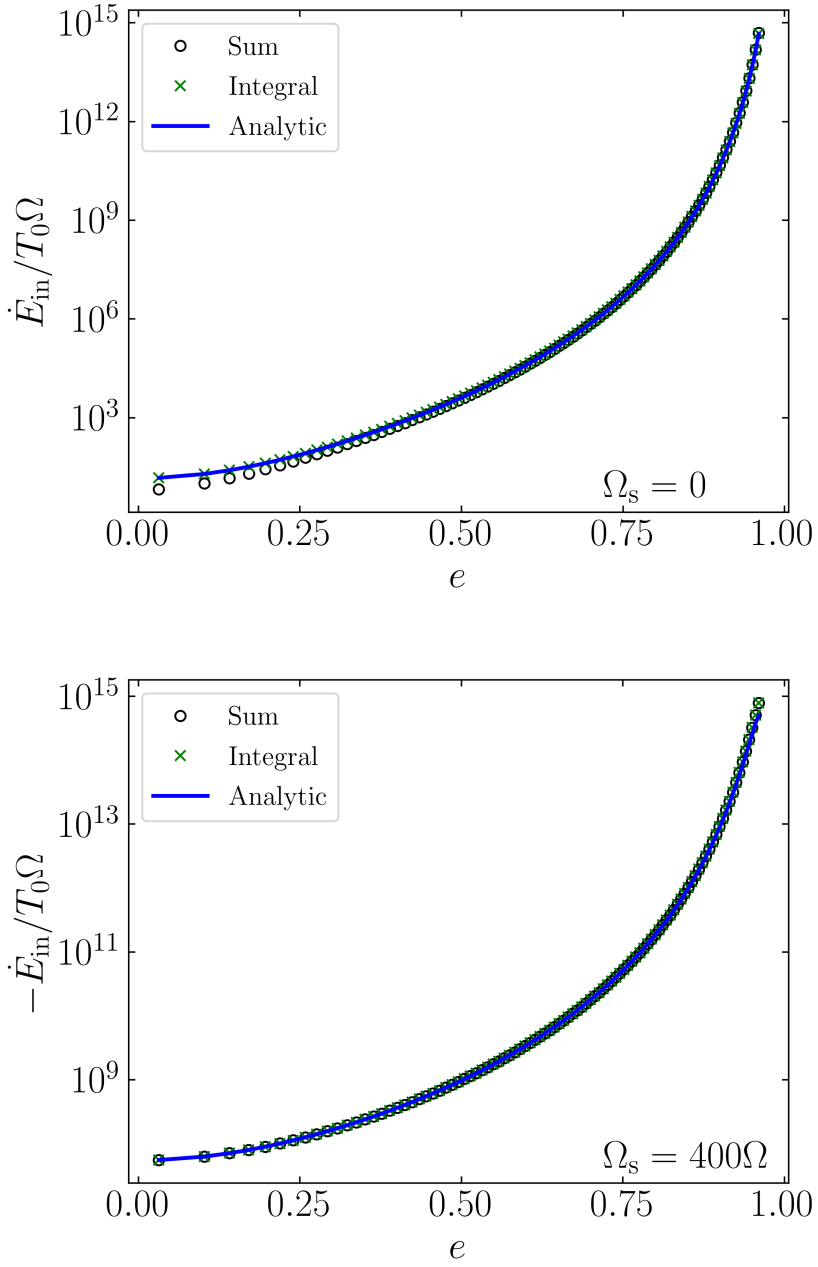

Figure 6.6: The tidal energy transfer rate $\dot{E}_{\rm in}$ for a non-rotating (top) and a rapidly rotating (bottom) star. The black circles represent direct summation of Eq. (6.16), green crosses the integral form Eq. (6.41), and the blue line the closed-form expression Eq. (6.46).

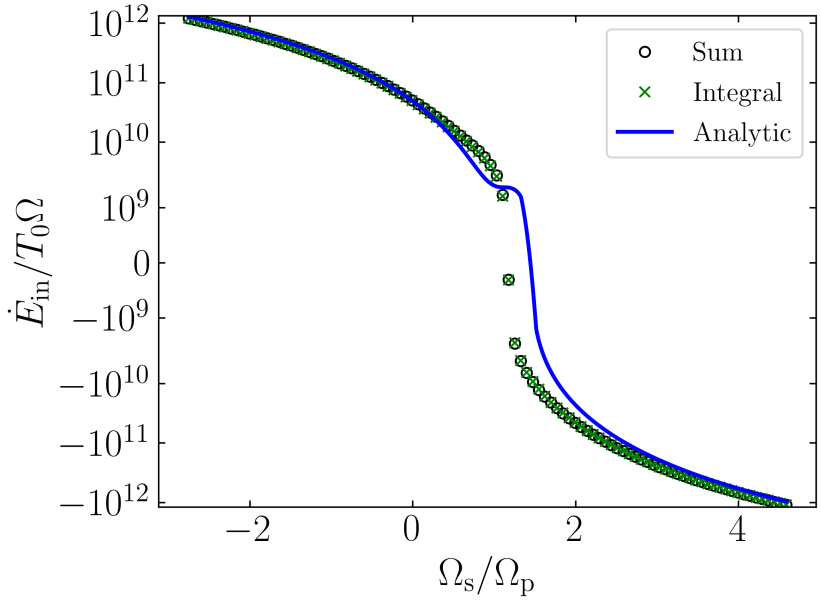

Figure 6.7: The tidal energy transfer rate $\dot{E}_{\rm in}$ as a function of spin [normalized by $\Omega_{\rm p}$; Eq. (6.17)] for a highly eccentric $e = 0.9$ companion. The black circles represent direct summation of Eq. (6.10), green crosses the integral approximation Eq. (6.41), and the blue line the analytic closed form Eq. (6.46).

6.4 PSR J0045-7319/B-Star Binary

As an application of our analytical results above, we consider the PSR J0045-7319/MS binary system [Kaspi et al., 1994] and attempt to explain its orbital decay via dynamical tides. This system is one of the few pulsar binaries discovered so far that have massive MS companions [the other known binaries are, PSR B1259-63, PSR J1740-3052, PSR J1638-4725, J2032+4127; Johnston et al., 1992, Stairs et al., 2001, Lorimer et al., 2006, Lyne et al., 2015]. These systems evolve from MS-MS binaries when one of the stars explodes in a supernova to form a neutron star (NS), and will eventually become double NS systems when the MS companion also explodes to form a NS. Thus, characterizing the evolution of such systems is important for understanding the formation of double NS binaries [e.g. Tauris et al., 2017]. The PSR J0045-7319 system contains a radio pulsar ($M_2 \simeq 1.4 M_\odot$)

and a massive B star ($M \simeq 8.8 M_\odot$) companion in an eccentric ($e = 0.808$) orbit with period $P = 51.17$ days, corresponding to a semi-major axis $a = 126 R_\odot$. Timing observation shows that the orbit is decaying at the rate $\dot{P} = -3.03 \times 10^{-7}$, or $P/\dot{P} \simeq -0.5$ Myr [Kaspi et al., 1996]. The measured B-star luminosity $L = 1.2 \times 10^4 L_\odot$ and surface temperature $T_{\rm surf} = (24000 \pm 1000)$ K imply a radius of $R = 6.4 R_\odot$ [Bell et al., 1995]. The B star has a projected surface rotation velocity $v \sin i = 113 \pm 10$ km/s [Bell et al., 1995], consistent with rapid rotation (the breakup velocity is $\sqrt{GM/R} = 512$ km/s). While there are uncertainties in some of these parameters (e.g., the pulsar and companion masses could be larger by about 10%; see Thorsett and Chakrabarty, 1999), we adopt the above values in our calculation below for better comparison with previous works.

Lai [1996] and Lai [1997] explained the observed orbital decay of the PSR J0045-7319 binary in terms of tidal excitations of discrete (rotation-modified) g-modes followed by radiative damping. He showed that retrograde rotation of the B-star [consistent with the observed nodal precession of the binary orbit; see Lai et al., 1995, Kaspi et al., 1996] can significantly enhance the strength of mode excitation, and potentially account for the observed orbital decay, although he did not compute the mode damping rate quantitatively. Kumar and Quataert [1997, 1998] examined the damping of g-modes and showed that radiative damping in rigidly rotating B-star is inadequate to explain the observed orbital decay rate, suggesting that in addition to retrograde rotation, significant differential rotation or nonlinear parametric mode decay may be required. Given the uncertainties in their estimates, it was not clear to what extent the observed orbital decay rate can be quantitatively explained. Moreover, both Lai et al. [1995] and Kumar and Quataert [1997, 1998] considered discrete g-modes, whereas absorption of tidally excited gravity waves near the stellar envelope, via either efficient radiative damping or nonlinear breaking [see Su et al., 2020], implies outgoing waves

(as adopted in the works of Zahn, 1975, Goldreich and Nicholson, 1989, Kushnir et al., 2017) rather than discrete g-modes.

We now consider the evolution of stellar spin and binary orbit for the PSR J0045-7319 system. For the adopted system parameters above, the pericentre distance is $a_{\rm p} \simeq 3.78R$, and pericentre frequency is $\Omega_{\rm p} = \sqrt{(1+e)GM_{\rm tot}/a_{\rm p}^3} \simeq 0.20\sqrt{GM/R^3}$. First we note that the tidal torque T and the energy transfer rate $\dot{E}_{\rm in}$ (dominated by the $m = 2$ term) are related by

$$\dot{E}_{\rm in} \simeq T\Omega_{\rm p} \frac{f_2}{5(1+e)^2 f_5}, \tag{6.47}$$

with $f_2 = 8.38$, $f_5 = 3.12$. Thus the spin evolution rate (for spin-orbit synchronization and alignment) is given by

$$\left|\frac{\dot{\mathbf{S}}}{S}\right| \simeq \frac{L}{S}\frac{5(1-e^2)f_5}{2f_2}\left|\frac{\dot{E}_{\rm in}}{E_{\rm orb}}\right|, \tag{6.48}$$

where $S = kMR^2\bar{\Omega}_{\rm s}$ is the spin angular momentum of the star (with $\bar{\Omega}_{\rm s}$ the mean rotation rate, and $k \simeq 0.1$), L is the orbital angular momentum, and $E_{\rm orb}$ is the orbital energy. Thus

$$\left|\frac{\dot{\mathbf{S}}}{S}\right| \simeq 6.3\,\frac{\Omega_{\rm p}}{\bar{\Omega}_{\rm s}}\left|\frac{\dot{a}}{a}\right|. \tag{6.49}$$

The observed nodal precession of the PSR J0045-7319 binary implies that the spin of the B-star is far from spin-orbit alignment and synchronization driven by tides [Lai et al., 1995]. Thus we require $\bar{\Omega}_{\rm s} \gtrsim 6.3\Omega_{\rm p} \sim \sqrt{GM/R^3}$, suggesting that the internal rotation rate of the star is much larger that the surface rate.

Using Eq. (6.46) with $e = 0.808$ (and keeping only the $m = 2$ term), we find that the orbital decay rate is given by

$$\left|\frac{\dot{a}}{a}\right| \simeq 1.6\times 10^5\,\Omega\,\frac{M_2}{M}\left(\frac{M_{\rm tot}}{M_{\rm c}}\right)^{4/3} \times \left(\frac{r_{\rm c}}{a}\right)^9 \frac{\rho_{\rm c}}{\bar{\rho}_{\rm c}}\left(1-\frac{\rho_{\rm c}}{\bar{\rho}_{\rm c}}\right)^2 \left|\frac{4}{\gamma_E}\left(1-\frac{\gamma_E\Omega_{\rm s}}{\eta_2\Omega}\right)\right|^{8/3}. \tag{6.50}$$

With $\eta_2 = 10.55$, $a \simeq 19.7R$, and adopting $\rho_c/\bar{\rho}_c \simeq 1/3$, we find the orbital decay rate

$$\left|\frac{\dot{P}}{P}\right| \simeq \frac{1}{0.5\,\mathrm{Myr}} \left(\frac{3M_\odot}{M_c}\right)^{4/3} \left(\frac{r_c}{0.54R}\right)^9 \left|1 - \frac{0.89\Omega_s}{\Omega_p}\right|^{8/3}. \tag{6.51}$$

Note Ω_s in the above expression refers to the rotation rate at the radiative-convective boundary (RCB) r_c, and we expect $\Omega_s \gtrsim \bar{\Omega}_s \gtrsim 6\Omega_p$.

To explain the observed orbital decay timescale $|P/\dot{P}| \simeq 0.5$ Myr, the most critical parameter is the core radius r_c. Kumar & Quataert (1998) adopted $M_c \simeq 3M_\odot$ and $r_c \simeq 1.38R_\odot$ (or $r_c \simeq 0.22R$) based on comparison with a Yale stellar evolution model. This value of r_c would require $\Omega_s/\Omega_p \simeq -24$, or $\Omega_s \simeq -4.8\sqrt{GM/R^3}$, to explain the observed decay rate. If we use a slightly larger core radius, $r_c = 1.5R_\odot \simeq 0.234R$, the required Ω_s would be $\Omega_s \simeq -18\Omega_p \simeq -3.6\sqrt{GM/R^3}$. In either case, extreme differential rotation (with $|\Omega_s|$ at the RCB at least a factor of few larger than the surface rotation) is required. In Fig. 6.8 we show $\dot{P}/P$ as a function of Ω_s, obtained using the exact expression Eq. (6.46) for four different values of r_c. In general, given that the surface rotation rate of the star is less than $\sqrt{GM/R^3}$, our calculation suggests that the B-star must have large, retrograde differential rotation in order to explain the observed orbital decay.

We note that our own exploration of stellar models using the Modules for Experiments in Stellar Astrophysics [MESA; Paxton et al., 2011, 2013, 2015, 2018, 2019] generally finds a small core radius ($r_c \lesssim R_\odot$) for the B-star in the PSR J0045-7319 system. Since the system is in the Small Magellanic Cloud, we use a typical metallicity $Z = 0.1Z_\odot$, where $Z_\odot$ is the solar metallicity. For a range of initial stellar masses, we begin with a non-rotating zero-age main sequence (ZAMS) stellar model, and evolve it until its core hydrogen is depleted. Among these evolutionary tracks, we select the model and stellar age that best matches the observed L and T_{surf} and record the core radius at that age. We then repeat this procedure with different values for the convective overshoot parameter, initial rotation rate (up to

nearly maximally rotating), and metallicity (up to $Z = 0.2Z_{\odot}$). For all parameter combinations, the predicted stellar masses lie in the range $8.8M_{\odot} \leq M \leq 10M_{\odot}$, in agreement with the estimates in the literature. However, the core radius for all stellar models is $r_c \lesssim R_{\odot} \approx 0.16R$. This reflects the fact that our best-fitting stellar models tend to be somewhat evolved from the ZAMS. For further details, see AppendiX E.1.

We caution that applying standard isolated stellar evolution to the B-star in the PSR J0045-7319 system can be fraught with uncertainties. The very rapid rotation may induce instabilities and allow the star to transport material from the hydrogen-rich envelope into the central burning region and vice versa, potentially making the convective core larger [e.g. Maeder, 1987, Heger and Langer, 2000]. This effect may be enhanced by the large misaligned, differential rotation. Related to the rotational effect is the mass transfer effect: The observed rapid orbital decay rate and general orbital evolution modeling sets an upper limit of about 1.4 Myr on the age of the binary system since the last supernova explosion [Lai, 1996], much shorter than the canonical MS lifetime. Thus the B-star must have accreted significant material from the pulsar progenitor in the recent past. Such accretion can affect the structure and evolution of the B-star in a significant way. Given these uncertainties, we think it is likely that the B-star has a larger core radius than the canonical value, rendering a less extreme differential rotation[3].

[3]We note that a recent study of intermediate and high-mass eclipsing binaries suggests that convective core masses are underpredicted by stellar structure codes [Tkachenko et al., 2020a].

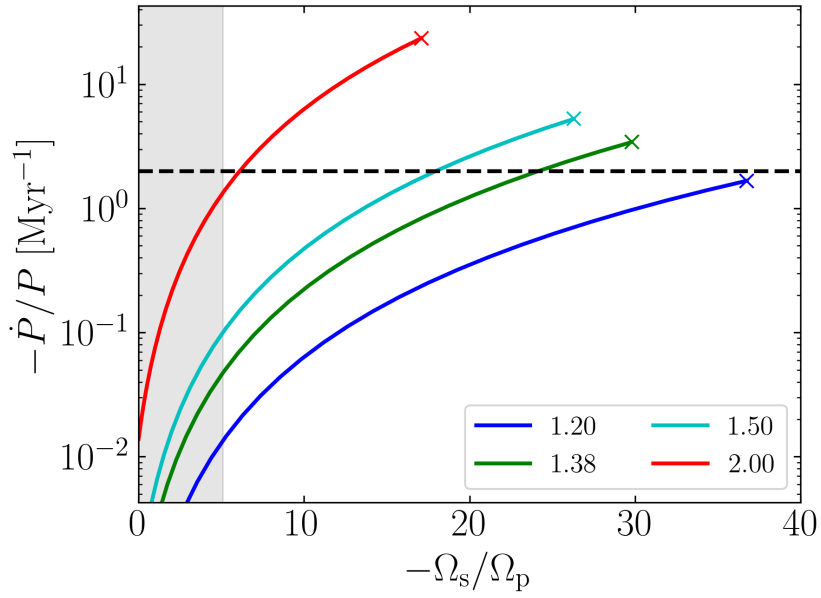

Figure 6.8: The orbital decay ratio $\dot{P}/P$ as a function of Ω_s for the canonical parameters of the PSR J0045-7319 binary system, as evaluated by Eq. (6.46), for four different values of r_c (legend, in units of $R_\odot$). The measured $\dot{P}/P = -(0.5\,\mathrm{Myr})^{-1}$ is shown by the horizontal dashed line. The vertical shaded region is the region where $|\Omega_s|$ is less than the breakup rotation rate of the star as a whole, given by $(GM/R^3)^{1/2}$. Each r_c is only shown for $|\Omega_s| \leq \Omega_{s,c} \equiv (GM_c/r_c^3)^{1/2}$, the *core* breakup rotation rate, and the colored crosses denote where $\Omega_s = \Omega_{s,c}$ for each value of r_c. Note that for $r_c \lesssim 1.3R_\odot$, even a maximally rotating core cannot generate enough tidal torque to match the observed $\dot{P}/P$.

6.5 Summary and Discussion

6.5.1 Key Results

The main goal of this paper is to derive easy-to-use, analytical expressions for the tidal torque T and tidal energy transfer rate $\dot{E}_{\rm in}$ due to internal gravity wave (IGW) dissipation in a massive, main-sequence (MS) star under the gravitational influence of an eccentric companion. Tidal evolution in such systems plays an important role in the formation scenarios of merging neutron-star (NS) binaries. For general eccentricities, these expressions are given by the sums, Eqs. (6.15) and (6.16), respectively. However, when the eccentricity is large, these sums require the evaluation of many terms to be accurate. We have derived approximate expressions in two regimes:

- For $e \gtrsim 0.2$, we show that the tidal torque and energy transfer rate can be accurately approximated by the integral expressions, Eqs. (6.32) and (6.41).
- If furthermore the spin of the stellar core is not very close to its pseudo-synchronized value (i.e. where the torque vanishes; see Section 6.3.2), we show that these two integral expressions can be well approximated by the closed-form expressions, Eqs. (6.37) and (6.46).

These analytical expressions for T and $\dot{E}_{\rm in}$ (particularly the closed-form expressions) can be easily applied to study the spin and orbital evolution of eccentric binaries consisting of massive MS stars, such as those found in the evolution scenarios leading to the formation of merging neutron star binaries.

We then apply our analytical expressions to the PSR J0045-7319 binary system, which has a massive B-star companion and a measured orbital decay rate.

This system provides a rare example to test/calibrate our theoretical understanding of IGW-mediated dynamical tides in massive stars. We show that for the "standard" radius of the convective core based on isolated non-rotating stellar modeling, the B-star must have a significant retrograde and differential rotation (with the rotation rate at the convective-radiative boundary at least a few times larger than the surface rotation rate of the star). Alternatively, we suggest that the convective core radius may be larger than the standard value as a result of rapid stellar rotation and/or mass transfer to the B-star in the recent past during the post-MS evolution of the pulsar progenitor. Overall, our attempt to explain the rapid orbital decay of the PSR J0045-7319 binary highlights the critical importance of internal stellar structure, particularly the size of the convective core, in determining the tidal evolution of eccentric binaries containing massive MS stars.

6.5.2 Caveats

Concerning our analytical expressions for the tidal torque and energy transfer rate, we note a few potential caveats:

(i) For simplicity, we have assumed that the stellar spin and orbit axes are aligned or anti-aligned. For general stellar obliquities (as in the case of the PSR J0045-7319 binary system), it is possible to decompose the tidal force into different Fourier components (see Appendix A of Lai, 1997), and this would be unlikely to yield qualitatively different result in terms of the orbital decay rate [cf. Lai, 2012].

(ii) More importantly, in our work we have assumed that all Fourier harmonics (with different forcing frequencies $N\Omega$ in the inertial frame, where Ω is the mean orbital frequency) of the tidal potential excite IGWs at the radiative-convective boundary that damp completely as they propagate towards the stellar surface.

This is known to be the case when the normalized tidal forcing frequency ω (equal to $N\Omega - 2\Omega_s$ for $m = 2$ and $N\Omega$ for $m = 0$) satisfies $|\omega| \ll \sqrt{GM/R^3}$ due to efficient radiative damping (Zahn, 1975, Kushnir et al., 2017; see also the review paper Ogilvie, 2014). Note that the dominant Fourier harmonics of the tidal potential have $N\Omega \sim \Omega_p$ (the orbital frequency at the pericentre). Thus, as long as $\Omega_p, |\Omega_s| \ll \sqrt{GM/R^3}$, the assumption of outgoing IGWs inherent in our theory is valid. When $|\omega|$ is comparable to $\sqrt{GM/R^3}$, it is traditionally thought that IGWs set up standing modes in the stellar interior. This is because IGWs are evanescent sufficiently near stellar surface, where the pressure scale height becomes smaller than the radial wavelength of the wave [Goldreich and Nicholson, 1989]. Moreover, Su et al. [2020] found that sufficiently large-amplitude IGWs can spontaneously cause a critical layer to form due to nonlinear wave breaking, causing incident IGWs to be efficiently absorbed. After such a critical layer forms, it can propagate to deep within the stellar interior and efficiently absorb IGWs even before they reach breaking amplitudes. Wave breaking and other nonlinear effects (such as nonlinear mode couplings) may be enhanced in an eccentric binary such as PSR J0045-7319, where IGWs with a wide range of frequencies are excited. Burkart et al. [2012] found that the frequency cutoff for g-modes in the eccentric heartbeat star system KOI-54 (with eccentricity $e = 0.83$, orbital period $P = 41.8$ days, and stellar mass $M \approx 2.3 M_\odot$) is in agreement with the frequency at which IGWs become efficiently damped by thermal diffusion. However, in higher-mass MS stars such as that in PSR J0045-7319, nonlinear wave breaking may be an important source of IGW damping due to the larger tidal torque. More work is needed to address whether our assumption of traveling IGWs in massive stars is accurate.

CHAPTER 7

SPIN-ORBIT MISALIGNMENTS IN TERTIARY-INDUCED BLACK-HOLE BINARY MERGERS: THEORETICAL ANALYSIS

Originally published in:
Yubo Su, Dong Lai, and Bin Liu. Spin-orbit misalignments in tertiary-induced binary black-hole mergers: Theoretical analysis. *Phys. Rev. D*, 103(6):063040, 2021a

7.1 Introduction

As LIGO/VIRGO continues to detect mergers of black hole (BH) binaries [e.g. Abbott et al., 2016, 2019], it is increasingly important to systematically study various formation channels of BH binaries and their observable signatures. The canonical channel consists of isolated binary evolution, in which mass transfer and friction in the common envelope phase cause the binary orbit to decay sufficiently that it subsequently merges via emission of gravitational waves (GW) within a Hubble time [e.g. Lipunov et al., 1997, 2017, Podsiadlowski et al., 2003, Belczynski et al., 2010, 2016, Dominik et al., 2012, 2013, 2015]. BH binaries formed via isolated binary evolution are generally expected to have small misalignment between the BH spin axis and the orbital angular momentum axis [Postnov and Kuranov, 2019, Belczynski et al., 2020]. On the other hand, various flavors of dynamical formation channels of BH binaries have also been studied. These involve either strong gravitational scatterings in dense clusters [e.g. Zwart and McMillan, 1999, O'leary et al., 2006, Miller and Lauburg, 2009, Banerjee et al., 2010, Downing et al., 2010, Ziosi et al., 2014, Rodriguez et al., 2015, Samsing and Ramirez-Ruiz, 2017, Samsing and D'Orazio, 2018, Rodriguez et al., 2018, Gondán et al., 2018] or more gentle "tertiary-induced mergers" [e.g. Liu and Lai, 2021, Liu and Lai, 2020, Liu et al., 2019b,a, Liu and Lai, 2019, Blaes et al., 2002, Miller and Hamilton, 2002, Wen, 2003, Antonini and Perets, 2012, Antonini et al., 2017, Silsbee and

Tremaine, 2017a, Liu and Lai, 2017, 2018, Randall and Xianyu, 2018b, Hoang et al., 2018]. The dynamical formation channels generally produce BH binaries with misaligned spins with respect to the orbital axes.

GW observations of binary inspirals can put constraints on BH masses and spins. Typically, the spin constraints come in the form of two dimensionless mass-weighted combinations of the component BH spins: (i) the aligned spin parameter

$$\chi_{\rm eff} \equiv \frac{m_1\chi_1\cos\theta_{\rm s_1l} + m_2\chi_2\cos\theta_{\rm s_2l}}{m_1+m_2}, \tag{7.1}$$

where $m_{1,2}$ are the masses of the BHs, $\theta_{\rm s_il}$ is the angle between the i-th spin and the binary orbital angular momentum axis, and $\chi_i \equiv cS_i/(Gm_i^2)$ is the dimensionless Kerr spin parameter; and (ii) the perpendicular spin parameter [Schmidt et al., 2015]

$$\chi_{\rm p} \equiv \max\left\{\chi_1\sin\theta_{\rm s_1l}, \frac{q(4q+3)}{4+3q}\chi_2\sin\theta_{\rm s_2l}\right\}, \tag{7.2}$$

where $q \equiv m_2/m_1$ and $m_1 \geq m_2$. The systems detected in the first and second observing runs (O1 and O2) of LIGO/VIRGO have $\chi_{\rm eff} \sim 0$ (but see [Zackay et al., 2019, Venumadhav et al., 2020] for exceptions). In the third observing run (O3) of LIGO/VIRGO, two events exhibit substantial spin-orbit misalignment. In GW190412 [Abbott et al., 2020a], the two BH component masses are $29^{+5.0}_{-5.3}M_\odot$ and $8.4^{+1.7}_{-1.0}M_\odot$. The primary (more massive) BH is inferred to have $\chi_1 = 0.43^{+0.16}_{-0.26}$, and the effective spin parameter of the binary is constrained to be $\chi_{\rm eff} = 0.25^{+0.09}_{-0.11}$, indicating a non-negligible spin-orbit misalignment angle. In GW190521 [Abbott et al., 2020b], the two component BHs have masses of $85^{+21}_{-14}M_\odot$ and $66^{+17}_{-18}M_\odot$ and spins of $\chi_1 = 0.69^{+0.27}_{-0.62}$ and $\chi_2 = 0.72^{+0.24}_{-0.64}$. The binary's aligned spin is $\chi_{\rm eff} = 0.08^{+0.27}_{-0.36}$ while the perpendicular spin is $\chi_{\rm p} = 0.68^{+0.25}_{-0.37}$, again suggesting significant spin-orbit misalignments.

Liu and Lai [2017, 2018, hereafter LL17, LL18], and Liu et al. [2019a] carried

out a systematic study of binary BH mergers in the presence of a tertiary companion. LL17 pointed out the important effect of spin-orbit coupling (de-Sitter precession) in determining the final spin-orbit misalignment angles of BH binaries in triple systems. They considered binaries with sufficiently compact orbits (so that mergers are possible even without a tertiary) and showed that the combination of LK oscillations (induced by a modestly inclined tertiary) and spin-orbit coupling gives rise to a broad range of final spin-orbit misalignments in the merging binary BHs. We call these mergers *LK-enhanced mergers*. On the other hand, LL18 considered the more interesting case of *LK-induced mergers*, in which an initially wide BH binary (too wide to merge in isolation) is pushed to extreme eccentricities (close to unity) by a highly inclined tertiary and merges within a few Gyrs. LL18 examined a wide range of orbital and spin evolution behaviors and found that LK-induced mergers can sometimes exhibit a "90° attractor" in the spin evolution: when the BH spin is initially aligned with the inner binary angular momentum axis ($\theta_{\rm sl,0} = 0$), it evolves towards a perpendicular state ($\theta_{\rm sl,f} \simeq 90°$) near merger (when the inner binary becomes gravitationally decoupled from the tertiary, and $\theta_{\rm sl}$ freezes). Qualitatively, they found that the attractor exists when the LK-induced orbital decay is sufficiently "gentle" and the octupole LK effects are unimportant. Figure 7.1 gives an example of a system evolving towards this attractor, where $\theta_{\rm sl}$ converges to $\approx 90°$ at late times in the bottom right panel. Figure 7.2 shows how $\theta_{\rm sl,f}$ varies when the initial inclination of the tertiary orbit I_0 (relative to the inner orbit) is varied. Note that for rapid mergers (when I_0 is close to 90°), the attractor does not exist; as I_0 deviates more from 90°, the merger time increases and $\theta_{\rm sl,f}$ becomes close to 90°. This "90° attractor" gives rise to a peak around $\chi_{\rm eff} = 0$ in the final $\chi_{\rm eff}$ distribution in tertiary-induced mergers [LL18; Liu et al., 2019a]. This peak was also found in the population studies of Antonini et al. [2018].

The physical origin of this "90° attractor" and under what conditions it can be achieved are not well understood. LL18 proposed an explanation based on analogy with an adiabatic invariant in systems where the inner binary remains circular throughout the inspiral (LL17; see also [Yu et al., 2020a]). However, the validity of this analogy is hard to justify, as significant eccentricity excitation is a necessary ingredient in LK-induced mergers. In addition, the LK-*enhanced* mergers considered in LL17 show no 90° attractor even though the orbital evolution is slow and regular.

In this paper, we present an analytic theory to explain the 90° attractor and to characterize its regime of validity. More generally, we develop a theoretical framework to help understand the BH spin evolution in LK-induced mergers. In Sections 7.2 and 7.3, we set up the relevant equations of motion for the orbital and spin evolution of the system. To simplify the theoretical analysis, we initially consider the cases where the tertiary mass is much larger than the binary mass. In Sections 7.4 and 7.5, we develop an analytic understanding of the spin evolution. In Section 7.6, we generalize our results to stellar-mass tertiary companions. We discuss and conclude in Section 7.7.

7.2 LK-Induced Mergers: Orbital Evolution

In this section we summarize the key features and relevant equations for LK-induced mergers to be used for our analysis in later sections. Consider a black hole (BH) binary with masses m_1 and m_2 having total mass m_{12}, reduced mass $\mu = m_1 m_2/m_{12}$, semimajor axis a and eccentricity e. This inner binary orbits around a tertiary with mass m_3, semimajor axis $a_{\rm out}$ and eccentricity $e_{\rm out}$ in a hierarchical configuration ($a_{\rm out} \gg a$). Unless explicitly stated, we assume $m_3 \gg m_1, m_2$ (e.g.

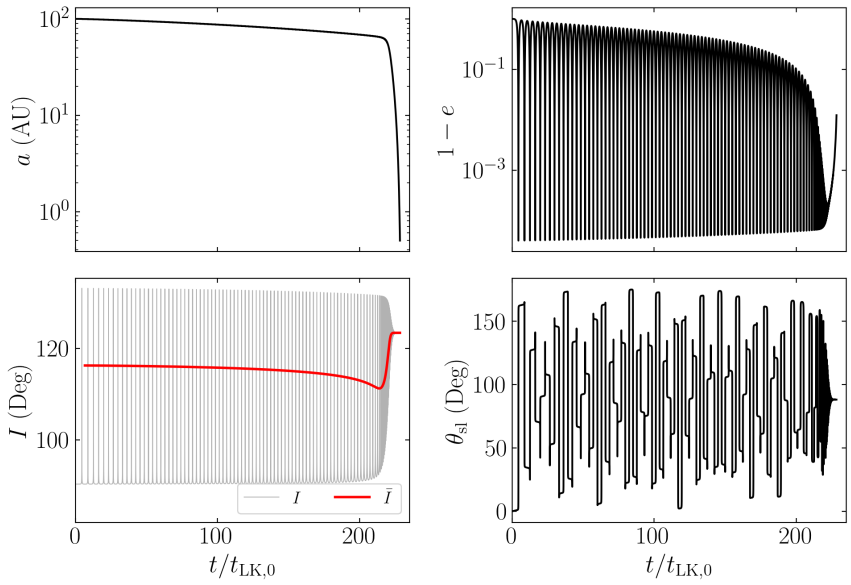

Figure 7.1: An example of the "90° spin attractor" in LK-induced BH binary mergers. The four panes show the time evolution of the binary semi-major axis a, eccentricity e, inclination I [the red line denotes the averaged $\bar{I}$ given by Eq. (7.29)], and spin-orbit misalignment angle $\theta_{\rm sl}$. The unit of time $t_{\rm LK,0}$ is the LK timescale [Eq. (7.9)] evaluated for the initial conditions. The inner binary has $m_1 = 30M_\odot$, $m_2 = 20M_\odot$, and initial $a_0 = 100$ AU, $e_0 = 0.001$, $I_0 = 90.35°$ (with respect to the outer binary), and $\theta_{\rm sl,0} = 0$. The tertiary has $a_{\rm out} = 2.2$ pc, $e_{\rm out} = 0$, and $m_3 = 3\times10^7 M_\odot$ (The result depends only on $m_3/\tilde{a}_{\rm out}^3$, provided that $L_{\rm out} \gg L$). It can be seen that $\theta_{\rm sl}$ evolves to $\sim 90°$ as a decays to smaller values, and we stop the simulation when $a = 0.5$ AU as the LK oscillation "freezes" and $\theta_{\rm sl}$ has converged to a constant value.

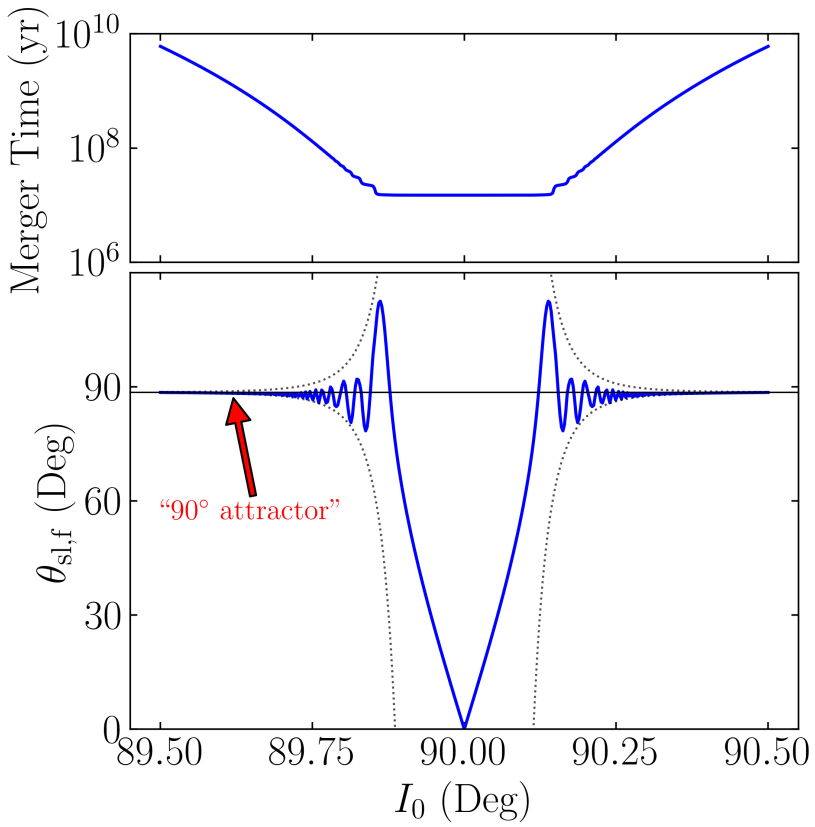

Figure 7.2: The merger time and the final spin-orbit misalignment angle $\theta_{\rm sl,f}$ as a function of the initial inclination I_0 for LK-induced mergers. The other parameters are the same as those in Fig. 7.1. For I_0 somewhat far away from 90°, the resulting $\theta_{\rm sl,f}$ are all quite near 90°. In the lower panel, the horizontal black solid line shows the predicted $\theta_{\rm sl,f}$ if $\bar{\theta}_{\rm e}$ is conserved, i.e. Eq. (7.57), and the black dashed line shows Eq. (7.61), which provides an estimate for the deviation from the 90° attractor.

the tertiary can be a supermassive black hole, or SMBH), although our analysis can be easily generalized to comparable masses (see Section 7.6). We denote the orbital angular momentum of the inner binary by $\mathbf{L} \equiv L\hat{\mathbf{L}}$ and the angular momentum of the outer binary by $\mathbf{L}_{\rm out} \equiv L_{\rm out}\hat{\mathbf{L}}_{\rm out}$. Since $L_{\rm out} \gg L$, we take $\mathbf{L}_{\rm out}$ to be fixed.

The equations of motion governing the orbital elements a, e, Ω, I, ω (where Ω, I, ω are the longitude of the ascending node, inclination, and argument of periapsis respectively) of the inner binary are

$$\frac{\mathrm{d}a}{\mathrm{d}t} = \left(\frac{\mathrm{d}a}{\mathrm{d}t}\right)_{\rm GW}, \tag{7.3}$$

$$\frac{\mathrm{d}e}{\mathrm{d}t} = \frac{15}{8t_{\rm LK}} e\, j(e) \sin 2\omega \sin^2 I + \left(\frac{\mathrm{d}e}{\mathrm{d}t}\right)_{\rm GW}, \tag{7.4}$$

$$\frac{\mathrm{d}\Omega}{\mathrm{d}t} = \frac{3}{4t_{\rm LK}} \frac{\cos I \left(5e^2\cos^2\omega - 4e^2 - 1\right)}{j(e)}, \tag{7.5}$$

$$\frac{\mathrm{d}I}{\mathrm{d}t} = -\frac{15}{16t_{\rm LK}} \frac{e^2 \sin 2\omega \sin 2I}{j(e)}, \tag{7.6}$$

$$\frac{\mathrm{d}\omega}{\mathrm{d}t} = \frac{3}{4t_{\rm LK}} \frac{2j^2(e) + 5\sin^2\omega(e^2 - \sin^2 I)}{j(e)} + \Omega_{\rm GR}, \tag{7.7}$$

where we have defined

$$j(e) = \sqrt{1-e^2}, \tag{7.8}$$

$$t_{\rm LK}^{-1} \equiv n\left(\frac{m_3}{m_{12}}\right)\left(\frac{a}{\tilde{a}_{\rm out}}\right)^3, \tag{7.9}$$

with $n \equiv \sqrt{Gm_{12}/a^3}$ the mean motion of the inner binary, and $\tilde{a}_{\rm out} = a_{\rm out}\sqrt{1-e_{\rm out}^2}$. The general relativity (GR) induced apsidal precession of the inner binary is given by

$$\Omega_{\rm GR}(e) = \frac{3Gnm_{12}}{c^2 a j^2(e)}. \tag{7.10}$$

The dissipative terms due to gravitational radiation are

$$\left(\frac{\mathrm{d}a}{\mathrm{d}t}\right)_{\rm GW} = -\frac{a}{t_{\rm GW}(e)}, \tag{7.11}$$

$$\left(\frac{\mathrm{d}e}{\mathrm{d}t}\right)_{\rm GW} = -\frac{304}{15}\frac{G^3\mu m_{12}^2}{c^5 a^4}\frac{1}{j^5(e)}\left(1 + \frac{121}{304}e^2\right)e, \tag{7.12}$$

where

$$t_{\rm GW}^{-1}(e) \equiv \frac{64}{5}\frac{G^3\mu m_{12}^2}{c^5 a^4}\frac{1}{j^7(e)}\left(1+\frac{73}{24}e^2+\frac{37}{96}e^4\right). \tag{7.13}$$

Equations (7.4–7.7) include only the effects of quadrupole perturbations from m_3 on the binary. The octupole effects depend on the parameter

$$\epsilon_{\rm oct} = \frac{m_1-m_2}{m_{12}}\frac{a e_{\rm out}}{a_{\rm out}(1-e_{\rm out}^2)}, \tag{7.14}$$

[see Liu et al., 2015a]. Throughout this paper, we consider systems where $\epsilon_{\rm oct} \ll 1$ so that the octupole effects are neglected.

In Fig. 7.1, we provide an example of an LK-induced merger for our fiducial parameters (described in the figure caption). The inner binary initially decays slowly as its eccentricity undergoes LK oscillations, with a nearly constant maximum eccentricity close to unity. Then, as a decreases and the minimum eccentricity within each LK cycle increases, the orbital decay of the inner binary accelerates. As apsidal precession further suppresses eccentricity oscillations, the eccentricity rapidly decays. We terminate the simulation at $a = 0.5$ AU as the spin-orbit misalignment angle $\theta_{\rm sl}$ has reached its final value, even though the binary still has non-negligible eccentricity. We refer to the example depicted in Fig. 7.1 as the fiducial example, and much of our analysis in later sections will be based on this example unless otherwise noted. Also note that the parameters of Fig. 7.1 give the same $t_{\rm LK}$ as Fig. 4 of LL18.

We next discuss the key analytical properties of the orbital evolution.

7.2.1 Analytical Results Without GW Radiation

First, neglecting the GW radiation terms, the system admits two conservation laws, the "Kozai constant" and energy conservation,

$$j(e)\cos I = \text{const}, \tag{7.15}$$

$$\frac{3}{8}\left[2e^2 + j^2(e)\cos^2 I - 5e^2\sin^2 I \sin^2\omega\right] + \frac{\epsilon_{\rm GR}}{j(e)} = \text{const}, \tag{7.16}$$

(see [Anderson et al., 2016] and LL18 for more general expressions when $L_{\rm out}$ is comparable to L), where

$$\epsilon_{\rm GR} \equiv (\Omega_{\rm GR} t_{\rm LK})_{e=0} = \frac{3Gm_{12}^2 \tilde{a}_{\rm out}^3}{c^2 m_3 a^4}. \tag{7.17}$$

The conservation laws can be combined to obtain the maximum eccentricity $e_{\max}$ as a function of the initial I_0 (and initial $e_0 \ll 1$). The largest value of $e_{\max}$ occurs at $I_0 = 90^\circ$ and is given by

$$j(e_{\max})_{I_0=90^\circ} = (8/9)\epsilon_{\rm GR}. \tag{7.18}$$

Eccentricity excitation then requires $\epsilon_{\rm GR} < 9/8$. Our fiducial examples in Figs. 7.1 and 7.2 satisfy $\epsilon_{\rm GR} \ll 1$ at $a = a_0$, leading to $e_{\max} \sim 1$ within a narrow inclination window around $I_0 = 90^\circ$.

Eqs. (7.15) and (7.16) imply that e is a function of $\sin^2\omega$ alone [see Kinoshita and Nakai, 1999, Storch and Lai, 2015, for the exact form], so an eccentricity maximum occurs every half period of ω. We define the LK period of eccentricity oscillation $P_{\rm LK}$ and its corresponding angular frequency $\Omega_{\rm LK}$ via

$$\pi = \int_0^{P_{\rm LK}} \frac{{\rm d}\omega}{{\rm d}t}\,{\rm d}t, \qquad\qquad \Omega_{\rm LK} \equiv \frac{2\pi}{P_{\rm LK}}. \tag{7.19}$$

In LK cycles, the inner binary oscillates between the eccentricity minimum $e_{\min}$ and maximum $e_{\max}$. The oscillation is "uneven": when $e_{\min} \ll e_{\max}$, the bi-

nary spends a fraction $\sim j(e_{\max})$ of the LK cycle, or time $\Delta t \sim t_{\rm LK} j(e_{\max})$, near $e \simeq e_{\max}$ [see Eq. (7.7)].

7.2.2 Behavior with GW Radiation

Including the effect of GW radiation, orbital decay predominantly occurs at $e \simeq e_{\max}$ with the timescale of $t_{\rm GW}(e_{\max})$ [see Eq. (7.13)]. On the other hand, Eq. (7.7) implies that, when $\epsilon_{\rm GR} \ll 1$, the binary spends only a small fraction ($\sim j(e_{\max})$) of the time near $e \simeq e_{\max}$. Thus, we expect two qualitatively different merger behaviors:

- "Rapid mergers": When $t_{\rm GW}(e_{\max}) \lesssim t_{\rm LK} j(e_{\max})$, the binary is "pushed" into high eccentricity and exhibits a "one shot merger" without any e-oscillations.
- "Smooth mergers": When $t_{\rm GW}(e_{\max}) \gtrsim t_{\rm LK} j(e_{\max})$, the binary goes through a phase of eccentricity oscillations while the orbit gradually decays. In this case, the LK-averaged orbital decay rate is $\sim j(e_{\max}) t_{\rm GW}^{-1}(e_{\max})$. As a decreases, $e_{\max}$ decreases slightly while the minimum eccentricity increases, approaching $e_{\max}$ (see Fig. 7.1). This eccentricity oscillation "freeze" ($e_{\min} \sim e_{\max}$) is due to GR-induced apsidal precession ($\epsilon_{\rm GR}$ increases as a decreases), and occurs when $\epsilon_{\rm GR}(a) \gg j(e_{\max})$. After the eccentricity is frozen, the binary circularizes and decays on the timescale $t_{\rm GW}(e_{\max})$.

7.3 Spin Dynamics: Equations

We are interested in the spin orientations of the inner BHs at merger as a function of initial conditions. Since they evolve independently to leading post-Newtonian

order, we focus on the dynamics of $\hat{\mathbf{S}}_1 = \hat{\mathbf{S}}$, the unit spin vector of m_1. Since the spin magnitude does not enter into the dynamics, we write $\mathbf{S} \equiv \hat{\mathbf{S}}$ for brevity (i.e. $\mathbf{S}$ is a unit vector). Neglecting spin-spin interactions, $\mathbf{S}$ undergoes de Sitter precession about $\mathbf{L}$ as

$$\frac{\mathrm{d}\mathbf{S}}{\mathrm{d}t} = \Omega_{\mathrm{SL}} \hat{\mathbf{L}} \times \mathbf{S}, \tag{7.20}$$

with

$$\Omega_{\mathrm{SL}} = \frac{3Gn\left(m_2 + \mu/3\right)}{2c^2 a j^2(e)}. \tag{7.21}$$

In the presence of a tertiary companion, the orbital axis $\hat{\mathbf{L}}$ of the inner binary precesses around $\hat{\mathbf{L}}_{\mathrm{out}}$ with rate $\mathrm{d}\mathfrak{O}/\mathrm{d}t$ and nutates with varying I [see Eqs. (7.5) and (7.6)]. To analyze the dynamics of the spin vector, we go to the co-rotating frame with $\hat{\mathbf{L}}$ about $\hat{\mathbf{L}}_{\mathrm{out}}$, in which Eq. (7.20) becomes

$$\left(\frac{\mathrm{d}\mathbf{S}}{\mathrm{d}t}\right)_{\mathrm{rot}} = \boldsymbol{\Omega}_{\mathrm{e}} \times \mathbf{S}, \tag{7.22}$$

where we have defined an effective rotation vector

$$\boldsymbol{\Omega}_{\mathrm{e}} \equiv \Omega_{\mathrm{L}} \hat{\mathbf{L}}_{\mathrm{out}} + \Omega_{\mathrm{SL}} \hat{\mathbf{L}}, \tag{7.23}$$

with [see Eq. (7.5)]

$$\Omega_{\mathrm{L}} \equiv -\frac{\mathrm{d}\mathfrak{O}}{\mathrm{d}t}. \tag{7.24}$$

In this rotating frame, the plane spanned by $\hat{\mathbf{L}}_{\mathrm{out}}$ and $\hat{\mathbf{L}}$ is constant in time, only the inclination angle I can vary.

7.3.1 Nondissipative Spin Dynamics

We first consider the limit where dissipation via GW radiation is completely neglected ($t_{\mathrm{GW}}(e) \to \infty$). Then $\boldsymbol{\Omega}_{\mathrm{e}}$ is exactly periodic with period P_{LK} [see Eq. (7.19)]

We can rewrite Eq. (7.22) in Fourier components

$$\left(\frac{\mathrm{d}\mathbf{S}}{\mathrm{d}t}\right)_{\mathrm{rot}} = \left[\overline{\mathbf{\Omega}}_{\mathrm{e}} + \sum_{N=1}^{\infty} \mathbf{\Omega}_{\mathrm{eN}} \cos\left(N\Omega_{\mathrm{LK}}t\right)\right] \times \mathbf{S}. \tag{7.25}$$

Note that $\overline{\mathbf{\Omega}}_{\mathrm{e}}$ is the zeroth Fourier component, where the bar denotes an average over a LK cycle. We have adopted the convention where $t = 0$ is the time of maximum eccentricity of the LK cycle, so that Eq. (7.25) does not have $\sin(N\Omega_{\mathrm{LK}}t)$ terms.

This system superficially resembles that considered in Storch and Lai [2015] (SL15), who studied the dynamics of the spin axis of a star when driven by a giant planet undergoing LK oscillations [see also Storch et al., 2014, 2017]. In their system, the spin-orbit coupling arises from Newtonian interaction between the planet (M_{p}) and the rotation-induced stellar quadrupole ($I_3 - I_1$), and the spin precession frequency is

$$\Omega_{\mathrm{SL}}^{(\mathrm{Newtonian})} = -\frac{3GM_{\mathrm{p}}(I_3 - I_1)}{2a^3 j^3(e)} \frac{\cos\theta_{\mathrm{sl}}}{I_3\Omega_{\mathrm{s}}}, \tag{7.26}$$

where $I_3\Omega_{\mathrm{s}}$ is the spin angular momentum of the star. SL15 showed that under some conditions that depend on a dimensionless adiabaticity parameter (roughly the ratio between the magnitudes of $\Omega_{\mathrm{SL}}^{(\mathrm{Newtonian})}$ and Ω_{L} when factoring out the eccentricity and obliquity dependence), the stellar spin axis can vary chaotically. One strong indicator of chaos in their study is the presence of irregular, fine structure in a bifurcation diagram [Fig. 1 of Storch and Lai [2015]] that shows the values of the spin-orbit misalignment angle θ_{sl} when varying system parameters in the "transadiabatic" regime, where the adiabaticity parameter crosses unity.

To generate an analogous bifurcation diagram for our problem, we consider a sample system with $m_{12} = 60M_{\odot}$, $m_3 = 3 \times 10^7 M_{\odot}$, $a = 0.1$ AU, $e_0 = 10^{-3}$, $I_0 = 70°$, $a_{\mathrm{out}} = 300$ AU, $e_{\mathrm{out}} = 0$, and initial $\theta_{\mathrm{sl}} = 0$ (note that these parameters are different from those in Fig. 7.1). We then evolve Eq. (7.20) together with the orbital

evolution equations [Eqs. (7.3–7.7) without the GW terms] while sampling both $\theta_{\rm sl}$ and $\theta_{\rm e}$ at eccentricity maxima, where $\theta_{\rm e}$ is the angle between $\overline{\mathbf{\Omega}}_{\rm e}$ and $\mathbf{S}$, i.e.

$$\cos\theta_{\rm e} = \frac{\overline{\mathbf{\Omega}}_{\rm e}}{\overline{\Omega}_{\rm e}} \cdot \mathbf{S}, \tag{7.27}$$

where $\overline{\Omega}_{\rm e} \equiv \left|\overline{\mathbf{\Omega}}_{\rm e}\right|$. We repeat this procedure with different mass ratios m_1/m_{12} of the inner binary, which only changes $\Omega_{\rm SL}$ without changing the orbital evolution (note that the LK oscillation depends only on m_{12} and not on individual masses of the inner binary). Analogous to SL15, we consider systems with a range of the adibaticity parameter $\mathscr{A}$ [to be defined later in Eq. (7.31)] that crosses order unity. Note that the fiducial system of Fig. 7.1 does not serve this purpose because the initial $\Omega_{\rm SL}$ is too small. Our result is depicted in Fig. 7.3.

While our bifurcation diagram has interesting structure, the features are all regular. This is in contrast to the star-planet system studied by SL15 (see their Fig. 1). A key difference is that in our system, $\Omega_{\rm SL}$ does not depend on $\theta_{\rm sl}$, while for the planet-star system, $\Omega_{\rm SL}^{\rm (Newtonian)}$ does, and this latter feature introduces nonlinearity to the dynamics.

A more formal understanding of the dynamical behavior of our spin-orbit system comes from Floquet theory[Floquet, 1883, Chicone, 2006], as Eq. (7.22) is a linear system with periodic coefficients (the system studied in SL15 is nonlinear). By Floquet's theorem, when a linear system with periodic coefficients is integrated over a period, the evolution can be described by the linear transformation

$$\mathbf{S}(t + P_{\rm LK}) = \tilde{\mathbf{M}}\mathbf{S}(t), \tag{7.28}$$

where $\tilde{\mathbf{M}}$ is called the *monodromy matrix* and is independent of $\mathbf{S}$.

For our system, while $\tilde{\mathbf{M}}$ can be easily defined, it cannot be evaluated in closed form. Instead, we can reason directly about the general properties of $\tilde{\mathbf{M}}$: it must

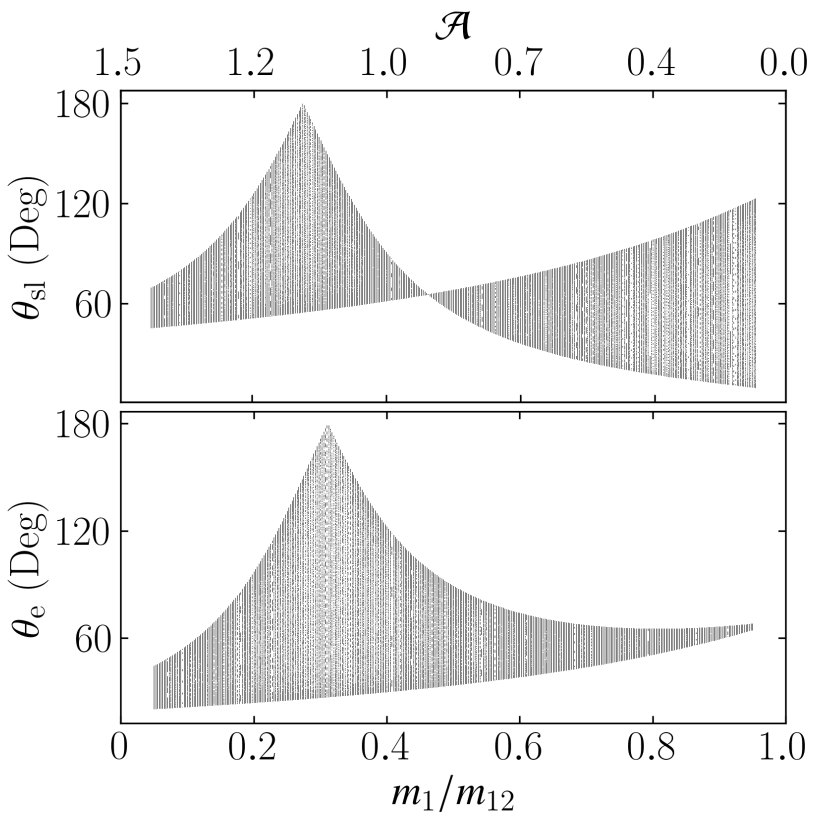

Figure 7.3: Bifurcation diagram for the BH spin orientation during LK oscillations. The physical parameters are $m_{12} = 60M_\odot$, $m_3 = 3 \times 10^7 M_\odot$, $a = 0.1$ AU, $e_0 = 10^{-3}$, $I_0 = 70^\circ$, $a_{\rm out} = 300$ AU, $e_{\rm out} = 0$, and initial condition $\theta_{\rm sl,0} = 0$. For each mass ratio m_1/m_{12}, the orbit-spin system is solved over 500 LK cycles, and both $\theta_{\rm sl}$ (the angle between $\mathbf{S}$ and $\hat{\mathbf{L}}$) and $\theta_{\rm e}$ [defined by Eq. (7.27)] are sampled at every eccentricity maximum and are plotted. The top axis shows the adiabaticity parameter $\mathcal{A}$ as defined by Eq. (7.31). Note that for a given m_{12}, changing the mass ratio m_1/m_{12} only changes the spin evolution and not the orbital evolution.

be a proper orthogonal matrix, or a rotation matrix, as it represents the effect of many infinitesimal rotations, each about the instantaneous $\mathbf{\Omega}_{\rm e}$[1]. Therefore, over each period $P_{\rm LK}$, the dynamics of $\mathbf{S}$ are equivalent to a rotation about a fixed axis, prohibiting chaotic behavior.

Another traditional indicator of chaos is a positive Lyapunov exponent, obtained when the separation between nearby trajectories diverges *exponentially* in time. In Floquet theory, the Lyapunov exponent is the logarithm of the largest eigenvalue of the monodromy matrix. Since $\tilde{\mathbf{M}}$ is a rotation matrix in our problem, the Lyapunov exponent must be 0, indicating no chaos. We have verified this numerically.

7.3.2 Spin Dynamics With GW Dissipation

When $t_{\rm GW}$ is finite, the coefficients $\mathbf{\Omega}_{\rm eN}$, including $\overline{\mathbf{\Omega}}_{\rm e}$ [see Eq. (7.25)], are no longer constant, but change over time. For "smooth" mergers (satisfying $t_{\rm GW}(e_{\rm max}) \gg t_{\rm LK} j(e_{\rm max})$; see Section 7.2), the binary goes through a sequence of LK cycles, and the coefficients vary on the LK-averaged orbital decay time $t_{\rm GW}(e_{\rm max})/j(e_{\rm max})$. After the LK oscillation freezes, we have $\mathbf{\Omega}_{\rm e} \simeq \overline{\mathbf{\Omega}}_{\rm e}$ (and $\mathbf{\Omega}_{\rm eN} \simeq 0$ for $N \geq 1$), which evolves on timesale $t_{\rm GW}(e)$ as the orbit decays and circularizes.

Once a is sufficiently small that $\Omega_{\rm SL} \gg \Omega_{\rm L}$, it can be seen from Eqs. (7.22–7.23) that $\theta_{\rm e} = \theta_{\rm sl}$ is constant, i.e. the spin-orbit misalignment angle is frozen (see bottom right panel of Fig. 7.1). This is the "final" spin-orbit misalignment, although the binary may still be far from the final merger. Note that at such

[1]More formally, $\tilde{\mathbf{M}} = \tilde{\mathbf{\Phi}}(P_{\rm LK})$ where $\tilde{\mathbf{\Phi}}(t)$ is the *principal fundamental matrix solution*: the columns of $\tilde{\mathbf{\Phi}}$ are solutions to Eq. (7.22) and $\tilde{\mathbf{\Phi}}(0)$ is the identity. By linearity, the columns of $\tilde{\mathbf{\Phi}}(t)$ remain orthonormal, while its determinant does not change, so $\tilde{\mathbf{M}}$ is a proper orthogonal matrix, or a rotation matrix.

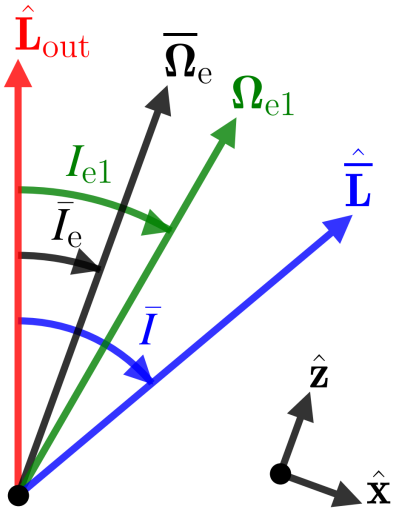

Figure 7.4: Definition of angles in the problem, shown in plane of the two angular momenta $\mathbf{L}_{\rm out}$ and $\mathbf{L}$. Here, $\overline{\mathbf{\Omega}}_{\rm e}$ is the LK-averaged $\mathbf{\Omega}_{\rm e}$, and $\mathbf{\Omega}_{\rm e1}$ is the first harmonic component (see Eqs. (7.23) and (7.25)). Note that for $I_0 > 90^\circ$, we choose $\bar{I}_{\rm e} \in (90^\circ, 180^\circ)$ so that $\overline{\Omega}_{\rm e} > 0$ (since $\Omega_{\rm L} < 0$). The bottom right shows our choice of coordinate axes with $\hat{\mathbf{z}} \propto \overline{\Omega}_{\rm e}$.

separations, $\epsilon_{\rm GR} \gg 1$ as well since $\Omega_{\rm SL} \sim \Omega_{\rm GR}$, and so LK eccentricity excitation is suppressed. For the fiducial examples depicted in Figs. 7.1–7.2, we stop the simulation at $a = 0.5\,\mathrm{AU}$, as $\theta_{\rm sl}$ has converged to its final value.

7.3.3 Spin Dynamics Equation in Component Form

For later analysis, it is useful to write Eq. (7.25) in component form. To do so, we define the inclination angle $\bar{I}_{\rm e}$ as the angle between $\overline{\mathbf{\Omega}}_{\rm e}$ and $\mathbf{L}_{\rm out}$ as shown in Fig. 7.4. To express $\bar{I}_{\rm e}$ algebraically, we define the LK-averaged quantities

$$\overline{\Omega_{\rm SL} \sin I} \equiv \overline{\Omega}_{\rm SL} \sin \bar{I}, \qquad \overline{\Omega_{\rm SL} \cos I} \equiv \overline{\Omega}_{\rm SL} \cos \bar{I}. \tag{7.29}$$

It then follows from Eq. (7.23) that

$$\tan \bar{I}_{\rm e} = \frac{\mathscr{A} \sin \bar{I}}{1 + \mathscr{A} \cos \bar{I}}, \tag{7.30}$$

where $\mathscr{A}$ is the adiabaticity parameter, given by

$$\mathscr{A} \equiv \frac{\overline{\Omega}_{\rm SL}}{\overline{\Omega}_{\rm L}}. \tag{7.31}$$

Note that in Eq. (7.30), $\bar{I}_{\rm e}$ is defined in the domain $[0°, 180°]$, i.e. $\bar{I}_{\rm e} \in (0, 90)$ when $\tan \bar{I}_{\rm e} > 0$ and $\bar{I}_{\rm e} \in (90, 180)$ when $\tan \bar{I}_{\rm e} < 0$.

We now choose a non-inertial coordinate system where $\hat{\mathbf{z}} \propto \overline{\mathbf{\Omega}}_{\rm e}$ and $\hat{\mathbf{x}}$ lies in the plane of $\mathbf{L}_{\rm out}$ and $\mathbf{L}$ (see Fig. 7.4). In this reference frame, the spin orientation is specified by the polar angle $\theta_{\rm e}$ as defined above in Eq. (7.27), and the spin evolution equation becomes

$$\left(\frac{{\rm d}\mathbf{S}}{{\rm d}t}\right)_{\rm xyz} = \left[\overline{\Omega}_{\rm e}\hat{\mathbf{z}} + \sum_{N=1}^{\infty} \mathbf{\Omega}_{\rm eN} \cos(N\Omega_{\rm LK} t)\right] \times \mathbf{S} - \dot{\bar{I}}_{\rm e}\hat{\mathbf{y}} \times \mathbf{S}. \tag{7.32}$$

One further simplification lets us cast this vector equation of motion into a scalar form. Break $\mathbf{S}$ into components $\mathbf{S} = S_x\hat{\mathbf{x}} + S_y\hat{\mathbf{y}} + \cos\theta_{\rm e}\hat{\mathbf{z}}$ and define complex variable

$$S_\perp \equiv S_x + iS_y. \tag{7.33}$$

Then, we can rewrite Eq. (7.32) as

$$\begin{aligned}\frac{{\rm d}S_\perp}{{\rm d}t} = i\overline{\Omega}_{\rm e}S_\perp - \dot{\bar{I}}_{\rm e}\cos\theta_{\rm e} + \sum_{N=1}^{\infty}\Big[&\cos(\Delta I_{\rm eN})S_\perp \\ &- i\cos\theta_{\rm e}\sin(\Delta I_{\rm eN})\Big]\Omega_{\rm eN}\cos(N\Omega_{\rm LK}t),\end{aligned} \tag{7.34}$$

where $\dot{\bar{I}}_{\rm e} = {\rm d}\bar{I}_{\rm e}/{\rm d}t$ and $\Omega_{\rm eN}$ is the magnitude of the vector $\mathbf{\Omega}_{\rm eN}$ [see Eq. (7.25)] and $\Delta I_{\rm eN} = I_{\rm eN} - \bar{I}_{\rm e}$, with $I_{\rm eN}$ the angle between $\mathbf{\Omega}_{\rm eN}$ and $\mathbf{L}_{\rm out}$ (see Fig. 7.4). Since $\cos\theta_{\rm e} = \pm\sqrt{1 - |S_\perp|^2}$, Eq. (7.34) is generally nonlinear in $S_\perp$, but becomes approximately linear when $|\theta_{\rm e}| \ll 1$.

7.4 Analysis: Approximate Adiabatic Invariant

In general, Eqs. (7.25) and (7.34) are difficult to study analytically. In this section, we neglect the harmonic terms and focus on how the varying $\overline{\mathbf{\Omega}}_{\rm e}$ affects the evolu-

tion of the BH spin axis. The effect of the harmonic terms is studied in Section 7.5.

7.4.1 The Adiabatic Invariant

When neglecting the $N \geq 1$ harmonic terms, Eq. (7.25) reduces to

$$\left(\frac{d\overline{\mathbf{S}}}{dt}\right)_{\rm rot} = \overline{\mathbf{\Omega}}_{\rm e} \times \overline{\mathbf{S}}. \tag{7.35}$$

It is not obvious to what extent the analysis of Eq. (7.35) is applicable to Eq. (7.25). From our numerical calculations, we find that the LK-average of $\mathbf{S}$ often evolves following Eq. (7.35), motivating our notation $\overline{\mathbf{S}}$. Over timescales shorter than the LK period $P_{\rm LK}$, Eq. (7.35) loses accuracy as the evolution of $\mathbf{S}$ itself is dominated by the $N \geq 1$ harmonics we have neglected. An intuitive interpretation of this result is that the $N \geq 1$ harmonics vanish when integrating Eq. (7.25) over a LK cycle.

Eq. (7.35) has one desirable property: $\bar{\theta}_{\rm e}$, defined by

$$\cos\bar{\theta}_{\rm e} \equiv \frac{\overline{\mathbf{\Omega}}_{\rm e}}{\overline{\Omega}_{\rm e}} \cdot \overline{\mathbf{S}}, \tag{7.36}$$

is an adiabatic invariant. This follows from the fact that $\overline{\mathbf{S}}_z$, the projection of $\overline{\mathbf{S}}$ on the $\overline{\mathbf{\Omega}}_{\rm e}$ axis, and φ, the precessional angle of $\overline{\mathbf{S}}$ around $\overline{\mathbf{\Omega}}_{\rm e}$, form a pair of action-angle variables. The adiabaticity condition requires that the precession axis $\hat{\mathbf{z}} = \overline{\mathbf{\Omega}}_{\rm e}/\overline{\Omega}_{\rm e}$ evolve slowly compared to the precession frequency at all times, i.e.

$$\left|\frac{d\bar{I}_{\rm e}}{dt}\right| \ll \overline{\Omega}_{\rm e}. \tag{7.37}$$

For our fiducial example depicted in Fig. 7.1, the values of $\dot{\bar{I}}_{\rm e}$ and $\overline{\Omega}_{\rm e}$ are shown in the top panel of Fig. 7.5, and the evolution of $\bar{\theta}_{\rm e}$ in the bottom panel. The net change in $\bar{\theta}_{\rm e}$ in this simulation is 0.01°, small as expected since $|\dot{\bar{I}}_{\rm e}| \ll \overline{\Omega}_{\rm e}$ at all times.

7.4.2 Deviation from Adiabaticity

The extent to which $\bar{\theta}_\mathrm{e}$ is conserved depends on how well Eq. (7.37) is satisfied. In this subsection, we derive a bound on the total non-conservation of $\bar{\theta}_\mathrm{e}$, then in the next subsection we show how this bound can be estimated from the initial conditions.

When neglecting harmonic terms, the scalar evolution equation Eq. (7.34) becomes

$$\frac{\mathrm{d}S_\perp}{\mathrm{d}t} = i\overline{\Omega}_\mathrm{e} S_\perp - \dot{\bar{I}}_\mathrm{e} \cos\bar{\theta}_\mathrm{e}. \tag{7.38}$$

This can be solved in closed form. Defining

$$\Phi(t) \equiv \int^t \overline{\Omega}_\mathrm{e}\, \mathrm{d}t, \tag{7.39}$$

we obtain the solution at time t:

$$e^{-i\Phi} S_\perp \Big|_0^t = -\int_0^t e^{-i\Phi(\tau)} \dot{\bar{I}}_\mathrm{e} \cos\bar{\theta}_\mathrm{e}\, \mathrm{d}\tau. \tag{7.40}$$

Recalling $|S_\perp| = \sin\bar{\theta}_\mathrm{e}$ and analyzing Eq. (7.40), we see that $\bar{\theta}_\mathrm{e}$ oscillates about its initial value with semi-amplitude

$$\left|\Delta\bar{\theta}_\mathrm{e}\right| \sim \left|\frac{\dot{\bar{I}}_\mathrm{e}}{\overline{\Omega}_\mathrm{e}}\right|. \tag{7.41}$$

In the adiabatic limit [Eq. (7.37)], $\bar{\theta}_\mathrm{e}$ is indeed conserved, as the right-hand side of Eq. (7.41) goes to zero. The bottom panel of Fig. 7.5 shows $\Delta\bar{\theta}_\mathrm{e}$ for the fiducial example. Note that $\bar{\theta}_\mathrm{e}$ is indeed mostly constant where Eq. (7.41) predicts small oscillations.

If we denote $\left|\Delta\bar{\theta}_\mathrm{e}\right|_\mathrm{f}$ to be the net change in $\bar{\theta}_\mathrm{e}$ over $t \in [0, t_\mathrm{f}]$, we can give a loose bound

$$\left|\Delta\bar{\theta}_\mathrm{e}\right|_\mathrm{f} \lesssim \left|\frac{\dot{\bar{I}}_\mathrm{e}}{\overline{\Omega}_\mathrm{e}}\right|_\mathrm{max}. \tag{7.42}$$

Inspection of Fig. 7.5 indicates that the spin dynamics are mostly uninteresting except near the peak of $|\dot{\bar{I}}_{\rm e}|$, which occurs where $\bar{\Omega}_{\rm SL} \simeq |\Omega_{\rm L}|$. We present a zoomed-in view of dynamical quantities near the peak of $|\dot{\bar{I}}_{\rm e}|$ in Fig. 7.6. In particular, in the bottom-rightmost panel, we see that the fluctuations in $\bar{\theta}_{\rm e}$ are dominated by a second contribution, the subject of the discussion in Section 7.5.

For comparison, we show in Fig. 7.7 a more rapid binary merger starting with $I_0 = 90.2°$, for which $|\Delta\theta_{\rm e}|_{\rm f} \approx 2°$. If we again examine the bottom-rightmost panel, we see that the net $\left|\Delta\bar{\theta}_{\rm e}\right|_{\rm f}$ obeys Eq. (7.42).

7.4.3 Estimate of Deviation from Adiabaticity from Initial Conditions

To estimate Eq. (7.42) as a function of initial conditions, we first differentiate Eq. (7.30),

$$\dot{\bar{I}}_{\rm e} = \left(\frac{\dot{\mathscr{A}}}{\mathscr{A}}\right) \frac{\mathscr{A} \sin \bar{I}}{1 + 2\mathscr{A} \cos \bar{I} + \mathscr{A}^2}. \tag{7.43}$$

It also follows from Eq. (7.23) that

$$\overline{\Omega}_{\rm e} = \left|\overline{\Omega}_{\rm L}\right| \left(1 + 2\mathscr{A} \cos \bar{I} + \mathscr{A}^2\right)^{1/2}, \tag{7.44}$$

from which we obtain

$$\frac{\left|\dot{\bar{I}}_{\rm e}\right|}{\overline{\Omega}_{\rm e}} = \left(\frac{\dot{\mathscr{A}}}{\mathscr{A}}\right) \frac{1}{\left|\overline{\Omega}_{\rm L}\right|} \frac{\mathscr{A} \sin \bar{I}}{\left(1 + 2\mathscr{A} \cos \bar{I} + \mathscr{A}^2\right)^{3/2}}. \tag{7.45}$$

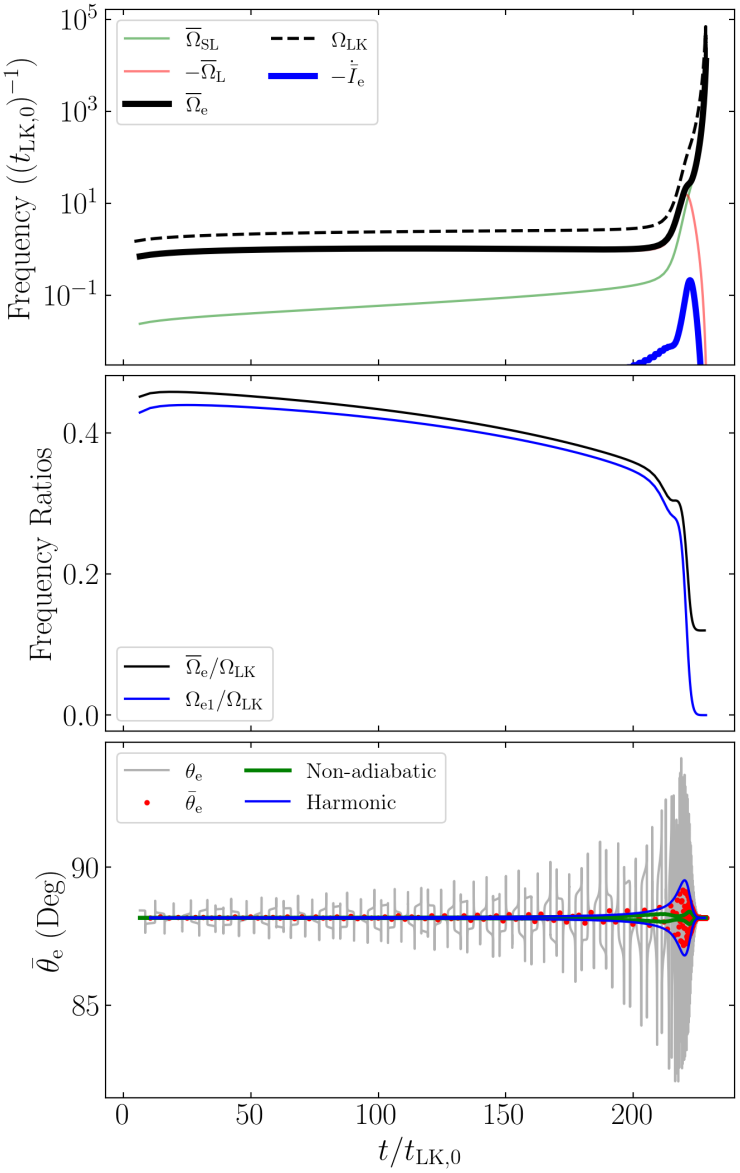

Figure 7.5: The same simulation as depicted in Fig. 7.1 but showing several calculated quantities relevant to the theory of the spin evolution. Top: the four characteristic frequencies of the system and $\mathrm{d}\bar{I}_{\rm e}/\mathrm{d}t$. Middle: the frequency ratios between the zeroth and first Fourier components of $\mathbf{\Omega}_{\rm e}$ to the LK frequency $\Omega_{\rm LK}$. Bottom: Time evolution of $\theta_{\rm e}$ [grey line; Eq. (7.27)], $\bar{\theta}_{\rm e}$ [red dots; Eq. (7.36)], as well as estimates of the deviations from perfect conservation of $\bar{\theta}_{\rm e}$ due to nonadiabaticity [green, Eq. (7.41)] and due to the resonance $\overline{\Omega}_{\rm e} \approx \Omega_{\rm LK}$ [blue, Eq. (7.81)].

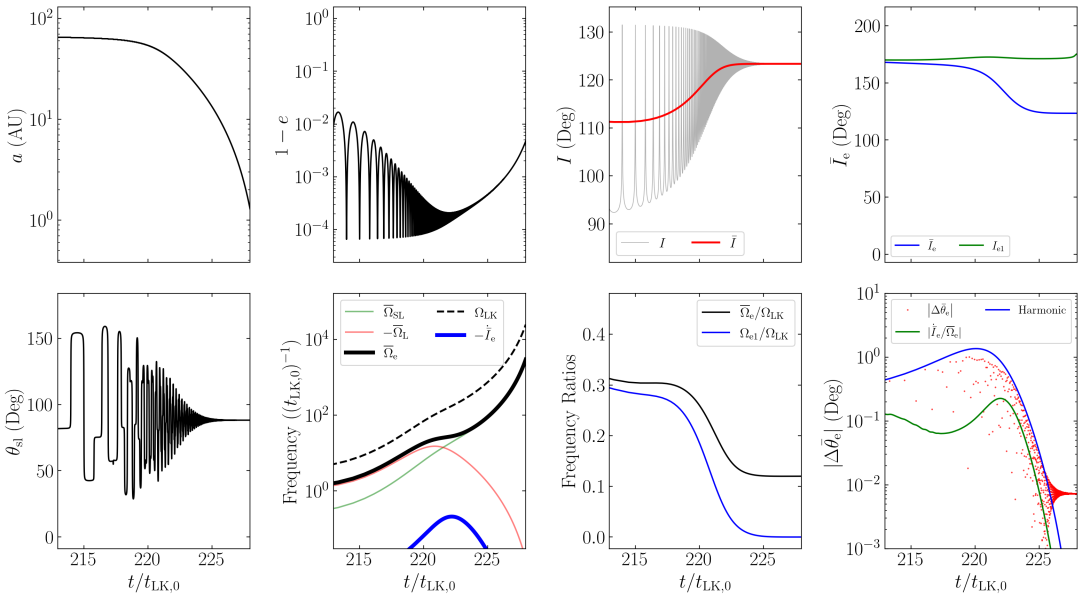

Figure 7.6: The same simulation as Fig. 7.1 but zoomed in on the region around $\mathscr{A} \equiv \overline{\Omega}_{SL}/\overline{\Omega}_L \simeq 1$ and showing a wide range of relevant quantities. The first three panels in the upper row depict a, e, I and $\bar{I}$ as in Fig. 7.1, while the fourth shows $\bar{I}_e$ [Eq. (7.30)] and I_{e1}. The bottom four panels depict θ_{sl}, the four characteristic frequencies of the system and $d\bar{I}_e/dt$ [Eqs. 7.23 and (7.24)] (as in the top panel of Fig. 7.5), the relevant frequency ratios (as in the middle panel of Fig. 7.5), and the deviation of $\bar{\theta}_e$ from its initial value compared to the predictions of Eqs. (7.41) and (7.81).

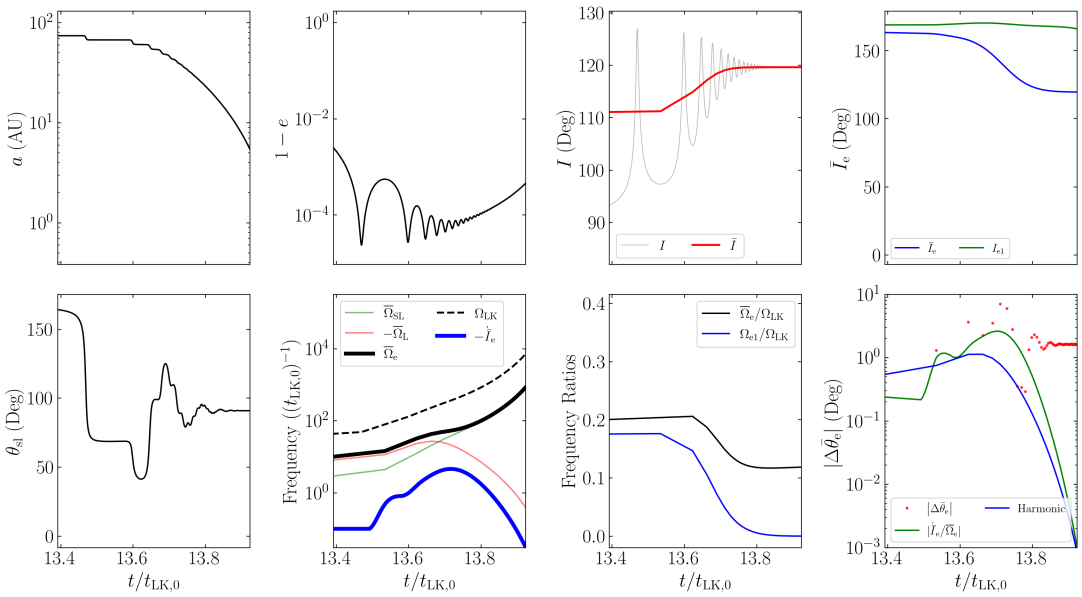

Figure 7.7: Same as Fig. 7.6 except for $I_0 = 90.2°$ (and all other parameters are the same as in Fig. 7.1), corresponding to a faster coalescence. The total change in $\bar{\theta}_e$ for this simulation is $\approx 2°$.

Moreover, if we assume the eccentricity is frozen around $e \simeq 1$ and use $\overline{\cos^2\omega} \simeq 1/2$ in $|\Omega_L| = |d\bigcirc\!\!\!\!\!\!\backslash/dt|$, we obtain the estimate

$$\mathscr{A} = \frac{\overline{\Omega}_{SL}}{\overline{\Omega}_L} \simeq \frac{3Gn\left(m_2+\mu/3\right)}{2c^2 a j^2(e)}\left[\frac{15\cos\bar{I}}{8t_{LK}j(e)}\right]^{-1}$$
$$\simeq \frac{4}{5}\frac{G(m_2+\mu/3)m_{12}\tilde{a}_{out}^3}{c^2 m_3 a^4 j(e)\cos\bar{I}}, \tag{7.46}$$

$$\frac{\dot{\mathscr{A}}}{\mathscr{A}} = -4\left(\frac{\dot{a}}{a}\right)_{GW} + \frac{e}{j^2(e)}\left(\frac{de}{dt}\right)_{GW}. \tag{7.47}$$

With these, we see that Eq. (7.45) is largest around $\mathscr{A} \simeq 1$, and so we find that the maximum $|\dot{\bar{I}}_e|/\overline{\Omega}_e$ is given by

$$\left|\frac{\dot{\bar{I}}_e}{\overline{\Omega}_e}\right|_{max} \simeq \left|\frac{\dot{\mathscr{A}}}{\mathscr{A}}\right| \frac{1}{\left|\overline{\Omega}_L\right|}\frac{\sin\bar{I}}{\left(2+2\cos\bar{I}\right)^{3/2}}. \tag{7.48}$$

To evaluate this, we make two assumptions: (i) $\bar{I}$ is approximately constant (see the third panels of Figs. 7.6 and 7.7), and (ii) $j(e)$ evaluated at $\mathscr{A} \simeq 1$ can be

approximated as a constant multiple of the initial $j(e_{\max})$, i.e.

$$j_\star \equiv j(e_\star) = f\sqrt{\frac{5}{3}\cos^2 I_0}, \tag{7.49}$$

where the star subscript denotes evaluation at $\mathscr{A} \simeq 1$ and $f > 1$ is a constant. Eq. (7.49) assumes that I_0 far enough from 90° that the GR effect is unimportant in determining $e_{\max}$. The value of f turns out to be relatively insensitive to I_0.

Using Eq. (7.47) and approximating $e_\star \approx 1$ in Eqs. (7.11) and (8.15) give

$$\left[\frac{\dot{\mathscr{A}}}{\mathscr{A}}\right]_\star \simeq \frac{G^3\mu m_{12}^2}{c^5 a_\star^4 j_\star^7}\frac{595}{3}. \tag{7.50}$$

To determine $a_\star$, we require Eq. (7.46) to give $\mathscr{A} = 1$ for $a_\star$ and $j_\star$. Taking this and Eq. (7.50), we rewrite Eq. (7.45) as

$$\left|\frac{\dot{\bar{I}}_{\rm e}}{\overline{\Omega}_{\rm e}}\right|_{\max} \approx \frac{595\sin\bar{I}\left|\cos\bar{I}\right|^{3/8}}{36\left(\cos\bar{I}+1\right)^{\frac{3}{2}}}\left[\frac{8000G^9 m_{12}^9 m_3^3\mu^8}{\tilde{a}_{\rm out}^9 j_\star^{37} c^{18}(m_2+\mu/3)^{11}}\right]^{1/8}. \tag{7.51}$$

We can also calculate $|\dot{\bar{I}}_{\rm e}|/\overline{\Omega}_{\rm e}$ from numerical simulations. Taking characteristic $\bar{I} \approx 120°$ (Figs. 7.6 and 7.7 show that this holds across a range of I_0), we fit the last remaining free parameter f [Eq. (7.49)] to the data from numerical simulations. This yields $f \approx 2.72$, leading to

$$\begin{aligned}\left|\frac{\dot{\bar{I}}_{\rm e}}{\overline{\Omega}_{\rm e}}\right|_{\max} \simeq\ & 0.98°\left(\frac{\cos I_0}{\cos(90.3°)}\right)^{-37/8}\left(\frac{\tilde{a}_{\rm out}}{2.2\,{\rm pc}}\right)^{-9/8} \\ & \times\left(\frac{m_3}{3\times10^7\,M_\odot}\right)^{3/8}\left(\frac{m_{12}^9\mu^8/(m_2+\mu/3)^{11}}{(28.64M_\odot)^6}\right)^{1/8}.\end{aligned} \tag{7.52}$$

Figure 7.8 shows that when the merger time $T_{\rm m}$ is much larger than the initial LK timescale, Eq. (7.52) provides an accurate estimate for $|\dot{\bar{I}}_{\rm e}/\bar{\Omega}_{\rm e}|_{\max}$ when compared with numerical results.

In the above, we have assumed that the system evolves through $\mathscr{A} \simeq 1$ when the eccentricity is mostly frozen (see Fig. 7.1 for an indication of how accurate this is for the parameter space explored in Fig. 7.8). It is also possible that $\mathscr{A} \simeq 1$ occurs

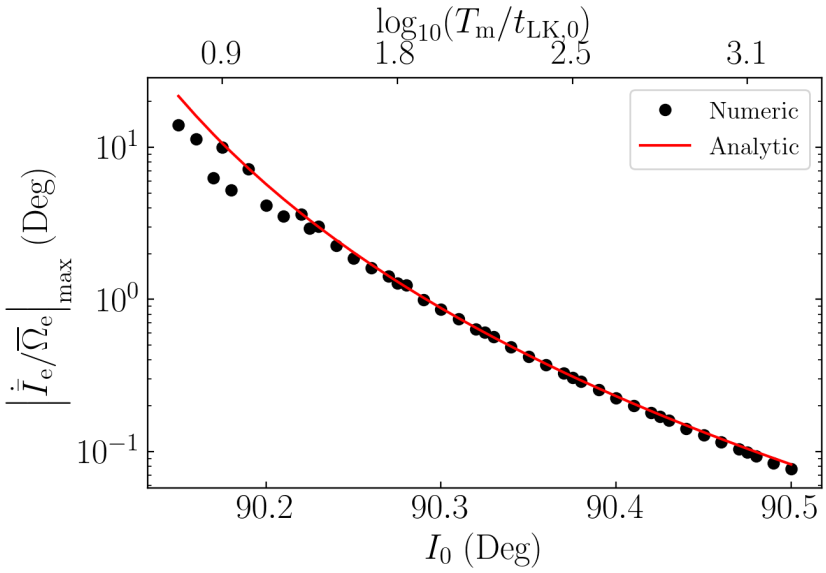

Figure 7.8: Comparison of $\left|\dot{\bar{I}}_e/\overline{\Omega}_e\right|_{max}$ obtained from simulations and from the analytical expression Eq. (7.52), where we take $f = 2.72$ in Eq. (7.49). The merger time T_m is shown along the top axis of the plot in units of the initial LK timescale $t_{LK,0}$. The agreement between the analytical and numerical results is excellent for $T_m \gg t_{LK,0}$.

when the eccentricity is still undergoing substantial oscillations. In fact, Eq. (7.52) remains accurate in this case when replacing e with $e_{\max}$, due to the following analysis. Recall that when $e_{\min} \ll e_{\max}$, the binary spends a fraction $\sim j(e_{\max})$ of the LK cycle near $e \simeq e_{\max}$. This fraction of the LK cycle dominates both GW dissipation and $\overline{\Omega}_{\rm e}$ precession. Thus, both $\dot{\bar{I}}_{\rm e}$ and $\overline{\Omega}_{\rm e}$ in the eccentricity-oscillating regime can be evaluated by setting $e \approx e_{\max}$ and multiplying by a prefactor of $j(e_{\max})$. This factor cancels when computing the quotient $|\dot{\bar{I}}_{\rm e}|/\overline{\Omega}_{\rm e}$.

The accuracy of Eq. (7.52) in bounding $\left|\Delta\bar{\theta}_{\rm e}\right|_{\rm f}$ is shown in Fig. 7.9, where we carry out simulations for a range of I_0, and for each I_0 we consider 100 different, isotropically distributed initial orientations for $\mathbf{S}$ (thus sampling a wide range of initial initial $\bar{\theta}_{\rm e}$). Note that conservation of $\bar{\theta}_{\rm e}$ is generally much better than Eq. (7.52) predicts. This is because cancellation of phases in Eq. (7.40) is generally more efficient than Eq. (7.52) assumes (recall that Eq. (7.41) only provides an estimate for the amplitude of "local" oscillations of $\bar{\theta}_{\rm e}$). Nevertheless, it is clear that Eq. (7.52) provides a robust upper bound of $\left|\Delta\bar{\theta}_{\rm e}\right|_{\rm f}$, and serves as a good indicator for the breakdown of adiabatic invariance.

7.4.4 Origin of the $\theta_{\rm sl,f} = 90^\circ$ Attractor

Using the approximate adiabatic invariant, we can now understand the origin of the $\theta_{\rm sl,f} = 90^\circ$ attractor as shown in Fig. 7.2.

Recall from Eq. (7.23)

$$\begin{aligned}\overline{\mathbf{\Omega}}_{\rm e} &= \overline{\Omega}_{\rm L}\hat{\mathbf{L}}_{\rm out} + \overline{\Omega_{\rm SL}\hat{\mathbf{L}}}, \\ &= \left(\overline{\Omega}_{\rm L} + \overline{\Omega}_{\rm SL}\cos\bar{I}\right)\hat{\mathbf{Z}} + \overline{\Omega}_{\rm SL}\sin\bar{I}\hat{\mathbf{X}}, \end{aligned} \tag{7.53}$$

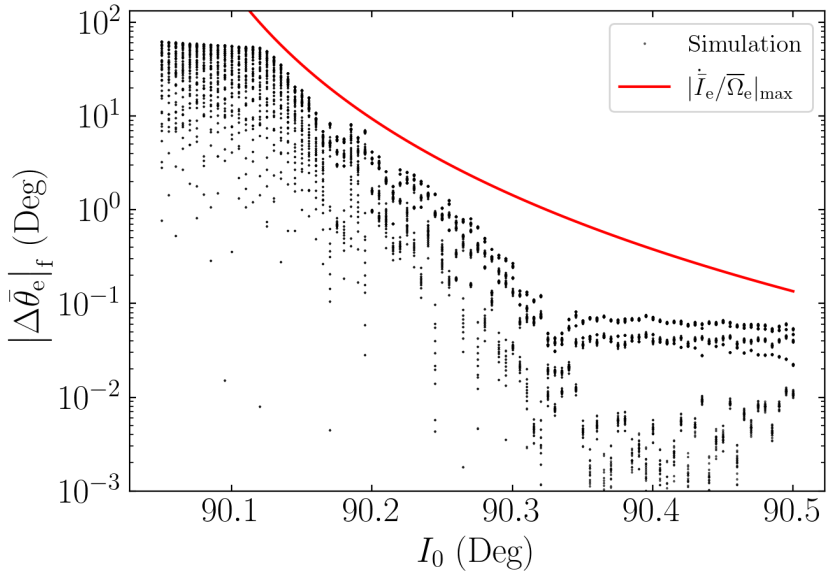

Figure 7.9: Net change in $\bar{\theta}_e$ over the binary inspiral as a function of initial inclination I_0. For each I_0, 100 simulations are run for **S** on a uniform, isotropic grid. Plotted for comparison is the bound $|\Delta\bar{\theta}_e|_f \lesssim \left|\dot{\bar{I}}_e/\overline{\Omega}_e\right|_{\max}$, using the analytical expression given by Eq. (7.52). It is clear that the expression provides a robust upper bound for the non-conservation of $\bar{\theta}_e$ due to nonadiabatic effects. Note that at the right of the plot, the numerical $|\Delta\bar{\theta}_e|_f$ saturates; this is because we compute the initial $\bar{\Omega}_e$ (in order to evaluate the initial $\bar{\theta}_e$) without GW dissipation, and such a procedure inevitably introduces fuzziness in $\bar{\theta}_e$.

where $\hat{\mathbf{Z}} = \hat{\mathbf{L}}_{\rm out}$ and $\hat{\mathbf{X}}$ is perpendicular to $\hat{\mathbf{Z}}$ in the $\hat{\mathbf{L}}_{\rm out}$–$\hat{\mathbf{L}}$ plane. Note that

$$\overline{\Omega}_{\rm L} \propto \frac{\cos\bar{I}}{t_{\rm LK}} \propto a^{3/2}\cos\bar{I}, \tag{7.54}$$

$$\overline{\Omega}_{\rm SL} \propto \frac{1}{a^{5/2}}. \tag{7.55}$$

Adiabatic invariance implies that $\bar{\theta}_{\rm e}$, the angle between $\mathbf{S}$ and $\overline{\mathbf{\Omega}}_{\rm e}$ is conserved between $t = 0$ and $t = t_{\rm f}$, i.e.

$$\bar{\theta}_{\rm e,f} \simeq \bar{\theta}_{\rm e,0}. \tag{7.56}$$

At $t = t_{\rm f}$, $\overline{\Omega}_{\rm SL} \gg \left|\overline{\Omega}_{\rm L}\right|$ and the spin-orbit misalignment angle $\theta_{\rm sl}$ is "frozen", implying $\overline{\mathbf{\Omega}}_{\rm e}$ is parallel to $\mathbf{L}$, and so $\bar{\theta}_{\rm e,f} = \theta_{\rm sl,f}$. Eq. (7.56) then gives

$$\theta_{\rm sl,f} \simeq \bar{\theta}_{\rm e,0}, \tag{7.57}$$

i.e. the final $\theta_{\rm sl}$ is determined by the initial angle between $\mathbf{S}$ and $\overline{\mathbf{\Omega}}_{\rm e}$.

Now, first consider the case where the initial spin $\mathbf{S}_0$ is aligned with the initial $\mathbf{L}_0$. This initial spin is inclined with respect to $\overline{\mathbf{\Omega}}_{\rm e}$ by $\bar{\theta}_{\rm e,0} = \left|I_0 - \bar{I}_{\rm e,0}\right|$, where I_0 is the initial inclination angle between $\mathbf{L}$ and $\mathbf{L}_{\rm out}$ and $\bar{I}_{\rm e,0}$ is the initial value of $\bar{I}_{\rm e}$. Thus, adiabatic invariance implies

$$\theta_{\rm sl,f} \simeq \left|I_0 - \bar{I}_{\rm e,0}\right|. \tag{7.58}$$

In the special case where the binary initially satisfies $\overline{\Omega}_{\rm SL} \ll \left|\overline{\Omega}_{\rm L}\right|$ or $|\mathscr{A}_0| \ll 1$, we find that $\overline{\mathbf{\Omega}}_{\rm e}$ is nearly parallel to $\mathbf{L}_{\rm out}$ (for $I_0 < 90^\circ$) or antiparallel to $\mathbf{L}_{\rm out}$ (for $I_0 > 90^\circ$). Thus,

$$\theta_{\rm sl,f} = \begin{cases} I_0 & I_0 < 90^\circ, \\ 180^\circ - I_0 & I_0 > 90^\circ. \end{cases} \tag{7.59}$$

Since LK-induced mergers necessarily require I_0 close to 90°, we find that $\theta_{\rm sl,f}$ is "attracted" to 90°.

Eq. (7.57) can be applied to more general initial spin orientations. For initial $|\mathscr{A}_0| \ll 1$ (as required for LK-induced mergers), $\overline{\Omega}_{\rm e,0}$ is parallel to $\pm\mathbf{L}_{\rm out}$. Suppose

the initial inclination between $\mathbf{S}$ and $\mathbf{L}_{\rm out}$ is $\theta_{\rm s,out,0}$, then $\bar{\theta}_{\rm e,0} = \theta_{\rm s,out,0}$ or $180^\circ - \theta_{\rm s,out,0}$ (depending on whether $I_0 < 90^\circ$ or $I_0 > 90^\circ$). Thus,

$$\theta_{\rm sl,f} \simeq \begin{cases} \theta_{\rm s,out,0} & I_0 < 90^\circ, \\ 180^\circ - \theta_{\rm s,out,0} & I_0 > 90^\circ, \end{cases} \tag{7.60}$$

[see also Yu et al., 2020a].

So far, we have analyzed the $\theta_{\rm sl,f}$ distribution for smooth mergers. Next, we can consider rapid mergers, for which $\bar{\theta}_{\rm e}$ conservation is imperfect. We expect

$$\left|\theta_{\rm sl,f} - \bar{\theta}_{\rm e,0}\right| \lesssim \left|\Delta\bar{\theta}_{\rm e}\right|_{\rm f}. \tag{7.61}$$

where $\left|\Delta\bar{\theta}_{\rm e}\right|_{\rm f}$ is given by Eq. (7.52). This is shown as the black dotted line in Fig. 7.2, and we see it predicts the maximum deviation of $\theta_{\rm sl,f}$ from $\sim 90^\circ$ except very near $I_0 = 90^\circ$. This is expected, as Eq. (7.52) is not very accurate very near $I_0 = 90^\circ$, where it diverges (see Fig. 7.9).

When $I_0 = 90^\circ$ exactly, Fig. 7.2 shows that $\theta_{\rm sl,f} = 0^\circ$. This can be understood: $I_0 = 90^\circ$ gives $\mathrm{d}I/\mathrm{d}t = 0$ by Eq. (7.6), so $I = 90^\circ$ for all time. This then yields $\mathrm{d}\mathcal{J}/\mathrm{d}t = 0$ [Eq. (7.5)], implying that $\mathbf{L}$ is constant. Thus, $\mathbf{L}$ is fixed as $\mathbf{S}$ precesses around it, and $\theta_{\rm sl}$ can never change. In Fig. 7.2, we take $\theta_{\rm sl,0} = 0$, so $\theta_{\rm sl,f} = 0$.

Finally, Fig. 7.2 shows that the actual $\theta_{\rm sl,f}$ are oscillatory within the envelope bounded by Eq. (7.61) above. This can also be understood: Eq. (7.42) only bounds the maximum of the absolute value of the change in $\bar{\theta}_{\rm e}$, while the actual change depends on the initial and final complex phases of $S_\perp$ in Eq. (7.40), denoted $\Phi(0)$ and $\Phi(t_{\rm f})$. When $\theta_{\rm sl,0} = 0$, we have $\Phi(0) = 0$, as $\mathbf{S}$ starts in the $\hat{\mathbf{x}}$-$\hat{\mathbf{z}}$ plane. Then, as I_0 is smoothly varied, the final phase $\Phi(t_{\rm f})$ must also vary smoothly [since $\overline{\Omega}_{\rm e}$ in Eq. (7.39) is a continuous function, $\Phi(t)$ must be as well], so the total phase difference between the initial and final values of $S_\perp$ varies smoothly. This means

the total change in $\bar{\theta}_{\rm e}$ will fluctuate smoothly between $\pm\left|\Delta\bar{\theta}_{\rm e}\right|_{\rm f}$ as I_0 is changed, giving rise to the sinusoidal shape seen in Fig. 7.2.

7.5 Analysis: Effect of Resonances

In the previous section, we have shown that the $\theta_{\rm sl,f}$ distribution in Fig. 7.2 and the "90° attractor" can be understood when neglecting the $N \geq 1$ Fourier harmonics in Eq. (7.25). In this section, we study the effects of these neglected terms and show that they have a negligible effect in LK-induced mergers. Separately, we will also consider the LK-enhanced regime and show that these Fourier harmonics play a dominant role in shaping the $\theta_{\rm sl,f}$ distribution.

For simplicity, we ignore the effects of GW dissipation in this section and assume the system is exactly periodic (so $\dot{\bar{I}}_{\rm e} = 0$). The scalar spin evolution equation Eq. (7.34) is then

$$\frac{{\rm d}S_\perp}{{\rm d}t} = i\overline{\Omega}_{\rm e} S_\perp + \sum_{N=1}^{\infty} \Big[\cos(\Delta I_{\rm eN}) S_\perp - i\cos\theta_{\rm e}\sin(\Delta I_{\rm eN}) \Big] \Omega_{\rm eN} \cos(N\Omega_{\rm LK} t). \tag{7.62}$$

7.5.1 Intuitive Analysis

We first restrict our attention to the effect of just the N-th Fourier harmonic, and Eq. (7.62) further simplifies to

$$\frac{{\rm d}S_\perp}{{\rm d}t} = \Big[i\overline{\Omega}_{\rm e} + \Omega_{\rm eN}\cos(\Delta I_{\rm eN})\cos(N\Omega_{\rm LK} t) \Big] S_\perp - i\Omega_{\rm eN}\cos\bar{\theta}_{\rm e}\sin(\Delta I_{\rm eN})\cos(N\Omega_{\rm LK} t). \tag{7.63}$$

There are two time-dependent perturbations, a modulation of the oscillation frequency (the term proportional to $S_\perp$ on the right-hand side) and a driving term. We can begin to understand the dynamics of $S_\perp$ by considering the effect of each of these two terms separately.

First, we consider the effect of frequency modulation alone. The equation of motion is

$$\frac{\mathrm{d}S_\perp}{\mathrm{d}t} \approx \left[i\overline{\Omega}_\mathrm{e} + \Omega_\mathrm{eN} \cos(\Delta I_\mathrm{eN}) \cos(N\Omega_\mathrm{LK} t) \right] S_\perp. \tag{7.64}$$

The exact solution is

$$S_\perp(t) = S_\perp(0) \exp\left[i\overline{\Omega}_\mathrm{e} t + \frac{\Omega_\mathrm{eN} \cos(\Delta I_\mathrm{eN})}{N\Omega_\mathrm{LK}} \sin(N\Omega_\mathrm{LK} t) \right]. \tag{7.65}$$

There is no combination of parameters for which the magnitude of $S_\perp$ diverges, so the modulation of the oscillation frequency does not cause any resonant behavior.

When considering only the time-dependent driving term instead, the equation of motion is

$$\frac{\mathrm{d}S_\perp}{\mathrm{d}t} \approx i\overline{\Omega}_\mathrm{e} S_\perp - i\Omega_\mathrm{eN} \cos\theta_\mathrm{e} \sin(\Delta I_\mathrm{eN}) \cos(N\Omega_\mathrm{LK} t). \tag{7.66}$$

We can approximate $\cos(N\Omega_\mathrm{LK} t) \approx e^{iN\Omega_\mathrm{LK} t}/2$, as the $e^{-iN\Omega_\mathrm{LK} t}$ component is always farther from resonance (as $\Omega_\mathrm{LK}, \overline{\Omega}_\mathrm{e} > 0$). Then the equation of motion has the solution

$$e^{-i\overline{\Omega}_\mathrm{e} t} S_\perp \Big|_0^t = -\int_0^t \frac{i\Omega_\mathrm{eN} \sin(\Delta I_\mathrm{eN})}{2} e^{-i\overline{\Omega}_\mathrm{e} t + iN\Omega_\mathrm{LK} t} \cos\theta_\mathrm{e} \, \mathrm{d}t. \tag{7.67}$$

Since $|S_\perp| = \sin\theta_\mathrm{e}$, the instantaneous oscillation amplitude $|\Delta\theta_\mathrm{e}|$ can be bound by

$$|\Delta\theta_\mathrm{e}| \sim \frac{1}{2} \left| \frac{\Omega_\mathrm{eN} \sin(\Delta I_\mathrm{eN})}{\overline{\Omega}_\mathrm{e} - N\Omega_\mathrm{LK}} \right|. \tag{7.68}$$

Thus, we see that large oscillation amplitudes in $\bar{\theta}_\mathrm{e}$ occur when $\overline{\Omega}_\mathrm{e} \approx N\Omega_\mathrm{LK}$, the frequency of the N-th Fourier harmonic.

7.5.2 General Solution

Single Fourier Harmonic

Above, we began the analysis of Eq. (7.63) by considering the two time-dependent perturbations separately. However, this is not necessary. Eq. (7.63) can be solved exactly:

$$\begin{aligned} e^{-i\Phi} S_\perp \Big|_0^t &= -i\Omega_{\mathrm{eN}} \cos\bar{\theta}_{\mathrm{e}} \sin\Delta I_{\mathrm{eN}} \int_0^t \cos(N\Omega\tau)\, e^{-i\Phi(\tau)}\, \mathrm{d}\tau, \\ &= iA \left[e^{-i\Phi}\Big|_0^t + i\overline{\Omega}_{\mathrm{e}} \int_0^t e^{-i\Phi(\tau)}\, \mathrm{d}\tau \right]. \end{aligned} \tag{7.69}$$

where $A = -\tan\Delta I_{\mathrm{eN}} \cos\bar{\theta}_{\mathrm{e}}$, and

$$\begin{aligned} i\Phi(t) &\equiv \int i\overline{\Omega}_{\mathrm{e}} + \Omega_{\mathrm{eN}} \cos(N\Omega_{\mathrm{LK}}\tau) \cos(\Delta I_{\mathrm{eN}})\, \mathrm{d}\tau, \\ &\equiv i\overline{\Omega}_{\mathrm{e}} t + \eta \sin(N\Omega_{\mathrm{LK}} t), \end{aligned} \tag{7.70}$$

where $\eta \equiv (\Omega_{\mathrm{eN}} \cos\Delta I_{\mathrm{eN}})/(N\Omega_{\mathrm{LK}})$. Eq. (7.69) shows that $|S_\perp|$ is bounded for all t unless the integral $\mathscr{I}(x)$, given by

$$\mathscr{I}(x) = \int_0^x e^{-i\xi - \eta\sin(\beta\xi)}\, \mathrm{d}\xi, \tag{7.71}$$

grows without bound as $x \to \infty$, where $x = \overline{\Omega}_{\mathrm{e}} t$ and $\beta = N\Omega_{\mathrm{LK}}/\overline{\Omega}_{\mathrm{e}}$.

To see where $\mathscr{I}(x)$ grows without bound, we rewrite

$$\mathscr{I}(x) = \sum_{k=0}^{\infty} \int_0^x (\cos\xi + i\sin\xi) \frac{\left(-\eta\sin\left(\beta\xi\right)\right)^k}{k!}\, \mathrm{d}\xi. \tag{7.72}$$

These $\sin^k\left(\beta\xi\right)$ terms can be expanded using the general trigonometric power-reduction identities [Zwillinger, 2003]:

$$\sin^{2n} y = \frac{1}{2^{2n}} \binom{2n}{n} + \frac{(-1)^n}{2^{2n-1}} \sum_{l=0}^{n-1} (-1)^l \binom{2n}{l} \cos[2(n-l)y], \tag{7.73}$$

$$\sin^{2n+1} y = \frac{(-1)^n}{4^n} \sum_{l=0}^{n} (-1)^l \binom{2n+1}{l} \sin[(2n+1-2l)y]. \tag{7.74}$$

Due to the orthogonality relations among the trigonometric functions, $\mathscr{I}(x)$ only grows without bound if $\sin^k(\beta\xi)$ contains a $\cos\xi$ or $\sin\xi$ term. Eqs. (7.73) and (7.74) show that $\sin^k\left(\beta\xi\right)$ only contains a term with unit frequency if $\beta = 1/q$ for some integer $q \geq 1$. When this is the case, all terms with $k \geq q$ in Eq. (7.72) contain a term with unit frequency. Among these terms, the $\sin^q\left(\beta\xi\right)$ term has the largest prefactor. Neglecting the other terms with $k > q$, we can evaluate $\mathscr{I}$ for any integer multiple m of its period $2\pi q$ to be

$$|\mathscr{I}(2\pi mq)| \approx 2\pi mq\left(\frac{\eta^q}{2^q q!}\right). \tag{7.75}$$

Within each period, $\mathscr{I}(x)$ has additional oscillatory behavior due to the other, off-resonance terms in Eq. (7.72). However, these oscillations are periodic and vanish at every $x = 2\pi mq$, so they are bounded and do not affect the divergence in Eq. (7.75). We conclude that $\mathscr{I}(x)$ grows without bound when $\beta = 1/q$, or

$$\overline{\Omega}_{\mathrm{e}} = Nq\Omega_{\mathrm{LK}}. \tag{7.76}$$

We see that this differs from the result of the intuitive analysis [Eq. (7.68)], as the N-th Fourier harmonic generates infinitely many resonances indexed by $q \geq 1$.

Instead, if β is near but not on a resonance, i.e. $0 < \left|1 - q\beta\right| \ll 1$, the amplitude of oscillation of $\mathscr{I}(x)$ is large but bounded. If we take q to be even, then the maximum value of $|\mathscr{I}(x)|$ is dominated by the near-resonance term in Eq. (7.72),

$$\begin{aligned} |\mathscr{I}(x)| &\simeq \left|\int_0^x \cos\xi \frac{\eta^q}{q!}\frac{1}{2^{q-1}}\cos\left(q\beta\xi\right)\,\mathrm{d}\xi\right| \\ &\leq \frac{|\eta|^q}{2^q q!}\frac{1}{\left|1-q\beta\right|}. \end{aligned} \tag{7.77}$$

If q is instead odd, we use Eq. (7.74) instead of Eq. (7.73) and integrate against $i\sin\xi$ instead of $\cos\xi$ in Eq. (7.72), which results in the same bound on the oscillation amplitude. Returning to Eq. (7.69), we neglect the first, bounded term

($\lesssim e^{\eta} \simeq 1$) on the right-hand side and obtain the total oscillation amplitude due to a q-th order resonance with the N-th Fourier harmonic

$$\left|\Delta\bar{\theta}_{\rm e}\right|_{Nq} \sim \frac{1}{2^q q!}\left|\tan\Delta I_{\rm eN}\left[\frac{\Omega_{\rm eN}\cos(\Delta I_{\rm eN})}{N\Omega_{\rm LK}}\right]^q\left(\frac{\overline{\Omega}_{\rm e}}{\overline{\Omega}_{\rm e}-qN\Omega_{\rm LK}}\right)\right|. \tag{7.78}$$

Since $\overline{\Omega}_{\rm e}/N\Omega_{\rm LK} \approx q$, this reduces to Eq. (7.68) when $q = 1$, as expected.

Generalization to Multiple Fourier Harmonics

After having understood the effect of a single Fourier harmonic, we now return to the spin evolution equation containing all of the Fourier harmonics [Eq. (7.62)]. If $\overline{\Omega}_{\rm e}/\Omega_{\rm LK} \approx M$, there can now be multiple N and q satisfying $Nq = M$. By linearity, the total $\left|\Delta\bar{\theta}_{\rm e}\right|$ is given by the sum over all of the resonances, so that

$$\left|\Delta\bar{\theta}_{\rm e}\right| \approx \sum_{N,q|Nq=M}\left|\Delta\bar{\theta}_{\rm e}\right|_{Nq}, \tag{7.79}$$

where $\left|\Delta\bar{\theta}_{\rm e}\right|_{Nq}$ is given by Eq. (7.78).

We next attempt to understand whether particular combinations of N and q dominate this sum. We make a few simplifying assumptions: (i) all N harmonics are approximately equal[2], (ii) $\Omega_{\rm eN} \sim \overline{\Omega}_{\rm e}$ and $\cos\Delta I_{\rm eN} \simeq 1$ (e.g. Figs. 7.5 and 7.6). Under these assumptions, $\left|\Delta\bar{\theta}_{\rm e}\right|_{Nq}$ with fixed $Nq = M$ scales with respect to q as

$$\left|\Delta\bar{\theta}_{\rm e}\right|_{Nq} \propto \frac{\cos^q(\Delta I_{\rm eN})\,q^q}{2^q q!}. \tag{7.80}$$

Stirling's formula then suggests that $\left|\Delta\bar{\theta}_{\rm e}\right|_{Nq} \propto (\cos(\Delta I_{\rm eN})e/2)^q/\sqrt{q} \sim 1$. Thus, we conclude that all combinations of N and q satisfying $Nq = M$ result in comparable oscillation amplitudes. For simplicity, we evaluate this amplitude for $q = 1$ and $N = M$. If we denote the number of pairs of N and q satisfying $Nq = M$ by $d(M)$

[2]This approximation is suitable for the problem studied in the main text because the only characteristic frequency scale is $j_{\rm min}^{-1} \gg 1$, so all Fourier harmonics $\mathbf{\Omega}_{\rm eN}$ for $N \lesssim j_{\rm min}^{-1}$ are similar.

(the number of positive divisors of M), we can approximate Eq. (7.79) by:

$$\begin{aligned}\left|\Delta\bar{\theta}_{\rm e}\right| &\approx d(M)\left|\Delta\bar{\theta}_{\rm e}\right|_{M1} \\ &\sim \frac{d(M)}{2}\left|\frac{\Omega_{\rm eM}\sin(\Delta I_{\rm eM})}{\overline{\Omega}_{\rm e}-M\Omega_{\rm LK}}\right|,\end{aligned} \tag{7.81}$$

Note that this agrees with Eq. (7.68) except for the factor of $d(M)$. Appendix F.1.3 demonstrates that Eq. (7.81) is in good agreement with detailed numerical simulations when $M = 1$ or $M = 2$, the two most relevant cases for our study.

7.5.3 Effect of Resonances in LK-Induced Mergers

We first consider the effect of these resonances ($\bar{\Omega}_{\rm e} = M\Omega_{\rm LK}$) on the LK-induced regime, using the fiducial parameters (as in Figs. 7.1 and 7.2). Numerically, we find that $\overline{\Omega}_{\rm e} < \Omega_{\rm LK}$ for the region of parameter space relevant to LK-induced mergers (see Fig. 7.10), so we focus on the effect of the $M = 1$ resonance. If, for the entire inspiral, $\overline{\Omega}_{\rm e} < \Omega_{\rm LK}$ by a sufficient margin that Eq. (7.81) remains small, then the conservation of $\bar{\theta}_{\rm e}$ cannot be significantly affected by this resonance. For the fiducial simulation, Fig. 7.5 shows the ratio $\overline{\Omega}_{\rm e}/\Omega_{\rm LK}$ in the middle panel (black) and the amplitude of oscillation of $\bar{\theta}_{\rm e}$ due to the $M = 1$ resonance [Eq. (7.81)] in the bottom panel (blue). We see that the system is never close to the resonant condition $\overline{\Omega}_{\rm e}/\Omega_{\rm LK} = 1$, and as a result the net effect of the resonance never exceeds a few degrees.

For a more precise comparison, the bottom-rightmost panel of Fig. 7.6 compares $\left|\Delta\bar{\theta}_{\rm e}\right|$ in the fiducial simulation to the expected contributions from nonadiabatic [Eq. (7.41)] and resonant [Eq. (7.81) for $M = 1$] effects in the regime where $\mathscr{A} \simeq 1$. We see that Eq. (7.81) for $M = 1$ describes the oscillations in $\bar{\theta}_{\rm e}$ very well. The agreement is poorer in the bottom-rightmost panel of Fig. 7.7, as the nonadiabatic effect is comparatively stronger.

It is somewhat surprising that the contribution of the resonances to the instantaneous $\left|\Delta\bar{\theta}_{\rm e}\right|$ when $\mathscr{A} \simeq 1$ is dominant over that of the nonadiabatic contribution. In Section 7.4, we have shown that neglecting resonant terms still allows for an accurate prediction of the final $\bar{\theta}_{\rm e}$ deviation [Eq. (7.52)]. This implies that, while the resonances have a larger contribution to $\left|\Delta\bar{\theta}_{\rm e}\right|$, the nonadiabatic effect is more important in determining $\left|\Delta\bar{\theta}_{\rm e}\right|_{\rm f}$. This also requires that a $\left|\Delta\bar{\theta}_{\rm e}\right|$ of up to a few degrees due to resonant effects not affect $\left|\Delta\bar{\theta}_{\rm e}\right|_{\rm f}$ by more than $\sim 0.01^\circ$. This differs from the nonadiabatic case, where we find $\left|\Delta\bar{\theta}_{\rm e}\right|_{\rm f} \sim \max\left|\Delta\bar{\theta}_{\rm e}\right|$. The origin of these differences in behaviors may be due to the complex phases cancelling differently in Eqs. (7.40) and (7.69) as the BH binary coalesces.

7.5.4 Effect of Resonances in LK-Enhanced Mergers

We turn now to the case of LK-enhanced mergers, as was studied in LL17, where the inner binary is sufficiently compact (~ 0.1 AU) that it can merge in isolation via GW radiation. We consider a set of parameters that has the same $t_{\rm LK,0}$ as the system studied in LL17 but has a tertiary SMBH: $m_1 = m_2 = 30M_\odot$, $a_0 = 0.1$ AU, $e_0 = 10^{-3}$, $m_3 = 3\times10^7 M_\odot$, $\tilde{a}_{\rm out} = 300$ AU, and $e_{\rm out} = 0$. We show that the resonances studied above play an important role in shaping the $\theta_{\rm sl,f}$ distribution for this regime.

First, we illustrate the $\theta_{\rm sl,f}$ distribution obtained via numerical simulation, shown as the blue dots in Fig. 7.11. The prediction assuming adiabatic invariance (i.e. the conservation of $\bar{\theta}_{\rm e}$) is shown in the red solid line. Good agreement is observed both when no eccentricity excitation occurs ($I_0 \lesssim 50^\circ$ and $I_0 \gtrsim 130^\circ$) and when $|\mathscr{A}| \gg 1$ ($80^\circ \lesssim I_0 \lesssim 100^\circ$). However, we see in Fig. 7.11 that for intermediate inclinations, $I_0 \in [50, 80]$ and $I_0 \in [100, 130]$, $\theta_{\rm sl,f}$ varies over a large range and

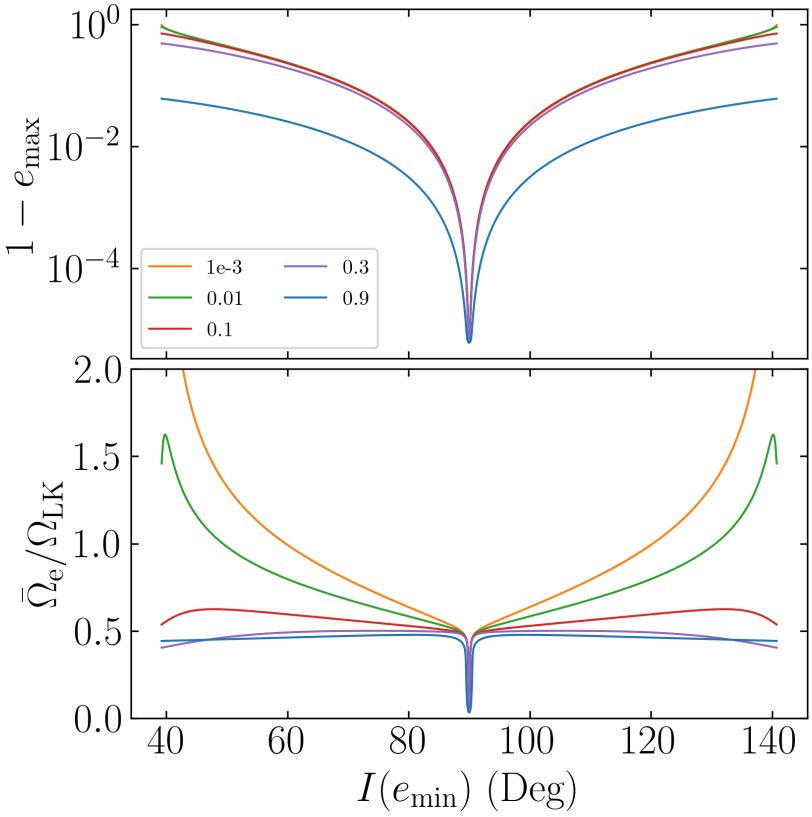

Figure 7.10: $e_{\rm max}$ and $\overline{\Omega}_{\rm e}/\Omega_{\rm LK}$ as a function of $I(e_{\rm min})$, the inclination of the inner binary at eccentricity minimum, for varying values of $e_{\rm min}$ (different colors as labeled) for a LK-induced merger (with the parameters the same as in Figs. 7.1 and 7.2). In this case, only systems with I_0 close to 90° will merge within a Hubble time, $I(e_{\rm min}) \sim 90°$ for most of the evolution (see Fig. 7.1) until $e_{\rm min} \approx 1$ is satisfied. This plot shows that $\overline{\Omega}_{\rm e} \lesssim 0.5\Omega_{\rm LK}$ is a general feature of LK-induced mergers, as is the case for the fiducial simulation (see Fig. 7.5).

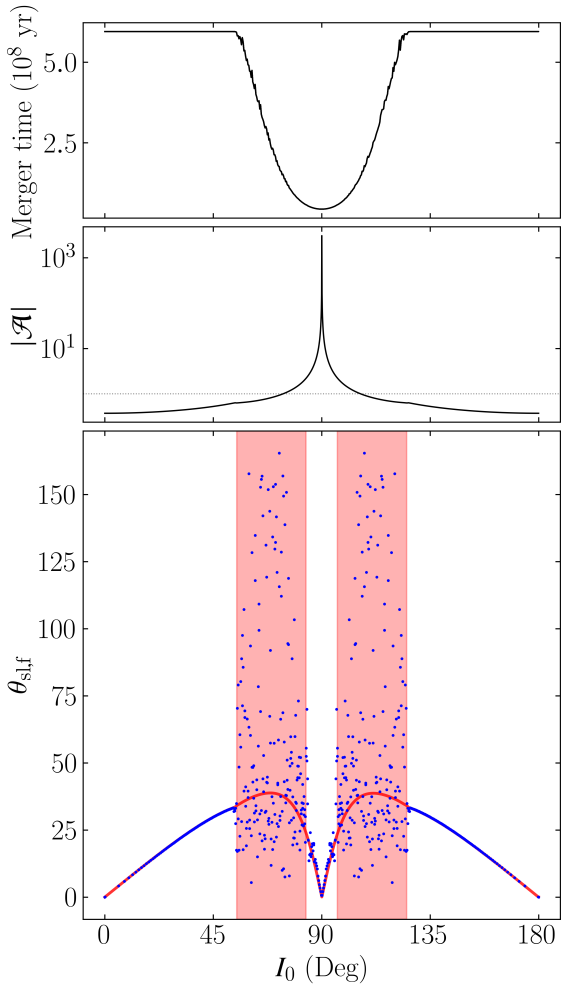

Figure 7.11: The merger time (top), the magnitude of the initial adiabaticity parameter $|\mathcal{A}| \equiv \overline{\Omega}_{\rm SL}/|\overline{\Omega}_{\rm L}|$ (middle), and the final spin-orbit misalignment angle $\theta_{\rm sl,f}$ (bottom) for LK-enhanced mergers, with $m_1 = m_2 = 30M_\odot$, $m_3 = 3\times10^7 M_\odot$, $a_0 = 0.1$ AU, $e_0 = 10^{-3}$, $\tilde{a}_{\rm out} = 300$ AU, and $e_{\rm out} = 0$. In the middle panel, the horizontal dashed line indicates $|\mathcal{A}| = 1$. In the bottom panel, the blue dots denote results from numerical simulations with $\theta_{\rm sl,0} = 0$ [these are symmetric about $I_0 = 90°$, as the equations of motion (7.3–7.7) are as well]. The prediction for $\theta_{\rm sl,f}$ assuming conservation of $\bar{\theta}_{\rm e}$ is shown as the red line, which agrees well with the data both when there is no eccentricity excitation ($I_0 \lesssim 50°$ and $I_0 \gtrsim 130°$) and when $|\mathcal{A}| \gg 1$. For a substantial range of intermediate inclinations ($I_0 \in [50°, 80°]$ and $I_0 \in [100°, 130°]$), $\theta_{\rm sl,f}$ is significantly affected by the resonances as they evolve (see Fig. 7.12). As such, these initial inclinations are expected to give rise to a wide range of $\theta_{\rm sl,f}$, and we denote this with broad red shaded regions.

does not agree with the prediction of $\bar{\theta}_e$ conservation. Note that these inclinations correspond to neither the fastest nor slowest merging systems.

We attribute the origin of this wide scatter to resonance interactions. Figure 7.12 illustrates that for these intermediate inclinations, the condition $\overline{\Omega}_e \sim \Omega_{LK}$ is satisfied. In addition, as the inner binary coalesces under GW radiation, e_{min} becomes larger (e.g. see Fig. 7.1). This causes the locations of the resonances at inclinations less than (greater than) $I = 90^\circ$ to evolve to smaller (larger) inclinations. As the location of the resonances is a sensitive function of e_{min}, resonance passage is nonadiabatic. Thus, we expect that all systems that encounter the resonance, i.e. all systems with intermediate initial inclinations, will experience an impulsive kick to $\bar{\theta}_e$, resulting in poor $\bar{\theta}_e$ conservation. This result is denoted by the two red shaded regions in Fig. 7.11.

While the outer edges of the red shaded regions described above are located at the critical I_0 required for nonzero eccentricity excitation, the inner edges are harder to characterize. Systems with initial inclinations close to 90° start at the edge of the $M = 1$ resonance and quickly evolve away from it (as e_{min} increases and a decreases). As such, they only interact briefly and weakly with the resonances, and the cumulative effect of the resonance interaction can be estimated by evaluating Eq. (7.81) for $M = 1$ at the initial conditions. We empirically choose the transition between such "weakly" and "strongly" resonant systems, i.e. the inner edge of the broad red shaded region in Fig. 7.11, when the oscillation semi-amplitude $\left|\Delta\bar{\theta}_e\right|$ predicted by Eq. (7.81) exceeds 3°.

To understand the general characteristics of systems that interact strongly with resonances, we examine the quantities in Eq. (7.81):

- $\sin(\Delta I_{eN})$ is small unless $\mathscr{A} \simeq 1$. Otherwise, $\mathbf{\Omega}_e$ does not nutate substan-

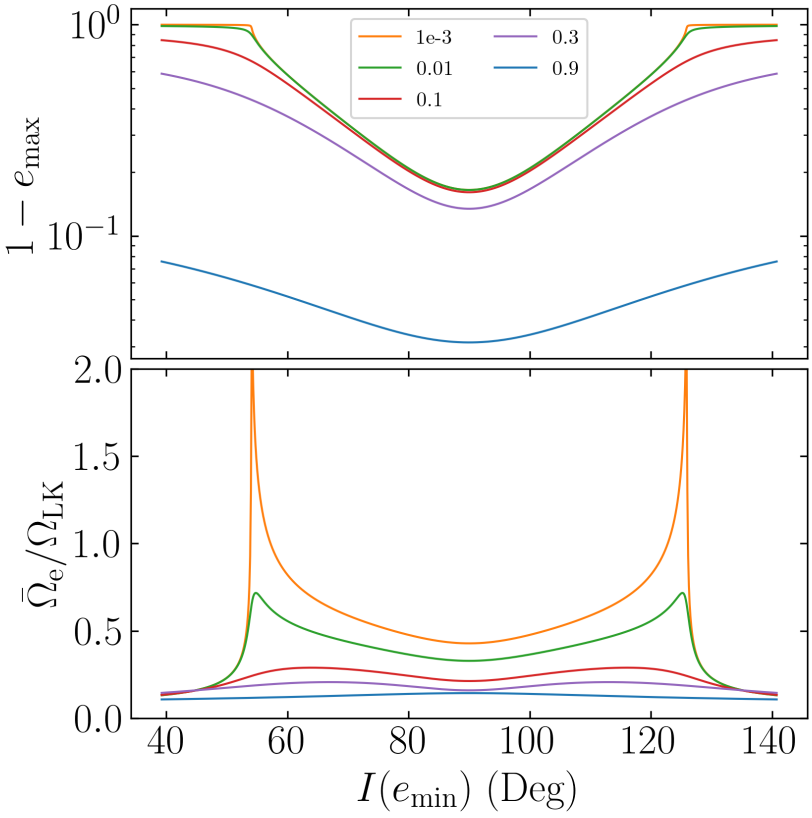

Figure 7.12: Same as Fig. 7.10, but for a LK-enhanced merger (with the parameters of Fig. 7.11). In the LK-enhanced regime, all initial inclinations merge within a Hubble time, and it is clear that $\overline{\Omega}_e \approx \Omega_{LK}$ can be satisfied for a wide range of initial inclinations when the initial eccentricity is sufficiently small.

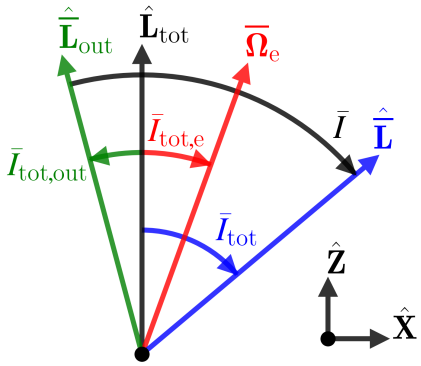

Figure 7.13: Definition of angles in the case where $L/L_{\rm out}$ is nonzero. Similar to before, we choose the convention where $I_{\rm tot,e} \in [0°, 90°]$ when $\overline{\Omega}_{\rm L} > 0$ and $I_{\rm tot,e} \in [90°, 180°]$ when $\overline{\Omega}_{\rm L} < 0$. Here, $\mathbf{L}_{\rm out}$ is not fixed, but $\mathbf{L}_{\rm tot} \equiv \mathbf{L} + \mathbf{L}_{\rm out}$ is. Note that the coordinate system is now oriented with $\hat{\mathbf{Z}} \propto \mathbf{L}_{\rm tot}$.

tially within a LK cycle, and all the $\mathbf{\Omega}_{\rm eN}$ are aligned with $\overline{\mathbf{\Omega}}_{\rm e}$ which implies that the $\Delta I_{\rm eN} \approx 0$ for all $N \geq 1$.

- Smaller values of $e_{\rm min}$ increase $\overline{\Omega}_{\rm e}/\Omega_{\rm LK}$, as shown in Fig. 7.12.

However, the timescales over which $\mathscr{A}$ increases and $e_{\rm min}$ decreases are comparable (see Fig. 7.1). This implies that, if $\mathscr{A} \ll 1$ initially, which is the case for LK-induced mergers, then $e_{\rm min}$ will be very close to unity when $\mathscr{A}$ grows to be $\simeq 1$, and the contribution predicted by Eq. (7.81) will remain small throughout the entire evolution. On the other hand, only if $\mathscr{A} \simeq 1$ and $e_{\rm min} \ll 1$ initially, as is the case for the intermediate inclinations in the LK-enhanced regime, are resonant interactions likely to be significant.

7.6 Stellar Mass Black Hole Triples

In this section, we extend our predictions for the final spin-orbit misalignment angle $\theta_{\rm sl,f}$ to systems where all three masses are comparable and the ratio of the

angular momenta of the two binaries, given by

$$\eta \equiv \left.\frac{L}{L_{\rm out}}\right|_{e=e_{\rm out}=0} = \frac{\mu}{\mu_{\rm out}}\left[\frac{m_{12}a}{m_{123}a_{\rm out}}\right]^{1/2}, \tag{7.82}$$

where $m_{123} = m_{12} + m_3$ and $\mu_{\rm out} = m_{12}m_3/m_{123}$, is not negligible. When $\eta \neq 0$, $\mathbf{L}_{\rm out}$ is no longer fixed, but the total angular momentum $\mathbf{L}_{\rm tot} \equiv \mathbf{L} + \mathbf{L}_{\rm out}$ is fixed. We choose the coordinate system with $\hat{\mathbf{Z}} = \hat{\mathbf{L}}_{\rm tot}$, shown in Fig. 7.13.

To analyze this system, we still assume $e_{\rm out} \ll 1$ so that the octupole-order effects are negligible. To calculate the evolution of $\mathbf{L}$, it is only necessary to evolve the orbital elements of the inner binary [a, e, Ω, $I_{\rm tot}$ (its inclination relative to $\hat{\mathbf{L}}_{\rm tot}$), and ω] and a single orbital element for the outer binary, its inclination $I_{\rm tot,out}$ relative to $\hat{\mathbf{L}}_{\rm tot}$. The equations of motion are given by [Liu et al., 2015a]:

$$\frac{{\rm d}a}{{\rm d}t} = \left(\frac{{\rm d}a}{{\rm d}t}\right)_{\rm GW}, \tag{7.83}$$

$$\frac{{\rm d}e}{{\rm d}t} = \frac{15}{8t_{\rm LK}} e\, j(e) \sin 2\omega \sin^2 I + \left(\frac{{\rm d}e}{{\rm d}t}\right)_{\rm GW}, \tag{7.84}$$

$$\frac{{\rm d}\Omega}{{\rm d}t} = \frac{L_{\rm tot}}{L_{\rm out}} \frac{3}{4t_{\rm LK}} \frac{\cos I\left(5e^2\cos^2\omega - 4e^2 - 1\right)}{j(e)}, \tag{7.85}$$

$$\frac{{\rm d}I_{\rm tot}}{{\rm d}t} = -\frac{15}{16t_{\rm LK}} \frac{e^2 \sin 2\omega \sin 2I}{j(e)}, \tag{7.86}$$

$$\frac{{\rm d}I_{\rm tot,out}}{{\rm d}t} = -\eta \frac{15}{8t_{\rm LK}}\left(e^2 \sin 2\omega \sin I\right), \tag{7.87}$$

$$\frac{{\rm d}\omega}{{\rm d}t} = \frac{3}{t_{\rm LK}}\left\{\frac{4\cos^2 I + (5\cos(2\omega) - 1)(1 - e^2 - \cos^2 I)}{8j(e)} + \frac{\eta\cos I}{8}\left[2 + e^2(3 - 5\cos(2\omega))\right]\right\} + \Omega_{\rm GR}, \tag{7.88}$$

where $I = I_{\rm tot} + I_{\rm tot,out}$ is the relative inclination between the two angular momenta. The spin evolution of one of the inner BHs is then described in the frame corotating with $\mathbf{L}$ about $\mathbf{L}_{\rm tot}$ by the equation of motion

$$\left(\frac{{\rm d}\mathbf{S}}{{\rm d}t}\right)_{\rm rot} = \mathbf{\Omega}_{\rm e} \times \mathbf{S}, \tag{7.89}$$

where

$$\mathbf{\Omega}_{\rm e} \equiv \Omega_{\rm SL}\hat{\mathbf{L}} + \Omega_{\rm L}\hat{\mathbf{L}}_{\rm tot}. \tag{7.90}$$

where $\Omega_{\rm L} = -{\rm d}\wp/{\rm d}t$ [Eq. (7.85)] is the rate of precession of $\mathbf{L}$ about $\mathbf{L}_{\rm tot}$. As in Section 7.4, we consider the LK-averaged $\boldsymbol{\Omega}_{\rm e}$ and neglect the harmonic terms:

$$\left(\frac{{\rm d}\overline{\mathbf{S}}}{{\rm d}t}\right)_{\rm rot} = \overline{\boldsymbol{\Omega}}_{\rm e} \times \overline{\mathbf{S}}, \tag{7.91}$$

where

$$\begin{aligned}\overline{\boldsymbol{\Omega}}_{\rm e} &= \overline{\Omega_{\rm SL}\sin I_{\rm tot}}\hat{\mathbf{X}} + \left(\overline{\Omega}_{\rm L} + \overline{\Omega_{\rm SL}\cos I_{\rm tot}}\right)\hat{\mathbf{Z}} \\ &\equiv \overline{\Omega}_{\rm SL}\sin\bar{I}_{\rm tot}\hat{\mathbf{X}} + \left(\overline{\Omega}_{\rm L} + \overline{\Omega}_{\rm SL}\cos\bar{I}_{\rm tot}\right)\hat{\mathbf{Z}}.\end{aligned} \tag{7.92}$$

The results of Section 7.4 suggest that the angle $\bar{\theta}_{\rm e}$ is an adiabatic invariant, where $\bar{\theta}_{\rm e}$ is given by

$$\cos\bar{\theta}_{\rm e} \equiv \frac{\overline{\boldsymbol{\Omega}}_{\rm e}}{\overline{\Omega}_{\rm e}} \cdot \overline{\mathbf{S}}, \tag{7.93}$$

where $\overline{\mathbf{S}}$ is the spin vector averaged over a LK cycle. The orientation of $\overline{\boldsymbol{\Omega}}_{\rm e}$ is described by the inclination angle $\bar{I}_{\rm tot,e}$ (Fig. 7.13), which can be expressed using Eq. (7.92)

$$\tan\bar{I}_{\rm tot,e} = \frac{\mathscr{A}\sin\bar{I}_{\rm tot}}{1+\mathscr{A}\cos\bar{I}_{\rm tot}}, \tag{7.94}$$

where $\mathscr{A} \equiv \overline{\Omega}_{\rm SL}/\overline{\Omega}_{\rm L}$ is the adiabaticity parameter.

At $t = t_{\rm f}$, the inner binary is sufficiently compact that $\theta_{\rm sl}$ is frozen (see bottom right panel of Fig. 7.1), and the system satisfies $\mathscr{A} \gg 1$ ($\overline{\Omega}_{\rm SL} \propto a^{-5/2}$ while $\overline{\Omega}_{\rm L} \propto a^{3/2}$). When this is the case, $\overline{\boldsymbol{\Omega}}_{\rm e} \parallel \mathbf{L}$, and so $\bar{\theta}_{\rm e,f} = \theta_{\rm sl,f}$. Then, since adiabatic invariance implies $\bar{\theta}_{\rm e,f} = \bar{\theta}_{\rm e,0}$,

$$\theta_{\rm sl,f} = \bar{\theta}_{\rm e,0}. \tag{7.95}$$

We first consider the case where $\mathbf{S}_0 \propto \mathbf{L}_0$. Then $\bar{\theta}_{\rm e,0} = \left|I_{\rm tot,0} - \bar{I}_{\rm tot,e,0}\right|$ (see Fig. 7.13), and so

$$\theta_{\rm sl,f} = \left|I_{\rm tot,0} - \bar{I}_{\rm e,0}\right|. \tag{7.96}$$

Suppose additionally that the binary initially satisfies $|\overline{\Omega}_{\rm L}| \gg \overline{\Omega}_{\rm SL}$, then $\overline{\mathbf{\Omega}}_{\rm e}$ is either parallel or anti-parallel to $\mathbf{L}_{\rm tot}$ depending on whether $\overline{\Omega}_{\rm L}$ is positive or negative. We denote the starting mutual inclination for which $\overline{\Omega}_{\rm L}$ changes sign by $I_{\rm c}$. Note that $I_{\rm c} > 90^\circ$: even though $\Omega_{\rm L}$ changes sign at $I_0 = 90^\circ$, the inclination decreases over a LK cycle for $I < I_{\rm lim}$ (where $I_{\rm lim} > 90^\circ$ is the starting mutual inclination that maximizes $e_{\rm max}$ [Liu and Lai, 2018]), so the sign of $\Omega_{\rm L}$ changes over a LK cycle for some $I_{\rm c} \in (90^\circ, I_{\rm lim})$. We then obtain that

$$\theta_{\rm sl,f} = \begin{cases} I_{\rm tot,0}, & I_0 < I_{\rm c}, \\ 180^\circ - I_{\rm tot,0}, & I_0 > I_{\rm c}. \end{cases} \tag{7.97}$$

More generally, so long as $\mathscr{A} \ll 1$ initially, we can specify the initial spin orientation by $\theta_{\rm s,tot,0}$, the initial angle between $\mathbf{S}$ and $\mathbf{L}_{\rm tot}$, giving

$$\theta_{\rm sl,f} = \begin{cases} \theta_{\rm s,tot,0}, & I < I_{\rm c}, \\ 180^\circ - \theta_{\rm s,tot,0}, & I > I_{\rm c}. \end{cases} \tag{7.98}$$

We first compare these results to numerical simulations by considering a stellar-mass BH triple that is in the LK-induced regime: we use the same inner binary parameters as the example of Fig. 7.1, but for a tertiary companion with $m_3 = 30 M_\odot$, $a_{\rm out} = 4500\,{\rm AU}$, and $e_{\rm out} = 0$. Figure 7.14 shows that Eq. (7.96) accurately predicts $\theta_{\rm sl,f}$ when $\theta_{\rm sl,0} = 0^\circ$ for this parameter regime when conservation of $\bar{\theta}_{\rm e}$ is good. Furthermore, deviations from exact $\bar{\theta}_{\rm e}$ conservation are well described by Eq. (7.61), the prediction of the theory in Section 7.4. Unlike the $\eta = 0$ case (Fig. 7.2), $\theta_{\rm sl,f}$ is not symmetric about $I_{\rm c} \approx 92.14^\circ$. This is because $|\overline{\Omega}_{\rm L}|$ is not exactly equal on either side of $I_{\rm c}$. Additionally, unlike in the $\eta = 0$ case, the minimum $\theta_{\rm sl,f}$ is not exactly zero. We showed in Section 7.4.4 that when $\eta = 0$, $\mathbf{L}$ is fixed when $I_0 = 90^\circ$, as $\mathrm{d}\Omega/\mathrm{d}t = \mathrm{d}I/\mathrm{d}t = 0$. For nonzero η, neither $\mathrm{d}\Omega/\mathrm{d}t$ nor $\mathrm{d}I_{\rm tot}/\mathrm{d}t$ is zero at $I_0 = I_{\rm c}$.

Eq. (7.96) also gives good agreement in the LK-enhanced merger regime. We

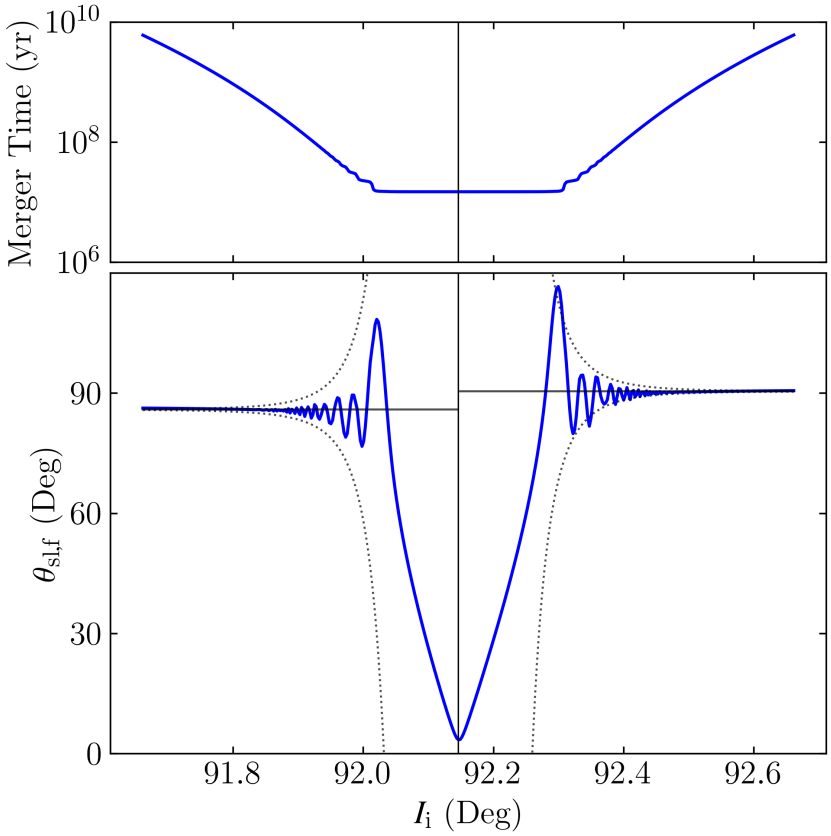

Figure 7.14: Similar to Fig. 7.2 but for stellar-mass tertiary $m_3 = 30M_\odot$ and $\tilde{a}_3 = 4500$ AU. The vertical black line denotes $I_{\rm c} \approx 92.14°$, the initial inclination for which $\overline{\Omega}_{\rm L}$ changes signs, and the two horizontal lines denote the predictions of Eq. (7.96). The dotted black lines bound the deviation due to non-adiabatic evolution, given by Eq. (7.61).

consider the same inner binary parameters as in Fig. 7.11 but use a tertiary companion with $m_3 = 30M_\odot$, $a_{\rm out} = 3$ AU, and $e_{\rm out} = 0$. The results are shown in Fig. 7.15.

7.7 Conclusion and Discussion

In this paper, we have carried out a theoretical study on the evolution of spin-orbit misalignments in tertiary-induced black-hole (BH) binary mergers. Recent nu-

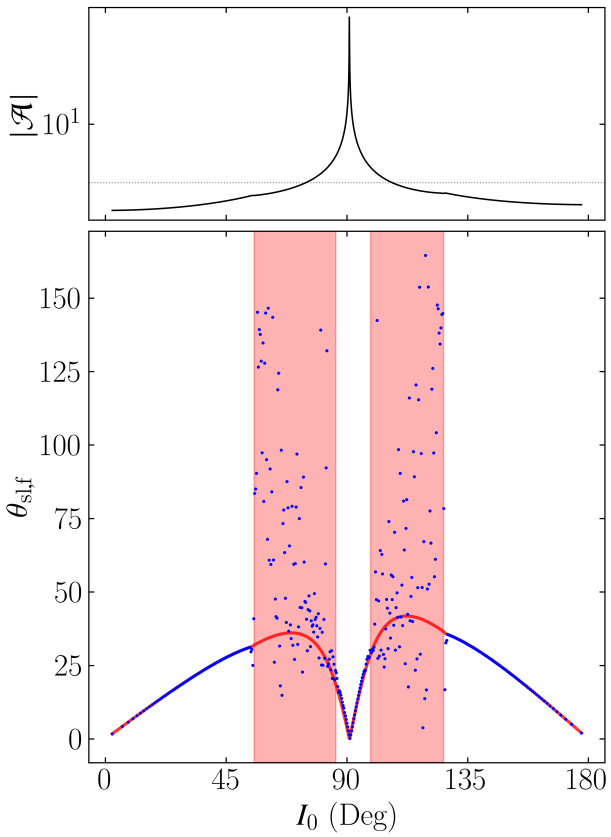

Figure 7.15: Similar to Fig. 7.11 except for a stellar mass tertiary $m_3 = 30M_\odot$ and $\tilde{a}_{\rm out} = 3\,{\rm AU}$.

merical works [Liu and Lai, 2017, 2018, Liu et al., 2019a, Antonini et al., 2018, Yu et al., 2020a] have revealed that when binary BHs undergo mergers due to Lidov-Kozai (LK) oscillations driven by a tertiary companion, the BH spin may evolve toward a perpendicular state where the final spin-orbit misalignment angle $\theta_{\rm sl}$ is close to 90°. Our theoretical analysis in this paper provides an understanding of this "90° attractor" and characterizes its regime of validity and various spin evolution behaviors during such LK-induced mergers. We focus on hierachical triple systems where the inner BH binary experiences the "standard" quadupole LK oscillations and eventually merges, with the octuple effects playing a negigible role [$\epsilon_{\rm oct} \ll 1$; see Eq. (7.14)]. For such systems, the spin vectors of the inner BHs obey a simple evolution equation, Eq. (7.22) or Eq. (7.91), where the "effective" precssion rate $\mathbf{\Omega}_{\rm e}$ varies quasi-periodically due to the combined effects of LK oscillations and gravitational radiation. Analysis of this equation yields the following conclusions:

- For BH binaries that have too large initial separations to merge in isolation, LK-induced mergers require large/extreme eccentricity excitations in the binary driven by a highly inclined tertiary companion. For such systems, the BH spin evolution behavior can be generally captured by replacing $\mathbf{\Omega}_{\rm e}$ with its LK-average $\overline{\mathbf{\Omega}}_{\rm e}$ [thus neglecting the Fourier harmonic terms in Eq. (7.25)]. If the orbital decay is sufficiently gradual, the angle $\bar{\theta}_{\rm e}$ [Eq. (7.36)] between the spin axis and $\overline{\mathbf{\Omega}}_{\rm e}$ is an adiabatic invariant. This naturally explains the "90° attractor" for the final spin-orbit misalignment angle when the initial tertiary inclination I_0 is not too close to 90° and the initial BH spin axis is aligned with the orbital angular momentum axis (see Fig. 7.2). We show that the deviation from perfect adiabaticity can be predicted from initial conditions [see Eq. 7.52 and Fig. 7.9].
- When the resonant condition $\overline{\Omega}_{\rm e} \approx M\Omega_{\rm LK}$ for integer M is satisfied, sig-

nificant variations in $\bar{\theta}_{\rm e}$ can arise. We derive an analytic estimate of this variation amplitude [Eq. (7.81)]. This estimate demonstrates that the resonances are unimportant for "LK-induced" mergers (as depicted in Figs. 7.1–7.2 and 7.14), but become important for "LK-enhanced" mergers, where the BH binaries exhibit only modest eccentricity excitations. Our analysis of the resonance effects qualitatively explain the behavior in $\theta_{\rm sl,f}$ as seen in LK-enhanced mergers (see Figs. 7.11 and 7.15).

- For LK-induced mergers of BH binaries with general tertiary companions, we provide an analytic prescription for calculating the final spin-orbit misalignment angle for arbitrary initial spin orientations (Section 7.6). This prescirption is based on the approximate adiabatic invariance of $\bar{\theta}_{\rm e}$, and produces results that are in agreement with numerical simulations (see Fig. 7.14) in the appropriate regime.

There are several simplificatons in our theoretical analysis that are worth mentioning. (i) We have neglected the octupole effects in the LK oscillations. This is appropriate for systems where the tertiary orbit is circular and/or the semi-major axis $a_{\rm out}$ is much larger than the inner binary (as in the case when the tertiary is a SMBH) and/or the inner binary BHs have nearly equal masses [see Eq. (7.14)]. The octupole effects are known to significantly broaden the inclination window for extreme eccentricity excitations, and therefore enhance the efficiency of LK-induced mergers [Liu and Lai, 2018]. When the octupole effects are significant, the LK orbital evolution is not integrable, and the eccentricity excitations are no longer regular. As a result, $\mathbf{\Omega}_{\rm e}$ has neither consistent direction nor magnitude, and our theory cannot be applied. In fact, the resulting $\theta_{\rm sl,f}$ distribution is largely unrelated to the initial $\bar{\theta}_{\rm e,0}$ and the "90° attractor" is significantly "erased" [Liu and Lai, 2018]. (ii) If the system is not sufficiently hierarchical ($a_{\rm out}$ is too small),

the double averaging approximation for the dynamics of the triple breaks down [Liu and Lai, 2018]. In this case, there is little reason to expect any relation between $\theta_{\rm sl,f}$ and $\bar{\theta}_{\rm e,0}$. However, Liu and Lai [2018] found that the double averaged orbital equations predict the correct merger window and merger fractions even beyond their regime of validity if the octupole effect is weak, so it is possible that our results concerning $\theta_{\rm sl,f}$ are also somewhat robust even when the double averaged equations formally break down. (iii) In this work, we only consider spin-orbit coupling, and follow the evolution of $\theta_{\rm sl}$ until the orbital separation is sufficiently small such that the inner binary is gravitationally decoupled from the tertiary and the spin-orbit misalignment angle is frozen. To leading post-Newtonian (PN) order, $\theta_{\rm sl}$ is constant for small separations until the spin-spin interaction (2 PN) becomes important. This interaction is non-negligible only when binary enters the LIGO band and when the spin magnitude of each BH is appreciable [Liu et al., 2019a, Yu et al., 2020a].

As noted in Section 7.1, the merging BH binaries detected by LIGO/VIRGO in O1 and O2 have $\chi_{\rm eff} \sim 0$ [Abbott et al., 2016, 2019]. One possible explanation for this is that BHs are born slowly rotating [e.g. Fuller and Ma, 2019]. But our "90° attractor" provides an alternative explanation with no assumptions on the BH spin magnitudes if the mergers are "LK-induced" and $\theta_{\rm sl,0} \approx 0^\circ$. In the O3 event GW190521, each BH has a significant spin magnitude and a large spin-orbit misalignment angle [Abbott et al., 2020b]. If the evolution history of the system resembled our LK-induced scenario [see Liu and Lai, 2021], a primordial $\theta_{\rm sl,0} \approx 0^\circ$ would be consistent with the observed outcome of $\theta_{\rm sl,f} \sim 90^\circ$.

CHAPTER 8

THE MASS RATIO DISTRIBUTION OF TERTIARY INDUCED BINARY BLACK HOLE MERGERS

Originally published in:
Yubo Su, Bin Liu, and Dong Lai. The mass-ratio distribution of tertiary-induced binary black hole mergers. *MNRAS*, 505(3):3681–3697, 2021b

8.1 Introduction

The 50 or so black hole (BH) binary mergers detected by the LIGO/VIRGO collaboration to date [Abbott et al., 2021] continue to motivate theoretical studies of their formation channels. These range from the traditional isolated binary evolution, in which mass transfer and friction in the common envelope phase cause the binary orbit to decay sufficiently that it subsequently merges via emission of gravitational waves (GWs) [e.g., Lipunov et al., 1997, 2017, Podsiadlowski et al., 2003, Belczynski et al., 2010, 2016, Dominik et al., 2012, 2013, 2015], to various flavors of dynamical formation channels that involve either strong gravitational scatterings in dense clusters [e.g., Zwart and McMillan, 1999, O'leary et al., 2006, Miller and Lauburg, 2009, Banerjee et al., 2010, Downing et al., 2010, Ziosi et al., 2014, Rodriguez et al., 2015, Samsing and Ramirez-Ruiz, 2017, Samsing and D'Orazio, 2018, Rodriguez et al., 2018, Gondán et al., 2018] or mergers in isolated triple and quadruple systems induced by distant companions [e.g., Miller and Hamilton, 2002, Wen, 2003, Antonini and Perets, 2012, Antonini et al., 2017, Silsbee and Tremaine, 2017b, Liu and Lai, 2017, 2018, Randall and Xianyu, 2018b,a, Hoang et al., 2018, Fragione and Kocsis, 2019, Fragione and Loeb, 2019, Liu and Lai, 2019, Liu et al., 2019a,b, Liu and Lai, 2020, Liu and Lai, 2021].

Given the large number of merger events to be detected in the coming years,

it is important to search for observational signatures to distinguish various BH binary formation channels. The masses of merging BHs obviously carry important information. The recent detection of BH binary systems with component masses in the mass gap (such in GW190521) suggests that some kinds of "hierarchical mergers" may be needed to explain these exceptional events (Abbott et al., 2020b; see Liu and Lai, 2021 for examples of such "hierarchical mergers" in stellar multiples). Another possible indicator is merger eccentricity: previous studies find that dynamical binary-single interactions in dense clusters [e.g., Samsing and Ramirez-Ruiz, 2017, Rodriguez et al., 2018, Samsing and D'Orazio, 2018, Fragione and Bromberg, 2019] or in galactic triples [Silsbee and Tremaine, 2017b, Antonini et al., 2017, Fragione and Loeb, 2019, Liu et al., 2019a] may lead to BH binaries that enter the LIGO band with modest eccentricities. The third possible indicator is the spin-orbit misalignment of the binary. In particular, the mass-weighted projection of the BH spins,

$$\chi_{\rm eff} = \frac{m_1 \boldsymbol{\chi}_1 + m_2 \boldsymbol{\chi}_2}{m_1 + m_2} \cdot \hat{\mathbf{L}}, \tag{8.1}$$

can be measured through the binary inspiral waveform [here, $m_{1,2}$ is the BH mass, $\boldsymbol{\chi}_{1,2} = c\boldsymbol{S}_{1,2}/(Gm_{1,2}^2)$ is the dimensionless BH spin, and $\hat{\mathbf{L}}$ is the unit orbital angular momentum vector of the binary]. Different formation histories yield different distributions of $\chi_{\rm eff}$ [Liu and Lai, 2017, 2018, Antonini et al., 2018, Rodriguez et al., 2018, Gerosa et al., 2018, Liu et al., 2019a, Su et al., 2021a].

The fourth possible indicator of BH binary formation mechanisms is the distribution of masses and mass ratios of merging BHs. In Fig. 8.1, we show the distribution of the mass ratio $q \equiv m_2/m_1$, where $m_1 \geq m_2$, for all LIGO/VIRGO binaries detected as of the O3a data release [Abbott et al., 2021][1]. The distribution

[1]Note that Fig. 8.1 should not be interpreted as directly reflecting the distribution of merging BH binaries, as there are many selection effects and observational biases, e.g. systems with smaller q are harder to detect for the same $M_{\rm chirp}$ or m_{12}. For a detailed statistical analysis, see Abbott et al. [2021].

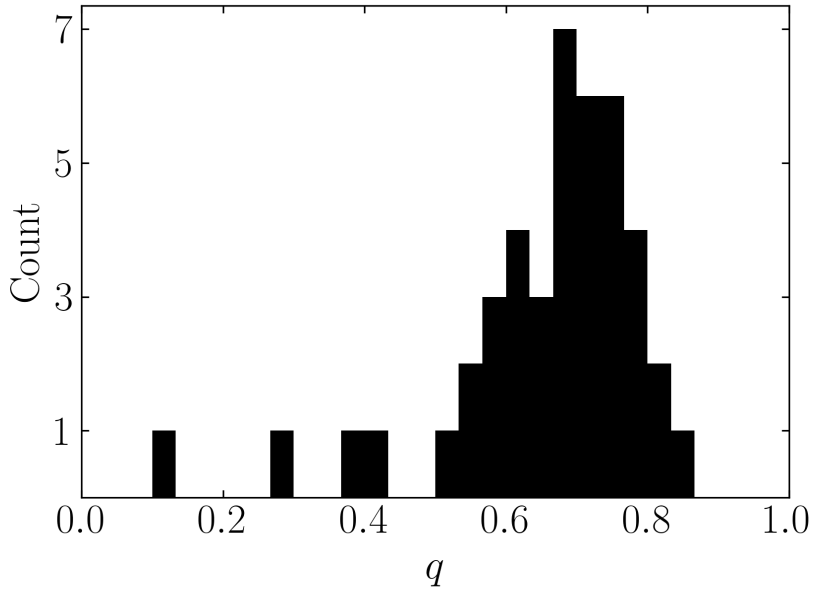

Figure 8.1: Histogram of the mass ratios $q \equiv m_2/m_1$ of binary BH mergers in the O3a data release, excluding the two NS-NS mergers but including GW190814, whose $2.5M_\odot$ secondary may be a BH [Abbott et al., 2021].

distinctly peaks around $q \sim 0.7$. BH binaries formed via isolated binary evolution are generally expected to have $q \gtrsim 0.5$ [Belczynski et al., 2016, Olejak et al., 2020]. On the other hand, dynamical formation channels may produce a larger variety of distributions for the binary mass ratio [e.g., Rodriguez et al., 2016, Silsbee and Tremaine, 2017b, Fragione and Kocsis, 2019].

In this paper, we study in detail the mass ratio distribution for BH mergers induced by tertiary companions in isolated triple systems. In this scenario, a tertiary BH on a sufficiently inclined (outer) orbit induces phases of extreme eccentricity in the inner binary via the von Zeipel-Lidov-Kozai (ZLK;von Zeipel, 1910, Lidov, 1962, Kozai, 1962) effect, leading to efficient gravitational radiation and orbital decay. While the original ZLK effect relies on the leading-order, quadrupolar gravitational perturbation from the tertiary on the inner binary, the octupole order terms can become important [sometimes known as the eccentric Kozai mech-

anism, e.g. Naoz, 2016] when the triple system is mildly hierarchical, the outer orbit is eccentric ($e_{\rm out} \neq 0$) and the inner binary BHs have unequal masses [e.g., Ford et al., 2000, Blaes et al., 2002, Lithwick and Naoz, 2011, Liu et al., 2015a]. The strength of the octupole effect depends on the dimensionless parameter

$$\epsilon_{\rm oct} = \frac{m_1 - m_2}{m_1 + m_2} \frac{a}{a_{\rm out}} \frac{e_{\rm out}}{1 - e_{\rm out}^2}. \tag{8.2}$$

where $a, a_{\rm out}$ are the semi-major axes of the inner and outer binaries, respectively. Previous studies have shown that the octupole terms generally increase the inclination window for extreme eccentricity excitation, and thus enhance the rate of successful binary mergers [Liu and Lai, 2018]. As $\epsilon_{\rm oct} \propto (1-q)/(1+q)$ increases with decreasing q, we expect that ZLK-induced BH mergers favor binaries with smaller mass ratios. The main goal of this paper is to quantify the dependence of the merger fraction/probability on q, using a combination of analytical and numerical calculations. We focus on the cases where the tertiary mass is comparable to the binary BH masses. When the tertiary mass m_3 is much larger than $m_{12} = m_1 + m_2$ (as in the case of a supermassive BH tertiary), dynamical stability of the triple requires $a_{\rm out}(1-e_{\rm out})/[a(1+e)] \gtrsim 3.7(m_3/m_{12})^{1/3} \gg 1$ [Kiseleva et al., 1996], which implies that the octupole effect is negligible.

This paper is organized as follows. In Section 8.2, we review some analytical results of ZLK oscillations and examine how the octupole terms affect the inclination window and probability for extreme eccentricity excitation. In Section 8.3, we study tertiary-induced BH mergers using a combination of numerical and analytical approaches. We propose new semi-analytical criteria (Section 8.3.2) that allow us to determine, without full numerical integration, whether an initial BH binary can undergo a "one-shot merger" or a more gradual merger induced by the octupole effect of an tertiary. In Section 8.4, we calculate the merger fraction as a function of mass ratio for some representative triple systems. In Section 8.5, we

study the mass ratio distribution of the initial BH binaries based on the properties of main-sequence (MS) stellar binaries and the MS mass to BH mass mapping. Using the result of Section 8.4, we illustrate how the final merging BH binary mass distribution may be influenced by the octupole effect for tertiary-induced mergers. We summarize our results and their implications in Section 8.6.

8.2 Von Zeipel-Lidov-Kozai (ZLK) Oscillations: Analytical Results

Consider two BHs orbiting each other with masses m_1 and m_2 on a orbit with semi-major axis a, eccentricity e, and angular momentum $\mathbf{L}$. An external, tertiary BH of mass m_3 orbits this inner binary with semi-major axis $a_{\rm out}$, eccentricity $e_{\rm out}$, and angular momentum $\mathbf{L}_{\rm out}$. The reduced masses of the inner and outer binaries are $\mu \equiv m_1 m_2/m_{12}$ and $\mu_{\rm out} \equiv m_{12} m_3/m_{123}$ respectively, where $m_{12} = m_1 + m_2$ and $m_{123} = m_{12} + m_3$. These two binary orbits are further described by three angles: the inclinations i and $i_{\rm out}$, the arguments of pericenters ω and $\omega_{\rm out}$, and the longitudes of the ascending nodes Ω and $\Omega_{\rm out}$. These angles are defined in a coordinate system where the z axis is aligned with the total angular momentum $\mathbf{J} = \mathbf{L} + \mathbf{L}_{\rm out}$ (i.e., the invariant plane is perpendicular to $\mathbf{J}$). The mutual inclination between the two orbits is denoted $I \equiv i + i_{\rm out}$. Note that $\Omega_{\rm out} = \Omega + 180^\circ$.

To study the evolution of the inner binary under the influence of the tertiary BH, we use the double-averaged secular equations of motion, including the interactions between the inner binary and the tertiary up to the octupole level of approximation as given by Liu et al. [2015a]. Throughout this paper, we restrict to hierarchical triple systems where the double-averaged secular equations are valid

– systems with relatively small $a_{\rm out}/a$ may require solving the single-averaged equations of motion or direct N-body integration [see Antonini and Perets, 2012, Antonini et al., 2014, Luo et al., 2016, Lei et al., 2018, Liu and Lai, 2019, Liu et al., 2019a, Hamers, 2020a][2]. For the remainder of this section, we include general relativistic apsidal precession of the inner binary, a first order post-Newtonian (1PN) effect, but omit the emission of GWs, a 2.5PN effect – this will be considered in Section 8.3. We group the results by increasing order of approximation, starting by ignoring the octupole-order effects entirely.

8.2.1 Quadrupole Order

At the quadrupole order, the tertiary induces eccentricity oscillations in the inner binary on the characteristic timescale

$$t_{\rm ZLK} = \frac{1}{n}\frac{m_{12}}{m_3}\left(\frac{a_{\rm out,eff}}{a}\right)^3, \tag{8.3}$$

where $n \equiv \sqrt{Gm_{12}/a^3}$ is the mean motion of the inner binary, and $a_{\rm out,eff} \equiv a_{\rm out}\sqrt{1-e_{\rm out}^2}$. During these oscillations, there are two conserved quantities, the total energy and the total orbital angular momentum. Through some manipulation, the total angular momentum can be written in terms of the conserved quantity K given by

$$K \equiv j(e)\cos I - \frac{\eta}{2}e^2. \tag{8.4}$$

Here, $j(e) \equiv \sqrt{1-e^2}$ and η is the ratio of the magnitudes of the angular momenta at zero inner binary eccentricity:

$$\eta \equiv \left(\frac{L}{L_{\rm out}}\right)_{e=0} = \frac{\mu}{\mu_{\rm out}}\left[\frac{m_{12}a}{m_{123}a_{\rm out}(1-e_{\rm out}^2)}\right]^{1/2}. \tag{8.5}$$

[2]Although we do not study such systems in this paper, we expect that a qualitatively similar dependence of the merger probability on the mass ratio remains, since the strength of the octupole effect in the single-averaged secular equations is also proportional to $(1-q)/(1+q)$ [see Eq. 25 of Liu and Lai, 2019].

Note that when $\eta = 0$, K reduces to the classical "Kozai constant", $K = j(e)\cos I$.

The maximum eccentricity $e_{\max}$ attained in these ZLK oscillations can be computed analytically at the quadrupolar order. It depends on the "competition" between the 1PN apsidal precession rate $\dot{\omega}_{\rm GR}$ and the ZLK rate $t_{\rm ZLK}^{-1}$. The relevant dimensionless parameter is

$$\epsilon_{\rm GR} \equiv (\dot{\omega}_{\rm GR} t_{\rm ZLK})_{e=0} = \frac{3Gm_{12}}{c^2}\frac{m_{12}}{m_3}\frac{a_{\rm out,eff}^3}{a^4}. \tag{8.6}$$

It can then be shown that, for an initially circular inner binary, $e_{\max}$ is related to the initial mutual inclination I_0 by [Liu et al., 2015a, Anderson et al., 2016]:

$$\frac{3}{8}\frac{j^2(e_{\max})-1}{j^2(e_{\max})}\left[5\left(\cos I_0 + \frac{\eta}{2}\right)^2 - \left(3 + 4\eta\cos I_0 + \frac{9}{4}\eta^2\right)j^2(e_{\max}) + \eta^2 j^4(e_{\max})\right] + \epsilon_{\rm GR}\left[1 - \frac{1}{j(e_{\max})}\right] = 0. \tag{8.7}$$

In the limit $\eta \to 0$ and $\epsilon_{\rm GR} \to 0$, we recover the well-known result

$$e_{\max} = \sqrt{1 - (5/3)\cos^2 I_0}. \tag{8.8}$$

For general η, $e_{\max}$ attains its limiting value $e_{\rm lim}$ when $I_0 = I_{0,\rm lim}$, where [see also Hamers, 2020b]

$$\cos I_{0,\rm lim} = \frac{\eta}{2}\left[\frac{4}{5}j^2(e_{\rm lim}) - 1\right]. \tag{8.9}$$

Note that $I_{0,\rm lim} \geq 90^\circ$ with equality only when $\eta = 0$. Substituting Eq. (8.9) into Eq. (8.7), we find that $e_{\rm lim}$ satisfies

$$\frac{3}{8}\left[j^2(e_{\rm lim}) - 1\right]\left[-3 + \frac{\eta^2}{4}\left(\frac{4}{5}j^2(e_{\rm lim}) - 1\right)\right] + \epsilon_{\rm GR}\left[1 - \frac{1}{j(e_{\rm lim})}\right] = 0. \tag{8.10}$$

On the other hand, eccentricity excitation ($e_{\max} \geq 0$) is only possible when $(\cos I_0)_- \leq \cos I_0 \leq (\cos I_0)_+$ where

$$(\cos I_0)_\pm = \frac{1}{10}\left(-\eta \pm \sqrt{\eta^2 + 60 - \frac{80}{3}\epsilon_{\rm GR}}\right). \tag{8.11}$$

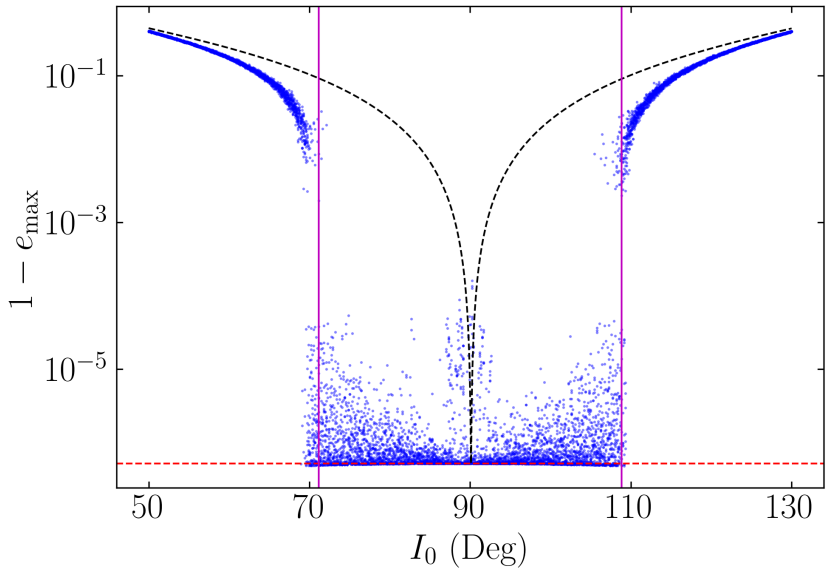

Figure 8.2: The maximum eccentricity achieved for an inner binary in the test-particle limit as a function of the initial inclination angle I_0. The triple system parameters are: $a = 100$ AU, $a_{\rm out,eff} = 3600$ AU, $m_{12} = 50M_\odot$, $m_3 = 30M_\odot$, and $e_{\rm out} = 0.6$; the corresponding octupole strength parameter is $\epsilon_{\rm oct} = 0.02$ and $\eta \simeq 0$. The octupole-level secular equations of motion are integrated for $2000t_{\rm ZLK}$ (see Eq. 8.3), and the maximum eccentricity attained during this time is recorded and shown as a blue dot for each initial condition. We consider 1000 initial inclinations in the range $50^\circ \le I_0 \le 130^\circ$, and each I_0 is simulated five times, with the initial orbital elements ω, $\omega_{\rm out}$, and $\Omega = \Omega_{\rm out} - \pi$ chosen randomly $\in [0, 2\pi)$ shows the quadrupole-level result (Eq. 8.7 with $\eta = 0$), and $e_{\rm lim}$ (Eq. 8.10) is shown as the horizontal red line. The vertical purple lines denote the boundary of the octupole-active inclination window, based on the fitting formula from Muñoz et al. [2016] (Eq. 8.13).

For I_0 outside of this range, no eccentricity excitation is possible. This condition reduces to the well-known $\cos^2 I_0 \le 3/5$ when $\eta = \epsilon_{\rm GR} = 0$.

8.2.2 Octupole Order: Test-particle Limit

The relative strength of the octupole-order potential to the quadrupole-order potential is determined by the dimensionless parameter $\epsilon_{\rm oct}$ (Eq. 8.2). When $\epsilon_{\rm oct}$ is

non-negligible, K is no longer conserved, and the system evolution becomes chaotic [Ford et al., 2000, Katz et al., 2011, Lithwick and Naoz, 2011, Li et al., 2014, Liu et al., 2015a]. As a result, analytical (and semi-analytical) results have only been given for the test-particle limit, where $m_2 = \eta = 0$. We briefly review these results below.

Due to the non-conservation of K, $e_{\max}$ evolves irregularly ZLK cycles, and the orbit may even flip between prograde ($I < 90°$) and retrograde ($I > 90°$) if K changes sign (in the test-particle limit, $K = j(e)\cos I$). During these orbit flips, the eccentricity maxima reach their largest values but do not exceed $e_{\lim}$ [Lithwick and Naoz, 2011, Liu et al., 2015a, Anderson et al., 2016]. These orbit flips occur on characteristic timescale $t_{\rm ZLK,oct}$, given by [Antognini, 2015]

$$t_{\rm ZLK,oct} = t_{\rm ZLK}\frac{128\sqrt{10}}{15\pi\sqrt{\epsilon_{\rm oct}}}. \tag{8.12}$$

The octupole potential tends to widen the inclination range for which the eccentricity can reach $e_{\lim}$; we refer to this widened range as the *octupole-active window*. Figure 8.2 shows the maximum eccentricity attained by an inner binary orbited by a tertiary companion with inclination I_0. The octupole-active window is visible as a range of inclinations centered on $I_0 = 90°$ that attain $e_{\lim}$ (the red horizontal dashed line in Fig. 8.2). Katz et al. [2011] show that this window can be approximated using analytical arguments when $\epsilon_{\rm oct} \ll 1$. Muñoz et al. [2016] give a more general numerical fitting formula describing the octupole-active window for arbitrary $\epsilon_{\rm oct}$. They find that orbit flips and extreme eccentricity excitation occur for $I_{\rm flip,-} \lesssim I_0 \lesssim I_{\rm flip,+}$ where

$$\cos^2 I_{\rm flip,\pm} = \begin{cases} 0.26\left(\frac{\epsilon_{\rm oct}}{0.1}\right) - 0.536\left(\frac{\epsilon_{\rm oct}}{0.1}\right)^2 & \\ \quad +12.05\left(\frac{\epsilon_{\rm oct}}{0.1}\right)^3 - 16.78\left(\frac{\epsilon_{\rm oct}}{0.1}\right)^4 & \epsilon_{\rm oct} \lesssim 0.05, \\ 0.45 & \epsilon_{\rm oct} \gtrsim 0.05. \end{cases} \tag{8.13}$$

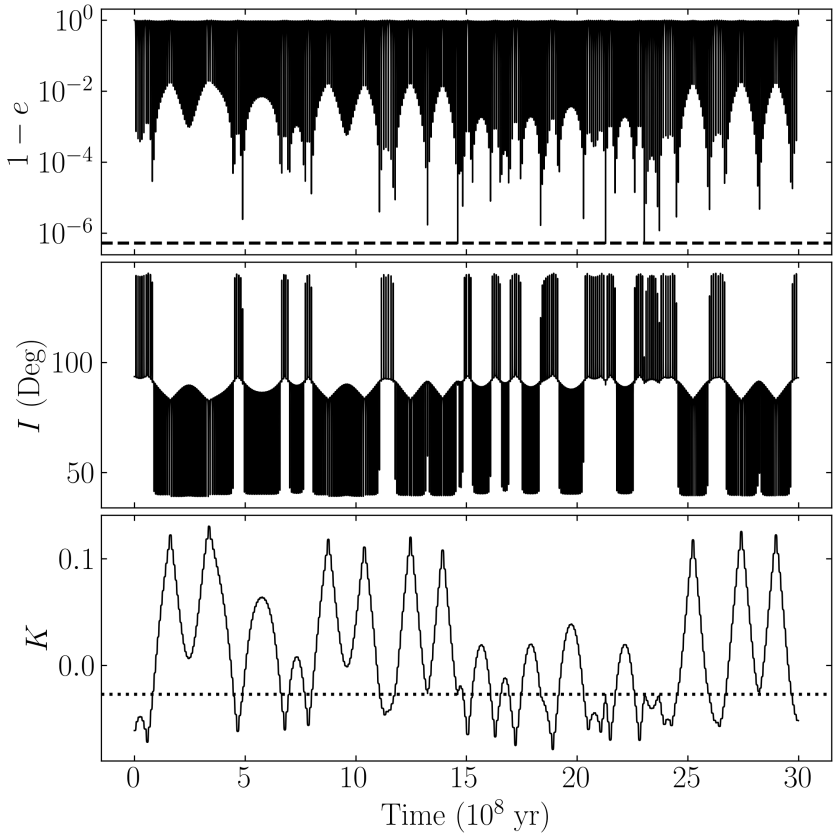

Figure 8.3: An example of the triple evolution for a system with significant octupole effects and finite η (see Eq. 8.5). We use the same system parameters as in Fig. 8.2 except for $q = 0.2$, corresponding to $\eta \approx 0.087$ and $\epsilon_{\rm oct} \approx 0.007$, and $I_0 = 93.5°$. The three panels show the inner orbit eccentricity, the mutual inclination, and the generalized "Kozai constant" K (Eq. 8.4). In the first panel, $e_{\rm lim}$ is denoted by the black dashed line. By comparing the second and third panels, we see that orbit flips occur when K crosses the dotted line, given by $K = K_{\rm c} \equiv -\eta/2$.

In Fig. 8.2, we see that with the octupole effect included, $e_{\rm max}$ indeed attains $e_{\rm lim}$ when I_0 is within the broad octupole-active window given by Eq. (8.13) (denoted by the vertical purple lines in Fig. 8.2).

8.2.3 Octupole Order: General Masses

For general inner binary masses, when the angular momentum ratio η is non-negligible, the octupole-level ZLK behavior is less well-studied [see Liu et al., 2015a]. Figure 8.3 shows an example of the evolution of a triple system with significant η and $\epsilon_{\rm oct}$. Many aspects of the evolution discussed in Section 8.2.2 are still observed: the ZLK eccentricity maxima and K evolve over timescales $\gg t_{\rm ZLK}$; the eccentricity never exceeds $e_{\rm lim}$; when K crosses $K_{\rm c} \equiv -\eta/2$, an orbit flip occurs (this follows by inspection of Eq. 8.4).

However, Eq. (8.13) no longer describes the octupole-active window as η is non-negligible [see also Rodet et al., 2021]. In the top panel of Fig. 8.4, the blue dots show the maximum achieved eccentricity of a system with the same parameters as Fig. 8.2 except with $q = 0.5$ (so $\epsilon_{\rm oct} = 0.007$ and $\eta = 0.087$). Here, it can be seen that no prograde systems can attain $e_{\rm lim}$, and only a small range of retrograde inclinations $\geq I_{0,\rm lim}$ (see Eq. 8.9) are able to reach $e_{\rm lim}$. In fact, there is even a clear double valued feature around $I \approx 75^\circ$ in the top panel of Fig. 8.4 that is not present in Fig. 8.2. If q is decreased to 0.3 (Fig. 8.5) or further to 0.2 (Fig. 8.6), $\epsilon_{\rm oct}$ increases while η decreases. This permits a larger number of prograde systems to reach $e_{\rm lim}$, though a small range of inclinations near $I_0 = 90^\circ$ still do not reach $e_{\rm lim}$; we call this range of inclinations the "octupole-inactive gap". On the other hand, if q is held at 0.5 as in Fig. 8.4 and $e_{\rm out}$ is increased to 0.9 while holding $a_{\rm out,eff} = 3600\,{\rm AU}$ constant, both $\epsilon_{\rm oct}$ and η increase; the top panel of Fig. 8.7 shows that prograde systems still fail to reach $e_{\rm lim}$ for these parameters, despite the increase in $\epsilon_{\rm oct}$. The top panel of Fig. 8.8 illustrates the behavior when the inner binary is substantially more compact ($a = 10\,{\rm AU}$): even though $\epsilon_{\rm oct}$ is larger than it is in any of Figs. 8.4–8.7, we see that prograde perturbers fail to attain $e_{\rm lim}$. All of these examples (top panels of Figs. 8.4–8.8) illustrate importance of η in

determining the range of inclinations for the system to be able to reach $e_{\rm lim}$.

In general, we find that a symmetric octupole-active window (as in Eq. 8.13) can be realized for sufficiently small η. Rodet et al. [2021] considered some examples of triple systems (consisting of MS stars with planetary companions and tertiaries, for which the short-range forces is dominated by tidal interaction) and found that $\eta \lesssim 0.1$ is sufficient for a symmetric octupole-active window. In the cases considered in this paper, a smaller η is necessary (e.g., $\eta \simeq 0.054$ in Fig. 8.6). Thus, the critical η above which the symmetry of the octupole-active window is significantly broken likely depends on the dominant short-range forces and $e_{\rm lim}$ [in Rodet et al. [2021], $1-e_{\rm lim} \sim 10^{-3}$, while in Figs. 8.2 and 8.4–8.8, $1-e_{\rm lim} \lesssim 10^{-5}$]. In general, when η is non-negligible, there are up to two octupole-active windows: a prograde window whose existence depends on the specific values of η and $\epsilon_{\rm oct}$, and a retrograde window that always exists.

8.3 Tertiary-Induced Black Hole Mergers

Emission of gravitational waves (GWs) affects the evolution of the inner binary, which can be incorporated into the secular equations of motion for the triple [e.g., Peters, 1964, Liu and Lai, 2018]. The associated orbital and eccentricity decay rates are [Peters, 1964]:

$$\left.\frac{1}{a}\frac{{\rm d}a}{{\rm d}t}\right|_{\rm GW} \equiv -\frac{1}{t_{\rm GW}} = -\frac{64}{5}\frac{G^3\mu m_{12}^2}{c^5 a^4 j^7(e)}\left(1+\frac{73}{24}e^2+\frac{37}{96}e^4\right), \tag{8.14}$$

$$\left.\frac{{\rm d}e}{{\rm d}t}\right|_{\rm GW} = -\frac{304}{15}\frac{G^3\mu m_{12}^2}{c^5 a^4}\frac{1}{j^5(e)}\left(1+\frac{121}{304}e^2\right). \tag{8.15}$$

GW emission can cause the orbit to decay significantly when extreme eccentricities are reached during the ZLK cycles described in the previous section. This

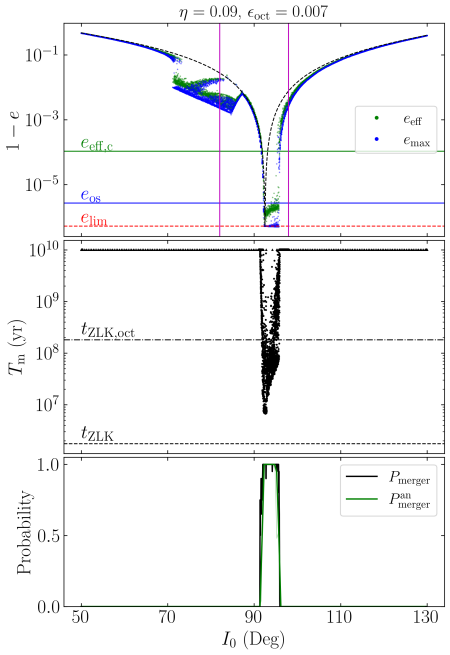

Figure 8.4: Eccentricity excitation and merger windows for the fiducial BH triple system ($a = 100\,\mathrm{AU}$, $a_{\rm out,eff} = 3600\,\mathrm{AU}$, $m_{12} = 50M_\odot$, $m_3 = 30M_\odot$) with $q = 0.5$ and $e_{\rm out} = 0.6$, corresponding to $\eta \approx 0.087$ and $\epsilon_{\rm oct} \approx 0.007$. In the top panel, for each of 1000 initial inclinations, we choose 5 different random ω, $\omega_{\rm out}$, and Ω as initial conditions and evolve the system for $2000t_{\rm ZLK}$ without GW radiation. The effective eccentricity $e_{\rm eff}$ (Eq. 8.22; green dots) as well as the maximum eccentricity $e_{\rm max}$ (blue dots) over this period are displayed. For comparison, $e_{\rm eff,c}$ (Eq. 8.23) is given by the horizontal green dashed line, $e_{\rm os}$ (Eq. 8.19) is shown as the horizontal blue line, and $e_{\rm lim}$ (Eq. 8.10) is shown as the horizontal red dashed line. The vertical purple lines denote the test-mass octupole-active window and are given by the fitting formula of Muñoz et al. [2016]; they do not longer accurately describe the $e_{\rm lim}$-attaining inclination window because η is finite. The black dashed line is is the quadrupole-level result as given by Eq. (8.7). In the middle panel, we show the binary merger times when including GW radiation and using the same range of initial conditions. Numerical integrations are terminated when $T_{\rm m} > 10$ Gyr and marked as unsuccessful mergers. The horizontal dashed line denotes $t_{\rm ZLK}$ (Eq. 8.3) while the horizontal dash-dotted line indicates $t_{\rm ZLK,oct}$ (Eq. 8.12). Here, each I_0 is run 20 times with uniform distributions of ω, $\omega_{\rm out}$, and Ω, so we can estimate the merger probability $P_{\rm merger}$ (Eq. 8.17) for each $I_0 - P_{\rm merger}$ is shown as the black line in the bottom panel. As described in Section 8.3.2, the merger probability can be predicted semi-analytically using the results of the top panel and Eq. (8.25), and is denoted by $P^{\rm an}_{\rm merger}$. In the bottom panel, the thick green line shows $P^{\rm an}_{\rm merger}$ when using an integration time of $2000t_{\rm ZLK} \approx 3$ Gyr for the non-dissipative simulations, and thin green line shows the prediction using an integration time of $500t_{\rm ZLK}$. The agreement of $P^{\rm an}_{\rm merger}$ with $P_{\rm merger}$ is good and improves when using the longer integration time.

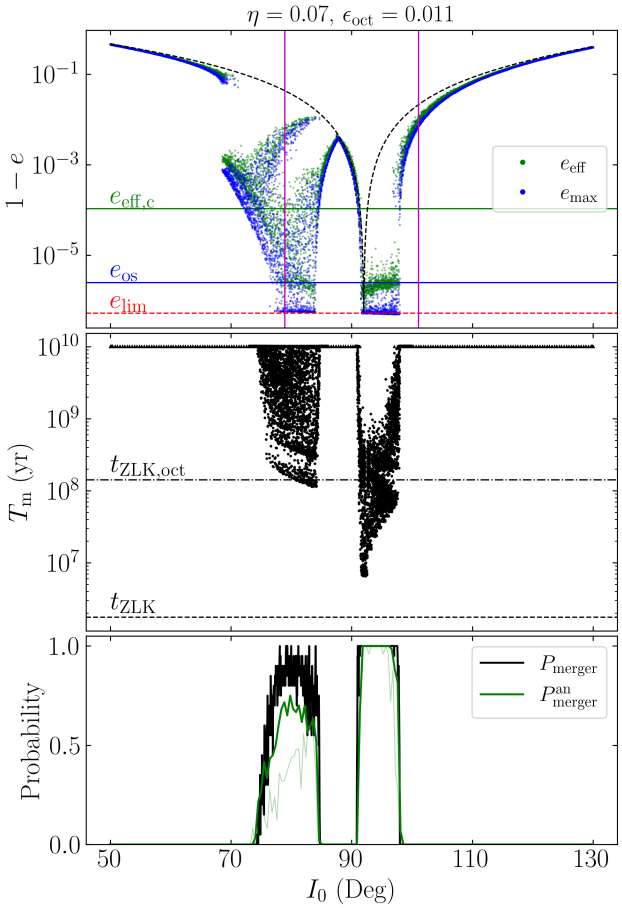

Figure 8.5: Same as Fig. 8.4 but for $q = 0.3$, corresponding to $\eta \approx 0.07$ and $\epsilon_{\rm oct} \approx 0.011$.

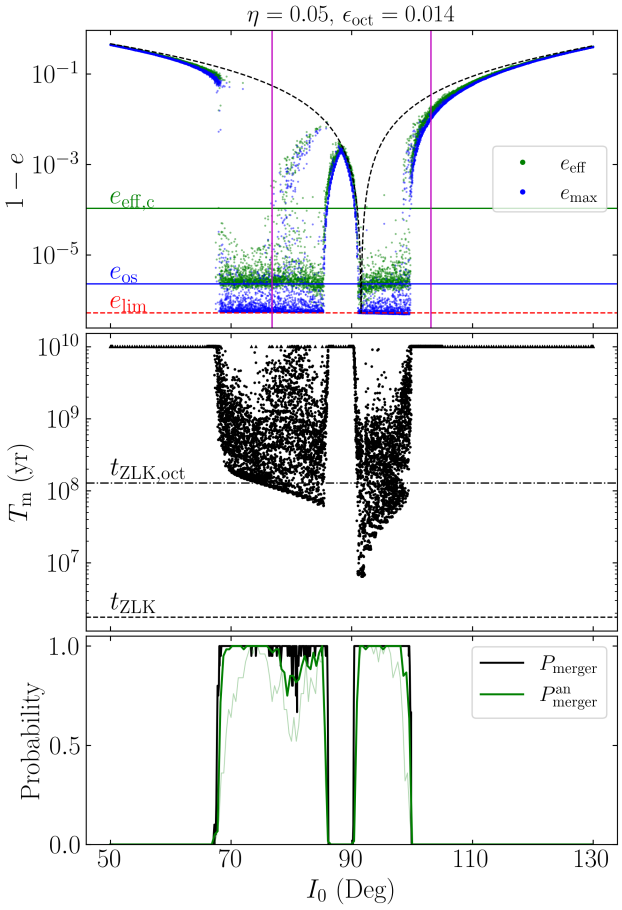

Figure 8.6: Same as Fig. 8.4 but for $q = 0.2$, corresponding to $\eta \approx 0.054$ and $\epsilon_{\rm oct} \approx 0.014$.

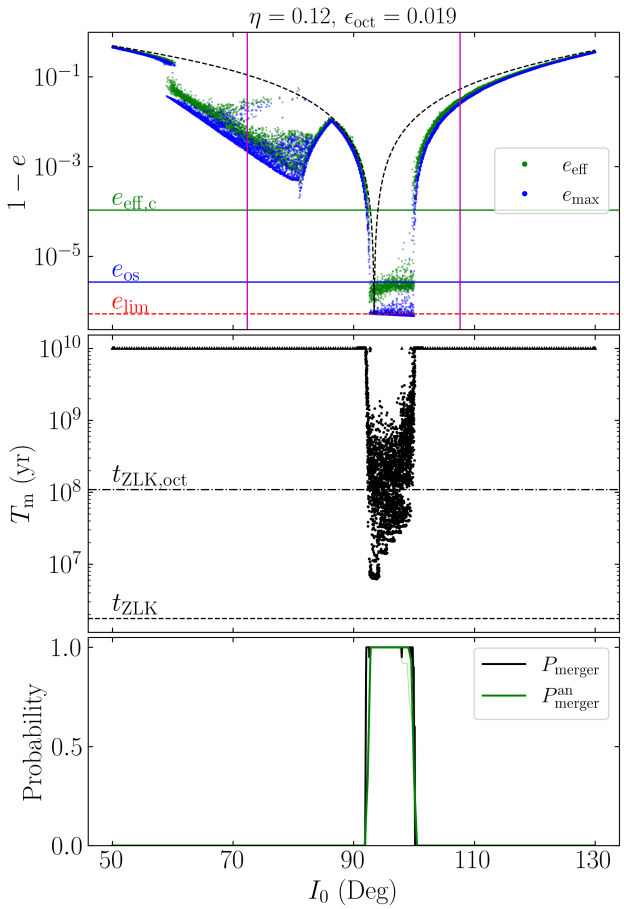

Figure 8.7: Same as Fig. 8.4 but for $e_{\rm out} = 0.9$ while holding $a_{\rm out,eff}$ the same, corresponding to $\eta = 0.118$ and $\epsilon_{\rm oct} = 0.019$.

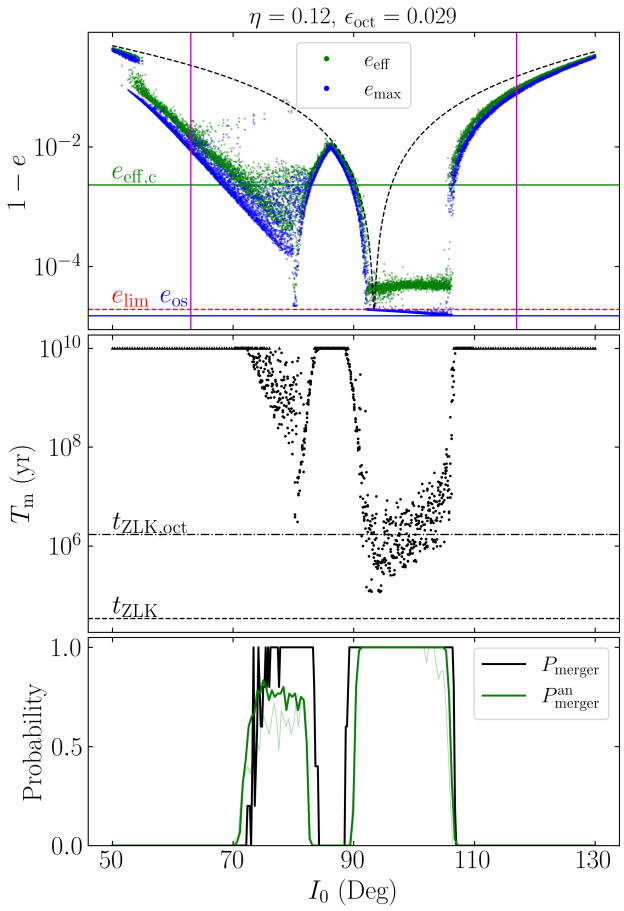

Figure 8.8: Same as Fig. 8.4 but for a more compact inner binary; the parameters are $a_0 = 10\,\mathrm{AU}$, $a_{\rm out,eff} = 700\,\mathrm{AU}$, $m_{12} = 50M_\odot$, $m_3 = 30M_\odot$, $e_{\rm out} = 0.9$, and $q = 0.4$, corresponding to $\eta = 0.118$ and $\epsilon_{\rm oct} = 0.029$. Here, $P_{\rm merger}$ is computed with only 5 integrations (for random ω, $\omega_{\rm out}$, and Ω) for each I_0.

allows even wide binaries (~ 100 AU) to merge efficiently within a Hubble time. While various numerical examples of such tertiary-induced mergers have been given before (e.g., Liu and Lai [2018]; see also Liu et al. [2019a] for "population synthesis"), in this section we examine the dynamical process in detail in order to develop an analytical understanding. Our fiducial system parameters are as in Fig. 8.3: $a_{\rm out,eff} = 4500\,{\rm AU}$, $e_{\rm out} = 0.6$, $m_{12} = 50M_\odot$ (with varying q), $m_3 = 30M_\odot$, and the inner binary has initial $a_0 = 100\,{\rm AU}$ and $e_0 = 10^{-3}$.

8.3.1 Merger Windows and Probability: Numerical Results

To understand what initial conditions lead to successful mergers within a Hubble time, we integrate the double-averaged octupole-order ZLK equations including GW radiation. We terminate each integration if either $a = 0.005a_0$ (a successful merger) or the system age reaches 10 Gyr. We can verify that the inner binary is effectively decoupled from the tertiary for this orbital separation by evaluating $\epsilon_{\rm GR}$ (Eq. 8.6):

$$\epsilon_{\rm GR} = 1.8\times 10^6 \left(\frac{m_{12}}{50M_\odot}\right)^2 \left(\frac{a_{\rm out,eff}}{3600\,{\rm AU}}\right)^3 \left(\frac{m_3}{30M_\odot}\right)^{-1} \left(\frac{a}{0.5\,{\rm AU}}\right)^{-4}. \tag{8.16}$$

The middle panel of Fig. 8.4 shows the merger time $T_{\rm m}$ as a function of I_0 for our fiducial parameters with $q = 0.5$. We note that only retrograde inclinations lead to successful mergers, and almost all successful mergers are rapid, with $T_{\rm m} \sim t_{\rm ZLK,oct}$. These are the result of a system merging by emitting a single large burst of GW radiation during an extreme-eccentricity ZLK cycle, which we term a "*one-shot merger*"[3]. In Fig. 8.5, q is decreased to 0.3, and some prograde systems are

[3]It is important to note that these "one-shot mergers" are distinct from the "fast" mergers previously discussed in the literature [e.g. Wen, 2003, Randall and Xianyu, 2018a, Su et al., 2021a]: The one-shot mergers discussed here occur when the maximum eccentricity attained by the inner binary over an *octupole* cycle (i.e. within the first $\sim t_{\rm ZLK,oct}$) is sufficiently large to produce a prompt merger, while the references cited above neglect octupole-order effects and study the scenario when

also able to merge successfully. However, these prograde systems exhibit a broad range of merger times, with $T_{\rm m} \gtrsim t_{\rm ZLK,oct}$. These occur when a system gradually emits a small amount of GW radiation at every eccentricity maximum – we term this a "*smooth merger*". Additionally, the octupole-inactive gap near $I_0 = 90^\circ$ is visible in the merger time plot (middle panel of Fig. 8.5). The middle panels of Figs. 8.6–8.8 show the behavior of $T_{\rm m}$ for the other parameter regimes and also exhibit these two categories of mergers and the octupole-inactive gap.

Due to the chaotic nature of the octupole-order ZLK effect, the initial inclination I_0 alone is not sufficient to determine with certainty whether a system can merge within a Hubble time. Instead, for a given I_0, we can use numerical integrations with various ω, $\omega_{\rm out}$, and Ω to compute a merger probability, denoted by

$$P_{\rm merger}(I_0; q, e_{\rm out}) = P\left(T_{\rm m} < 10\,{\rm Gyr}\right), \tag{8.17}$$

where the notation $P_{\rm merger}(I_0; q, e_{\rm out})$ highlights the dependence of $P_{\rm merger}$ on q and $e_{\rm out}$, two of the key factors that determine the strength of the octupole effect (of course $P_{\rm merger}$ depends on other system parameters such as m_{12}, a_0, $a_{\rm out}$, etc.). The bottom panels of Figs. 8.4–8.8 show our numerical results. In all of these plots, there is a retrograde inclination window for which successful merger is guaranteed. In Fig. 8.5, it can be seen that a large range of prograde inclinations have a probabilistic outcome. In Fig. 8.6, while the enhanced octupole strength allows for most of the prograde inclinations to merge with certainty, there is still a region around $I_0 \approx 80^\circ$ where $P_{\rm merger} < 1$.

---

the maximum eccentricity attained in a *quadrupole* ZLK cycle (i.e. within the first $\sim t_{\rm ZLK}$) is sufficiently large to produce a prompt merger. When the octupole effect is non-negligible, it can drive systems to much more extreme eccentricities than can the quadrupole-order effects alone (compare the blue dots and black dashed line in Fig. 8.4), and thus our "one-shot mergers" occur for a larger range of I_0 than do quadrupole-order "fast" mergers.

8.3.2 Merger Probability: Semi-analytic Criteria

By comparing the top and bottom panels of Figs. 8.4–8.8, it is clear that their features are correlated: in all five cases, the retrograde merger window occupies the same inclination range as the retrograde octupole-active window, while $P_{\rm merger}$ is only nonzero for prograde inclinations where $e_{\max}$ nearly attains $e_{\lim}$. Here, we further develop this connection and show that the non-dissipative simulations can be used to predict the outcomes of simulations with GW dissipation rather reliably.

In Section 8.3.1, we identified both one-shot and smooth mergers in our simulations. Towards understanding the one-shot mergers, we first define $e_{\rm os}$ to be the $e_{\max}$ required to dissipate an order-unity fraction of the binary's orbital energy via GW emission in a single ZLK cycle. Since a binary spends a fraction $\sim j(e_{\max})$ of each ZLK cycle near $e_{\max}$ [e.g., Anderson et al., 2016], we set

$$j(e_{\rm os})\left.\frac{{\rm d}\ln a}{{\rm d}t}\right|_{e=e_{\rm os}} = -\frac{1}{t_{\rm ZLK}}, \tag{8.18}$$

where ${\rm d}(\ln a)/{\rm d}t$ is given by Eq. (8.14). This yields

$$j^6(e_{\rm os}) \equiv \frac{425 t_{\rm ZLK}}{96 t_{\rm GW,0}} = \frac{170}{3}\frac{G^3\mu m_{12}^3}{m_3 c^5 a^4 n}\left(\frac{a_{\rm out,eff}}{a}\right)^3, \tag{8.19}$$

where $t_{\rm GW,0} = (t_{\rm GW})_{e=0}$ (see Eq. 8.14) is given by

$$t_{\rm GW,0}^{-1} = \frac{64}{5}\frac{G^3\mu m_{12}^2}{c^5 a^4}, \tag{8.20}$$

we have approximated $e_{\rm os} \approx 1$. Eq. (8.19) is equivalent to

$$\begin{aligned} 1 - e_{\rm os} \approx 3\times 10^{-6}&\left(\frac{m_{12}}{50M_\odot}\right)^{7/6}\left(\frac{q/(1+q)^2}{1/4}\right)^{1/3}\left(\frac{m_3}{30M_\odot}\right)^{-1/3} \\ &\times\left(\frac{a_{\rm out,eff}}{3600\,{\rm AU}}\right)\left(\frac{a}{100\,{\rm AU}}\right)^{-11/6}. \end{aligned} \tag{8.21}$$

Then, if a system satisfies $e_{\max} > e_{\rm os}$ with $e_{\max}$ based on non-dissipative integration, it is expected attain a sufficiently large eccentricity to undergo a one-shot merger.

Towards understanding smooth mergers, we seek a characteristic eccentricity that captures GW emission over many ZLK cycles. We define $e_{\rm eff}$ as an effective ZLK maximum eccentricity, i.e.

$$\begin{aligned}\left\langle \frac{\mathrm{d}\ln a}{\mathrm{d}t} \right\rangle &= -\frac{1}{t_{\rm GW,0}} \left\langle \frac{1+73e^2/24+37e^4/96}{j^7(e)} \right\rangle \\ &\equiv -\frac{425/96}{t_{\rm GW,0}} \frac{1}{j^6(e_{\rm eff})},\end{aligned} \tag{8.22}$$

where the angle brackets denote averaging over many $t_{\rm ZLK,oct}$ in order to capture the characteristic eccentricity behavior over many octupole cycles. In the second line of Eq. (8.22), we have essentially replaced the ZLK-averaged orbital decay rate by $\mathrm{d}(\ln a)/\mathrm{d}t$ evaluated at $e_{\rm eff}$ multiplied by $j(e_{\rm eff})$. In practice (see Figs. 8.4–8.8), we typically average over $2000 t_{\rm ZLK}$ of the non-dissipative simulations to compute $e_{\rm eff}$.

With $e_{\rm eff}$ computed using Eq. (8.22), we can define the critical effective eccentricity $e_{\rm eff,c}$ such that the ZLK-averaged inspiral time is a Hubble time, i.e. $\langle \mathrm{d}(\ln a)/\mathrm{d}t \rangle \equiv -(10\,\mathrm{Gyr})^{-1}$. This gives

$$j^6\left(e_{\rm eff,c}\right) \equiv \frac{425}{96} \frac{10\,\mathrm{Gyr}}{t_{\rm GW,0}}, \tag{8.23}$$

or equivalently

$$1 - e_{\rm eff,c} \approx 10^{-4} \left(\frac{m_{12}}{50 M_\odot}\right) \left(\frac{q/(1+q)^2}{1/4}\right)^{1/3} \left(\frac{a}{100\,\mathrm{AU}}\right)^{-4/3}. \tag{8.24}$$

Thus, if a system is evolved using the non-dissipative equations of motion and satisfies $e_{\rm eff} > e_{\rm eff,c}$, then it is expected to successfully undergo a smooth merger within a Hubble time.

Therefore, a system can be predicted to merge successfully if it satisfies either the one-shot or smooth merger criteria. The semi-analytical merger probability (as a function of I_0 and other parameters) is:

$$P^{\rm an}_{\rm merger}(I_0; q, e_{\rm out}) = P\left(e_{\rm eff} > e_{\rm eff,c} \text{ or } e_{\rm max} > e_{\rm os}\right). \tag{8.25}$$

Although not fully analytical (since numerical integrations of non-dissipative systems are needed to obtain $e_{\rm eff}$ and $e_{\rm max}$ in general), Eq. (8.25) provides efficient computation of the merger probability without full numerical integrations including GW radiation.

The top panels of Figs. 8.4–8.8 show $e_{\rm eff}$ and $e_{\rm max}$, and their critical values, $e_{\rm eff,c}$ and $e_{\rm os}$. Using these, we compute the semi-analytical merger probability, shown as the thick green lines in the bottom panels of Figs. 8.4–8.8. We generally observe good agreement with the numerical $P_{\rm merger}$. However, $P^{\rm an}_{\rm merger}$ slightly but systematically underpredicts $P_{\rm merger}$ for some configurations, such as the prograde inclinations in Figs. 8.5 and 8.8. These regions coincide with the inclinations for which the merger outcome is uncertain. This underprediction is due to the restricted integration time of $2000t_{\rm ZLK} \approx 3$ Gyr used for the non-dissipative simulations. To illustrate this, we also calculate $P^{\rm an}_{\rm merger}$ using a shorter integration time of $500t_{\rm ZLK}$ for our non-dissipative simulations. The results are shown as the light green lines in the bottom panels of Figs. 8.4–8.8, performing visibly worse. A more detailed discussion of this issue can be found in Section 8.4.4.

A few observations about Eq. (8.25) can be made. First, it explains why some prograde systems merge probabilistically ($0 < P_{\rm merger} < 1$): for the prograde inclinations in Fig. 8.5, the $e_{\rm eff}$ values scatter widely around $e_{\rm eff,c}$ [or more precisely, $j(e_{\rm eff})$ scatters around $j(e_{\rm eff,c})$], even for a given I_0, so the detailed merger outcome depends on the initial conditions. For the prograde inclinations in Fig. 8.6, the double-valued feature in the $e_{\rm max}$ plot (the top panel) pointed out in Section 8.2.3 represents a sub-population of systems that do not satisfy Eq. (8.25). Second, $e_{\rm max} > e_{\rm os}$ often ensures $e_{\rm eff} > e_{\rm eff,c}$ in practice, as the averaging in Eq. (8.22) is heavily weighted towards extreme eccentricities. As such, $e_{\rm eff} > e_{\rm eff,c}$ alone is often a sufficient condition in Eq. (8.25).

The one-shot merger criterion ($e_{\max} > e_{\rm os}$) can also be used to distinguish two different types of system architectures: if $e_{\rm lim} \gtrsim e_{\rm os}$ for a particular architecture, then all initial conditions leading to orbit flips (i.e., in an octupole-active window) also execute one-shot mergers. For $e_{\rm lim} \approx 1$, Eq. (8.10) reduces to

$$j(e_{\rm lim}) \approx \frac{8\epsilon_{\rm GR}}{9}\left(1+\frac{\eta^2}{12}\right)^{-1}. \tag{8.26}$$

which lets us rewrite the constraint $e_{\rm lim} \gtrsim e_{\rm os}$ as

$$\left(\frac{a}{a_{\rm out,eff}}\right) \gtrsim 0.0186\left(\frac{a_{\rm out,eff}}{3600\,{\rm AU}}\right)^{-7/37}\left(\frac{m_{12}}{50M_\odot}\right)^{17/37} \times \left(\frac{30M_\odot}{m_3}\right)^{10/37}\left(\frac{q/(1+q)^2}{1/4}\right)^{-2/37}. \tag{8.27}$$

For the system architecture considered in Figs. 8.4–8.7, this condition is satisfied, and we see indeed that wherever the top panel suggests orbit flipping ($e_{\max} = e_{\rm lim}$), the bottom panel shows $P_{\rm merger} \approx 1$. When the condition (Eq. 8.27) is not satisfied, one-shot mergers are not possible, and $P_{\rm merger}$ is generally only nonzero for a small range about $I_{0,\rm lim}$.

8.4 Merger Fraction as a Function of Mass Ratio

Having developed an semi-analytical understanding of the binary merger window and probability in the last section (particularly Section 8.3.2), we now study the fraction of BH binaries in triples that successfully merge under various conditions – we call this the merger fraction.

8.4.1 Merger Fraction for Fixed Tertiary Eccentricity

We first consider the simple case where $e_{\rm out}$ is fixed at a few specific values and compute the merger fraction as a function of the mass ratio q. We consider

isotropic mutual orientations between the inner and outer binaries, i.e. we draw $\cos I_0$ from a uniform grid over the range $[-1,1]$ (recall that ω, $\omega_{\rm out}$, and Ω are drawn uniformly from the range $[0,2\pi)$ when computing the merger probability $P_{\rm merger}$ at a given I_0). The merger fraction is then given by:

$$f_{\rm merger}(q,e_{\rm out}) \equiv \frac{1}{2}\int_{-1}^{1} {\rm d}\cos I_0\, P_{\rm merger}(I_0;q,e_{\rm out}). \tag{8.28}$$

This is proportional to the integral of the black lines (weighted by $\sin I_0$) in the bottom panels of Figs. 8.4–8.7. We can also use semi-analytical criteria introduced in Section 8.3.2 to predict the outcome and merger fraction. This is computed by using $P^{\rm an}_{\rm merger}$ as the integrand in Eq. (8.28), or by evaluating the integral of the thick green lines (weighted by $\sin I_0$) in the bottom panels of Figs. 8.4–8.7. Figure 8.9 shows the resulting $f_{\rm merger}$ and the analytical estimates for all combinations of $q \in \{0.2, 0.3, 0.4, 0.5, 0.7, 1.0\}$ and $e_{\rm out} \in \{0.6, 0.8, 0.9\}$. It is clear that the numerical $f_{\rm merger}$ and the analytical estimate agree well, and that the merger fraction increases steeply for smaller q.

To explore the impact of our choice of isotropic mutual orientations between the two binaries, we also consider a wedge-shaped distribution of $\cos I_0$ as was found in the population synthesis studies of Antonini et al. [2017]. We still use the same uniform grid of $\cos I_0$ as before, but weight each eccentricity by its probability probability density following the distribution:

$$P(\cos I_0) = \frac{1}{4} + \frac{|\cos I_0|}{2}. \tag{8.29}$$

The resulting $f_{\rm merger}$ for a tertiary with $\cos I_0$ distributed like Eq. (8.29) is shown as the dashed lines in Fig. 8.9. While the total merger fractions decrease, the strong enhancement of the merger fraction at smaller q is unaffected.

In the right panel of Fig. 8.9, we see that the merger fractions for the three $e_{\rm out}$ values overlap for small $\epsilon_{\rm oct}$. This implies that $f_{\rm merger}$ depends only on $\epsilon_{\rm oct}$

in this regime, and not on the values of q and $e_{\rm out}$ independently. From Fig. 8.4 (which has $\epsilon_{\rm oct} = 0.007$), we see that this suggests that the size of the retrograde merger window only depends on $\epsilon_{\rm oct}$, much like what Eq. (8.13) shows for the test-particle limit. However, once $\epsilon_{\rm oct}$ is increased sufficiently, the three curves in the right panel of Fig. 8.9 cease to overlap. This can be attributed to their different η values: for sufficiently small $\epsilon_{\rm oct}$, no prograde initial inclinations successfully merge (e.g., Fig. 8.4), and the merger fraction is solely determined by the size of the retrograde octupole-active window. But once $\epsilon_{\rm oct}$ is sufficiently large, prograde mergers become possible, and the merger fraction is also affected by the size of the octupole-inactive gap, which depends on η. This again illustrates the importance of the octupole-inactive gap, which we comment on in Appendix G.1.

Figure 8.10 depicts the merger fractions for systems with $a_0 = 50\,\mathrm{AU}$ (the other parameters are the same as in Fig. 8.9). According to Eq. (8.27), these systems no longer satisfy $e_{\rm lim} \gtrsim e_{\rm os}$, so the merger fraction is expected to diminish strongly and vary much more weakly with q, as one-shot mergers are no longer possible. This is indeed observed, particularly for the $e_{\rm out} = 0.6$ curve in Fig. 8.10. We also remark that the semi-analytical prediction accuracy is poorer in this case than in Fig. 8.9. This is because the only mergers in this regime are smooth mergers. As can be seen for the prograde I_0 in Figs. 8.5 and 8.8, smooth mergers occur over a wide range of merger times $T_{\rm m}$, and the specific $T_{\rm m}$ that a system experiences depends sensitively on its chaotic evolution. Thus, Eq. (8.22) is a rather approximate estimate of the amount of GW emission that a real system emits during a smooth merger; indeed, the prograde regions of Figs. 8.5 and 8.8 show that the merger times for smooth mergers are systematically underpredicted by the semi-analytic merger criterion (see discussion in Section 8.4.4). The non-monotonicity of the semi-analytic merger fraction for $e_{\rm out} = 0.6$ from $q = 0.2$ to $q = 0.3$ is due to small sample sizes and finite grid spacing in $\cos I_0$.

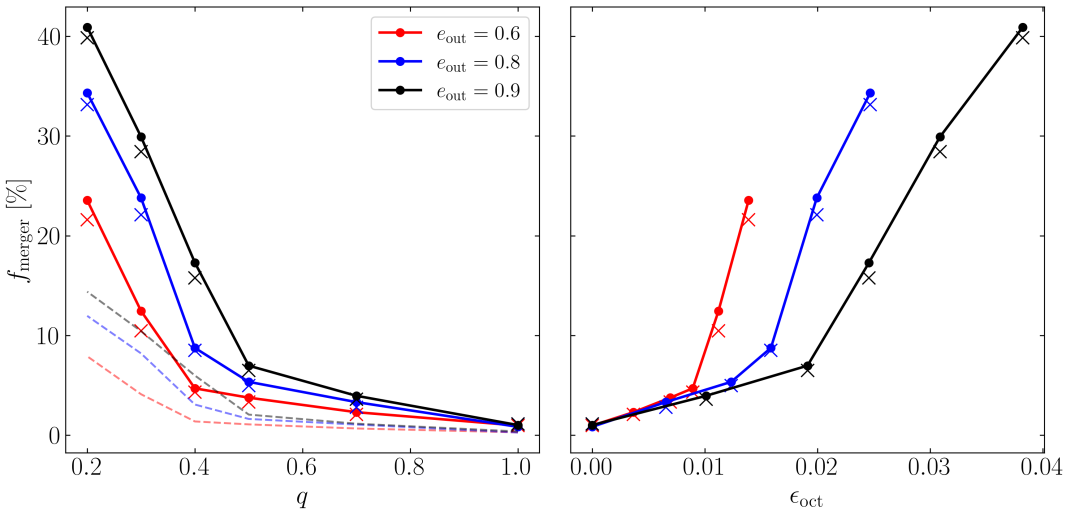

Figure 8.9: Merger fraction (Eq. 8.17) of BH binaries in triples as a function of mass ratio q (left panel) for several values of outer binary eccentricities. The other system parameters are the same as in Figs. 8.4–8.7. The right panel shows the same merger fraction, but plotted against the octupole parameter $\epsilon_{\rm oct}$. The filled circles joined by the solid lines are numerical results (based on integrations for full triple system evolution including GW emission; see the black solid lines in the bottom panels of Figs. 8.4–8.7) assuming random mutual inclinations between the inner and outer binaries (uniform in $\cos I_0$), and the dashed lines denote the merger fractions if the mutual inclinations are distributed according to Eq. (8.29). The crosses are semi-analytical results using an integration time of $2000 t_{\rm ZLK}$ (see the thick green lines in the bottom panels of Figs. 8.4–8.7).

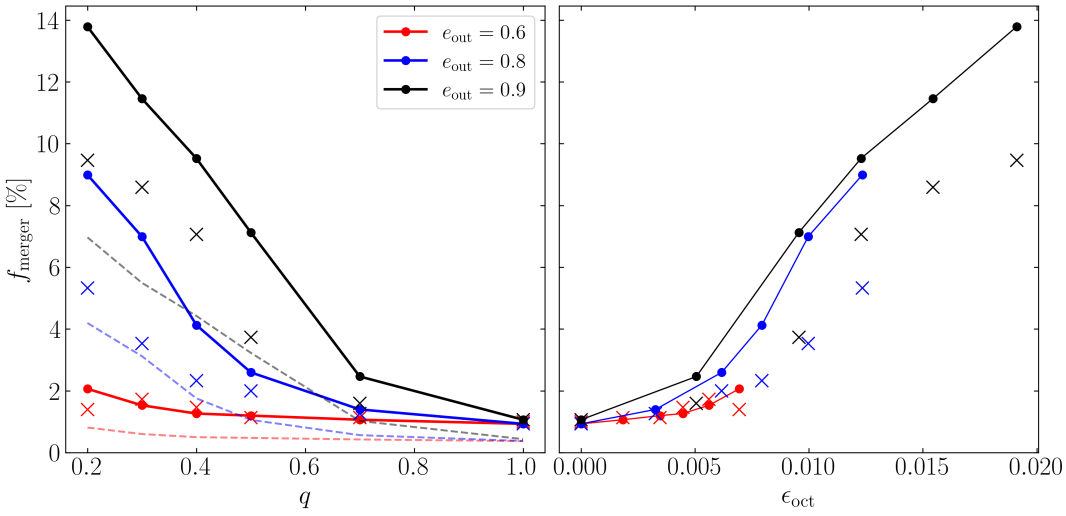

Figure 8.10: Same as Fig. 8.9 but for $a_0 = 50\,{\rm AU}$.

8.4.2 Merger Fraction for a Distribution of Tertiary Eccentricities

For a distribution of tertiary eccentricities, denoted $P(e_{\rm out})$, the merger fraction is given by

$$\begin{aligned}\eta_{\rm merger}(q) &= \int {\rm d}e_{\rm out}\, P(e_{\rm out}) f_{\rm merger}(q, e_{\rm out}), \\ &= \int {\rm d}e_{\rm out}\, \frac{P(e_{\rm out})}{2} \int_{-1}^{1} {\rm d}\cos I_0\, P_{\rm merger}(I_0; q, e_{\rm out}). \end{aligned} \tag{8.30}$$

We consider two possible $P(e_{\rm out})$ with $e_{\rm out} \in [0, 0.9]$: (i) a uniform distribution, $P(e_{\rm out}) = $ constant, and (ii) a thermal distribution, $P(e_{\rm out}) \propto e_{\rm out}$.

The top panel of Fig. 8.11 shows $\eta_{\rm merger}$ (black dots) for the fiducial triple systems (with the same parameters as in Figs. 8.4–8.7). For each q, the integral in Eq. (8.30) is computed using 1000 realizations of random $e_{\rm out}$, $\cos I_0$, ω, $\omega_{\rm out}$, and Ω. Not surprisingly, we see $\eta_{\rm merger}$ increases with decreasing q. When q is small, a thermal distribution of $e_{\rm out}$ tends to yield higher $\eta_{\rm merger}$ than does a uniform distribution. We also compute the merger fraction using the semi-analytical merger probability of Eq. (8.25) on a dense grid of initial conditions uniformly sampled in $e_{\rm out}$ and $\cos I_0$; the result is shown as the blue dotted line in Fig. 8.11, which is in good agreement with the uniform-$e_{\rm out}$ simulation result (black).

To characterize the properties of merging binaries, the middle and bottom panels of Fig. 8.11 show the distributions of merger times and merger eccentricities (at both the LISA and LIGO bands) for different mass ratios. To obtain the LISA and LIGO band eccentricities (with GW frequency equal to 0.1 Hz and 10 Hz respectively), the inner binaries are evolved from when they reach $0.005 a_0$ (at which point we terminate the integration of the triple system evolution as the inner binary's evolution is decoupled from the tertiary; see Eq. 8.16) to physical merger

using Eqs. (8.14–8.15). While the LIGO band eccentricities are all quite small ($\lesssim 10^{-3}$), the LISA band eccentricities (at 0.1 Hz) are significant, with median $\gtrsim 0.2$ for $q \lesssim 0.5$. We note that these eccentricities are generally smaller than those found in the population studies of Liu et al. [2019a]. This is because in this paper we consider only sufficiently hierarchical systems for which double-averaged evolution equations are valid, whereas Liu et al. [2019a] included a wider range of triple hierarchies and had to use N-body integrations to evolve some of the systems.

For comparison, Figure 8.12 shows the results when $a_{\rm out,eff} = 5500$ AU (instead of $a_{\rm out,eff} = 3600$ AU for Fig. 8.11) with all other parameters unchanged. While $\eta_{\rm merger}$ is lower than it is for $a_{\rm out,eff} = 3600$ AU, there is still a large increase of $\eta_{\rm merger}$ with decreasing q. Since Eq. (8.27) is still satisfied, this is expected.

8.4.3 $q \ll 1$ Limit

For fixed m_{12} (and other parameters), even though the octupole strength $\epsilon_{\rm oct}$ increases as q decreases, the efficiency of GW radiation also decreases. It is therefore natural to ask at what q these competing effects become comparable and the merger fraction is maximized. We show that this does not happen until q is extremely small.

We see from Figs. 8.4–8.7 that $e_{\rm lim} > e_{\rm os}$ for our fiducial triple systems. Indeed, from Eq. (8.27), we see that even for q as small as 10^{-5}, the condition $e_{\rm lim} > e_{\rm os}$ is satisfied. This implies that most binaties execute one-shot mergers when undergoing an orbit flip. In addition, recall that the characteristic time for the binary to approach $e_{\rm lim}$ can be estimated by Eq. (8.12), which, for our fiducial

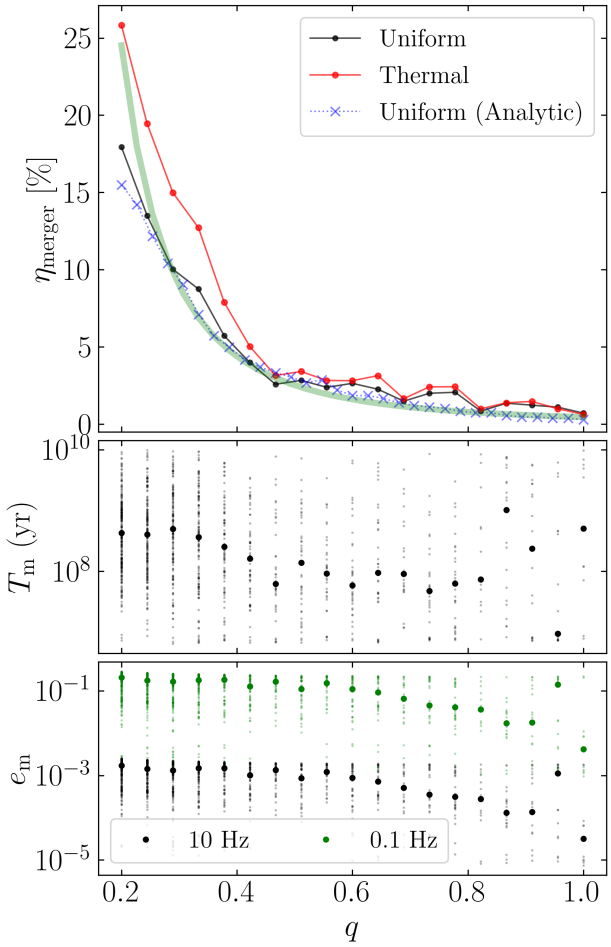

Figure 8.11: *Upper panel:* Binary BH merger fraction as a function of mass ratio q for the fiducial triple systems (with parameters the same as in Figs. 8.4–8.7), assuming random mutual inclinations (uniform in $\cos I_0$), and either uniform (black dots) or thermal distribution (red dots) for the tertiary eccentricity distribution [with $e_{\rm out} \in [0, 0.9]$]. These are obtained numerically using Eq. (8.30) by sampling 1000 combinations of $e_{\rm out}$, $\cos I_0$, ω, $\omega_{\rm out}$, and Ω. The blue dotted line is the semi-analytical result obtained by applying Eq. (8.25) in Eq. (8.30) (evaluated using a dense uniform grid of $\cos I_0$ and $e_{\rm out}$). The thick green line is a power-law fit to the analytical $\eta_{\rm merger}$ with a power law index of -2.5. *Middle panel:* Merger times of successful mergers for a uniform $e_{\rm out}$ distribution (the median is denoted with the large black dot). *Bottom panel:* Merging binary eccentricities (again, for a uniform $e_{\rm out}$ distribution) in the LISA band (0.1 Hz; green) and in the LIGO band (10 Hz; black), with medians marked with large dots.

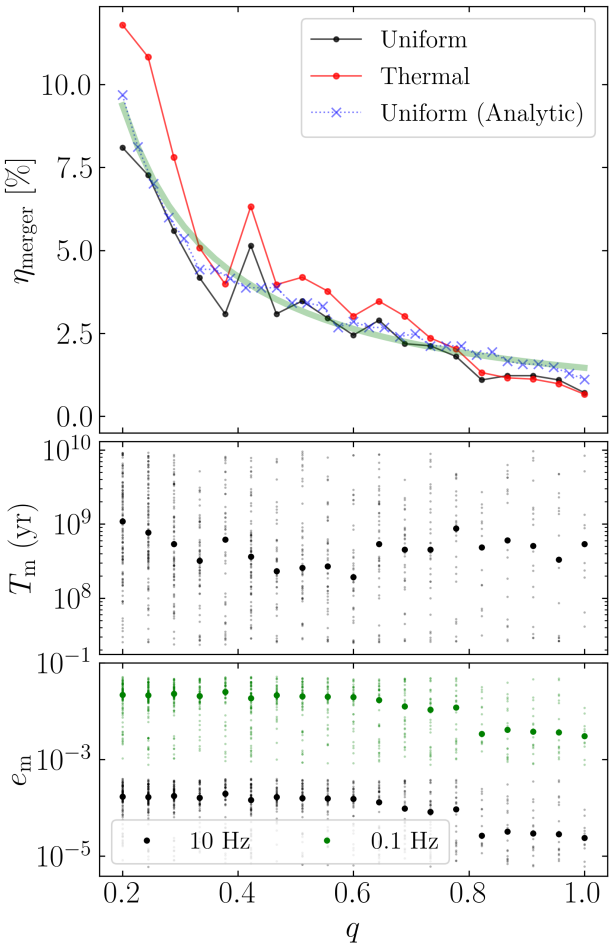

Figure 8.12: Same as Fig. 8.11 but for $a_{\rm out,eff} = 5500$ AU. The power law index of the fit to the analytical $\eta_{\rm merger}$ is -1.15.

triple systems, is given by

$$t_{\rm ZLK,oct} \simeq 10^8 \left(\frac{m_{12}}{50M_\odot}\right)^{1/2} \left(\frac{a_{\rm out,eff}}{3600\,{\rm AU}}\right)^{7/2} \left(\frac{a}{100\,{\rm AU}}\right)^{-2} \times \left(\frac{m_3}{30M_\odot}\right)^{-1} \left[\frac{1-q}{1+q}\frac{e_{\rm out}}{\sqrt{1-e_{\rm out}^2}}\right]^{-1/2} {\rm yr}. \quad (8.31)$$

Since $t_{\rm ZLK,oct} \ll 10\,{\rm Gyr}$, this implies that the octupole-ZLK-induced binary merger fractions are primarily determined by what initial conditions would lead to extreme eccentricity excitation and only weakly depend on the GW radiation rate. Indeed, Eq. (8.27) shows that, while $e_{\rm lim} > e_{\rm os}$ is indeed violated if q is decreased sufficiently, the dependence is extremely weak. Thus, $\eta_{\rm merger}$ is expected to be very nearly constant for all physically relevant values of q, as can be seen in Fig. 8.13.

8.4.4 Limitations of semi-analytic Calculation

It can be seen in Fig. 8.9 that the semi-analytical merger fractions are systematically lower than the values obtained from the direct simulations. One reason that this discrepancy arises is because the non-dissipative simulations used to compute $e_{\rm eff}$ and $e_{\rm max}$ are only run for $2000t_{\rm LK} \approx 3$ Gyr, while the full simulations including GW dissipation are run for 10 Gyr. Owing to the chaotic nature of the octupole-order ZLK effect, this means that, if an initial condition leads to extreme eccentricities only after many Gyrs, then $e_{\rm eff}$ and $e_{\rm max}$ are underpredicted by the non-dissipative simulations. Additionally, there are times when eccentricity vector of the inner binary is librating, during which orbit flips are strongly suppressed [Katz et al., 2011]. Since the librating phase can last an unpredictable amount of time, this suggests that the semi-analytical merger criteria can become more complete as the integration time is increased.

We quantify the "completeness" of the semi-analytical merger fraction via the

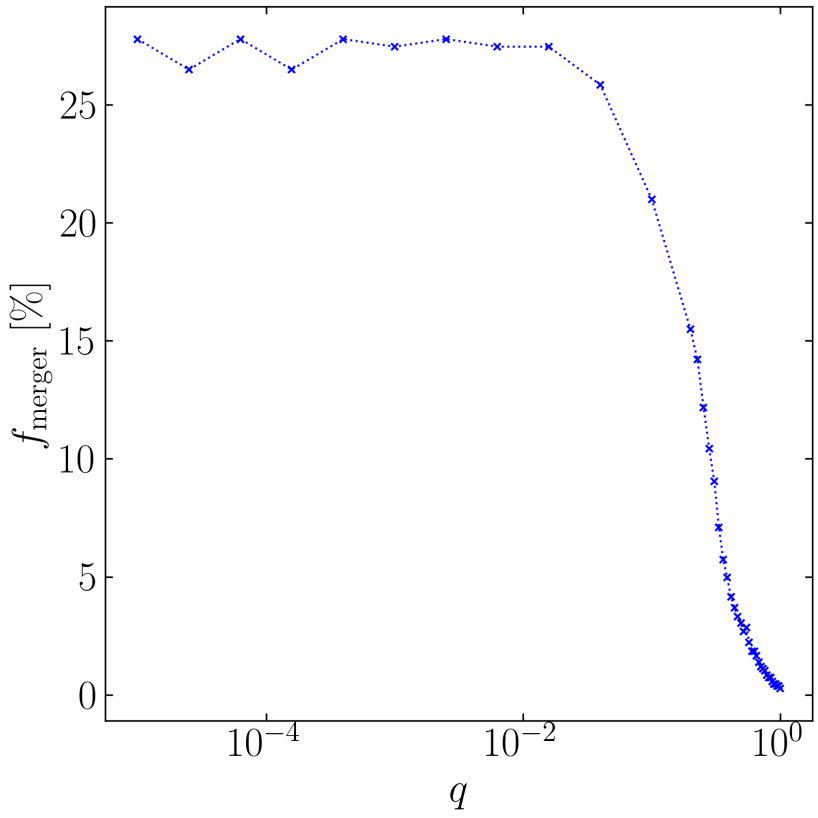

Figure 8.13: Same as blue dashed line of the top panel of Fig. 8.11 but extended to very small q. Due to the very weak q dependence in Eq. (8.27), $f_{\rm merger}$ is expected to depend very weakly on q when $q \ll 1$ (such that $\epsilon_{\rm oct}$ is approximately constant), which agrees with the simulation results.

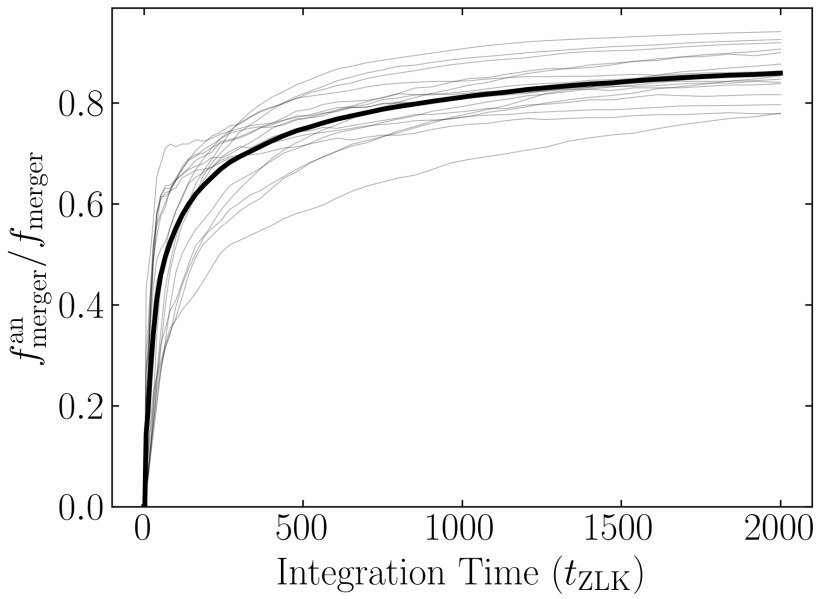

Figure 8.14: Completeness of the semi-analytical merger fraction, defined as $f^{\rm an}_{\rm merger}/f_{\rm merger}$, as a function of the integration time used for the non-dissipative simulations, in the fiducial parameter regime while $e_{\rm out}$ is fixed at a few values. The thin grey lines indicate the completeness for particular combinations of $(q, e_{\rm out})$, and the thick black line denotes their average. We see that completeness is still increasing as the integration time approaches $2000 t_{\rm ZLK} \approx 3$ Gyr.

ratio $f^{\rm an}_{\rm merger}/f_{\rm merger}$ as a function of non-dissipative integration time. We focus on the fiducial triple systems for demonstrative purposes and compute the completeness for each of the q and $e_{\rm out}$ combinations shown in Fig. 8.9. Figure 8.14 shows the completeness for each of these simulations in light grey lines and their mean in the thick black line. We see that the completeness is still increasing even as the non-dissipative simulation time is increased to $2000 t_{\rm ZLK}$, so we expect that even longer integration times would give even better agreement with the dissipative simulations.

8.5 Mass Ratio Distribution of Merging BH Binaries

In Section 4, we have calculated the binary BH merger fractions $f_{\rm merger}$ and $\eta_{\rm merger}$ as a function of the mass ratio q for some representative triple systems. To determine the distribution in q and m_{12} (total mass) of the merging binaries, we would need to know both the initial distribution in q, m_{12} and a_0 of the inner BH binaries and the distribution in m_3, $a_{\rm out}$ and $e_{\rm out}$ of the outer binaries, denoted by:

$$\frac{{\rm d}F}{{\rm d}q{\rm d}m_{12}{\rm d}a_0}, \quad \frac{{\rm d}F_{\rm out}}{{\rm d}m_3{\rm d}a_{\rm out}{\rm d}e_{\rm out}}. \tag{8.32}$$

The distribution in q and m_{12} of the merging binaries is then

$$\begin{aligned}\frac{{\rm d}F_{\rm merger}}{{\rm d}q{\rm d}m_{12}} = &\int {\rm d}a_0 {\rm d}m_{\rm out} {\rm d}a_{\rm out} {\rm d}e_{\rm out} \frac{{\rm d}F}{{\rm d}q{\rm d}m_{12}{\rm d}a_0} \\ &\times \frac{{\rm d}F_{\rm out}}{{\rm d}m_3{\rm d}a_{\rm out}{\rm d}e_{\rm out}} f_{\rm merger}(q, e_{\rm out}; m_{12}, a_0, m_3, a_{\rm out}, e_{\rm out}),\end{aligned} \tag{8.33}$$

where $f_{\rm merger}$ is given by Eq. (8.28) (assuming random mutual inclinations between the inner and outer binaries), and we have spelled out its dependence on various system parameters. Some examples of $f_{\rm merger}$ are shown in Figs. 8.9–8.10. If we further specify the eccentricity distribution of the outer binaries, we have

$$\begin{aligned}\frac{{\rm d}F_{\rm merger}}{{\rm d}q{\rm d}m_{12}} = &\int {\rm d}a_0 {\rm d}m_3 {\rm d}a_{\rm out} \frac{{\rm d}F}{{\rm d}q{\rm d}m_{12}{\rm d}a_0} \\ &\times \frac{{\rm d}F_{\rm out}}{{\rm d}m_3{\rm d}a_{\rm out,eff}} \eta_{\rm merger}(q; m_{12}, a_0, m_3, a_{\rm out,eff}),\end{aligned} \tag{8.34}$$

where $\eta_{\rm merger}$ is given by Eq. (8.30). Some examples of $\eta_{\rm merger}$ are shown in the top panels of Figs. 8.11–8.12.

Clearly, to properly evaluate Eq. (8.33) or (8.34) would require large population synthesis calculations and in any case would involve significant uncertainties, a task beyond the scope of this paper. For illustrative purposes, we consider the

fiducial triple systems as studied in Section 8.4, and estimate the mass-ratio distribution of BH mergers as

$$\frac{\mathrm{d}F_{\mathrm{merger}}}{\mathrm{d}q} \sim \frac{\mathrm{d}F}{\mathrm{d}q}\,\eta_{\mathrm{merger}}(q). \tag{8.35}$$

8.5.1 Initial q-distribution of BH Binaries

The initial mass-ratio distribution of BH binaries, $\mathrm{d}F/\mathrm{d}q$, is uncertain. It can be derived from the the mass distributions of of main-sequence (MS) binaries, together with the MS mass (m_{ms}) to BH mass (m) relation.

For the distribution of MS binary masses, we assume that each MS component mass is drawn from a Salpeter-like initial mass function (IMF) independently, with

$$\frac{\mathrm{d}F_{\mathrm{ms}}}{\mathrm{d}m_{\mathrm{ms}}} \propto m_{\mathrm{ms}}^{-\alpha}, \tag{8.36}$$

in the range $m_{\mathrm{min}} \leq m_{\mathrm{ms}} \leq m_{\mathrm{max}}$. Note in this case the MS binary mass-ratio distribution is (for $q \leq 1$)

$$\frac{\mathrm{d}F_{\mathrm{ms}}}{\mathrm{d}q} \propto q^{\alpha-2}\left[1-\left(\frac{q}{q_{\mathrm{min}}}\right)^{2-2\alpha}\right], \tag{8.37}$$

where $q_{\mathrm{min}} = m_{\mathrm{min}}/m_{\mathrm{max}}$ is the minimum possible binary mass ratio [this is a generalization of the result of Tout, 1991]. We consider two representative values of α: (i) $\alpha = 2.35$, the canonical Salpeter IMF [Salpeter, 1955], and (ii) $\alpha = 2$, resulting in a uniform q distribution (for $q \gtrsim 2q_{\mathrm{min}}$). The latter case is consistent with observational studies of the mass ratio of high-mass MS binaries [Sana et al., 2012, Duchêne and Kraus, 2013, Kobulnicky et al., 2014, Moe and Di Stefano, 2017].

To obtain $\mathrm{d}F/\mathrm{d}q$, we compute the BH binary mass ratio when each main sequence mass m_{ms} is mapped to its corresponding BH mass m. This mapping is

taken from Spera and Mapelli [2017] for the mass range $25M_\odot \leq m_{\rm ms} \leq 117M_\odot$. We consider both the case where $Z = 0.02$ ("high Z") and where $Z = 2.0\times10^{-4}$ ("low Z"), the two limiting metallicities used in Spera and Mapelli [2017]. We can then numerically compute $\mathrm{d}F/\mathrm{d}q$ by sampling masses for stellar binaries from the IMF, translating these into BH masses, then calculating the resulting BH mass ratios for each binary. The upper panel of Fig. 8.15 shows the $\mathrm{d}F/\mathrm{d}q$ obtained via this procedure for a Salpeter IMF ($\alpha = 2.35$) when sampling 10^5 MS binaries for each metallicity. In the lower four panels, we also show $\mathrm{d}F/\mathrm{d}q$ restricted to particular ranges of m_{12}. Note that the distributions differ significantly among the m_{12} ranges and also between the two metallicities. Figure 8.16 shows the case when $\alpha = 2$, which mostly resembles Fig. 8.15.

8.5.2 q-distribution of Merging BH Binaries

Using the results of Section 8.5.1, we can also estimate the mass ratio distribution of merging BHs using Eq. (8.35). We consider representative triple systems considered in Section 8.4: for $\eta_{\rm merger}$, we use a simple approximation that lies roughly between the two cases shown in Figs. 8.11–8.12:

$$\eta_{\rm merger}(q) \approx 0.2 \times [\max(q, 0.2)]^{-2}. \tag{8.38}$$

The results for $\mathrm{d}F_{\rm merger}/\mathrm{d}q$ are displayed as the dotted curves in Figs. 8.15–8.16 in each panel. Broadly speaking, $\mathrm{d}F_{\rm merger}/\mathrm{d}q$ peaks around $q \sim 0.3$ for low-Z systems, and around $q \sim 0.4$ for high-Z systems, the latter reflecting the peak in the initial BH binary q-distribution. Also note that $\mathrm{d}F_{\rm merger}/\mathrm{d}q$ can be quite different for different m_{12} ranges. For example, merging BH binaries with $m_{12} > 42M_\odot$ are only produced in low-Z systems, and $\mathrm{d}F_{\rm merger}/\mathrm{d}q$ peaks around $q \sim 0.3$ for $m_{12} \in [42, 67]M_\odot$, and is roughly uniform between $q \sim 0.2$ to 1 for $m_{12} \gtrsim 67M_\odot$.

We emphasize that these results for $\mathrm{d}F_{\rm merger}/\mathrm{d}q$ refer to the representative triple systems studied in Sections 8.2–8.4, and thus should be considered for illustrative purposes only. As noted above, the merger fraction $\eta_{\rm merger}$ depends on various parameters of the triple systems. While we have not attempted to quantify $\eta_{\rm merger}$ for all possible triple system parameters, it is clear that the principal finding of Section 8.4 (i.e., $\eta_{\rm merger}$ increases with decreasing q) applies only for systems with sufficiently strong octupole effects. In fact, from Figs. 8.9 and 8.10 we can estimate that the octupole-induced feature in $\eta_{\rm merger}$ becomes prominent only when $\epsilon_{\rm oct} \gtrsim 0.005$, or equivalently

$$\frac{a}{a_{\rm out,eff}} \gtrsim 0.005 \left(\frac{1+q}{1-q}\right) \frac{\sqrt{1-e_{\rm out}^2}}{e_{\rm out}} \simeq \frac{0.01}{e_{\rm out}}, \tag{8.39}$$

where in the second step we have used $q \sim 0.5$ and $e_{\rm out} \sim 0.6$. When this condition is satisfied, the inner binary can usually also undergo a one-shot merger (see Eq. 8.27), leading to strong dependence of the merger fraction on q. For triple systems with $a/a_{\rm out,eff} \lesssim 0.01$ (such as the case when the tertiary is a supermassive BH with $m_3 \gtrsim 10^6 m_{12}$), the octupole effect is unimportant (see the discussion following Eq. 8.2), and we expect the merger fraction to be almost independent of q. Indeed, an analytical fitting formula for BH mergers induced by pure quadrupole-ZLK effect shows $\eta_{\rm merger} \propto \mu^{0.16} \propto q^{0.16}/(1+q)^{0.32}$ (see Eq. 53 of Liu and Lai, 2018, or Eq. 26 of Liu and Lai, 2021). For such systems, we expect $\mathrm{d}F_{\rm merger}/\mathrm{d}q$ to be mainly determined by the initial q-distribution of BH binaries at their formation.

8.6 Summary and Discussion

We have studied the dynamical formation of merging BH binaries induced by a tertiary companion via the von Zeipel-Lidov-Kozai (ZLK) effect, focusing on the expected mass ratio distribution of merging binaries. The octupole potential of the

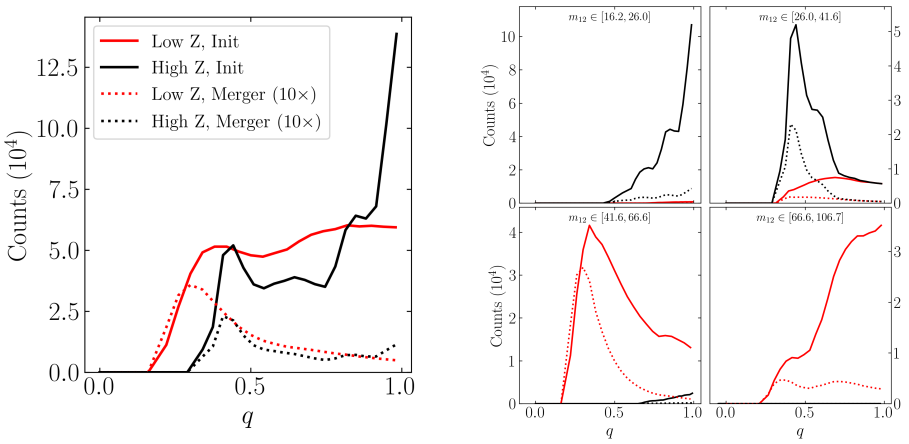

Figure 8.15: Mass ratio distributions of the initial BH binaries (solid lines) and merging BH binaries (dotted lines) when using $\alpha = 2.35$ for the MS stellar initial mass function (see Sections 8.5.1 and 8.5.2). *Top panel:* Distribution of binary mass ratio at formation and merger for all possible total binary BH masses. Each BH mass is obtained from the MS mass using the fitting formula of Spera and Mapelli [2017] for metallicities of 2×10^{-4} (Low Z) and 0.02 (High Z), while the merger fraction of BH binaries is given by Eq. (8.38). To produce these distributions, 10^5 initial MS binaries are used for each metallicity, and the number of merging BH binaries has been scaled up by a factor of 10 for visibility. The counts refer to the number per $\Delta q = 0.05$ bin. *Bottom four panels:* Same as the top panel but with specific ranges of m_{12}, the total BH mass of the binary (as labeled). Note that low-m_{12} systems are mainly produced from high-Z MS binaries, while high-m_{12} systems are mainly produced in low-Z MS binaries.

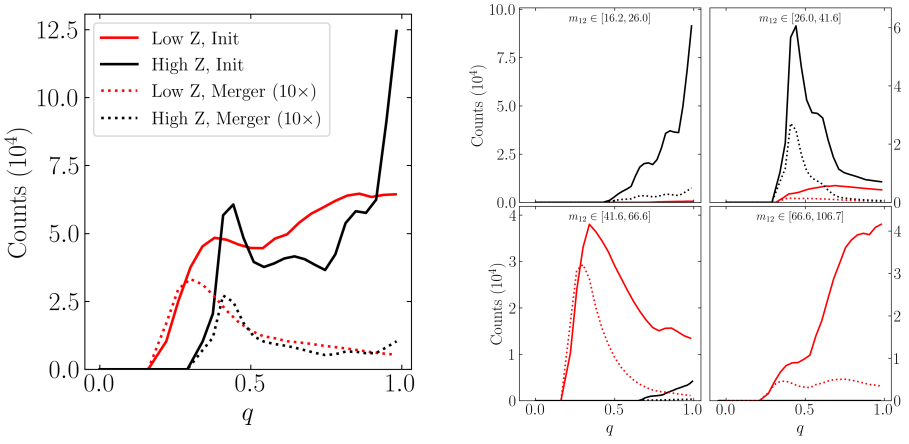

Figure 8.16: Same as Fig. 8.15 but for $\alpha = 2$, i.e. a nearly uniform distribution of the main sequence binary mass ratio. The results are very similar to Fig. 8.15.

tertiary, when sufficiently strong, can increase the inclination window and probability of extreme eccentricity excitation, and thus enhance the rate of successful binary mergers. Since the octupole strength $\epsilon_{\rm oct} \propto (1-q)/(1+q)$ (see Eq. 8.2) increases with decreasing binary mass ratio q, it is expected that ZLK-induced BH mergers favor binaries with smaller mass ratios. We quantify the dependence of the merger fraction/probability on q using a combination of numerical integrations and analytical calculations, based on the secular evolution equations for hierarchical triples. We develop new analytical criteria (Section 8.3.2) that allow us to determine, without full numerical integrations, whether an initial BH binary can undergo a "one-shot merger" or a more gradual merger under the influence of a tertiary companion. These allow us to compute the merger probability semi-analytically by only studying non-dissipative (i.e. no GWs) triple systems (see Eq. 8.25). We show that for hierarchical triples with semi-major axis ratio $a/a_{\rm out} \gtrsim 0.01-0.02$ (see Eq. 8.39), the BH binary merger fraction ($f_{\rm merger}$ or $\eta_{\rm merger}$) can increase by a larger factor (up to ~ 20) as q decreases from unity to 0.2 (see Figs. 8.9–8.13). When combined with a reasonable estimate of the mass ratio distribution of the initial BH binaries (Section 8.5.1), our results for the merger fraction suggest that the final merging BH binaries have an overall mass ratio distribution that peaks around $q = 0.3$ or 0.4, although very different distributions can be produced when restricting to specific ranges of total binary masses (see Figs. 8.15 and 8.16).

Taking our final results (Figs. 8.15 and 8.16) at face value, we tentatively conclude that the mass-ratio distribution $\mathrm{d}F_{\rm merger}/\mathrm{d}q$ of BH binary mergers induced by a comparable-mass companion is inconsistent with the current LIGO/VIRGO result (see Fig. 8.1), suggesting that such tertiary-induced mergers may not be the dominant formation channel for the majority of the detected LIGO/VIRGO events. However, there are at least two important issues/caveats to keep in mind:

(i) $\mathrm{d}F_{\rm merger}/\mathrm{d}q$ depends strongly on the initial mass-ratio distribution of BH binaries at their formation ($\mathrm{d}F/\mathrm{d}q$), which is uncertain and depends sensitively on the metalicity of the binary formation environment (see Section 8.5.1). It is also possible that the initial BH binary mass ratio distribution is much more skewed towards equal masses than what we found in Section 8.5.1 (e.g. if stellar binaries with significantly asymmetric masses become unbound due to mass loss and supernova kicks as their components become BHs). Such a distribution was found by population synthesis studies that include octupole-order ZLK effects and models of stellar evolution [e.g. Hamers et al., 2013, Toonen et al., 2018]. These studies find that ZLK oscillations in stellar binaries with small q can experience mass transfer and merge without forming a compact object binary; as a result, most compact object binaries form with large mass ratios. The prevalence of this phenomenon likely depends on the initial semimajor axes of the inner binaries. Further study would be required to understand the competition between this primordial large-q enhancement and the elevated merger fractions for small q found in the present study in an astrophysically realistic population.

(ii) When the tertiary mass m_3 is much larger than the BH binary mass m_{12}, as in the case of a supermassive BH tertiary, dynamical stability of the triple requires $a_{\rm out} \gg a$, which implies that the octupole effect is negligible ($\epsilon_{\rm oct} \ll 1$). For such triple systems, we expect the merger fraction to depend very weakly on the mass ratio, and the final $\mathrm{d}F_{\rm merger}/\mathrm{d}q$ to depend entirely on the initial $\mathrm{d}F/\mathrm{d}q$. Although the merger fraction of such "pure quadrupole" triples is small ($\lesssim 6\%$; see Eq. 53 of Liu and Lai, 2018), additional "external" effects can enhance the merger efficiency significantly [e.g., when the outer orbit experiences quasi-periodic torques from the galactic potential (Petrovich and Antonini, 2017; see also Hamers and Lai, 2017), or from the spin of a supermassive BH [Liu et al., 2019b]].

Near the completion of this paper, we became aware of the simultaneous work by Martinez et al. [2021], who study a similar topic using a population synthesis approach.

APPENDIX A

APPENDICIES TO DYNAMICS OF COLOMBO'S TOP: DISSIPATING DISK

A.1 Cassini State Local Dynamics

In this appendix, we linearize the equations of motion near each CS and determine its stability. We derive the local libration frequency or growth rate for perturbations around each CS.

A.1.1 Canonical Equations of Motion and Solutions

We adopt spherical coordinate system where $\hat{\mathbf{l}} = \hat{\mathbf{z}}$ and θ, ϕ are the polar and azimuthal angle of $\hat{\mathbf{s}}$. We choose $\hat{\mathbf{l}}_{\rm d}$ at coordinates $\theta = I, \phi = \pi$ (see Figs. 2.1 and 3.1). We use the convention $0 \le \theta < \pi$ and $0 \le \phi < 2\pi$.

The equations of motion in $\left(\phi, \cos\theta\right)$ follow by applying Hamilton's equations to the Hamiltonian [Eq. (3.8)]:

$$\frac{\mathrm{d}\phi}{\mathrm{d}t} = \frac{\partial \mathscr{H}}{\partial(\cos\theta)} = -\cos\theta + \eta\left(\cos I + \sin I \cot\theta \cos\phi\right), \tag{A.1a}$$

$$\frac{\mathrm{d}(\cos\theta)}{\mathrm{d}t} = -\frac{\partial \mathscr{H}}{\partial\phi} = -\eta \sin I \sin\theta \sin\phi. \tag{A.1b}$$

These agree with Eq. (2.9).

The CSs satisfy $\dot{\phi} = \dot{\theta} = 0$. For convenience, we give approximate solutions for the CSs in the limits $\eta \ll 1$ and $\eta \gg 1$. For $\eta \ll 1$:

- CS1: $\phi_1 = 0$, $\theta_1 \simeq \eta \sin I$.

- CS2: $\phi_2 = \pi$, $\theta_2 \simeq \pi/2 - \eta\cos I$.
- CS3: $\phi_3 = 0$, $\theta_3 \simeq \pi - \eta\sin I$.
- CS4: $\phi_4 = 0$, $\theta_4 \simeq \pi/2 - \eta\cos I$.

For $\eta \gg 1$, only CS2 and CS3 exist and are given by:

- CS2: $\phi_2 = \pi$, $\theta_2 \simeq I + \eta^{-1}\sin I\cos I$.
- CS3: $\phi_3 = 0$, $\theta_3 \simeq \pi - I + \eta^{-1}\sin I\cos I$.

Note that in the convention of Fig. 3.1, CS1, CS3 and CS4 have negative θ values since $\phi = 0$.

A.1.2 Stability and Frequency of Local Oscillations

To examine stability of each CS, we linearize Eqs. (A.1) about an equilibrium located at $\phi_{\rm cs} = 0$ (CS 1, 3, 4) or π (CS2) but arbitrary $\theta_{\rm cs}$. Setting $\phi = \phi_{\rm cs} + \delta\phi, \theta = \theta_{\rm cs} + \delta\theta$ yields

$$\frac{{\rm d}\delta\phi}{{\rm d}t} = \sin\theta_{\rm cs}\delta\theta \mp \eta\frac{\sin I}{\sin^2\theta_{\rm cs}}\delta\theta, \tag{A.2a}$$

$$\frac{{\rm d}\delta\theta}{{\rm d}t} = \pm\eta\sin I\delta\phi, \tag{A.2b}$$

where the upper sign corresponds to $\phi_{\rm cs} = 0$. Eliminating $\delta\theta$ gives

$$\frac{{\rm d}^2\delta\phi}{{\rm d}t^2} \equiv \lambda^2\delta\phi, \tag{A.3}$$

where

$$\lambda^2 \equiv \left(\sin\theta_{\rm cs} \mp \eta\sin I\csc^2\theta\right)\left(\pm\eta\sin I\right). \tag{A.4}$$

A plot of λ^2 for each of the CSs is given in Fig. A.1. It is clear that CS4 is unstable while the other three are stable. The local libration frequency for these stable CSs is simply $\omega_{\rm lib} = \sqrt{-\lambda^2}$.

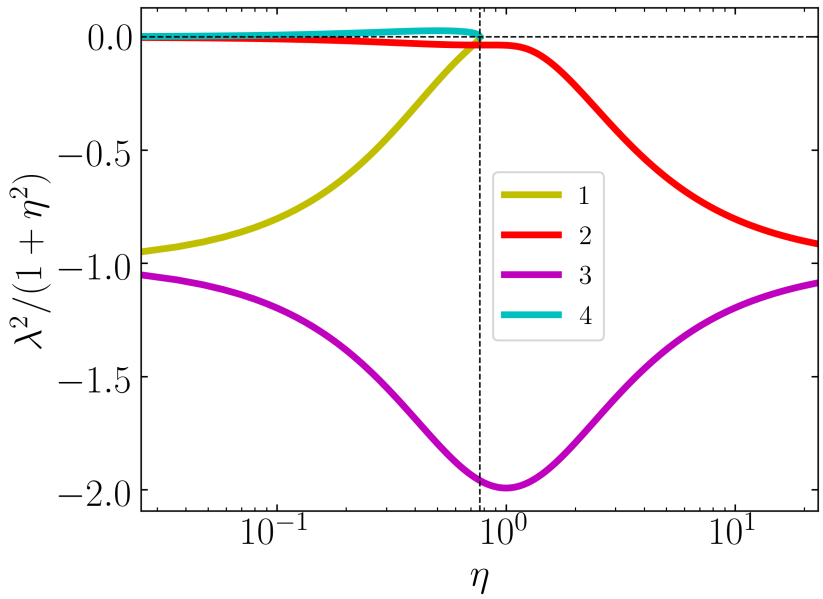

Figure A.1: λ^2, given by Eq. (A.3), evaluated at each of the Cassini States. The vertical axis is rescaled for clarity. Note that CS4 is unstable ($\lambda^2 > 0$) when it exists while all others are stable ($\lambda^2 < 0$). The thin horizontal dashed line is the instability boundary $\lambda^2 = 0$ while the thin vertical dashed line labels $\eta = \eta_c$ [Eq. (2.14)].

A.2 Approximate Adiabatic Evolution

In this appendix, we will use approximations valid for small η to derive the explicit analytic expressions for the final obliquities at small $\theta_{sd,i}$ and the associated probabilities for the II → I and II → III tracks. These are the only possible tracks for small η.

We first seek a simple parameterization for the separatrix, the level curve of the Hamiltonian intersecting the unstable equilibrium CS4. Points along the separatrix, parameterized by $\left(\phi, \theta_{sep}(\phi)\right)$, satisfy $\mathscr{H}\left(\phi, \theta_{sep}(\phi)\right) = \mathscr{H}\left(\phi_4, \theta_4\right)$ where ϕ_4 and θ_4 are given in Appendix A.1.1. We obtain two solutions for θ_{sep}, given to leading order in η by:

$$\cos\theta_{sep}(\phi) \approx \cos\theta_4 \pm \sqrt{2\eta \sin I \left(1 - \cos\phi\right)}. \tag{A.5}$$

These two solutions parameterize the two legs of the separatrix. Integration of the phase area enclosed by the separatrix yields then

$$\mathscr{A}_{\mathrm{II}}(\eta) \approx 16\sqrt{\eta \sin I}. \tag{A.6}$$

We can now compute the final obliquities and their associated probabilities for each track as follows:

1. For a given $\theta_{\mathrm{sd,i}}$, we know that if $\eta \to \infty$ then the trajectory executes simple libration about $\hat{\mathbf{I}}_{\mathrm{d}}$, and so $A = 2\pi\left(1-\cos\theta_{\mathrm{sd,i}}\right) \approx \pi\theta_{\mathrm{sd,i}}^2$. This then implies $\eta_\star$ must be the solution to $\mathscr{A}_{\mathrm{II}}(\eta_\star) = A$, or

$$\eta_\star \approx \left(\frac{2\pi\left(1-\cos\theta_{\mathrm{sd,i}}\right)}{16}\right)^2 \frac{1}{\sin I} \approx \left(\frac{\pi\theta_{\mathrm{sd,i}}^2}{16}\right)^2 \frac{1}{\sin I}. \tag{A.7}$$

2. Upon separatrix encounter, a transition to either zone I or zone III occurs. These can be calculated to have the associated probabilities [using the approximate area Eq. (A.6) and Eqs. (2.25)]

$$\Pr(\mathrm{II} \to \mathrm{I}) \approx \frac{2\pi\eta_\star \cos I + 4\sqrt{\eta_\star \sin I}}{8\sqrt{\eta_\star \sin I}}, \tag{A.8a}$$

$$\Pr(\mathrm{II} \to \mathrm{III}) \approx \frac{-2\pi\eta_\star \cos I + 4\sqrt{\eta_\star \sin I}}{8\sqrt{\eta_\star \sin I}}. \tag{A.8b}$$

3. Upon a transition to zone I or zone III, the final obliquity can be predicted by observing the final adiabatic invariant $A_{\mathrm{f}} = -\mathscr{A}_{\mathrm{I}}(\eta_\star)$ in the zone I case and $A_{\mathrm{f}} = \mathscr{A}_{\mathrm{I}}(\eta_\star) + \mathscr{A}_{\mathrm{I}}I(\eta_\star)$ in the zone III case. As $\eta \to 0$, these correspond to obliquities

$$(\cos\theta_{\mathrm{f}})_{\mathrm{II}\to\mathrm{I}} \approx \left(\frac{\pi\theta_{\mathrm{sd,i}}^2}{16}\right)^2 \cot I + \frac{\theta_{\mathrm{sd,i}}^2}{4}, \tag{A.9a}$$

$$(\cos\theta_{\mathrm{f}})_{\mathrm{II}\to\mathrm{III}} \approx \left(\frac{\pi\theta_{\mathrm{sd,i}}^2}{16}\right)^2 \cot I - \frac{\theta_{\mathrm{sd,i}}^2}{4}. \tag{A.9b}$$

These are the black dotted lines overplotted in Fig. 2.5.

APPENDIX B

APPENDICIES TO COLOMBO'S TOP: WEAK TIDAL FRICTION

B.1 Convergence of Initial Conditions Inside the Separatrix to CS2

In Section **??**, we studied the stability of the CSs under of tidal alignment torque given by Eq. (4.7), finding that CS2 is locally stable. Later, in Section 3.3.3, we found that all initial conditions within the separatrix converge to CS2, which is not guaranteed by local stability of CS2. In this section, we give an analytic demonstration that all points inside the separatrix indeed converge to CS2, focusing on the case where $\eta \ll 1$.

Similarly to the analytic calculation in Section 3.3.4, we seek to compute the change in the unperturbed Hamiltonian over a single libration cycle. To calculate the evolution of H, we first parameterize the unperturbed trajectory (similarly to Eq. 3.27). For initial conditions inside the separatrix, the value of H can be written $H = H_{\rm sep} + \Delta H$ where $\Delta H > 0$, and the two legs of the libration trajectory can be written:

$$\cos\theta_{\pm} \approx \eta\cos I \pm \sqrt{2\eta\left[\sin I\left(1-\cos\phi\right) - \Delta H\right]}. \tag{B.1}$$

We have taken $\sin\theta \approx 1$, a good approximation in zone II when $\eta \ll 1$. Note that there are some values of ϕ for which no solutions of θ exist, reflecting the fact that the libration cycle does not extend over the full interval $\phi \in [0, 2\pi]$. During a libration cycle, θ_- [θ_+] is traversed while $\phi' > 0$ [$\phi' < 0$], i.e. the trajectory librates counterclockwise in $(\cos\theta, \phi)$ phase space (see Fig. 3.2).

The leading order change to H over a single libration cycle can then computed

by integrating $\mathrm{d}H/\mathrm{d}t$ along this trajectory, yielding:

$$\begin{aligned}\oint \frac{\mathrm{d}H}{\mathrm{d}t}\,\mathrm{d}t &= \oint \left(\frac{\mathrm{d}(\cos\theta)}{\mathrm{d}t}\right)_{\mathrm{tide}} \mathrm{d}\phi, \\ &= \int_{\phi_{\min}}^{\phi_{\max}} \frac{1}{t_{\mathrm{s}}}\left(\sin^2\theta_- - \sin^2\theta_+\right)\,\mathrm{d}\phi \\ &\approx \frac{1}{t_{\mathrm{s}}}\int_{\phi_{\min}}^{\phi_{\max}} 4\eta\cos I\sqrt{2\eta\left[\sin I\left(1-\cos\phi\right)-\Delta H\right]}\,\mathrm{d}\phi > 0. \end{aligned} \tag{B.2}$$

Here, $\phi_{\min} > 0$ and $\phi_{\max} < 2\pi$ are defined such that the trajectory librates over $\phi \in [\phi_{\min}, \phi_{\max}]$. Thus, H is strictly increasing for all initial conditions inside the separatrix, and they all converge to CS2.

B.2 Approximate TCE2 Probability for Small η_{sync}

In this appendix, we seek a tentative analytic understanding for the probability of convergence to tCE2 when η_{sync} is small, i.e. the left extremes of Figs. 3.20 and 3.21. In this regime, following the discussions in Sections 3.3.4 and 3.4.3, we understand that initial conditions (ICs) in zone I always converge to tCE1, ICs in zone II always converge to tCE2, and ICs in zone III experience separatrix encounter and probabilistically converge to either one of the tCE. To further proceed, we will assume an isotropic distribution of initial spin orientations; different distributions again will only change the quantitative but not qualitative character of the discussion. Then the tCE2 probability, which we denote by P_{tCE2}, can be expressed as the sum of: (i) the probability that an IC is in zone II, and (ii) the probability that an IC is both in zone III and undergoes a III $\rightarrow$ II transition. To simplify the discussion, we will approximate that P_{tCE2} can be calculated as

$$P_{\mathrm{tCE2}} \sim \frac{A_{\mathrm{II}}}{4\pi} + \frac{A_{\mathrm{III}}}{4\pi}\left\langle P_{\mathrm{III}\rightarrow\mathrm{II}}\right\rangle, \tag{B.3}$$

where $A_{\rm II}$ and $A_{\rm III}$ are the phase space areas of zones II and III respectively, and $\langle P_{\rm III\to II}\rangle$ is the *average* III $\to$ II transition probability for a random IC in zone III. Next, we evaluate each of the expressions in Eq. (B.3).

We first consider $A_{\rm II}$ and $A_{\rm III}$. Exact analytic forms for both $A_{\rm II}$ and $A_{\rm III}$ is known (Ward and Hamilton, 2004, Paper I), but an accurate approximation can be obtained using Eq. (3.27) since $\eta_{\rm i} \ll 1$. We obtain that:

$$\frac{A_{\rm II}}{4\pi} = \frac{4}{\pi}\sqrt{\eta_{\rm i}\sin I}, \tag{B.4}$$

$$\frac{A_{\rm III}}{4\pi} = \frac{1+\eta_{\rm i}\cos I}{2} - \frac{2}{\pi}\sqrt{\eta_{\rm i}\sin I}. \tag{B.5}$$

Next, we need to evaluate $\langle P_{\rm III\to II}\rangle$, for which we must understand the outcomes of the separatrix encounters that ICs in zone III experience. We proceed by analytically calculating $\Delta K_\pm$ (Eq. 3.45) for use in Eq. (3.46) to obtain the probabilities of the outcomes of separatrix encounter. We first rewrite Eq. (3.45) as:

$$\begin{aligned}\Delta K_\pm &= \oint_{\mathscr{C}_\pm} \frac{{\rm d}H}{{\rm d}t} - \frac{{\rm d}H_{\rm sep}}{{\rm d}t}\,{\rm d}t \\ &= \oint_{\mathscr{C}_\pm} \left(\frac{{\rm d}(\cos\theta)}{{\rm d}t}\right)_{\rm tide} + \frac{\dot\Omega_{\rm s}}{\dot\phi}\left(\frac{\partial H}{\partial\Omega_{\rm s}} - \frac{\partial H_{\rm sep}}{\partial\Omega_{\rm s}}\right){\rm d}\phi.\end{aligned} \tag{B.6}$$

Then, using the full equations of motion for the planet's spin including weak tidal friction in component form, given by Eqs. (3.34–3.36), we can evaluate $\Delta K_\pm$ by integrating along the two legs of the separatrix $\mathscr{C}_\pm$ (see Fig. 3.2). Note that we must use the value of η at the moment of separatrix encounter, which we denote $\eta_{\rm cross}$, as the evolution of $\Omega_{\rm s}$ changes the spin-orbit precession frequency α and

thus η itself:

$$
\begin{aligned}
t_{\rm s}\Delta K_{\pm} \approx \frac{\eta_{\rm cross}^2}{\eta_{\rm sync}}\Bigg[& -2\cos I\left(\pm 2\pi\eta_{\rm cross}\cos I + 8\sqrt{\eta_{\rm cross}\sin I}\right) \mp 4\pi\sin I \\
& - 8\cos I\sqrt{\eta_{\rm cross}\sin I} + \frac{4\eta_{\rm sync}}{\eta_{\rm cross}}\sqrt{\sin I/\eta_{\rm cross}}\Bigg] \\
& + \frac{2\eta_{\rm cross}}{\eta_{\rm sync}}\left(\mp 2\pi\left(1-2\eta_{\rm cross}\sin I\right) + 16\cos I\,\eta_{\rm cross}^{3/2}\sqrt{\sin I}\right) + 8\sqrt{\eta_{\rm cross}\sin I} \\
& \pm 2\pi\eta_{\rm cross}\cos I - \frac{64}{3}\left(\eta_{\rm cross}\sin I\right)^{3/2}. \qquad \text{(B.7)}
\end{aligned}
$$

The resulting $P_{\rm III\to II}$ obtained using this analytic $\Delta K_{\pm}$ in Eq. (3.46) is shown as the green dashed line in the top panel of Fig. 3.18, where it can be seen that agreement is reasonable for $\eta_{\rm cross} \lesssim 0.05$. For the purposes of this section, we drop all but the leading order terms in both the numerator and denominator of Eq. (3.46) and obtain:

$$
P_{\rm III\to II} \simeq \frac{6\eta_{\rm sync}}{\pi}\sqrt{\frac{\sin I}{\eta_{\rm cross}}}. \qquad \text{(B.8)}
$$

However, $\eta_{\rm cross}$ cannot be expressed in closed form as a function of the ICs. Based on the bottom panel of Fig. 3.18, we make the crude approximation that $\eta_{\rm cross}$ is uniformly distributed between $\eta_{\rm i}$ and $\eta_{\rm sync}$. Note that if $\Omega_{\rm s} \simeq n$, then this approximation is invalid: since nearly anti-aligned spins ($\theta_{\rm i} \approx 180^\circ$) will undergo significant spin-down before tidal friction can realign the spin orientation, $\Omega_{\rm s,i}$ being too close to n results in $\eta_{\rm cross} \ll \eta_{\rm sync}$. We thus obtain:

$$
\begin{aligned}
\langle P_{\rm III\to II}\rangle &\sim \frac{1}{\eta_{\rm sync}-\eta_{\rm i}}\int_{\eta_{\rm i}}^{\eta_{\rm sync}} P_{\rm III\to II}\,{\rm d}\eta_{\rm cross} \\
&= \frac{12\sqrt{\eta_{\rm sync}\sin I}}{\pi\left(1+\sqrt{n/\Omega_{\rm s,i}}\right)}. \qquad \text{(B.9)}
\end{aligned}
$$

With this result, we can finally express Eq. (B.3) as:

$$
P_{\rm tCE2} \simeq \frac{4\sqrt{\eta_{\rm sync}\sin I}}{\pi}\left[\sqrt{n/\Omega_{\rm s,i}} + \frac{3}{2\left(1+\sqrt{n/\Omega_{\rm s,i}}\right)}\right] + \mathcal{O}\left(\eta_{\rm sync}\right). \qquad \text{(B.10)}
$$

This is exactly Eq. (3.47). We remark again that this is valid in the regime where $\eta_{\rm sync} \ll 1$ and $\Omega_{\rm s} \gtrsim n$.

APPENDIX C

APPENDICIES TO COLOMBO'S TOP: MULTIPLANETARY SYSTEMS

C.1 Inclination Modes of 3-Planet Systems

In the linear regime, the evolution of the orbital inclinations in a multi-planet system is described by the Laplace-Lagrange theory [Murray and Dermott, 1999, Pu and Lai, 2018]. In this section, we consider 3-planet systems. We denote the magnitude of the angular momentum of each planet by L_j and the inclination relative to the total angular momentum axis $\hat{\mathbf{J}}$ by I_j, and we define the complex inclination $\mathscr{I}_j = I_j \exp[i\Omega_i]$. The evolution equations for $\mathscr{I}_1$, $\mathscr{I}_2$, and $\mathscr{I}_3$ are

$$\frac{\mathrm{d}}{\mathrm{d}t}\begin{pmatrix}\mathscr{I}_1\\ \mathscr{I}_2\\ \mathscr{I}_3\end{pmatrix} = i\begin{pmatrix}-\omega_{12}-\omega_{13} & \omega_{12} & \omega_{13}\\ \omega_{21} & -\omega_{21}-\omega_{23} & \omega_{23}\\ \omega_{31} & \omega_{32} & -\omega_{31}-\omega_{32},\end{pmatrix}\begin{pmatrix}\mathscr{I}_1\\ \mathscr{I}_2\\ \mathscr{I}_3\end{pmatrix}, \tag{C.1}$$

where ω_{jk} is the precession rate of the j-th planet induced by the k-th planet, and is given by

$$\omega_{jk} = \frac{m_k}{4M_\star}\frac{a_j a_<}{a_>^2} n_j b^{(1)}_{3/2}(\alpha), \tag{C.2}$$

where $a_< = \min(a_j, a_k)$, $a_> = \max(a_j, a_k)$, $n_j = (GM_\star/a_j^3)^{1/2}$, $\alpha = a_</a_>$, and

$$b^{(1)}_{3/2}(\alpha) = 3\alpha\left(1 + \frac{15}{8}\alpha^2 + \frac{175}{64}\alpha^4 + \ldots\right) \tag{C.3}$$

is the Laplace coefficient. Eq. (C.1) can be solved in general, giving two non-trivial eigenmodes. In the limit $L_1 \ll L_2, L_3$, the two eigenmodes have simple solutions and interpretations:

- Mode I has frequency

$$g_{(\mathrm{I})} = -(\omega_{12} + \omega_{13}). \tag{C.4}$$

It corresponds to free precession of $\hat{\mathbf{L}}_1$ around the total angular momentum $\mathbf{J} = \mathbf{L}_2 + \mathbf{L}_3$. The amplitude of oscillation of $\hat{\mathbf{L}}_1$, $I_{(\mathrm{I})}$, is simply the inclination of $\hat{\mathbf{L}}_1$ with respect to $\hat{\mathbf{J}}$.

- Mode II has frequency

$$g_{(\mathrm{II})} = -(\omega_{23} + \omega_{32}) = -\frac{J}{L_3}\omega_{23}, \tag{C.5}$$

which is simply the precession frequency of $\hat{\mathbf{L}}_2$ (or $\hat{\mathbf{L}}_3$) about $\hat{\mathbf{J}}$. The forced oscillation of $\hat{\mathbf{L}}_1$ has an amplitude

$$I_{(\mathrm{II})} = \frac{\omega_{12}L_3 - \omega_{13}L_2}{\left(g_{(\mathrm{II})} - g_{(\mathrm{I})}\right)J} I_{23}, \tag{C.6}$$

where I_{23} is the mutual inclination between the two outer planets and is constant.

We consider two archetypal 3-planet configurations, systems with three super Earths (SEs) and systems with two inner SEs and an exterior cold Jupiter (CJ). In both cases, we take the inner two planets to have $m_1 = M_\oplus$, $m_2 = 3M_\oplus$, $a_1 = 0.1\,\mathrm{AU}$, and we consider three values of $a_2 = \{0.15, 0.2, 0.25\}$ AU. For the 3SE case, we take $m_3 = 3M_\oplus$ and the characteristic inclinations $I_1 \simeq I_{23} \simeq 2^\circ$ [corresponding to three nearly-coplanar SEs; see Fabrycky et al., 2014, Dai et al., 2018]. For the 2SE + CJ case, we take $m_3 = 0.5M_\mathrm{J}$ and the characteristic inclinations $I_1 \simeq I_{23} \simeq 10^\circ$ [corresponding to a mildly inclined CJ; see Masuda et al., 2020]. In both cases, we compute the mode precession frequencies $g_{(\mathrm{I,II})}$ and characteristic mode amplitudes $I_{(\mathrm{I,II})}$ for a range of a_3. Figures C.1–C.3 show examples of our results.

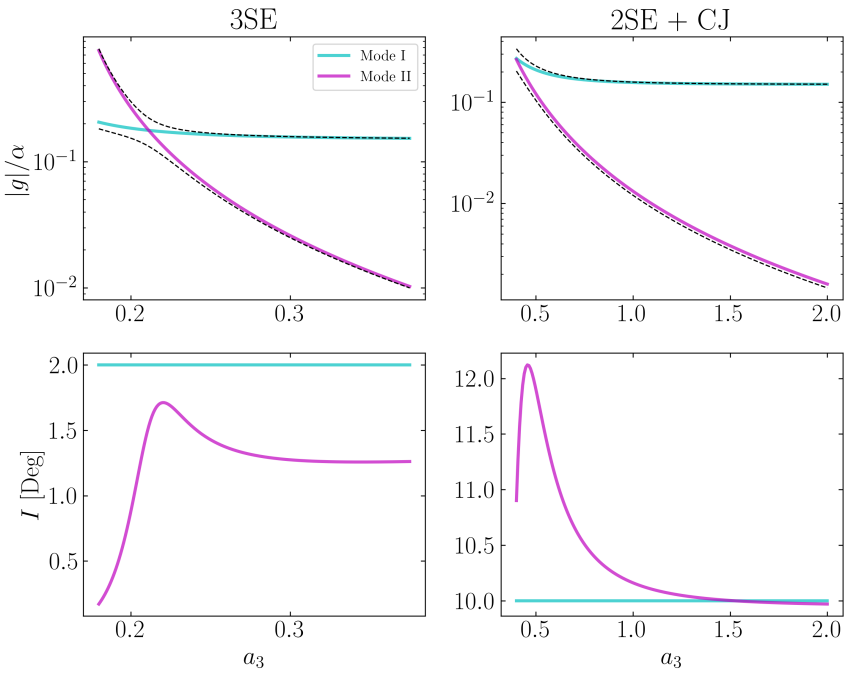

Figure C.1: Inclination mode frequencies and amplitudes for the 3SE (left) and 2SE + CJ (right) systems. In both systems, the inner planets' parameters are $m_1 = M_\oplus$, $m_2 = 3M_\oplus$, $a_1 = 0.1$ AU, $a_2 = 0.15$ AU. In the 3SE case, $m_3 = 3M_\oplus$ and $I_1 = I_{23} = 2°$, while in the 2SE + CJ case, $m_3 = 0.5M_J$ and $I_1 = I_{23} = 10°$, In the top panels, the black dashed lines show the mode frequencies from the exact solution of Eq. (C.1), while the solid, colored lines are given by Eqs. (C.4, C.5).

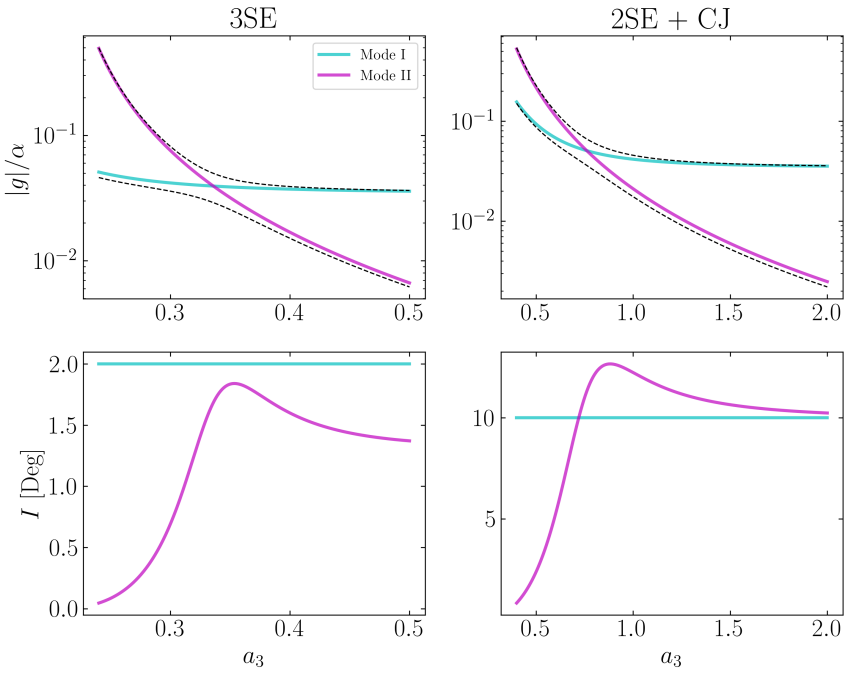

Figure C.2: Same as Fig. C.1 but for $a_2 = 0.2\,\mathrm{AU}$.

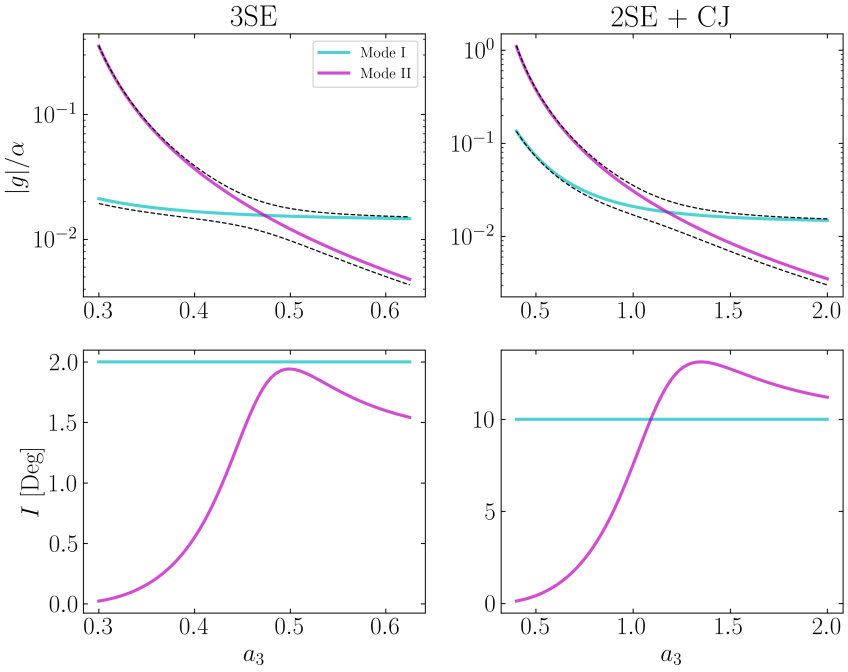

Figure C.3: Same as Fig. C.1 but for $a_2 = 0.25\,\mathrm{AU}$.

C.2 Additional Comments and Results on Mixed Mode Equilibria

In the main text, we provided an example of the spin evolution into a mixed-mode equilibrium in Fig. 4.2 for the parameters $I_{(\mathrm{I})} = 10^\circ$, $I_{(\mathrm{II})} = 1^\circ$, $\alpha = 10\left|g_{(\mathrm{I})}\right|$, and $g_{(\mathrm{II})} = 10g_{(\mathrm{I})}$. In Fig. C.4, we provide several further examples of the evolution into other mixed-mode equilibria with different values of g_{res} when $I_{(\mathrm{II})} = 3^\circ$ is used. We find that their average equilibrium obliquities θ_{eq} are still well-described by Eq. (4.15). Furthermore, we find that, if $g_{\mathrm{res}}/\Delta g = p/q$ for integers p and q, then the steady-state oscillations of θ_{sl} are periodic with period $2\pi q/|\Delta g|$ (see bottom example in Fig. 4.2 for the case of $g_{\mathrm{res}} = \Delta g/2$).

Figure C.5 shows the equilibrium obliquity θ_{eq} as a function of g_{res} for a system with $I_{(\mathrm{II})} = 3^\circ$ and $g_{(\mathrm{II})} = 8.5g_{(\mathrm{I})}$. We can see for $g_{\mathrm{res}} = \Delta g$ that there are three distinct equilibrium values of θ_{sl}. The largest-obliquity equilibrium is CS2(II), and the equilibrium with an intermediate obliquity is a mixed-mode equilibrium with $g_{\mathrm{res}} = \Delta g$, as it directly intersects the green line (Eq. 4.15). The existence and stability of this equilibrium is responsible for the extra dot a few degrees below the CS2(II) curve in the bottom panels of Figs. 4.6, 4.9, and 4.11 (e.g. most visible for $g_{(\mathrm{II})}/g_{(\mathrm{I})} = 6.5$, 7.5, and 8.5 in Fig. 4.9). The origin of the lowest-obliquity equilibrium at $g_{\mathrm{res}} = \Delta g$ in Fig. C.5 is distinct, though it is within the range of oscillation of θ_{sl} of the mixed-mode steady state.

In Fig. 4.4, we presented the numerical stability analysis of initial conditions in the neighborhood of the mixed-mode equilibrium for the $I_{(\mathrm{II})} = 1^\circ$ case. When $I_{(\mathrm{II})}$ is increased to 3°, the amplitudes of oscillations of the mixed-mode equilibria begin to overlap (see Fig. 4.8), and so we might expect that the basins of attraction for the resonances overlap in $\theta_{\mathrm{sl},0}$ space. Figure C.6 shows that this is indeed the

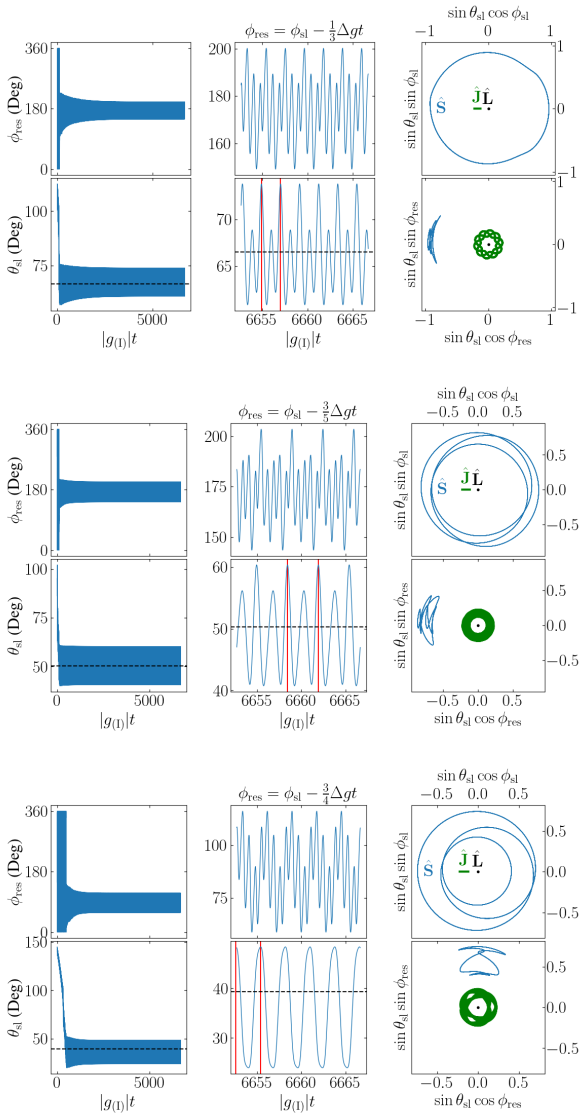

Figure C.4: Same as Fig. 4.2 but for $g_{(\mathrm{II})} = 10g_{(\mathrm{I})}$ and $I_{(\mathrm{II})} = 3°$. The three examples correspond to capture into mixed-mode equilibria with resonant angles corresponding to $g_{\mathrm{res}} = \Delta g/3$, $g_{\mathrm{res}} = 3\Delta g/5$, and $g_{\mathrm{res}} = 3\Delta g/4$ respectively. The three pairs of vertical red lines are separated by $6\pi/|\Delta g|$, $10\pi/|\Delta g|$, and $8\pi/\Delta g$ in the three examples respectively.

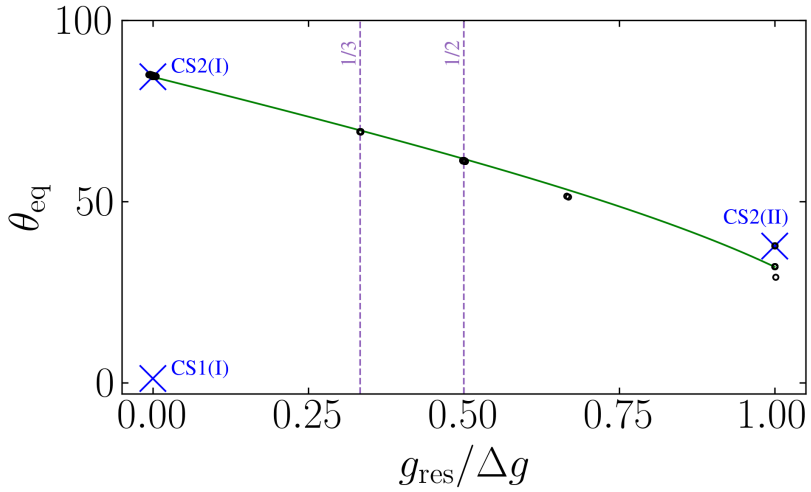

Figure C.5: Same as Figs. 4.5 and 4.8 but for $I_{(\rm II)} = 3°$ and $g_{(\rm II)} = 8.5 g_{(\rm I)}$, where ranges of oscillation in $\theta_{\rm sl}$ have been suppressed for clarity.

case, and that the basins of attraction of the mixed modes are very distorted (likely due to interactions among the resonances) compared to those seen in the $I_{(\rm II)} = 1°$ case.

Finally, in the main text, we have focused on the regime where $I_{(\rm II)} \ll I_{(\rm I)}$. In Fig. C.7, we show the effect of choosing $I_{(\rm II)} = 9°$ (with the same that $I_{(\rm I)} = 10°$). It can be seen that the $g_{\rm res} = \Delta g/2$ mixed mode is the most common outcome when $|g_{(\rm II)}| \gg |g_{(\rm I)}|$, as it is the preferred low-obliquity equilibrium ($\theta_{\rm eq} \lesssim 20°$) for $g_{(\rm II)} = 15 g_{(\rm I)}$. The degraded agreement of the $\theta_{\rm eq}$ values with Eq. (4.15) is because our theoretical results assume $I_{(\rm II)} \ll I_{(\rm I)}$. A broad range of final obliquities is observed when $g_{(\rm II)} = 6.5 g_{(\rm I)}$, very close to the critical value of $g_{(\rm II)}$ (denoted by the vertical dashed line) where the number of mode II CSs changes from 4 to 2 [Su and Lai, 2021]. This is likely due to the unusual phase space structure near this bifurcation.

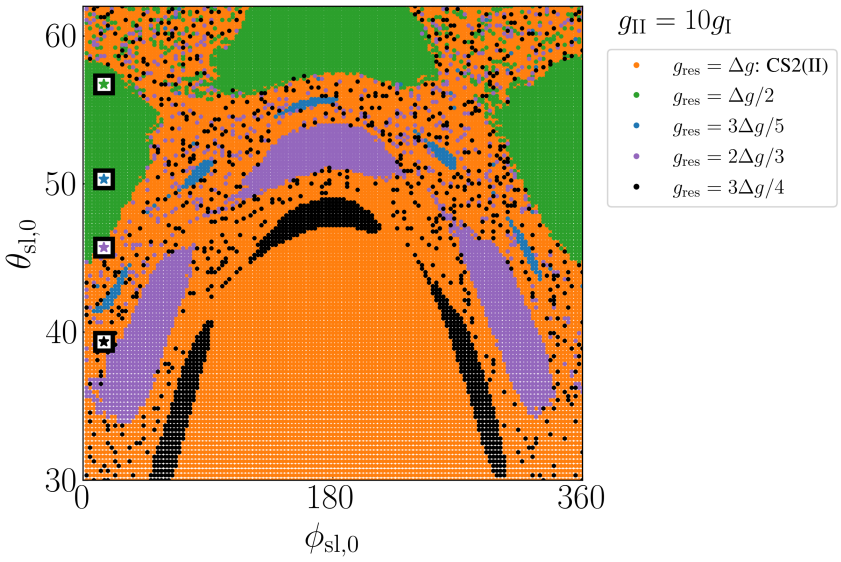

Figure C.6: Same as Fig. 4.4 but for $I_{\rm (II)} = 3°$. The range of the vertical axis is chosen to include the ranges of oscillation of the 1/2, 3/5, 2/3, and 3/4 mixed mode resonances (see Fig. 4.8). The decreasing density of points as $\theta_{\rm sl,0}$ decreases is because the grid of initial conditions is uniform in $\cos\theta_{\rm sl,0}$ rather than $\theta_{\rm sl,0}$ itself.

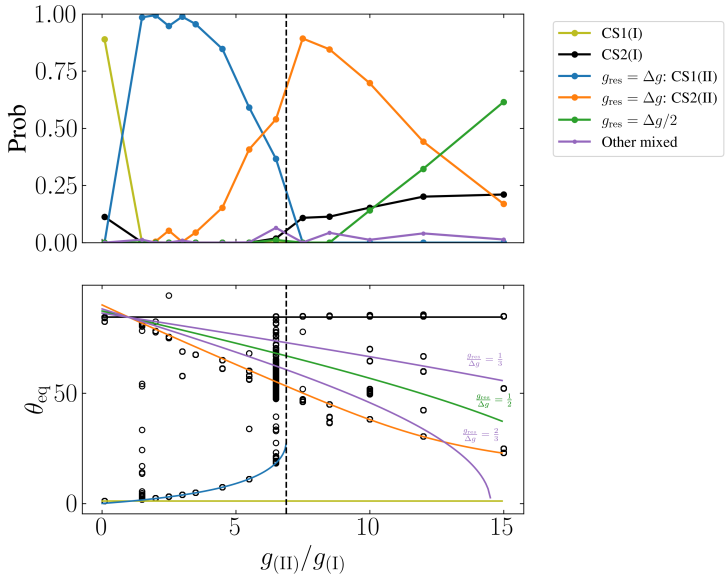

Figure C.7: Same as Fig. 4.6 but for $I_{\rm (II)} = 9°$.

APPENDIX D

APPENDICIES TO PHYSICS OF TIDAL DISSIPATION

D.1 Derivation of Fluid Equations

We aim to model wave dynamics over multiple density and pressure scaleheights. Start with the compressible Euler equations.

$$\partial_t \rho + (\mathbf{u}\cdot\nabla)\rho + \rho\nabla\cdot\mathbf{u} = 0, \tag{D.1}$$

$$\partial_t s + (\mathbf{u}\cdot\nabla)s = 0, \tag{D.2}$$

$$\partial_t \mathbf{u} + (\mathbf{u}\cdot\nabla)\mathbf{u} + \frac{1}{\rho}\nabla p = \mathbf{g}, \tag{D.3}$$

where s is the entropy. The pressure is calculated from the entropy and density using the equation of state

$$\frac{s}{c_p} = \log\frac{p^{1/\gamma}}{\rho}, \tag{D.4}$$

where c_p is the specific heat at constant pressure, and γ is the ratio of specific heats. For computational ease, it is convenient to filter out the fast sound waves from these equations. One approach is to assume pressure perturbations are small [yielding the "pseudo-incompressible" equations, Vasil et al., 2013], or that all thermodynamic perturbations are small [yielding the "anelastic" equations, Brown et al., 2012]. In these approximations, one of the thermodynamic equations is replaced by a constraint equation: $\nabla\cdot\left(p_0^{1/\gamma}\mathbf{u}\right) = 0$ for pseudo-incompressible; $\nabla\cdot\left(\rho_0\mathbf{u}\right) = 0$ for anelastic. Here p_0 and ρ_0 are the background density and pressure profiles. The pressure in the momentum equation can be interpreted as a Lagrange multiplier which enforces the constraint [Vasil et al., 2013]. Upon linearization, both approximations conserve a wave energy

$$E_w = \frac{1}{2}\rho_0|\mathbf{u}|^2 + \frac{1}{2}\frac{g^2}{N^2}\frac{(\rho')^2}{\rho_0} = \frac{1}{2}\rho_0|\mathbf{u}|^2 + \frac{1}{2}\rho_0 N^2\frac{(s')^2}{|\nabla s_0|^2}, \tag{D.5}$$

where ρ' and s' represent the density and entropy perturbations.

Rather than assume thermodynamic perturbations are small, we instead filter out sound waves by taking the limit $\gamma \to \infty$. Then the entropy and log density are proportional to each other, and the entropy equation becomes

$$\partial_t \log \rho + (\mathbf{u} \cdot \nabla) \log \rho = 0. \tag{D.6}$$

Together with mass conservation, this implies

$$\nabla \cdot \mathbf{u} = 0. \tag{D.7}$$

We solve these equations together with the normal momentum equation.

Although these equations are non-standard, they have various desirable properties. They conserve mass and momentum, and the linearized equations conserve the wave energy E_w [Eq. (D.5) above] similar to the pseudo-incompressible equations and anelastic equations. Our equations also satisfy the same linear dispersion relation as the fully compressible equations in the limit of large sound speed [this is also true for the anelastic equations, but not pseudo-incompressible, Brown et al., 2012, Vasil et al., 2013]. Thus, the vertical propagation of internal gravity waves is similar to the pseudo-incompressible equations and anelastic equations.

In this work we are interested in waves which reach large amplitudes and break. For breaking waves, Achatz et al. [2010] suggests that the anelastic equations may miss important effects. Although the pseudo-incompressible equations may capture wave-breaking more accurately, they are more complicated, and do not satisfy the correct dispersion relation to order $(k_z H)^{-2}$ [Vasil et al., 2013]. In the absence of a clear choice to study this wave breaking problem, we have elected to use these simple equations derived in the $\gamma \to \infty$ limit.

D.2 Forcing Solution

To solve for the linear excited IGW amplitude due to bulk forcing (see Eq. (5.13)), we consider the linearized system of equations, with all dynamical variables having dependence $u_z(x,z,t) = \tilde{u_z}(z)e^{ik_x x - i\omega t}$. Thus, $\partial/\partial t \to -i\omega t$, $\frac{\partial}{\partial x} \to ik_x$, and the dynamical fluid equations become (see Eqs. (5.2) and (5.5)):

$$\begin{aligned}
\frac{\mathrm{d}u_z}{\mathrm{d}z} + ik_x u_x &= 0, \\
-i\omega u_x + ik_x \varpi + gHik_x \Upsilon &= 0, \\
-i\omega u_z + \frac{\mathrm{d}\varpi}{\mathrm{d}z} + gH\frac{\mathrm{d}\Upsilon}{\mathrm{d}z} - \frac{\varpi}{H} &= 0, \\
-i\omega\Upsilon - \frac{u_z}{H} &= C\exp\left[-\frac{(z-z_0)^2}{2\sigma^2}\right] \equiv \mathscr{C}(z).
\end{aligned}$$

These can be recast solely in terms of u_z as

$$\frac{\mathrm{d}^2 u_z}{\mathrm{d}z^2} - k_x^2 u_z - \frac{1}{H}\frac{\mathrm{d}u_z}{\mathrm{d}z} + u_z\frac{N^2 k_x^2}{\omega^2} = -\frac{gk_x^2}{\omega^2}\mathscr{C}(z)..$$

The homogeneous solutions are of form $u_{z,\pm}(z) = \exp\left[\left(\frac{1}{2H} \pm ik_z\right)(z-z_0)\right]$ where k_z satisfies the dispersion relation (Eq. (5.7)). We compute the solution to the inhomogeneous ODE by the method of variation of parameters. The Wronskian is

$$W \equiv \det\begin{vmatrix} u_{z,+} & u_{z,-} \\ \mathrm{d}u_{z,+}/\mathrm{d}z & \mathrm{d}u_{z,-}/\mathrm{d}z \end{vmatrix} = -2ik_z e^{z/H}. \tag{D.8}$$

The general solution is then

$$u_z = -u_{z,+}\int \frac{1}{W}u_{z,-}\left(-\frac{gk_x^2}{\omega^2}\mathscr{C}(z)\right)\mathrm{d}z + u_{z,-}\int \frac{1}{W}u_{z,+}\left(-\frac{gk_x^2}{\omega^2}\mathscr{C}(z)\right)\mathrm{d}z. \tag{D.9}$$

Taking these integrals and applying the boundary conditions $u_z(z\to\infty)=u_{z,+}$, $u_z(z\to-\infty)=u_{z,-}$ give the exact solution:

$$u(z)=\frac{\sqrt{\pi}C\sigma}{2^{3/2}ik_z}\frac{gk_x^2}{\omega^2}\exp\left[\frac{\left(\frac{\sigma^2}{2H}\pm ik_z\sigma^2\right)^2}{2\sigma^2}\right]\left[-u_{z,+}(1+\mathrm{erf}(\xi_+))+u_{z,-}(\mathrm{erf}(\xi_-)-1)\right], \tag{D.10}$$

$$\xi_\pm\equiv\left[\frac{z-z_0}{\sqrt{2\sigma^2}}+\frac{\sigma}{2^{3/2}H}\pm\frac{ik_z\sigma}{\sqrt{2}}\right] \tag{D.11}$$

Here, the error function is defined $\mathrm{erf}(z)\equiv\left(2/\sqrt{\pi}\right)\int_0^z\exp\left(-t^2\right)\,\mathrm{d}t$. If we are concerned with only z scales significantly larger than σ, then we may take $\mathrm{erf}(\xi_\pm)\approx\Theta(z-z_0)$ (the Heaviside step function). If we further assume $|k_zH|\gg1$ and restore the $e^{ik_xx-i\omega t}$ factor, we recover Eq. (5.14) in the main text

$$u_z(x,z,t)=-\frac{C}{2ik_z}\frac{gk_x^2}{\omega^2}e^{-k_z^2\sigma^2/2}\sqrt{2\pi\sigma^2}e^{ik_xx-i\omega t}\times\begin{cases}\exp\left[\left(\frac{1}{2H}+ik_z\right)(z-z_0)+i\frac{k_z\sigma^2}{2H}\right] & \text{for } z>z_0,\\ \exp\left[\left(\frac{1}{2H}-ik_z\right)(z-z_0)-i\frac{k_z\sigma^2}{2H}\right] & \text{for } z>z_0.\end{cases} \tag{D.12}$$

Note that in the main text, this approximate form is used to compute $\mathbf{u}_{\mathrm{an}}$, as it is easier to work with and sufficiently accurate in the regions of interest (many σ away from z_0).

D.3 Equation Implementation

The system of equations we wish to simulate consists of Eqs. (5.2a), (5.5b), and (5.13). The nonlinear terms in the these equations will transfer energy from lower wavenumbers to higher wavenumbers. Since spectral codes have no numerical diffusion, explicit diffusion must be added. To ensure the non-ideal system conserves horizontal momentum exactly, we begin by adding diffusion terms to the flux-conservative

form of the Euler fluid equations (equivalent to Eqs. 5.2):

$$\nabla \cdot \mathbf{u} = 0, \tag{D.13a}$$

$$\partial_t \rho + \nabla \cdot (\rho \mathbf{u} - \nu \nabla(\rho - \overline{\rho})) = 0, \tag{D.13b}$$

$$\partial_t(\rho \mathbf{u}) + \nabla \cdot (\rho \mathbf{u}\mathbf{u} + \mathrm{diag}(\rho \varpi) - \nu \rho \nabla \mathbf{u}) + \rho g \hat{\mathbf{z}} = 0. \tag{D.13c}$$

For simplicity, we use the same diffusivity ν for both the momentum and mass diffusivities. Although mass diffusivity is not physical, we include it for numerical stability. We choose the mass diffusion term to conserve mass, and not to affect the background density profile.

It is necessary to mask out nonlinear terms in the forcing zone using a form similar to Eq. (5.27). In the absence of this mask, a nonphysical mean flow localized to the forcing zone develops. We use the mask

$$\Gamma_{NL}(z) = \frac{1}{2}\left[2 + \tanh\frac{z - (z_0 + 8\sigma)}{\sigma} - \tanh\frac{z - z_B}{\sigma}\right]. \tag{D.14}$$

Including the damping zones and forcing terms as described in Section 5.4, and again making change of variables to Υ, ϖ, we finally obtain the full system of

equations as simulated in Dedalus:

$$\nabla \cdot \mathbf{u} = 0, \tag{D.15a}$$

$$\begin{aligned}\partial_t \Upsilon - \frac{u_z}{H} = &-\Gamma(z)\Upsilon + \frac{F}{\overline{\rho}(z)} e^{-\frac{(z-z_0)^2}{2\sigma^2}} \cos(k_x x - \omega t) \\ &+ \Gamma_{NL}\Big[-(\mathbf{u}\cdot\nabla)\Upsilon + \nu\left(\nabla^2\Upsilon + (\nabla\Upsilon)\cdot(\nabla\Upsilon) - \frac{2}{H}\partial_z\Upsilon + \frac{1-e^{-\Upsilon}}{H^2}\right)\Big],\end{aligned} \tag{D.15b}$$

$$\begin{aligned}\frac{\partial u_x}{\partial t} + \frac{\partial \varpi'}{\partial x} + gH\frac{\partial \Upsilon}{\partial x} = &-\Gamma(z)u_x + \Gamma_{NL}\Big[\nu\nabla^2 u_x - u_x\nu\left(\nabla^2\Upsilon + (\nabla\Upsilon)\cdot(\nabla\Upsilon) - \frac{2}{H}\partial_z\Upsilon + \frac{1-e^{-\Upsilon}}{H^2}\right) \\ &+ 2\nu\left(((\nabla\Upsilon)\cdot\nabla)u_x - \frac{1}{H}\partial_z u_x\right) - (\mathbf{u}\cdot\nabla)u_x - \varpi'\frac{\partial\Upsilon}{\partial x}\Big],\end{aligned} \tag{D.15c}$$

$$\begin{aligned}\frac{\partial u_z}{\partial t} + \frac{\partial \varpi'}{\partial z} + gH\frac{\partial \Upsilon}{\partial z} - \frac{\varpi'}{H} = &-\Gamma(z)u_z + \Gamma_{NL}\Big[\nu\nabla^2 u_z - u_z\nu\left(\nabla^2\Upsilon + (\nabla\Upsilon)\cdot(\nabla\Upsilon) - \frac{2}{H}\partial_z\Upsilon + \frac{1-e^{-\Upsilon}}{H^2}\right) \\ &+ 2\nu\left(((\nabla\Upsilon)\cdot\nabla)u_z - \frac{1}{H}\partial_z u_z\right) - (\mathbf{u}\cdot\nabla)u_z - \varpi'\frac{\partial\Upsilon}{\partial z}\Big].\end{aligned} \tag{D.15d}$$

APPENDIX E

APPENDICIES TO DYNAMICAL TIDES IN ECCENTRIC BINARIES

E.1 Stellar Structure calculations with MESA

We attempt to reproduce the stellar structure parameters for the main-sequence star in PSR J0045-7319 as reported from the so-called "Yale model" of [Kumar and Quataert, 1998] using the stellar evolution code Modules for Experiments in Stellar Astrophysics [MESA; Paxton et al., 2011, 2013, 2015, 2018, 2019]. In particular, the most relevant parameter to our results is the radius of the convective core. To calculate this quantity, we perform a multi-step procedure, described below:

- First, we pick a set of parameters for the stellar evolution (we explored different values of stellar rotation, metallicity, and convective overshoot parameter α). For the stellar rotation, we tried both non-rotating and critically-rotating models. The non-rotating models are expected to be inaccurate since B stars are typically rapidly rotating. The measured $v \sin i \approx 110$ km/s at the surface [Kaspi et al., 1994], so we assume that $v_{\rm surf} \sim 160$ km/s, which is a substantial fraction of the critical $v_{\rm c} \equiv \sqrt{GM/R} \sim 500$ km/s. Since PSR J0045-7319 is in the SMC, its metallicity can be taken from measurements of the typical SMC metallicity. We find that this value is in the range $Z = 0.1Z_{\odot}$–$0.2Z_{\odot}$ [Piatti, 2012, Bolatto et al., 2011]. For the solar metallicity, this value ranges from 0.012–0.02 [Vagnozzi, 2019]. Finally for convective overshoot, we used a value of $\alpha_{\rm ov} = 0.6$, satisfying the value required to match the larger convective core masses reported in recent literature [Tkachenko et al., 2020b].

- For each set of parameters, we initialize stellar models with a range of ZAMS masses. We then evolve each of these models until core hydrogen depletion.
- For each model, we can find the age at which its luminosity and effective temperature best match the observed values of $T_{\rm eff} = 2.4 \times 10^4$ K and $L = 1.2 \times 10^4 L_\odot$. This gives us a single stellar model, described by its hyperparameters, mass, and age, that best matches the observed properties of the MS star in PSR J0045-7319.
- For this best-fit stellar model, we calculate its core radius as the innermost radius at which its Brunt-Väisälä frequency $N^2 > 0$, i.e. the innermost radius at which it is convectively stable.

This procedure is illustrated for a few of these models in Figs. E.1–**??**. We see that the core radii do not exceed $\sim R_\odot$, though larger convective overshoot and metallicity improve agreement. The values of the convective core radius are in disagreement with the conclusions shown in Fig. 6.8, which require a core radius $r_{\rm c} \gtrsim 1.3 R_\odot$.

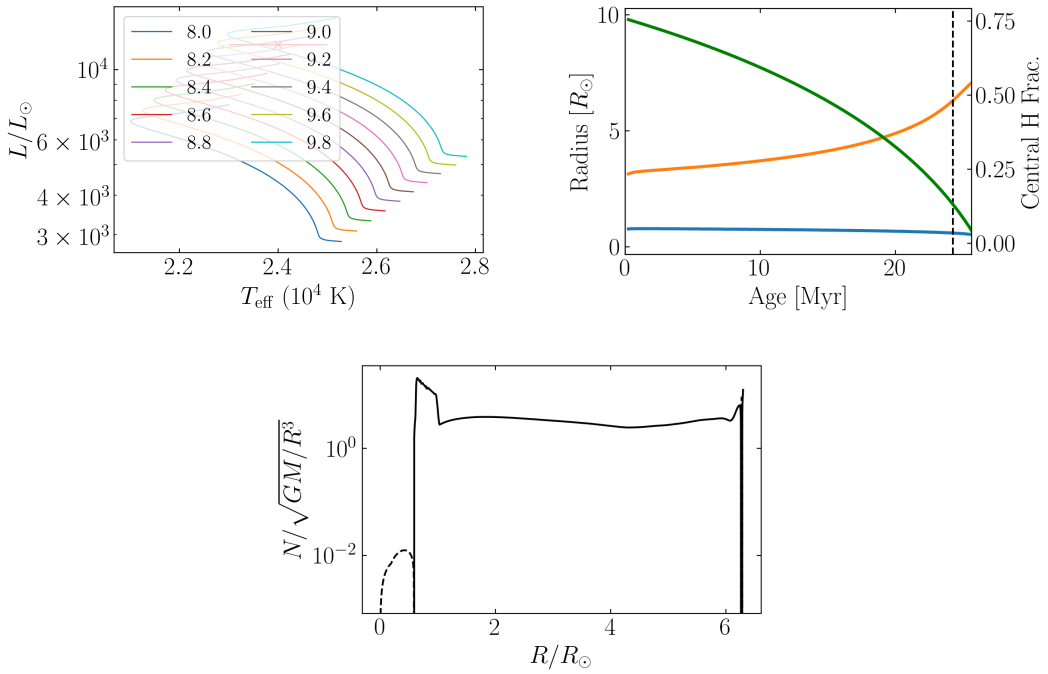

Figure E.1: Plots illustrating the procedure used to find the best-fitting stellar model to the properties of PSR J0045-7319 using a near-critically rotating stellar model with no convective overshoot, and metallicity $Z = 0.1Z_\odot = 0.0012$. In the top-left panel, the plots show the fit to the observed stellar luminosity and surface temperature (red dot) as a function of the ZAMS stellar mass (each line is an evolutionary track for a star with mass denoted in the legend). In the top-right column, the plots show the evolution of the best-fitting star as a function of stellar age: the orange line shows the overall stellar radius, the blue line the radius of the convective core, and the green line the central hydrogen fraction (right axis). The vertical black line denotes the age at which the stellar model best matches the observed luminosity and surface temperature (i.e. the age used for the third column). In the bottom panel, the plots show the signed Brunt-Väisälä frequency N^2 as a function of the stellar radius for the best-fitting stellar mass and age combination.

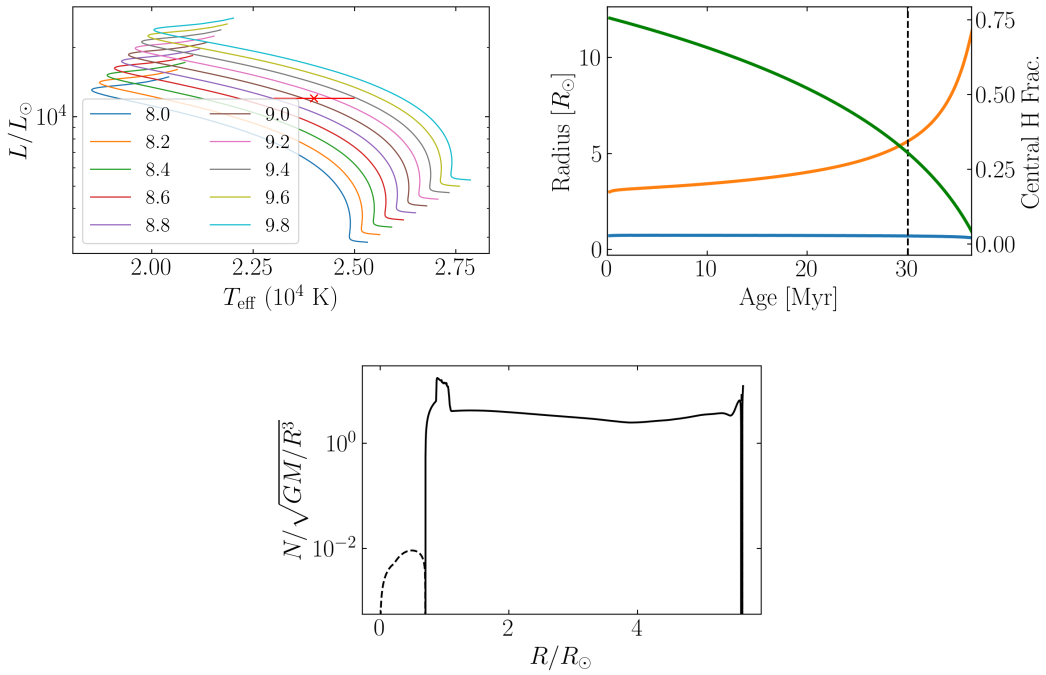

Figure E.2: Same as Fig. E.1 but with a convective overshoot parameter of 0.04 (see MESA documentation).

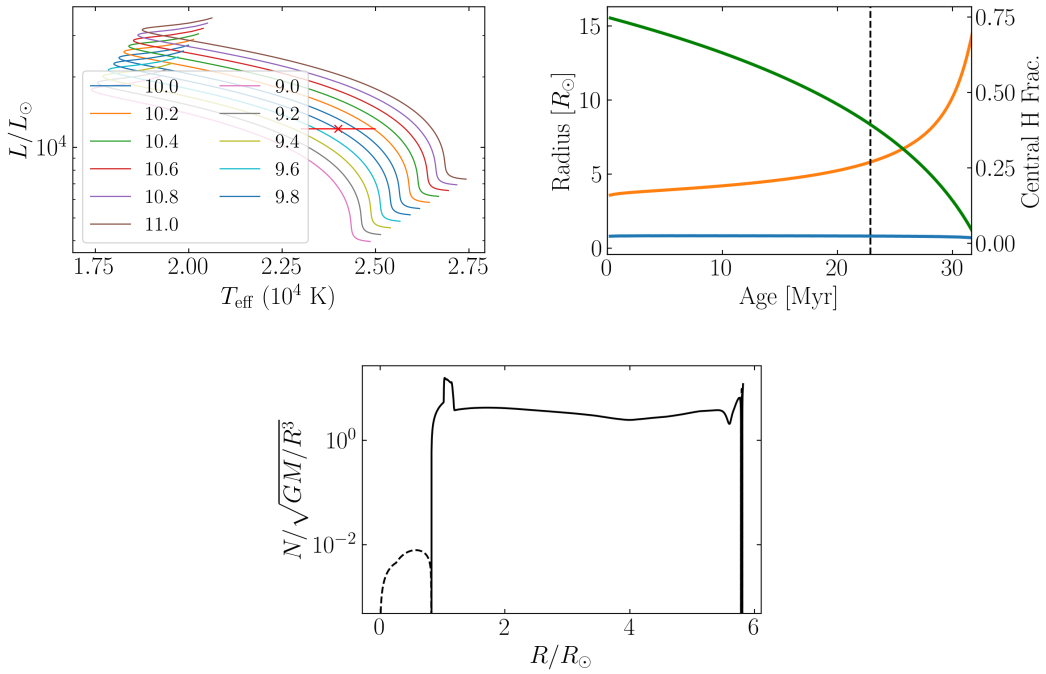

Figure E.3: Same as Fig. E.1 but with a convective overshoot parameter of 0.04 (see MESA documentation) and with $Z = 0.2Z_\odot = 0.004$

APPENDIX F

APPENDICIES TO SPIN DYNAMICS OF TERTIARY-INDUCED BLACK HOLE MERGERS

F.1 Floquet Theory Analysis

In this appendix, we provide an alternative approach to analyzing the BH spin dynamics based on Floquet theory [Chicone, 2006] that provides results complementary to those in the main text. Although the resulting equations cannot be analytically solved, they place strong constraints on the allowed behavior of the system. Additionally, Eq. (7.81) has a natural interpretation in this formulation, and its accuracy is numerically tested in Appendix F.1.3. We again work in the corotating frame and neglect GW dissipation, so the equation of motion is given by Eq. (7.22). If we define the matrix operator $\tilde{\mathbf{A}}$ satisfying $\tilde{\mathbf{A}}\mathbf{S} = \boldsymbol{\Omega}_{\rm e} \times \mathbf{S}$, then the equation of motion is

$$\left(\frac{\mathrm{d}\mathbf{S}}{\mathrm{d}t}\right)_{\rm rot} = \tilde{\mathbf{A}}\mathbf{S}. \tag{F.1}$$

Here, $\tilde{\mathbf{A}}$ is periodic with period $P_{\rm LK}$ [see Eq. (7.19)].

F.1.1 Without Nutation

First, for simplicity, let us assume that $\boldsymbol{\Omega}_{\rm e}$ does not nutate, so its orientation is fixed. In this case, Eq. (F.1) admits an exact conserved quantity:

$$\frac{\mathrm{d}}{\mathrm{d}t}\left[e^{-\Phi}\mathbf{S}\right] = 0, \tag{F.2}$$

where

$$\Phi(t) \equiv \int^{t} \tilde{\mathbf{A}}\,\mathrm{d}t. \tag{F.3}$$

Separately, since Eq. (F.1) is linear and has periodic coefficients, Floquet theory tells us that $\mathbf{S}(t+P_{\rm LK})$ is related to $\mathbf{S}(t)$ by the monodromy matrix $\tilde{\mathbf{M}}$:

$$\mathbf{S}(t+P_{\rm LK}) = \tilde{\mathbf{M}}\mathbf{S}(t). \tag{F.4}$$

Comparing Eqs. (F.2) and (F.4), we immediately find that

$$\begin{aligned}\tilde{\mathbf{M}} &= \exp\left[\int_0^{P_{\rm LK}} \tilde{\mathbf{A}}\,\mathrm{d}t\right], \\ &= \exp\left[P_{\rm LK}\overline{\tilde{\mathbf{A}}}\right],\end{aligned} \tag{F.5}$$

where again the overbar denotes time averaging. Note that $\tilde{\mathbf{M}}$ is a rotation matrix, so it must have exactly one eigenvector with eigenvalue 1; call this eigenvector $\mathbf{R}$. But $\mathbf{R} = \hat{\mathbf{\Omega}}_{\rm e}$, so $\mathbf{S}\cdot\hat{\mathbf{\Omega}}_{\rm e}$ must be constant for every $t = NP_{\rm LK}$.

This example is somewhat trivial: since $\mathbf{\Omega}_{\rm e}$ does not nutate, $\mathbf{S}$ just precesses around fixed $\mathbf{R} = \hat{\mathbf{\Omega}}_{\rm e}$ at a variable rate, and $\mathbf{S}\cdot\hat{\mathbf{\Omega}}_{\rm e}$ is conserved. However, the equation of motion studied in Section 7.4 [Eq. (7.35)] neglects nutation yet provides a good description of the evolution of $\bar{\theta}_{\rm e}$. For the fiducial LK-induced merger, Fig. 7.6 shows that $\mathbf{\Omega}_{\rm e}$ nutates substantially within a LK period when $\mathscr{A} \simeq 1$ (nutation is equivalent to $\Omega_{\rm e1} \neq 0$ and $\Delta I_{\rm e1} \neq 0°$). We infer that, even when $\mathbf{\Omega}_{\rm e}$ does nutate appreciably, the nutation can sometimes be neglected to good approximation.

In Section 7.5, we showed that being close to a resonance $\overline{\Omega}_{\rm e} \approx M\Omega_{\rm LK}$ results in non-conservation of $\bar{\theta}_{\rm e}$. However, the converse is not obviously true: our approximate analysis does not prove that being far from these resonances guarantees good conservation of $\bar{\theta}_{\rm e}$. In the next section, we argue that, for the dynamics studied in this paper, this converse is likely true as well.

F.1.2 With Nutation

When $\boldsymbol{\Omega}_\mathrm{e}$ is allowed to nutate within P_LK, the quantity given by Eq. (F.2) is no longer conserved, as

$$\frac{\mathrm{d}}{\mathrm{d}t}\left[e^{-\Phi}\mathbf{S}\right] = e^{-\Phi}\frac{\mathrm{d}\mathbf{S}}{\mathrm{d}t} - \tilde{A}e^{-\Phi}\mathbf{S} \neq e^{-\Phi}\left[\frac{\mathrm{d}\mathbf{S}}{\mathrm{d}t} - \tilde{\mathbf{A}}\mathbf{S}\right] = 0. \tag{F.6}$$

Instead, we define two new quantities Φ' and $\tilde{\mathbf{B}}$ via

$$\Phi'(t) \equiv \int^{t} \left(\tilde{\mathbf{A}} + \tilde{\mathbf{B}}\right)\,\mathrm{d}t, \tag{F.7}$$

$$\frac{\mathrm{d}}{\mathrm{d}t}\left[e^{-\Phi'}\mathbf{S}\right] = 0. \tag{F.8}$$

This requires

$$\tilde{\mathbf{B}} = \left[e^{-\Phi'}, \tilde{\mathbf{A}}\right] e^{\Phi'}, \tag{F.9}$$

where the square brackets denote the commutator. The monodromy matrix is then

$$\tilde{\mathbf{M}} = \exp\left[\int_0^{P_\mathrm{LK}} \left(\tilde{\mathbf{A}} + \tilde{\mathbf{B}}\right)\,\mathrm{d}t\right]. \tag{F.10}$$

We next want to understand when Eq. (F.10) can be well approximated by Eq. (F.5). We first expand the matrix exponential using the Zassenhaus formula [the inverse of the well-known Baker-Campbell-Hausdorff formula, see e.g. Magnus, 1954]

$$\tilde{\mathbf{M}} = e^{P_\mathrm{LK}\bar{\tilde{\mathbf{A}}}} e^{P_\mathrm{LK}\bar{\tilde{\mathbf{B}}}} \exp\left[-\frac{P_\mathrm{LK}^2\left[\bar{\tilde{\mathbf{A}}}, \bar{\tilde{\mathbf{B}}}\right]}{2} + \ldots\right]. \tag{F.11}$$

Note that since $\tilde{\mathbf{M}}$ is a rotation matrix (see Section 7.3.1), and $\exp\left[P_\mathrm{LK}\bar{\tilde{\mathbf{A}}}\right]$ is also a rotation matrix ($\tilde{\mathbf{A}}$ is skew-symmetric), the remainder of the right-hand side above must also be a rotation matrix (as the rotation matrices are closed under matrix multiplication). For convenience, define

$$\tilde{\mathbf{R}}_\mathrm{A} \equiv e^{P_\mathrm{LK}\bar{\tilde{\mathbf{A}}}} \qquad \tilde{\mathbf{R}}_\mathrm{B} \equiv e^{P_\mathrm{LK}\bar{\tilde{\mathbf{B}}}} \exp\left[-\frac{P_\mathrm{LK}^2\left[\bar{\tilde{\mathbf{A}}}, \bar{\tilde{\mathbf{B}}}\right]}{2} + \ldots\right], \tag{F.12}$$

where $\tilde{\mathbf{R}}_\mathrm{A}$ and $\tilde{\mathbf{R}}_\mathrm{B}$ are rotation matrices that effect rotations by angles θ_A and θ_B about their respective axes.

When can $\tilde{\mathbf{R}}_\mathrm{B}$ be neglected? From Eq. (F.9), we see that $\tilde{\mathbf{B}} = 0$ vanishes ($\theta_\mathrm{B} = 0$) when $\left[\tilde{\mathbf{A}}, \Phi\right] = 0$, which occurs when $\boldsymbol{\Omega}_\mathrm{e}$ does not nutate, and we recover Eq. (F.5). In fact, we will argue later that θ_B is generally small for the spin dynamics studied in the main text. However, a small θ_B alone is not sufficient to guarantee $\tilde{\mathbf{M}} \approx \tilde{\mathbf{R}}_\mathrm{A}$. To see this, note if θ_B is small, then $\tilde{\mathbf{R}}_\mathrm{B} \approx \mathbf{1}$ where $\mathbf{1}$ is the 3×3 identity matrix. On the other hand, $\theta_\mathrm{A} = \overline{\Omega}_\mathrm{e} T_\mathrm{LK}$. Then, if θ_A is not too near an integer multiple of 2π, $\tilde{\mathbf{M}} \approx \tilde{\mathbf{R}}_\mathrm{A}$ and $\tilde{\mathbf{M}} \approx \tilde{\mathbf{R}}_\mathrm{A}$ as before. However, if $\overline{\Omega}_\mathrm{e} T_\mathrm{LK} \approx 2\pi M$ for integer M, then $\tilde{\mathbf{R}}_\mathrm{A}$ itself is near the identity as well, and $\tilde{\mathbf{R}}_\mathrm{B}$ *cannot* be neglected when calculating $\tilde{\mathbf{M}}$. The criterion for neglecting $\tilde{\mathbf{R}}_\mathrm{B}$ is then clear: θ_B must be much closer to an integer multiple of $2\pi M$ than θ_A.

To complete this picture, we argue that, for the spin dynamics studied in the main text, θ_B is small, so generally $\tilde{\mathbf{R}}_\mathrm{B} \approx \mathbf{1}$, and $\overline{\Omega}_\mathrm{e} \approx M\Omega_\mathrm{LK}$ is a *necessary* condition for $\mathbf{R}$ to differ significantly from $\hat{\overline{\boldsymbol{\Omega}}}_\mathrm{e}$. To do this, we recall that $\overline{\Omega}_\mathrm{e} P_\mathrm{LK} \lesssim 2\pi$ (Figs. 7.10 and 7.12), and we seek to show that θ_B must generally be small compared to θ_A, which would imply $\theta_\mathrm{B} \ll 2\pi$. We first approximate that $e^{\Phi'} \approx e^{\Phi}$ in Eq. (F.9) (requiring $\theta_\mathrm{B} \ll \theta_\mathrm{A}$, which we will verify retroactively, and being far from resonance, $\theta_\mathrm{A} \neq 2\pi$), which gives

$$\tilde{\mathbf{B}} \approx \left[e^{-\Phi}, \tilde{\mathbf{A}}\right] e^{\Phi}. \tag{F.13}$$

Next, recall that Φ is the integral of $-\tilde{\mathbf{A}}$, and so the magnitude of $\overline{\tilde{\mathbf{B}}}$ [$\tilde{\mathbf{B}}$ primarily affects $\tilde{\mathbf{M}}$ via its average, see Eq. (F.10)] depends on the average misalignment between the vectors $\boldsymbol{\Omega}_\mathrm{e}$ and $\int^t \boldsymbol{\Omega}_\mathrm{e}\, \mathrm{d}t \simeq \overline{\boldsymbol{\Omega}}_\mathrm{e}$. There are a few possible regimes to consider: (i) if $\mathscr{A} \gg 1$, then LK oscillations are frozen, and $\boldsymbol{\Omega}_\mathrm{e}$ does not nutate; (ii) if $\mathscr{A} \ll 1$, then $\hat{\Omega}_\mathrm{e} \approx \hat{\mathbf{L}}_\mathrm{tot} \approx \hat{\overline{\boldsymbol{\Omega}}}_\mathrm{e}$ for almost all of T_Lk; and (iii) if $\mathscr{A} \simeq 1$, then e_max cannot be too large [Eq. (7.18)], and so Ω_L and Ω_SL cannot vary too much

within an LK cycle and the nutation of $\mathbf{\Omega}_e$ is limited. This analysis suggests that, at least far from resonance, the nutation of $\mathbf{\Omega}_e$ is limited, and the commutator in Eq. (F.13) is small in the sense that $\theta_B \ll \theta_A$, justifying our earlier claim. While this analysis is not rigorous, it suggests that the only resonances present in the system are near $\overline{\Omega}_e = M\Omega_{LK}$ and that otherwise $\mathbf{R} \parallel \overline{\mathbf{\Omega}}_e$, in agreement with the results of the main text.

F.1.3 Quantitative Effect

Above, we have given a qualitative analysis of the exact solution for the monodromy matrix $\tilde{\mathbf{M}}$. In this section, we aim to reconcile this with the quantitative, approximate results in the text and suggest that the results in the text constitute a complete characterization of the spin dynamics.

In Section 7.5, we found that one effect of the Fourier harmonics in Eq. (7.25) are fluctuations in $\bar{\theta}_e$ when $\overline{\Omega}_e \approx M\Omega_{LK}$ for some integer M with amplitude given by Eq. (7.81). On the other hand, in Appendix F.1.2, we found that $\mathbf{R}$ is aligned with $\overline{\mathbf{\Omega}}_e$ except when $\overline{\Omega}_e$ is sufficiently close to $M\Omega_{LK}$ that the nutation of $\mathbf{\Omega}_e$ becomes important, but we were not able to determine a closed-form expression for the misalignment. In this section, we show numerically that the formulas given in the main text give good predictions for the orientation of $\mathbf{R}$.

To validate the analytic prediction given by Eq. (7.81), we numerically compute $\tilde{\mathbf{M}}$. We study the $\eta \neq 0$, LK-enhanced regime ($m_1 = m_2 = m_3 = 30M_\odot$, $a_0 = 0.1$ AU, $e_0 = 10^{-3}$,$\tilde{a}_{out} = 3$ AU). We still neglect GW dissipation in order for Floquet analysis to be applicable. For 2000 different I_0 of the inner binary, we construct $\tilde{\mathbf{M}}$ by evolving the spin equation of motion Eq. (7.22) starting with the three initial conditions $\mathbf{S}_0 = \hat{\mathbf{x}}$, $\mathbf{S}_0 = \hat{\mathbf{y}}$, and $\mathbf{S}_0 = \mathbf{z}$ (see Fig. F.1) over a single LK period, then

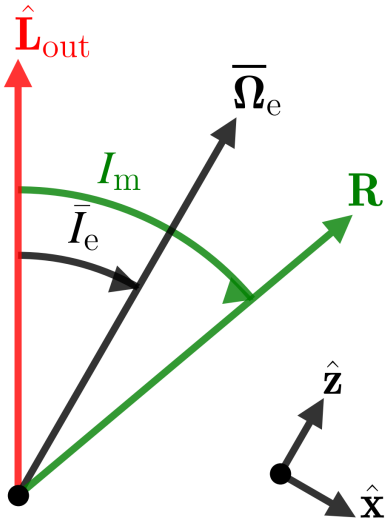

Figure F.1: Definition of angles for numerical study of the monodromy matrix rotation axis. $\mathbf{R}$ is the eigenvector of the monodromy matrix $\tilde{\mathbf{M}}$ with eigenvalue 1.

using

$$\tilde{\mathbf{M}} = \mathbf{\Phi}(P_{\rm LK})\mathbf{\Phi}^{-1}(0) = \mathbf{\Phi}(P_{\rm LK}), \tag{F.14}$$

where $\mathbf{\Phi}(t)$ is the *principal fundamental matrix solution* whose columns are solutions to Eq. (7.22) and $\mathbf{\Phi}(0)$ is the identity. $\mathbf{R}$ is then the eigenvector that has eigenvalue 1. Note that if $\mathbf{v}$ is an eigenvector, so too is $-\mathbf{v}$; we choose convention that $\mathbf{R}$ points in the same direction as $\overline{\mathbf{\Omega}}_{\rm e}$, i.e. $\Delta I_{\rm m} \equiv \left|I_{\rm m} - \bar{I}_{\rm e}\right| < 90^\circ$.

The orientation of $\mathbf{R}$ is related to the $\left|\Delta\bar{\theta}_{\rm e}\right|$ predicted by Eq. (7.81): if $\mathbf{R}$ and $\overline{\mathbf{\Omega}}_{\rm e}$ are misaligned by angle $\Delta I_{\rm m}$, then $\bar{\theta}_{\rm e}$ oscillates with semi-amplitude $\Delta I_{\rm m}$. Thus, we can infer $\Delta I_{\rm m}$ in the vicinity of each $\overline{\Omega}_{\rm e} = M\Omega_{\rm LK}$ resonance from Eq. (7.81), and we obtain by linearity that

$$\Delta I_{\rm m} \sim \sum_{M=1}^{\infty} \frac{d(M)}{2} \left| \frac{\Omega_{\rm eM} \sin \Delta I_{\rm eM}}{\overline{\Omega}_{\rm e} - M\Omega_{\rm LK}} \right|. \tag{F.15}$$

Figure F.2 shows that this calculation predicts the numeric $\Delta I_{\rm m}$ well. In particular, the amplitude of both resonances are well predicted, suggesting that the approximate factor $d(M)$ introduced in Eq. (7.81) is accurate. This supports our

assertion that $\mathbf{R}$ deviates from $\hat{\overline{\mathbf{\Omega}}}_{\rm e}$ at resonances $\overline{\Omega}_{\rm e} \approx M\Omega_{\rm LK}$, and the misalignment is captured by Eq. (7.81).

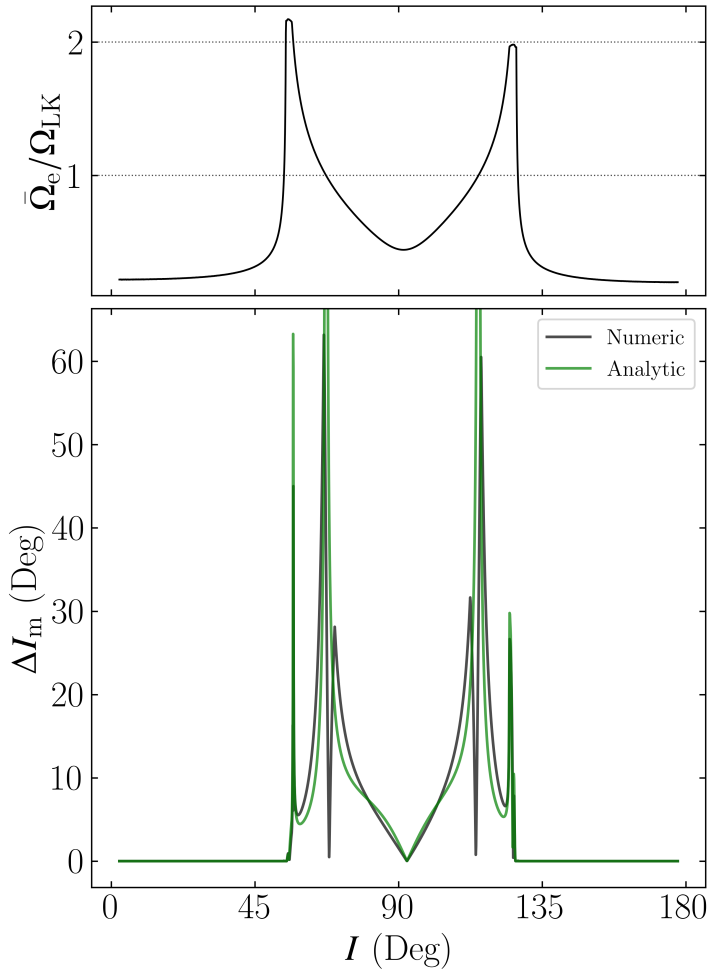

Figure F.2: Comparison of the orientation $\mathbf{R}$ obtained from numerical simulations of Eq. (7.22) in the $\eta \neq 0$, LK-enhanced parameter regime ($m_1 = m_2 = m_3 = 30M_\odot$, $a_0 = 0.1$ AU, $e_0 = 10^{-3}$,$\tilde{a}_{\rm out} = 3$ AU) with the analytic resonance formula given by Eq. (F.15) as a function of initial inclination, in the absence of GW dissipation. The top panel shows the ratio $\overline{\Omega}_e/\Omega_{LK}$ is shown as the solid black line, while the horizontal dashed lines denote $\overline{\Omega}_e = \Omega_{LK}$ and $\overline{\Omega}_e = 2\Omega_{LK}$. The bottom panel shows the misalignment angle between the numerically-computed $\mathbf{R}$ and $\overline{\mathbf{\Omega}}_e$ as the black line. Separately, the predicted misalignment ΔI_m due to interaction with the Fourier harmonics is given by Eq. (F.15). We see that the scaling of the misalignment angle near resonances is well captured by our analytic formula, but the numerical misalignment angle crosses 0 within the $M = 1$ resonance, which is not predicted by our simple theory.

APPENDIX G

APPENDICIES TO MASS RATIO DISTRIBUTION OF TERTIARY-INDUCED BLACK HOLE MERGERS

G.1 Origin of Octupole-Inactive Gap

We investigate the origin of the "octupole-inactive gap", an inclination range near $I_0 \approx 90^\circ$ for which $e_{\max}$ does not attain $e_{\lim}$ despite being in between two octupole-active windows. This gap was first identified in Section 8.2.3, and is seen in both the non-dissipative and full simulations with GW dissipation (see Figs. 8.4–8.8).

To better understand this gap, we first review the mechanism by which extreme eccentricity excitation occurs. In the test-particle limit, Katz et al. [2011] showed that K (Eq. 8.4) oscillates over long timescales when ω, the argument of pericenter of the inner orbit, is circulating. This then leads to orbit flips (and extreme eccentricity excitation) between prograde and retrograde inclinations when K changes signs: since $j(e)$ is nonnegative, the sign of K determines the sign of $\cos I$. Katz et al. [2011] obtained coupled oscillation equations in K and Ω_e, the azimuthal angle of the inner eccentricity vector in the inertial reference frame. The amplitude of oscillation of K can then be analytically computed, and the octupole-active window (the range of I_0 over which orbit flips occur) is the region for which the range of these oscillations encompasses $K = 0$ [Katz et al., 2011]. When ω is librating instead, Ω_e jumps by $\sim 180^\circ$ every ZLK cycle, and the oscillations in K are suppressed.

In the finite-η case, we commented in Section 8.2.3 that the relation between K oscillations and extreme eccentricity excitation (and orbit flipping) can be generalized even when η is nonzero. K still oscillates over timescales $\gg t_{\rm ZLK}$ when

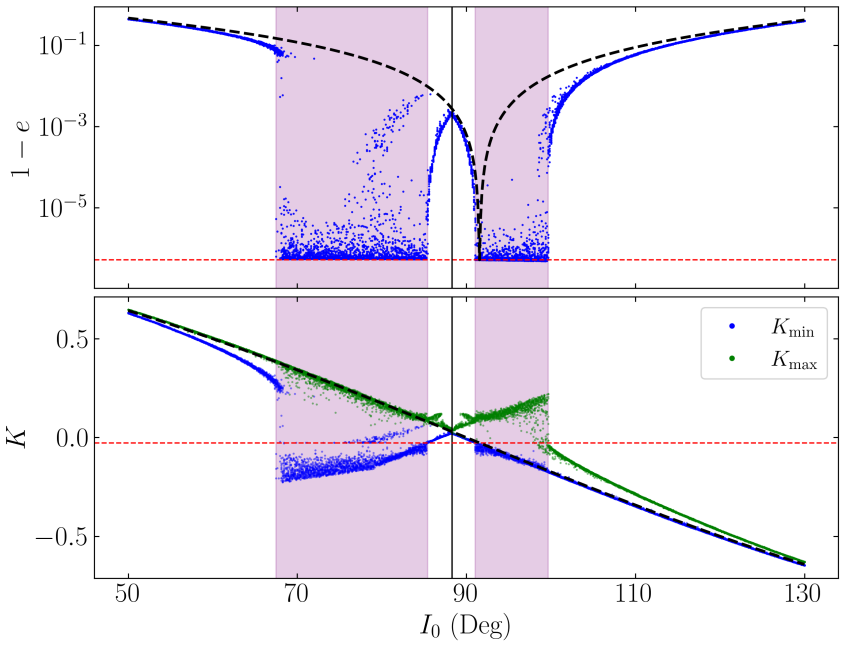

Figure G.1: Octupole-active windows and amplitude of oscillation of K (Eq. 8.4). *Top panel:* Maximum eccentricity $e_{\max}$ attained by the inner binary with initial tertiary inclination I_0 when integrated for $2000 t_{\rm ZLK}$ (blue dots), reproduced from the top panel of Fig. 8.6. Also shown are $e_{\rm lim}$ (Eq. 8.10, horizontal red dashed line), the quadrupole-level result for $e_{\max}$ (Eq. 8.7, dashed black line), the empirically-determined center of the gap, located at $I_0 \approx 88.32°$ (vertical black line), and the inclinations that can lead to extreme eccentricities (shaded purple regions). *Bottom panel:* Minimum and maximum values of K, denoted $K_{\min}$ and $K_{\max}$, attained by the systems. Also shown are the initial K for a given I_0 (black dashed line) and the critical $K_{\rm c} = -\eta/2$ for orbit flipping (horizontal red dashed line). The center of the octupole-inactive gap and the octupole-active windows are labeled as in the top panel.

ω is circulating, and if its range of oscillation contains $K_c \equiv -\eta/2$, then the inner orbit flips, in the process attaining extreme eccentricities. To be precise, orbit flips are defined to be when the range of inclination oscillations changes from $(\cos I_0)_- < \cos I < \cos I_{0,\rm lim}$ to $\cos I_{0,\rm lim} < \cos I < (\cos I_0)_+$ or vice versa, where $(\cos I_0)_\pm$ are given by Eq. (8.11) and $I_{0,\rm lim}$ satisfies Eq. (8.9).

However, the range of oscillation of K is more complex than it is in the test-particle limit. Figure G.1 compares the behavior of $e_{\rm max}$ in the non-dissipative simulations (top panel; reproduced from the top panel of Fig. 8.6) to the range of oscillations in K (bottom panel). Denote the center of the gap $I_{0,\rm gap}$ (shown as the vertical black line in both panels of Fig. G.1). Near $I_{0,\rm gap}$, K oscillates about $K(I_{0,\rm gap})$, which is *positive*, and the oscillation amplitude goes to zero at $I_{0,\rm gap}$. On the other hand, orbit flips (and extreme eccentricity excitation) are possible when the range of oscillation of K encloses K_c (i.e., $K_{\rm min} < K_c < K_{\rm max}$). The purple shaded regions in both panels of Fig. G.1 illustrate this equivalence, as they show both the $e_{\rm lim}$-attaining inclinations in the top panel and the inclinations where $K_{\rm min} < K_c < K_{\rm max}$ in the bottom panel. But since $K\left(I_{0,\rm gap}\right) > 0$ while $K_c < 0$, there will always be a range of I_0 about $I_{0,\rm gap}$ for which the oscillation amplitude is smaller than $K\left(I_{0,\rm gap}\right) - K_c$, and orbit flips are impossible in this range. This range then corresponds to the octupole-inactive gap.

This analysis has simply pushed our lack of understanding onto a new quantity: why are K oscillations suppressed in the neighborhood of $I_{0,\rm gap}$? A quantitative answer to this question is beyond the scope of this paper, but for a qualitative understanding, we can examine the evolution of a system in the octupole-inactive gap. The left panel of Fig. G.2 shows the same simulation as Fig. 8.3 but with an additional panel showing Ω_e, while the right panel shows a simulation with the same parameters except $I_0 = 88^\circ$, which is near $I_{0,\rm gap}$ (see Fig. G.1). The oscilla-

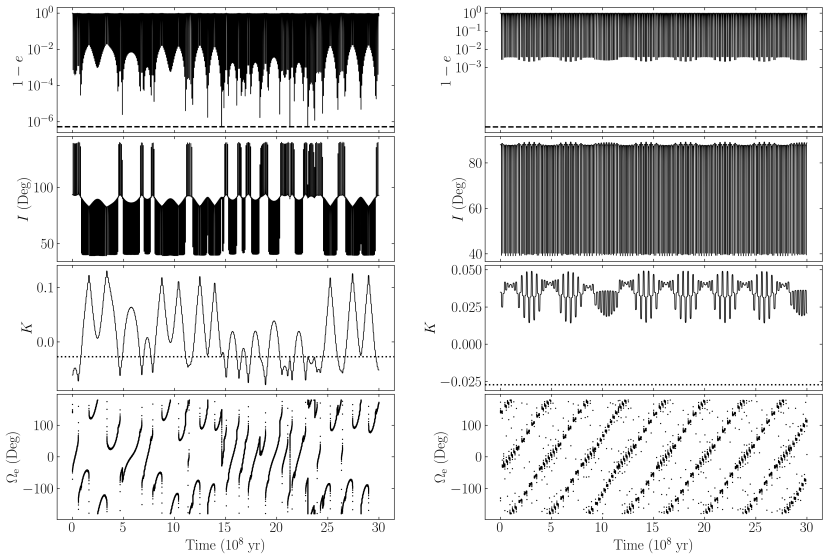

Figure G.2: The left panel is the same as Fig. 8.3 but includes the evolution of the azimuthal angle of the eccentricity vector, Ω_e. The right panel is the same as the left but for $I_0 = 88°$. For both of these examples, we have used $\omega_0 = 0$, but the evolution is similar for all ω_0.

tions in K (third panels) are much smaller for $I_0 = 88°$ than for $I_0 = 93.5°$, and no orbit flips occur. Most interestingly, the fourth panel shows that the evolution of Ω_e is much less smooth than in Fig. 8.3, jumping at almost every other eccentricity maximum. Katz et al. [2011] have already pointed out that jumps in Ω_e occur when ω is *librating*, rather than circulating.

When the octupole-order terms are neglected, the circulation-libration boundary is a boundary in e-ω space: as long as the ZLK separatrix exists in the e-ω plane and $e_0 > 0$, then an initial $\omega_0 = 0$ causes ω to circulate, while an initial $\omega_0 = \pi/2$ causes ω to librate [e.g., Kinoshita and Nakai, 1999, Shevchenko, 2016]. However, when including octupole-order terms, this picture breaks down. To illustrate this, for a range of I_0 and both $\omega_0 = 0$ and $\omega_0 = \pi$, we evolve the fiducial system parameters for a single ZLK cycle, using $q = 0.2$ as is used for Figs. G.1 and G.2, and consider both the dynamics with and without the octupole-order terms. Figure G.3 gives the resulting changes in Ω_e over a single ZLK period

when the octupole-order effects are neglected (top) and when they are not (bottom). Two observations can be made: (i) $I_{0,\mathrm{gap}}$ is approximately where $\Delta\Omega_\mathrm{e} = 0$ for circulating initial conditions when neglecting octupole-order terms, and (ii) the inclusion of the octupole-order terms seem to cause Ω_e to exclusively vary slowly ($|\Delta\Omega_\mathrm{e}| \ll 180°$) except for $I_{0,\mathrm{gap}} < I_0 < I_{0,\mathrm{lim}}$. The former is plausible: if $K(I_{0,\mathrm{gap}})$ is the location of an equilibrium in K-Ω_e space, then it must satisfy $\Delta\Omega_\mathrm{e} = 0$. The latter suggests that the assumption of circulation of ω in Katz et al. [2011] may be satisfied for many more initial conditions than the quadrupole-level analysis suggests, as long as they are not in octupole-inactive gap.

Finally, examination of the bottom panel of Fig. G.1 suggests that the oscillation amplitude in K grows roughly linearly with $\left|I_0 - I_{0,\mathrm{gap}}\right|$ in the vicinity of $I_{0,\mathrm{gap}}$ [this may be because, in the test-particle limit, librating ω give oscillation amplitudes in K that are higher-order in K and Ω_e, as pointed out by Katz et al., 2011]. Assuming this, the gap width can then be given by

$$\text{Gap Width} = 2\left(I_{0,\mathrm{lim}} - I_{0,\mathrm{gap}}\right). \tag{G.1}$$

This explains why the gap does not exist in the test-particle regime, as $I_{0,\mathrm{lim}} = I_{0,\mathrm{gap}} = 90°$ by symmetry of the equations of motion.

It is clear from the preceding discussion and Fig. G.3 that the octupole-order, finite-η dynamics are complex, and our discussion can only be considered heuristic. Nevertheless, in the absence of a closed form solution to the octupole-order ZLK equations of motion or a full generalization of the work of Katz et al. [2011], they provide a preliminary understanding of the octupole-inactive gap.

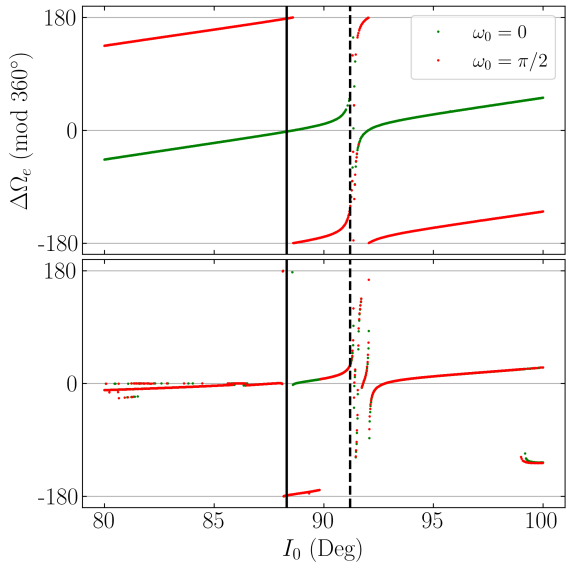

Figure G.3: Plot of $\Delta\Omega_e$, the change in Ω_e over a single ZLK cycle, for $q = 0.2$ and the fiducial parameters using different initial conditions. In the top panel, octupole-order terms are neglected, while in the lower panel, they are not. The solid and dashed vertical black lines denote $I_{0,\mathrm{gap}}$ and $I_{0,\mathrm{lim}}$ respectively.

BIBLIOGRAPHY

Benjamin P Abbott, Richard Abbott, TD Abbott, MR Abernathy, Fausto Acernese, Kendall Ackley, Carl Adams, Thomas Adams, Paolo Addesso, RX Adhikari, et al. GW150914: Implications for the stochastic gravitational-wave background from binary black holes. *Phys. Rev. Lett.*, 116(13):131102, 2016.

Benjamin P Abbott, Richard Abbott, TD Abbott, MR Abernathy, Fausto Acernese, Kendall Ackley, Carl Adams, Thomas Adams, Paolo Addesso, RX Adhikari, et al. GW190412: Observation of a binary-black-hole coalescence with asymmetric masses. *Phys. Rev. D*, 102:043015, 2020a.

BP Abbott, R Abbott, TD Abbott, S Abraham, F Acernese, K Ackley, C Adams, RX Adhikari, VB Adya, C Affeldt, et al. Binary black hole population properties inferred from the first and second observing runs of advanced LIGO and advanced VIRGO. *ApJ*, 882(2):L24, 2019.

R Abbott, TD Abbott, S Abraham, F Acernese, K Ackley, C Adams, RX Adhikari, VB Adya, C Affeldt, M Agathos, et al. Properties and astrophysical implications of the 150m binary black hole merger GW190521. *ApJ*, 900(1):L13, 2020b.

Rich Abbott, TD Abbott, S Abraham, F Acernese, K Ackley, A Adams, C Adams, RX Adhikari, VB Adya, C Affeldt, et al. Population properties of compact objects from the second LIGO–VIRGO gravitational-wave transient catalog. *ApJ*, 913 (1):L7, 2021.

Ulrich Achatz, Rupert Klein, and Fabian Senf. Gravity waves, scale asymptotics and the pseudo-incompressible equations. *J. Fluid Mech.*, 663:120–147, 2010.

Arthur D Adams, Sarah Millholland, and Gregory P Laughlin. Signatures of obliquity in thermal phase curves of hot Jupiters. *AJ*, 158(3):108, 2019.

M.E. Alexander. The weak friction approximation and tidal evolution in close binary systems. *Ap&SS*, 23:459, 1973.

Kassandra R Anderson and Dong Lai. Teetering stars: Resonant excitation of stellar obliquities by hot and warm Jupiters with external companions. *MNRAS*, 480(1):1402–1414, 2018.

Kassandra R Anderson, Natalia I Storch, and Dong Lai. Formation and stellar spin-orbit misalignment of hot Jupiters from Lidov–Kozai oscillations in stellar binaries. *MNRAS*, 456(4):3671–3701, 2016.

Joseph MO Antognini. Timescales of Kozai–Lidov oscillations at quadrupole and octupole order in the test particle limit. *MNRAS*, 452(4):3610–3619, 2015.

Fabio Antonini and Hagai B Perets. Secular evolution of compact binaries near massive black holes: Gravitational wave sources and other exotica. *ApJ*, 757(1): 27, 2012.

Fabio Antonini, Norman Murray, and Seppo Mikkola. Black hole triple dynamics: A breakdown of the orbit average approximation and implications for gravitational wave detections. *ApJ*, 781(1):45, Jan 2014. doi: 10.1088/0004-637x/781/1/45.

Fabio Antonini, Silvia Toonen, and Adrian S Hamers. Binary black hole mergers from field triples: Properties, rates, and the impact of stellar evolution. *ApJ*, 841(2):77, 2017.

Fabio Antonini, Carl L Rodriguez, Cristobal Petrovich, and Caitlin L Fischer. Precessional dynamics of black hole triples: Binary mergers with near-zero effective spin. *MNRASLett.*, 480(1):L58–L62, 2018.

JC Armstrong, R Barnes, S Domagal-Goldman, J Breiner, TR Quinn, and VS Meadows. Effects of extreme obliquity variations on the habitability of exoplanets. *Astrobiology*, 14(4):277–291, 2014.

Uri M Ascher, Steven J Ruuth, and Raymond J Spiteri. Implicit-explicit runge-kutta methods for time-dependent partial differential equations. *Appl. Numer. Math.*, 25(2-3):151–167, 1997.

MP Baldwin, LJ Gray, TJ Dunkerton, K Hamilton, PH Haynes, WJ Randel, JR Holton, MJ Alexander, I Hirota, T Horinouchi, et al. The quasi-biennial oscillation. *Rev. Geophys.*, 39(2):179–229, 2001.

Sambaran Banerjee, Holger Baumgardt, and Pavel Kroupa. Stellar-mass black holes in star clusters: Implications for gravitational wave radiation. *MNRAS*, 402(1):371–380, 2010.

Adrian J Barker. Tidal dissipation in evolving low-mass and solar-type stars with predictions for planetary orbital decay. *MNRAS*, 498(2):2270–2294, 2020.

Adrian J Barker and Gordon I Ogilvie. On internal wave breaking and tidal dissipation near the centre of a solar-type star. *MNRAS*, 404(4):1849–1868, 2010.

Konstantin Batygin and Fred C Adams. Magnetic and gravitational disk-star interactions: An interdependence of pms stellar rotation rates and spin-orbit misalignments. *ApJ*, 778(2):169, 2013.

K Belczynski, J Klencki, CE Fields, A Olejak, E Berti, G Meynet, CL Fryer, DE Holz, R O'Shaughnessy, DA Brown, et al. Evolutionary roads leading to low effective spins, high black hole masses, and o1/o2 rates for LIGO/VIRGO binary black holes. *A&A*, 636:A104, 2020.

Krzysztof Belczynski, Michal Dominik, Tomasz Bulik, Richard O'Shaughnessy, Chris Fryer, and Daniel E Holz. The effect of metallicity on the detection prospects for gravitational waves. *ApJ*, 715(2):L138, 2010.

Krzysztof Belczynski, Daniel E Holz, Tomasz Bulik, and Richard O'Shaughnessy. The first gravitational-wave source from the isolated evolution of two stars in the 40–100 solar mass range. *Nature*, 534(7608):512–515, 2016.

JF Bell, MS Bessell, BW Stappers, M Bailes, and VM Kaspi. Psr J0045–7319: A dual-line binary radio pulsar. *ApJ*, 447(2):L117, 1995.

W Benz, WL Slattery, and AGW Cameron. Tilting Uranus in a giant impact. *Meteoritics*, 24:251, 1989.

Omer Blaes, Man Hoi Lee, and Aristotle Socrates. The Kozai mechanism and the evolution of binary supermassive black holes. *ApJ*, 578(2):775, 2002.

Alberto D. Bolatto, Adam K. Leroy, Katherine Jameson, Eve Ostriker, Karl Gordon, Brandon Lawton, Snežana Stanimirović, Frank P. Israel, Suzanne C. Madden, Sacha Hony, Karin M. Sandstrom, Caroline Bot, Mónica Rubio, P. Frank Winkler, Julia Roman-Duval, Jacco Th. van Loon, Joana M. Oliveira, and Rémy Indebetouw. The state of the gas and the relation between gas and star formation at low metallicity: The Small Magellanic Cloud. *ApJ*, 741(1):12, Oct 2011. doi: 10.1088/0004-637x/741/1/12.

ALDO STEFANO Bonomo, Silvano Desidera, SERENA Benatti, Francesco Borsa, S Crespi, Mario Damasso, Antonino Francesco Lanza, Alessandro Sozzetti, G Lodato, F Marzari, et al. The gaps programme with harps-n at tng-xiv. investigating giant planet migration history via improved eccentricity and mass determination for 231 transiting planets. *A&A*, 602:A107, 2017.

John R. Booker and Francis P. Bretherton. The critical layer for internal gravity waves in a shear flow. *J. Fluid Mech.*, 27(3):513–539, 1967.

John P Boyd. *Chebyshev and Fourier Spectral Methods*. Courier Corporation, 2001.

Benjamin P Brown, Geoffrey M Vasil, and Ellen G Zweibel. Energy conservation and gravity waves in sound-proof treatments of stellar interiors. part I. anelastic approximations. *ApJ*, 756(2):109, 2012.

SN Brown and K Stewartson. On the nonlinear reflection of a gravity wave at a critical level. part 2. *J. Fluid Mech.*, 115:217–230, 1982.

Marta L Bryan, Björn Benneke, Heather A Knutson, Konstantin Batygin, and Brendan P Bowler. Constraints on the spin evolution of young planetary-mass companions. *Nat. Astron*, 2(2):138–144, 2018.

Marta L Bryan, Heather A Knutson, Eve J Lee, BJ Fulton, Konstantin Batygin, Henry Ngo, and Tiffany Meshkat. An excess of Jupiter analogs in super-Earth systems. *AJ*, 157(2):52, 2019.

Marta L Bryan, Eugene Chiang, Brendan P Bowler, Caroline V Morley, Sarah Millholland, Sarah Blunt, Katelyn B Ashok, Eric Nielsen, Henry Ngo, Dimitri Mawet, et al. Obliquity constraints on an extrasolar planetary-mass companion. *AJ*, 159(4):181, 2020.

Marta L Bryan, Eugene Chiang, Caroline V Morley, Gregory N Mace, and Brendan P Bowler. Obliquity constraints on the planetary-mass companion hd 106906 b. *AJ*, 162(5):217, 2021.

Joshua Burkart, Eliot Quataert, Phil Arras, and Nevin N Weinberg. Tidal asteroseismology: Kepler's KOI-54. *MNRAS*, 421(2):983–1006, 2012.

Joshua Burkart, Eliot Quataert, Phil Arras, and Nevin N Weinberg. Tidal resonance locks in inspiraling white dwarf binaries. *MNRAS*, 433(1):332–352, 2013.

K. J. Burns, G. M. Vasil, J. S. Oishi, D. Lecoanet, and B. Brown. Dedalus: Flexible framework for spectrally solving differential equations. Astrophysics Source Code Library, March 2016.

Keaton J Burns, Geoffrey M Vasil, Jeffrey S Oishi, Daniel Lecoanet, and Benjamin P Brown. Dedalus: A flexible framework for numerical simulations with spectral methods. *Physical Review Research*, 2(2):023068, 2020.

David J Champion, Scott M Ransom, Patrick Lazarus, Fernando Camilo, Cees Bassa, Victoria M Kaspi, David J Nice, Paulo CC Freire, Ingrid H Stairs, Joeri Van Leeuwen, et al. An eccentric binary millisecond pulsar in the galactic plane. *Science*, 320(5881):1309–1312, 2008.

Carmen Chicone. *Ordinary Differential Equations with Applications*, volume 34. Springer Science & Business Media, 2006.

G Colombo. Cassini's second and third laws. *AJ*, 71:891, 1966.

Alexandre CM Correia, Jacques Laskar, and Olivier Néron de Surgy. Long-term evolution of the spin of Venus: I. theory. *Icarus*, 163(1):1–23, 2003.

Alexandre CM Correia, Gwenaël Boué, Jacques Laskar, and Adrián Rodríguez. Deformation and tidal evolution of close-in planets and satellites using a maxwell viscoelastic rheology. *A&A*, 571:A50, 2014.

Louis-Alexandre Couston, Daniel Lecoanet, Benjamin Favier, and Michael Le Bars. Order out of chaos: Slowly reversing mean flows emerge from turbulently generated internal waves. *Phys. Rev. Lett.*, 120:244505, Jun 2018. doi: 10.1103/PhysRevLett.120.244505.

Fei Dai, Kento Masuda, and Joshua N Winn. Larger mutual inclinations for the shortest-period planets. *ApJ*, 864(2):L38, 2018.

Michal Dominik, Krzysztof Belczynski, Christopher Fryer, Daniel E Holz, Emanuele Berti, Tomasz Bulik, Ilya Mandel, and Richard O'Shaughnessy. Double compact objects. I. the significance of the common envelope on merger rates. *ApJ*, 759(1):52, 2012.

Michal Dominik, Krzysztof Belczynski, Christopher Fryer, Daniel E Holz, Emanuele Berti, Tomasz Bulik, Ilya Mandel, and Richard O'Shaughnessy. Double compact objects. II. cosmological merger rates. *ApJ*, 779(1):72, 2013.

Michal Dominik, Emanuele Berti, Richard O'Shaughnessy, Ilya Mandel, Krzysztof Belczynski, Christopher Fryer, Daniel E Holz, Tomasz Bulik, and Francesco Pannarale. Double compact objects. III. gravitational-wave detection rates. *ApJ*, 806(2):263, 2015.

Luke Dones and Scott Tremaine. Why does the Earth spin forward? *Science*, 259 (5093):350–354, 1993.

Hayley V Dosser and Bruce R Sutherland. Anelastic internal wave packet evolution and stability. *J. Atmos. Chem.*, 68(12):2844–2859, 2011a.

HV Dosser and BR Sutherland. Weakly nonlinear non-boussinesq internal gravity wavepackets. *Physica D: Nonlinear Phenomena*, 240(3):346–356, 2011b.

JMB Downing, MJ Benacquista, M Giersz, and R Spurzem. Compact binaries in star clusters–I. black hole binaries inside globular clusters. *MNRAS*, 407(3): 1946–1962, 2010.

PG Drazin. On the instability of an internal gravity wave. *Proc. R. Soc. Lond. A*, 356(1686):411–432, 1977.

Courtney D. Dressing, Andrew Vanderburg, Joshua Schlieder, Ian J. M. Crossfield, Heather A. Knutson, Elisabeth R. Newton, David R. Ciardi, Benjamin J. Fulton, Erica J. Gonzales, Andrew W. Howard, Howard Isaacson, John Livingston, Erik A. Petigura, Evan Sinukoff, Mark Everett, Elliott Horch, and Steve B. Howell. Characterizing K2 candidate planetary systems orbiting low-mass stars. II. planetary systems observed during campaigns 1-7. *AJ*, 154(5):207, November 2017.

Gaspard Duchêne and Adam Kraus. Stellar multiplicity. *ARA&A*, 51(1):269–310, 2013. doi: 10.1146/annurev-astro-081710-102602.

Reed Essick and Nevin N Weinberg. Orbital decay of hot Jupiters due to nonlinear tidal dissipation within solar-type hosts. *ApJ*, 816(1):18, 2015.

Daniel C Fabrycky, Eric T Johnson, and Jeremy Goodman. Cassini states with dissipation: Why obliquity tides cannot inflate hot Jupiters. *ApJ*, 665(1):754, 2007.

Daniel C. Fabrycky, Jack J. Lissauer, Darin Ragozzine, Jason F. Rowe, Jason H. Steffen, Eric Agol, Thomas Barclay, Natalie Batalha, William Borucki, David R. Ciardi, Eric B. Ford, Thomas N. Gautier, John C. Geary, Matthew J. Holman, Jon M. Jenkins, Jie Li, Robert C. Morehead, Robert L. Morris, Avi Shporer, Jeffrey C. Smith, Martin Still, and Jeffrey Van Cleve. Architecture of Kepler's multi-transiting systems. II. new investigations with twice as many candidates. *ApJ*, 790(2):146, August 2014. doi: 10.1088/0004-637X/790/2/146.

David Ferreira, John Marshall, Paul A. O'Gorman, and Sara Seager. Climate at high-obliquity. *Icarus*, 243:236–248, November 2014. doi: 10.1016/j.icarus.2014.09.015.

Joseph E Flaherty and FC Hoppensteadt. Frequency entrainment of a forced van der pol oscillator. *Stud. Appl. Math.*, 58(1):5–15, 1978.

Gaston Floquet. Sur les équations différentielles linéaires à coefficients périodiques. In *ANNALES SCIENTIFIQUES DE L'ÉCOLE NORMALE SUPÉRIEURE*, volume 12, pages 47–88, 1883.

Eric B Ford, Boris Kozinsky, and Frederic A Rasio. Secular evolution of hierarchical triple star systems. *ApJ*, 535(1):385, 2000.

Giacomo Fragione and Omer Bromberg. Eccentric binary black hole mergers in globular clusters hosting intermediate-mass black holes. *MNRAS*, 488(3):4370–4377, 2019.

Giacomo Fragione and Bence Kocsis. Black hole mergers from quadruples. *MNRAS*, 486(4):4781–4789, May 2019. ISSN 0035-8711. doi: 10.1093/mnras/stz1175.

Giacomo Fragione and Abraham Loeb. Black hole–neutron star mergers from triples. *MNRAS*, 486(3):4443–4450, 2019.

W Fricke. Joint report of the working groups of iau com. 4 on precession, planetary ephemerides, units and time-scales. *Trans. Int. Astron. Union, Series B*, 16:56, 1977.

Jim Fuller and Dong Lai. Tidal excitations of oscillation modes in compact white dwarf binaries–I. linear theory. *MNRAS*, 412(2):1331–1340, 2011.

Jim Fuller and Dong Lai. Dynamical tides in compact white dwarf binaries: Tidal synchronization and dissipation. *MNRAS*, 421(1):426–445, 2012a.

Jim Fuller and Dong Lai. Tidal novae in compact binary white dwarfs. *ApJ*, 756 (1):L17, 2012b.

Jim Fuller and Dong Lai. Dynamical tides in compact white dwarf binaries: Helium core white dwarfs, tidal heating and observational signatures. *MNRAS*, 430(1):274–287, 2013.

Jim Fuller and Linhao Ma. Most black holes are born very slowly rotating. *ApJ*, 881(1):L1, 2019.

Shuang Gao, Chao Liu, Xiaobin Zhang, Stephen Justham, Licai Deng, and Ming Yang. The binarity of Milky Way F,G,K stars as a function of effective temperature and metallicity. *ApJ*, 788(2):L37, June 2014. doi: 10.1088/2041-8205/788/2/L37.

Davide Gerosa, Emanuele Berti, Richard O'Shaughnessy, Krzysztof Belczynski, Michael Kesden, Daniel Wysocki, and Wojciech Gladysz. Spin orientations of merging black holes formed from the evolution of stellar binaries. *Phys. Rev. D*, 98:084036, Oct 2018. doi: 10.1103/PhysRevD.98.084036.

Michaël Gillon, Amaury HMJ Triaud, Brice-Olivier Demory, Emmanuël Jehin, Eric Agol, Katherine M Deck, Susan M Lederer, Julien De Wit, Artem Burdanov, James G Ingalls, et al. Seven temperate terrestrial planets around the nearby ultracool dwarf star trappist-1. *Nature*, 542(7642):456–460, 2017.

Brett Gladman. Dynamics of systems of two close planets. *Icarus*, 106(1):247–263, 1993.

Peter Goldreich and Philip D Nicholson. Tidal friction in early-type stars. *ApJ*, 342(2):1079–1084, 1989.

Peter Goldreich and Stanton Peale. Spin-orbit coupling in the solar system. *AJ*, 71:425, 1966.

László Gondán, Bence Kocsis, Péter Raffai, and Zsolt Frei. Eccentric black hole gravitational-wave capture sources in galactic nuclei: Distribution of binary parameters. *ApJ*, 860(1):5, 2018.

Jeremy Goodman and Eric S Dickson. Dynamical tide in solar-type binaries. *ApJ*, 507(2):938, 1998.

Erwin Groten. Fundamental parameters and current (2004) best estimates of the parameters of common relevance to astronomy, geodesy, and geodynamics. *J. Geod.*, 77(10):724–797, Apr 2004. ISSN 1432-1394. doi: 10.1007/s00190-003-0373-y.

John Guckenheimer and Philip J. Holmes. *NONLINEAR OSCILLATIONS, DYNAMICAL SYSTEMS, AND BIFURCATIONS OF VECTOR FIELDS*. Springer-Verlag, New York, 1983. ISBN 978-1-4612-1140-2.

A. S. Hamers, O. R. Pols, J. S. W. Claeys, and G. Nelemans. Population synthesis of triple systems in the context of mergers of carbon-oxygen white dwarfs. *MNRAS*, 430(3):2262–2280, April 2013. doi: 10.1093/mnras/stt046.

Adrian S Hamers. Secular dynamics of hierarchical multiple systems composed of nested binaries, with an arbitrary number of bodies and arbitrary hierarchical structure III. suborbital effects: Hybrid integration techniques and orbit-averaging corrections. *MNRAS*, 494(4):5492–5506, April 2020a. ISSN 0035-8711. doi: 10.1093/mnras/staa1084.

Adrian S Hamers. Properties of von Zeipel-Lidov-Kozai oscillations in triple systems at the quadrupole order: Relaxing the test particle approximation. *MNRAS*, 500(3):3481–3496, November 2020b. ISSN 0035-8711. doi: 10.1093/mnras/staa3498.

Adrian S Hamers and Dong Lai. Secular chaotic dynamics in hierarchical quadruple systems, with applications to hot Jupiters in stellar binaries and triples. *MNRAS*, 470(2):1657–1672, 2017.

Douglas P Hamilton and William R Ward. Tilting Saturn. II. numerical model. *AJ*, 128(5):2510, 2004.

Chihiro Hayashi. *Nonlinear Oscillations in Physical Systems*. Princeton University Press, 2014.

Philip Hazel. The effect of viscosity and heat conduction on internal gravity waves at a critical level. *J. Fluid Mech.*, 30(4):775–783, 1967.

Matthias Y. He, Eric B. Ford, Darin Ragozzine, and Daniel Carrera. Architectures of exoplanetary systems. III. eccentricity and mutual inclination distributions of amd-stable planetary systems. *AJ*, 160(6):276, December 2020. doi: 10.3847/1538-3881/abba18.

Matthias Y. He, Eric B. Ford, and Darin Ragozzine. Architectures of exoplanetary systems. II. an increase in inner planetary system occurrence toward later spectral types for Kepler's fgk dwarfs. *AJ*, 161(1):16, January 2021. doi: 10.3847/1538-3881/abc68b.

Leslie Hebb, A Collier-Cameron, B Loeillet, D Pollacco, G Hébrard, RA Street, F Bouchy, HC Stempels, C Moutou, E Simpson, et al. Wasp-12b: The hottest transiting extrasolar planet yet discovered. *ApJ*, 693(2):1920, 2009.

A. Heger and N. Langer. Presupernova evolution of rotating massive stars. II. evolution of the surface properties. *ApJ*, 544(2):1016–1035, December 2000. doi: 10.1086/317239.

Jacques Henrard. Capture into resonance: An extension of the use of adiabatic invariants. *Celest. Mech. Dyn. Astron.*, 27(1):3–22, 1982.

Jacques Henrard and Charles Murigande. Colombo's Top. *Phys. Rev.*, 40(3-4): 345–366, 1987.

Bao-Minh Hoang, Smadar Naoz, Bence Kocsis, Frederic A Rasio, and Fani Dosopoulou. Black hole mergers in galactic nuclei induced by the eccentric Kozai–Lidov effect. *ApJ*, 856(2):140, 2018.

James R Holton. The influence of gravity wave breaking on the general circulation of the middle atmosphere. *J. Atmos. Sci.*, 40(10):2497–2507, 1983.

Yu-Cian Hong, Dong Lai, Jonathan I. Lunine, and Philip D. Nicholson. Spin dynamics of extrasolar giant planets in planet-planet scattering. *ApJ*, 920(2):151, October 2021. doi: 10.3847/1538-4357/ac1a14.

Andrew W Howard, Geoffrey W Marcy, Stephen T Bryson, Jon M Jenkins, Jason F Rowe, Natalie M Batalha, William J Borucki, David G Koch, Edward W Dunham, Thomas N Gautier III, et al. Planet occurrence within 0.25 au of solar-type stars from Kepler. *ApJS*, 201(2):15, 2012.

Jarrod R Hurley, Christopher A Tout, and Onno R Pols. Evolution of binary stars and the effect of tides on binary populations. *MNRAS*, 329(4):897–928, 2002.

Nawal Husnoo, Frédéric Pont, Guillaume Hébrard, Elaine Simpson, Tsevi Mazeh, François Bouchy, Claire Moutou, Luc Arnold, Isabelle Boisse, Rodrigo F Díaz, et al. Orbital eccentricity of WASP-12 and WASP-14 from new radial velocity monitoring with SOPHIE. *MNRAS*, 413(4):2500–2508, 2011.

P Hut. Tidal evolution in close binary systems. *A&A*, 99:126–140, 1981.

Niraj K Inamdar and Hilke E Schlichting. The formation of super-Earths and mini-Neptunes with giant impacts. *MNRAS*, 448(2):1751–1760, 2015.

Niraj K Inamdar and Hilke E Schlichting. Stealing the gas: Giant impacts and the large diversity in exoplanet densities. *ApJ*, 817(2):L13, 2016.

Andre Izidoro, Masahiro Ogihara, Sean N Raymond, Alessandro Morbidelli, Arnaud Pierens, Bertram Bitsch, Christophe Cossou, and Franck Hersant. Breaking the chains: Hot super-Earth systems from migration and disruption of compact resonant chains. *MNRAS*, 470(2):1750–1770, 2017.

H Janka, Annop Wongwathanarat, Michael Kramer, et al. Supernova fallback as origin of neutron star spins and spin-kick alignment. *arXiv*, 2021.

R. Michael Jennings and Eugene Chiang. Primordial obliquities of brown dwarfs and super-Jupiters from fragmenting gravito-turbulent discs. *MNRAS*, 507(4): 5187–5194, November 2021. doi: 10.1093/mnras/stab2429.

Simon Johnston, R. N. Manchester, A. G. Lyne, M. Bailes, V. M. Kaspi, Guojun Qiao, and N. D'Amico. Psr 1259-63: A binary radio pulsar with a be star companion. *ApJ*, 387:L37, March 1992. doi: 10.1086/186300.

Simon Johnston, RN Manchester, AG Lyne, L Nicastro, and J Spyromilio. Radio and optical observations of the PSR B1259–63/SS 2883 Be star binary system. *MNRAS*, 268(2):430–436, 1994.

VM Kaspi, S Johnston, JF Bell, RN Manchester, M Bailes, M Bessell, AG a Lyne, and N D'amico. A massive radio pulsar binary in the Small Magellanic Cloud. *ApJ*, 423:L43–L45, 1994.

VM Kaspi, M Bailes, RN Manchester, BW Stappers, and JF Bell. Evidence from

a processing pulsar orbit for a neutron-star birth kick. *Nature*, 381(6583):584–586, 1996.

Boaz Katz, Subo Dong, and Renu Malhotra. Long-term cycling of Kozai-Lidov cycles: Extreme eccentricities and inclinations excited by a distant eccentric perturber. *Phys. Rev. Lett.*, 107(18):181101, 2011.

Hiroshi Kinoshita and Hiroshi Nakai. Analytical solution of the Kozai resonance and its application. *Celest. Mech. Dyn. Astron.*, 75(2):125–147, 1999.

L. G. Kiseleva, S. J. Aarseth, P. P. Eggleton, and R. de La Fuente Marcos. Formation and evolution of hierarchical triple systems in open clusters. In E. F. Milone and J. C. Mermilliod, editors, *THE ORIGINS, EVOLUTION, AND DESTINIES OF BINARY STARS IN CLUSTERS*, volume 90 of *Astronomical Society of the Pacific Conference Series*, page 433, January 1996.

J. Klostermeyer. Two- and three-dimensional parametric instabilities in finite-amplitude internal gravity waves. *Geophys. Astrophys. Fluid Dyn.*, 61(1-4):1–25, 1991. doi: 10.1080/03091929108229035.

Heather A Knutson, Benjamin J Fulton, Benjamin T Montet, Melodie Kao, Henry Ngo, Andrew W Howard, Justin R Crepp, Sasha Hinkley, Gaspar Á Bakos, Konstantin Batygin, et al. Friends of hot Jupiters. I. a radial velocity search for massive, long-period companions to close-in gas giant planets. *ApJ*, 785(2):126, 2014.

Henry A. Kobulnicky, Daniel C. Kiminki, Michael J. Lundquist, Jamison Burke, James Chapman, Erica Keller, Kathryn Lester, Emily K. Rolen, Eric Topel, Anirban Bhattacharjee, Rachel A. Smullen, Carlos A. Vargas Álvarez, Jessie C. Runnoe, Daniel A. Dale, and Michael M. Brotherton. Toward complete statistics of

massive binary stars: Penultimate results from the Cygnus OB2 radial velocity survey. *ApJS*, 213(2):34, Aug 2014. doi: 10.1088/0067-0049/213/2/34.

DG Korycansky, P Bodenheimer, P Cassen, and JB Pollack. One-dimensional calculations of a large impact on Uranus. *Icarus*, 84(2):528–541, 1990.

Yoshihide Kozai. Secular perturbations of asteroids with high inclination and eccentricity. *AJ*, 67:591, 1962.

Pawan Kumar and Eliot J Quataert. Differential rotation enhanced dissipation of tides in the PSR J0045–7319 binary. *ApJ*, 479(1):L51, 1997.

Pawan Kumar and Eliot J Quataert. On the orbital decay of the PSR J0045–7319 binary. *ApJ*, 493(1):412, 1998.

Doron Kushnir, Matias Zaldarriaga, Juna A Kollmeier, and Roni Waldman. Dynamical tides reexpressed. *MNRAS*, 467(2):2146–2149, 2017.

Dong Lai. Orbital decay of the PSR J0045–7319 binary system: Age of radio pulsar and initial spin of neutron star. *ApJ*, 466(1):L35, 1996.

Dong Lai. Dynamical tides in rotating binary stars. *ApJ*, 490(2):847–862, December 1997. doi: 10.1086/304899.

Dong Lai. Tidal dissipation in planet-hosting stars: Damping of spin–orbit misalignment and survival of hot Jupiters. *MNRAS*, 423(1):486–492, 2012.

Dong Lai. Star–disc–binary interactions in protoplanetary disc systems and primordial spin–orbit misalignments. *MNRAS*, 440(4):3532–3544, 2014.

Dong Lai and Bonan Pu. Hiding planets behind a big friend: Mutual inclinations of multi-planet systems with external companions. *AJ*, 153(1):42, Dec 2017. doi: 10.3847/1538-3881/153/1/42.

Dong Lai, Lars Bildsten, and Victoria M. Kaspi. Spin-orbit interactions in neutron star/main-sequence binaries and implications for pulsar timing. *ApJ*, 452:819, October 1995. doi: 10.1086/176350.

Dong Lai, David F Chernoff, and James M Cordes. Pulsar jets: Implications for neutron star kicks and initial spins. *ApJ*, 549(2):1111, 2001.

Valéry Lainey. Quantification of tidal parameters from solar system data. *Celest. Mech. Dyn. Astron.*, 126(1-3):145–156, 2016.

Jacques Laskar and Philippe Robutel. The chaotic obliquity of the planets. *Nature*, 361(6413):608–612, 1993.

D. Lecoanet, G. M. Vasil, J. Fuller, M. Cantiello, and K. J. Burns. Conversion of internal gravity waves into magnetic waves. *MNRAS*, 466(2):2181–2193, Dec 2016. ISSN 0035-8711. doi: 10.1093/mnras/stw3273.

Daniel Lecoanet, Benjamin P. Brown, Ellen G. Zweibel, Keaton J. Burns, Jeffrey S. Oishi, and Geoffrey M. Vasil. Conduction in low mach number flows. I. linear and weakly nonlinear regimes. *ApJ*, 797(2):94, Dec 2014. doi: 10.1088/0004-637x/797/2/94.

Eve J Lee and Eugene Chiang. Magnetospheric truncation, tidal inspiral, and the creation of short-period and ultra-short-period planets. *ApJ*, 842(1):40, 2017.

Hanlun Lei, Christian Circi, and Emiliano Ortore. Modified double-averaged hamiltonian in hierarchical triple systems. *MNRAS*, 481(4):4602–4620, September 2018. ISSN 0035-8711. doi: 10.1093/mnras/sty2619.

Morris E. Levenson. Harmonic and subharmonic response for the duffing equation $\ddot{x} + \alpha x + \beta x^3 = F \cos \omega t$ ($\alpha > 0$). *J. Appl. Phys.*, 20(11):1045–1051, November 1949. doi: 10.1063/1.1698272.

B. Levrard, A. C. M. Correia, G. Chabrier, I. Baraffe, F. Selsis, and J. Laskar. Tidal dissipation within hot Jupiters: A new appraisal. *A&A*, 462(1):L5–L8, January 2007. doi: 10.1051/0004-6361:20066487.

Gongjie Li. Tilting planets during planet scattering. *ApJ*, 915(1):L2, July 2021. doi: 10.3847/2041-8213/ac0620.

Gongjie Li, Smadar Naoz, Matt Holman, and Abraham Loeb. Chaos in the test particle eccentric Kozai-Lidov mechanism. *ApJ*, 791(2):86, 2014.

Jiaru Li and Dong Lai. Planetary spin and obliquity from mergers. *ApJ*, 898(1): L20, 2020.

Jiaru Li, Dong Lai, Kassandra R Anderson, and Bonan Pu. Giant planet scatterings and collisions: Hydrodynamics, merger-ejection branching ratio, and properties of the remnants. *MNRAS*, 501(2):1621–1632, 2021.

Michael L Lidov. The evolution of orbits of artificial satellites of planets under the action of gravitational perturbations of external bodies. *Planet. Space Sci.*, 9(10):719–759, 1962.

Richard S Lindzen. Turbulence and stress owing to gravity wave and tidal breakdown. *J. Geophys. Res.: Oceans*, 86(C10):9707–9714, 1981.

Richard S. Lindzen and James R. Holton. A theory of the quasi-biennial oscillation. *J. Atmos. Sci.*, 25(6):1095–1107, 1968. doi: 10.1175/1520-0469(1968)025<1095:ATOTQB>2.0.CO;2.

VM Lipunov, KA Postnov, and ME Prokhorov. Black holes and gravitational waves: Possibilities for simultaneous detection using first-generation laser interferometers. *Astron. Lett.*, 23:492–497, 1997.

VM Lipunov, V Kornilov, E Gorbovskoy, DAH Buckley, N Tiurina, P Balanutsa, A Kuznetsov, J Greiner, V Vladimirov, D Vlasenko, et al. First gravitational-wave burst GW150914: Master optical follow-up observations. *MNRAS*, 465(3): 3656–3667, 2017.

Jack J Lissauer, Alice F Berman, Yuval Greenzweig, and David M Kary. Accretion of mass and spin angular momentum by a planet on an eccentric orbit. *Icarus*, 127(1):65–92, 1997.

Jack J Lissauer, Darin Ragozzine, Daniel C Fabrycky, Jason H Steffen, Eric B Ford, Jon M Jenkins, Avi Shporer, Matthew J Holman, Jason F Rowe, Elisa V Quintana, et al. Architecture and dynamics of Kepler's candidate multiple transiting planet systems. *ApJS*, 197(1):8, 2011.

Yoram Lithwick and Smadar Naoz. The eccentric Kozai mechanism for a test particle. *ApJ*, 742(2):94, 2011.

Bin Liu and Dong Lai. Spin–orbit misalignment of merging black hole binaries with tertiary companions. *ApJ*, 846(1):L11, 2017.

Bin Liu and Dong Lai. Black hole and neutron star binary mergers in triple systems: Merger fraction and spin–orbit misalignment. *ApJ*, 863(1):68, 2018.

Bin Liu and Dong Lai. Enhanced black hole mergers in binary-binary interactions. *MNRAS*, 483(3):4060–4069, March 2019. doi: 10.1093/mnras/sty3432.

Bin Liu and Dong Lai. Merging compact binaries near a rotating supermassive black hole: Eccentricity excitation due to apsidal precession resonance. *Phys. Rev. D*, 102(2):023020, July 2020. doi: 10.1103/PhysRevD.102.023020.

Bin Liu and Dong Lai. Hierarchical black hole mergers in multiple systems: Con-

strain the formation of GW190412-, GW190814-, and GW190521-like events. *MNRAS*, 502(2):2049–2064, 2021.

Bin Liu, Diego J Muñoz, and Dong Lai. Suppression of extreme orbital evolution in triple systems with short-range forces. *MNRAS*, 447(1):747–764, 2015a.

Bin Liu, Dong Lai, and Yi-Han Wang. Black hole and neutron star binary mergers in triple systems. II. merger eccentricity and spin-orbit misalignment. *ApJ*, 881 (1):41, August 2019a. doi: 10.3847/1538-4357/ab2dfb.

Bin Liu, Dong Lai, and Yi-Han Wang. Binary mergers near a supermassive black hole: Relativistic effects in triples. *ApJ*, 883(1):L7, September 2019b. doi: 10. 3847/2041-8213/ab40c0.

Shang-Fei Liu, Yasunori Hori, DNC Lin, and Erik Asphaug. Giant impact: An efficient mechanism for the devolatilization of super-Earths. *ApJ*, 812(2):164, 2015b.

Mario Livio and Paolo Mazzali. On the progenitors of type ia supernovae. *Physics Reports*, 736:1–23, 2018.

Ana H Lobo and Simona Bordoni. Atmospheric dynamics in high obliquity planets. *Icarus*, 340:113592, 2020.

D. R. Lorimer, A. J. Faulkner, A. G. Lyne, R. N. Manchester, M. Kramer, M. A. McLaughlin, G. Hobbs, A. Possenti, I. H. Stairs, F. Camilo, M. Burgay, N. D'Amico, A. Corongiu, and F. Crawford. The parkes multibeam pulsar survey - VI. discovery and timing of 142 pulsars and a galactic population analysis. *MNRAS*, 372(2):777–800, October 2006. doi: 10.1111/j.1365-2966.2006.10887.x.

Liantong Luo, Boaz Katz, and Subo Dong. Double-averaging can fail to characterize the long-term evolution of Lidov-Kozai cycles and derivation of an analytical

correction. *MNRAS*, 458(3):3060–3074, March 2016. ISSN 0035-8711. doi: 10.1093/mnras/stw475.

A. G. Lyne, B. W. Stappers, M. J. Keith, P. S. Ray, M. Kerr, F. Camilo, and T. J. Johnson. The binary nature of PSR J2032+4127. *MNRAS*, 451(1):581–587, July 2015. doi: 10.1093/mnras/stv236.

G Maciejewski, D Dimitrov, M Seeliger, M Kitze, R Errmann, G Nowak, A Niedzielski, V Popov, C Marka, K Goździewski, et al. Multi-site campaign for transit timing variations of WASP-12b: Possible detection of a long-period signal of planetary origin. *A&A*, 551:A108, 2013.

G Maciejewski, D Dimitrov, Matilde Fernández, A Sota, G Nowak, J Ohlert, G Nikolov, TC Hinse, E Pallé, B Tingley, et al. Departure from the constant-period ephemeris for the transiting exoplanet WASP-12b. *A&A*, 588:L6, 2016.

A. Maeder. Evidences for a bifurcation in massive star evolution. the on-blue stragglers. *A&A*, 178:159–169, May 1987.

Wilhelm Magnus. On the exponential solution of differential equations for a linear operator. *Commun. Pure Appl. Math.*, 7(4):649–673, 1954.

Miguel A. S. Martinez, Carl L. Rodriguez, and Giacomo Fragione. On the mass ratio distribution of black hole mergers in triple systems. *arXiv*, art. arXiv:2105.01671, May 2021.

Kento Masuda, Joshua N Winn, and Hajime Kawahara. Mutual orbital inclinations between cold Jupiters and inner super-Earths. *AJ*, 159(2):38, 2020.

Yamila Miguel and Adrián Brunini. Planet formation: Statistics of spin rates and obliquities of extrasolar planets. *MNRAS*, 406(3):1935–1943, 2010.

M Coleman Miller and Douglas P Hamilton. Four-body effects in globular cluster black hole coalescence. *ApJ*, 576(2):894, 2002.

M Coleman Miller and Vanessa M Lauburg. Mergers of stellar-mass black holes in nuclear star clusters. *ApJ*, 692(1):917, 2009.

Sarah Millholland and Konstantin Batygin. Excitation of planetary obliquities through planet–disk interactions. *ApJ*, 876(2):119, 2019.

Sarah Millholland and Gregory Laughlin. Obliquity tides may drive WASP-12b's rapid orbital decay. *ApJ*, 869(1):L15, 2018.

Sarah Millholland and Gregory Laughlin. Obliquity-driven sculpting of exoplanetary systems. *Nat. Astron*, 3(5):424–433, 2019.

Sarah C Millholland and Christopher Spalding. Formation of ultra-short-period planets by obliquity-driven tidal runaway. *ApJ*, 905(1):71, 2020.

Maxwell Moe and Rosanne Di Stefano. Mind your ps and qs: The interrelation between period (p) and mass-ratio (q) distributions of binary stars. *ApJS*, 230 (2):15, 2017.

Alessandro Morbidelli, Kleomenis Tsiganis, Konstantin Batygin, Aurelien Crida, and Rodney Gomes. Explaining why the Uranian satellites have equatorial prograde orbits despite the large planetary obliquity. *Icarus*, 219(2):737–740, 2012.

Diego J Muñoz, Dong Lai, and Bin Liu. The formation efficiency of close-in planets via Lidov–Kozai migration: Analytic calculations. *MNRAS*, 460(1):1086–1093, 2016.

Carl D Murray and Stanley F Dermott. *Solar System Dynamics*. Cambridge university press, 1999.

Smadar Naoz. The eccentric Kozai-Lidov effect and its applications. *ARA&A*, 54: 441–489, 2016.

Gordon I. Ogilvie. Tidal dissipation in stars and giant planets. *ARA&A*, 52:171–210, August 2014. doi: 10.1146/annurev-astro-081913-035941.

Gordon I Ogilvie. Tidal dissipation in stars and giant planets. *ARA&A*, 52:171–210, 2014.

Yoshimitsu Ogura and Norman A Phillips. Scale analysis of deep and shallow convection in the atmosphere. *J. Atmos. Sci.*, 19(2):173–179, 1962.

Kazumasa Ohno and Xi Zhang. Atmospheres on nonsynchronized eccentric-tilted exoplanets. II. thermal light curves. *ApJ*, 874(1):2, 2019.

Ryan M. O'Leary and Joshua Burkart. It takes a village to raise a tide: Non-linear multiple-mode coupling and mode identification in KOI-54. *MNRAS*, 440 (4):3036–3050, April 2014. ISSN 0035-8711. doi: 10.1093/mnras/stu335.

Ryan M O'leary, Frederic A Rasio, John M Fregeau, Natalia Ivanova, and Richard O'Shaughnessy. Binary mergers and growth of black holes in dense star clusters. *ApJ*, 637(2):937, 2006.

A. Olejak, M. Fishbach, K. Belczynski, D. E. Holz, J. P. Lasota, M. C. Miller, and T. Bulik. The origin of inequality: Isolated formation of a 30+10 $m_\odot$ binary black hole merger. *ApJ*, 901(2):L39, October 2020. doi: 10.3847/2041-8213/abb5b5.

J. C. B. Papaloizou and P. B. Ivanov. Dynamic tides in rotating objects: A numerical investigation of inertial waves in fully convective or barotropic stars and planets. *MNRAS*, 407(3):1631–1656, Sept 2010. ISSN 0035-8711. doi: 10.1111/j.1365-2966.2010.17011.x.

Kishore C Patra, Joshua N Winn, Matthew J Holman, Liang Yu, Drake Deming, and Fei Dai. The apparently decaying orbit of WASP-12b. *AJ*, 154(1):4, 2017.

Kishore C. Patra, Joshua N. Winn, Matthew J. Holman, Michael Gillon, Artem Burdanov, Emmanuel Jehin, Laetitia Delrez, Francisco J. Pozuelos, Khalid Barkaoui, Zouhair Benkhaldoun, Norio Narita, Akihiko Fukui, Nobuhiko Kusakabe, Kiyoe Kawauchi, Yuka Terada, L. G. Bouma, Nevin N. Weinberg, and Madelyn Broome. The continuing search for evidence of tidal orbital decay of hot Jupiters. *AJ*, 159(4):150, April 2020. doi: 10.3847/1538-3881/ab7374.

B. Paxton, L. Bildsten, A. Dotter, F. Herwig, P. Lesaffre, and F. Timmes. Modules for experiments in stellar astrophysics (MESA). *ApJS*, 192:3, January 2011. doi: 10.1088/0067-0049/192/1/3.

B. Paxton, M. Cantiello, P. Arras, L. Bildsten, E. F. Brown, A. Dotter, C. Mankovich, M. H. Montgomery, D. Stello, F. X. Timmes, and R. Townsend. Modules for experiments in stellar astrophysics (MESA): Planets, oscillations, rotation, and massive stars. *ApJS*, 208:4, Sep 2013. doi: 10.1088/0067-0049/208/1/4.

B. Paxton, P. Marchant, J. Schwab, E. B. Bauer, L. Bildsten, M. Cantiello, L. Dessart, R. Farmer, H. Hu, N. Langer, R. H. D. Townsend, D. M. Townsley, and F. X. Timmes. Modules for experiments in stellar astrophysics (MESA): Binaries, pulsations, and explosions. *ApJS*, 220:15, Sep 2015. doi: 10.1088/0067-0049/220/1/15.

B. Paxton, J. Schwab, E. B. Bauer, L. Bildsten, S. Blinnikov, P. Duffell, R. Farmer, J. A. Goldberg, P. Marchant, E. Sorokina, A. Thoul, R. H. D. Townsend, and F. X. Timmes. Modules for experiments in stellar astrophysics (MESA): Convective

boundaries, element diffusion, and massive star explosions. *ApJS*, 234:34, Feb 2018. doi: 10.3847/1538-4365/aaa5a8.

Bill Paxton, R. Smolec, Josiah Schwab, A. Gautschy, Lars Bildsten, Matteo Cantiello, Aaron Dotter, R. Farmer, Jared A. Goldberg, Adam S. Jermyn, S. M. Kanbur, Pablo Marchant, Anne Thoul, Richard H. D. Townsend, William M. Wolf, Michael Zhang, and F. X. Timmes. Modules for experiments in stellar astrophysics (MESA): Pulsating variable stars, rotation, convective boundaries, and energy conservation. *ApJS*, 243(1):10, Jul 2019. doi: 10.3847/1538-4365/ab2241.

SJ Peale. Obliquity tides in hot Jupiters. In *EXTREME SOLAR SYSTEMS*, volume 398, page 281, 2008.

Stanton J Peale. Generalized Cassini's laws. *AJ*, 74:483, 1969.

Stanton J Peale. Possible histories of the obliquity of Mercury. *AJ*, 79:722, 1974.

Philip Carl Peters. Gravitational radiation and the motion of two point masses. *Phys. Rev.*, 136(4B):B1224, 1964.

Antoine C Petit, Gabriele Pichierri, Melvyn B Davies, and Anders Johansen. The path to instability in compact multi-planetary systems. *A&A*, 641:A176, 2020.

Cristobal Petrovich and Fabio Antonini. Greatly enhanced merger rates of compact-object binaries in non-spherical nuclear star clusters. *ApJ*, 846(2):146, 2017.

Cristobal Petrovich, Emily Deibert, and Yanqin Wu. Ultra-short-period planets from secular chaos. *AJ*, 157(5):180, 2019.

Andrés E. Piatti. The star field age-metallicity relationship of the Small Magellanic Cloud. *MNRAS*, 422(2):1109–1121, April 2012. ISSN 0035-8711. doi: 10.1111/j.1365-2966.2012.20684.x.

Ph Podsiadlowski, Saul Rappaport, and Zhanwen Han. On the formation and evolution of black hole binaries. *MNRAS*, 341(2):385–404, 2003.

KA Postnov and AG Kuranov. Black hole spins in coalescing binary black holes. *MNRAS*, 483(3):3288–3306, 2019.

Bonan Pu and Dong Lai. Eccentricities and inclinations of multiplanet systems with external perturbers. *MNRAS*, 478(1):197–217, 2018.

Bonan Pu and Dong Lai. Low-eccentricity migration of ultra-short-period planets in multiplanet systems. *MNRAS*, 488(3):3568–3587, 2019.

Lisa Randall and Zhong-Zhi Xianyu. An analytical portrait of binary mergers in hierarchical triple systems. *ApJ*, 864(2):134, 2018a.

Lisa Randall and Zhong-Zhi Xianyu. Induced ellipticity for inspiraling binary systems. *ApJ*, 853(1):93, 2018b.

Laetitia Rodet, Yubo Su, and Dong Lai. On the correlation between hot Jupiters and stellar clustering: High-eccentricity migration induced by stellar flybys. *ApJ*, 913(2):104, 2021.

Carl L Rodriguez, Meagan Morscher, Bharath Pattabiraman, Sourav Chatterjee, Carl-Johan Haster, and Frederic A Rasio. Binary black hole mergers from globular clusters: Implications for advanced LIGO. *Phys. Rev. Lett.*, 115(5):051101, 2015.

Carl L Rodriguez, Sourav Chatterjee, and Frederic A Rasio. Binary black hole

mergers from globular clusters: Masses, merger rates, and the impact of stellar evolution. *Phys. Rev. D*, 93(8):084029, 2016.

Carl L Rodriguez, Pau Amaro-Seoane, Sourav Chatterjee, and Frederic A Rasio. Post-newtonian dynamics in dense star clusters: Highly eccentric, highly spinning, and repeated binary black hole mergers. *Phys. Rev. Lett.*, 120(15):151101, 2018.

Zeeve Rogoszinski and Douglas P Hamilton. Tilting ice giants with a spin–orbit resonance. *ApJ*, 888(2):60, 2020.

Lee J Rosenthal, Heather A Knutson, Yayaati Chachan, Fei Dai, Andrew W Howard, Benjamin J Fulton, Ashley Chontos, Justin R Crepp, Paul A Dalba, Gregory W Henry, et al. The california legacy survey III. on the shoulders of (some) giants: The relationship between inner small planets and outer massive planets. *arXiv*, 2021.

Javier Roulet, Horng Sheng Chia, Seth Olsen, Liang Dai, Tejaswi Venumadhav, Barak Zackay, and Matias Zaldarriaga. Distribution of effective spins and masses of binary black holes from the LIGO and VIRGO O1-O3a observing runs. *Phys. Rev. D*, 104(8):083010, October 2021. doi: 10.1103/PhysRevD.104.083010.

VS Safronov and EV Zvjagina. Relative sizes of the largest bodies during the accumulation of planets. *Icarus*, 10(1):109–115, 1969.

Melaine Saillenfest, Giacomo Lari, and Ariane Courtot. The future large obliquity of Jupiter. *A&A*, 640:A11, 2020.

Melaine Saillenfest, Giacomo Lari, and Gwenaël Boué. The large obliquity of Saturn explained by the fast migration of titan. *Nat. Astron*, 5(4):345–349, 2021.

Edwin E Salpeter. The luminosity function and stellar evolution. *ApJ*, 121:161, 1955.

Johan Samsing and Daniel J D'Orazio. Black hole mergers from globular clusters observable by lisa i: Eccentric sources originating from relativistic n-body dynamics. *MNRAS*, 481(4):5445–5450, 2018.

Johan Samsing and Enrico Ramirez-Ruiz. On the assembly rate of highly eccentric binary black hole mergers. *ApJ*, 840(2):L14, 2017.

Hugues Sana, SE De Mink, Alex de Koter, N Langer, CJ Evans, M Gieles, Eric Gosset, RG Izzard, J-B Le Bouquin, and FRN Schneider. Binary interaction dominates the evolution of massive stars. *Science*, 337(6093):444–446, 2012.

Roberto Sanchis-Ojeda, Saul Rappaport, Joshua N Winn, Michael C Kotson, Alan Levine, and Ileyk El Mellah. A study of the shortest-period planets found with Kepler. *ApJ*, 787(1):47, 2014.

Emily Sandford, David Kipping, and Michael Collins. The multiplicity distribution of Keplerxoplanets. *MNRAS*, 489(3):3162–3173, 2019.

GJ Savonije and JCB Papaloizou. On the tidal spin up and orbital circularization rate for the massive x-ray binary systems. *MNRAS*, 203(3):581–593, 1983.

Patricia Schmidt, Frank Ohme, and Mark Hannam. Towards models of gravitational waveforms from generic binaries: II. modelling precession effects with a single effective precession parameter. *Phys. Rev. D*, 91(2):024043, 2015.

S Seager and Lam Hui. Constraining the rotation rate of transiting extrasolar planets by oblateness measurements. *ApJ*, 574(2):1004, 2002.

Ivan I Shevchenko. *The Lidov-Kozai Effect: Applications in Exoplanet Research*

and Dynamical Astronomy, volume 441 of *Astrophysics and Space Science Library*. Springer, 2016.

Frank H Shu. *The Physics of Astrophysics: Gas Dynamics*, volume 2. University Science Books, 1991.

Kedron Silsbee and Scott Tremaine. Lidov–Kozai cycles with gravitational radiation: Merging black holes in isolated triple systems. *ApJ*, 836(1):39, 2017a.

Kedron Silsbee and Scott Tremaine. Lidov–Kozai cycles with gravitational radiation: Merging black holes in isolated triple systems. *ApJ*, 836(1):39, 2017b.

Ignas AG Snellen, Bernhard R Brandl, Remco J de Kok, Matteo Brogi, Jayne Birkby, and Henriette Schwarz. Fast spin of the young extrasolar planet β pictoris b. *Nature*, 509(7498):63–65, 2014.

Mario Spera and Michela Mapelli. Very massive stars, pair-instability supernovae and intermediate-mass black holes with the sevn code. *MNRAS*, 470(4):4739–4749, 2017.

David S Spiegel, Sean N Raymond, Courtney D Dressing, Caleb A Scharf, and Jonathan L Mitchell. Generalized milankovitch cycles and long-term climatic habitability. *ApJ*, 721(2):1308, 2010.

I. H. Stairs, R. N. Manchester, A. G. Lyne, V. M. Kaspi, F. Camilo, J. F. Bell, N. D'Amico, M. Kramer, F. Crawford, D. J. Morris, A. Possenti, N. P. F. McKay, S. L. Lumsden, L. E. Tacconi-Garman, R. D. Cannon, N. C. Hambly, and P. R. Wood. Psr j1740-3052: A pulsar with a massive companion. *MNRAS*, 325(3): 979–988, August 2001. doi: 10.1046/j.1365-8711.2001.04447.x.

Jason H Steffen and Will M Farr. A lack of short-period multiplanet systems with close-proximity pairs and the curious case of Kepler-42. *ApJ*, 774(1):L12, 2013.

Elias M Stein and Rami Shakarchi. *Real Analysis: Measure Theory, Integration, and Hilbert Spaces*. Princeton University Press, 2009.

Natalia I. Storch and Dong Lai. Viscoelastic tidal dissipation in giant planets and formation of hot Jupiters through high-eccentricity migration. *MNRAS*, 438(2): 1526–1534, December 2013. ISSN 0035-8711. doi: 10.1093/mnras/stt2292.

Natalia I Storch and Dong Lai. Chaotic dynamics of stellar spin driven by planets undergoing Lidov–Kozai oscillations: Resonances and origin of chaos. *MNRAS*, 448(2):1821–1834, 2015.

Natalia I Storch, Kassandra R Anderson, and Dong Lai. Chaotic dynamics of stellar spin in binaries and the production of misaligned hot Jupiters. *Science*, 345(6202):1317–1321, 2014.

Natalia I Storch, Dong Lai, and Kassandra R Anderson. Dynamics of stellar spin driven by planets undergoing Lidov–Kozai migration: Paths to spin–orbit misalignment. *MNRAS*, 465(4):3927–3942, 2017.

Yubo Su and Dong Lai. Dynamics of Colombo's Top: Generating exoplanet obliquities from planet-disk interactions. *ApJ*, 903(1):7, Oct 2020. doi: 10.3847/1538-4357/abb6f3.

Yubo Su and Dong Lai. Dynamics of Colombo's Top: Tidal dissipation and resonance capture, with applications to oblique super-Earths, ultra-short-period planets and inspiraling hot Jupiters. *MNRAS*, 509(3):3301–3320, November 2021. ISSN 0035-8711. doi: 10.1093/mnras/stab3172.

Yubo Su and Dong Lai. Dynamics of Colombo's Top: Non-trivial oblique spin equilibria of super-Earths in multi-planetary systems. *MNRAS*, 2022a.

Yubo Su and Dong Lai. Dynamical tides in eccentric binaries containing massive main-sequence stars: Analytical expressions. *MNRAS*, 510(4):4943–4951, 2022b.

Yubo Su, Daniel Lecoanet, and Dong Lai. Physics of tidal dissipation in early-type stars and white dwarfs: Hydrodynamical simulations of internal gravity wave breaking in stellar envelopes. *MNRAS*, 495(1):1239–1251, May 2020. ISSN 0035-8711. doi: 10.1093/mnras/staa1306.

Yubo Su, Dong Lai, and Bin Liu. Spin-orbit misalignments in tertiary-induced binary black-hole mergers: Theoretical analysis. *Phys. Rev. D*, 103(6):063040, 2021a.

Yubo Su, Bin Liu, and Dong Lai. The mass-ratio distribution of tertiary-induced binary black hole mergers. *MNRAS*, 505(3):3681–3697, 2021b.

T. M. Tauris, M. Kramer, P. C. C. Freire, N. Wex, H. T. Janka, N. Langer, Ph. Podsiadlowski, E. Bozzo, S. Chaty, M. U. Kruckow, E. P. J. van den Heuvel, J. Antoniadis, R. P. Breton, and D. J. Champion. Formation of double neutron star systems. *ApJ*, 846(2):170, September 2017. doi: 10.3847/1538-4357/aa7e89.

The LIGO Scientific Collaboration, the Virgo Collaboration, the KAGRA Collaboration, R. Abbott, T. D. Abbott, F. Acernese, K. Ackley, C. Adams, N. Adhikari, R. X. Adhikari, V. B. Adya, C. Affeldt, D. Agarwal, M. Agathos, K. Agatsuma, N. Aggarwal, O. D. Aguiar, L. Aiello, A. Ain, P. Ajith, T. Akutsu, S. Albanesi, A. Allocca, P. A. Altin, A. Amato, C. Anand, S. Anand, A. Ananyeva, S. B. Anderson, W. G. Anderson, M. Ando, T. Andrade, N. Andres, T. Andrić, S. V. Angelova, S. Ansoldi, J. M. Antelis, S. Antier, F. Antonini, S. Appert, Koji Arai, Koya Arai, Y. Arai, S. Araki, et al. The population of merging compact binaries inferred us-

ing gravitational waves through GWTC-3. *arXiv e-prints*, art. arXiv:2111.03634, November 2021a.

The LIGO Scientific Collaboration, the Virgo Collaboration, the KAGRA Collaboration, R. Abbott, T. D. Abbott, F. Acernese, K. Ackley, C. Adams, N. Adhikari, R. X. Adhikari, V. B. Adya, C. Affeldt, D. Agarwal, M. Agathos, K. Agatsuma, N. Aggarwal, O. D. Aguiar, L. Aiello, A. Ain, et al. GWTC-3: Compact binary coalescences observed by LIGO and VIRGO during the second part of the third observing run. *arXiv e-prints*, art. arXiv:2111.03606, November 2021b.

Stephen E Thorsett and Deepto Chakrabarty. Neutron star mass measurements. I. radio pulsars. *ApJ*, 512(1):288, 1999.

A Tkachenko, K Pavlovski, C Johnston, MG Pedersen, M Michielsen, DM Bowman, J Southworth, V Tsymbal, and C Aerts. The mass discrepancy in intermediate-and high-mass eclipsing binaries: The need for higher convective core masses. *A&A*, 637:A60, 2020a.

A Tkachenko, K Pavlovski, C Johnston, MG Pedersen, M Michielsen, DM Bowman, J Southworth, V Tsymbal, and C Aerts. The mass discrepancy in intermediate-and high-mass eclipsing binaries: The need for higher convective core masses. *A&A*, 637:A60, 2020b.

Odette Toloza, Elme Breedt, Domitilla De Martino, Jeremy Drake, Boris Gansicke, Matthew Green, Alessandro Ederoclite, Johnson Jennifer, Kollmeier Juna, Christian Knigge, Thomas Kupfer, Knox Long, Thomas Marsh, Anna Pala, Steven Parsons, Tom Prince, Roberto Raddi, Alberto Rebassa-Manserga, Pablo Rodriguez-Gil, Simone Scaringi, Linda Schmidtobreick, Matthias Schreiber, Axel Schwope, Ken Shen, Danny Steeghs, Paula Szkody, Claus Tappert, Silvia

Toonen, Dean Townsley, and Monica Zorotovic. Understanding the evolution of close white dwarf binaries. *BAAS*, 51(3):168, May 2019.

S Toonen, HB Perets, and AS Hamers. Rate of WD-WD head-on collisions in isolated triples is too low to explain standard type ia supernovae. *A&A*, 610: A22, 2018.

Jihad Touma and Jack Wisdom. The chaotic obliquity of Mars. *Science*, 259(5099): 1294–1297, 1993.

Christopher A. Tout. On the relation between the mass-ratio distribution in binary stars and the mass function for single stars. *MNRAS*, 250(4):701–706, June 1991. ISSN 0035-8711. doi: 10.1093/mnras/250.4.701.

S. Tremaine. On the origin of the obliquities of the outer planets. *Icarus*, 89(1): 85–92, January 1991. doi: 10.1016/0019-1035(91)90089-C.

Scott Tremaine and Subo Dong. The statistics of multi-planet systems. *AJ*, 143 (4):94, April 2012. doi: 10.1088/0004-6256/143/4/94.

Jake D. Turner, Andrew Ridden-Harper, and Ray Jayawardhana. Decaying orbit of the hot Jupiter WASP-12b: Confirmation with tess observations. *AJ*, 161(2): 72, February 2021. doi: 10.3847/1538-3881/abd178.

Sunny Vagnozzi. New solar metallicity measurements. *Atoms*, 7(2), 2019. ISSN 2218-2004. doi: 10.3390/atoms7020041.

Geoffrey M Vasil, Daniel Lecoanet, Benjamin P Brown, Toby S Wood, and Ellen G Zweibel. Energy conservation and gravity waves in sound-proof treatments of stellar interiors. II. Lagrangian constrained analysis. *ApJ*, 773(2):169, 2013.

Tejaswi Venumadhav, Barak Zackay, Javier Roulet, Liang Dai, and Matias Zaldarriaga. New binary black hole mergers in the second observing run of advanced LIGO and advanced VIRGO. *Phys. Rev. D*, 101(8):083030, 2020.

Michelle Vick, Dong Lai, and Jim Fuller. Tidal dissipation and evolution of white dwarfs around massive black holes: An eccentric path to tidal disruption. *MNRAS*, 468(2):2296–2310, 2017.

Michelle Vick, Morgan MacLeod, Dong Lai, and Abraham Loeb. Tidal dissipation impact on the eccentric onset of common envelope phases in massive binary star systems. *MNRAS*, 503(4):5569–5582, June 2021. doi: 10.1093/mnras/stab850.

Alejandro Vigna-Gómez, Morgan MacLeod, Coenraad J Neijssel, Floor S Broekgaarden, Stephen Justham, George Howitt, Selma E de Mink, Serena Vinciguerra, and Ilya Mandel. Common envelope episodes that lead to double neutron star formation. *Publ. Astron. Soc. Aust.*, 37, 2020.

David Vokrouhlickỳ and David Nesvornỳ. Tilting Jupiter (a bit) and Saturn (a lot) during planetary migration. *ApJ*, 806(1):143, 2015.

Hugo von Zeipel. Sur l'application des séries de m. Lindstedt à l'étude du mouvement des comètes périodiques. *Astronomische Nachrichten*, 183:345, 1910.

William R Ward and Robin M Canup. The obliquity of Jupiter. *ApJ*, 640(1):L91, 2006.

William R Ward and Douglas P Hamilton. Tilting Saturn. I. analytic model. *AJ*, 128(5):2501, 2004.

William Roger Ward. Tidal friction and generalized Cassini's laws in the solar system. *AJ*, 80:64–70, 1975.

Nevin N Weinberg, Meng Sun, Phil Arras, and Reed Essick. Tidal dissipation in WASP-12. *ApJ*, 849(1):L11, 2017.

Linqing Wen. On the eccentricity distribution of coalescing black hole binaries driven by the Kozai mechanism in globular clusters. *ApJ*, 598(1):419, 2003.

Joshua N Winn, Roberto Sanchis-Ojeda, and Saul Rappaport. Kepler-78 and the ultra-short-period planets. *New A Rev.*, 83:37–48, 2018.

K. B. Winters and E. A. D'Asaro. Three-dimensional wave instability near a critical level. *J. Fluid Mech.*, 272:255–284, 1994.

Jia-Yi Yang, Ji-Wei Xie, and Ji-Lin Zhou. Occurrence and architecture of Kepler planetary systems as functions of stellar mass and effective temperature. *AJ*, 159(4):164, April 2020. doi: 10.3847/1538-3881/ab7373.

Hang Yu, Sizheng Ma, Matthew Giesler, and Yanbei Chen. Spin and eccentricity evolution in triple systems: From the Lidov-Kozai interaction to the final merger of the inner binary. *Phys. Rev. D*, 102(12):123009, 2020a.

Hang Yu, Nevin N Weinberg, and Jim Fuller. Non-linear dynamical tides in white dwarf binaries. *MNRAS*, 496(4):5482–5502, 2020b.

Hang Yu, Jim Fuller, and Kevin B Burdge. Tidally excited oscillations in hot white dwarfs. *MNRAS*, 501(2):1836–1851, 2021.

Haibo Yuan, Xiaowei Liu, Maosheng Xiang, Yang Huang, Bingqiu Chen, Yue Wu, Yonghui Hou, and Yong Zhang. Stellar loci II. a model-FREE estimate of the binary fraction for field FGK stars. *ApJ*, 799(2):135, Jan 2015. doi: 10.1088/0004-637x/799/2/135. URL `https://doi.org/10.1088/0004-637x/799/2/135`.

Barak Zackay, Tejaswi Venumadhav, Liang Dai, Javier Roulet, and Matias Zaldarriaga. Highly spinning and aligned binary black hole merger in the advanced LIGO first observing run. *Phys. Rev. D*, 100(2):023007, 2019.

J-P Zahn. The dynamical tide in close binaries. *A&A*, 41:329–344, 1975.

J-P Zahn. Tidal friction in close binary stars. *A&A*, 57:383–394, 1977.

Matias Zaldarriaga, Doron Kushnir, and Juna A Kollmeier. The expected spins of gravitational wave sources with isolated field binary progenitors. *MNRAS*, 473 (3):4174–4178, 2018.

JJ Zanazzi and Dong Lai. Planet formation in discs with inclined binary companions: Can primordial spin–orbit misalignment be produced? *MNRAS*, 478(1): 835–851, 2018.

Wei Zhu and Yanqin Wu. The super Earth–cold Jupiter relations. *AJ*, 156(3):92, 2018.

Wei Zhu, Cristobal Petrovich, Yanqin Wu, Subo Dong, and Jiwei Xie. About 30% of sun-like stars have Kepler-like planetary systems: A study of their intrinsic architecture. *ApJ*, 860(2):101, 2018.

Brunetto Marco Ziosi, Michela Mapelli, Marica Branchesi, and Giuseppe Tormen. Dynamics of stellar black holes in young star clusters with different metallicities–II. black hole–black hole binaries. *MNRAS*, 441(4):3703–3717, 2014.

Simon F Portegies Zwart and Stephen LW McMillan. Black hole mergers in the universe. *ApJ*, 528(1):L17, 1999.

Daniel Zwillinger. *CRC Standard Mathematical Tables and Formulae*. CRC press, 2003.